Conference Proceedings of the Society for Experimental Mechanics Series

Matthew R.W. Brake
Ludovic Renson
Robert J. Kuether
Paolo Tiso *Editors*

Nonlinear Structures & Systems, Volume 1

Proceedings of the 41st IMAC, A Conference and Exposition on Structural Dynamics 2023

Springer

Conference Proceedings of the Society for Experimental Mechanics Series

Series Editor

Kristin B. Zimmerman
Society for Experimental Mechanics, Inc.,
Bethel, CT, USA

The Conference Proceedings of the Society for Experimental Mechanics Series presents early findings and case studies from a wide range of fundamental and applied work across the broad range of fields that comprise Experimental Mechanics. Series volumes follow the principle tracks or focus topics featured in each of the Society's two annual conferences: IMAC, A Conference and Exposition on Structural Dynamics, and the Society's Annual Conference & Exposition and will address critical areas of interest to researchers and design engineers working in all areas of Structural Dynamics, Solid Mechanics and Materials Research.

Matthew R. W. Brake • Ludovic Renson • Robert J. Kuether • Paolo Tiso
Editors

Nonlinear Structures & Systems, Volume 1

Proceedings of the 41st IMAC, A Conference and Exposition on Structural Dynamics 2023

Springer

Editors
Matthew R. W. Brake
Department of Mechanical Engineering
Rice University
Houston, TX, USA

Robert J. Kuether
Sandia National Laboratories
Albuquerque, NM, USA

Ludovic Renson
Department of Mechanical Engineering
Imperial College London
London, UK

Paolo Tiso
D-MAVT, LEE Building, Room LEE M205
ETH Zürich
Zürich, Zürich, Switzerland

ISSN 2191-5644 ISSN 2191-5652 (electronic)
Conference Proceedings of the Society for Experimental Mechanics Series
ISBN 978-3-031-36998-8 ISBN 978-3-031-36999-5 (eBook)
https://doi.org/10.1007/978-3-031-36999-5

This Springer imprint is published by the registered company Springer Nature Switzerland AG
The registered company address is: Gewerbestrasse 11, 6330 Cham, Switzerland

Paper in this product is recyclable.

Preface

Nonlinear Structures and Systems represents one of ten volumes of technical papers presented at the 41st IMAC, A Conference and Exposition on Structural Dynamics, organized by the Society for Experimental Mechanics, held February 13–16, 2023. The full proceedings also include volumes on Dynamics of Civil Structures; Model Validation and Uncertainty Quantification; Dynamic Substructures; Special Topics in Structural Dynamics and Experimental Techniques; Computer Vision and Laser Vibrometry; Dynamic Environments Testing; Sensors and Instrumentation and Aircraft/Aerospace Testing Techniques; Topics in Modal Analysis and Parameter Identification; and Data Science in Engineering.

Each collection presents early findings from experimental and computational investigations on an important area within Structural Dynamics. Nonlinearity is one of these areas.

The vast majority of real engineering structures behave nonlinearly. Therefore, it is necessary to include nonlinear effects in all of the steps of the engineering design: both in the experimental analysis tools (so that the nonlinear parameters can be correctly identified) and in the mathematical and numerical models of the structure (in order to run accurate simulations). In so doing, it is possible to create a model representative of the reality which, once validated, can be used for better predictions.

Several nonlinear papers address theoretical and numerical aspects of nonlinear dynamics (covering rigorous theoretical formulations and robust computational algorithms) as well as experimental techniques and analysis methods. There are also papers dedicated to nonlinearity in practice where real-life examples of nonlinear structures will be discussed.

The organizers would like to thank the authors, presenters, session organizers, and session chairs for their participation in this track.

Houston, TX, USA — Matthew R. W. Brake
London, UK — Ludovic Renson
Albuquerque, NM, USA — Robert J. Kuether
Zürich, Zürich, Switzerland — Paolo Tiso

Contents

Chapter 1
On the Detection and Quantification of Nonlinearity via Statistics of the Gradients of a Black-Box Model

Georgios Tsialiamanis and Charles R. Farrar

Abstract Detection and identification of nonlinearity is a task of high importance for structural dynamics. On the one hand, identifying nonlinearity in a structure would allow one to build more accurate models of the structure. On the other hand, detecting nonlinearity in a structure, which has been designed to operate in its linear region, might indicate the existence of damage within the structure. Common damage cases which cause nonlinear behaviour are breathing cracks and points where some material may have reached its plastic region. Therefore, it is important, even for safety reasons, to detect when a structure exhibits nonlinear behaviour. In the current work, a method to detect nonlinearity is proposed, based on the distribution of the gradients of a data-driven model, which is fitted on data acquired from the structure of interest. The data-driven model selected for the current application is a neural network. The selection of such a type of model was done in order to not allow the user to decide how linear or nonlinear the model shall be, but to let the training algorithm of the neural network shape the level of nonlinearity according to the training data. The neural network is trained to predict the accelerations of the structure for a time-instant using as input accelerations of previous time-instants, i.e. one-step-ahead predictions. Afterwards, the gradients of the output of the neural network with respect to its inputs are calculated. Given that the structure is linear, the distribution of the aforementioned gradients should be unimodal and quite peaked, while in the case of a structure with nonlinearities, the distribution of the gradients shall be more spread and, potentially, multimodal. To test the above assumption, data from an experimental structure are considered. The structure is tested under different scenarios, some of which are linear and some of which are nonlinear. More specifically, the nonlinearity is introduced as a column-bumper nonlinearity, aimed at simulating the effects of a breathing crack and at different levels, i.e. different values of the initial gap between the bumper and the column. Following the proposed method, the statistics of the distributions of the gradients for the different scenarios can indeed be used to identify cases where nonlinearity is present. Moreover, via the proposed method one is able to quantify the nonlinearity by observing higher values of standard deviation of the distribution of the gradients for lower values of the initial column-bumper gap, i.e. for "more nonlinear" scenarios.

Keywords Structural health monitoring (SHM) · Structural dynamics · Nonlinear dynamics · Machine learning · Neural networks

1.1 Introduction

In the pursuit of making everyday life safer, humans have extensively tried to model the environment around them. Structures are an important part of the environment, in which humans live. They are man-made and should be safe throughout their lifetime. Structures are exposed to numerous environmental factors, which may cause them to fail. Moreover, during operation, structures are subjected to dynamic loads, which, in time, may cause failure. Such failures will most probably result in economic damage to society and may even result in loss of human lives. Therefore, for the purpose of maintaining structures safe, the field of *structural health monitoring* (SHM) [1] has emerged.

G. Tsialiamanis (✉)
Dynamics Research Group, Department of Mechanical Engineering, University of Sheffield, Sheffield, UK
e-mail: g.tsialiamanis@sheffield.ac.uk

C. R. Farrar
Engineering Institute, MS T-001, Los Alamos National Laboratory, Los Alamos, NM, USA
e-mail: farrar@lanl.gov

M. R. W. Brake et al. (eds.), *Nonlinear Structures & Systems, Volume 1*, Conference Proceedings of the Society for Experimental Mechanics Series, https://doi.org/10.1007/978-3-031-36999-5_1

The discipline of SHM is the subdiscipline of structural dynamics, which focuses on using data acquired from sensors to evaluate the condition of a structure. There are several tasks that are performed during an SHM project. A convenient categorization of these tasks has been proposed by Rytter in [2], extended in [1] and is given by the hierarchical structure:

1. Is there damage in the system (*existence*)?
2. Where is the damage in the system (*location*)?
3. What kind of damage is present (*type/classification*)?
4. How severe is the damage (*extent/severity*)?
5. How much useful (safe) life remains (*prognosis*)?

The order of the tasks in the above hierarchy may also be viewed as being defined according to their difficulty. The first step, that of identifying whether damage exists in a structure, is considered the most simple one. Several approaches exist, but a quite common one is *outlier detection* [3]. Such approaches could range from fitting simple probability density functions to the data to fitting an *autoencoder neural network* (ANN) to the data to calculate a novelty index [4]. A general strategy for this task is to define a baseline model of the structure, which accurately explains the healthy state, and indicate any state of the structure, which may not be adequately explained by this model, as a potentially damaged state [5].

The second and the third steps of the hierarchy, the localization or the classification of damage, require more specialized tools than the case of detecting damage. As in many cases of modelling systems, there are two types of models to adopt to localize damage, *physics-based* models (e.g. *finite element models* [6]) and *data-driven* or *machine learning* models [7]. The first category refers to models which are built according to one's understanding of the physics of damage, e.g. cracks [8]. The second type of models, machine learning models, is built using mainly data and algorithms which perform pattern recognition to indicate the position of the damage within the structure [9].

The next two steps are considered to be the most difficult ones. To define the extent of damage or how much useful life the structure has, one should have adequate knowledge about the physics of the mechanism of the specific type of damage that affects the structure [10]. In order to perform these processes in a data-driven manner, one should have data available of the evolution of damage of the structure, which might be difficult to acquire. Therefore, a way to deal with problems of the fourth and fifth step of Rytter's hierarchy might be to follow a *population-based structural health monitoring* (PBSHM) framework [11], in order to exploit data from structures in a population, which have already failed, to make predictions about the evolution of damage of existing structures in the same population. In every case, these steps (especially the last one) involve many uncertain parameters, such as the environmental and operational conditions of the structure in the future, making them quite complicated tasks.

All of the steps of the hierarchy have been approached in both a physics-based and a data-driven way and each of these ways has its advantages and disadvantages. On the one hand, physics-based models are based on the underlying physics of the structure and the damage mechanism; therefore, if the formulation of the physics matches or is "close" to the real underlying physics, the models should make accurate predictions about it. However, because of the uncertainties of the environment, capturing accurately the underlying physics for a structure does not ensure that other structures—even identical ones—shall behave the same way.

Data-driven models, on the other hand, do not require definition of analytical expressions regarding the underlying physics of a structure. They rely exclusively on data. An apparent drawback of such models is that it might be challenging to consider them in cases where data from a structure are not available. Moreover, since the main object of study of SHM is damage, data-driven methods are even more difficult to be applied, because, when structures are damaged, they are often quickly repaired, making the access to data from damaged structures even more restricted. Even if one acquires data from the damaged structure, the models trained according to these data may not be efficient for the repaired structure, because the structural parameters may change, as a result of the repair procedure [12].

The current work is mainly focused on the first step of the hierarchy, that of identifying whether a structure is damaged or not. The approach followed herein is motivated by Farrar et al. [13] and Worden et al. [14], where it is assumed that a damaged structure should provide more complex data than a healthy structure—the complexity being measured by several complexity metrics. The approach proposed herein is that of a metric of complexity of the gradients of a neural network model that sufficiently explains the data acquired from a structure. As it will be discussed, the proposed metric is based on the statistics of the gradients of the model and provides a way of discriminating states of the structure that indicate nonlinear behaviour. Moreover, the proposed metric can be calculated for different degrees of freedom of the structure so it may also be used as a tool for the second step of the hierarchy, the localization of damage. Finally, being a scalar metric, in the example presented here, it's magnitude may also be used as an indication of "how intensely nonlinear" a structure is.

The layout of the paper is the following. In the second section, a brief discussion is provided about machine learning in structural dynamics and more specifically SHM and the reasons that it has been widely exploited in many disciplines, including engineering. In the third section, the dataset which is used in the current work is presented and aspects of the

specific dataset are discussed. In the fourth section, the proposed methodology is presented and the results of applying it on the dataset. In the final section, conclusions are drawn regarding the proposed algorithm and future steps are discussed.

1.2 Machine Learning for Structural Dynamics

In recent years, machine learning has been widely developed for computer science and many other disciplines as well. One would argue that machine learning gets so much attention because of the impressiveness of the results of its algorithms. For example, machine learning algorithms have achieved generation of real-looking images [15], translation of text into artificially generated images [16] and prediction of the structure of proteins [17], achievements that before the rise of machine learning would have been considered very difficult or even impossible. However, an equally important reason of the success of machine learning is that it has provided an alternative solution to problems that classical approaches have failed.

One of the problems that machine learning has solved quite successfully is that of image recognition [18]. A basic application of image recognition is to simply classify images in classes, regarding the content of the image. The advantage of using machine learning is that the model which takes an image as an input and predicts the class of the image is learnt exclusively from the available data. A classical approach to this problem may have been very difficult to be attained. One may have had to manually identify patterns in the images that point towards each class. Afterwards, one would have to define, also manually, a model that quantifies how plausible it is for every image to belong to a class, according to these patterns. Machine learning and specifically the *convolutional neural network* (CNN) [18] provided a solution to these problems without any need of human intervention in the parameters of the model (only the *hyperparameters* of a machine learning algorithm need manual tuning).

Similarly, for SHM, one of the problems of Rytter's hierarchy can be solved via the use of classification machine learning algorithms. An excellent example of such a solution is presented in [9], where a neural network is built to predict the category of damage on a wing of an aircraft. The damage was simulated by removing panels from the wing and data were acquired during nine different damage cases. The model is trained according to data corresponding to the damaged states and it achieves quite high accuracy in classifying unseen data into the nine damage classes. The image recognition and the damage classification applications reveal a major advantage of machine learning, the bypassing of manually defining a model to perform the desired task. Especially for the damage classification task, one would need extended understanding of the way that the removed panels should affect the recorded data, something that might be quite structure-specific as results in [12] reveal. However, because of the uncertainties of such a phenomenon, machine learning proves a far more convenient and effective solution.

The two examples mentioned in the previous paragraphs refer to problems whose solution in a traditional way may have been infeasible, i.e. the definition of closed form equations that would classify the images into the desired classes or the sensor signals into the damage classes. However, machine learning can provide solutions in a similar manner in case of problems for which one may have available equations. An example of such a problem is that of system identification [19]. Quite often, one may have a parametric set of equations for a system but the set of equations may suffer from *epistemic uncertainty*, i.e. the equations may not resemble the completely true underlying physics of the problem. Therefore, such a set of equations may not be able to sufficiently explain the phenomenon and make accurate predictions. In such cases, a *black-box* modelling approach can be followed. A black-box model is simply a model that learns exclusively from data the relationship between some input and some output quantities of interest. A characteristic example of such a model is a neural network [7].

In the current work, a functionality of neural networks which has become popular in the community of scientific machine learning is exploited. This functionality refers to the calculation of gradients of neural network models with respect to their inputs. Differentiation is a very important part of defining and training a neural network, because *backpropagation*, the algorithm used to train a neural network, is based on calculating the derivatives of a *loss function* with respect to the tunable parameters of the network. Recently, the calculation of derivatives has been extended to the inputs of the neural network because of the definition of *physics-informed neural networks* (PINN) [20]. For such a type of neural networks, the researchers impose their knowledge of the underlying physics of the studied system as part of the loss function. This knowledge often involves relationships of the derivatives of the defined model; therefore, the calculation of derivatives with respect to input quantities has been utilized. In the case of PINNs the gradient is used as a means of imposing physical knowledge into the model. However, in the current work the gradients are studied after training the model as a way of analysing the model, aiming at a better study and higher explainability of the model.

1.3 A Three-Storey Building Dataset

The dataset which is used in the current work comes from a three-storey structure, shown in Fig. 1.1, which was tested in the laboratory. The structure was considered in 17 different states, but the 14 of those are of interest of the current work. State 1 is considered the baseline state, states 2–9 are considered to be undamaged, and states 10–14 are considered the damaged ones. The difference between states 2–9 from the baseline state is regarding the stiffness of different columns of the structure or some added mass on a floor. For example, state 3 has an extra 1.2 kg on the first floor and state 6 has a stiffness reduction on the front column of the first floor. In large scale structures, such stiffness reductions could be observed in cases of temperature differences between two parts of the structure, e.g. a bridge whose deck is heated by the sun, but the underneath structure is heated slower. The damage for states 10–14 is simulated by engaging the bumper and the column between the second and the third floor, shown within the dashed box in Fig. 1.1. A damage type, which could be simulated by such a column-bumper setup, could be a breathing crack. The difference between the damaged states is the width of the initial gap between the column and the bumper, and for higher number of state, the gap becomes smaller, which can be considered an increase in how harsh the nonlinearity of the structure is, because the smaller the gap, the more often the two elements will collide and probably with higher velocity. Namely, the gap was 0.20 mm, 0.15 mm, 0.13 mm, 0.10 mm and 0.05 mm for states 10–14, respectively.

The structure was excited using a white noise signal on its base. The acquired data came from accelerometers placed on each floor and the base. For every state of the structure, the experiment was repeated 50 times, and for every repetition the excitation and the recording of the data lasted 25.6 s and the data were recorded in a sampling frequency of 320 Hz, resulting in 8192 data points for each one of the 50 repetitions. Therefore, for every state, a dataset of 409600 points is available.

The aim of the current work is to define a metric which shall be used to identify the existence of damage and which shall have a higher value for greater extent of damage. As mentioned, in the current dataset, the damaged states are considered the ones which have a nonlinearity. Furthermore, the nonlinearity of the structure is considered to be increasing as the gap between the column and the bumper is decreasing. On the contrary, states 2–9 are different compared to the baseline state 1, but are still linear and not considered as damaged. As a result, the desired metric should be a metric of nonlinearity which should have a higher value as the structure becomes more nonlinear or, in the current case, as the gap between the bumper and the column becomes smaller. As a first step, a model is desired, which can be used to make accurate predictions and be studied in order to define a metric with the aforementioned properties.

Following a physics-based framework, such a model, which would be fitted to the data, would have a predefined form, for example:

$$[M]\{\ddot{\mathbf{y}}\} + [C]\{\dot{\mathbf{y}}\} + [K]\{\mathbf{y}\} = F \tag{1.1}$$

where $[M]$, $[C]$, $[K]$ are the mass, damping and stiffness matrices, respectively, $\{\ddot{\mathbf{y}}\}$, $\{\dot{\mathbf{y}}\}$, $\{\mathbf{y}\}$ are the acceleration, velocity and displacement vectors and F is the forcing vector of the system. A major problem of such an approach is that if the

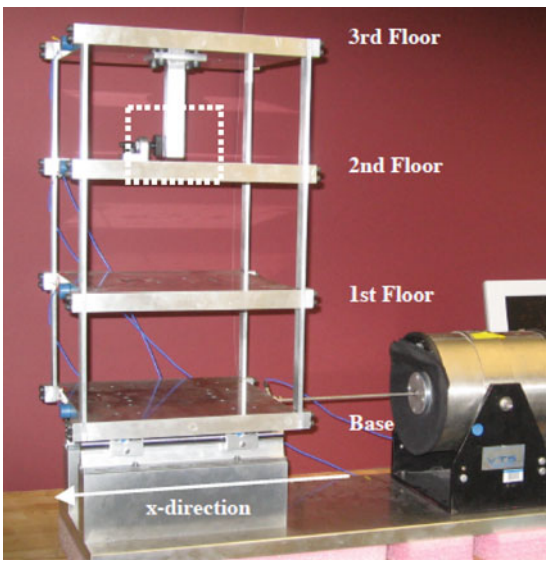

Fig. 1.1 Experimental setup of three floors and the bumper nonlinearity between the second and third floor shown in the dashed box [21]

predefined equation does not match the underlying physics of the structure, the model may not be sufficient to make accurate predictions. Although the structure is considered linear for states 1–9, there might be nonlinearities, for example, in the joints or the damping.

Another approach for a model that can be studied in order define the desired metric is to define a machine learning model. For this purpose, in the current work, a neural network is chosen as such a model. The reasons to use a neural network are two. First, a neural network is a universal approximator [22], making it a great model in the case of unknown underlying physics. An example of a model which does not have such a property is a polynomial regression model of predefined order. The second reason is that a neural network can be recalibrated from its baseline state according to data from a new state. The desired approach herein is to define a model for the baseline state and to recalibrate it for new data. Following this approach, the change of the model can be studied and compared to the baseline model to define the aforementioned metric.

1.4 Statistics of the Model Gradients as a Nonlinearity Metric

For a single-degree-of-freedom system, a general equation that can be considered for dynamic systems is given by:

$$m\ddot{y} + c\dot{y} + ky + g(y, \dot{y}) = F(t) \tag{1.2}$$

where m, c, k are the mass, damping and stiffness of the oscillator, $\ddot{y}$, $\dot{y}$, y are the acceleration, velocity and displacement of the system, $F(t)$ is the force signal applied to the system and $g(y, \dot{y})$ is a function of nonlinear terms of y. A common way to solve such an equation is in a discrete-time framework, by replacing $\ddot{y}$ and $\dot{y}$ by their finite difference approximation, i.e. $\dot{y} = \frac{y_t - y_{t-1}}{dt}$ and $\ddot{y} = \frac{\dot{y}_t - \dot{y}_{t-1}}{dt}$. The solution then is a *one-step-ahead* (OSA) model having the form:

$$y_t = f(y_{t-1}, y_{t-2}, \dots y_{t-l}) \tag{1.3}$$

where f is a model and l is the *lag*, which is number of timesteps before the timestep t that are used as inputs to the model. For the linear case, the equation above becomes $y_t = (2 - \frac{c\Delta t}{m} - \frac{k\Delta t^2}{m})y_{t-1} + (\frac{c\Delta t}{m} - 1)y_{t-2} + \frac{\Delta t^2}{m}F_{t-1}$ [1].

From Eq. (1.3) the gradients of y_t with respect to y_{t-i} can be calculated as:

$$\frac{\partial y_t}{\partial y_{t-i}}|_{y_0} = \frac{\partial f}{\partial y_{t-i}}|_{y_0} \quad i = 1, 2, \dots l \tag{1.4}$$

where y_0 is the value of y_{t-i} for which the derivative is calculated. The distribution of these derivatives is a meaningful object which characterizes the system. For the linear case, the value of $g(y, \dot{y})$ of Eq. (1.2) is zero, making the relationship of Eq. (1.3) linear and the value of the aforementioned gradients constant. The distribution of the gradients should be a Kronecker delta. However, since the model f is a statistical model and noise will be present in the data, the distribution is expected to be a quite narrow Gaussian-like distribution.

For a wide range of types of nonlinearity, the distribution of the gradients is expected to spread. Quite often, nonlinear systems exhibit nonlinear behaviour for larger values of displacements, e.g. the Duffing oscillator. In these cases, the value of $g(y, \dot{y})$ of Eq. (1.2) is not equal to zero, but as the magnitude of y increases, the contribution of g to the movement of the system becomes more evident. For an example of the Duffing oscillator $g(y, \dot{y}) = k_3 y^3$; therefore, the derivative will have constant terms, because of the linear part of the system, and nonlinear terms proportional to y^2, which for small values of y is almost equal to zero, but for larger values affects the value of the derivative. As a result, the distribution of the derivatives will not be as narrow as in the linear case.

Using the available dataset from the three-storey building, an OSA model can be defined using a neural network. The model can be defined as:

$$\{\ddot{\mathbf{y}}_t\} = f(\{\ddot{\mathbf{y}}_{t-1}\}, \{\ddot{\mathbf{y}}_{t-2}\}, \dots \{\ddot{\mathbf{y}}_{t-l}\}) \tag{1.5}$$

where $\{\ddot{\mathbf{y}}_t\} = [y_t^1, y_t^2, y_t^3, y_t^4]$ is the vector of accelerations of the four degrees of freedom for timestep t, f is the neural network model and l is the *lag*, which is number of timesteps before the timestep t that are used as inputs to the model. To emulate a real situation where the forcing vector is not available to use for modelling, it is not used as an input to the model; however, the accelerations of the base can be considered the forcing of the rest of the building, as in an earthquake situation.

Having defined a model such as the one defined in Eq. (1.5) allows studying its gradients with respect to its inputs. More specifically, for the acceleration of the ith degree of freedom, the derivative with respect to the acceleration of the same degree of freedom but of the previous timestep is defined as:

$$\frac{\partial y_t^i}{\partial y_{t-1}^i}|_{y_0^i} = \frac{\partial f^i}{\partial y_{t-1}^i}|_{y_0^i} \tag{1.6}$$

where f^i is the ith output of the neural network model of Eq. (1.5). The quantity of the above equation is calculated for a specific value of $y_{t-1}^i = y_0^i$. Therefore, by calculating the derivative for several values of y_{t-1}^i one can calculate the distribution of these derivatives.

For the three-storey structure, a simple feedforward neural network is chosen as the model, which will be fitted on the available data. The considered neural network had three layers, an input layer, a hidden layer and an output layer. The dimensionality of the input layer is defined by the size of the lag, which is one of the hyperparameters of the algorithm and should be optimized. The size of the output layer can be equal to the number of degrees of freedom of the system, according to Eq. (1.5), but to allow the model to be specialized separately to each degree of freedom, in the current work, different models are trained for the accelerations of each degree of freedom, i.e. $\ddot{y}_t^i = f(\{\ddot{\mathbf{y}}_{t-1}\}, \{\ddot{\mathbf{y}}_{t-2}\}, \dots \{\ddot{\mathbf{y}}_{t-l}\})$.

The size of the hidden layer is also a hyperparameter. A common approach for the size of the hidden layer is to train the neural network using a part of the available dataset, called the training dataset, and calculate the error on a second part of the dataset, called the validation dataset. Then the optimal size of the hidden layer is considered one with which the minimum error on the validation dataset is achieved. Although this is an effective strategy to optimize the size of the hidden layer, in the current work, it is predefined by the authors. The size is predefined because the model is fitted on the baseline state data and then shall be recalibrated according to the data from the new states. Having the same model offers the chance for a comparison between the distribution of the gradients of the baseline state and that of the new states. Therefore, the size of the hidden layer should be chosen in a way to allow the neural network to have approximation capabilities for a wide range of linear and nonlinear states. The size is chosen to be 100 neurons, which is considered a decent size. In every case, the model is tested on unseen data to ensure that the error on these data is not high, i.e. it is not overfitted to the training data.

As mentioned, proper training requires splitting the complete dataset in a training and a validation dataset. In order to test the algorithm on unseen data, a third part is considered, the testing dataset. The whole procedure followed to train the baseline model was to split the whole dataset of state 1 into the three aforementioned parts. Afterwards different values for the lag were studied, to train the model on the training dataset and to pick the one model that performs best on the validation dataset. It was noted that a lag value of 2 was sufficient for the model to perform satisfactorily on the validation dataset.

The performance of the model was examined using the *normalized mean-square error* (NMSE), given by $\frac{100}{N\sigma_y^2}\sum_{i=1}^{N}(\hat{y}_i - y_i)^2$, where N is the number of available samples in the dataset, σ_y is the standard deviation of the target values, $\hat{y}_i$ are the predictions of the model and y_i are the actual target values. The NMSE is a convenient measure of error in regression problems, since it provides an objective measure of the accuracy, regardless of the scale of the data. NMSE values close to 100% indicate that the model does no better than simply using the mean value of the data, while the lower the value the better the model is calibrated. From experience, values of NMSE lower than 5% indicate a well-fitted model, and values lower than 1% show an excellent model. For the applications presented here, the NMSE was for every state lower than 5% for all three datasets (training, validation, testing), indicating that the models were not overfitted.

Another aspect of training, which is considered important in the current work, was the use of *regularization* [23]. Regularization is often used to prevent overfitting by enforcing smoother mappings between the input and the output quantities of the neural network. In the current work, its benefit is considered to be the smoothness of the mapping, which shall allow the gradients to smoothly change and provide more smooth distributions. For the same reason, the activation functions of the neural network are *hyperbolic tangent* (tanh) activation functions for the hidden layer and a linear activation function for the output layer.

After fitting the model to the baseline state, for every new state, the model was recalibrated. This procedure is simply the training of the neural network considering as the initial state of its trainable parameters the trained-on-the-baseline-data model. After retraining for each different state, the gradients were calculated for the accelerations of every degree of freedom with respect to every input variable (the lagged accelerations). For these distributions three moments were calculated: the standard deviation, the skewness and the kurtosis. The standard deviation and the inverse of the kurtosis exhibited good results and are presented herein; the skewness did not exhibit any worth-presenting results. More specifically, the mean values of the moments are used, given by:

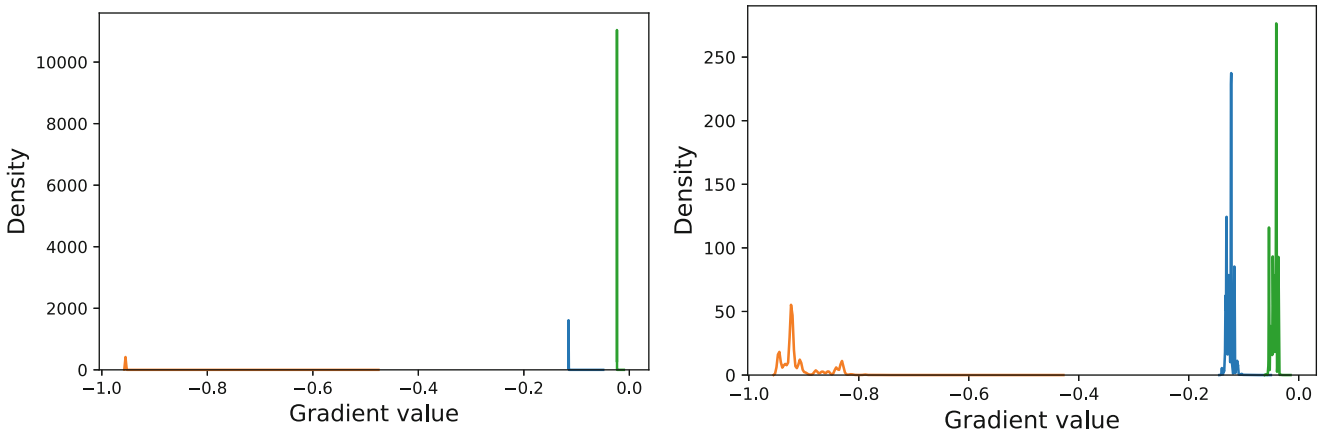

Fig. 1.2 Distribution of the gradients of the model for the predictions of the third floor with respect to the accelerations of the previous timestep of the base (blue line), the first floor (orange line) and the second floor (green line). The distributions are shown for two cases, for the baseline state (left) and for state 14 (right), the most nonlinear case

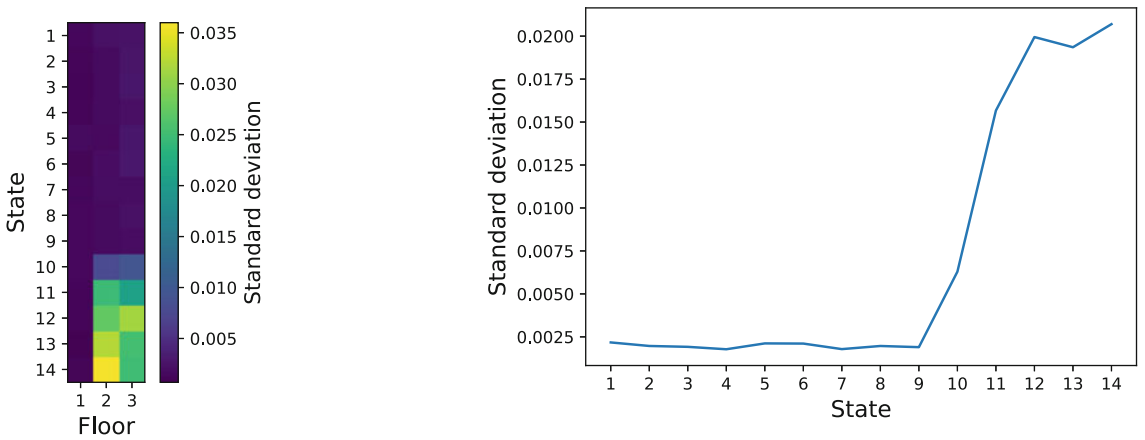

Fig. 1.3 The values of the metric of Eq. (1.7) using the standard deviation as M, for the accelerations of the three floors of the structure (left) and the average value of all three floors of the metric for the different states (right)

$$\bar{M}^i = \frac{1}{D}\sum_{j=1}^{D} M\left[\frac{\partial f^i}{\partial y_{t-1}^j}|_{y_0^j}\right] \quad i = 1, 2, \ldots n_{dof} \tag{1.7}$$

where M is a moment (standard deviation or inverse kurtosis herein), D is the dimensionality of the input, n_{dof} is the number of degrees of freedom of the system and y_0^j are the points for which the gradients are calculated—these points in the current work are all the available points in the three-storey-building dataset. Essentially, the moments are calculated separately for the distributions of the gradients with respect to every input quantity and the average of these values is used as a metric.

At first, the aforementioned distributions are presented to provide a visual confirmation of the intuition presented in the previous paragraphs. Since samples of the gradients are available, a probability density function (PDF) needs to be defined for the purpose of visualizing the distributions. The PDF was calculated using a kernel density estimation and the Silverman's algorithm [24]. The results for the baseline state (state 1) and for the most nonlinear case (state 14) are presented in Fig. 1.2. From the plots, it is clear that for the undamaged state the distribution of the gradients is much more peaked than in the case of the nonlinear structure, where the expected spread of the distributions is clearly observed.

Subsequently, using Eq. (1.7) two metrics are calculated. The first metric is the standard deviation of the distributions of the gradients. The standard deviation is a metric of spreadness of the distribution. Higher values of standard deviation mean a more spread distribution. In Fig. 1.3 on the left, using Eq. (1.7), the average standard deviation of the model of the acceleration of the three floors is shown for different states. On the right of the figure, the mean values of the rows of the left-side plot are shown. The results reveal that using the standard deviation as a metric, the nonlinear states can be identified.

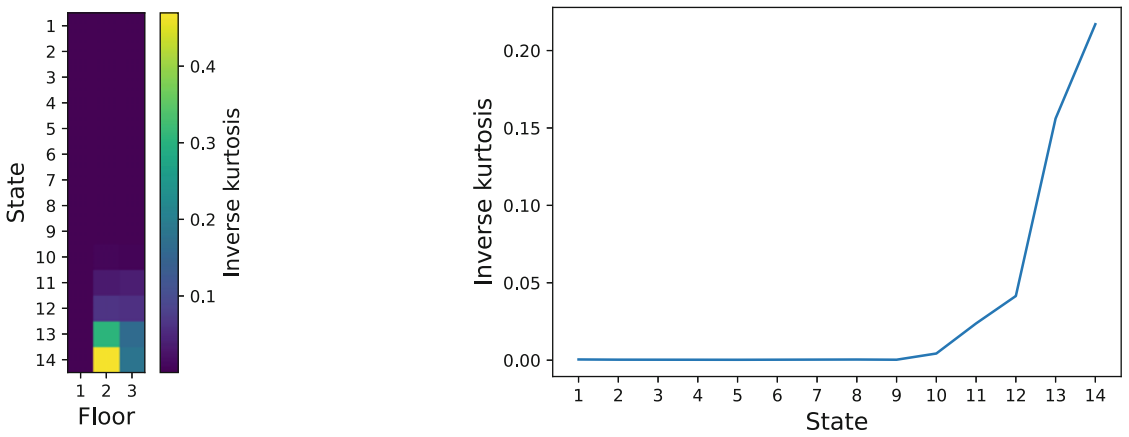

Fig. 1.4 The values of the metric of Eq. (1.7) using inverse kurtosis as M, for the accelerations of the three floors of the structure (left) and the average value of all three floors of the metric for the different states (right)

Moreover, a monotonic increase on the value of the metric is observed, as the column-bumper gap becomes smaller, except for state 13, where a small decrease is observed, compared to states 12 and 14. Another interesting aspect of the metric is that its value is increasing mainly for the second and third floors, where the nonlinearity is introduced, making it a candidate metric for localization of damage.

The second metric examined is the inverse of the kurtosis of the distributions. Kurtosis is the fourth moment of the distributions and is a metric of how concentrated the mass of the distribution is around its mean. Higher values of kurtosis mean a greater concentration around the mean value and lower values mean more spread values further away from the mean. Therefore, because of its definition, kurtosis is higher for more peaked distributions, and its inverse is lower, making it a metric whose value increases as the distributions spread. The results for the inverse kurtosis are presented in a similar way to the standard deviation results in Fig. 1.4. The results in this case seem even better than in the case of using the standard deviation. For the undamaged states, the metric is almost equal to zero and it monotonically increases only for the second and the third floors. The average also exhibits better results than the standard deviation, being monotonically higher for smaller values of the column-bumper gap.

1.5 Conclusions

In the current paper, a metric for detecting and quantifying the nonlinearity of a structure is presented. The metric is based on the calculation of the statistics of the gradients of a model, which is trained as a one-step-ahead model for the data acquired from a structure. The model is built for the baseline undamaged state of a structure, having as input lagged accelerations of the structure and as outputs the values of the acceleration one step ahead in time. For new testing states of the structure, the model is recalibrated to the newly acquired data. The gradients for every output of the model are then calculated with respect to the different inputs of the model for the available data samples of the dataset. The distribution of the values of these gradients is then studied. It is expected that for linear cases the distribution shall be quite peaked and as damage evolves within the structure, it shall cause nonlinear effects and affect the distribution of the gradients. The expected effect is a spread of the values. The spread is studied in the current work using two statistical moments, the standard deviation and the inverse of the kurtosis of the distributions.

The aforementioned methodology is tested on a dataset from a three-storey experimental structure. The structure is tested at 14 different states, 9 of which are considered undamaged and the rest 5 are considered damaged. The difference between the undamaged states is in the stiffness of the columns of the structure, and, for the damaged states, the damage is simulated as an added column-bumper setup between two floors of the structure, with varying initial gap between the two elements.

The proposed methodology was applied on the data from the experimental structure and the results revealed that the proposed metrics works as intended. The value of the metric is higher for the damaged cases, making it a tool for identification of damaged states. As the gap between the column and the bumper becomes smaller, making the structure more intensely

nonlinear, the metric also increases, which means that the metric could potentially be used for the definition of the severity of damage. Furthermore, the metric is higher for the distributions of the gradients of the accelerations of the two floors, between which the column and the bumper are placed, making it also a potential metric for damage localization.

Further validation of the methodology is needed. However, being tested on experimental data the methodology proves quite efficient. Real-life structures which are designed to operate mainly in the linear region of their members exist, e.g. nuclear plants. Therefore, a similar situation with the experimental setup of the current work could be encountered in such structures. In these cases a methodology similar to the one presented here could be used for identification, localization and quantification of damage within the structure. Moreover, in future work, analysis of the form of the distributions could be made to infer the type of nonlinearity and other comparisons between the different-state distributions could be made to extract further information about the source of the nonlinearity or even to differentiate the linear cases.

Acknowledgments G. Tsialiamanis would like to acknowledge the support of the UK Engineering & Physical Sciences Research Council (EPSRC) via the Programme Grant EP/R006768/1 and European Union's Horizon 2020 research and innovation programme under the Marie Sklodowska-Curie grant agreement No. 764547. For the purpose of open access, the authors have applied a Creative Commons Attribution (CC BY) licence to any author accepted manuscript version arising.

References

1. Farrar, C.R., Worden, K.: Structural Health Monitoring: A Machine Learning Perspective. Wiley, New York (2011)
2. Rytter, A.: Vibrational Based Inspection of Civil Engineering Structures. PhD thesis, Aalborg University, Denmark (1993)
3. Barnett, V., Lewis, T.: Outliers in Statistical Data. Wiley, Chichester (1994)
4. Worden, K., Manson, G., Allman, D.: Experimental validation of a structural health monitoring methodology: Part I. Novelty detection on a laboratory structure. J. Sound Vib. **259**(2), 323–343 (2003)
5. Sohn, H., Farrar, C.R.: Damage diagnosis using time series analysis of vibration signals. Smart Mater. Struct. **10**(3), 446 (2001)
6. Bathe, K.-J.: Finite Element Procedures. Klaus-Jurgen Bathe, Berlin (2006)
7. Bishop, C.M.: Pattern Recognition and Machine Learning. Springer, Berlin (2006)
8. Agathos, K., Chatzi, E., Bordas, S.: Multiple crack detection in 3d using a stable XFEM and global optimization. Comput. Mech. **62**(4), 835–852 (2018)
9. Manson, G., Worden, K., Allman, D.: Experimental validation of a structural health monitoring methodology: Part III. Damage location on an aircraft wing. J. Sound Vib. **259**(2), 365–385 (2003)
10. Corbetta, M., Sbarufatti, C., Giglio, M., Todd, M.D.: Optimization of nonlinear, non-Gaussian Bayesian filtering for diagnosis and prognosis of monotonic degradation processes. Mech. Syst. Signal Process. **104**, 305–322 (2018)
11. Gardner, P., Bull, L.A., Gosliga, J., Dervilis, N., Cross, E.J., Papatheou, E., Worden, K.: Population-Based Structural Health Monitoring. In: Structural Health Monitoring Based on Data Science Techniques, pp. 413–435. Springer, New York (2022)
12. Gardner, P.A., Bull, L.A., Dervilis, N., Worden, K.: Challenges for SHM from structural repairs: An outlier-informed domain adaptation approach. In: Data Science in Engineering, vol. 9, pp. 75–86. Springer, New York (2022)
13. Farrar, C., Park, G., Worden, K.: Complexity: A new axiom for structural health monitoring? Technical report, Los Alamos National Laboratory, New Mexico (2010)
14. Worden, K., Dervilis, N., Farrar, C.: Applying the concept of complexity to structural health monitoring. Struct. Health Monit. **2019** (2019)
15. Goodfellow, I., Pouget-Abadie, J., Mirza, M., Xu, B., Warde-Farley, D., Ozair, S. Courville, A., Bengio, Y.: Generative adversarial nets. Adv. Neural Inf. Proces. Syst. **27** (2014)
16. Ramesh, A., Dhariwal, P., Nichol, A., Chu, C., Chen, M.: Hierarchical text-conditional image generation with clip latents. arXiv preprint arXiv:2204.06125 (2022)
17. Jumper, J., Evans, R., Pritzel, A., Green, T., Figurnov, M., Ronneberger, O., Tunyasuvunakool, K., Bates, R., Žídek, A., Potapenko, A., et al.: Highly accurate protein structure prediction with alphafold. Nature **596**(7873), 583–589 (2021)
18. LeCun, Y., Bengio, Y., et al.: Convolutional networks for images, speech, and time series. The Handbook of Brain Theory and Neural Networks **3361**(10), 1995 (1995)
19. Rogers, T.J., Worden, K., Cross, E.J.: On the application of gaussian process latent force models for joint input-state-parameter estimation: With a view to Bayesian operational identification. Mech. Syst. Signal Process. **140**, 106580 (2020)
20. Raissi, M., Perdikaris, P., Karniadakis, G.E.: Physics-informed neural networks: A deep learning framework for solving forward and inverse problems involving nonlinear partial differential equations. J. Comput. Phys. **378**, 686–707 (2019)
21. Figueiredo, E., Park Gyuhae, G., Figueiras, J., Farrar, C., Worden Keith, K.: Structural health monitoring algorithm comparisons using standard data sets. Technical report, Los Alamos National Lab.(LANL), Los Alamos, NM (United States) (2009)
22. Csáji, B.C., et al.: Approximation with artificial neural networks. Faculty of Sciences, Eotovs Lorand University, Hungary **24**(48), 7 (2001)
23. Krogh, A., Hertz, J.: A simple weight decay can improve generalization. Adv. Neural Inf. Proces. Syst. **4** (1991)
24. Silverman, B.W.: Using kernel density estimates to investigate multimodality. J. R. Stat. Soc. Ser. B Methodol. **43**(1), 97–99 (1981)

Chapter 2
Robust Identification of Nonlinear Oscillators from Frequency Response Data

Thomas Breunung, Lautaro Cilenti, Jae Min You, and Balakumar Balachandran

Abstract While experimental modal analysis for linear systems is well established and widely used, no universal procedure for identification of nonlinear oscillatory systems is currently available. Thus, the authors develop an automated tool to robustly identify nonlinear oscillators from data. Frequency response curves measured with periodic shaker excitation are arguably the best source to obtain a robust model for nonlinear oscillators. In this setting, an analysis in the frequency domain beneficially reduces noise and helps compress information. Then, data-driven identification techniques, curve fitting, as well as a judicious parameter elimination are combined to yield a low-order and sparse nonlinear oscillator, which can be used to accurately capture the considered system's forced response curve.

Keywords System identification · Experimental technique · Nonlinear vibrations · Data-driven technique · Reduced-order modeling

2.1 Introduction

Modal analysis is the workhorse of modern structural engineering and in the experimental implementation, experimental modal analysis, modal parameters are extracted from measurements. For the associated tools, one assumes an underlying linear structure, which impedes the methodology's extension to analyzing nonlinear behavior. Thus, no universal method for system identification of nonlinear oscillatory systems has emerged.

Most common excitation methods for modal testing are impact and shaker testing. These excitation sources remain relevant for nonlinear oscillators. Indeed, free-decay measurements have been used for identification of nonlinear oscillators, via, for example, the Hilbert transformation [1], fitting NARMAX models [2], or extracting zero-crossings [3]. The excitation for free-decay measurements is relatively simply generated by using impact hammers or impactors. However, repeatability remains an issue and the signal processing is evolved [4]. Furthermore, the excitation amplitude is not easily controlled; this is crucial for nonlinear oscillators which have amplitude-dependent modal properties.

Excitation via shakers on the other hand is highly repeatable and controllable. Despite the possibility for shaker-structure interaction and the need for higher instrumentation effort, this type of excitation remains the industry standard to obtain high-quality linear models [5]. Due to these advantages, shaker testing is the natural candidate for identification of nonlinear oscillators. Shakers can generate a wide variety of signals, including sinusoidal, chirp, and random signals. The responses of nonlinear oscillators due to these types of excitations, however, remain largely not well characterized. Without doubt, the best explored and understood behavior is the periodic response of nonlinear oscillators to sinusoidal excitation. Thus, it is only logical to build on this prior knowledge and exploit the periodic response of nonlinear oscillators to sinusoidal excitation for system identification.

The Hilbert transformation can be used to extract damping and stiffness of nonlinear systems from forced vibration measurements [6]. The Hilbert transformation, a signal processing tool, can be most appropriately interpreted as shifting the phase of a signal by $\pi/2$. With this characteristic, an instantaneous amplitude and phase can be defined, which, in turn, can be related to nonlinear damping and stiffness terms. However, this method is designed for single-degree-of-freedom systems and it does not apply to nonlinear terms depending on the velocity and position simultaneously [7].

T. Breunung (✉) · L. Cilenti · J. M. You · B. Balachandran
Department of Mechanical Engineering, University of Maryland, College Park, MD, USA
e-mail: thomasbr@umd.edu; lcilenti@umd.edu; Jmyou00@terpmail.umd.edu; balab@umd.edu

M. R. W. Brake et al. (eds.), *Nonlinear Structures & Systems, Volume 1*, Conference Proceedings of the Society for Experimental Mechanics Series, https://doi.org/10.1007/978-3-031-36999-5_2

Alternatively, the response surface method can be utilized to identify nonlinear systems [8]. For a single-degree-of-freedom system, with this method, one plots the difference between the measured acceleration and excitation signal over velocity and position and, thereby, obtains the response force as a surface. Curve fitting methods are then required to find a model representing the response surface. While this method can be extended to multi-degree-of-freedom systems, curve fitting in high-dimensional spaces remains challenging. Moreover, position, velocity, and acceleration signals are required. In practice, often only one measurement is available and numerical differentiation or integration to obtain the others can introduce errors.

Through many computational and several experimental studies, nonlinear modes [9] have been identified as a powerful basis for understanding and studying the dynamics of smooth nonlinear oscillatory systems. These modes are defined as families of periodic solutions of the underlying conservative system. With this concept, one can extend the eigenfrequencies and eigenfunctions of linear systems to the nonlinear setting. Based on their properties a series of system identification methods utilizing, for example, nonlinear phase lag-criterion [10] or control-based continuation [11], have been proposed. The experimental identification of nonlinear modes, however, remains challenging and it is often carried out in a case-by-case basis.

To enable a robust and automated system identification procedure for nonlinear oscillators, the authors utilize a transformation into the Fourier domain, curve fitting tools, and a judicious parameter reduction. The obtained models are sparse and accurately capture the forced response data.

2.2 System Identification

In this work, the authors develop a uniform methodology to robustly identify nonlinear oscillatory systems from measured frequency response curves. Exciting the structure with a periodic forcing, the periodic steady state is recorded for various forcing frequencies Ω. To fit these measurements the general, nonlinear oscillatory system

$$\mathbf{M}\ddot{\mathbf{q}} + \mathbf{C}\dot{\mathbf{q}} + \mathbf{K}\mathbf{q} + \mathbf{S}(\dot{\mathbf{q}}, \mathbf{q}) = \mathbf{f}(t), \tag{2.1}$$

is employed, whereby the forcing $\mathbf{f}(t)$ is periodic. The nonlinearity $\mathbf{S}(\dot{\mathbf{q}}, \mathbf{q})$ is a function of the velocity $\dot{\mathbf{q}}$ and position $\mathbf{q}$. Expanding the observed periodic orbit into a Fourier series yields

$$\mathbf{q} := \sum_{k=-K}^{K} \mathbf{q}^k e^{\mathrm{i}k\Omega t}, \qquad \dot{\mathbf{q}} = \sum_{k=-K}^{K} \mathrm{i}k\Omega \mathbf{q}^k e^{\mathrm{i}k\Omega t}, \qquad \ddot{\mathbf{q}} = \sum_{k=-K}^{K} -k^2\Omega^2 \mathbf{q}^k e^{\mathrm{i}k\Omega t}. \tag{2.2}$$

Thus, from measuring either position, velocity, or acceleration, the other two signals can be recovered without numerical differentiation and integration. After substituting the expansion (2.2) into Eq. (2.1), projecting the nonlinearities onto the first K Fourier modes and imposing a balance for the first K Fourier modes, the result is a linear set of equations. Collecting multiple measurements for different forcing frequencies Ω yields an overdetermined set of linear equations

$$\mathbf{A}\mathbf{p} = \mathbf{B}, \tag{2.3}$$

which can be solved in the least squares sense. While assembling the linear equations, terms beyond the noise floor are terminated and the column space of $\mathbf{A}$ is checked for linear dependencies to increase the robustness of the fit. Finally, the number of parameters is iteratively reduced until the residual error reaches a predetermined threshold. This procedure yields a low-order and sparse nonlinear oscillatory system, which can be used to accurately capture the forced response curve.

2.3 Results

The proposed methodology is tested on the clamped-free cantilever shown in Fig. 2.1a. The shaker is used to excite the first bending mode, and within this frequency range, a single-degree-of-freedom system is fitted. The proposed fitting methodology automatically leads to the following oscillatory system:

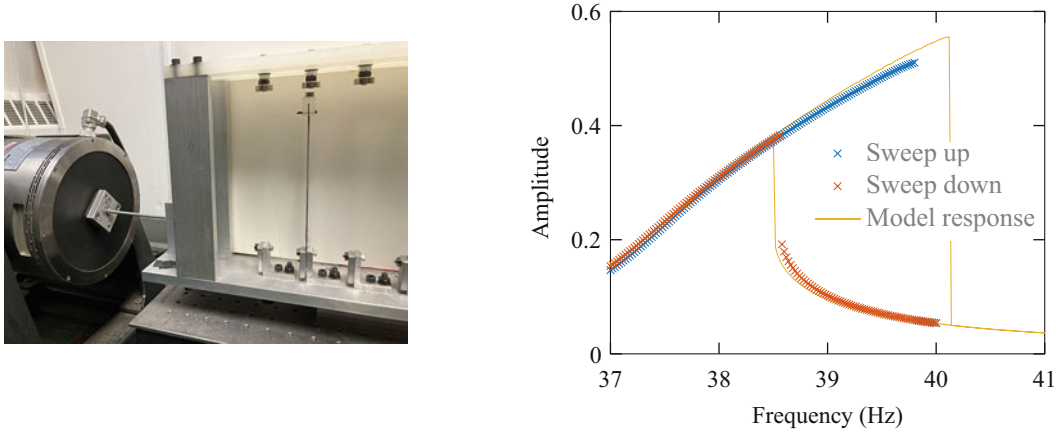

(a) (b)

Fig. 2.1 Experimental setup and obtained forced response curves. (**a**) Experiment. (**b**) Measured and simulated responses

$$\ddot{q} + c\dot{q} + \omega_1^2 q + k_2 q^2 + k_3 q^3 = a\cos(\Omega t), \tag{2.4}$$

which accurately captures the measured response as shown in Fig. 2.1b.

2.4 Conclusions

The proposed, automated methodology yields sparse and robust models which can be used to accurately capture the experimentally observed forced response. The present work paves the path to an automated and universal fitting routine for nonlinear oscillators. In the talk, results obtained with multi-degree-of-freedom systems will also be presented and discussed.

References

1. Feldman, M.: Non-linear system vibration analysis using hilbert transform–i. free vibration analysis method'freevib. Mech. Syst. Signal Process. **8**(2), 119–127 (1994)
2. Leontaritis, I.J., Billings, S.A.: Input-output parametric models for non-linear systems part I: deterministic non-linear systems. Int. J. Control. **41**(2), 303–328 (1985)
3. Londoño, J.M., Neild, S.A., Cooper, J.E.: Identification of backbone curves of nonlinear systems from resonance decay responses. J. Sound Vib. 348, 224–238 (2015)
4. Ewins, D.J.: Modal Testing: Theory, Practice and Application. Wiley, New York (2009)
5. Modal Impact Postprocessing: Getting the Best FRF. https://community.sw.siemens.com/s/article/Modal-Impact-Testing-Getting-the-Best-FRF. Accessed: 2022-10-20
6. Feldman, M.: Non-linear system vibration analysis using hilbert transform–ii. forced vibration analysis method 'forcevib'. Mech. Syst. Signal Process. **8**(3), 309–318 (1994)
7. Kerschen, G., Worden, K., Vakakis, A.F., Golinval, J.-C.: Past, present and future of nonlinear system identification in structural dynamics. Mech. Syst. Signal Process. **20**(3), 505–592 (2006)
8. Masri, S.F., Caughey, T.K.: A nonparametric identification technique for nonlinear dynamic problems. J. Appl. Mech. **46**(2), 433–447 (1979)
9. Kerschen, G., Peeters, M., Golinval, J.-C., Vakakis, A.F.: Nonlinear normal modes, part I: A useful framework for the structural dynamicist. Mech. Syst. Signal Process. **23**(1), 170–194 (2009)
10. Peeters, M., Kerschen, G., Golinval, J.-C.: Dynamic testing of nonlinear vibrating structures using nonlinear normal modes. J. Sound Vib. **330**(3), 486–509 (2011)
11. Renson, L., Gonzalez-Buelga, A., Barton, D.A.W., Neild, S.A.: Robust identification of backbone curves using control-based continuation. J. Sound Vib. **367**, 145–158 (2016)

Chapter 3
Creating Data-Driven Reduced-Order Models for Nonlinear Vibration via Physics-Informed Neural Networks

Alex J. Elliott

Abstract Modern engineering solutions often aim to improve the energy efficiency of their structures by including lightweight, flexible, and slender designs. In practice, it is not always possible to maximise these characteristics and hence the efficiency of the structures, as they exhibit complex, nonlinear structural dynamics. Unless this behaviour is accurately predicted or controlled, the system may encounter extremely destructive behaviour, which can lead to catastrophic mechanical failure. Non-intrusive reduced-order models (NIROMs)—which project the system dynamics onto a reduced set of modes and approximate the nonlinear components of the behaviour—have, therefore, been of great interest and have the potential to greatly increase the industrial uptake of high-efficiency, nonlinear structures. Existing methodologies for NIROM generation apply linear regression to static force and displacement cases, but this approach has previously been demonstrated to be overly dependent on the scale of these characteristics, a point that has prevented wider application. In this work, initial steps are taken to utilise physics-informed recurrent neural networks (RNNs) in place of the static step, allowing the dynamic behaviour to be more accurately captured in the NIROM. First, the use of random and periodic data series is applied in the training stage, with low-pass filtered white noise shown to provide the more reliable model. Following this, long short-term memory RNNs are developed both with and without a physics-informed loss function, with the former demonstrating faster convergence and more accurate predictions. This study represents the first steps taken in a wider project that aims to improve the accuracy and reliability of nonlinear NIROMs, so that they may be more readily applied in a real-world setting.

Keywords Nonlinear vibrations · Long short-term memory · Physics-informed neural networks · Reduced-order model

3.1 Introduction

The global climate effort is increasingly dependent on lightweight, flexible designs to provide engineering solutions capable of meeting ambitious emissions targets. Examples of these designs include high-aspect ratio wings [1, 2], which are capable of achieving extended flight times using significantly less energy, but their complexity introduces geometric nonlinearity to the system, leading to a substantial increase in complexity [3]. Both the structural behaviour and the mathematical techniques required to capture it provide a much greater modelling challenge. The potential benefits offered by these next-generation designs necessitate accurate and responsive modelling techniques, leading to a marked interest in reliable, non-intrusive reduced-order models (NIROMs) in recent years.

The application of NIROMs to efficiently calculate nonlinear structural behaviour is well-established, with the associated literature including examples of their use to capture local [4] and global nonlinearities [5]. For the designs mentioned above, the increased flexibility and associated strains lead to nonlinearity on the global scale, so this is the focus of the present work. As outlined in [5], NIROM generation traditionally applies nonlinear regression to a series of static cases to estimate the nonlinear coefficients in the force-displacement relationship. This is particularly important for models developed using commercial finite element software, in which the black-box nature of the source code prevents NIROMs from being generated directly.

Naturally, there are two major strategies for generating the aforementioned static cases. In the first of these, often referred to as the implicit condensation [6] (and expansion [7]), a static *force* is applied and the resulting displacements are recorded. Alternatively, it is possible to apply a series of static displacements to the system and record the resultant forces [8].

A. J. Elliott (✉)
School of Aerospace, Transport and Manufacturing, Cranfield University, Wharley End, England
e-mail: Alex.J.Elliott@cranfield.ac.uk

M. R. W. Brake et al. (eds.), *Nonlinear Structures & Systems, Volume 1*, Conference Proceedings of the Society for Experimental Mechanics Series, https://doi.org/10.1007/978-3-031-36999-5_3

Given their similarity, the comparison of these methodologies has been relatively common [9], with the authors of [10] investigating the impact that their differences have on the accuracy of the associated NIROMs. A key finding of this work was that accurately capturing the cross-coupling of the vibration modes was fundamental to achieving an accurate NIROM, an attribute that was not consistently observed for either method.

In light of this underperformance, the recent literature has started to explore the use of machine learning, and particularly recurrent neural networks (RNNs), to overcome this barrier [11–14]. Simpson et al. [11] employ several toy models to investigate the use of long short-term memory (LSTM) RNNs [15], utilising an autoencoder that reduces the order of the model. In contrast, Cenedese et al. [12, 13] expand the spectral submanifold approach to nonlinear normal modes by incorporating a data-driven learning of the dynamics on the submanifold. Across these examples, the methodologies show exceptional promise, though their relative complexity restricts their applicability by a non-expert in a real-world setting.

This paper explores the initial steps in the development of an analogous strategy that aims to directly address this need. A simple, five-degree-of-freedom (5DOF) mass-spring model, including nonlinear springs, is introduced to explore the fundamental accuracy and practicability of the proposed methodology. The application of physics-informed (PI) RNNs, in which verifiable knowledge of the physics of the system is used to guarantee convergence to a physically interpretable solution [16], is identified as a key strategy in achieving this overall aim.

3.2 Methodology

The general equations of motion for a nonlinear mechanical system are given by

$$\mathbf{M}\ddot{\mathbf{x}} + \mathbf{C}_{\mathbf{x}}\dot{\mathbf{x}} + \mathbf{K}\mathbf{x} + \mathbf{F}_{\mathrm{NL,x}}(\mathbf{x}) = \mathbf{F}_{\mathbf{x}}, \tag{3.1}$$

where $\mathbf{x}$ denotes the physical coordinates and $\mathbf{M}$, $\mathbf{C}$, and $\mathbf{K}$ denote the mass, damping, and stiffness matrices, respectively. $\mathbf{F}_{\mathrm{NL}}(\mathbf{x})$ and $\mathbf{F}_x$ represent the vectors of nonlinear and external forces; note that the subscript x on the forces and damping matrix denotes the fact that this vector is in physical coordinates, rather than modal, as this will simplify the notation below.

It is common practice to consider this system in terms of the basis of modal coordinates—denoted by $\mathbf{q}$—which can be found through the application of the mass-normalised eigenvector matrix, Φ, with $\mathbf{x} = \Phi\mathbf{q}$. Through this transformation, Eq. (3.1) can be rewritten as [3]

$$\ddot{\mathbf{q}} + \mathbf{C}\dot{\mathbf{q}} + \Lambda\mathbf{q} + \mathbf{F}_{\mathrm{NL}}(\mathbf{q}) = \mathbf{F}, \tag{3.2}$$

where Λ is the diagonal matrix of the squared natural frequencies (i.e. the nth diagonal entry is ω_n^2) and $\mathbf{F}_{\mathrm{NL}}(\mathbf{q}) = \Phi^{\mathrm{T}}\mathbf{F}_{\mathrm{NL,x}}(\Phi\mathbf{q})$.

The NIROM methodologies discussed in the Introduction are designed to preserve the structure of Eq. (3.2), but reducing the number of modes retained in the model. Specifically, the NIROM is defined in terms of some subset $\{\hat{q}\} \subset \{q\}$, with associated reduced eigenvector matrix $\hat{\Phi}$. The number of modes retained in $\{\hat{q}\}$ will be denoted by R. The reduced equations of motion can now be written in the form

$$\ddot{\hat{\mathbf{q}}} + \hat{\mathbf{C}}\dot{\hat{\mathbf{q}}} + \hat{\Lambda}\hat{\mathbf{q}} + \hat{\mathbf{F}}_{\mathrm{NL}}(\hat{\mathbf{q}}) = \hat{\mathbf{F}}. \tag{3.3}$$

Both the linear components of Eq. (3.1) and $\hat{\Phi}$ can be readily obtained, either analytically or from the finite element software, so the linear elements of Eq. (3.3) can be easily calculated. In contrast, the nonlinear function is typically complicated and is often approximated through a numerical methodology that is not made available to the user. Thus, the main aim of the NIROM generation strategy is to analytically approximate this behaviour in the function $\hat{\mathbf{F}}_{\mathrm{NL}}$.

Since the motivation for developing NIROMs is frequently driven by a need for significant improvements in response time, $\hat{\mathbf{F}}_{\mathrm{NL}}$ is usually written as a cubic polynomial in terms of the elements of $\hat{\mathbf{q}}$. The m^{th} element of this vector is given by

$$\hat{\mathbf{F}}_{\mathrm{NL},m} = \sum_{i=1}^{R}\sum_{j=1}^{R}\sum_{k=1}^{R} A_{i,j,k}^{(m)}\hat{q}_i\hat{q}_j\hat{q}_k + \sum_{i=1}^{R}\sum_{j=1}^{R} B_{i,j}^{(m)}\hat{q}_i\hat{q}_j, \tag{3.4}$$

where the coefficients, $A_{i,j,k}$ and $B_{i,j}$, are the terms estimated by the reduction steps. With the nonlinear terms approximated as in Eq. (3.4), the static cases applied to the system take the form

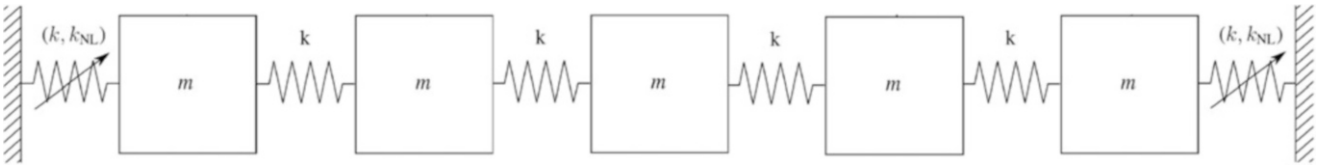

Fig. 3.1 Schematic for a 5DOF mass-spring system with nonlinear grounding springs

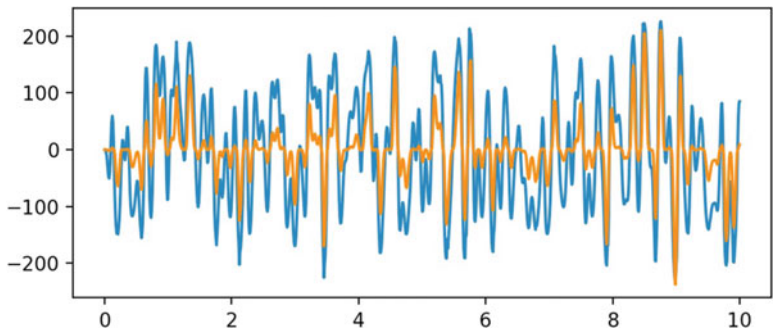

Fig. 3.2 Relative magnitudes of the linear (blue) and nonlinear (orange) forces observed for the 5DOF mass-spring system

$$\omega_m^2 \hat{q}_m + \sum_{i=1}^{R}\sum_{j=1}^{R}\sum_{k=1}^{R} A_{i,j,k}^{(m)} \hat{q}_i \hat{q}_j \hat{q}_k + \sum_{i=1}^{R}\sum_{j=1}^{R} B_{i,j}^{(m)} \hat{q}_i \hat{q}_j = \hat{\mathbf{F}}_m. \tag{3.5}$$

In Eq. (3.5), it is only the nonlinear coefficients that are unknown. Therefore, by generating a sufficient number of these cases, it will be possible to apply linear regression to estimate the value for $A_{i,j,k}$ and $B_{i,j}$. The details for both methodologies are outlined in [10], so they are not provided here.

3.2.1 Example: Five-Degree-of-Freedom, Nonlinear Mass-Spring Model

To allow the accuracy and usability of the methods to be compared, a simple toy model is introduced and presented in Fig. 3.1. This consists of five masses, of mass $m = 0.1$ kg, arranged in parallel and connected by linear springs with stiffness coefficient $k = 100$ N/m and an associated damping coefficient of $c = 0.1$ kg/s. The end masses are grounded by springs that include an additional cubic component with stiffness, $k_{\mathrm{NL}} = 25$ N/m^3, so that its force is defined by the equation $F(x_n) = kx_n + k_{\mathrm{NL}}x_n^3$, where x_n denotes the horizontal displacement of the nth mass.
The forcing of the system is scaled by the amplitude vector $\mathbf{A} = [75, 0, 0, 0, 75]^{\mathrm{T}}$. As can be observed in Fig. 3.2, this forcing level results in the linear and nonlinear forces observed in the system time histories being of a similar magnitude. This has been selected to mirror the typical approach for the static methodologies, which utilise a user-defined scaling factor to ensure that the modal cross-couplings have been sufficiently activated [5, 10].

3.2.2 Data Generation

The longer-term vision for this approach is that knowledge of the system can be used to strategically force the system and generate data that leads to an optimal NIROM, though this is beyond the scope of the present work. Instead, two types of forcing are considered:

- *Sinusoidal:* A simple sinusoidal function with amplitude vector $\mathbf{A}$ and frequency Ω is applied to one or multiple masses, i.e., $\hat{\mathbf{F}} = \mathbf{A}\sin(\Omega t)$.
- *Random:* Low-pass filtered white noise, with cut-off frequency of 7.5 Hz is applied to one or multiple masses.

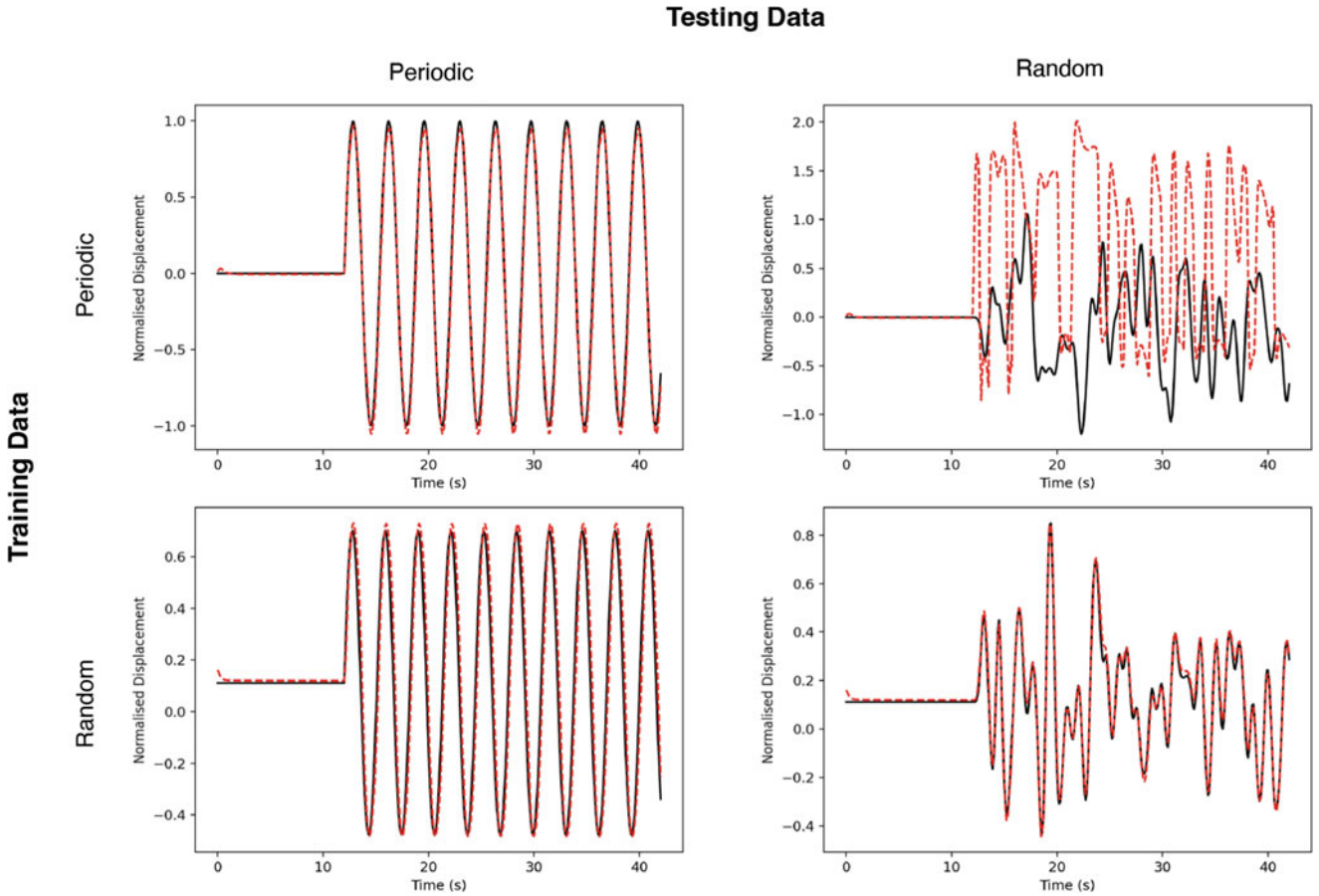

Fig. 3.3 Representative model performance for models trained using periodic and random data

In both cases, each time history is preceded by a period of zero forcing to improve the prediction if the system is forced from a resting position, as recommended in [11].

The relative performance of models generated with periodic and random forcing data is presented in Fig. 3.3. For both cases, the prediction of periodic data is observed to be accurate. It can be noted that there are minor discrepancies in the predicted amplitude, with slight improvements in the periodic model, though these are negligible in relation to the full vibration magnitude. In contrast, there are significant differences in the accuracy of the prediction of randomly forced data. As expected, the model that is also trained with random data predicts the system response very accurately, with no real change in performance between the periodic and random test cases. However, the periodic model performs very poorly, failing to predict the structural dynamics as soon as the force is applied. These initial results highlight the importance of representative data in the NIROM training phase. This point is particularly important for the aforementioned longer-term data generation strategy, which must incorporate the full range of system behaviour if it is to be reliably used in the real world.

3.2.3 Long Short-Term Memory

In this work, we investigate the application of LSTM [15] as a strategy for incorporating the dynamical behaviour of the system into the NIROMs generated. LSTM networks are a specific (and popular) subcategory of RNNs, which use gated activation functions to up the "cell state". This cell has the ability to remember the system values over a pre-selected number of steps, allowing longer-term behaviour to be captured; this is of particular interest for nonlinear structures, for which the behaviour is often hysteretic in nature. As the exact details of the LSTM mechanism are of little relevance to the generated NIROMs—and with the wider project aiming to remove the need for the user to have in-depth technical knowledge of machine learning—further these details are not provided here, and the reader is instead directed to [15] for this information.

3.2.4 *Physics-Informed Loss Function*

While LSTM is a proven strategy for developing surrogate models and NIROMs, there is no explicit guarantee that the model developed is consistent with physical laws that define the system behaviour. To address this concern, this section investigates the application of PI RNNs—as introduced in [16]—to allow the existing knowledge of the system to be incorporated into the process.

As has been discussed throughout the previous sections, the underlying linear system (which can be found by simply removing the nonlinear force function from Eq. (3.1) or (3.2)) has been extensively studied and defines a large amount of the structural dynamics. By incorporating this knowledge into the loss function utilised in the LSTM network, it is possible to create a PI loss function that can aid the accuracy, physical interpretability, and convergence of the NIROM. In the vanilla LSTM approach, the loss function consists solely of the standard mean squared error (MSE) applied to displacement and velocity:

$$L(\hat{\mathbf{q}}, \dot{\hat{\mathbf{q}}}) = \|\mathbf{z}_1 - \hat{\mathbf{q}}\|_2^2 + \|\mathbf{z}_2 - \dot{\hat{\mathbf{q}}}\|_2^2, \tag{3.6}$$

where $\mathbf{z}_1$ and $\mathbf{z}_2$ denote the true values of the modal displacements and velocities, respectively, and $\|\bullet\|_2$ denotes the standard ℓ^2-norm. In practical terms, the loss function in Eq. (3.6) will aid the convergence to a surrogate model that accurately predicts behaviour similar to what it has been trained with, but there is no guarantee that this will be sufficient to capture unseen physical phenomena. This is something that a PI loss function should address, with the added benefit that convergence may occur more quickly.

The changes required to update Eq. (3.6) are relatively minimal and take advantage of the fact that the unknown nonlinear function, $\hat{F}_{\mathrm{NL}}$, can be expressed in terms of the known linear terms by rearranging Eq. (3.3). Therefore, Eq. (3.6) can be adapted to also assess the error in the prediction of the nonlinear term, as follows:

$$L(\hat{\mathbf{q}}, \dot{\hat{\mathbf{q}}}) = \|\mathbf{z}_1 - \hat{\mathbf{q}}\|_2^2 + \|\mathbf{z}_2 - \dot{\hat{\mathbf{q}}}\|_2^2 + \|\hat{\mathbf{F}}_{\mathrm{NL}}(\mathbf{z}_1) - \hat{\mathbf{F}}_{\mathrm{NL}}(\hat{\mathbf{q}})\|_2^2. \tag{3.7}$$

The impact of this additional term can be observed in Fig. 3.4, which compares the convergence and performance of NIROMs generated using the MSE and PI loss functions. The performance of both models is strong, though the vanilla NIROM slightly underperforms in both amplitude and phase, which could prove problematic for systems with very high-frequency components of the response. However, there is a much clearer difference in the convergence of the model. While the first 1000 epochs of training show lower losses for the MSE model, it eventually takes over 4000 iterations to show signs of real convergence. In contrast, the PI loss values are much more volatile for the initial 1500 epochs, but converge by 2000 epochs. This suggests that the use of a PI loss function can more than halve the computation time.

3.3 Conclusions

This paper presents initial insights into the use of physics-informed neural networks in the development of NIROMs for nonlinear mechanical systems. It is envisaged that this approach will eventually provide a more accurate and reliable methodology than current approaches that utilise static forces and displacements to approximate the dynamic nonlinear behaviour. A 5DOF mass-spring model with nonlinear grounding springs is used to explore the generation of data that leads to robust NIROMs that are capable of capturing complex, nonlinear behaviour, with random data providing clear advantages over simpler periodic time histories. This model is further applied to investigate the use of an LSTM-based machine learning methodology. This approach has been demonstrated to accurately capture the system dynamics, with additional accuracy and savings in computation being achieved through the inclusion of a PI loss function. Future work on this topic will focus on developing this strategy to be able to capture the dynamics of much larger systems, including those built with commercial finite element packages, as well as incorporating uncertainty quantification and optimisation.

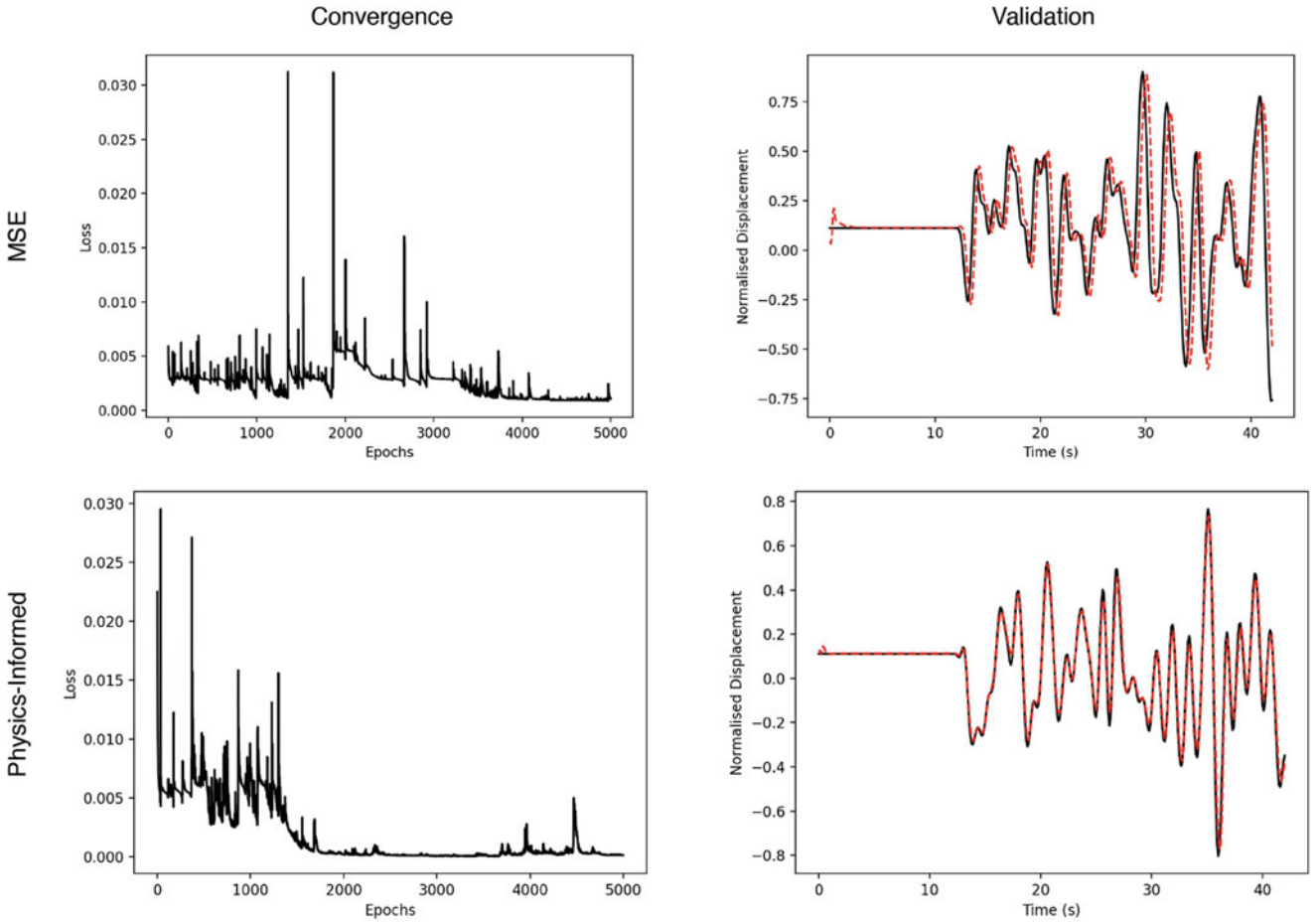

Fig. 3.4 Convergence and performance data for NIROMs generated using MSE and PI loss functions

References

1. Glauert, H.: The elements of aerofoil and airscrew theory. In: Cambridge Science Classics. Cambridge University Press, Cambridge (1983)
2. Chen, T., Katz, J.: Induced Drag of High-Aspect Ratio Wings (2004)
3. Wagg, D., Neild, S.: Nonlinear vibration with control. In: Solid Mechanics and Its Applications, vol. 218. Springer International Publishing, Cham (2015)
4. Krattiger, D., Wu, L., Zacharczuk, M., Buck, M., Kuether, R.J., Allen, S.M., Tiso, P., Brake, M.R.W.: Interface reduction for Hurty/Craig-Bampton substructured models: Review and improvements. Mech. Syst. Signal Process. **114**, 579–603 (2019)
5. A review of indirect/non-intrusive reduced order modeling of nonlinear geometric structures. J. Sound Vib. **332**(10), 2437–2460 (2013)
6. McEwan, M.I., Wright, J.R., Cooper, J.E., Leung, A.Y.T.: A combined modal/finite element analysis technique for the dynamic response of a non-linear beam to harmonic excitation. J. Sound Vib. **243**(4), 601–624 (2001)
7. Hollkamp, J.J., Gordon, R.W.: Reduced-order models for nonlinear response prediction: implicit condensation and expansion. J. Sound Vib. **318**(4), 1139–1153 (2008)
8. Muravyov, A.A., Rizzi, S.A.: Determination of nonlinear stiffness with application to random vibration of geometrically nonlinear structures. Comput. Struct. **81**(15), 1513–1523 (2003)
9. Kuether, R.J., Allen, M.S.: A numerical approach to directly compute nonlinear normal modes of geometrically nonlinear finite element models. Mech. Syst. Signal Process. **46**(1), 1–15 (2014)
10. Tartaruga, I., Elliott, A., Hill, T.L., Neild, S.A., Cammarano, A.: The effect of nonlinear cross-coupling on reduced-order modelling. Int. J. Non Linear Mech. **116**, 7–17 (2019)
11. Simpson, T., Dervilis, N., Chatzi, E.: Machine learning approach to model order reduction of nonlinear systems via autoencoder and LSTM networks. J. Eng. Mech. **147**(10), 04021061 (2021)
12. Cenedese, M., Axås, J., Bäuerlein, B., Avila, K., Haller, G.: Data-driven modeling and prediction of non-linearizable dynamics via spectral submanifolds. Nat. Commun. **13**(1), 872 (2022)
13. Cenedese, M., Axås, J., Yang, H., Eriten, M., Haller, G.: Data-driven nonlinear model reduction to spectral submanifolds in mechanical systems. Philos. Trans. R. Soc. A Math. Phys. Eng. Sci. **380**(2229), 20210194 (2022)

14. Fresca, S., Gobat, G., Fedeli, P., Frangi, A., Manzoni, A.: Deep learning-based reduced order models for the real-time simulation of the nonlinear dynamics of microstructures. Int. J. Numer. Methods Eng. **123**(20), 4749–4777 (2022)
15. Hochreiter, S., Schmidhuber, J.: Long short-term memory. Neural Comput. **9**(8), 1735–1780 (1997)
16. Raissi, M., Perdikaris, P., Karniadakis, G.E.: Physics-informed neural networks: A deep learning framework for solving forward and inverse problems involving nonlinear partial differential equations. J. Comput. Phys. **378**, 686–707 (2019)

Chapter 4
Effect of Structural Parameters on the Nonlinear Vibration of L-Shaped Beams

Yigitcan Ekici, Ender Cigeroglu, and Yigit Yazicioglu

Abstract In this chapter, nonlinear vibration analysis of L-shaped beams is performed for different structural parameters, and the effects of these parameters are observed. The L-shaped beam is composed of two beams joined end to end and perpendicular to each other; therefore, the system is considered as two separate beams with the same boundary conditions at their mutual ends. In addition to this, concentrated masses are attached to each beam on the L-shaped beam. The dynamic model is obtained by using Euler-Bernoulli Beam Theory and Hamilton's principle. These equations are further simplified by disregarding the axial motions of the beams and only the transverse motions are considered in calculations. Galerkin's method is utilized to discretize the obtained nonlinear partial differential equations into a set of nonlinear ordinary differential equations. These nonlinear ordinary differential equations are converted into a set of nonlinear algebraic equations by using Harmonic Balance Method (HBM), which are then solved numerically by using Newton's method with arc-length continuation. In order to observe the effect of the nonlinearity, a linear solution is also obtained and compared with the nonlinear solution. Several case studies are performed in order to observe the effect of system parameters on the nonlinear steady-state response of the L-shaped beam.

Keywords Nonlinear beams · Nonlinear L-shaped beams · Structural dynamics · Euler-Bernoulli beam theory

4.1 Introduction

L-shaped beams are considered to be one of the most important components in engineering structures [1]. These beams are a subclass of beams, which are commonly used in many applications such as buildings, aerospace structures, naval structures, and vehicles. Because of this reason, they are investigated in many studies. L-shaped beams using linear Euler-Bernoulli beam models are studied in earlier papers, since it is easy to derive the governing differential equations and it is possible to obtain the analytical solution. However, the linear Euler-Bernoulli beam model is valid only for small deflections. In order to obtain accurate solution for large deflections, nonlinear Euler-Bernoulli models are considered in later studies.

Besides analytical and finite element modeling methods, many numerical methods exist to discretize the Euler-Bernoulli beam equation in the spatial domain and turn it into an ordinary differential equation. The most common ones are the Galerkin, the Collocation, and the Assumed Modes methods [2, 3]. Alongside these methods, Samandari and Cigeroglu [1] employed Differential Quadrature Method [4, 5] to discretize the nonlinear equations of motion of an L-shaped beam. Apart from these, Morales [6] applied the Rayleigh-Ritz-Meirovitch Substructure Synthesis method (RRMSSM) [7] to discretize the linear equation of motion of the L-shaped beam and compared the results with the results obtained using analytical and FEM solutions. In his later work [8], generic expressions of RRMSSM mass and stiffness matrices of the L-shaped beam were presented.

Some studies focus on the analytical solution of L-shaped beams. Bang's study [9] is one of the most prominent one among these studies. In his study, an analytical solution for linearized equations of motion of the L-shaped beam is obtained. Gurgoze detected some mistakes on this study and corrected them [10] and later improved this study by obtaining analytical solution of the linear L-shaped beam with a point mass attached to its end [11]. Oguamanam et al. [12] obtained linearized

Y. Ekici
Roketsan Inc., Ankara, Turkey

E. Cigeroglu (✉) · Y. Yazicioglu
Department of Mechanical Engineering, Middle East Technical University, Ankara, Turkey
e-mail: ender@metu.edu.tr

M. R. W. Brake et al. (eds.), *Nonlinear Structures & Systems, Volume 1*, Conference Proceedings of the Society for Experimental Mechanics Series, https://doi.org/10.1007/978-3-031-36999-5_4

equations of motion for a two-member open frame structure with an arbitrary angle between them and compared the natural frequencies obtained by analytical method and finite element method. Georgiades et al. [13] studied in-plane and out-of-plane modal analysis of L-shaped beams. In this study, the analytical solutions are compared with the results of finite element analysis and it is observed that for in-plane bending, the effects of shear and inertia are not significant and for out-of-plane bending, the effects of shear and inertia are more important, especially, for the second beam.

Since the linearized models for L-shaped beams are not valid for large deflections, many researches considered the nonlinear models for L-shaped beams. In [14], nonlinear equations of motion of an L-shaped beam were formulated and global mode approach is used to obtain mode shapes and natural frequencies of the system. The results were compared with FEM results to illustrate the validity of this approach. In the study of Georgiades, nonlinear model for L-shaped beams was developed [15]. This study was the first to describe the out-of-plane motion of nonlinear L-shaped beams, which had been neglected in the literature for many years.

Besides the studies that focus on analysis and mathematical modeling of L-shaped beams, many researches were performed to observe the dynamical behaviors of these beams, both mathematically and experimentally. Most of these studies consider L-shaped beams with two-to-one internal resonance to a primary resonance [16–21]. The study of Haddow et al. [16] is one of the first studies that compared the natural frequencies and planar dynamic responses of an L-shaped beam obtained by mathematical model and experiments. In addition to this, saturation, jump conditions, and the nonexistence of a steady-state response were also demonstrated experimentally. In [17–21], experimental responses of an L-shaped beam were compared to the results obtained by nonlinear mathematical modeling. Experimentally, it is observed that periodic, quasi-periodic, and chaotic responses occur when an L-shaped beam with quadratic nonlinearities is excited with extremely small excitation levels, as predicted by the nonlinear theory.

In this study, nonlinear mathematical model of an L-shaped beam, one end of which is fixed to the ground, is developed. In addition to the L-shaped beam, point masses are attached to each beam, since they have a considerable effect on the response of the system. HBM is employed to convert the nonlinear differential equations of motion into nonlinear algebraic equations, which are solved by Newton's methods with arc-length continuation. In order to validate the model developed, results obtained for the linear L-shaped beam are compared with the ones obtained from the commercial finite element software ANSYS. Several case studies are carried out in order to see the effects of system parameters on the vibration characteristics of the L-shaped beam. Moreover, responses of the linear system and nonlinear system are compared and it is observed that as the excitation amplitude increases, it is necessary to consider the nonlinear effects in order to capture the dynamics of the L-shaped beam accurately.

4.2 Background

4.2.1 Formulation of the L-Shaped Beam

In this section, the nonlinear partial differential equations of motion of an L-shaped beam are derived. The equations of motions are derived for a transversally excited beam with symmetric cross sections with respect to the respective longitudinal directions. Because of that, only the in-plane axial and transverse motions of the beam are considered and torsional and out-of-plane motions are neglected. The beam is modeled as two beams with different coordinate frames attached to their respective ends as shown in Fig. 4.1. In addition, point masses are attached to each beam in order to study the effects of such masses on dynamic response of the L-shaped beam.

Using Von Karman displacement field and strain relationship based on Euler-Bernoulli Beam theory [22], nonlinear strain equation can be written as follows:

$$\varepsilon_r\left(x_r, z_r\right) = \frac{\partial u_r}{\partial x_r} + \frac{1}{2}\left(\frac{\partial w_r}{\partial x_r}\right)^2 - z_r \frac{\partial^2 w_r}{\partial {x_r}^2}, \tag{4.1}$$

where subscript r stands for the beam 1 and 2 and u_r and w_r represent the axial and transverse deflections of the rth beam, respectively. These deflections are functions of both spatial (x_r) and temporal (t) independent variables. Using Eq. (4.1), potential energy of the beams can be written as

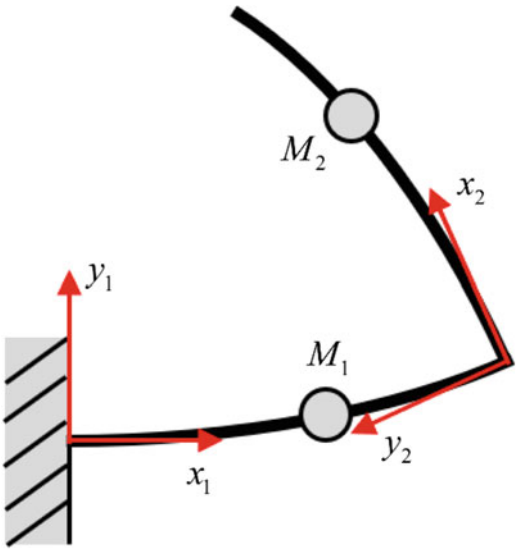

Fig. 4.1 Schematic of an L-shaped beam

$$V_r = \frac{1}{2}\int_0^{L_r} A_r \int E_r \left(\frac{\partial u_r}{\partial x_r} + \frac{1}{2}\left(\frac{\partial w_r}{\partial x_r}\right)^2 - z_r \frac{\partial^2 w_r}{\partial {x_r}^2}\right)^2 dA_r dx_r. \tag{4.2}$$

For symmetric cross section with respect to axis normal to the beam plane, Eq. (4.2) becomes

$$V_r = \frac{E_r}{2}\int_0^{L_r} \left(A_r\left(\frac{\partial u_r}{\partial x_r} + \frac{1}{2}\left(\frac{\partial w_r}{\partial x_r}\right)^2\right)^2 + I_r\left(\frac{\partial^2 w_r}{\partial {x_r}^2}\right)^2\right) dx_r. \tag{4.3}$$

Total kinetic energy of the L-shaped beam can be written as

$$\begin{aligned} T = {} & \tfrac{1}{2}\textstyle\int_0^{L_1} \left(\rho_1 A_1 + M_1 \delta\left(x_1 - L_{M_1}\right)\right)\left(\dot{u}_1^2 + \dot{w}_1^2\right) dx_1 \\ & + \tfrac{1}{2}\textstyle\int_0^{L_2} \left(\rho_2 A_2 + M_2 \delta\left(x_2 - L_{M_2}\right)\right)\left(\left(\dot{u}_2 + \dot{w}_1|_{x_1=L_1}\right)^2 + \left(x_2 \tfrac{\partial \dot{w}_1}{\partial x_1}|_{x_1=L_1} + \dot{w}_2 - \dot{u}_1\big|_{x_1=L_1}\right)^2\right) dx_2. \end{aligned} \tag{4.4}$$

Since coordinate frame attached to the second beam is a moving frame, the motion of the first beam at the end is included in the kinetic energy of the second beam. Hamilton's principle can be written as follows:

$$\int_{t_1}^{t_2} \delta L dt = \int_{t_1}^{t_2} \delta T dt - \int_{t_1}^{t_2} \delta V dt = 0. \tag{4.5}$$

where $V = V_1 = V_2$. By inserting Eqs. (4.3) and (4.4) into Eq. (4.5) and applying integration by parts (IBP), governing nonlinear partial differential equations (PDEs) are obtained by setting coefficients of δu_r and δw_r to 0:

$$-\left(\rho_1 A_1 + M_1 \delta\left(x_1 - L_{M_1}\right)\right)\ddot{u}_1 + \frac{\partial}{\partial x_1}\left(E_1 A_1\left(\frac{\partial u_1}{\partial x_1} + \frac{1}{2}\left(\frac{\partial w_1}{\partial x_1}\right)^2\right)\right) = 0, \tag{4.6}$$

$$-\left(\rho_1 A_1 + M_1 \delta\left(x_1 - L_{M_1}\right)\right)\ddot{w}_1 - E_1 I_1 \frac{\partial^4 w_1}{\partial {x_1}^4} + \frac{\partial}{\partial x_1}\left(E_1 A_1\left(\frac{\partial u_1}{\partial x_1} + \frac{1}{2}\left(\frac{\partial w_1}{\partial x_1}\right)^2\right)\frac{\partial w_1}{\partial x_1}\right) = 0, \tag{4.7}$$

$$-\left(\rho_2 A_2 + M_2 \delta\left(x_2 - L_{M_2}\right)\right)\left(\ddot{u}_2 + \ddot{w}_1\left(L_1\right)\right) + \frac{\partial}{\partial x_1}\left(E_2 A_2\left(\frac{\partial u_2}{\partial x_2} + \frac{1}{2}\left(\frac{\partial w_2}{\partial x_2}\right)^2\right)\right) = 0, \tag{4.8}$$

$$-\left(\rho_2 A_2+M_2\delta\left(x_2-L_{M_2}\right)\right)\left(\ddot{w}_2+x_2\frac{\partial\ddot{w}_1\left(L_1\right)}{\partial x_1}-\ddot{u}_1\left(L_1\right)\right)-E_2I_2\frac{\partial^4 w_1}{\partial {x_1}^4}+\frac{\partial}{\partial x_2}\left(E_2A_2\left(\frac{\partial u_2}{\partial x_2}+\frac{1}{2}\left(\frac{\partial w_2}{\partial x_2}\right)^2\right)\frac{\partial w_2}{\partial x_2}\right)=0. \tag{4.9}$$

The PDEs given above can be reduced to two equations by neglecting the acceleration due to the axial motion of the beams ($\ddot{u}_r = 0$), integrating Eqs. (4.6) and (4.8) along their respective beam lengths, and substituting them into Eqs. (4.7) and (4.9). Then, the reduced PDEs are obtained as follows:

$$-\left(\rho_1 A_1+M_1\delta\left(x_1-L_{M_1}\right)\right)\ddot{w}_1-E_1I_1\frac{\partial^4 w_1}{\partial {x_1}^4}+\frac{E_1A_1}{2L_1}\int_0^{L_1}\left(\frac{\partial w_1}{\partial x_1}\right)^2 dx_1\frac{\partial^2 w_1}{\partial {x_1}^2}=0, \tag{4.10}$$

$$\begin{aligned}&-\left(\rho_2 A_2+M_2\delta\left(x_2-L_{M_2}\right)\right)\left(\ddot{w}_2+x_2\tfrac{\partial\ddot{w}_1(L_1)}{\partial x_1}-\ddot{w}_1\left(L_1\right)\tfrac{\partial w_2}{\partial x_2}\right)\\&\quad+\left(\rho_2 A_2\left(x_2-\tfrac{L_2}{2}\right)+M_2\left(H\left(x_2-L_{M_2}\right)-\tfrac{L_2-L_{M_2}}{L_2}\right)\right)\ddot{w}_1\left(L_1\right)\tfrac{\partial^2 w_2}{\partial {x_2}^2}-E_2I_2\tfrac{\partial^4 w_2}{\partial {x_2}^4}+\tfrac{E_2A_2}{2L_2}\textstyle\int_0^{L_2}\left(\tfrac{\partial w_2}{\partial x_2}\right)^2 dx_2\tfrac{\partial^2 w_2}{\partial {x_2}^2}=0.\end{aligned} \tag{4.11}$$

Furthermore, by applying the same substitution to the by-products of the IBP and neglecting the acceleration due to the axial motion of the beams, boundary conditions (BCs) are obtained as follows:

$$w_1(0)=0, \tag{4.12}$$

$$\left.\frac{\partial w_1}{\partial x_1}\right|_{x_1=0}=0, \tag{4.13}$$

$$\frac{E_1A_1}{2L_1}\left(\int_0^{L_1}\left(\frac{\partial w_1}{\partial x_1}\right)^2 dx_1\right)\left.\frac{\partial w_1}{\partial x_1}\right|_{x_1=L_1}-E_1I_1\left.\frac{\partial^3 w_1}{\partial {x_1}^3}\right|_{x_1=L_1}+\int_0^{L_2}\left(\rho_2A_2+M_2\delta\left(x_2-L_{M_2}\right)\right)dx_2\ddot{w}_1\left(L_1\right)=0, \tag{4.14}$$

$$\int_0^{L_2}\begin{pmatrix}\rho_2A_2\\+M_2\delta\left(x_2-L_{M_2}\right)\end{pmatrix}\begin{pmatrix}\ddot{w}_2\\+x_2\left.\frac{\partial w_1}{\partial x_1}\right|_{x_1=L_1}\end{pmatrix}x_2dx_2+E_1I_1\left.\frac{\partial^2 w_1}{\partial {x_1}^2}\right|_{x_1=L_1}=0, \tag{4.15}$$

$$w_2(0)=0, \tag{4.16}$$

$$\left.\frac{\partial w_2}{\partial x_2}\right|_{x_2=0}=0, \tag{4.17}$$

$$\left(\frac{\rho_2A_2L_2}{2}+\frac{M_2L_{M_2}}{L_2}\right)\ddot{w}_1\left(L_1\right)-E_2I_2\left.\frac{\partial^3 w_2}{\partial {x_2}^3}\right|_{x_2=L_2}+\frac{E_2A_2}{2L_1}\left(\int_0^{L_2}\left(\frac{\partial w_2}{\partial x_2}\right)^2 dx_2\right)\left.\frac{\partial w_2}{\partial x_2}\right|_{x_2=L_2}=0, \tag{4.18}$$

$$\left.E_2I_2\frac{\partial^2 w_2}{\partial {x_2}^2}\right|_{x_2=L_2}=0. \tag{4.19}$$

4.2.2 Discretization of the Nonlinear PDEs by Using Galerkin's Method

Nonlinear PDEs can be discretized and converted into nonlinear ordinary differential equations (ODEs) by using Galerkein's method. The following solution for the response is assumed,

$$w_{r,n}(x_r, t) = \sum_{i=1}^{n} \left(\phi_{r,i}(x_r)\, q_{r,i}(t)\right), \tag{4.20}$$

where $\phi_{r,i}(x)$ is an admissible function, $q_{r,i}(t)$ is generalized coordinate, and n is the number of admissible functions used. The following admissible functions are considered, which satisfy all geometric BCs.

$$\phi_{r,i}(x_r) = \left(\frac{x_r}{L_r}\right)^{i+1}. \tag{4.21}$$

Applying Galerkin's method with relaxation of BCs to Eqs. (4.10) and (4.11), the following discretized equations are obtained:

$$\begin{aligned}
&-\sum_{j=1}^{n_1}\left(\ddot{q}_{1,j}\left(\frac{\rho_1 A_1 L_1}{i+j+3} + M_1 \frac{{L_{M_1}}^{i+j+2}}{{L_1}^{i+j+2}} + M_2 + \rho_2 A_2 L_2 + (i+1)(j+1)\frac{{L_2}^2}{{L_1}^2}\left(\frac{\rho_2 A_2 L_2}{3} + M_2 \frac{{L_{M_2}}^2}{{L_2}^2}\right)\right)\right)\\
&-\sum_{j=1}^{n_2}\left(\ddot{q}_{2,j}(i+1)\frac{L_2}{L_1}\left(\frac{\rho_2 A_2 L_2}{j+3} + M_2 \frac{{L_{M_2}}^{j+2}}{{L_2}^{j+2}}\right)\right) - \sum_{j=1}^{n_1}\left(q_{1,j}\frac{E_1 I_1}{{L_1}^3}\frac{(i+1)i(j+1)j}{i+j-1}\right)\\
&-\sum_{j=1}^{n_1}\sum_{k=1}^{n_1}\sum_{l=1}^{n_1}\left(q_{1,j}q_{1,k}q_{1,l}\frac{E_1 A_1}{2{L_1}^3}\frac{(i+1)(j+1)(k+1)(l+1)}{(i+l+1)(j+k+1)}\right) = 0,
\end{aligned} \tag{4.22}$$

$$\begin{aligned}
&-\sum_{j=1}^{n_2}\left(\ddot{q}_{2,j}\left(\frac{\rho_2 A_2 L_2}{i+j+3} + M_2\left(\frac{L_{M_2}}{L_2}\right)^{i+j+2}\right)\right) - \sum_{j=1}^{n_1}\left(\ddot{q}_{1,j}(j+1)\frac{L_2}{L_1}\left(\frac{\rho_2 A_2 L_2}{i+3} + M_2 \frac{{L_{M_2}}^{i+2}}{{L_2}^{i+2}}\right)\right)\\
&-\sum_{j=1}^{n_2}\left(q_{2,j}\frac{E_2 I_2}{{L_2}^3}\frac{(i+1)i(j+1)j}{i+j-1}\right) - \sum_{j=1}^{n_1}\sum_{k=1}^{n_2}\left(\ddot{q}_{1,j}q_{2,k}\frac{(i+1)(k+1)}{L_2(i+k+1)}\left(\rho_2 A_2 L_2 \frac{i+k}{i+k+2} + M_2\frac{L_{M_2}}{L_2}\left(1-\left(\frac{L_{M_2}}{L_2}\right)^{i+k}\right)\right)\right)\\
&-\sum_{j=1}^{n_2}\sum_{k=1}^{n_2}\sum_{l=1}^{n_2}\left(q_{2,j}q_{2,k}q_{2,l}\frac{E_2 A_2}{2{L_2}^3}\frac{(i+1)(j+1)(k+1)(l+1)}{(i+l+1)(j+k+1)}\right) = 0.
\end{aligned} \tag{4.23}$$

A sinusoidal force is assumed to be applied on one of the beams at location x_f.

$$F_r\left(x_f, t\right) = F_0\delta\left(x_f\right)\sin(\omega t). \tag{4.24}$$

Galerkin's method is applied to Eq. (4.24) to discretize it as

$$Q_{r_i} = F_0 \sin(\omega t)\left(\frac{x_f}{L_r}\right)^{i+1}. \tag{4.25}$$

Using Eqs. (4.22), (4.23) and (4.25), nonlinear ODE system can be represented in matrix form as

$$\mathbf{M}\ddot{\mathbf{q}} + (1 + i\gamma)\,\mathbf{K}\mathbf{q} + \mathbf{f_{NL}} = \mathbf{f}, \tag{4.26}$$

where $\mathbf{M}$ and $\mathbf{K}$ are mass and stiffness matrices respectively, $\ddot{\mathbf{q}}$, $\mathbf{f_{NL}}$, and $\mathbf{f}$ are generalized coordinate, nonlinear force, and external force vectors, respectively, and γ is the structural damping coefficient.

4.2.3 Multiharmonic Harmonic Balance Method (HBM)

HBM is used to calculate steady-state responses of nonlinear systems by transforming nonlinear ODEs into nonlinear algebraic equations in frequency domain. In HBM, displacement, excitation force, and nonlinear internal forcing vectors are represented by Fourier series as periodic function and similar terms are balanced to obtain the nonlinear algebraic equations. Therefore, generalized coordinate vector is written as follows:

$$\mathbf{q}(\theta) = \mathbf{q}_0 + \sum_{h=1}^{N_h}\mathbf{q}_s^h \sin(h\theta) + \mathbf{q}_c^h \cos(h\theta),\ \theta = \omega t, \tag{4.27}$$

where N_h is the number of harmonics used in the representation. Similarly, excitation force vector and nonlinear internal forcing vectors can be written as follows:

$$\mathbf{f}(\theta) = \mathbf{f}_0 + \sum_{h=1}^{N_h} \mathbf{f}_s^h \sin(h\theta) + \mathbf{f}_c^h \cos(h\theta), \tag{4.28}$$

$$\mathbf{f}_N(\theta) = \mathbf{f}_{N0} + \sum_{h=1}^{N_h} \mathbf{f}_{Ns}^h \sin(h\theta) + \mathbf{f}_{Nc}^h \cos(h\theta). \tag{4.29}$$

In addition to this, nonlinear terms are transformed into nonlinear equations in frequency domain by using Fourier transformation for each harmonic. By balancing each harmonic, steady-state response of the system is obtained. The formulation of HBM with double harmonic solution is as follows:

$$\begin{aligned} &\mathbf{K}\mathbf{q}_0 + \mathbf{f}_{N0} - \mathbf{f}_0 = 0, \\ &\begin{bmatrix} \mathbf{K} - (h\omega)^2\mathbf{M} & -\gamma\mathbf{K} \\ \gamma\mathbf{K} & \mathbf{K} - (h\omega)^2\mathbf{M} \end{bmatrix} \begin{bmatrix} \mathbf{q}_s^h \\ \mathbf{q}_c^h \end{bmatrix} + \begin{bmatrix} \mathbf{f}_{Ns}^h \\ \mathbf{f}_{Nc}^h \end{bmatrix} - \begin{bmatrix} \mathbf{f}_s^h \\ \mathbf{f}_s^h \end{bmatrix} = 0, \quad h = 1, 2, \ldots, N_h. \end{aligned} \tag{4.30}$$

Equation (4.30) is solved by Newton's method with arc-length continuation. Details on the solution method can be found in [23, 24]. After solving the equation for generalized coordinates, responses of the beams with respect to a fixed point represented in an inertial frame (i.e., earth frame) can be obtained as follows:

$$w_1{}^{(e)}(x_1, t) = \sum_{i=1}^{n_1} \left(\left(\frac{x_1}{L_1} \right)^{i+1} q_{1,i}(t) \right), \tag{4.31}$$

$$w_2{}^{(e)}(x_2, t) = \sum_{i=1}^{n_2} \left(\left(\frac{x_2}{L_2} \right)^{i+1} q_{2,i}(t) \right) + \frac{x_2}{L_2} \frac{L_2}{L_1} \sum_{i=1}^{n_2} \left((i+1)\, q_{1,i}(t) \right). \tag{4.32}$$

4.3 Results and Discussions

In this section, frequency responses of the L-shaped beam at selected locations are obtained by applying the methodology explained in the previous section for several case studies. In order to reduce the number of system parameters, it is assumed that the materials and cross sections of the first and second beams are the same, that is, $\rho = \rho_1 = \rho_2$, $E = E_1 = E_2$, $A = A_1 = A_2$, $I = I_1 = I_2$. Structural damping coefficient of 0.01 is used in the case studies.

4.3.1 Linear Model Results

First, validity of the linear model is checked by comparing the results obtained with results obtained by commercial finite element (FE) software ANSYS. BEAM189 elements are used in the model. Moreover, in order model to perform only in-plane motion, other translational DOFs are fixed. Several studies are performed for the system parameters given in Table 4.1. Using these parameters, other system parameters could be obtained such as L_{M_1}/L_1, $EI/{L_2}^3$, and $EA/2{L_2}^3$. Results of the linear system are compared to the FE software results in Fig. 4.2:

It can be seen that results obtained are identical to each other, which verifies the linear model developed.

Table 4.1 Selected system parameters for Case 1

System parameters	Case 1	System parameters	Case 1	System parameters	Case 1	System parameters	Case 1
$\rho A L_1$	0.3925 kg	M_2	0.1 kg	$\frac{EI}{{L_1}^3}$	1333.3 $\frac{\text{N}}{\text{m}}$	F_0	1 N
$\rho A L_2$	0.3925 kg	L_{M_1}/L_1	0.5	$\frac{EA}{2{L_1}^3}$	8×10^7 $\frac{\text{N}}{\text{m}^3}$	x_f/L_r	$x_f/L_1 = 1$
M_1	0.1 kg	L_{M_2}/L_2	1	L_2	0.5 m		

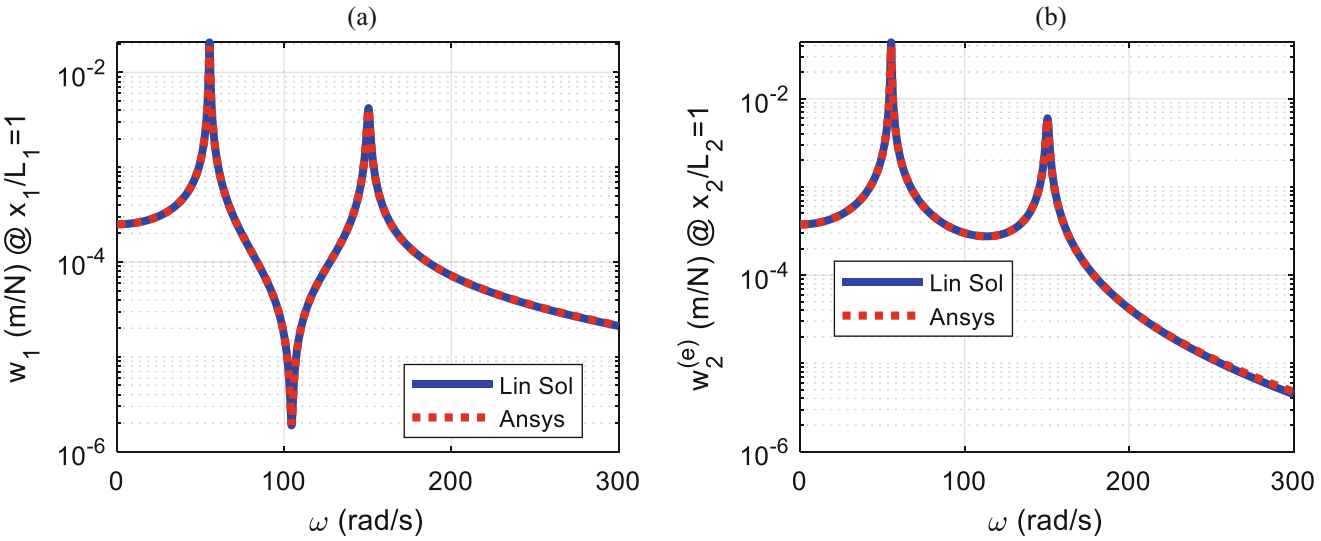

Fig. 4.2 Comparison of the frequency response with ANSYS for Case 1 at (**a**) $x_1/L_1 = 1$, (**b**) $x_2/L_2 = 1$

Table 4.2 Controlled variables and their values

Controlled variable	Case 2: ρAL_1	Case 3: ρAL_2	Case 4: M_1	Case 5: M_2	Case 6: L_{M_1}/L_1	Case 7: L_{M_2}/L_2	Case 8: $EI/L_1{}^3$
Value	0.19625 kg	0.19625 kg	0.5 kg	0.5 kg	1	0.5	666.67 N/m

Table 4.3 Natural frequencies for each case

	ANSYS	Case 1	Case 2	Case 3	Case 4	Case 5	Case 6	Case 7	Case 8
ω_1 (rad/s)	55.365	55.37	29.57	89.557	54.812	35.75	53.796	62.223	39.152
ω_2 (rad/s)	150.36	150.44	118.25	295.91	143.77	106.95	145.64	170.97	106.38

4.3.2 Case Studies

After verifying the linear model, several case studies are performed. Case 1 is used as the basis for the system parameters and for each study, one of the parameters is selected as the controlled variable, while others are kept constant in order to observe its effects on the nonlinear response of the system. The selected controlled variables and their values are given in Table 4.2. Natural frequencies of the linear system for each case are presented in Table 4.3.

In the first case study, in order to observe the effect of forcing amplitude on the nonlinear response of the model, different excitation forcing amplitudes are considered and the normalized responses with respect to forcing amplitudes are compared with each other. It can be seen from Fig. 4.3 that when the forcing is very small, the response is very similar to the response of the linear system. When a forcing with an amplitude of 0.05 N is applied, cubic stiffness nonlinearity starts to take effect. As the forcing amplitude increases, the resonance frequency shifts to the right, which is the outcome of the cubic stiffness nonlinearity dominant in this system. Moreover, when the forcing amplitude is 2 N, the squared nonlinearity becomes effective as seen from the notch at the first resonance.

For the second case study, the effect of the masses of the first and the second beams (ρAL_1 and ρAL_2) on the vibration characteristics are compared. These are labeled as Case 2 and Case 3, respectively. Since densities and areas of each beam are equal to each other, changing these parameters results in the change of the ratio of the beam lengths. The steady-state frequency responses at $x_1/L_1 = 1$ and $x_2/L_2 = 1$ are given in Fig. 4.4. It can be seen from the figures that decreasing the mass of the first beam causes a decrease in the resonance frequencies, whereas decreasing the mass of the second beam causes an increase in the resonance frequencies in contrast to Case 2. Additionally, decrease in the L_2/L_1 ratio makes cubic stiffness more dominant at the first resonance frequency. Moreover, increasing the mass of the first beam amplifies the resonance response at the tip of the beam; similarly, increase in the mass of the second beam amplifies the response at the tip point of the second beam.

The third case study investigates the effect of the concentrated masses connected to the first and second beams (M_1 and M_2) on the vibration characteristics. These are labeled as Case 4 and Case 5, respectively. The frequency responses at $x_1/L_1 = 1$ and $x_2/L_2 = 1$ are obtained and given in Fig. 4.5. It can be clearly seen that increase in the mass of the

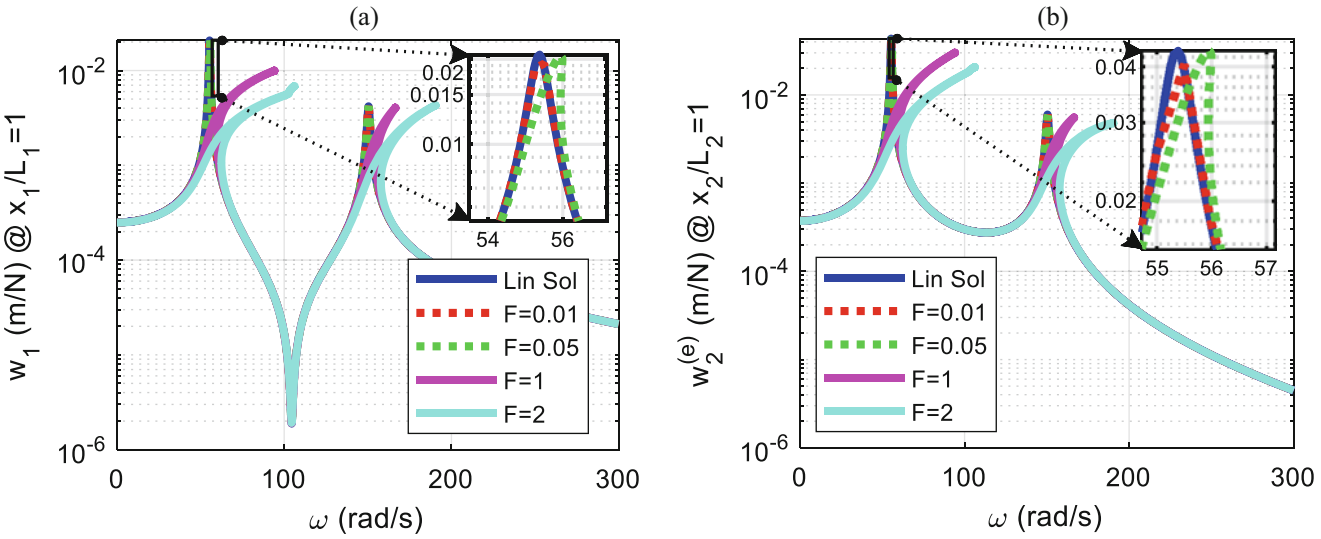

Fig. 4.3 Effect of the forcing amplitude on the response of the beam for Case 1 at (**a**) $x_1/L_1 = 1$, (**b**) $x_2/L_2 = 1$

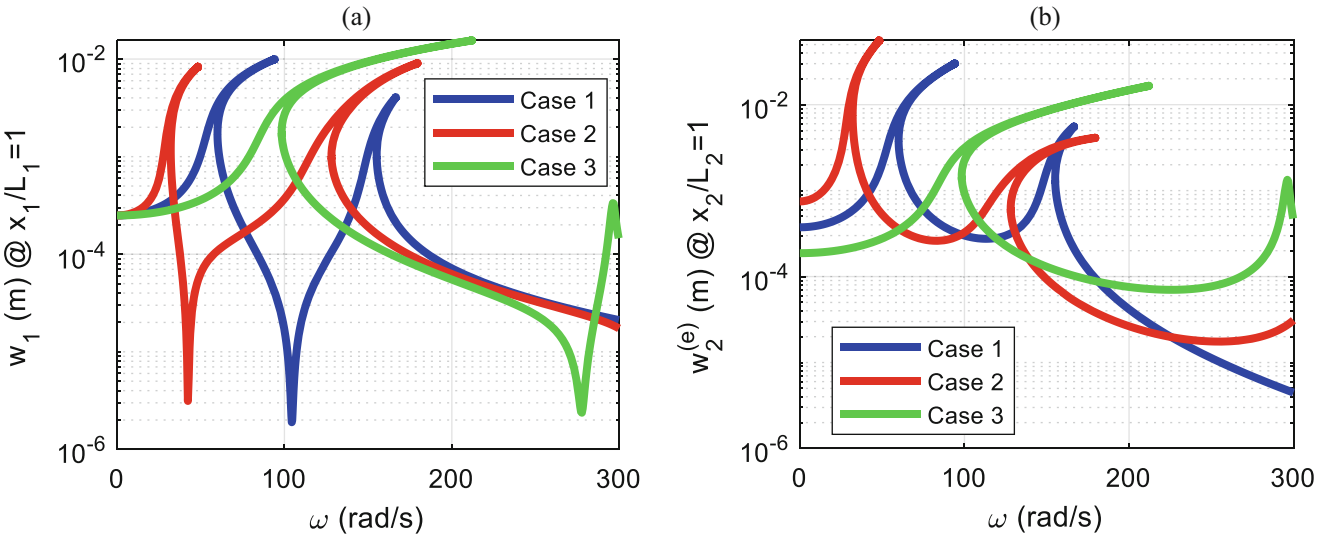

Fig. 4.4 Comparison of the frequency response of the Cases 1, 2, and 3 at (**a**) $x_1/L_1 = 1$, (**b**) $x_2/L_2 = 1$

concentrated mass attached to the first beam has slight effect on the resonance frequencies and frequency responses compared to the concentrated mass attached to the second beam. The increase in the second concentrated mass causes a decrease in the resonance frequencies, which is an expected result. Moreover, increase in the second concentrated mass decreases the resonance amplitude at the tip of the second beam significantly around the second resonance frequency of the L-shaped beam.

The fourth case study investigates the effect of the locations of the first and second concentrated masses (L_{M_1}/L_1 and L_{M_2}/L_2) on the vibration characteristics. These are labeled as Case 6 and Case 7, respectively. The steady-state frequency responses obtained at $x_1/L_1 = 1$ and $x_2/L_2 = 1$ are given in Fig. 4.6. As it can be seen from the results of Case 6, change in the ratio of L_{M_1}/L_1 has negligible effect on the system. On the other hand, decrease in the L_{M_2}/L_2 ratio causes an increase in the resonance frequencies.

In the final case study, the effect of the stiffness of the first beam ($EI/{L_1}^3$) is investigated, which is Case 8. Since the length ratio of the beams is 1.0 for Case 1, the stiffness of the second beam is the same, which means that this parameter affects the stiffness of both the first and second beams. Responses of the L-shaped beam obtained at $x_1/L_1 = 1$ and $x_2/L_2 = 1$ are given in Fig. 4.7. It is observed from the figure that when the stiffness is decreased, the resonance frequencies also decrease. Additionally, as the linear stiffness decreases, the effect of the nonlinear stiffness becomes more dominant. It should be noted

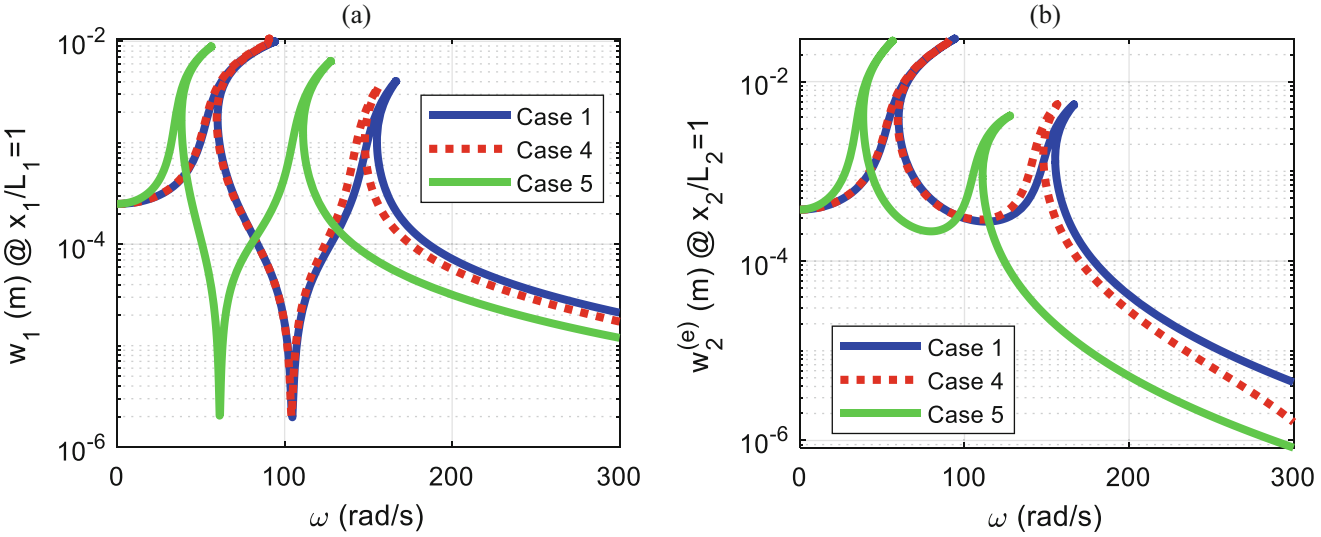

Fig. 4.5 Comparison of the frequency response of the Cases 1, 4, and 5 at (**a**) $x_1/L_1 = 1$, (**b**) $x_2/L_2 = 1$

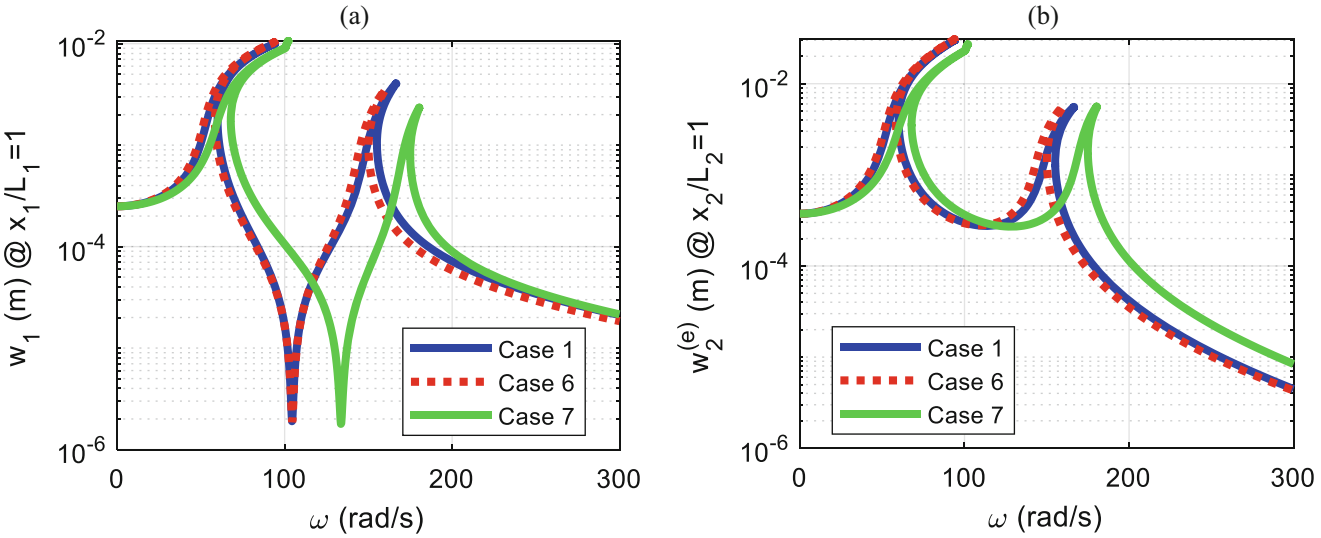

Fig. 4.6 Comparison of the frequency response of the Cases 1, 6, and 7 at (**a**) $x_1/L_1 = 1$, (**b**) $x_2/L_2 = 1$

that quadratic nonlinearity becomes more apparent in the results around the first resonance frequency. It is also observed that the responses at the tips of each beam at the resonance frequencies increase as well.

4.4 Conclusion

In this chapter, the effects of the system parameters on the vibration characteristics of an L-shaped beam are investigated. To do that, the nonlinear equation of motion of an L-shaped beam fixed from one end is derived. The linear mathematical model is verified by using commercial FE software. Finally, the effects of the system parameters are investigated by performing several case studies.

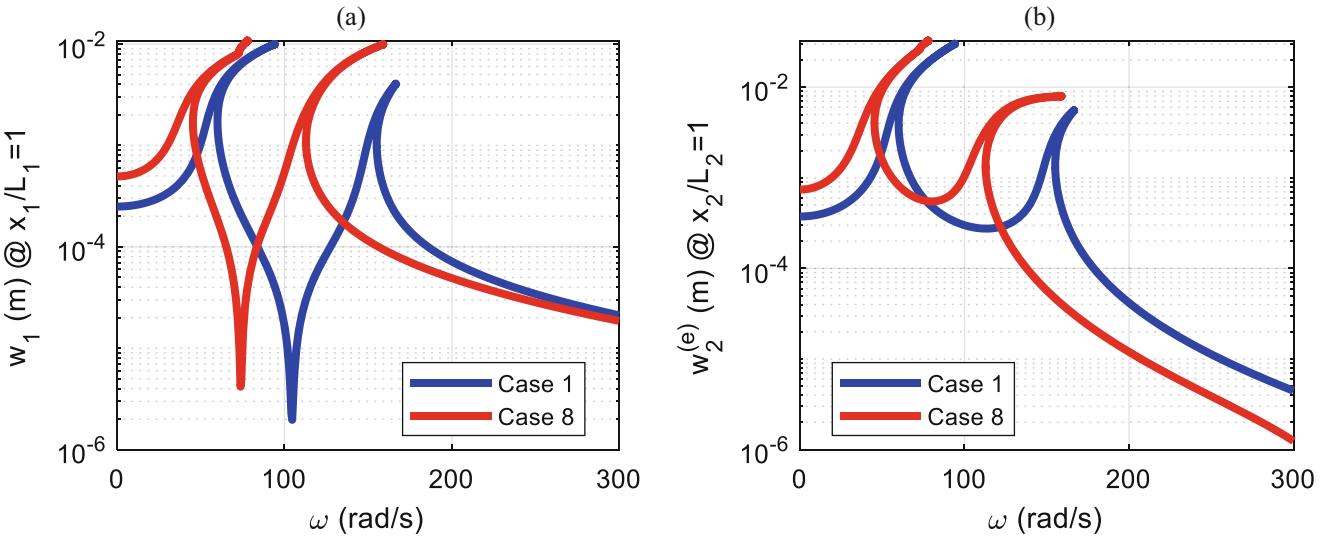

Fig. 4.7 Comparison of the frequency response of the Cases 1 and 8 at (**a**) $x_1/L_1 = 1$, (**b**) $x_2/L_2 = 1$

References

1. Samandari, H., Cigeroglu, E.: Nonlinear vibrations of a flexible L-shaped beam using differential quadrature method. In: Conference Proceedings of the Society for Experimental Mechanics Series, pp. 145–154. Springer New York LLC (2016)
2. Rao, S.S.: Vibration of Continuous Systems. Wiley (2019)
3. Wagg, D., Neild, S.: Nonlinear vibration with control. Solid Mech. Appl. **170**, 215–254 (2010)
4. Tornabene, F., Fantuzzi, N., Ubertini, F., Viola, E.: Strong formulation finite element method based on differential quadrature: a survey. Appl. Mech. Rev. **67**(2), 020801 (2015)
5. Cigeroglu, E., Samandari, H.: Nonlinear free vibrations of curved double walled carbon nanotubes using differential quadrature method. Physica E. **64**, 95–105 (2014)
6. Morales, C.A.: Dynamic analysis of an L-shaped structure by Rayleigh-Ritz substructure synthesis method. Meccanica. **44**(3), 339–343 (2009)
7. Meirovitch, L., Kwak, M.K.: Rayleigh-Ritz based substructure synthesis for flexible multibody systems. AIAA J. **29**(10), 1709 (1991)
8. Morales, C.A.: L-shaped structure mass and stiffness matrices by substructure synthesis. Meccanica. **45**(2), 279–282 (2010)
9. Bang, H.: Analytical solution for dynamic analysis of a flexible L-shaped structure. J. Guid. Control. Dyn. **19**(1), 248–250 (1996)
10. Gürgöze, M.: Comment on "Analytical solution for dynamic analysis of a flexible L-shaped structure". J. Guid. Control. Dyn. **21**(2), 359–359 (1998)
11. Gürgöze, M.: On the dynamic analysis of a flexible L-shaped structure. J. Sound Vib. **211**(4), 683–688 (1998)
12. Oguamanam, D., Hansen, J., Heppler, G.: Vibration of arbitrarily oriented two-member open frames with tip mass. J. Sound Vib. **209**, 651–669 (1998)
13. Georgiades, F., Warminski, J., Cartmell, M.P.: Linear modal analysis of L-shaped beam structures. Mech. Syst. Signal Process. **38**(2), 312–332 (2013)
14. Wei, J., Cao, D., Yang, Y., Huang, W.: Nonlinear dynamical modeling and vibration responses of an L-shaped beam-mass structure. J. Appl. Nonlinear Dyn. **6**(1), 91–104 (2017)
15. Georgiades, F.: Nonlinear equations of motion of L-shaped beam structures. Eur. J. Mech. A. Solids. **65**, 91–122 (2017)
16. Haddow, A.G., Barr, A.D.S., Mook, D.T.: Theoretical and experimental study of modal interaction in a two-degree-of-freedom structure. J. Sound Vib. **97**, 451–473 (1984)
17. Nayfeh, A.H., Zavodney, L.D.: Experimental observation of amplitude-and phase-modulated responses of two internally coupled oscillators to a harmonic excitation. J. Appl. Mech. **55**, 706–710 (1988)
18. Nayfeh, A.H., Balachandran, B., Colbert, M.A., Nayfeh, M.A.: An experimental investigation of complicated responses of a two-degree-of-freedom structure. J. Appl. Mech. **56**(4), 960–967 (1998)
19. Nayfeh, A.H., Balachandran, B.: Experimental investigation of resonantly forced oscillations of a two-degree-of-freedom structure. Int. J. Nonlinear Mech. **25**, 199–209 (1990)
20. Balachandran, B., Nayfeh, A.H.: Nonlinear motions of beam-mass structure. Nonlinear Dyn. **1**, 39–61 (1990)
21. Balachandran, B., Nayfeh, A.H.: Observations of modal interactions in resonantly forced beam-mass structures. Nonlinear Dyn. **2**, 77–117 (1991)
22. Reddy, J.N.: An Introduction to Nonlinear Finite Element Analysis, 2nd edn. Springer (2015)
23. von Groll, G., Ewins, D.J.: The harmonic balance method with arc-length continuation in rotor/stator contact problems. J. Sound Vib. **241**(2), 223–233 (2001)
24. Cigeroglu, E., Samandari, H.: Nonlinear free vibration of double walled carbon nanotubes by using describing function method with multiple trial functions. Physica E. **46**, 160–173 (2012)

Chapter 5
Importance of Virtual Sensing and Model Reduction in the Structural Identification of Bolted Assemblies

Sina Safari and Julian M. Londoño Monsalve

Abstract Creating mathematical models of mechanical structures with bolted joints is still a challenging topic, which is the base of ongoing research efforts to develop methods to characterize and quantify nonlinearities in mechanical structures. An approach to efficiently handle the identification of large nonlinear structural systems using measured data is to formulate the identification problem in a low-dimensional space, that is, nonlinear modal reduced order model (NMROM). This chapter discusses the effects of truncating the order of reduced order model in their prediction accuracy and its impact on the nonlinear model identification process that uses the reduced order model. This chapter also presents results of a virtual sensing strategy that is used alongside to the model reduction to lift the necessity of direct measurement of the degrees of freedom where the active nonlinear element is located. An experimental setup of a bolted joint structure is used to demonstrate the application of reduced order modeling for identification purpose. The results quantify the accuracy of the selected model in predicting global responses of the structure such as amplitude-dependent frequencies and damping ratios.

Keywords Damping nonlinearity · Structural identification · Bolted joints · Virtual sensing · Model reduction

5.1 Introduction

Efficient and lightweight structures developed for the industrial application like aerospace exhibit levels of nonlinearity during vibration test. The development of effective system identification techniques applicable to nonlinear systems is a major demand by dynamitists [1]. In this context, nonlinear characterization and quantification regarded as nonlinear model selection and parameter estimation using measured data is still a challenging task [2]. Although it is possible to build low-dimensional parametric models via nonlinear modal reduced order modeling (NMROM), these techniques usually demand high number of modal bases to accurately approximate the responses of large structural models when modal couplings are present [1]. This issue often compromises the efficiency of model reduction for nonlinear structures and consequently nonlinear identification. This chapter explores ways to efficiently determine the minimum number of modal bases needed to successfully perform the nonlinear identification problem. This is accomplished through a data-driven methodology for the structural identification of nonlinear assemblies with mechanical joints (localized nonlinearities) in which model reduction and virtual sensing are employed to allow identifying nonlinearities in known but inaccessible-to-measure locations.

5.2 Methodology

Consider a multi-degree-of-freedom mechanical system of the form below in the physical domain

$$\boldsymbol{M}\ddot{\boldsymbol{q}}(t) + \boldsymbol{C}\dot{\boldsymbol{q}}(t) + \boldsymbol{K}\boldsymbol{q}(t) + \sum\nolimits_{i=1}^{r} \boldsymbol{\rho}_i^{\mathrm{T}} f_{\mathrm{nl}i}\big(\boldsymbol{\rho}_i \boldsymbol{q}(t), \boldsymbol{\rho}_i \dot{\boldsymbol{q}}(t)\big) = \boldsymbol{F}(t) \tag{5.1}$$

S. Safari (✉) · J. M. Londoño Monsalve
Faculty of Environment, Science and Economy (ESE), University of Exeter, Exeter, UK
e-mail: ss1072@exeter.ac.uk

M. R. W. Brake et al. (eds.), *Nonlinear Structures & Systems, Volume 1*, Conference Proceedings of the Society for Experimental Mechanics Series, https://doi.org/10.1007/978-3-031-36999-5_5

where $\boldsymbol{M}$, $\boldsymbol{C}$, and $\boldsymbol{K}$ are the $m \times m$ matrices of mass, damping, and stiffness, $\boldsymbol{F}$ is the force vector, $\boldsymbol{q}$, $\dot{\boldsymbol{q}}$, and $\ddot{\boldsymbol{q}}$ are, accordingly, the displacement, velocity, and displacement $m \times n$ vectors. Here m is the number of degrees of freedom (DOF) and n is the number of time-domain samples. The nonlinear force vector f_{nl} contains all conservative and nonconservative forces, and $\boldsymbol{\rho}$ is a location vector of the r nonlinear elements. In order to keep the equations short, the time instance t is omitted in the later equations. In the first step, the Iterative Improved Reduced System (IIRS) method [3] is employed for model reduction in the physical domain considering measurement and joint degrees of freedoms as master DOFs and the remaining as slave DOFs. The transformation matrix ($\boldsymbol{T}_{\text{IIRS}}$) obtained using IIRS method is used in the Eq. (5.1) by replacing $\boldsymbol{q} = \boldsymbol{T}_{\text{IIRS}}\boldsymbol{x}$ as follows:

$$\boldsymbol{M}_{\text{IIRS}}\ddot{\boldsymbol{x}} + \boldsymbol{C}_{\text{IIRS}}\dot{\boldsymbol{x}} + \boldsymbol{K}_{\text{IIRS}}\boldsymbol{x} + \sum_{i=1}^{r} \boldsymbol{T}_{\text{IIRS}}{}^{\text{T}}\boldsymbol{\rho}_i^{\text{T}} f_{\text{nl}i}\left(\boldsymbol{\rho}_i \boldsymbol{T}_{\text{IIRS}}\boldsymbol{x}, \boldsymbol{\rho}_i \boldsymbol{T}_{\text{IIRS}}\dot{\boldsymbol{x}}\right) = \boldsymbol{F}_{\text{IIRS}} \tag{5.2}$$

where $\boldsymbol{M}_{\text{IIRS}}$, $\boldsymbol{C}_{\text{IIRS}}$, and $\boldsymbol{K}_{\text{IIRS}}$ are the reduced mass, damping, and stiffness matrices, respectively, and the external force is projected based on $\boldsymbol{F}_{\text{IIRS}} = \boldsymbol{T}_{\text{IIRS}}{}^{\text{T}}\boldsymbol{F}$. Once model reduction in physical domain has been completed, the reduced system in Eq. (5.2) is projected into the modal domain using the matrix of linear mode shapes $\boldsymbol{x} = \boldsymbol{\Phi}\boldsymbol{u}$, which results in Eq. (5.3). Thus, system dynamics can be expressed in terms of the linear modal coordinates $\boldsymbol{u}$:

$$\boldsymbol{M}_{\text{s}}\ddot{\boldsymbol{u}} + \boldsymbol{C}_{\text{s}}\dot{\boldsymbol{u}} + \boldsymbol{K}_{\text{s}}\boldsymbol{u} + \sum_{i=1}^{r} \boldsymbol{\Phi}^{\text{T}}\boldsymbol{T}_{\text{IIRS}}{}^{\text{T}}\boldsymbol{\rho}_i^{\text{T}} f_{\text{nl}i}\left(\boldsymbol{\rho}_i \boldsymbol{T}_{\text{IIRS}}\boldsymbol{\Phi}\boldsymbol{u}, \boldsymbol{\rho}_i \boldsymbol{T}_{\text{IIRS}}\boldsymbol{\Phi}\dot{\boldsymbol{u}}\right) = \boldsymbol{\Phi}^{\text{T}}\boldsymbol{F}_{\text{IIRS}} \tag{5.3}$$

where $\boldsymbol{M}_{\text{s}} = \boldsymbol{\Phi}^{\text{T}}\boldsymbol{M}_{\text{IIRS}}\boldsymbol{\Phi}$, $\boldsymbol{C}_{\text{s}} = \boldsymbol{\Phi}^{\text{T}}\boldsymbol{C}_{\text{IIRS}}\boldsymbol{\Phi}$, and $\boldsymbol{K}_{\text{s}} = \boldsymbol{\Phi}^{\text{T}}\boldsymbol{K}_{\text{IIRS}}\boldsymbol{\Phi}$ are the diagonal modal matrices for mass, damping, and stiffness. Diagonal modal matrices indicate decoupling of the equations of motion in the linear part; however, coupling among linear modes remains and is due to the presence of nonlinear terms in the summation in Eq. (5.3). The displacement $\boldsymbol{x}$ in Eq. (5.2) is divided into two parts: measured DOFs ($\boldsymbol{x}^m$), and unmeasured DOFs ($\boldsymbol{x}^u$). Similarly, the matrix of linear mode shapes $\boldsymbol{\Phi}$ is partitioned into $\boldsymbol{\Phi}^m$ and $\boldsymbol{\Phi}^u$. Using modal expansion approach $\boldsymbol{u}$ can be estimated using $\boldsymbol{x}^m$ and $\boldsymbol{\Phi}^m$; consequently, the response time histories at the unmeasured DOFs, $\boldsymbol{x}^u$, can be estimated as

$$\boldsymbol{x}^u = \boldsymbol{\Phi}^u\left(\boldsymbol{\Phi}^m\right)^{\dagger}\boldsymbol{x}^m \tag{5.4}$$

in which $(\boldsymbol{\Phi}^m)^{\dagger}$ indicates the left pseudo-inverse of matrix $\boldsymbol{\Phi}^m$. Ultimately, it is evident that the modal responses $\boldsymbol{u}$ are projected into the location of each nonlinear element using the transformations: modal transformation $\boldsymbol{\Phi}$, improved transformation matrix $\boldsymbol{T}_{\text{IIRS}}$, and binary location matrix $\boldsymbol{\rho}$. Equation (5.3) can be used directly to discover the nonlinear model and estimate unknown parameters using an optimization problem defined below:

$$\text{Minimize : MSE} = \frac{1}{n}\sum_{i=1}^{n}\left(\boldsymbol{y}^*_{\text{mm}_i} - \boldsymbol{y}_{\text{mm}i}\right)^2 + \frac{1}{n_{\text{c}}}\sum_{j=1}^{n_{\text{c}}}\frac{1}{n}\sum_{i=1}^{n}\left(\boldsymbol{y}^*_{\text{cm}(j)_i} - \boldsymbol{y}_{\text{cm}(j)_i}\right)^2 \tag{5.5a}$$

$$\boldsymbol{y}^* = \boldsymbol{\varphi}^{\text{T}}\boldsymbol{T}_{\text{IIRS}}{}^{\text{T}}\boldsymbol{F}, \text{ and } \boldsymbol{y} = \boldsymbol{M}_{\text{s}}\ddot{\boldsymbol{u}} + \boldsymbol{C}_{\text{s}}\dot{\boldsymbol{u}} + \boldsymbol{K}_{s}\boldsymbol{u} + \sum_{i=1}^{r}\boldsymbol{\varphi}^{\text{T}}\boldsymbol{T}_{\text{IIRS}}{}^{\text{T}}\boldsymbol{\rho}_i^{\text{T}} f_{\text{nl}i}\left(\boldsymbol{\rho}_i \boldsymbol{T}_{\text{IIRS}}\boldsymbol{\varphi}\boldsymbol{u}, \boldsymbol{\rho}_i \boldsymbol{T}_{\text{IIRS}}\boldsymbol{\varphi}\dot{\boldsymbol{u}}\right) \tag{5.5b}$$

where n is the size of the time-series data; $\boldsymbol{y}^*$ and $\boldsymbol{y}$ are the input force and internal force vectors, respectively. Subscripts mm and cm indicate the mode number for main and coupled modes, and n_{c} is the number of coupled modes. The mode in which the structure is excited close to its natural frequency is chosen to be the main mode. Coupled modes are those in which a strong coupling to the main mode is anticipated.

5.3 Analysis and Discussion

The application of the proposed approach to the case of the length-modified Brake–Reuß beam (LBRB) with frictional three-bolted lap-joint is discussed. The LBRB consists of two beam components with square cross-section that are bolted through a three-bolted lap-joint together to form a long beam. The total length of the beam is about 1080 mm (42.5 in) and the cross-section of the beams is a 25.4 mm × 25.4 mm (1 in × 1 in) square. Three sets of M8 bolts, nuts, and standard washers are used for the assembly, which has a 120 mm × 25.4 mm contacting interface. For modeling the bolted lap-joint, we considered the "whole-joint" approach presented by Lacayo et al. [4]. The whole-joint model is characterized by a linear spring in the normal direction and a nonlinear element in the tangential direction. For this virtual experiment example, all five whole-joint models consist of a linear spring with stiffness 1×10^8 Nm^{-1} connecting the normal (Y) direction DOF

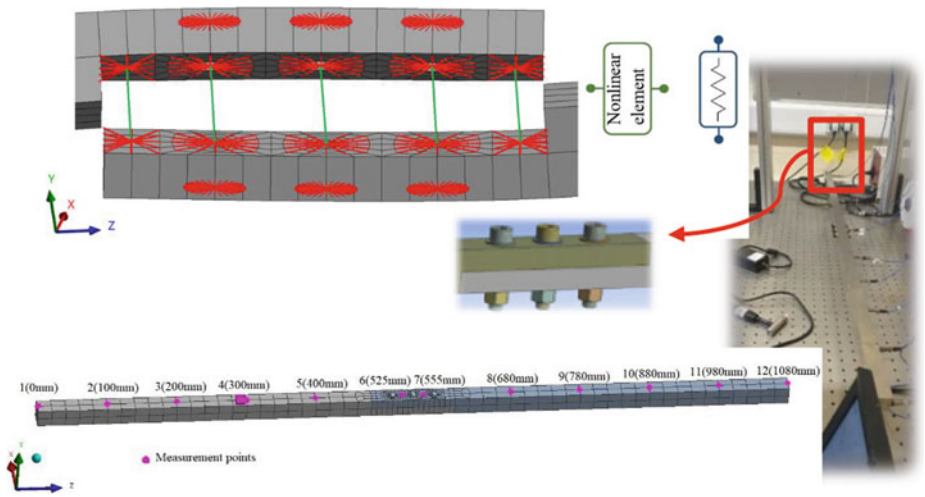

Fig. 5.1 LBRB structure with joint modeling detail

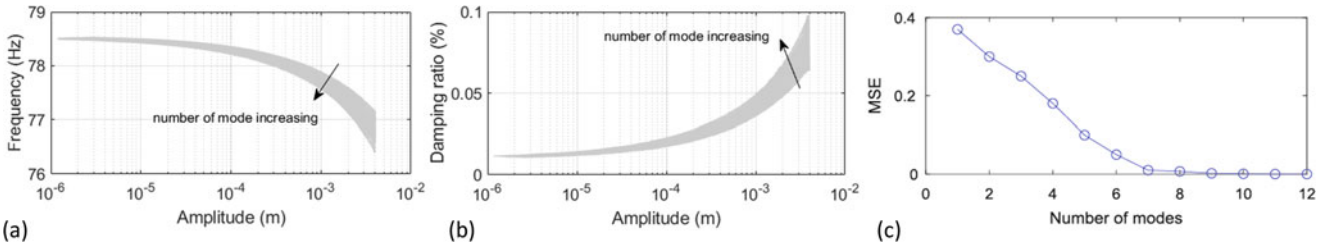

Fig. 5.2 (**a**) Instantaneous frequency, (**b**) instantaneous damping ratio, and (**c**) prediction error

and a 4-parameter Iwan element [4] with parameters $f_y = 2000$ N, $k_t = 1 \times 10^8$ Nm^{-1}, $\chi = -0.5$, and $\beta = 0.1$ connecting the axial (z) direction DOF. During the model reduction, 12 DOFs are retained as measurement points (see Fig. 5.1) and 20 DOFs retained kept in the joint location so that the reduced model in physical space has 32 DOFs.

Modal displacement of 0.004 m at the beam tip for the first mode is considered to initialize the simulations and the free decay response is recorded in the same location. Figure 5.2a, b shows the variation of amplitude-dependent response of the structure when the number of modes is increasing and Fig. 5.2c shows the prediction error based on Eq. (5.5). It can be seen that using almost 7 first mode is adequate for accurate identification of this specific structure.

5.4 Conclusion

Nonlinear system identification of bolted structure is conducted here using an optimization-based identification method employing reduced order modeling. The importance of considering a number of modes during the identification process is addressed based on the prediction error of the identified model. It is also shown that virtual sensing can help to build nonlinear models of engineering structures with local nonlinearities.

Acknowledgments Mr. Safari is support by the scholarship from the College of Engineering, Mathematics, and Physical Sciences, University of Exeter, which is gratefully acknowledged.

References

1. Noël, J.P., Kerschen, G.: Nonlinear system identification in structural dynamics: 10 more years of progress. Mech. Syst. Signal Process. **83**, 2–35 (2017)

2. Safari, S., Londoño Monsalve, J.M.: Direct optimisation based model selection and parameter estimation using time-domain data for identifying localised nonlinearities. J. Sound Vib. **501**, 116056 (2021)
3. Friswell, M.I., Garvey, S.D., Penny, J.E.T.: Model reduction using dynamic and iterated IRS techniques. J. Sound Vib. **186**, 311–323 (1995)
4. Lacayo, R., Pesaresi, L., Groß, J., Fochler, D., Armand, J., Salles, L., Schwingshackl, C., Allen, M., Brake, M.: Nonlinear modeling of structures with bolted joints: a comparison of two approaches based on a time-domain and frequency-domain solver. Mech. Syst. Sig. Process. **114**, 413–438 (2019)

Chapter 6
On the Harmonic Balance Method Augmented with Nonsmooth Basis Functions for Contact/Impact Problems

Brian Evan Saunders, Robert J. Kuether, Rui M. G. Vasconcellos, and Abdessattar Abdelkefi

Abstract In this work, we evaluate the usefulness of nonsmooth basis functions for representing the periodic response of a nonlinear system subject to contact/impact behavior. As with sine and cosine basis functions for classical Fourier series, which have C^{∞} smoothness, nonsmooth counterparts with C^0 smoothness are defined to develop a nonsmooth functional representation of the solution. Some properties of these basis functions are outlined, such as periodicity, derivatives, and orthogonality, which are useful for functional series applied via the Galerkin method. Least-squares fits of the classical Fourier series and nonsmooth basis functions are presented and compared using goodness-of-fit metrics for time histories from vibro-impact systems with varying contact stiffnesses. This formulation has the potential to significantly reduce the computational cost of harmonic balance solvers for nonsmooth dynamical systems. Rather than requiring many harmonics to capture a system response using classical, smooth Fourier terms, the frequency domain discretization could be captured by a combination of a finite Fourier series supplemented with nonsmooth basis functions to improve convergence of the solution for contact-impact problems.

Keywords Harmonic balance · Contact/impact · Nonsmooth · Basis functions · Galerkin method

6.1 Introduction

The harmonic balance method (HBM) is now widely used in recent years to obtain periodic responses to both weakly and strongly nonlinear dynamical systems. Recent developments have allowed HBM to be efficiently combined with numerical continuation for both small- and large-scale systems and for stability analysis, bifurcation detection and tracking, and nonlinear modal analysis [1]. Some researchers have worked to expand HBM to nonsmooth nonlinearities such as friction and contact [2]. A major difficulty with nonsmooth nonlinearities is the Gibbs phenomenon, which leads to inaccuracies near nonsmooth points with discontinuous derivatives. Also, nonsmooth solutions only converge polynomially unlike exponentially for smooth solutions [3]. To resolve this problem, some researchers used Lanczos filtering to improve the values of the Fourier coefficients [2]. Some work has been done on appending additional, nonsmooth, or discontinuous terms to a system's solution [4], as well as replacing some or all the terms in classical Fourier series with nonsmooth terms [5]. A priori knowledge of the state transition times may be required. Other works utilized event-driven schemes to find and integrate between the state transition times to compute nonlinear forces [6]. Nonsmooth temporal and spatial transformations have also been studied in detail [7].

In this work, we evaluate the usefulness of nonsmooth basis functions for efficiently representing the periodic response of a nonlinear system subject to contact/impact behavior. The objective is to combine desirable traits from previous works and eventually create an improved harmonic balance formulation that supplements the Fourier series with additional nonsmooth terms. Nonsmooth functions with C^0 smoothness are defined to develop a nonsmooth functional representation of a solution. Rather than using Fourier series with many harmonics to capture a nonsmooth system response, it may instead be obtainable

B. E. Saunders (✉) · A. Abdelkefi
Mechanical & Aerospace Engineering Department, New Mexico State University, Las Cruces, NM, USA
e-mail: bevan343@nmsu.edu

R. J. Kuether
Sandia National Laboratories, Albuquerque, NM, USA

R. M. G. Vasconcellos
Campus of São João da Boa Vista, São Paulo State University, São João da Boa Vista, Brazil

M. R. W. Brake et al. (eds.), *Nonlinear Structures & Systems, Volume 1*, Conference Proceedings of the Society for Experimental Mechanics Series, https://doi.org/10.1007/978-3-031-36999-5_6

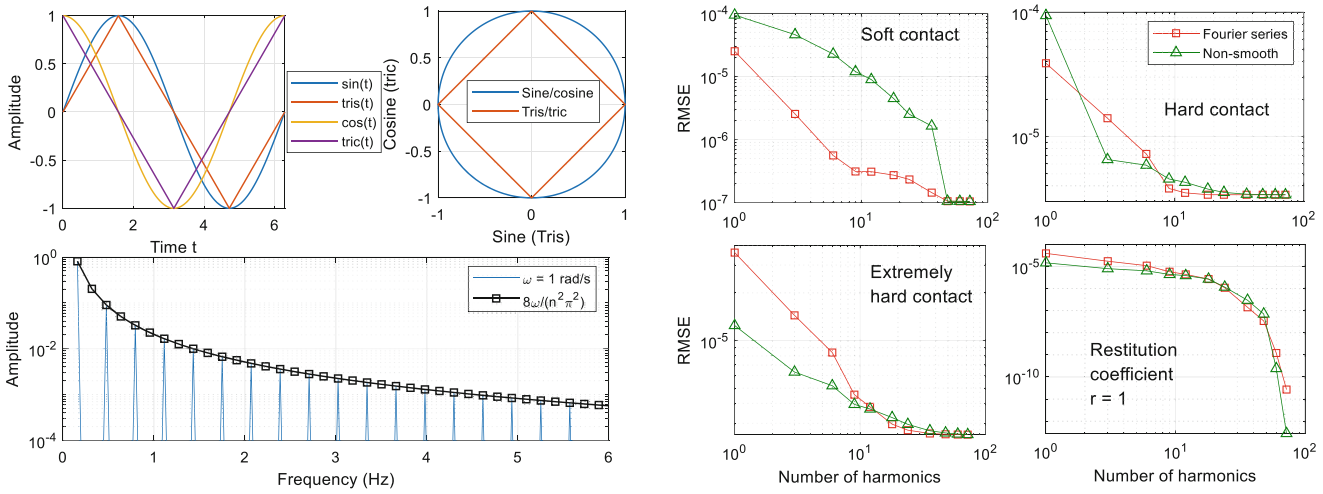

Fig. 6.1 (**a**) Time histories, phase portraits, and FFT spectra comparing the sine/cosine functions to their nonsmooth counterparts. (**b**) RMSE of Fourier series and nonsmooth series curve fits to time data of dynamical systems with three levels of penalty stiffness, and with a perfectly elastic, restitution-based contact law

by combining a truncated Fourier series with a number of nonsmooth basis functions. This highlights a potential to significantly reduce the computational cost of harmonic balance solvers for nonsmooth dynamical systems. Properties, such as periodicity, derivatives, and orthogonality are outlined. Goodness-of-fit metrics are used to evaluate the classical Fourier series and the nonsmooth basis functions, using time data from different contact systems, to provide a proof of concept for the formulation.

6.2 Nonsmooth Galerkin Formulation

The nonsmooth basis functions investigated here are periodic triangle waves with the same periodicity, maxima, minima, and roots as sine and cosine waves. The basis functions are denoted as "triangle sine" tris(ωt) and "triangle cosine" tric(ωt), respectively, for frequency ω and time t. The basis functions can be mathematically defined and used in a nonsmooth series:

$$\text{tris}(\omega t) = \begin{cases} \frac{4}{T}t_m, & t_m < \frac{T}{4} \\ \frac{-4}{T}t_m + 2, & \frac{T}{4} \leq t_m \leq \frac{3T}{4} \\ \frac{4}{T}t_m - 4, & t_m > \frac{3T}{4} \end{cases}, \quad \text{tric}\,(\omega t) = \begin{cases} \frac{-4}{T}t_m + 1, & t_m \leq \frac{T}{2} \\ \frac{4}{T}t_m - 3, & t_m > \frac{T}{2} \end{cases}, \tag{6.1a, b}$$

$$f(t) = a_0 + \textstyle\sum_{n=1}^{\infty} a_n \text{tric}\,(n\omega t) + b_n \text{tris}\,(n\omega t)\,, \tag{6.2}$$

where $t_m = \omega t (\text{mod} T)$ ensures periodicity of the function over a time period $T = 2\pi$, and the values a_0, a_n, b_n denote weighting coefficients that scale each function. Given a time history, a nonsmooth series can be curve-fitted to the data using least-squares regression. Figure 6.1a shows the time histories, phase portraits, and FFT spectra comparing the sine and cosine functions to their nonsmooth counterparts tris and tric. The nonsmooth functions parametrize the unit diamond, and the FFT peaks follow a known pattern, which is mathematically derived to decay polynomially.

6.3 Least-Squares Regression Analysis

Figure 6.1b presents the root mean square error (RMSE) of the Fourier series and nonsmooth series curve fits to different sets of contact/impact time data for a periodic orbit, as the number of harmonics increases. The time histories were obtained from a forced Duffing oscillator with freeplay using two different contact laws, shown in Eq. (6.3). Three responses use a penalty

stiffnesses (soft, hard, and extremely hard), namely linear stiffness K_c added when the system crosses contact boundaries $x = -j_1$ or $x = j_2$. A fourth case uses an elastic coefficient of restitution ($r = 1$) to relate the velocities right before and after an impact, x^-, x^+. The third stiffness case produces a response, which resembles the restitution-based response.

$$m\ddot{x} + c\dot{x} + kx + \alpha x^3 + F_c(x) = p\cos(\omega t)\,, \tag{6.3a}$$

$$F_c(x) = \begin{cases} K_c\,(x + j_1)\,, & x < -j_1 \\ 0, & -j_1 \le x \le j_2 \\ K_c\,(x - j_2)\,, & x > j_2 \end{cases}, \quad x^+ = -rx^-, r = 1 \tag{6.3b, c}$$

For soft contact, the system response is smooth, and classical Fourier series converges much faster than the nonsmooth series. Hard contact produces a less-smooth response, and both curve fits tend to swap accuracy. Extremely hard stiffness leads to a strong nonsmooth response, and the nonsmooth series converges faster than Fourier series until approximately 12 harmonics are used. Elastic rigid impact leads to a perfectly nonsmooth response, and the nonsmooth series produces closer results if either few or many harmonics are used.

6.4 Conclusion

In this work, we evaluated the usefulness of nonsmooth basis functions for efficiently obtaining the response of a nonlinear system subject to contact/impact behavior. The nonsmooth functions were defined, their similarities to sine and cosine functions were highlighted, and different cases of contact/impact time histories were curve-fitted with Fourier series and the nonsmooth series. Results show Fourier series is superior for smooth responses, but the nonsmooth series becomes superior for increasingly nonsmooth responses. However, Fourier series tends to become more accurate again when many harmonics are used. This behavior will be explored in the final conference presentation, along with other methods for defining the nonsmooth series to represent periodic orbits from vibro-impact systems.

Acknowledgments The authors B. Saunders and A. Abdelkefi gratefully acknowledge the support from Sandia National Laboratories. This study describes objective technical results and analysis. Any subjective views or opinions that might be expressed in this chapter do not necessarily represent the views of the U.S. Department of Energy or the United States Government. Supported by the Laboratory Directed Research and Development program at Sandia National Laboratories, a multimission laboratory managed and operated by National Technology and Engineering Solutions of Sandia LLC, a wholly owned subsidiary of Honeywell International Inc. for the U.S. Department of Energy's National Nuclear Security Administration under contract DE-NA0003525. SAND2022-14790 C. R. Vasconcellos acknowledges the financial support of the Brazilian agency CAPES (grant 88881.302889/2018-01).

References

1. Detroux, T., Renson, L., Masset, L., Kerschen, G.: The harmonic balance method for bifurcation analysis of large-scale nonlinear mechanical systems. Comput. Methods Appl. Mech. Eng. **296**, 18–38 (2015). https://doi.org/10.1016/j.cma.2015.07.017
2. Colaïtis, Y., Batailly, A.: The harmonic balance method with arc-length continuation in blade-tip/casing contact problems. J. Sound Vib. **502**, 116070 (2021). https://doi.org/10.1016/j.jsv.2021.116070
3. Wang, W., Lu, Z.R., Liu, J.: Convergence rates of harmonic balance method for periodic solution of smooth and non-smooth systems. Commun. Nonlinear Sci. Numer. Simul. **99**, 105826 (2021). https://doi.org/10.1016/j.cnsns.2021.105826
4. Brake, M.R., Segalman, D.J.: Modelling localized nonlinearities in continuous systems via the method of augmentation by non-smooth basis functions. Proc. R. Soc. A Math. Phys. Eng. Sci. **469**(2158), 20130260 (2013). https://doi.org/10.1098/rspa.2013.0260
5. Kim, W.J., Perkins, N.C.: Harmonic balance/Galerkin method for non-smooth dynamic systems. J. Sound Vib. **261**(2), 213–224 (2003). https://doi.org/10.1016/S0022-460X(02)00949-5
6. Krack, M., Panning-von Scheidt, L., Wallaschek, J.: A high-order harmonic balance method for systems with distinct states. J. Sound Vib. **332**(21), 5476–5488 (2013). https://doi.org/10.1016/j.jsv.2013.04.048
7. Pilipchuk, V.N.: Nonlinear Dynamics: Between Linear and Impact Limits, vol. 52. Springer Science & Business Media (2010)

Chapter 7
Periodic Response Prediction for Hybrid and Piecewise Linear Systems

G. Manson

Abstract This chapter presents a completely novel framework for the prediction and understanding of nonlinear system behavior. The idea is simply that all nonlinear systems can be represented as a combination of linear systems between which information is exchanged. Under harmonic excitation, the periodic responses of such hybrid systems may be easily calculated when the switching between linear systems is specified in terms of time. These time-switching hybrid systems provide a useful stepping stone to more realistic piecewise linear systems where the switching criteria are specified in terms of displacement and/or velocity. This chapter details the framework and illustrates its ability to efficiently predict the periodic responses from piecewise linear systems. The framework is also shown to be capable of predicting both stable and unstable periodic responses for conditions where jump behavior is possible. The extension of the work to continuous nonlinear systems is also briefly discussed.

Keywords Nonlinear · Hybrid systems · Piecewise linear

7.1 Introduction

The environmental and economic pressures of the last couple of decades have resulted in an unprecedented effort on the part of structural design engineers to design structures that are more lightweight than, yet are at least as strong as, their structural ancestors. While this drive for strong, lightweight structures is clearly desirable, in many cases, this will also result in the structural response becoming significantly nonlinear. While research has been conducted into nonlinear system behavior for centuries, the current situation appears to be, as Worden and Tomlinson wrote in their monograph "Nonlinearity in Structural Dynamics" [1] that "there is no unique approach to dealing with the problem of nonlinearity either analytically or experimentally and thus we must be prepared to experiment with several approaches." The primary aim of this monograph was to introduce and explain a number of these approaches that would belong in a "toolbox" for the analysis of nonlinear structural systems and included Harmonic Balance [2], Hilbert Transform [3], NARMAX modeling [4], the Masri-Caughey Restoring Force Surface method [5], Direct Parameter Estimation [6], and the Volterra Series approximation [7]. Approaches not considered in the monograph included perturbation methods [8], multiple scales [9], and nonlinear normal modes [10]. The research conducted using the aforementioned approaches over the last five or so decades has undoubtedly led to much greater understanding of the behavior of nonlinear systems and has resulted in countless applications. That said, it is fair to say that all approaches are not without their limitations. These limitations are often associated with the need for approximation or, where infinite series are being employed, are associated with the related issues of series convergence and truncation. Another limitation with the bulk of these approaches is that they are only capable of representing what is often termed "weak nonlinearity."

One of the reasons as to why there has not yet emerged a General Theory of Nonlinearity may be in the nonlinear dynamicists' simple system of choice, namely, the Duffing oscillator [11]. While the classical Duffing oscillator model of a linear plus cubic stiffness term lends itself as a good approximation for many real engineering systems, it may not have been the best starting point for the development of a General Theory. The author would instead like to propose that a better starting point may be provided via hybrid systems and, their close counterparts, piecewise linear systems. The reason behind this proposal is that the responses of such systems may be written in terms of linear steady-state and linear transient

G. Manson (✉)
Dynamics Research Group, Department of Mechanical Engineering, University of Sheffield, Sheffield, UK
e-mail: graeme.manson@sheffield.ac.uk

M. R. W. Brake et al. (eds.), *Nonlinear Structures & Systems, Volume 1*, Conference Proceedings
of the Society for Experimental Mechanics Series, https://doi.org/10.1007/978-3-031-36999-5_7

components without any recourse to a framework that presupposes the nature of the resulting response. Within the field of Control Engineering, hybrid systems are very well known and there have been several papers [12–14] that have demonstrated that such systems are capable of the most extreme form of nonlinear behavior, namely, chaos. It should be stated however that these papers all relied upon numerical simulation as opposed to any theoretical framework, which is the purpose of this chapter.

The layout of this chapter is as follows: Sect. 7.2 develops the closed-form solution for the periodic response of a harmonically-excited time-switched hybrid system. Section 7.3 introduces an iterative approach that allows the closed-form solution of the previous section to be used for the prediction of periodic responses of piecewise linear systems, including the identification of stable and unstable solutions when the jump phenomenon is present. Section 7.4 rounds off with some discussion including how the approach may eventually be extended to predict the periodic responses of the Duffing oscillator.

7.2 Periodic Response of Harmonically-Excited Time-Switched Hybrid Systems

In this section, the format of the hybrid system will be introduced, followed by the development of the theory regarding the calculation of the periodic responses of these systems. The hybrid system will be composed of n linear systems with a single linear system being active at any point in time. The equation of motion for the ith linear system is written in nondimensional form:

$$\ddot{Y}(\tau) + \underbrace{2\zeta_i \left(\dot{Y}(\tau) - \dot{Y}_{\text{offset}_i}\right)}_{F_{\text{d}_i}} + \underbrace{\gamma_i \left(Y(\tau) - Y_{\text{offset}_i}\right)}_{F_{\text{s}_i}} = \cos(\alpha\tau) \tag{7.1}$$

The above equation allows each linear system to have individual damping and stiffness parameters ζ_i and γ_i. The inclusion of $\dot{Y}_{\text{offset}_i}$ and Y_{offset_i} means that the zero values of damping force F_{d_i} and stiffness force F_{s_i} may occur at nonzero values of velocity and displacement, respectively.

The time point at which the active system changes will be referred to as a time switch. There will be multiple time switches and therefore, there will be multiple response segments. Assuming that the jth response segment occurs when the ith linear system is active, the total output displacement and velocity response segments, $Y_j(\tau)$ and $\dot{Y}_j(\tau)$, respectively, may be expressed as a sum of the steady-state and transient response segments:

$$\begin{aligned} Y_j(\tau) &= Y_{\text{ss}_j}(\tau) + Y_{\text{tr}_j}(\tau) \\ \dot{Y}_j(\tau) &= \dot{Y}_{\text{ss}_j}(\tau) + \dot{Y}_{\text{tr}_j}(\tau) \end{aligned} \tag{7.2}$$

The steady-state displacement response segment $Y_{\text{ss}_j}(\tau)$ may be written as follows:

$$Y_{\text{ss}_j}(\tau) = \frac{2\zeta_i}{\gamma_i}\dot{Y}_{\text{offset}_i} + Y_{\text{offset}_i} + |H_i(\alpha)| \cos\left(\alpha\tau + \angle H_i(\alpha)\right) \tag{7.3}$$

where $H_i(\alpha)$, the frequency response function (FRF) of the ith linear system, is given by

$$H_i(\alpha) = \frac{1}{\gamma_i - \alpha^2 + i2\zeta_i\alpha} \tag{7.4}$$

The steady-state velocity response segment $\dot{Y}_{\text{ss}_j}(\tau)$ is the derivative of Eq. (7.3):

$$\dot{Y}_{\text{ss}_j}(\tau) = -\alpha\,|H_i(\alpha)| \sin\left(\alpha\tau + \angle H_i(\alpha)\right) \tag{7.5}$$

The transient displacement response segment $Y_{\text{tr}_j}(\tau)$ will be written as follows:

$$Y_{\text{tr}_j}(\tau) = \exp\left(-\zeta_i\left(\Delta\tau_j\right)\right)\left[A_j \cos\left(\beta_i\left(\Delta\tau_j\right)\right) + B_j \sin\left(\beta_i\left(\Delta\tau_j\right)\right)\right] \tag{7.6}$$

where $\beta_i = \sqrt{\gamma_i - \zeta_i^2}$ and $\Delta\tau_j$ is the dimensionless time measured from the point at which the system became active. The transient parameters A_j and B_j will be calculated to ensure that the displacement and velocity values of the newly active system and those of the previously active system are the same at the point of switching.

The transient velocity response segment $\dot{Y}_{\mathrm{tr}_j}(\tau)$ is the derivative of Eq. (7.6):

$$\dot{Y}_{\mathrm{tr}_j}(\tau) = \exp\left(-\zeta_i\left(\Delta\tau_j\right)\right)\left[\left(\beta_i B_j - \zeta_i A_j\right)\cos\left(\beta_i\left(\Delta\tau_j\right)\right) + \left(-\beta_i A_j - \zeta_i B_j\right)\sin\left(\beta_i\left(\Delta\tau_j\right)\right)\right] \tag{7.7}$$

The above equations may now be used for the first idea of this chapter, namely, that the periodic response of harmonically-excited hybrid systems, subjected to time switches that occur at the same point in the forcing cycle, may be expressed in a closed-form. It is assumed that the system parameters will be specified for each system as will the forcing frequency ratio α. Information regarding the times at which specific linear systems become active will also need to be specified. If there are a total of m time switches, vectors of size $1 \times m$ must be specified that state which linear system becomes active at each switch and the time at which that switch occurs. The active system vector will be labeled S and the time switch vector will be labeled τ_{sw}. All elements S_j (where $j = 1, \ldots, m$) must be integers between 1 and n, while all elements τ_{sw_j} (where $j = 1, \ldots, m$) must be between zero and the repeat period $\tau_{\mathrm{period}} = 2\pi/\alpha$. It is also necessary that successive elements of τ_{sw} must increase in value (in order to give a positive value for time spent in each active system) – there can be a single decrease in value, which will describe a "wrap-around" effect into the next forcing period. This concept should become clearer when an illustrative example is considered shortly. Once the τ_{sw} vector has been specified, the $\Delta\tau$ vector that details the time spent in each active system segment may be calculated.

The time spent in system S_j (if $j \neq m$) is given by

$$\begin{aligned} \Delta\tau_j &= \tau_{\mathrm{sw}_{j+1}} - \tau_{\mathrm{sw}_j} \text{ if } \tau_{\mathrm{sw}_{j+1}} > \tau_{\mathrm{sw}_j} \\ \Delta\tau_j &= \tau_{\mathrm{period}} + \tau_{\mathrm{sw}_{j+1}} - \tau_{\mathrm{sw}_j} \text{ if } \tau_{\mathrm{sw}_{j+1}} < \tau_{\mathrm{sw}_j} \end{aligned} \tag{7.8}$$

and, if $j = m$, the time spent in system S_j is given by

$$\begin{aligned} \Delta\tau_j &= \tau_{\mathrm{sw}_1} - \tau_{\mathrm{sw}_m} \text{ if } \tau_{\mathrm{sw}_1} > \tau_{\mathrm{sw}_m} \\ \Delta\tau_j &= \tau_{\mathrm{period}} + \tau_{\mathrm{sw}_1} - \tau_{\mathrm{sw}_m} \text{ if } \tau_{\mathrm{sw}_1} < \tau_{\mathrm{sw}_m} \end{aligned} \tag{7.9}$$

As stated previously, the closed-form expression for the periodic responses of harmonically-excited hybrid systems will be derived via equating the displacement of the newly active system to that of the previously active system at each time switch and doing the same with the velocity. Expressing the displacements and velocities in terms of steady-state and transient components gives rise to expressions that equate the steady-state differences to the transient differences as shown below (for $j \neq 1$):

$$\begin{aligned} Y_{\mathrm{tr}_j}\left(\tau_{\mathrm{sw}_j}\right) - Y_{\mathrm{tr}_{j-1}}\left(\tau_{\mathrm{sw}_j}\right) &= Y_{\mathrm{ss}_{j-1}}\left(\tau_{\mathrm{sw}_j}\right) - Y_{\mathrm{ss}_j}\left(\tau_{\mathrm{sw}_j}\right) \\ \dot{Y}_{\mathrm{tr}_j}\left(\tau_{\mathrm{sw}_j}\right) - \dot{Y}_{\mathrm{tr}_{j-1}}\left(\tau_{\mathrm{sw}_j}\right) &= \dot{Y}_{\mathrm{ss}_{j-1}}\left(\tau_{\mathrm{sw}_j}\right) - \dot{Y}_{\mathrm{ss}_j}\left(\tau_{\mathrm{sw}_j}\right) \end{aligned} \tag{7.10}$$

and, for $j = 1$,

$$\begin{aligned} Y_{\mathrm{tr}_1}\left(\tau_{\mathrm{sw}_1}\right) - Y_{\mathrm{tr}_m}\left(\tau_{\mathrm{sw}_1}\right) &= Y_{\mathrm{ss}_m}\left(\tau_{\mathrm{sw}_1}\right) - Y_{\mathrm{ss}_1}\left(\tau_{\mathrm{sw}_1}\right) \\ \dot{Y}_{\mathrm{tr}_1}\left(\tau_{\mathrm{sw}_1}\right) - \dot{Y}_{\mathrm{tr}_m}\left(\tau_{\mathrm{sw}_1}\right) &= \dot{Y}_{\mathrm{ss}_m}\left(\tau_{\mathrm{sw}_1}\right) - \dot{Y}_{\mathrm{ss}_1}\left(\tau_{\mathrm{sw}_1}\right) \end{aligned} \tag{7.11}$$

The steady-state displacement for the jth response segment (i.e., when system S_j is active) at the kth time switch is given by

$$Y_{\mathrm{ss}_j}\left(\tau_{\mathrm{sw}_k}\right) = \frac{2\zeta_{\mathrm{S}_j}}{\gamma_{S_j}}\dot{Y}_{\mathrm{offset}_{S_j}} + Y_{\mathrm{offset}_{S_j}} + \left|H_{S_j}(\alpha)\right|\cos\left(\alpha\tau_{\mathrm{sw}_k} + \angle H_{S_j}(\alpha)\right) \tag{7.12}$$

and the corresponding steady-state velocity is

$$\dot{Y}_{\mathrm{ss}_j}\left(\tau_{\mathrm{sw}_k}\right) = -\alpha\left|H_{S_j}(\alpha)\right|\sin\left(\alpha\tau_{\mathrm{sw}_k} + \angle H_{S_j}(\alpha)\right) \tag{7.13}$$

The transient displacement and velocity expressions at each time switch are a little less straightforward, and it is also necessary to develop expressions that relate the transient behavior between successive time switches. The transient displacement for the *j*th response segment (i.e., when system S_j is active) is given by

$$Y_{\mathrm{tr}_j}\left(\tau_{\mathrm{sw}_j}+\tau_j\right)=\exp\left(-\zeta_{S_j}\tau_j\right)\left[A_j\cos\left(\beta_{S_j}\tau_j\right)+B_j\sin\left(\beta_{S_j}\tau_j\right)\right] \tag{7.14}$$

where τ_j varies from 0 (when system S_j becomes active) to $\Delta\tau_j$ (when system S_j stops being active). Similarly, the velocity response for the *j*th response segment is given by a slightly modified version of Eq. (7.16):

$$\dot{Y}_{\mathrm{tr}_j}\left(\tau_{\mathrm{sw}_j}+\tau_j\right)=\exp\left(-\zeta_{S_j}\tau_j\right)\left[\left(\beta_{S_j}B_j-\zeta_{S_j}A_j\right)\cos\left(\beta_{S_j}\tau_j\right)+\left(-\beta_{S_j}A_j-\zeta_{S_j}B_j\right)\sin\left(\beta_{S_j}\tau_j\right)\right] \tag{7.15}$$

Setting τ_j equal to zero in the above two expressions and rearranging a little gives expressions for the transient parameters A_j and B_j in terms of the transient displacement and velocity at the time switch where system S_j becomes active. Similarly, setting τ_j equal to $\Delta\tau_j$ in Eqs. (7.14) and (7.15) gives expressions for the transient displacement and velocity for system S_j at the time switch where it stops being active. These four equations may be combined to express the equality of the displacements and velocities of the previously active and newly active systems at any switch point. For τ_{sw_j}, the displacement and velocity equalities may be presented in matrix form:

$$\begin{bmatrix} \mathrm{ec}_{j-1}+\frac{\zeta_{S_{j-1}}}{\beta_{S_{j-1}}}\mathrm{es}_{j-1} & \frac{1}{\beta_{S_{j-1}}}\mathrm{es}_{j-1} & 1 & 0 \\ \frac{-\beta_{S_{j-1}}^2-\zeta_{S_{j-1}}^2}{\beta_{S_{j-1}}}\mathrm{es}_{j-1} & \mathrm{ec}_{j-1}-\frac{\zeta_{S_{j-1}}}{\beta_{S_{j-1}}}\mathrm{es}_{j-1} & 0 & 1 \end{bmatrix}\begin{Bmatrix} Y_{\mathrm{tr}_{j-1}}\left(\tau_{\mathrm{sw}_{j-1}}\right) \\ \dot{Y}_{\mathrm{tr}_{j-1}}\left(\tau_{\mathrm{sw}_{j-1}}\right) \\ Y_{\mathrm{tr}_j}\left(\tau_{\mathrm{sw}_j}\right) \\ \dot{Y}_{\mathrm{tr}_j}\left(\tau_{\mathrm{sw}_j}\right) \end{Bmatrix}=\begin{Bmatrix} Y_{\mathrm{ss}_{j-1}}\left(\tau_{\mathrm{sw}_j}\right)-Y_{\mathrm{ss}_j}\left(\tau_{\mathrm{sw}_j}\right) \\ \dot{Y}_{\mathrm{ss}_{j-1}}\left(\tau_{\mathrm{sw}_j}\right)-\dot{Y}_{\mathrm{ss}_j}\left(\tau_{\mathrm{sw}_j}\right) \end{Bmatrix} \tag{7.16}$$

where the shorthand notation ec_{j-1} represents $\exp\left(-\zeta_{S_{j-1}}\left(\Delta\tau_{j-1}\right)\right)\cos\left(\beta_{S_{j-1}}\left(\Delta\tau_{j-1}\right)\right)$ and es_{j-1} represents $\exp\left(-\zeta_{S_{j-1}}\left(\Delta\tau_{j-1}\right)\right)\sin\left(\beta_{S_{j-1}}\left(\Delta\tau_{j-1}\right)\right)$.

Repeating this for all m time switches results in the matrix expression $[\lambda]\{T\}=\{\phi\}$ where $[\lambda]$ is a $2m\times 2m$ matrix given by

$$[\lambda]=\begin{bmatrix} q_1 & r_1 & 1 & 0 & 0 & 0 & \cdots & 0 & 0 \\ s_1 & t_1 & 0 & 1 & 0 & 0 & \cdots & 0 & 0 \\ 0 & 0 & q_2 & r_2 & 1 & 0 & \cdots & 0 & 0 \\ 0 & 0 & s_2 & t_2 & 0 & 1 & \cdots & 0 & 0 \\ \vdots & \vdots & \vdots & \vdots & \vdots & \vdots & \ddots & \vdots & \vdots \\ 1 & 0 & 0 & 0 & 0 & 0 & \cdots & q_m & r_m \\ 0 & 1 & 0 & 0 & 0 & 0 & \cdots & s_m & t_m \end{bmatrix} \tag{7.17}$$

where

$$\begin{aligned} q_j &= \mathrm{ec}_j+\frac{\zeta_{S_j}}{\beta_{S_j}}\mathrm{es}_j, \quad & r_j &= \frac{1}{\beta_{S_j}}\mathrm{es}_j, \\ s_j &= \frac{-\beta_{S_j}^2-\zeta_{S_j}^2}{\beta_{S_j}}\mathrm{es}_j, \quad & t_j &= \mathrm{ec}_j-\frac{\zeta_{S_j}}{\beta_{S_j}}\mathrm{es}_j \end{aligned} \tag{7.18}$$

$\{T\}$ and $\{\phi\}$ are $2m\times 1$ column vectors given by

$$\{T\}=\begin{Bmatrix} Y_{\mathrm{tr}_1}\left(\tau_{\mathrm{sw}_1}\right) \\ \dot{Y}_{\mathrm{tr}_1}\left(\tau_{\mathrm{sw}_1}\right) \\ Y_{\mathrm{tr}_2}\left(\tau_{\mathrm{sw}_2}\right) \\ \dot{Y}_{\mathrm{tr}_2}\left(\tau_{\mathrm{sw}_2}\right) \\ \vdots \\ Y_{\mathrm{tr}_m}\left(\tau_{\mathrm{sw}_m}\right) \\ \dot{Y}_{\mathrm{tr}_m}\left(\tau_{\mathrm{sw}_m}\right) \end{Bmatrix}, \qquad \{\phi\}=\begin{Bmatrix} Y_{\mathrm{ss}_1}\left(\tau_{\mathrm{sw}_2}\right)-Y_{\mathrm{ss}_2}\left(\tau_{\mathrm{sw}_2}\right) \\ \dot{Y}_{\mathrm{ss}_1}\left(\tau_{\mathrm{sw}_2}\right)-\dot{Y}_{\mathrm{ss}_2}\left(\tau_{\mathrm{sw}_2}\right) \\ Y_{\mathrm{ss}_2}\left(\tau_{\mathrm{sw}_3}\right)-Y_{\mathrm{ss}_3}\left(\tau_{\mathrm{sw}_3}\right) \\ \dot{Y}_{\mathrm{ss}_2}\left(\tau_{\mathrm{sw}_3}\right)-\dot{Y}_{\mathrm{ss}_3}\left(\tau_{\mathrm{sw}_3}\right) \\ \vdots \\ Y_{\mathrm{ss}_m}\left(\tau_{\mathrm{sw}_1}\right)-Y_{\mathrm{ss}_1}\left(\tau_{\mathrm{sw}_1}\right) \\ \dot{Y}_{\mathrm{ss}_m}\left(\tau_{\mathrm{sw}_1}\right)-\dot{Y}_{\mathrm{ss}_1}\left(\tau_{\mathrm{sw}_1}\right) \end{Bmatrix} \tag{7.19}$$

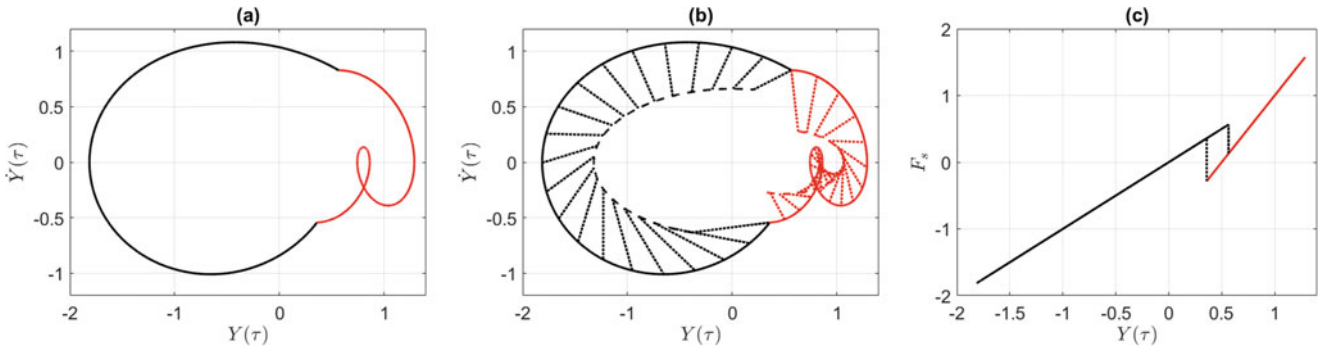

Fig. 7.1 System response of the hybrid SDOF system composed of two linear systems. (**a**) The phase plane plot of total displacement against total velocity. (**b**) The same phase plane plot with the steady-state and transient responses superimposed. (**c**) The spring force versus displacement for the two linear systems with the dotted lines showing the switch discontinuities. In all three plots, the black lines show the response when linear system 1 is active and the red lines show the response when linear system 2 is active

The transient displacements and velocities required at each switch point to ensure a periodic response may then be calculated using $\{T\} = [\lambda]^{-1}\{\phi\}$. Once the time switch transient displacements and velocities have been calculated, the values of the transient parameters A_j and B_j may then be calculated, followed by the segment responses. Note that it would have been no more complicated to formulate an expression to directly calculate the transient parameters A_j and B_j but it was felt that the current formulation would be more consistent with any future plans to extend the approach for multi-degree-of-freedom (MDOF) hybrid systems.

A numerical example will now be given to illustrate the previous theory. A hybrid system composed of two linear systems will be considered. The first linear system parameters are $\zeta_1 = 0.1$, $\gamma_1 = 1$, and $Y_{\text{offset}_1} = \dot{Y}_{\text{offset}_1} = 0$, while the second linear system parameters are $\zeta_2 = 0.1$, $\gamma_2 = 2$, $\dot{Y}_{\text{offset}_2} = 0$, and $Y_{\text{offset}_2} = 0.5$. It may be observed that the two linear systems only differ in their spring force versus displacement relationships, which are shown above in Fig. 7.1c. The forcing frequency ratio is $\alpha = 0.5$ meaning that the repeat period will be $\tau_{\text{period}} = 4\pi$. The active system vector S is [1 2] and the time switch vector will initially be set as $\tau_{\text{sw}} = [4\ 10]$. This means that linear system 1 will become active at $\tau = 4$ and remain so until $\tau = 10$, at which point linear system 2 will become active. Linear system 2 will remain active until $\tau = 4$ in the next forcing cycle and so on. Using Eqs. (7.8) and (7.9) gives a $\Delta\tau$ vector (time spent in each active system segment) as $\Delta\tau = [6\ 6.57]$. Note that these two time values sum to give the τ_{period} value. The 4×4 $[\lambda]$ matrix and the 4×1 $\{\phi\}$ column vector can then be constructed and substituted into Eqs. (7.17) and (7.19) to give the 4×1 $\{T\}$ column vector that will result in a periodic response. The various steady-state, transient, and total displacement and velocity response segments may then be calculated. These are plotted in Fig. 7.1 in the form of two phase planes and a spring force versus displacement plot. The phase plane in Fig. 7.1a shows the phase plane segments of the linear system 1 total response as a black trajectory line and the phase plane segments of the linear system 2 total response as a red trajectory line and the continuity between the two segments is clear to see. Figure 7.1b shows the same phase plane plot but with the inclusion of both the steady-state and transient phase plane segments. The dashed black and red lines show the steady-state phase plane segments of linear system 1 and linear system 2, respectively, and may be seen to take the form of elliptical arcs. Emanating from the steady-state arcs and terminating at the solid total response segments are shown a series of dotted lines that depict the progression of the transient response segments. While this plot may appear a little more cluttered than the top left plot, it does contain valuable information about how the total periodic response arises from the equilibrium between the steady-state and transient components. Figure 7.1c shows the spring force versus displacement plot for the two active systems. The discontinuities of spring force at the switches are shown by the dotted vertical lines – in the next section, an approach for eliminating these discontinuities, thereby resulting in prediction of periodic responses of piecewise linear systems, will be discussed.

7.3 Periodic Response of Harmonically-Excited Piecewise Linear Systems

The previous section presented a relatively straightforward methodology for calculating the periodic response of a harmonically excited hybrid system composed of a number of linear systems assuming that all of the switches between systems were conducted on the basis of time and were fully specified. While there may be situations, particularly in control systems, where switches are conducted on the basis of time, it will be much more common for switches between linear

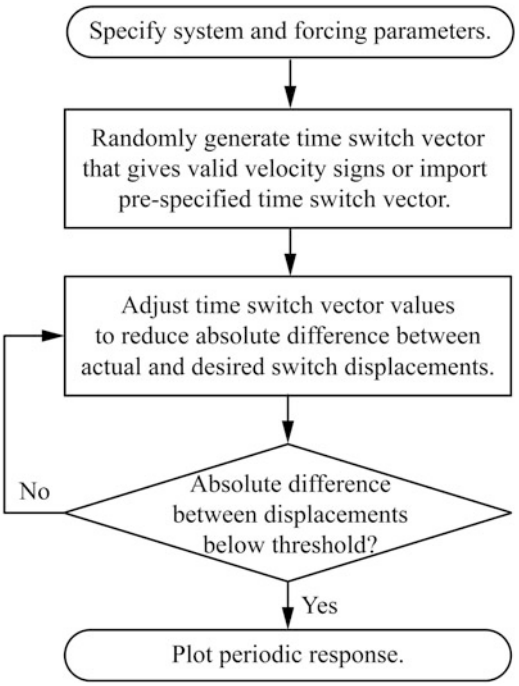

Fig. 7.2 Flowchart illustrating the iterative optimization approach for identifying the time switches to give the desired displacement switch behavior

systems to occur on the basis of displacement and/or velocity. This section will be concerned with how the time-switching method of the previous section may be exploited to predict the periodic responses of piecewise linear systems whose system parameters change on the basis of displacement. All of the ideas that are introduced here will be easily extendable to hybrid systems whose system parameters change on the basis of velocity or a combination of displacement and velocity.

For hybrid systems that require only two time switches (such as that shown in the previous section), it will be possible to conduct an exhaustive search to identify the correct time switch values to give the desired displacement switch values. For situations where there are more than two time switches, it will be preferable to adopt an iterative approach to finding the correct time switch values. This iterative approach is best described using the flowchart of Fig. 7.2. As may be seen from the flowchart, the process begins with the specification of the system parameters for each linear system and the specification of the forcing frequency ratio α. The active system vector S must also be specified to state the order in which the systems will become active – this will also specify the number of switches m. The next step of the process is to generate, or specify, a valid initial time switch vector. This may be done via the specification of an initial time switch vector that is believed to be in close proximity to the required time switch vector – this approach will be used later to calculate periodic responses over a range of frequencies. For situations where a nearby initial time switch vector cannot be specified, a randomly generated initial time switch vector may be used. It has been found that the overall method is more computationally efficient if the random generation process is repeated until the generation of an initial time switch vector that results in the desired signs for each of the velocities at the switch points. The iterative part of the process is simply updating the time switch vector values so as to reduce the difference between the desired and actual switch displacements. The size of the time switch increments will depend upon the values of the displacement differences. This process is repeated until the sum of the absolute displacement differences is less than some pre-specified threshold level, at which point the overall periodic response may be plotted.

The iterative process described above will now be employed to demonstrate how the steady-state and transient components combine to produce the overall system response for a trilinear system as the forcing frequency ratio changes. The first linear system parameters are $\zeta_1 = 0.1$, $\gamma_1 = 2$, $Y_{\text{offset}_1} = -0.5$, and $\dot{Y}_{\text{offset}_1} = 0$, the second linear system parameters are $\zeta_2 = 0.1$, $\gamma_2 = 1$, and $Y_{\text{offset}_2} = \dot{Y}_{\text{offset}_2} = 0$, and the third linear system parameters are $\zeta_3 = 0.1$, $\gamma_3 = 2$, $Y_{\text{offset}_3} = 0.5$, and $\dot{Y}_{\text{offset}_3} = 0$. This hybrid system would be a trilinear stiffness oscillator if the switches between linear system 1 and linear system 2 occurred when the displacement $Y = -1$ and the switches between linear system 2 and linear system 3 occurred when the displacement $Y = 1$. Forcing frequency ratios from $\alpha = 0.2$ to $\alpha = 1.2$ in steps of 0.2 were investigated. The active system vector S is [1 2 3 2]. The resulting phase plane plots are shown in Fig. 7.3. The solid lines again show the overall phase plane with the following colors being used: black for segment 1 (linear system 1 active), red for segment 2 (linear system 2 active for the first time), green for segment 3 (linear system 3 active), and blue for segment 4 (linear system 2 active for the second time). The dashed lines show the steady-state response segments for when each system is active and the dotted lines show the transient response segments for the same period. These plots hopefully show how the interaction between the

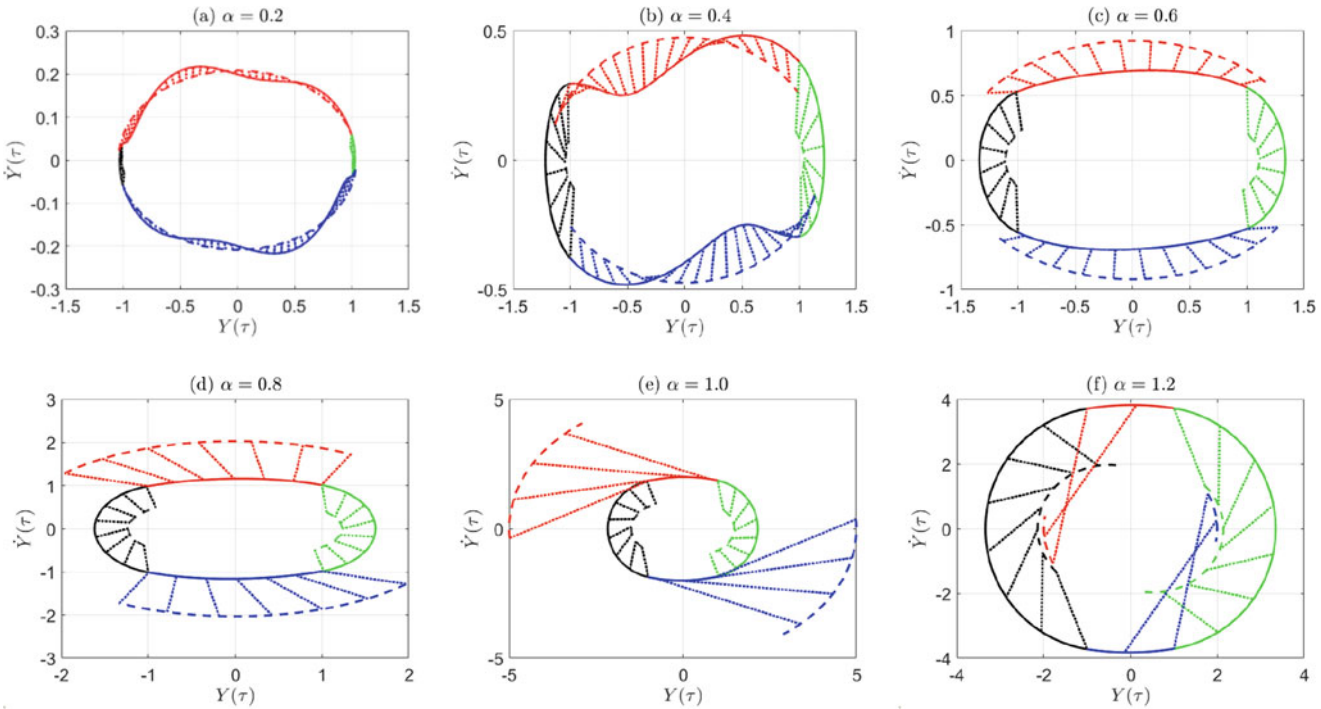

Fig. 7.3 System response of a trilinear system for various forcing frequency ratios. In all plots, the black lines show the response during segment 1, the red lines show the segment 2 response, the green lines show the segment 3 response, and the blue lines show the segment 4 response. Solid lines denote the phase plane of the overall response, while dashed lines show the steady-state components of the response when each system is active. The dotted lines emanating from the steady-state arcs show the progression of the transient components of the response

steady-state and transient responses results in the overall response. This explains how the distorted phase planes for $\alpha = 0.2$ and $\alpha = 0.4$ arise and also how the steady-state phase mismatch at $\alpha = 1.2$ results in large transient responses and a large overall response. Note that it is not possible for the trilinear system to maintain a nonlinear periodic response for $\alpha \geq 1.4$ with the only possible periodic response being the steady-state response of linear system 2.

In the previous example, there was only one possible periodic response for all forcing frequency ratios – this response was nonlinear for $\alpha < 1.4$ and linear for $\alpha \geq 1.4$. It will now be shown that, by increasing the values of the linear stiffness terms, the iterative method can identify a stable nonlinear periodic response, an unstable nonlinear periodic response in addition to the linear periodic response for a region of frequency ratios $\alpha \geq 1.4$. The stiffness parameters for linear system 1 and 3 will now be increased in value, with linear system 2 remaining the same as in the previous example. The first linear system parameters are now $\zeta_1 = 0.1$, $\gamma_1 = 5$, $Y_{\text{offset}_1} = -0.8$, and $\dot{Y}_{\text{offset}_1} = 0$; the second linear system parameters are still $\zeta_2 = 0.1$, $\gamma_2 = 1$, and $Y_{\text{offset}_2} = \dot{Y}_{\text{offset}_2} = 0$; and the third linear system parameters are $\zeta_3 = 0.1$, $\gamma_3 = 5$, $Y_{\text{offset}_3} = 0.8$, and $\dot{Y}_{\text{offset}_3} = 0$. Again, this hybrid system would be a trilinear stiffness oscillator if the switches between linear system 1 and linear system 2 occurred when the displacement $Y = -1$ and the switches between linear system 2 and linear system 3 occurred when the displacement $Y = 1$. The active system vector S is again [1 2 3 2]. The same iterative process described above was employed to identify the stable and unstable nonlinear periodic responses along with the stable linear periodic response for the region between $1.4 \leq \alpha \leq 1.8$. The process for consistently maintaining the stable or unstable nonlinear branch was through "seeding" the approach with the previous time switch vector. The active system vector S is [1 2 3 2]. The resulting phase plane plots for forcing frequency ratios from $\alpha = 1.4$ to $\alpha = 1.8$ in steps of 0.1 are shown in Fig. 7.4. On this occasion, the black lines depict the stable nonlinear response, the green lines depict the stable linear response and the red lines depict the unstable nonlinear response. The progression of the red unstable nonlinear response from being very near to the green linear response at $\alpha = 1.4$ to being very near to the black stable nonlinear response at $\alpha = 1.8$ may be clearly observed. Note that it is not possible for this trilinear system to maintain a nonlinear periodic response for $\alpha \geq 1.8$ with the only possible periodic response being the steady-state response of linear system 2.

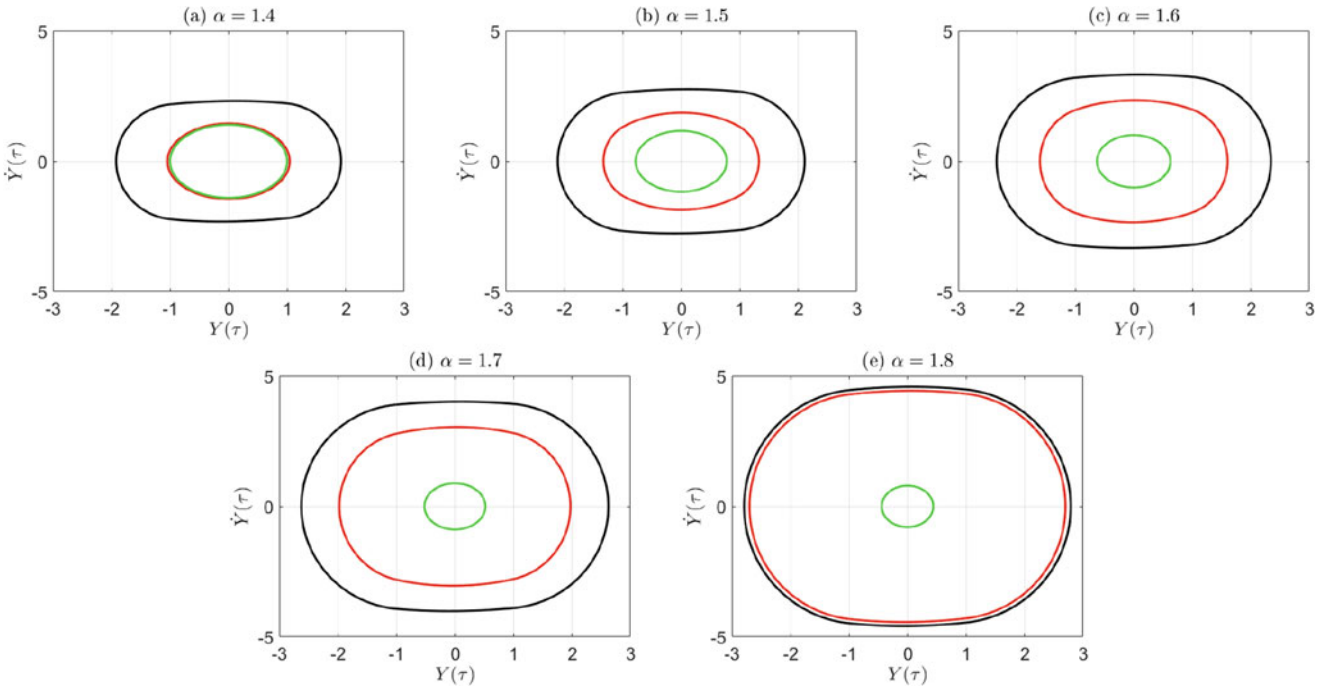

Fig. 7.4 System response of a trilinear system for various forcing frequency ratios. In all plots, the black lines show the nonlinear stable response, the red lines show the nonlinear unstable response, while the green lines show the linear stable response

7.4 Discussion and Conclusion

This chapter has presented a closed-form solution for the periodic response of a time-switched hybrid system. As stated earlier, this may be of use in some control engineering applications but the main thrust of this chapter was how this closed-form solution could be wrapped into an efficient iterative approach for the calculation of periodic responses of piecewise linear systems, including the prediction of stable and unstable solutions in the jump frequency range. The method shown can very easily be extended to other piecewise linear systems – this could include systems whereby nonlinear damping (e.g., combinations of friction and viscous damping) is represented via a number of linear systems.

That said, the true potential of this work, in the author's view, will be its possibility to be extended to continuous nonlinear systems, such as the Duffing oscillator. It is a simple matter to include more linear systems into the piecewise linear model and thereby start to approach the Duffing oscillator's stiffness curve. It is hoped that, by considering the overall response as the combination of linear steady-state and linear transient components, the ever-surprising Duffing oscillator may reveal all of its secrets.

Acknowledgments The author would like to acknowledge all the useful discussions with Professor Keith Worden regarding many things nonlinear, both in the past 25 or so years and in the last few years, since the inception of this work.

References

1. Worden, K., Tomlinson, G.: Nonlinearity in Structural Dynamics: Detection, Identification and Modelling. IoP Publishing, Bristol and Philidelphia (2001)
2. Maas, S.: Nonlinear Microwave and RF Circuits, 2nd edn. Artech House (2003)
3. Peters, J.: A beginner's guide to the Hilbert transform. Int. J. Math. Educ. Sci. Technol. **1**, 89–106 (1995)
4. Chen, S., Billings, S.: Representation of non-linear systems: the NARMAX model. Int. J. Control. **49**, 1013–1032 (1989)
5. Masri, S., Caughey, T.: A nonparametric identification technique for nonlinear dynamical problems. J. Appl. Mech. **46**, 433–447 (1979)
6. Mohammad, K., Worden, K., Tomlinson, G.: Direct parameter estimation for linear and nonlinear structures. J. Sound Vib. **152**, 471–499 (1991)
7. Volterra, V.: Theory of Functionals and Integral Equations. Dover, New York (1959)
8. Nayfeh, A.: Perturbation Methods. Wiley, New York (1973)

9. Nayfeh, A., Mook, D.: Nonlinear Oscillations. Wiley, New York (1979)
10. Vakakis, A., Manevitch, L., Mikhlin, Y., Pilipchuk, V., Zevin, A.: Normal Modes and Localization in Nonlinear Systems. Wiley-Interscience, New York (1996)
11. Kovacic, I., Brennan, M.: The Duffing Equation: Nonlinear Oscillators and their Behaviour. Wiley-Blackwell (2011)
12. Xie, L., Zhou, Y., Zhao, Y.: Criterion of chaos for switched linear systems with controllers. Int. J. Bifurcation Chaos. **20**, 4103–4109 (2010)
13. El Guezar, F., Bouzahir, H.: Chaotic behavior in a switched dynamical system. Model. Simul. Eng. **2008**, 798395 (2008)
14. Lu, J., Zhou, T., Chen, G., Yang, X.: Generating chaos with a switching piecewise-linear controller. Chaos. **12**, 344–349 (2002)

Chapter 8
A Tutorial on Data-Driven Methods in Nonlinear Dynamics

Keith Worden and Elizabeth J. Cross

Abstract In the past two decades, it is fair to say that there has been an explosion in the use of machine learning technology or 'data-driven' methods, across the whole subject of engineering; this is no less true of the subdiscipline of structural dynamics. A modern dynamicist needs, at the least, some familiarity with these technologies. This paper attempts to give an overview of some of the main ideas in 'data-based' engineering, by focussing on the (comparatively) smaller area of nonlinear dynamics—indeed on nonlinear system identification. A particular viewpoint is adopted, based on modern Bayesian methods of regression. Considerable attention is paid here to the desirability of combining measured data with physical insight when modelling dynamic systems and structures. Although this view naturally begins with the idea of 'grey-box' models, this generalises into the emerging subject of *physics-informed machine learning*. Although this tutorial necessarily focusses down on a narrow application context, the many references allow the curious reader to explore further afield.

Keywords Tutorial · Data-based methods · Nonlinear dynamics

8.1 Introduction

At the risk of beginning this tutorial paper with a contentious statement, one might argue that *all* of science and engineering is *data-based*. It is certainly true that the acid test of any physical theory is that it be consistent with previous observations (data), and that it make predictions that can be confirmed by further new observations. As all of science and engineering is arguably founded in physics, the opening statement follows. Adopting the term 'data-driven' narrows the field a little; however, even then the subject is far too large to address in a single paper. Focussing down further, this paper is concerned with 'data-driven methods', and in the recent past, this term has come to mean a specific class of algorithms derived from statistics and machine learning, with which one can model some aspect of reality armed with some prior assumptions and a set of measured observations from the system of interest. Finally, the paper will concentrate on the specific context of nonlinear dynamics. With this remit, one might arguably do justice to the subject matter with a single book; the recent [1] is a nice attempt. However, this is a paper, not a book, so it will reflect some hard choices on the part of the authors.

The term 'model' here will be applied to any *mathematical* construct which can be used to explain observations of physical reality and predict the observations that would entail for the system under previously unobserved stimuli. The discipline of *machine learning* will be understood to mean the body of theory and practice which allows one to infer a model from some subset of the known observations, possibly augmented by some prior knowledge. To establish some concrete terminology here, any model derived entirely from the data alone will be referred to as a 'black-box' model. If a model has been derived purely by the application of existing laws of physics, it will be referred to as a 'white-box' model.[1] A model, which is inferred from prior physics *and* and observed data, will be called a 'grey-box' model.

Of course, learning a model from data has been an established discipline within engineering for decades—that of *system identification* (SI). As such, the overall problem breaks down into two essential components *structure detection* and

[1] This definition will gloss over the fact that 'existing' laws of physics will, at some point, have been based on observational evidence (data).

K. Worden (✉) · E. J. Cross
Dynamics Research Group, Department of Mechanical Engineering, University of Sheffield, Sheffield, UK
e-mail: k.worden@sheffield.ac.uk; e.j.cross@sheffield.ac.uk

M. R. W. Brake et al. (eds.), *Nonlinear Structures & Systems, Volume 1*, Conference Proceedings
of the Society for Experimental Mechanics Series, https://doi.org/10.1007/978-3-031-36999-5_8

parameter estimation.[2] A 'model' is defined above as a 'mathematical construct'; often this means a mathematical equation, or system of equations. With this in mind, the problem of structure detection is simply that of determining the functional form of the equations which govern the model; they may be algebraic, differential, integral, etc. The equations will need to contain all of the variables which control or describe some aspect of reality (temperature, current, acceleration, etc.) and may well contain constants or parameters, some of which will be fixed by the physics and some will need to be determined. The latter parameters give rise to the problem of parameter estimation and will need to be inferred from measured data. As a concrete example (which will recur throughout the paper), one might consider a dynamical system of the form:

$$m\ddot{y} + c\dot{y} + ky = x(t) \tag{8.1}$$

which is a simple linear mass-spring-damper system. In the usual frame of engineering dynamics, $x(t)$ would be a force (the stimulus), and $y(t)$ would be a displacement (the response); m, c and k would be constants for a given system (mass, damping and stiffness, respectively). The overdots in the equation denote differentiation with respect to time; thus the model *structure* here represents a second-order differential equation. If the structure and values of the constants are known a priori from physics, this is a white-box model; if the structure is known, but the parameters need to be inferred from measured data, this is a *grey-box* model.

The problem of inferring model parameters from data is commonly called *regression* within the statistics and machine learning communities [2]. Few would argue that the mathematical basis for regression began with the method of *least squares*. This algorithm for fitting a model to data was first published by Legendre [3], although Gauss subsequently claimed precedence.[3] Regardless of the dispute on precedence, Gauss certainly extended the algorithm in important ways; in particular, the *Gaussian* or *normal* probability distribution was introduced as a means of handling measurement errors in a rigorous fashion. In any case, both Legendre and Gauss developed and used the method in order to solve problems in celestial mechanics, which were highly nonlinear. The point here is that it would appear that the discipline of machine learning was originally motivated by problems in nonlinear dynamics.

Given that the subject of 'data-driven' methods is vast, the 'hard choices' mentioned earlier come into play. Given the experience and preferences of the authors, this tutorial will concentrate on system identification. Furthermore, as this paper is a tutorial as opposed to original research, it will make no attempt at a comprehensive or balanced survey of the literature, but will rather lean on the papers by the authors and their colleagues with which they are most familiar. A more balanced viewpoint can be found by following the references in those papers.

The identification of linear systems (LSI) is arguably so well developed now that it is comprehensively covered in textbooks [5, 6]. In contrast, nonlinear system identification (NLSI) is by no means as well developed [7]. Part of the problem with NLSI is that the structure detection problem is much more complicated. For a general linear differential equation model, the only freedom in the model structure is in the number of derivatives of the variables; furthermore, the model parameters only appear as multipliers of terms, there are no parameters 'hidden' in nonlinear functions, like the a in e^{ay}. Such parameters require more sophisticated means of estimation, whereas the *linear-in-the-parameters* problems can sometimes yield to algorithms as 'simple' as basic least squares. An NLSI model structure could in principle contain *any* nonlinear functions of the variables of interest and their derivatives and any parameters. The complexities of NLSI have meant that, in the past, there has been no single algorithm which can address the completely general problem; the NLSI practitioner has instead relied on a 'toolbox' philosophy, with different approaches used for different classes of problem.

This situation persisted until recently, when two methodologies emerged in the NLSI community, each offering the prospect of a general framework. The first group of algorithms, based on *evolutionary optimisation*, starting with the genetic algorithm [8], can handle difficult technical problems in NLSI, like nonlinearity in the model parameters and the existence of unmeasured states [9, 10]. The second group exploited *Bayesian Inference*. Although this idea originated over 20 years ago [11, 12], it really flourished in the last decade or so, when dynamicists began to take advantage of concepts from machine learning [13]. Bayesian methods overcome the same technical problems as evolutionary methods [14] and offer additional benefits; they allow model selection simultaneously with parameter estimation [15], can estimate parameter *distributions* and can propagate uncertainty in a principled manner. Because of its power and generality, this tutorial will mainly focus on Bayesian methods.

Having said that the focus here will be on NLSI, it is important to note that there are many other problems in nonlinear dynamics for which a data-driven approach has been adopted. In fact, data-driven methods have proved vital in the development of the subject for a fundamental and important reason. Problems in nonlinear dynamics almost never have

[2] The first author first learned these terms from the seminal work of Steve Billings; however, they may well predate that work.

[3] Legendre published in 1805, Gauss in 1809; however, Gauss claimed to have had the method since 1793. The whole story is discussed in [4].

analytical solutions. To be more precise, nonlinear equations of motion almost never have exact closed-form solutions. Suppose one were to take the linear equation in Eq. (8.1) and add the 'simplest' nonlinear term (which turns out to be cubic in y), the result is *Duffing's equation* [16]:

$$m\ddot{y} + c\dot{y} + ky + k_3 y^3 = x(t) \tag{8.2}$$

To this day, there are no exact solutions of this equation, except in the very restricted undamped ($c = 0$) and unforced ($x(t)$) case. For the restricted case, Duffing himself provided an exact solution involving elliptic functions in 1918; however, there has been no progress to speak of on the general case since then. Unfortunately, this general lack of exact solutions means that all of the fascinating nonlinear phenomena discovered in the twentieth century—like bifurcations and chaos—present intractable problems for exact analytical methods. One way around this issue has been to rely on simulations; one numerically simulates the system responses of interest and characterises the responses. Initially these simulations were carried out using analogue computers incorporating bespoke nonlinear circuits, but with the advent of (and explosion in) digital computers, it became possible to solve the nonlinear initial value problems in order to simulate samples of response data for further computational analysis. For example, if one wishes to analyse the stability or chaotic nature of a system, the Lyapunov exponents can be estimated from a time series [17] (in fact, the algorithm in that paper was designed for use with experimental data, but the principle is the same). Discrete wavelet analysis has also proved powerful in the analysis of chaotic time series [18]; apart from estimating certain chaotic invariants, the analysis can also detect coherent structures. Finally, on the subject of coherent structures, the interesting book [19] details how coherent structures and low-dimensional structure can be found in data from turbulent flows; one of the main algorithms discussed is the Karhunen-Loéve expansion or principal orthogonal decomposition (POD). Perhaps a little ironically, the POD is basically a variant of principal component analysis (PCA), which is a *linear* projection method often used in applied machine learning for data visualisation and dimension reduction. Turbulence is of course one of the major outstanding problems in nonlinear science generally.

Even within the restricted scope of NLSI, this paper will omit one very important class of models—the 'black-box' models mentioned earlier. In principle, such models can work without any physical insight whatsoever; they work by proposing some basis of functions which spans the function space of interest, much as a Fourier expansion does for the space of periodic functions on some finite interval. The important point of such models is not that they encode some prior physical knowledge, but rather that they have a *universal approximation property*, which is to say that they can represent some target function with arbitrary accuracy (as long as they include enough terms). Such 'learners' include neural networks (deep or shallow), radial-basis function (RBF) networks, Gaussian processes, etc. [2]. In principle, one could download software for such a learner, input some data and run the software with default settings, and out would pop a model. Such a model would be 'pitch black'.[4] The authors would always caution against this practice; it seldom produces good research and could produce catastrophic results when applied in real life. Black boxes will surface later in the discussion of grey boxes and *physics-informed machine learning* (PIML).

The layout of the paper is as follows. The next section presents the arguments for adopting a Bayesian approach to NLSI and this is followed by a discussion of a specific parameter estimation method based around Markov chain Monte Carlo (MCMC). Section 8.4 then presents a case study of MCMC applied to the identification of a Duffing oscillator system. Section 8.5 discusses the combined problem of parameter estimation and model selection and is followed by another case study involving equation discovery for hysteretic oscillators. Section 8.7 then presents some ideas on combining physics-based and data-based approaches in the form or grey-box modelling, or more generally *physics-informed machine learning*. The paper ends with brief conclusions.

8.2 Bayesian Inference and System Identification

This section will give a precise definition of the system identification problem and will outline the advantages of taking a Bayesian probabilistic viewpoint. The input (stimulus) variable will be denoted $x(t)$ and the output (response) variable by $y(t)$. Suppose that one has a set of data $\mathcal{D} = \{(x_i, y_i), i = 1, \ldots, N\}$ of sampled system inputs x_i and outputs y_i. If one assumes that there is no measurement noise, and the model structure is known, then the application of an identification algorithm will yield (assuming that the problem is well-conditioned) a deterministic estimate of the system parameters $\underline{w}$:

$$\underline{w} = id(\mathcal{D}) \tag{8.3}$$

[4] The authors thank Johan Schoukens for introducing them to this term.

where the function id represents the application of the identification algorithm to the data $\mathcal{D}$. If one were concerned with the Duffing system of Eq. (8.2), then one would have $\underline{w} = (m, c, k, k_3)^T$. Now, if noise $\epsilon(t)$ is present on the input or output data (or both), $\underline{w}$ will become a *random variable* conditioned on the data. In this context one no longer wishes to find an *estimate* of $\underline{w}$, but rather to specify one's belief in its value. To simplify matters here, it will be assumed that the noise is Gaussian with (unknown) variance σ_ϵ; also, the parameter σ_ϵ will be subsumed into $\underline{w}$, since it is to be inferred along with the model. In probabilistic terms, instead of Eq. (8.3) one now has:

$$\underline{w} \sim p(\underline{w}|\mathcal{D}, \mathcal{M}) \tag{8.4}$$

where $\mathcal{M}$ represents the choice of model (the Duffing oscillator in the current case). Knowing the full parameter distribution means that one can construct confidence intervals (or error bars) for the parameter estimates; this is the first major advantage of a probabilistic viewpoint. In particular, the *Bayesian* approach to SI is that one uses Bayes' theorem in the form:

$$p(\underline{w}|\mathcal{D}) = \frac{p(\mathcal{D}|\underline{w})\, p(\underline{w})}{p(\mathcal{D})} \tag{8.5}$$

to convert an a priori probability distribution for the parameters $\underline{w}$ into a posterior distribution having seen the data $\mathcal{D}$. If one desires a so-called point estimate of the parameters, the usual course of action is to choose that which maximises the posterior probability $p(\underline{w}|\mathcal{D})$. Now, as the data $\mathcal{D}$ are a constant of the identification problem, one is reduced to maximising $p(\mathcal{D}|\underline{w})p(\underline{w})$. It is often the case at this point that an uninformative constant (and hence improper) prior $p(\underline{w})$ is chosen, and this reduces the problem to that of maximising $p(\mathcal{D}|\underline{w})$, which is simply the likelihood of the data. The *maximum a posteriori* (MAP) estimate then becomes *maximum likelihood*. If the noise is assumed Gaussian, the problem essentially becomes one of minimising a least-squares cost/error function.

The usual objective of SI is to provide a *predictive model*, i.e. one which can estimate or predict system outputs if a different system input were provided. In the probabilistic context described above, the best that one could do is to determine a *predictive distribution*. Suppose a new input sequence $\underline{x}^*$ were applied to the system, one would wish to determine the density for the predicted outputs:

$$\underline{y}^* \sim p(\underline{y}^*|\underline{x}^*, \underline{w}, \mathcal{D}, \mathcal{M}) \tag{8.6}$$

noting all the dependencies.

The mean of this distribution would give the 'best' estimates for the predictions and the covariance would allow one to establish confidence intervals for them. However, one notes the presence of the parameter vector $\underline{w}$. In practice, one might use the $\underline{w}$ value corresponding to the mean or the mode of the posterior parameter distribution; however, a truly Bayesian viewpoint on the prediction would require one to marginalise over the parameter estimates, i.e. to derive:

$$p(\underline{y}^*|\underline{x}^*, \mathcal{D}, \mathcal{M}) = \int p(\underline{y}^*|\underline{x}^*, \underline{w}, \mathcal{M})\, p(\underline{w}|\mathcal{D}, \mathcal{M}) d\underline{w} \tag{8.7}$$

This is a very powerful idea: allowing for a fixed model *structure*, *one is making predictions using an entire set of parameters consistent with the training data*, with each point in the space of parameters weighted according to its probability given the data. In practice, there are considerable problems in implementing the full Bayesian approach, i.e. performing the intractable integral 8.7. For the purposes of this section, the main issue for discussion will be the problem of inferring the distributions for the parameters as given in Eq. (8.4).

Another potential advantage of a Bayesian approach is that it may be possible to assess the relative evidence for a number of competing model structures, i.e. to solve the *structure detection* problem. Suppose that one believes that the true model structure is one of a finite number $\{\mathcal{M}_i, i = 1, \ldots, M\}$ (the discussion here will closely follow [13]). In principle, one could imagine computing the probability of observing the data $P(\mathcal{D}|\mathcal{M}_i)$, given the particular model structure (noting that this is a from a discrete distribution). If this quantity were available, one could select the model with the highest probability. Even more in the spirit of Bayesian inference, one could marginalise over *all possible* model structures weighted according to their probability; in terms of prediction, one would have:

$$p(\underline{y}^*|\underline{x}^*, \mathcal{D}) = \sum_{i=1}^{M} p(\underline{y}^*|\underline{x}^*, \mathcal{M}_k, \mathcal{D})\, P(\mathcal{M}_k|\mathcal{D}) \tag{8.8}$$

Unfortunately, the posterior over models $P(\mathcal{M}_i|\mathcal{D})$ is difficult to compute. If one appeals to Bayes theorem in the form:

$$P(\mathcal{M}_i|\mathcal{D}) = \frac{p(\mathcal{D}|\mathcal{M}_i)P(\mathcal{M}_i)}{p(\mathcal{D})} \tag{8.9}$$

and assumes equal priors on the models, one arrives at a comparison ratio or *Bayes factor*:

$$B_{ij} = \frac{P(\mathcal{M}_i|\mathcal{D})}{P(\mathcal{M}_j|\mathcal{D})} = \frac{p(\mathcal{D}|\mathcal{M}_i)}{p(\mathcal{D}|\mathcal{M}_j)} \tag{8.10}$$

which weights the evidence for two models in terms of marginal likelihoods of the data given the models. Unfortunately, the marginal likelihoods themselves are expressed as an integral over all possible parameters, i.e.

$$p(\mathcal{D}|\mathcal{M}) = \int p(\mathcal{D}|\underline{w}, \mathcal{M})p(\underline{w}|\mathcal{M})d\underline{w} \tag{8.11}$$

and this integral is analytically intractable and numerically challenging because it can be high-dimensional [20].

One can resort to less informative model selection indicators which are simpler to compute, e.g., the *deviance information criterion* (DIC) [21], as applied in [14].

Leaving aside model selection for the moment, the next section will discuss a Bayesian approach to parameter estimation—*Markov chain Monte Carlo* (MCMC), a powerful approach for sampling from probability distributions.

8.3 System Identification Using Markov Chain Monte Carlo

As stated in the previous section, one of the central problems discussed in this paper is that of determining the posterior probability function for parameters, given data from a differential equation system. This distribution will not take any particular form (e.g. Gaussian) and in the absence of the normalising constant $p(\mathcal{D}|\mathcal{M})$ can only be evaluated up to proportionality. One ideally wishes to adopt a nonparametric approach to the problem so that the true statistics of the parameter density are obtained. An obvious step in the direction of nonparametric estimation is to sample from the parameter distribution itself and thus build a picture; however, the distribution in question is unknown. Fortunately, there exists a very powerful class of numerical methods which allow sampling from such densities—the class of *Markov chain Monte Carlo (MCMC)* methods [22]. MCMC methods are well-known in the context of Bayesian inference; however, for completeness a summary of the method used here—the *Metropolis-Hasting* (MH) algorithm—is provided here.

It is sufficient for now to assume that one has a single random variable x with true, but unknown, density $p(x)$. The MH method actually works even if $p(x)$ is too complicated to sample from directly. First of all, one assumes that one can at least *evaluate* $p(x)$, given a candidate value for x; in fact, one only needs to evaluate a density $p^*(x)$, where $p^*(x) = Z_p p(x)$, i.e. the density of interest up to a multiplicative constant. The method hinges on the use of a *proposal distribution* $q(x)$, which is simpler than $p(x)$ and can also be evaluated up a multiplicative constant. The use of the proposal distribution is common to many methods like importance and rejection sampling [22]. The unique feature of MCMC methods is that a sequence of samples or states x^i are generated, with the proposal distribution a function of the state at any given time. One estimates the probability for the next state in the sequence (a *Markov chain*—hence the name) by conditioning on the current state, the proposal distribution is $q(x'|x^i)$. Another way of regarding q is as a transition probability density for a jump in the state/sample space. Often q is taken as a simple distribution, i.e. a Gaussian. Under the latter assumption, one can see that a large variance for the proposal distribution will lead to higher probabilities of jumps in the state/sample space. One also immediately sees that a small variance, leading to small jumps in the space, will produce (at least locally) correlated states/samples.

The MH algorithm proceeds as follows. Assume one is at iteration i in the process:

1. Sample from the proposal density $q(x'|x^i)$ to generate a candidate state x'.
2. Evaluate the quantity:

$$a = \frac{p^*(x^i)q(x^i|x')}{p^*(x')q(x'|x^i)}$$

3. If $a \geq 1$, the new state is accepted; *otherwise* the new state is accepted with probability a.
4. If the new state is accepted, set $x^{i+1} = x'$; else set $x^{i+1} = x^i$.

As a full description of why this procedure leads to sampling from $p(x)$ is beyond the scope of this tutorial, the curious reader should consult [22].

Two practical issues arise with the iteration above. The first concerns initial conditions. As in any iterative process, initial conditions matter; depending on these there will be a transient period before the sequence becomes stationary and is consistently generating samples from $p(x)$. In order to allow for this, the algorithm is usually run for a *burn-in* period before samples are drawn. The second issue is concerned with independence; as observed above, the proposal density may only allow small jumps in the state/sample space, so states close together in the sequence will be *correlated*. To obtain independent samples, one only saves every $n_i{}^{\text{th}}$ state; this process is called *thinning*. Ideally, one chooses the thinning interval long enough for the states to potentially travel across the whole support of the density.

The ability to sample from a distribution provides access to a great deal of information. Suppose one is interested in a function F of the random variables of interest $\underline{x}$; the main quantity of interest is likely to be the expectation:

$$E[F(\underline{x})] = \int F(\underline{x}) p(\underline{x}) d\underline{x} \tag{8.12}$$

The basis of the Monte Carlo (MC) method is that, if one can draw a sequence of samples $\{\underline{x}_1, \ldots, \underline{x}_N\}$, from $p(\underline{x})$, one has the approximation:

$$E[F(\underline{x})] = \int F(\underline{x}) p(\underline{x}) d\underline{x} \approx \frac{1}{N} \sum_{i=1}^{N} F(\underline{x}_i) \tag{8.13}$$

which has the critical property that the accuracy of the estimates *does not depend on the dimension of* $\underline{x}$ [22].

Furthermore, if samples from the distribution are available, one can easily construct parametric and nonparametric (e.g. kernel density) estimates of the distribution.

Given that MCMC, in particular the MH method, allows one to draw samples from a given distribution and earlier discussions explained how this can lead to system identification via estimation of parameter distributions and statistics, what remains to be explained is the specific detail of how this is implemented here.

In order to implement MCMC, it is necessary to evaluate the density $p^*(\underline{w}|\mathcal{D})$, which is the required $p(\underline{w}|\mathcal{D})$ up to a constant multiple. Using Bayes theorem, one has:

$$p(\underline{w}|\mathcal{D}) = \frac{p(\mathcal{D}|\underline{w}) p(\underline{w})}{p(\mathcal{D})} \tag{8.14}$$

and as $p(\mathcal{D})$ is fixed by the data (and cannot be evaluated anyway), one has:

$$p^*(\underline{w}|\mathcal{D}) = p(\mathcal{D}|\underline{w}) p(\underline{w}) \tag{8.15}$$

as the required density (p, up to a constant). This object is the product of a likelihood for the data (which can be computed under the assumption that the noise is Gaussian—the log likelihood is then related to the least-squared error between predictions using the candidate parameters and the measured data) and a prior for the parameters. If very little is known about the system, an uninformative (constant, and therefore improper) prior can be assumed, and then one can take:

$$p^*(\underline{w}|\mathcal{D}) = p(\mathcal{D}|\underline{w}) \tag{8.16}$$

The only thing needed now for the MH algorithm is the proposal distribution $q(\underline{x}'|\underline{x}^i)$, and arguably the simplest prescription for this is a spherical Gaussian distribution:

$$q(\underline{x}'|\underline{x}^i) \sim N(\underline{x}^i, \sigma_p I) \tag{8.17}$$

controlled by a single scale parameter σ_p (I is the identity matrix).

None of the above discussion is specific to differential equation models; in fact the algorithm is applicable to any type of predictive model. Differential equations are singled out here because they often represent systems in structural dynamic problems.

8.4 Case Study in Parameter Estimation: The Duffing Oscillator

The training data for the current study were generated by simulation. The equation of motion considered will be the classical Duffing oscillator of Eq. (8.2). The data were generated here using Matlab [23], using a fixed-step fourth-order Runge-Kutta scheme for initial value problems [24]. The parameters for the baseline system here were: $m = 1$, $c = 20$, $k = 1.0 \times 10^4$ and $k_3 = 5 \times 10^9$. The excitation $x(t)$ was initially a Gaussian random sequence with mean zero and standard deviation 10.0. The step size (or sampling interval) was taken as 0.001 s, corresponding to a sampling frequency of 1000 Hz. Noise of RMS 1% of the response was added to the displacement signal which was used, with the corresponding samples of excitation force, as 'training data' for the algorithm. The training set used here was composed of 500 points corresponding to a record duration of 0.5 s. The clean training set, force and displacement (before the addition of the noise) is shown in Fig. 8.1.

Once the data had been generated, the MCMC algorithm discussed in the last section was applied to the identification problem. The MCMC identification routine was coded in the Python language using the package PyMC [25]. As well as the four parameters: m, c, k and k_3, the MCMC routine also learned the output noise variance; however, for convenience this was encoded as a precision parameter $\beta = 1/\sigma_\epsilon^2$. Because of the differences in scale between the parameters, log values were used in the algorithm to improve conditioning. All of the model parameters were given uniform priors spanning a range one order of magnitude above and below the true parameter values; the initial conditions for the Markov chain were set close to the true parameter values. The proposal distribution q was set as a spherical Gaussian with variance of 0.1 in each direction. The MCMC algorithm was set to run for 25,000 samples, thinning by taking every 10^{th} sample, and a burn-in of 5000 samples was used. The results from the MCMC run, summarising 2000 samples altogether, are shown in Fig. 8.2. Each of the subfigures shows the sequence of MC samples for the parameter of interest, followed by a frequency histogram giving a coarse view of the parameter density.

The first observation one can make from Fig. 8.2 is that the chains for the parameters m, c and β are largely stationary immediately following the burn-in period, while the parameters k and k_3 may still be undergoing some longer scale fluctuations. One also observes that the long-term behaviours of the latter two parameters are anticorrelated. This is understandable in that some of the true cubic behaviour can be accommodated by biasing the linear term. There is also (less evident) longer-term variation in the m parameter which is correlated with the k parameter. This is also understandable;

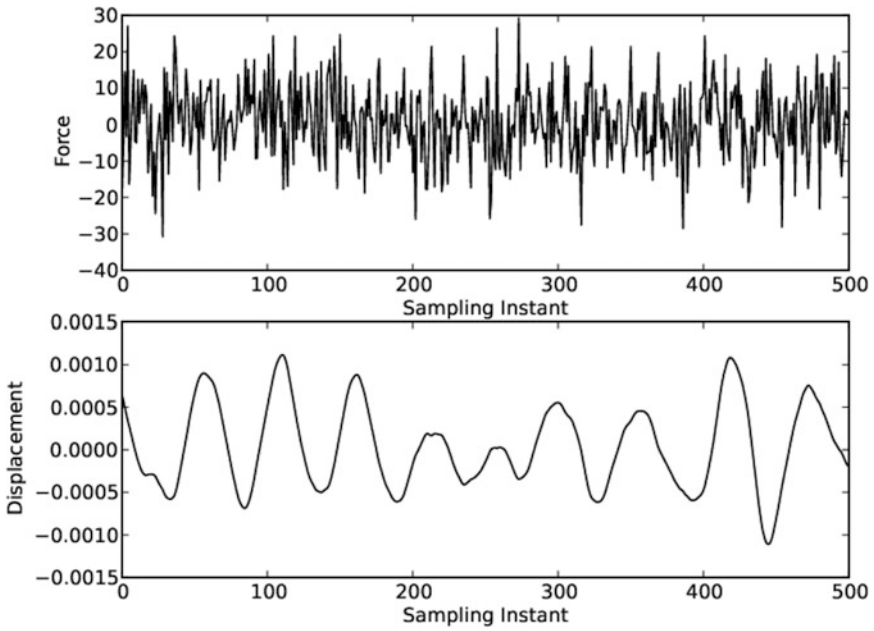

Fig. 8.1 Training data for Duffing system case study

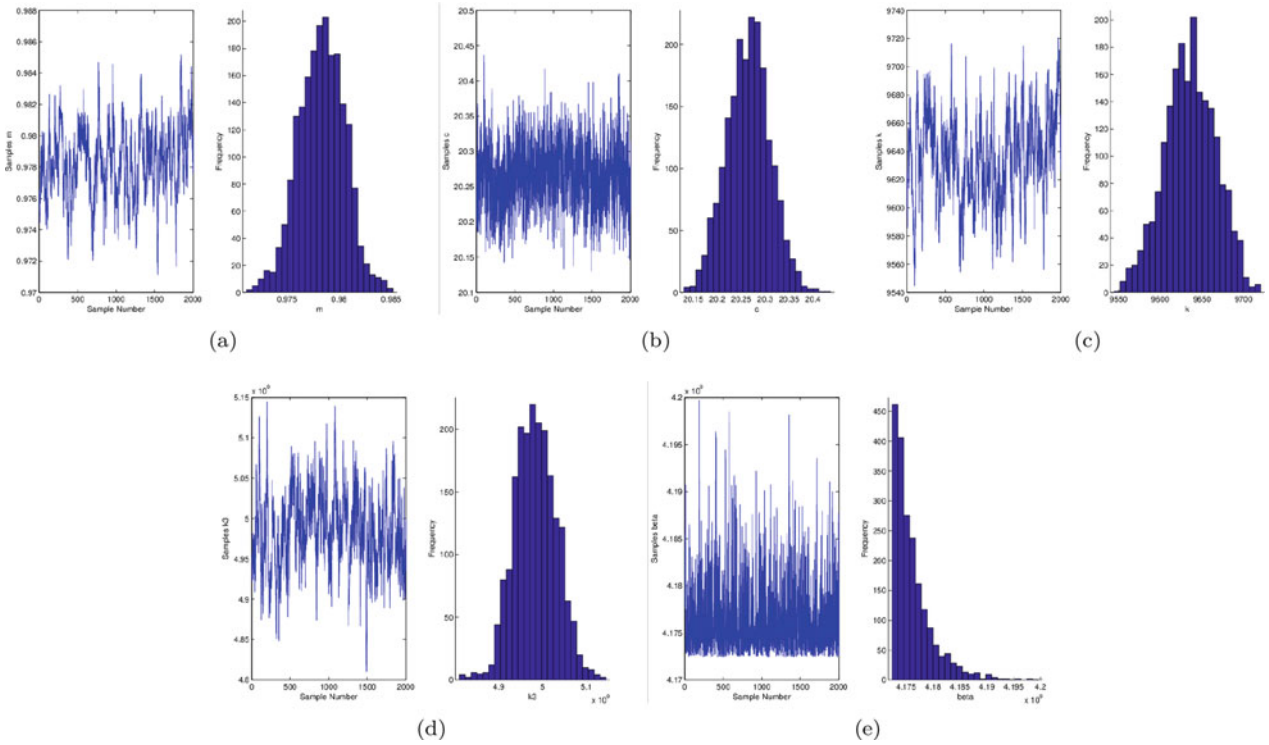

Fig. 8.2 Results from MCMC identification of Duffing oscillator system. (**a**) m. (**b**) c. (**c**) k. (**d**) k_3. (**e**) β

Table 8.1 Parameter estimates for Duffing oscillator model

Parameter	True value	MC mean	MC std
m	1.0	0.978	0.002
c	20.0	20.265	0.045
k	1.0×10^4	9635.7	30.7
k_3	5.0×10^9	4.983×10^9	0.048×10^9

in order to explain the data, the model needs to have the correct natural frequency $\omega_n = \sqrt{k/m}$, and any fluctuations in k should be mirrored in m in order to keep the correct ω_n for the system. When the mean and standard deviations for the parameters were estimated over the samples in each chain, the results were as summarised in Table 8.1.

The results show a little bias in the sense that the true parameters are not within the 3σ bounds of the estimates. This bias is because the chains are not yet stationary by the end of the calculation, partly because of the long-run correlations between the parameters.

As an objective measure of fidelity of the model predictions, one can define a *normalised mean-square error* by:

$$NMSE(y^*) = \frac{100}{N\sigma_y^2}\sum_{i=1}^{N}(y_i - \backslash ys_i)^2 \tag{8.18}$$

where the y_i are the observed outputs and the y_i^* are the predictions. Experience with this measure has shown that a value of less than 5.0 generally indicates a good model, while a value less than 1.0 suggests excellence. With the MCMC parameters, the NMSE for the predictions here is 0.53, which indicates an excellent fit to the data. In contrast to an identification scheme where the parameter distributions are *assumed* Gaussian, the parameter samples are available here so that a test can be carried out to check. Also nonparametric estimators for the densities can be applied. Using the last 50 samples from the chains, the predicted responses for the training inputs were computed and are shown superimposed on the true response in Fig. 8.3. There is very little variation between the realisations; this requires further discussion.

The low degree of variation between realisations is a consequence of the way the predictions have been made and is on the optimistic side. By integrating the differential equations across the entire time with a single realisation of the parameters, the predictions ignore the component of uncertainty associated with *state estimation*. One might argue that the correct course

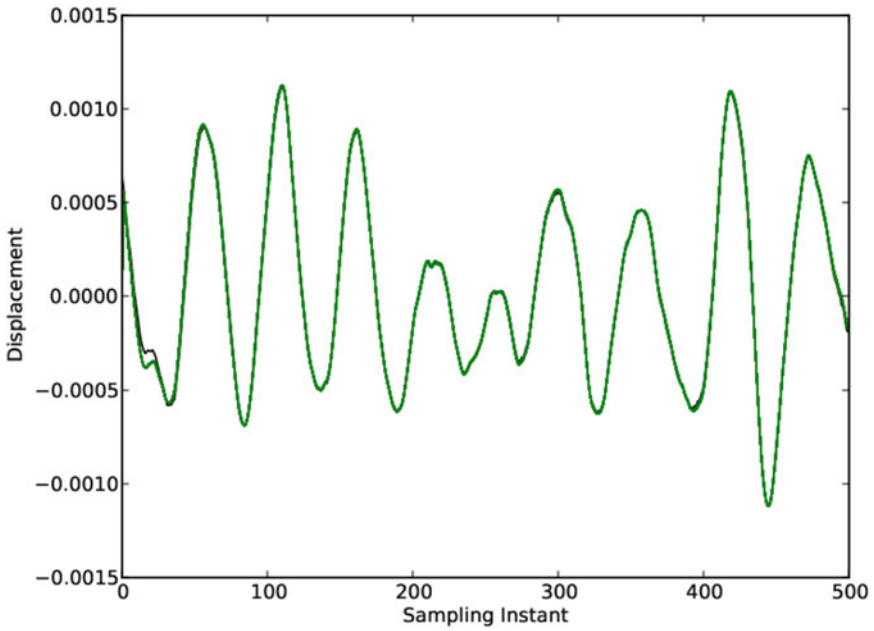

Fig. 8.3 Predictions using parameters from MCMC parameter samples, superimposed on observed data

Table 8.2 Parameter estimates for Duffing oscillator model: high noise case

Parameter	True value	MC mean	MC std
m	1.0	0.982	0.01
c	20.0	20.40	0.13
k	1.0×10^4	9693.3	81.5
k_3	5.0×10^9	4.99×10^9	0.13×10^9

of action would be to integrate forward one step at a time, sampling from the parameter distribution, to make an estimate of the response at the next time step. This strategy will clearly increase the overall bounds on the predictions. In order to expose the effect under discussion more clearly, a further identification of the Duffing data was carried out, this time adding noise of standard deviation of 5% of the signal before the MCMC process. The training data is as before for the system, but for this example an independent test set of data was used to assess the predictive capability of the model. The parameter estimates in this case are summarised in Table 8.2.

As one would expect, the parameter estimates in the higher noise case have greater standard deviations as compared to those in Table 8.1. This time, in order to show the effects of state estimation, the predictions were repeated but this time sampling from the MCMC parameter samples at *each time step* in the Runge-Kutta process. 50 realisations were made and the mean prediction was extracted as was the variance in the predictions. In order to accommodate the fact that the 'measured' data here are noisy, one has to add the MCMC-estimated noise variance for the computed bounds. The result of this calculation is shown in Fig. 8.4, which now has the measured data falling within the prediction intervals.

8.5 Model Selection and Approximate Bayesian Computation

The problem of *structure detection* or *model selection* discussed in the introduction here is extremely difficult when approached in its full generality. Unlike parameter estimation which searches some finite-dimensional parameter space to find a minimum according to some error criterion, structure detection requires searching some infinite-dimensional function space. In the simplest case, one imagines replacing the y^3 in Duffing Eq. (8.2), with some arbitrary stiffness function $f(y)$; even with constraints like continuity or differentiability, the search space is infinite-dimensional. Leaving aside intermediate possibilities for the moment, the most severe constraint one could impose is to propose a finite set of *candidate functions*, from which to choose. An offline approach to the identification would then be to run the MCMC algorithm for each candidate model and then select the best according to some validation criterion. Although this would work, it involves multiple identification runs and would potentially be computationally expensive; it also lacks elegance. A more elegant solution

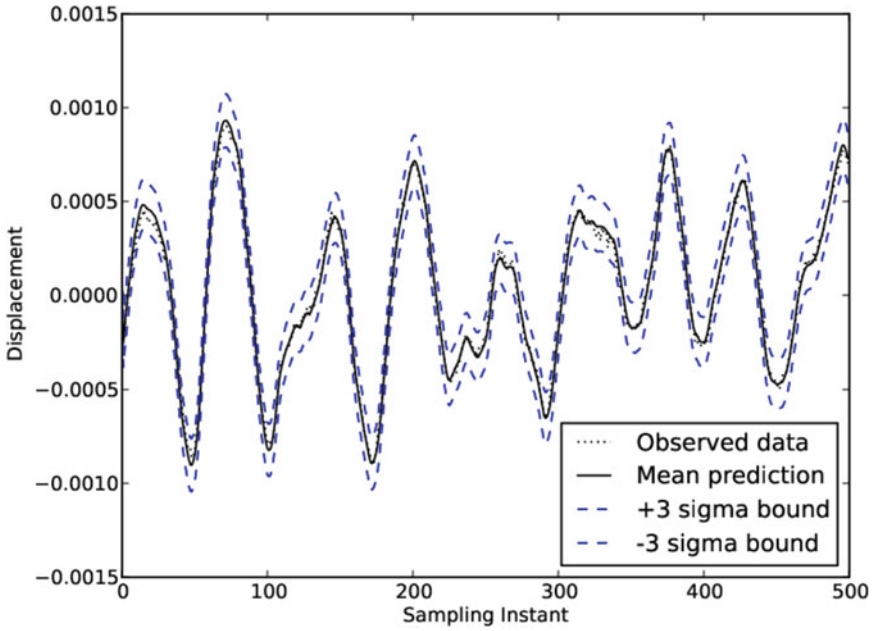

Fig. 8.4 Predictions using parameters from MCMC parameter samples identified in higher noise case. Bounds take into account parameter and state uncertainty and noise variance

would carry out both structure detection and parameter identification within one identification run. Such an algorithm would ideally trade off model complexity against model fidelity and thereby protect against the possibility of *overfitting*. Such algorithms which carry out both model selection and parameter estimation have recently been grouped under the term *equation discovery*. As Bayesian algorithms immediately suggest themselves, they implicitly implement such a trade-off [22].

What then would such a model look like? Having just seen the power of MCMC for parameter estimation, one might conceive of a similar algorithm where the Markov chain not only jumps between values in the parameter space but also jumps between models in the candidate set. Such methods do exist, but they are necessarily more complex than the MH algorithm discussed earlier. One of the problems can be seen immediately by considering the situation where the candidate set is {linear, Duffing}, where the linear model structure $\mathcal{M}_1$ is given by Eq. (8.1) and the Duffing structure $\mathcal{M}_2$ is given by (8.2). In this case, the parameter space for $\mathcal{M}_1$ is three-dimensional, while that for $\mathcal{M}_2$ is four-dimensional; the Markov chain would need to move between spaces of different dimension. Designing an MCMC algorithm with such a capability turns out to be quite difficult if one wishes for the convergence guarantees that hold for MH, etc. [22]. One algorithm with the desired properties is the *reversible-jump MCMC* algorithm [26]. While RJ-MCMC has been applied for NLSI [27, 28], it is difficult to code, is computationally expensive and depends on a number of algorithm parameters (hyperparameters), which require careful tuning. Fortunately, there is a 'simpler' alternative—*approximate Bayesian computing* (ABC).

The ABC algorithm has been applied in many contexts for equation discovery: genetics [29], biology [30, 31] and psychology [32]. It soon attracted attention as a promising method in NLSI [15, 33]. There are a number of variations on the ABC algorithm; for example, the approach in [33] was based on subset selection, while that of [15] was based on sequential MC (SMC). The SMC variant of the algorithm will be described and applied in the following. ABC offers the possibility of managing larger datasets and higher numbers of competing models with different dimensionalities, circumventing the limitations of RJ-MCMC.

In the core ABC algorithm, the objective is to obtain a good and computationally affordable approximation to the posterior distribution:

$$p(\underline{w}|\mathcal{D}^*, \mathcal{M}) \propto p(\mathcal{D}^*|\underline{w}, \mathcal{M})\, p(\underline{w}|\mathcal{M}) \tag{8.19}$$

where $\mathcal{M}$ is the model controlled by the set of parameters $\underline{w}$, $p(\underline{w}|\mathcal{M})$ denotes the prior distribution over the parameter space and $p(\mathcal{D}^*|\underline{w}, \mathcal{M})$ is the likelihood of the observed data $\mathcal{D}^*$ for a given parameter vector $\underline{w}$.

ABC was originally designed as a *likelihood-free* method to overcome issues from the intractable likelihood functions encountered in various real-world problems; as such, it relies on systematic comparisons between *observed* and *simulated*

data. The main principle consists of comparing the simulated data, $\mathcal{D}$, with observed data $\mathcal{D}^*$, and accepting simulations if a suitable distance measure between them, $\Delta(\mathcal{D}, \mathcal{D}^*)$, is less than a specified threshold ε, defined by the user. The ABC algorithm thus provides a sample from the approximate posterior of the form:

$$p(\underline{w}|\mathcal{D}^*, \mathcal{M}) \approx p_\varepsilon(\underline{w}|\mathcal{D}^*, \mathcal{M}) \propto \int f(\mathcal{D}^*|\underline{w}, \mathcal{M})\mathbf{1}\left(\Delta(\mathcal{D}, \mathcal{D}^*) \leq \varepsilon\right) p(\underline{w}|\mathcal{M})\mathrm{d}\mathcal{D} \tag{8.20}$$

where $\mathbf{1}\left(\Delta(\mathcal{D}, \mathcal{D}^*) \leq \varepsilon\right)$ is an indicator function which is unity if the bracketed condition is met and zero otherwise. When ε is small enough, $p_\varepsilon(\underline{w}|\mathcal{D}^*, \mathcal{M})$ will be a good approximation to the true posterior distribution.

In this work, the ABC-SMC algorithm of [30] will be illustrated. Generally speaking, the algorithm works as a *particle filter* which can be used to identify nonlinear dynamical systems [34]. The algorithm is based on the *sequential importance sampling* (SIS) algorithm, the Monte Carlo (MC) method which has formed the basis for most (SMC) algorithms developed in the past [35]. The key idea of ABC-SMC is to represent the required posterior density function by a set of random samples (*particles*) with associated weights. The algorithm iterates via a number of intermediate posterior distributions, before converging to the optimal approximate posterior distribution satisfying a convergence criterion defined by the user.

Algorithm 1 ABC-SMC for model selection

Input: Observed data u^*, n competing models $\mathcal{M}_{k=1}^n$, tolerance threshold ε_1, prior distributions $\pi(\alpha)$, $\pi(\mathcal{M}_k)$
Output: Model posterior probabilities, parameter distributions

At iteration t = 1,
for $i = 1 : N$ **do**
  repeat
    Select $\mathcal{M}^* = m_k$ from the prior distribution.
    Select α_k^* from the prior: $\pi(\alpha_k|m_k)$.
    Simulate u from $\mathcal{M}_k(u|\alpha_k^*)$.
    until $\Delta(u^*, u) < \varepsilon_1$.
  Set the particle as $\mathcal{M}_1^{(i)} = m_k$ and $\alpha_{\mathcal{M}_1}^{(i)} = \alpha_k^*$ with weight $\omega_1^{(i)} = \frac{1}{N}$.
end for
for $t = 2, \ldots, T$ **do**
  for $i = 1, \ldots, N$ **do**
    repeat
      Select $\mathcal{M}^* = m_k$ from the prior distribution.
      Sample $\alpha_{k,t-1}^{(i)}$ with corresponding weights $\omega_{t-1}^{(j)}$ and perturb the particle by generating α_k^*.
      Simulate u from $\mathcal{M}(u|\alpha^*)$.
      until $\pi(\alpha_k^*|m_k) > 0$ and $\Delta(u, u_k^*) < \varepsilon_k$
      Set the particle as $\mathcal{M}_t^{(i)} = m_k$ and $\alpha_{\mathcal{M}_t}^{(i)} = \alpha_k^*$ with weight:

$$\omega_t^{(i)} = \frac{\pi(\alpha_k^*|m_k)}{\sum_{j=1}^{N} \omega_{t-1}^{(j)} K_\alpha\left(\alpha_k^*|\alpha_{k,t-1}^{(j)}\right)}$$

  end for
For every m_k, $k = 1, \ldots, \ell$, normalise the weights.
end for

Following the scheme shown in Algorithm 1, one starts the iteration with an arbitrarily large tolerance threshold ε_1 to avoid a low acceptance rate and thus computational inefficacy. One selects directly from the prior distributions $p(\mathcal{M})$ and $p(\underline{w})$, evaluates the distance $\Delta(\mathcal{D}^*, \mathcal{D})$ and then compares this distance to ε_1, in order to accept or reject the $(\mathcal{M}, \underline{w})$ selection. This process is repeated until N particles distributed over the competing models are accepted. One then assigns equal weights to the accepted particles for each model. For the next iterations ($t > 1$) the tolerance thresholds are set such that $\varepsilon_1 > \varepsilon_2 > \ldots > \varepsilon_t$. The choice of the final tolerance schedule denoted here by ε_t depends mainly on the goals of the practitioner.

The dynamics by which ε evolves is a matter of choice; there is no general prescription. The tolerance threshold can be selected manually or adaptively, based on the distribution of the accepted distances in the previous iteration, $t - 1$. For example, the threshold of the second iteration can be set to the p^{th} percentile of the distances in the first iteration. This would seem to be the most common choice of tolerance threshold sequence since it is intuitive and simple to define. Both methods were used in this work and seem to do very well, in the sense that an appropriate acceptance rate is maintained over the populations. For the second strategy, it was found that a percentile between 20 and 40 is a rational choice. Once ε_2 is set,

one selects a model and a particle from the previous weighted set of particles and perturbs it via a predefined kernel; again the selection of the kernel is a matter of choice. A widely used option is to define the perturbation kernel as a multivariate Gaussian centred on the mean of the particle population, with a covariance matrix set to the covariance of the population obtained in the previous iteration. For a deep discussion of various schemes for specifying the perturbation kernels, the reader is referred to [36].

In this study, the particle perturbation distribution is uniform and symmetric around zero, with the interval width (for each parameter) taken as the range of the parameter in the previous population. One then calculates the distance $\Delta(\mathcal{D}^*, \mathcal{D})$, compares to the new tolerance threshold and accepts the new particle if $\Delta(\mathcal{D}^*, \mathcal{D}) \leq \varepsilon_2$; otherwise the particle is rejected. This process is repeated until a new set of N particles is assembled. One then updates the particle's weight according to the kernel. The entire procedure is repeated until convergence is met. One way to accept convergence is to impose a target threshold close to zero; another is to control the acceptance ratio, which is measured at each iteration. This ratio is the quotient of the number of proposals to the full number of proposed particles at every step. When this ratio falls below some given limit, the algorithm is halted. There are actually numerous meaningful ways to establish convergence [15].

When the algorithm halts, the approximate marginal posterior distribution for model candidate $\mathcal{M}_i$ is estimated by:

$$P(\mathcal{M}_i|\mathcal{D}^*) \approx \frac{\text{Accepted particles for } \mathcal{M}_i}{\text{Total number of particles } N} \tag{8.21}$$

As one can see, the algorithm does require the selection of a number of hyperparameters—the sequence of acceptance thresholds. A careful choice of those hyperparameters is important, since they will affect performance of the algorithm. A bad choice may lead to computational expense and/or biased parameter estimates.

8.6 Case Study in Equation Discovery: Hysteretic Systems

Hysteretic systems—or systems with *memory*—have always presented problems in terms of system modelling. The models often contain terms which are highly (and/or discontinuously) nonlinear in the parameters, and they may also evolve via unmeasured states. Even parameter estimation can be challenging. One compact and versatile model class which is popular for hysteretic SI is the *Bouc-Wen* (BW) class [37, 38].

The general single-degree-of-freedom (SDOF) hysteretic system described in the terms of Wen [38] is represented below, where $g(y, \dot{y})$ is the polynomial part of the internal restoring force, $z(y, \dot{y})$ is the hysteretic part and $x(t)$ is the excitation, as usual:

$$m\ddot{y} + g(y, \dot{y}) + z(y, \dot{y}) = x(t) \tag{8.22}$$

where m is the system mass. In the following discussion, the polynomial part of the internal force will be considered linear: i.e. $g(y, \dot{y}) = c\dot{y} + ky$.

The hysteretic component is defined by Wen [38], via the additional equation of motion:

$$\dot{z} = \begin{cases} -\alpha|\dot{y}|z^n - \beta\dot{y}|z^n| + A\dot{y}, & \text{for } n \text{ odd} \\ -\alpha|\dot{y}|z^{n-1}|z| - \beta\dot{y}|z^n| + A\dot{y}, & \text{for } n \text{ even} \end{cases} \tag{8.23}$$

The parameters α, β and n govern the shape and the smoothness of the hysteretic loop. The equations offer a simplification from the point of view of parameter estimation, in that the linear stiffness term from g in Eq. (8.22) can be combined with the $A\dot{y}$ term in the state equation for z. The reader can refer to [14] for full details.

In this illustration, the response output will be assumed to be displacement. Data were simulated in the same manner as for the Duffing example earlier. The sampling interval was taken as 0.001 s, corresponding to a sampling frequency of 1000 Hz. Here, as in the first example, the excitation is Gaussian with zero mean, but with a standard deviation of 10. The exact parameter values used to generate the training data and the parameter ranges are summarised in Table 8.3. Figure 8.5 shows the BW model response with $n = 2$. The training data used here were composed of 1001 points, corresponding to a record duration of 1 s.

Table 8.3 Parameter ranges of the Bouc-Wen model

Parameter	True value	Lower bound	Upper bound
m	1	0.1	10
c	20	2	200
α	1.5	0.15	15
β	−1.5	−15	−0.15
A	6680	668	66,800

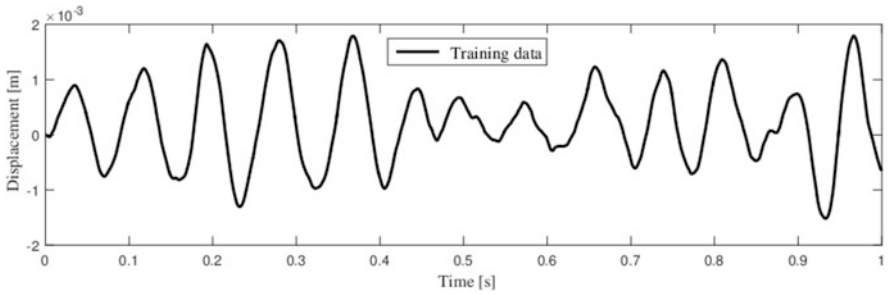

Fig. 8.5 Training data

The equation discovery problem here is created by proposing a range of potential models: a linear model and four BW models with different values of n.[5] Thus, five competing models are considered, denoted by,

$$\mathcal{M}_1 \quad : \quad m\ddot{y} + c\dot{y} + Ay = x(t) \tag{8.24}$$

$$\mathcal{M}_{2:5} \quad : \quad \text{Eqs. (8.22) and (8.23)}, \; n = 1:4 \tag{8.25}$$

To implement the ABC-SMC algorithm here, equal prior probabilities $p(\mathcal{M}_{i=1:5}) = \frac{1}{5}$ were assumed. In this example, the tolerance threshold sequence is adaptively defined. It was found that a tolerance threshold set at 20^{th} percentile of the particle distances from the previous iteration maintained a quite satisfactory acceptance rate through the algorithm run. The number of particles in the population was taken as 1000, and the distance metric simply used the NMSE defined in Eq. (8.18) earlier. The algorithm stopped when the difference between two consecutive tolerance thresholds was less or equal to 5×10^{-4}. The results obtained are summarised below (using noisy measurements, 1% RMS was added to the response).

Figure 8.6 shows how the ABC-SMC algorithm progressively eliminated the least likely models. One observes that $\mathcal{M}_5$ was the first to be eliminated which means that it is least adequate to explain the data. The linear model is removed in the population after. The models $\mathcal{M}_{2\to4}$ appear to be the most likely candidates to explain the data, since after eliminating $\mathcal{M}_5$ and $\mathcal{M}_1$, it seems quite difficult to favour one model above the other. Only at Population 18 ($\varepsilon = 0.0058$) does the algorithm start to favour $\mathcal{M}_3$; this would suggest that, at this level of error, even $\mathcal{M}_2$ and $\mathcal{M}_4$ may explain the data reasonably well, with preference for $\mathcal{M}_3$. The algorithm converges on the true model at Population 19 ($\varepsilon = 0.0042$). Figure 8.7 shows the histograms of the model parameter values, derived from the final population; the parameter statistics are presented in Table 8.4. Apart from α, which is outside the (5th, 95th) percentiles, the other parameters are well estimated. The training data and the model prediction are shown in Fig. 8.8, from which one can see the accuracy of the model.

The ABC-SMC algorithm is shown to be efficient in problems with several competing models; significantly, those models are quite similar.

Of course, there are many other approaches to equation discovery; the subject is currently experiencing a great deal of interest. One class of algorithms which is currently popular is based on the idea of a linear expansion over a dictionary. The idea is quite simple in principle; the equation required is proposed to be of the form (consistent with applications in structural dynamics):

$$\sum_{i=1}^{N} w_i f_i(\ddot{y}, \dot{y}, y, x) = 0 \tag{8.26}$$

[5] Of course, one could simply consider n as one of the parameters to be estimated, but this creates problems of its own.

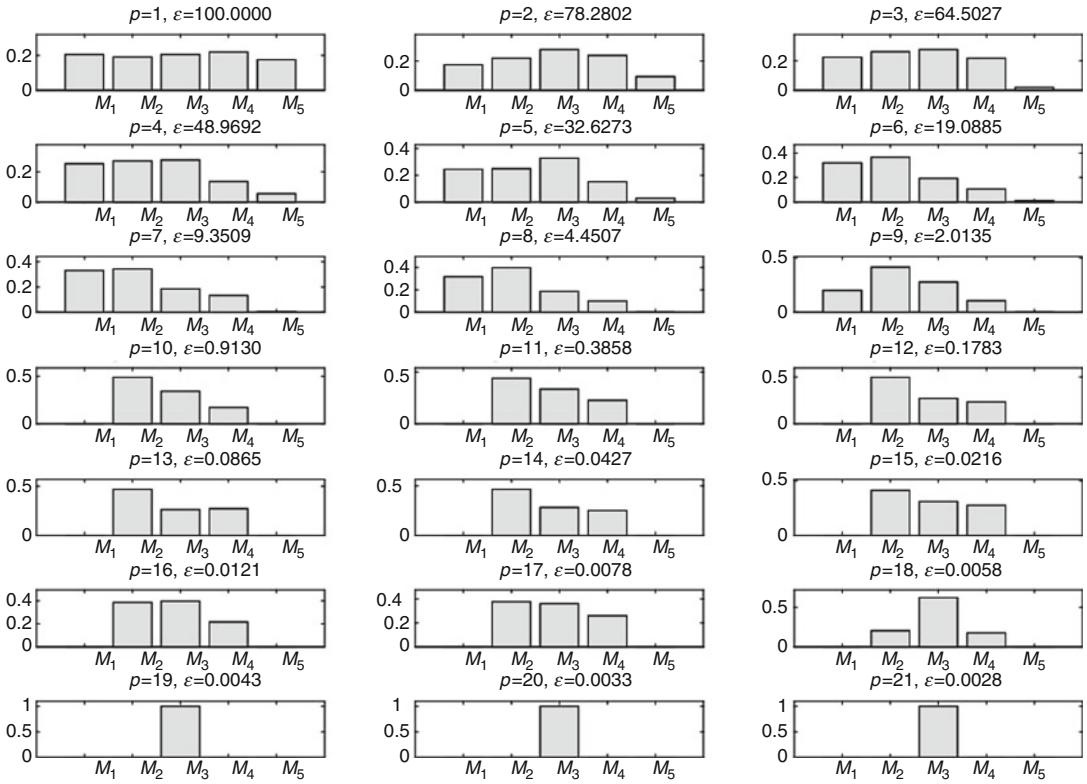

Fig. 8.6 Model posterior probabilities of the Bouc-Wen model over the populations

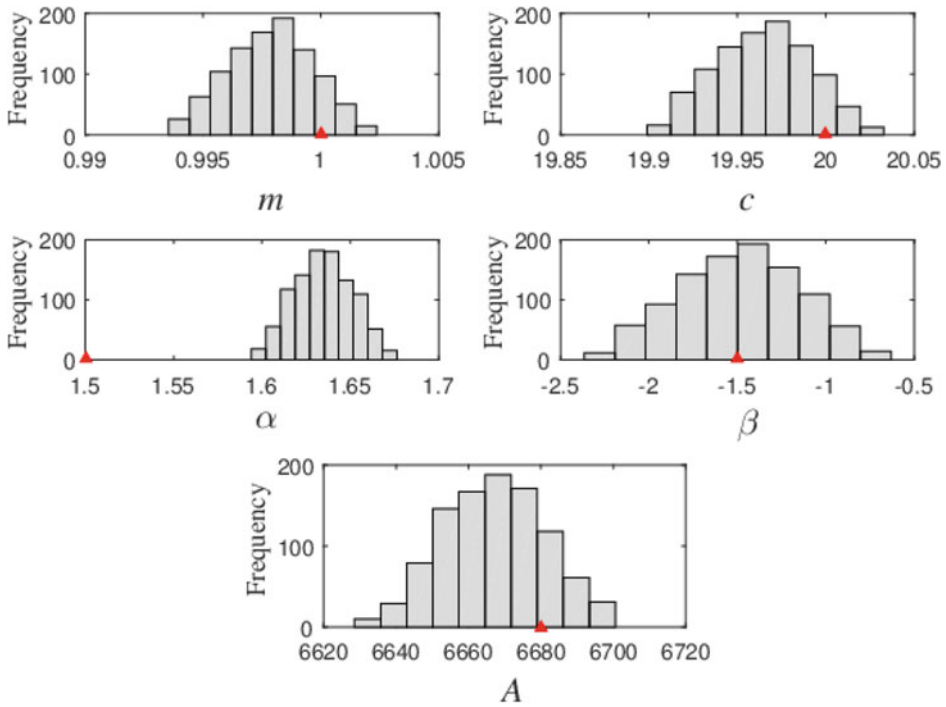

Fig. 8.7 Histograms of the identified BW model parameters (the red triangles show the true values)

where the w_i are tunable parameters and the f_i are N functions of the variables of interest (and their derivatives), *without* tunable parameters. The f_i are selected from a potentially large set of candidate terms—the *directionary*. In principle, there is no demand that the f_i form a complete set of basis functions. To give a concrete example, the dictionary $\{\ddot{y}, \dot{y}, y, y^3, x\}$ would

Table 8.4 Model parameter estimates from the last population

Parameter	True value	Mean, μ	Std. dev, σ	[5th, 95th] percentiles
m	1	0.9976	0.0017	[0.9947, 1.0004]
c	20	19.965	0.0248	[19.9241, 20.006]
α	1.5	1.6339	0.0149	[1.6083, 1.6577]
β	−1.5	−1.5005	0.3124	[−2.031, −0.9937]
A	6680	6665.1173	13.148	[6643.3231, 6687.1163]

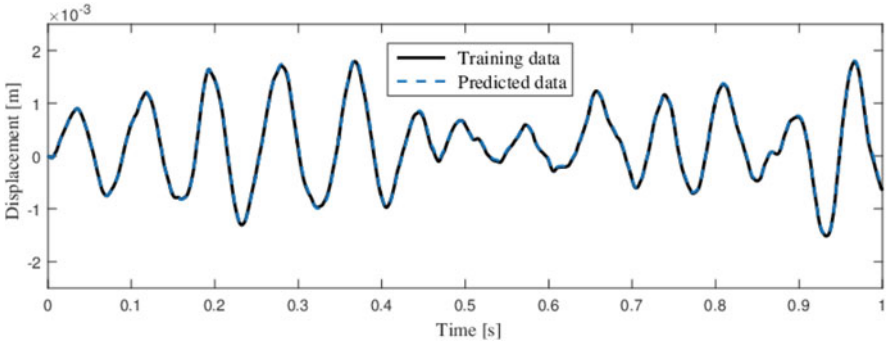

Fig. 8.8 Comparison between the training and predicted data

be sufficient to identify both the linear system in (8.1) and the Duffing oscillator in (8.2). In general, the dictionary would have very many terms, to increase the probability of discovering the correct equation; the issue then becomes the classic problem of overfitting. The solution is to find some means of enforcing sparsity in the model, i.e. driving the algorithm to select as few terms as possible in the model, by forcing as many parameters w_i as possible to zero [39–41]. One simple *shrinkage* approach is to monitor the contributions of individual terms to the overall variance and then zero any terms with contributions below some small threshold. There are many elegant Bayesian approaches to the problem, including using *automatic relevance determination* (ARD) priors over the parameters [2, 42]. More recent developments include the use of technology like *spike-and-slab* priors [43, 44].

8.7 Coloured Boxes and Physics-Informed Machine Learning

Here they come, every colour of the rainbow: black, white, brown.[6]

This section will return to the discussion of white, grey and black boxes; most of the material here follows the work of the second author during a recent fellowship. Before launching into a discussion of the technology, it is useful to revisit the basic terminology. In the introduction, a model which was determined *completely* by physics was termed a *white-box* model; in fact, it will be useful to relax this definition somewhat. While true white-box models do crop up in physics, they are comparatively rare in engineering. This fact occurs because even the most well-constructed systems and structures will deviate from their designs in some way, because of the imperfect nature of fabrication. In reality, one may know the *structure* of system equations of motion, but the exact parameters in operation will deviate from the design. For this reason, a white-box model here will be redesignated as one in which the model structure is not completely determined by the physics. If one needs to refer to the original concept, one could use the term *snow-white* model. With this amendment, a *grey-box* model is one for which the model structure and any parameters are undetermined by physics alone.

As stated in the introduction, it is generally unwise to construct pitch-black models using machine learners uninformed at all by physics. In some cases, this course of action is forced upon the modeller, but in general, some physical or engineering insight will be present and it is simply wasteful to ignore it. There are potentially many ways to construct a grey box model, but the simplest in principle is to form a direct sum of a white box and a black box, as in:

$$y(t) = F_t[\tilde{y}, \tilde{x}] + \Delta_t[\tilde{y}, \tilde{x}] + \varepsilon(t) \tag{8.27}$$

[6] Anonymous British snooker commentator.

where F_t is the white component and Δ_t is the black;[7] $\varepsilon(t)$ is assumed to be a noise sequence. In general F_t will be a structure suggested by physics with undetermined parameters with some physical significance; in contrast, Δ_t will be a nonparametric learner with parameters (and hyperparameters), devoid of physical significance.

Even this *basic* grey box presents technical problems if F_t and Δ_t are to be fitted simultaneously. One simple alternative strategy is to fit the white-box model, assuming that $y(t) = F_t[\tilde{y}, \tilde{x}]$, to then form the *residual* $r(t) = y(t) - F_t[\tilde{y}, \tilde{x}]$, and finally to fit $r(t) = \Delta_t[\tilde{y}, \tilde{x}]$. With this approach, the white-box model is primary, and the black box is considered a *residual model*, mopping up any systematic behaviour in y that is unaccounted for in F_t. Philosophically, Δ_t is countering any epistemic uncertainty in the physics and can be regarded as a *model discrepancy* term [45]. In the much simpler situation where y is a direct static function of x, the decomposition becomes:

$$y = \underbrace{f(x)}_{White-box} + \underbrace{\delta(x) + \varepsilon}_{Black-box} \tag{8.28}$$

A nice example of the application of a residual model can be found in [46], which is concerned with predicting wave-loading forces on offshore structure. For many years, the industry standard in predicting wave forces has been *Morison's equation*. However, Morison's equation is well-known to predict badly under certain Circumstances, e.g. when vortex shedding is present in the fluid kinematics. The approach in [46] adopts Morison's equation as the white-box component of the model:

$$y_t = \underbrace{C'_d U_t |U_t| + C'_m \dot{U}_t}_{Morison's\ Equation} + \underbrace{f([u_t,\ u_{t-1}, \ldots,\ u_{t-l_u},\ y_{t-1},\ y_{t-2}, \ldots,\ y_{t-l_y}]) + \varepsilon}_{GP-NARX} \tag{8.29}$$

where y_t is the wave force, C'_d is the *drag coefficient*, C'_m is the *inertia coefficient*, U is the wave velocity and $\dot{U}$ is the wave acceleration. In this case, the black-box component is a Gaussian process nonparametric learner, made dynamic by imposing a NARX structure which regresses the output on past inputs and outputs—a GP-NARX model [47]. In the GP-NARX component, $u_{t:t-l_u}$ are lagged exogenous inputs and $y_{t-1:t-l_u}$ are the lagged wave force; see [46] for more details. The grey box gives significant improvements on Morison's equation alone.

The term 'grey-box model' is perhaps most familiar to those from a control engineering background. Sohlberg [48, 49] provides a useful review and overview of grey-box models in this context. The term 'hybrid model' is sometimes used as a synonym for a grey box. Figure 8.9 attempts to capture and summarise some of the currently available modelling approaches relevant for challenges in structural dynamics on the white to black spectrum. Note that the "degree of greyness" of the models in the middle region will change according to implementation and application.

At the whiter end of the spectrum are modelling approaches where data are used for parameter estimation or model form selection (with equation discovery fitting in here). Considering the spectrum beyond residual models, the term *hybrid architectures* reflects the wider possibilities for combinations of white and black models (which could include the summation forms of (8.27) and (8.28)). The remainder of the spectrum contains models with structures that are more data-driven/black-box in nature. Sohlberg [49]) describes *semi-physical modelling* as when features are subject to a nonlinear transformation before being used as inputs to a black-box model; this is also referred to as *input augmentation*, see [50, 51] for more examples. These examples are placed under the heading of 'manipulation of black-box inputs'. *Constraints for machine learning algorithms* refers to methods that allow one to constrain the predictions of a machine learner so that they comply with physical assumptions. The final grouping of grey-box approaches mentioned here is *physics-guided black-box learners*. These are methods that use physical insight to attempt to improve model optimisation and include the construction of physics-guided loss functions and the use of physics-guided initialisation; these will not be discussed further here, but see, e.g. [52] for more details. The whole spectrum (with the exception of the pitch black) delineates the modern field of *physics-informed machine learning*.

The next illustration will concern *constraints for machine learning algorithms*; the machine learning approach here will be *Gaussian process* (GP) regression. GPs have been shown to be a powerful tool for regression tasks [53], which are becoming common in structural dynamic applications. Their use here and throughout the work of the authors is because of their (semi)non-parametric nature, their ability to function with a small number of training points and most importantly, the Bayesian framework within which they naturally work. The Gaussian process formulation provides a predictive *distribution*

[7] The notation here is intended to be flexible enough that it can represent many of the standard mathematical structures. The tilde is used to suggest that information for all times is available for the x and y. F_t and Δ_t are then *functionals* which can make use of any variable information *up to* time t. In this sense the notation is purely formal.

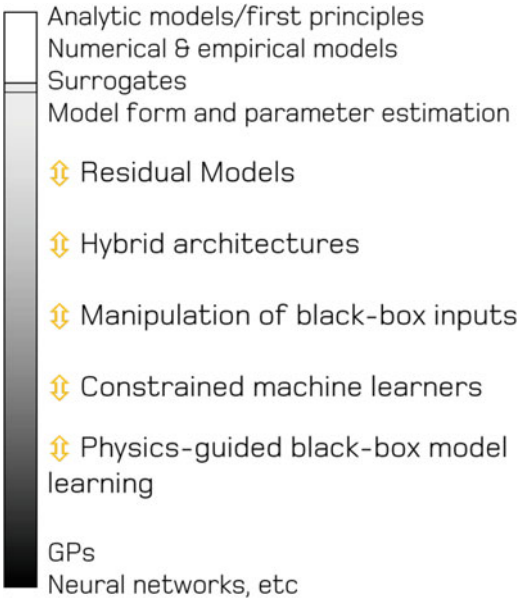

Fig. 8.9 Some modelling approaches on the white-black spectrum

rather than a single prediction point, allowing confidence intervals to be calculated and uncertainty to be propagated forward into any following analysis (see, e.g. [54]). As the use of GPs is now quite common, their complete formulation will not be introduced here. Suffice it to say that a GP requires a mean *function* $m(\underline{x})$ to be specified, rather than a constant vector, and a covariance function $k(\underline{x}, \underline{x}')$, rather than a matrix. The mean function expresses the central tendency of a process as it varies with time or space; the covariance expresses the variability. In the context of physics-informed machine learning, physical laws and constraints can be designed into the mean and covariance functions; in particular, for black-box models, the prior mean is often simply set to zero. The next case study illustrates how one can introduce physics into the mean function of a GP.

8.7.1 Case Study: Prior Mean Functions—Residual Modelling

The application domain here is in the performance monitoring of a cable-stayed bridge. The Tamar bridge is a cable-supported suspension bridge connecting Saltash and Plymouth in the South West of England, which has been monitored by the Vibration Engineering Section at the University of Exeter [55]. The interest here is in the development of a model to predict bridge-deck deflections that can be used as a performance indicator (see [56, 57]). The variations in deck deflections are driven by a number of factors, including fluctuating temperature and loading from traffic (which are included as inputs to the model). Figure 8.10a shows the regression target considered in this example, which is a longitudinal deflection. The monitoring period shown is from September (Autumn) to January (Winter). In this figure, one can see short-term fluctuations (daily), and a longer-term trend which is seasonal and driven by the increased hogging of the bridge deck as the ambient temperature decreases into the winter months. To mimic the situation where only a limited period of monitoring data is available for the establishment of an SHM algorithm, data from the initial month of the monitoring period are used to establish a GP regression model for deflection prediction (see [58] for more details).

A GP prediction, using the standard approach of a zero-mean prior, is shown in Fig. 8.10b. Here one can see exactly the behaviour that is expected; the model is able to predict the deck deflections well, in and around the training period, but is unable to predict the deflections in colder periods towards the end of the time series. The confidence intervals widen to reflect the fact that the inputs to the model towards the end of the period are different from those in the training set—this demonstrates the usefulness of the GP approach, as one knows not to trust the predictions in this period.

To formulate a grey-box model for this scenario, a physics-informed prior mean function is adopted that encodes the expected linear expansion behaviour of stay-cables with temperature [59]. Figure 8.10c shows the GP prediction with a linear prior mean function, where one can see a significant enhancement of predictive capability across the monitoring period. Where temperatures are at their lowest, the model predictions fall back on the prior mean function—which then

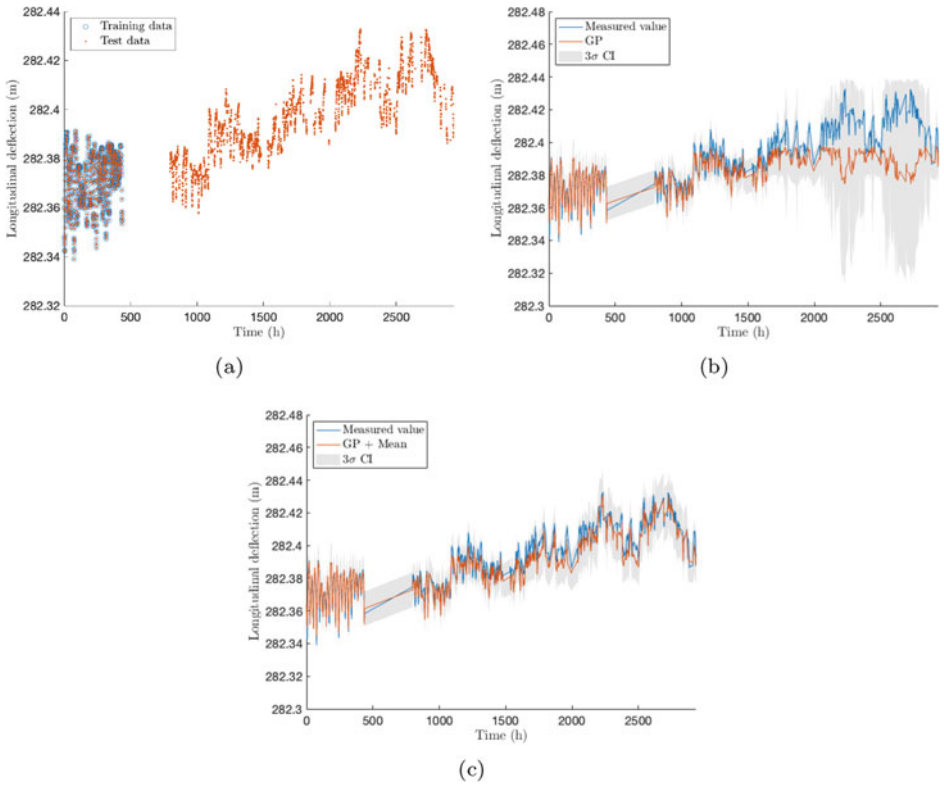

Fig. 8.10 Model for bridge deck deflections: (**a**) shows the training and test datasets for the GPs, (**b**) is a GP prediction with a zero mean function prior, and (**c**) shows the prediction when a simple physics-informed mean function is incorporated. See [58] for more details

behaves as a white box, allowing some extrapolative capability. The prediction error is significantly smaller for the grey-box model.

This example shows one of the significant strengths of a physics-informed approach. A nonparametric black-box learner will always be subject to generalisation issues; it will lose predictive capability if the conditions change from those experienced in the training set; it fails to extrapolate. In contrast, the grey-box model shows enhanced capability because it retains some explanatory power under any conditions in which the underlying physics hold.

Another advantage of grey-box models relates to the required quantity of the training data. If the white-box explains a significant part of the system behaviour, typically with a small number of meaningful parameters, this will reduce the necessary complexity of the black-box part. A simpler black-box model with a reduced parameter count then allows a reduction in the training data; this can be a significant advantage in engineering problems, where measured data may be expensive or difficult to obtain.

As mentioned above, using a GP as the nonparametric learner also allows physical insight to be included via the covariance function [60]. Although detailed case studies will not be presented here, the interested reader can consult [61] for a study relating to guided-wave structural health monitoring. In [62, 63], the physical boundary conditions for a plate structure are used to constrain GP predications on locating structural damage using acoustic emission signals.

8.8 Conclusions

This paper presents a tutorial treatment of certain data-based methods in nonlinear dynamics. The sheer size of the general subject has meant that only a small fraction of possible areas have been covered. The application domain within nonlinear dynamics has largely been restricted to the subject of *nonlinear system identification* (NLSI). Within NLSI, the choice was made to focus on Bayesian methodologies centred on white-box and grey-box models, although a large number of references have been cited, so that the interested reader can explore a little further afield. The paper also expands on the use

of combining physics-based and data-based models via the technology provided in the burgeoning field of *physics-informed machine learning*.

Acknowledgments The authors gratefully acknowledge the help of their colleagues and friends in the research presented here: Anis Bin Abdessalem, Will Becker, James Brownjohn, Nikos Devilis, Ramon Fuentes, Sam Gibson, Marcus Haywood-Alexander, James Hensman, Geoff Holmes, Matty Jones, Ki-Young Koo, Graeme Manson, Rajdip Nayek, Dan Pitchforth, Tim Rogers and Sikai Zhang. KW would like to thank the Engineering and Physical Sciences Research Council (EPSRC) for funding from the Programme Grant EP/R006768/1. EJC would like to thank EPSRC for funding via the Innovation Fellowship EP/S001565/1. For the purpose of open access, the authors have applied a Creative Commons Attribution (CC BY) licence to any author accepted manuscript version arising.

References

1. Brunton, S.L., Kutz, J.N.: Data-Driven Science and Engineering: Machine Learning, Dynamical Systems and Control. Cambridge University Press, Cambridge (2019)
2. Bishop, C.M.: *Pattern Recognition and Machine Learning*. Springer, New York (2013)
3. Legendre, A.M.: Nouvelles méthodes pour la détermination des orbites des comètes. Didot, F., Paris (1805)
4. Stigler, S.M.: Gauss and the invention of least squares. Ann. Stat. **9**, 475–474 (1981)
5. Ljung, L.: System Identification: Theory for the User, 2nd edn. Prentice-Hall, Englewood Cliffs (1998)
6. Sodersröm, T., Stoica, P.: System Identification. Prentice-Hall, Englewood Cliffs (1994)
7. Worden, K., Tomlinson, G.R.: Nonlinearity in Structural Dynamics. Institute of Physics Press, New York (2001)
8. Goldberg, D.E.: Genetic Algorithms in Search, Optimization and Machine Learning. Addison-Wesley, Reading (1989)
9. Worden, K., Manson, G.: On the identification of hysteretic systems, Part I: fitness landscapes and evolutionary identification. Mech. Syst. Signal Process. **29**, 201–212 (2012)
10. Worden, K., Becker, W.E.: On the identification of hysteretic systems, Part II: Bayesian sensitivity analysis and parameter confidence. Mech. Syst. Signal Process. **29**, 213–227 (2012)
11. Beck, J.L., Katafygiotis, L.S.: Updating models and their uncertainties. I: Bayesian statistical framework. ASCE J. Eng. Mech. **124**, 455–461 (1998)
12. Beck, J.L., Au, S.-K.: Bayesian updating of structural models and reliability using Markov chain Monte Carlo simulation. ASCE J. Eng. Mech. **128**, 380–391 (2002)
13. Girolami, M.: Bayesian inference for differential equations. Theor. Comput. Sci. **408**, 4–16 (2008)
14. Worden, K., Hensman, J.J.: Parameter estimation and model selection for a class of hysteretic systems using Bayesian inference. Mech. Syst. Signal Process. **32**, 153–169 (2012)
15. Abdessalem, A.B., Dervilis, N., Wagg, D.J., Worden, K.: Model selection and parameter estimation in structural dynamics using approximate Bayesian computation. Mech. Syst. Signal Process. **99**, 306–325 (2018)
16. Kovacic, I., Brennan, M.J.: The Duffing Equation: Nonlinear Oscillators and their Behaviour. Wiley, New York (2011)
17. Wolf, A., Swift, J.B., Swinney, H.L., Vastano, J.A.: Determining Lyapunov exponents from a time series. Physica D: Nonlinear Phenomena **16**, 285–317 (1985)
18. Staszewski, W.J., Worden, K.: Wavelet analysis of time-series: coherent structures, chaos and noise. Int. J. Bifurcation Chaos **9**, 455–471 (1997)
19. Holmes, P., Lumley, J.L., Berkooz, G.: Turbulence, Coherent Structures, Dynamical Systems and Symmetry. Cambridge University Press, Cambridge (1996)
20. Calderhead, B., Girolami, M., Higham, D.J.: Is it safe to go out yet? Statistical inference in a zombie outbreak model. Technical report, University of Strathclyde, Department of Mathematics and Statistics, Glasgow (2010)
21. Gelman, A., Carlin, J.B., Stern, H.S., Rubin, D.B.: Bayesian Data Analysis, 2nd edn.. Chapman and Hall/CRC, London (2004)
22. Mackay, M.J.C.: Information Theory, Inference and Learning Algorithms. Cambridge University Press, Cambridge (2003)
23. The Mathworks. Matlab V7 (2004)
24. Press, W.H., Teukolsky, S.A., Vetterling, W.T., Flannery, B.P.: Numerical Recipes: The Art of Scientific Computing, 3rd edn. Cambridge University Press, Cambridge (2007)
25. Patil, A., Huard, D., Fonnesbeck, C.J.: PyMC: Bayesian stochastic modelling in Python. J. Stat. Softw. **35**, 81 (2010)
26. Green, P.J.: Reversible jump Markov chain Monte Carlo computation and Bayesian model determination. Biometrika **82**, 711–732 (1995)
27. Tiboaca, O.D., Green, P.L., Barthorpe, R.J., Worden, K.: Bayesian parameter estimation and model selection of a nonlinear dynamical system using reversible jump Markov chain Monte Carlo. In: Proceedings of 26th International Conference on Noise and Vibration Engineering, Leuven (2014)
28. Tiboaca, O.D., Green, P.L., Barthorpe, R.J., Antoniadou, I., Worden, K.: Bayesian inference and RJMCMC in structural dynamics—on experimental data. In: Proceedings of the 34rd International Modal Analysis Conference, Orlando, FL (2016)
29. Beaumont, M., Cornuet, J., Marin, J., Robert, C.: Adaptive approximate Bayesian computation. Biometrika **96**, 983–990 (2009)
30. Toni, T., Stumpf, M.P.H.: Simulation-based model selection for dynamical systems in systems and population biology. Bioinformatics **26**, 104–110 (2010)
31. Barnes, C., Silk, D., Stumpf, P.: Bayesian design strategies for synthetic biology. Interface Focus **1**, 895–908 (2011)
32. Turner, B.M., Van Zandt, T.: A tutorial on approximate Bayesian computation. J. Math. Psychol. **56**, 69–85 (2012)
33. Chiachio, M., Beck, J.L., Chiachio, J., Rus, G.: Approximate Bayesian computation by subset simulation. SIAM J. Sci. Comput. **36**, A1339–A1338 (2014)

34. Ching, J., Beck, J.L., Porter, K.: Bayesian state and parameter estimation of uncertain dynamical systems. Probab. Eng. Mech. **21**, 81–96 (2006)
35. Doucet, A., Godsill, S., Andrieu, C.: On sequential Monte Carlo sampling methods for Bayesian filtering. Stat. Comput. **10**, 197–208 (2000)
36. Filippi, S., Barnes, C.P., Cornebise, J., Stumpf, M.P.H.: On optimality of kernels for approximate Bayesian computation using sequential Monte Carlo. Stat. Appl. Genet. Mol. Biol. **12**, 87–107 (2013)
37. Bouc, R.: Forced vibration of mechanical system with hysteresis. In: Proceedings of 4th Conference on Nonlinear Oscillation, Prague (1967)
38. Wen, Y.K.: Method for random vibration of hysteretic systems. Proceedings of the American Society of Civil Engineers Journal of the Engineering Mechanics Division, pp. 102 (1976)
39. Wipf, D.P., Rao, B.D.: Sparse Bayesian learning for basis selection. IEEE Trans. Signal Process. **52**, 2153–2164 (2004)
40. Brunton, S.L., Proctor, J.L., Kutz, J.N.: Discovering governing equations from data by sparse identification of nonlinear dynamical systems. Proc. Natl. Acad. Sci. **113**, 3932–3937 (2016)
41. Fuentes, R., Dervilis, N., Worden, K., Cross, E.J.: Efficient parameter identification and model selection in nonlinear dynamical systems via sparse Bayesian learning. In: Journal of Physics: Conference Series, vol. 1264, pp. 012050 (2019)
42. Tipping, M.E.: Sparse Bayesian learning and the relevance vector machine. J. Mach. Learn. Res. **1**, 211–244 (2001)
43. Ishwaran, H., Rao, J.S.: Spike and slab variable selection: Frequentist and Bayesian strategies. Ann. Stat. **33**, 730–773 (2005)
44. Nayek, R., Fuentes, R., Worden, K., Cross, E.J.: On spike-and-slab priors for Bayesian equation discovery of nonlinear dynamical systems via sparse linear regression. Mech. Syst. Signal Process. **161**, 107986 (2021)
45. Kennedy, M., O'Hagan, A.: Bayesian calibration of computer models. J. R. Stat. Soc. Ser. B **63**, 425–464 (2005)
46. Pitchforth, D.J., Rogers, T.J., Tygesen, U.T., Cross, E.J.: Grey-box models for wave loading prediction. Mech. Syst. Signal Process. **159**, 107741 (2021)
47. Worden, K., Becker, W.E., Rogers, T.J., Cross, E.J.: On the confidence bounds of Gaussian process NARX models and their higher-order frequency response functions. Mech. Syst. Signal Process. **104**, 188–223 (2018)
48. Sohlberg, B.: Supervision and Control for Industrial Processes: Using Grey Box Models, Predictive Control and Fault Detection Methods. Springer Science and Business Media, Berlin (2012)
49. Sohlberg, B., Jacobsen, E.W.: Grey box modelling—branches and experiences. IFAC Proceedings Volumes **41**, 11415–11420 (2008)
50. Rogers, T.J., Holmes, G.R., Cross, E.J., Worden, K.: On a grey box modelling framework for nonlinear system identification. In: Special Topics in Structural Dynamics, vol. 6, pp. 167–178. Springer, Berlin (2017)
51. Worden, K., Barthorpe, R.J., Cross, E.J., Dervilis, N., Holmes, G.R., Manson, G., Rogers, T.J.: On evolutionary system identification with applications to nonlinear benchmarks. Mech. Syst. Signal Process. **112**, 194–232 (2018)
52. Willard, J., Jia, X., Xu, S., Steinbach, M., Kumar, V.: Integrating physics-based modeling with machine learning: A survey. arXiv preprint arXiv:2003.04919 (2020)
53. Rasmussen, C.E., Williams, C.K.I.: Gaussian Processes for Machine Learning. The MIT Press, New York (2006)
54. Gibson, S.J., Rogers, T.J., Cross, E.J.: Data-driven strain prediction models and fatigue damage accumulation. In: Proceedings of the 29th International Conference on Noise and Vibration Engineering (ISMA 2020) (2020)
55. Koo, K.Y., Brownjohn, J.M.W., List, D.I., Cole, R.: Structural health monitoring of the Tamar suspension bridge. Struct. Control. Health Monit. **20**, 609–625 (2013)
56. Cross, E.J., Worden, K., Koo, K.Y., Brownjohn, J.M.W.: Filtering environmental load effects to enhance novelty detection on cable-supported bridge performance. In: Bridge Maintenance, Safety and Management. CRC Press, New York (2012), pp. 745–752
57. Cross, E.J.: On Structural Health Monitoring in Changing Environmental and Operational Conditions. PhD thesis, University of Sheffield, Sheffield (2012)
58. Zhang, S., Rogers, T.J., Cross, E.J.: Gaussian process based grey-box modelling for SHM of structures under fluctuating environmental conditions. In: Proceedings of 10th European Workshop on Structural Health Monitoring (EWSHM 2020) (2020)
59. Westgate, R.: Environmental Effects on a Suspension Bridge's Performance. PhD thesis, University of Sheffield, Sheffield (2012)
60. Cross, E.J., Rogers, T.J.: Physics-derived covariance functions for machine learning in structural dynamics. In: SYSID 2021, Padova, Italy (2021)
61. Haywood-Alexander, M., Dervilis, N., Worden, K., Cross, E.J., Mills, R.S., Rogers, T.J.: Structured machine learning tools for modelling characteristics of guided waves. arXiv preprint arXiv:2101.01506 (2021)
62. Jones, M.R., Rogers, T.J., Gardner, P.A., Cross, E.J.: Constraining Gaussian processes for grey-box acoustic emission source localisation. In: Proceedings of the 29th International Conference on Noise and Vibration Engineering (ISMA 2020) (2020)
63. Jones, M.R., Rogers, T.J., Martinez, I.E., Cross, E.J.: Bayesian localisation of acoustic emission sources for wind turbine bearings. In: Health Monitoring of Structural and Biological Systems XV, International Society for Optics and Photonics, vol. 11593 (2021)

Chapter 9
Modeling Nonlinear Structures Using Physics-Guided, Machine-Learnt Models

Michal J. Szydlowski, Christoph Schwingshackl, and Ludovic Renson

Abstract The constant drive to improve the performance of aeronautic structures is leading to new designs where nonlinearity is ubiquitous. Accurately predicting the dynamic behavior of nonlinear systems is very challenging because they can exhibit a wide range of behaviors that have no linear equivalent and are very sensitive to parameter changes. In this work, we consider a physics-based model to capture the underlying linear behavior of the system. This linear model is then augmented with a data-driven, machine-learnt model that captures the nonlinearities present in the system. Standard ML models have, however, several important shortcomings from an engineering point of view. They often require large training datasets, do not generalize well to unseen conditions, and can even be physically inconsistent. To overcome these limitations, we investigate the use of Lagrangian Neural Networks (LNNs) where a neural network is used to directly model the Lagrangian function of the system. To enforce physical consistency, the Euler-Lagrange equations of motion of the system are obtained by differentiating this neural network using automatic differentiation techniques. The potential of this modeling approach is numerically and experimentally shown on a range of systems with stiffness and damping nonlinearities.

Keywords Nonlinear systems · Physics-guided machine learning · Data-driven models

9.1 Introduction

Aerospace structures, rotating machines, turbines, pumps, and aero engines are complex dynamical systems that are known to suffer from vibration-related problems. Uncontrolled vibration leads to high cycle fatigue that might result in catastrophic failure [1]. Novel designs, strict regulations, and composite materials in aerospace structures make predicting vibration responses of already complex structures even more challenging, as they inherently exhibit nonlinearity. Predicting the dynamic behavior of nonlinear systems is difficult because of the wide range of behaviors that have no linear equivalent and are very sensitive to parameter changes. Identifying the source of nonlinearity and modeling requires domain-specific knowledge and experience and, to this day, poses a significant challenge [2–4].

In recent years, machine learning (ML) models started playing an important role in not only commercial applications but also in advancing scientific discovery in engineering [5–8]. Using state-of-the-art ML modeling techniques is tempting, especially in domains that are not fully understood, or where other well-established methods are computationally unfeasible. However, ML methods suffer from two main flaws: inefficient learning – as the models require large datasets, and lack of generalization beyond the training dataset – as the results often lack physical consistency [5, 9]. Therefore, in most cases, neither knowledge nor black-box approaches provide sufficient means to solve complex engineering problems. A recent research direction to address those issues is to implement the current understanding of physics in the data-driven or machine learning model [7, 9–15]. Such physics-guided data-driven machine-learnt models provide an opportunity to capitalize on existing domain knowledge and fill in the lack of understanding with black-box ML approaches.

In this work, we introduce an approach that uses a linear model that is augmented with a modified Lagrangian Neural Network (LNN) proposed by Cranmer et al. [16]. We demonstrate how to expand the LNN formulation to an externally forced and dissipative system and show how to use this approach in a nonlinear structural dynamic context.

M. J. Szydlowski · C. Schwingshackl · L. Renson (✉)
Imperial College London, South Kensington, London, UK
e-mail: l.renson@imperial.ac.uk

M. R. W. Brake et al. (eds.), *Nonlinear Structures & Systems, Volume 1*, Conference Proceedings of the Society for Experimental Mechanics Series, https://doi.org/10.1007/978-3-031-36999-5_9

9.2 Background

LNNs [16] provide a way to parametrize an arbitrary Lagrangian of a dynamical system. The well-established Lagrangian mechanics are based on the principle of least action [17] given by (9.1)

$$\mathcal{S} = \int_{t_0}^{t_1} \left(T\left(q_t, \dot{q_t}\right) - V\left(q_t\right)\right) dt = \int_{t_0}^{t_1} \mathcal{L}\left(q_t, \dot{q_t}\right) dt \tag{9.1}$$

where $\mathcal{S}$ is the scalar value of the action, $q, \dot{q}$ are generalized coordinates of the system, and $\mathcal{L}$ is the Lagrangian defined as the difference between kinetic energy T and potential energy V. The Euler-Lagrange equation

$$\frac{d}{dt}\frac{\partial \mathcal{L}}{\partial \dot{q}} = \frac{\partial \mathcal{L}}{\partial q} \tag{9.2}$$

can be expanded to the following equation of motion (EOM) in vector form

$$\ddot{q} = \left(\nabla_{\dot{q}} \nabla_q^T \mathcal{L}\right)^{-1} \left[\nabla_q \mathcal{L} - \left(\nabla_q \nabla_{\dot{q}}^T \mathcal{L}\right) \dot{q}\right], \tag{9.3}$$

as shown by Cranmer et al. [16].

The resulting EOM enables calculating $\ddot{q_t}$ for given a set of coordinates $q_t, \dot{q_t}$. In this work, we consider the case where $\mathcal{L}$ is an arbitrary Lagrangian function parametrized by a neural network. As integrating (9.3) yields the dynamics of the system, it is, therefore, possible to use it in a loss function that minimizes the discrepancy between model predictions, $\ddot{q_t}$, and experimental measurements, $\ddot{q_t}^{\text{true}}$. It is also worth noting that modern automatic differentiation frameworks have no problem with deriving the Jacobian, and hessian of $\mathcal{L}$ found in Eq. (9.3).

9.3 Introducing Nonconservative Forces

To expand the use of LNN to an engineering setting, let us consider a nonconservative system, with the presence of damping forces D, and other external excitation forces F. For such a system, one can modify (9.2), and write the following expression:

$$\frac{d}{dt}\frac{\partial \mathcal{L}}{\partial \dot{q}} - \frac{\partial \mathcal{L}}{\partial q} + \frac{\partial D}{\partial \dot{q}} + \frac{\partial F}{\partial q} = 0. \tag{9.4}$$

Similarly, to how Eq. (9.3) was achieved, expanding (9.4) yields the following expression:

$$\ddot{q} = \left(\nabla_{\dot{q}} \nabla_q^T \mathcal{L}\right)^{-1} \left[\nabla_q \mathcal{L} + \nabla_q E - \left(\nabla_q \nabla_{\dot{q}}^T \mathcal{L} + \nabla_{\dot{q}} F\right) \dot{q}\right]. \tag{9.5}$$

Here both $\mathcal{L}$ and the dissipative forces D are parametrized by a neural network, and the external forces $\nabla_q F$ are assumed to be measured directly from the experiment.

9.4 Experimental Analysis

To test the application of the extended LNN, a set of numerical experiments was conducted. A damped nonlinear mechanical system excited externally by a harmonic force F was simulated. The system comprised of a mass m, a linear k, a nonlinear cubic spring k_3, and a proportional damper c. The training data for the proposed presented method was simulated numerically using the following parameters $m = 0.64$, $k = 1$, $k_3 = 0.5$, and $c = 0.0064$, and for a set of different excitation frequencies as well as forces. Solutions were obtained using shooting with pseudo-arc length continuation methods [3] by fixing one parameter, the excitation frequency, or forcing amplitude and using the other one as a continuation parameter. This provided

frequency and S-shaped response curves [4] for the studied system. The training, testing, and validation data set was built using families of periodic solutions, where each training point contained the state variables and the value of the excitation force.

Figures 9.1 and 9.2 show an excellent agreement between the model of the system and the trained LNN. The LNN can also be used to extract the stiffness and damping characteristics of the system, informing more detailed physics-based modeling of the system of interest.

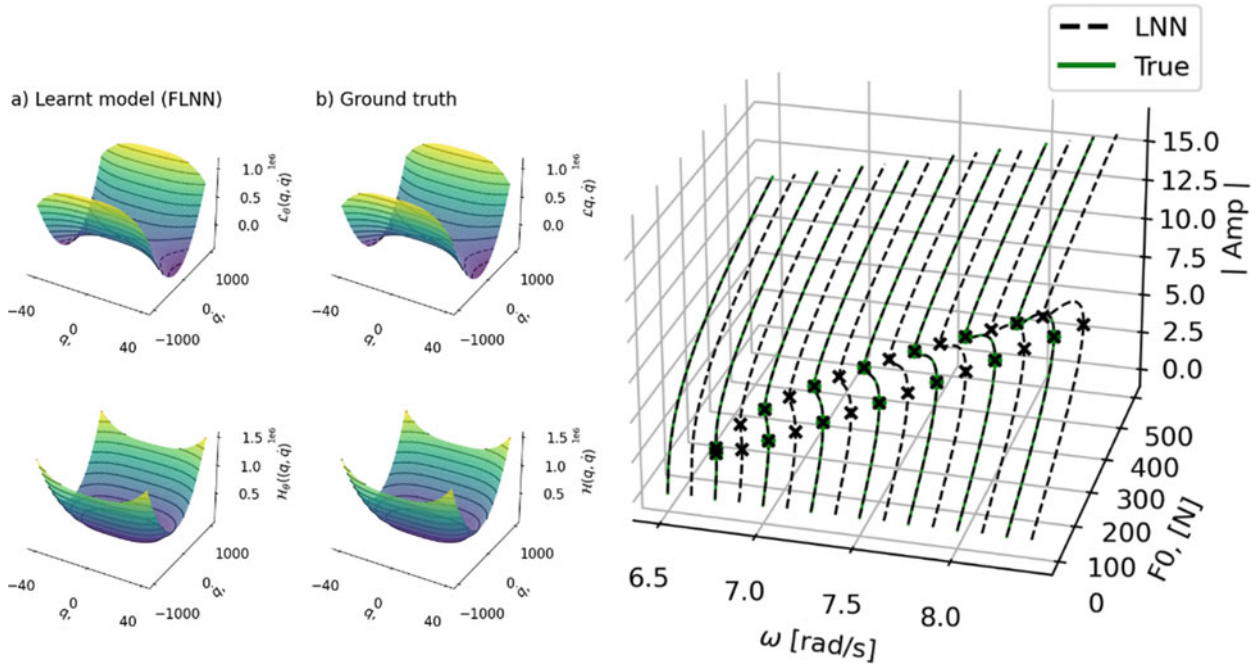

Fig. 9.1 (Left) Lagrangian and Hamiltonian of the trained LNN and the analytical model. (Right) Comparison between the response obtained from the model (solid green) and the response obtained from the LNN (dashed black). For both models, shooting and pseudo-arc length continuation were used to obtain the response curves. Crosses highlight the location of the fold points

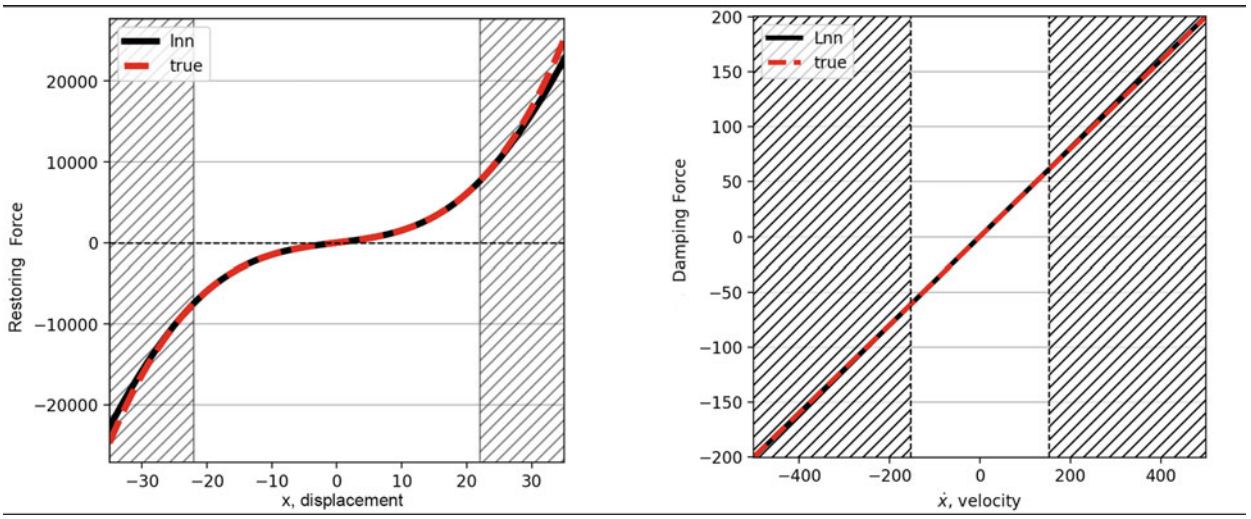

Fig. 9.2 Comparison between the stiffness and damping forces obtained from the model (dashed-red) and derived from the LNN (solid black). The shaded area represents displacement/velocity amplitudes outside the training data set

9.5 Exploiting Known Physics

As demonstrated in the previous paragraph, LNNs provide an elegant way to model a nonlinear dynamical system, without any assumptions about the underlying nonlinearity. In structural dynamics, a linear model of the structure is often known in the form of, for instance, a Finite Element Model. With LNNs, it is possible to exploit this prior knowledge about the system by simply adding the quadratic terms $\mathcal{L}_{\text{lin}}$ associated with the linear model to the LNN. The total Lagrangian of the system is thus given by

$$\mathcal{L}\left(q, \dot{q}\right) = \mathcal{L}_{\text{lin}}\left(q, \dot{q}\right) + \mathcal{L}_{\text{NN}}\left(q, \dot{q}\right), \tag{9.6}$$

where $\mathcal{L}_{\text{NN}}$ is an arbitrary function parametrized by a neural network that serves as a correction to the inaccuracies of the linear model and captures the nonlinear behavior of the system. Our work further discusses how Eq. (9.6) can be used to apply LNNs to more complex structures.

Acknowledgments Thanks to Rolls-Royce plc and the EPSRC for the support under the Prosperity Partnership Grant "Cornerstone: Mechanical Engineering Science to Enable Aero Propulsion Futures," Grant Ref: EP/R004951/1 for supporting this work and allowing to publish its outcomes. L.R. acknowledges the financial support of the Royal Academy of Engineering, Research Fellowship #RF1516/15/11.

References

1. Friswell, M.I., Penny, J.E.T., Garvey, S.D., Lees, A.W.: Dynamics of Rotating Machines. Cambridge University Press, Cambridge (2010). https://doi.org/10.1017/CBO9780511780509
2. Worden, K., Tomlinson, G.R.: Nonlinearity in Structural Dynamics: Detection, Identification and Modelling. CRC Press, New York (2019). https://doi.org/10.1201/9780429138331
3. Noël, J.P., Kerschen, G.: Nonlinear system identification in structural dynamics: 10 more years of progress. Mech. Syst. Signal Process. **83**, 2–35 (Jan. 2017). https://doi.org/10.1016/j.ymssp.2016.07.020
4. Renson, L.: Identification of backbone curves and nonlinear frequency responses using control-based continuation and local Gaussian process regression. In: Nonlinear Structures & Systems, vol. 1, pp. 83–85, Cham (2021). https://doi.org/10.1007/978-3-030-47626-7_13
5. Willard, J., Jia, X., Xu, S., Steinbach, M., Kumar, V.: Integrating physics-based modeling with machine learning: a survey. ArXiv200304919 Phys. Stat. (2020). [Online]. Available: http://arxiv.org/abs/2003.04919. Accessed 19 May 2021
6. Tan, Y., Saif, M.: Neural-networks-based nonlinear dynamic modeling for automotive engines. Neurocomputing. **30**(1), 129–142 (2000). https://doi.org/10.1016/S0925-2312(99)00121-6
7. Haghighat, E., Raissi, M., Moure, A., Gomez, H., Juanes, R.: A deep learning framework for solution and discovery in solid mechanics. ArXiv200302751 Cs Stat. (2020). [Online]. Available: http://arxiv.org/abs/2003.02751. Accessed 10 June 2021
8. Wu, R.-T., Jahanshahi, M.R.: Deep convolutional neural network for structural dynamic response estimation and system identification. J. Eng. Mech. **145**(1), 04018125 (2019). https://doi.org/10.1061/(ASCE)EM.1943-7889.0001556
9. Karpatne, A., et al.: Theory-guided data science: a new paradigm for scientific discovery from data. IEEE Trans. Knowl. Data Eng. **29**(10), 2318–2331 (2017). https://doi.org/10.1109/TKDE.2017.2720168
10. Brunton, S.L., Proctor, J.L., Kutz, J.N.: Discovering governing equations from data by sparse identification of nonlinear dynamical systems. Proc. Natl. Acad. Sci. **113**(15), 3932–3937 (2016). https://doi.org/10.1073/pnas.1517384113
11. Battaglia, P.W., Pascanu, R., Lai, M., Rezende, D., Kavukcuoglu, K.: Interaction Networks for learning about objects, relations and physics. ArXiv161200222 Cs. (2016). [Online]. Available: http://arxiv.org/abs/1612.00222. Accessed 19 May 2021
12. Chen, T.Q., Rubanova, Y., Bettencourt, J., Duvenaud, D.K.: Neural ordinary differential equations. In: Advances in Neural Information Processing Systems, p. 13 (2018)
13. Raissi, M.: Deep hidden physics models: Deep learning of nonlinear partial differential equations. ArXiv180106637 Cs Math. Stat. (2018). [Online]. Available: http://arxiv.org/abs/1801.06637. Accessed 10 June 2021
14. Lee, K.H., Barton, D.A.W., Renson, L.: Reduced-order modelling of flutter oscillations using normal forms and scientific machine learning. ArXiv201102041 Phys. (2020). [Online]. Available: http://arxiv.org/abs/2011.02041. Accessed 03 Oct 2021
15. Greydanus, S., Dzamba, M., Yosinski, J.: Hamiltonian neural networks. ArXiv190601563 Cs. (2019). [Online]. Available: http://arxiv.org/abs/1906.01563. Accessed 19 May 2021
16. Cranmer, M., Greydanus, S., Hoyer, S., Battaglia, P., Spergel, D., Ho, S.: Lagrangian neural networks. ArXiv200304630 Phys. Stat. (2020). [Online]. Available: http://arxiv.org/abs/2003.04630. Accessed 19 May 2021
17. Meirovitch, L.: Methods of Analytical Dynamics. Courier Corporation (2010)

Chapter 10
Bypassing the Repeatability Issue in Nonlinear Experimental Modal Analysis of Jointed Structures by Using the RCT-HFS Framework

M. Fatih Gürbüz, Taylan Karaağaçlı, M. Bülent Özer, and H. Nevzat Özgüven

Abstract Mechanical joints, which are indispensable for almost all mechanical systems, are often an important source of nonlinearity due to frictional, backlash, and/or preload effects. Recent studies have shown that the contact pressure distribution at bolted joint interfaces is the key parameter that governs joint friction and, therefore, the nonlinear damping mechanism in these systems. The problem is that this pressure distribution is susceptible to several different factors: bolt preload, bolt tightening order, surface roughness, surface flatness, and misalignments during the assembly process. These issues lead to considerable variability and repeatability problems in the nonlinear dynamics of jointed structures. Consequently, the accurate identification of nonlinear damping in jointed structures is still a challenging task. The combined use of the response-controlled stepped-sine testing (RCT) and the harmonic force surface concept (HFS) constitutes a framework that determines frequency response curves from the same measurement in two different ways: either by directly measuring them or by synthesizing them from the identified nonlinear modal parameters. Since any possible discrepancy of the frequency response curves obtained from the same measurement cannot be attributed to the repeatability issue, the RCT-HFS framework validates the accuracy of the identified nonlinear modal parameters in a sense bypassing the repeatability problem. In this study, this novel feature of the RCT-HFS framework is used in identifying and validating the accuracy of the modal model of a benchmark beam with a bolted lap joint.

Keywords Joint nonlinearity · Friction nonlinearity · Response-controlled stepped-sine testing · Harmonic force surface · Repeatability

10.1 Repeatability Issue

Vibration responses of jointed structures repeatedly measured under the same excitation condition can be very different from each other [1]. This poor repeatability in measurements makes it difficult to understand the nonlinear dynamics of mechanical joints and to develop a reliable and accurate mathematical model from experiments. Remarkable studies have been published recently that clarify the causes of the repeatability issue in jointed structures (e.g., [2, 3]). In these studies, it is shown that the interfacial contact pressure distribution is the key metric that affects the nonlinear dynamics of mechanical joints as well as the measurement repeatability. It is also shown that this pressure distribution is very sensitive to various factors such as the topography of the contact interface (flatness and surface roughness), bolt tightening order, bolt preload, and alignment issues during the assembly process. Some of these factors change considerably not only in the case of disassembly/reassembly but even in the case of the repeated measurements of the same assembly, which highly affects the contact pressure and therefore the measurement repeatability. In [2], it is demonstrated that a well-controlled assembly procedure can highly improve measurement repeatability. Furthermore, it is revealed that lower surface roughness considerably reduces the sensitivity of the contact pressure to bolt preload and bolted tightening order, which also results in better repeatability.

Although significant progress has been made in understanding the nonlinear characteristics of mechanical joints and improving repeatability as discussed above, developing an accurate mathematical model for joints still remains a challenging

M. F. Gürbüz · M. B. Özer · H. N. Özgüven
Department of Mechanical Engineering, Middle East Technical University, Ankara, Turkey

T. Karaağaçlı (✉)
The Scientific and Technological Research Council of Turkey, Defense Industries Research and Development Institute, TÜBİTAK-SAGE, Ankara, Turkey
e-mail: taylan.karaagacli@tubitak.gov.tr

M. R. W. Brake et al. (eds.), *Nonlinear Structures & Systems, Volume 1*, Conference Proceedings of the Society for Experimental Mechanics Series, https://doi.org/10.1007/978-3-031-36999-5_10

problem. In a recent joint work [4], the nonlinear dynamics of a jointed beam has been studied by applying several different identification methods such as the Hilbert Transform method, Peak Finding and Fitting method to the free decay response data measured by impact testing and shaker ringdown testing. In the same work, a significant discrepancy was reported between the backbone curves and nonlinear modal damping curves identified from these methods with the ones obtained from classical force-controlled stepped-sine testing. Whether this discrepancy is due to the theoretical/practical limitations of the studied identification methods or the repeatability issue remains ambiguous. On the other side, since the modal damping obtained from force-controlled testing is identified indirectly by assuming the input energy provided by the shaker is equal to the energy dissipated by bolted joints of the beam, it is also disputable whether this modal damping constitutes an accurate reference to validate other identification techniques.

An important advantage of the RCT-HFS identification framework [5] compared to the aforementioned identification methods is that it is capable of determining frequency response curves from the *same measurement* data set in two different ways: either by extracting them from the HFS or by synthesizing them from the identified nonlinear modal parameters based on the Single Nonlinear Mode (SNM) theory [6]. Since any possible discrepancy of the frequency response curves reproduced from the same measurement by two different approaches cannot be attributed to the repeatability issue, the RCT-HFS framework provides a reliable mean of validating its theoretical foundation, that is, the SNM theory, in a sense bypassing the repeatability problem. Of course, if the structure suffers from poor repeatability, the problem is still there and can be studied separately by applying the RCT-HFS framework on repeated measurements and obtaining uncertainty bounds of identified nonlinear modal parameters as shown in the case of a real missile in [5].

In a short period of time, the RCT-HFS identification framework has been successfully applied to a wide range of nonlinear systems; a T-beam benchmark with local cubic stiffness nonlinearity and a real missile with moderate damping nonlinearity due to bolted joints [5], a metal strip that exhibits strong geometrical (distributed) nonlinearity [7, 8], a nonlinear micro-electromechanical device with stack-type piezo-actuator [9], and the control fin actuation mechanism of a real missile [10]. In this study, the framework is successfully applied to a recently proposed benchmark beam with bolted lap joint, namely, the Orion beam [11].

10.2 Application of the RCT-HFS Framework to the Orion Beam

In this study, the RCT-HFS identification method is applied to a benchmark structure, the so-called Orion beam recently proposed in [11]. The structure consists of two thin beams connected by three bolted joints with contact patches on each connecting bolt. In [11], the Orion beam is subjected to a series of constant-force stepped-sine testing by using the experimental setup shown in Fig. 10.1. The beam is excited by a modal shaker at a point close to its clamped end. The response is measured by a laser vibrometer. All the details about the dimensions of the beam, data acquisition and control strategy can be found in [11]. Frequency response functions (FRFs) measured at different levels of excitation force amplitude and tightening torque are also provided in [12] as an open-source dataset to help different research groups to test the identification methods they have developed.

In the RCT-HFS framework, the usual practice is to conduct a series of response-controlled stepped-sine testing by keeping the displacement amplitude of a selected control point (usually the driving point) constant and to measure constant-response receptances, which turn out to be quasi-linear even in the case of strongly nonlinear systems [5, 7–10]. Then, these receptances are processed by using standard linear modal analysis techniques to extract response-level-dependent nonlinear modal parameters (natural frequency, modal damping ratio, and modal constant). On the other side, the HFS is constructed by using harmonic force spectra measured at different constant displacement amplitude levels. By cutting the HFS with constant-force planes, one can extract constant-force frequency response curves including unstable branches if there are any. Finally, the accuracy of the identified nonlinear modal parameters is validated by comparing constant-force receptances synthesized from these parameters (in a Newton-Raphson solution scheme) with the ones extracted from the HFS. However, [11, 12] provide only the constant-force FRFs for the Orion beam but not the constant-response FRFs. In this study, this issue is solved by using the HFS concept in a novel way different from its usual implementation as explained below.

In [12], constant-force mobility (velocity/force) data are measured around the 3rd mode of the Orion beam at 20 cNm tightening torque level. These data are converted into frequency response curves as shown in Fig. 10.2a. Since the nonlinearity is relatively weak, the frequency response curves do not exhibit any jump and are very smooth. Consequently, these curves are merged to construct a smooth HFS as shown in Fig. 10.2b. Cutting this HFS with constant-displacement amplitude planes gives V-shaped harmonic force spectra. Finally, dividing selected constant-displacement amplitudes with corresponding harmonic force spectra gives the quasi-linear constant-response FRFs as shown in Fig. 10.3. It is important to note that the main motivation behind the invention of the HFS was accurately identifying unstable branches and turning points of

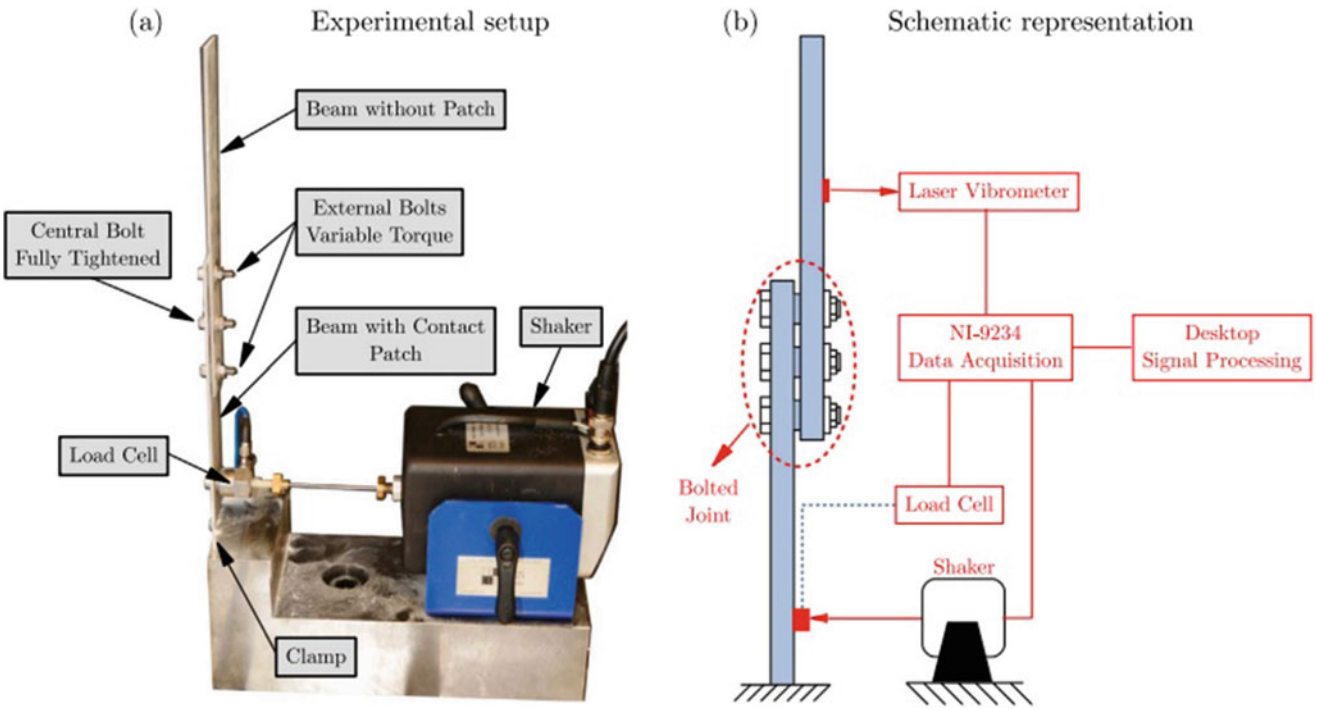

Fig. 10.1 Orion beam experimental setup [11]

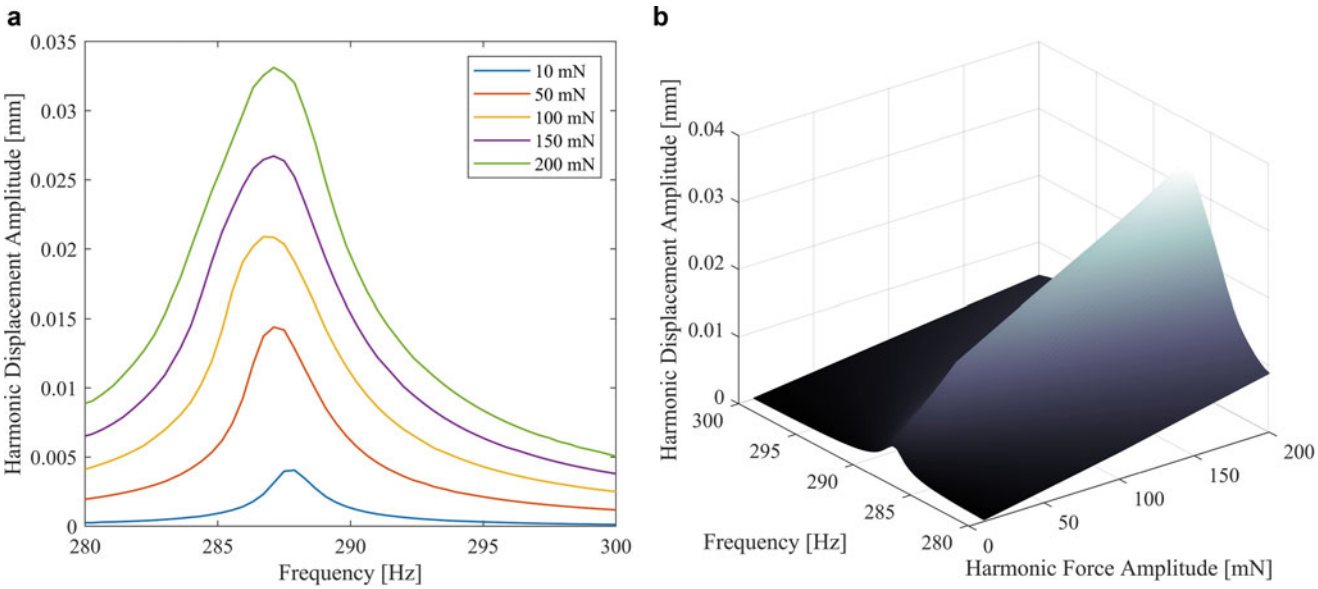

Fig. 10.2 Construction of the HFS from the constant-force frequency response curves for the 3rd bending mode at 20 cNm tightening torque: (**a**) constant-force frequency response curves, (**b**) harmonic force surface (HFS)

constant-force FRFs that exhibit the jump phenomenon in the case of classical constant-force testing. Therefore, in the case of strongly nonlinear systems, the HFS is used to obtain constant-force FRFs from the measured constant-response measurements. However, as shown in this study, this procedure can be reversed in the case of weakly nonlinear systems. This novel implementation of the HFS concept can be very useful to identify the model parameters of nonlinear structures very accurately as shown below.

Once the quasi-linear constant-response FRFs are obtained from the HFS as shown in Fig. 10.3, they can be processed by using standard linear modal analysis techniques to extract modal parameters corresponding to each displacement amplitude level. In this study, constant-response FRFs are processed by using the simple peak-picking algorithm, and response-

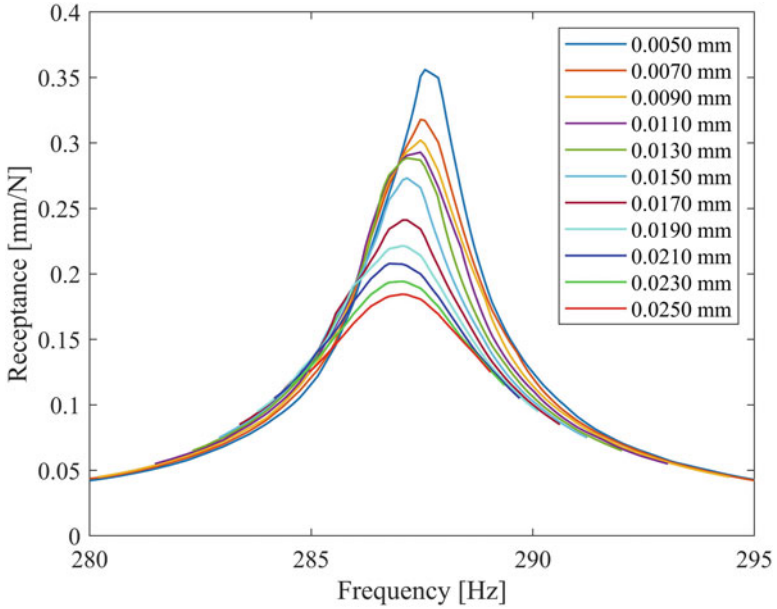

Fig. 10.3 Extraction of the quasi-linear constant-displacement FRFs from the HFS for the 3rd bending mode at 20 cNm tightening torque

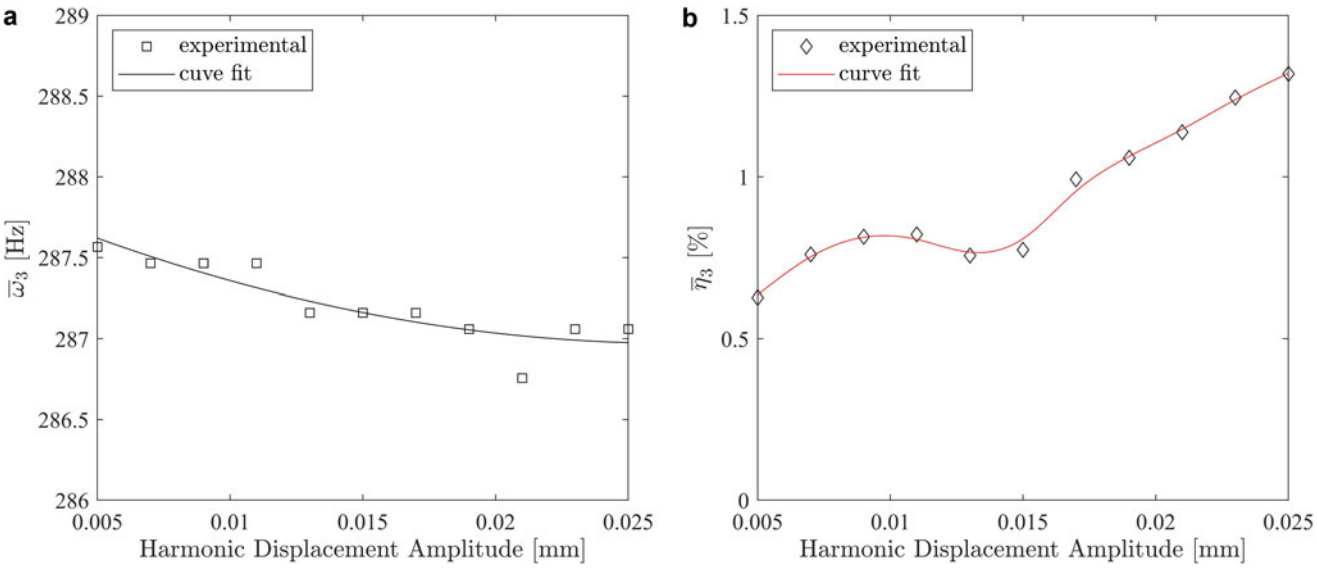

Fig. 10.4 Variation of modal parameters with response amplitude: (**a**) natural frequency, (**b**) modal damping ratio

level-dependent nonlinear modal parameters are obtained as shown in Fig. 10.4. An important advantage of the RCT-HFS framework over most of the state-of-the-art identification techniques is that it identifies accurate modal models of nonlinear structures without necessitating the a priori knowledge of the location and/or the type of nonlinearity, and it can be used even for distributed nonlinearity. In [11], a Duffing-Van der Pol oscillator model is assumed for the Orion beam, and the parameters of that model are determined iteratively by using the measured constant-force FRFs. The issue with such parametric modeling is that it can be computationally expensive or not possible at all in the case of complex engineering systems.

The final step of the RCT-HFS framework is the demonstration of the accuracy of the identified nonlinear modal parameters. To achieve this goal, constant-force FRFs are synthesized from the identified nonlinear modal model by using the SNM theory [6] and the Newton-Raphson solution scheme. These synthesized FRFs are compared with the ones directly measured by constant-force testing [11, 12] in Fig. 10.5. As can be seen from the figure, the match between the synthesized and directly measured data is perfect, which proves the accuracy of the identified nonlinear modal model.

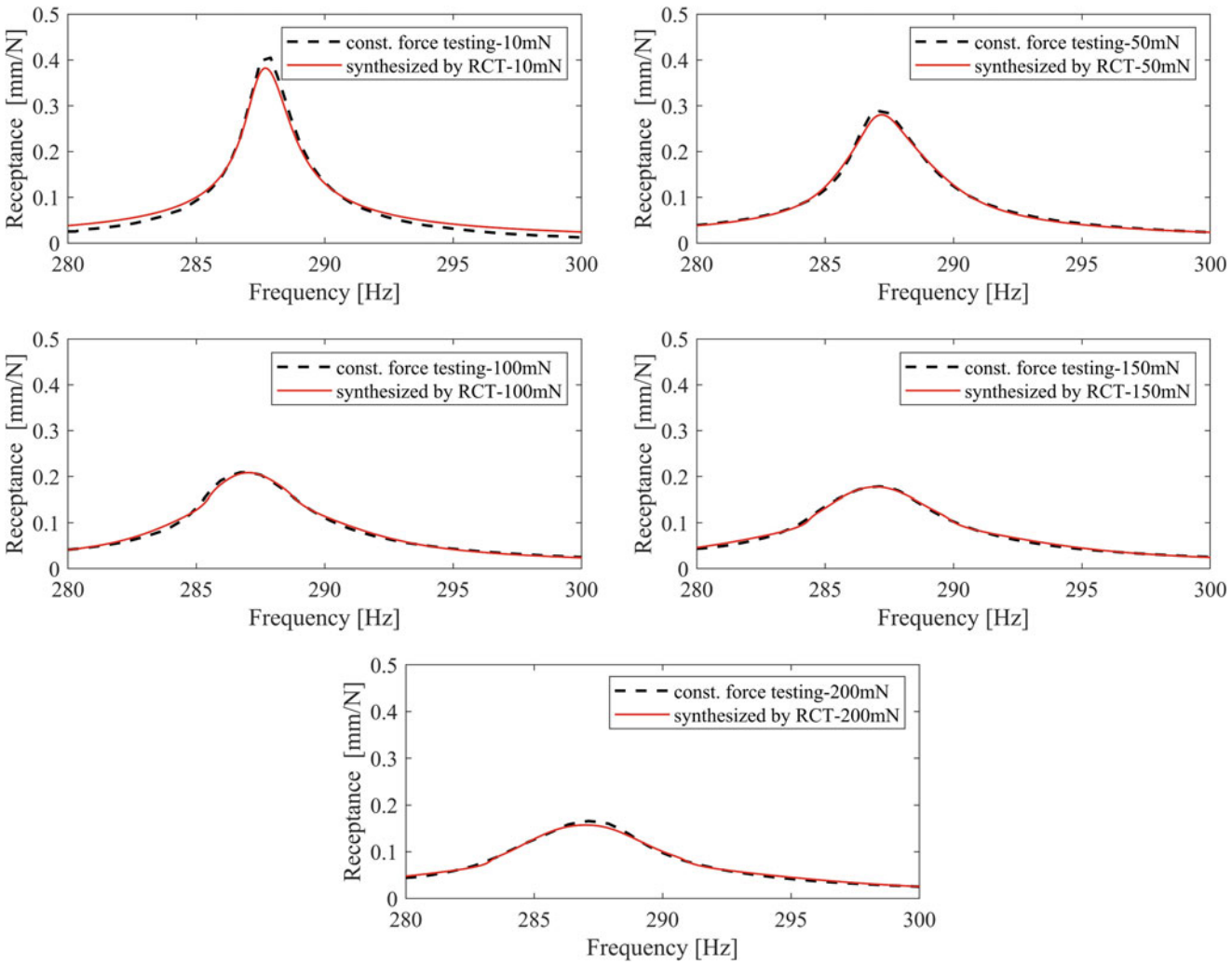

Fig. 10.5 Validation of the identified nonlinear modal parameters by comparing constant-force FRFs synthesized from these parameters with the ones directly measured by constant-force testing

A very interesting and important observation that can be made from Figs. 10.4 and 10.5 is that although the nonlinear model parameters were experimentally obtained for the displacement levels between 0.005 and 0.025 mm as seen in Fig. 10.4, the constant-force FRFs corresponding to the 10 mN and 200 mN covering response amplitudes below 0.005 mm and above 0.025 mm are also very accurately synthesized as shown in Fig. 10.5. This is achieved by a successful curve fitting and extrapolation process using the *fit* function of Matlab. A second-order polynomial is fitted to the natural frequency and smoothing spline curves are fitted to the modal damping ratio and modal constant, which satisfactorily extrapolates the modal parameters at amplitude levels below 0.005 mm and above 0.025 mm.

10.3 Discussions and Conclusions

Poor repeatability in measurements of jointed structures makes it a challenging task to understand the nonlinear dynamics of mechanical joints and to develop reliable and accurate mathematical models from experiments. In this study, the RCT-HFS framework, which has been successfully applied to a wide range of structures in a short period of time, is applied for the nonlinear modal identification of a recently proposed benchmark beam with a lap joint, the so-called Orion beam. Since the experimental data available in the literature consists of constant-force FRFs, the HFS is constructed in a novel way by merging constant-force frequency response data, contrary to its usual implementation, which uses constant-response

measurements. Cutting the HFS with constant-displacement amplitude planes gives quasi-linear constant-response FRFs. These FRFs are then processed with a simple peak-picking method to identify nonlinear modal parameters as functions of response amplitude. The perfect match between the constant-force FRFs obtained from direct measurement and the ones synthesized from the identified nonlinear modal parameters demonstrates the accuracy of the RCT-HFS method. Since the constant-force FRFs are obtained from the *same measurement* in two different ways, the accuracy of the identified nonlinear modal parameters is shown in a sense bypassing the repeatability problem. Of course, the repeatability problem is still there and can be studied separately by applying the RCT-HFS framework on repeated measurements and obtaining uncertainty bounds of identified nonlinear modal parameters. Also, since the nature of the RCT measurements requires keeping the vibration amplitude of the excitation point constant, unlike the constant amplitude forcing testing approach, the system does not move into an uncontrolled high amplitude oscillation regime at and around the resonance frequencies. In an RCT-HFS framework, the resonance is observed with decreased forcing amplitudes only; therefore, it avoids drastic changes in alignments and contact conditions as well as reduces the stress levels around the joint region, which is expected to reduce the severity of the repeatability problem in comparison to constant amplitude forcing measurements. This point will be studied in future work.

References

1. Brake, M.R.W. (ed.): The Mechanics of Jointed Structures. Springer (2018)
2. Brake, M.R.W., Schwingshackl, C.W., Reuß, P.: Observations of variability and repeatability in jointed structures. Mech. Syst. Signal Process. **129**, 282–307 (2019)
3. Dreher, T., Brake, M.R.W., Seeger, B., Krack, M.: In situ, real-time measurements of contact pressure internal to jointed interfaces during dynamic excitation of an assembled structure. Mech. Syst. Signal Process. **160**, 107859 (2021)
4. Jin, M., Kosova, G., Cenedese, M., Chen, W., Singh, A., Jana, D., Brake, M.R.W., et al.: Measurement and identification of the nonlinear dynamics of a jointed structure using full-field data, Part II: Nonlinear system identification. Mech. Syst. Signal Process. **166**, 108402 (2022)
5. Karaağaçlı, T., Özgüven, H.N.: Experimental modal analysis of nonlinear systems by using response-controlled stepped-sine testing. Mech. Syst. Signal Process. **146**, 107023 (2021)
6. Szemplinska-Stupnicka, W.: The modified single mode method in the investigation of the resonant vibration of nonlinear systems. J. Sound Vib. **63**(4), 475–489 (1979)
7. Karaağaçlı, T., Özgüven, H.N.: Experimental quantification and validation of modal properties of geometrically nonlinear structures by using response-controlled stepped-sine testing. Exp. Mech. **62**, 199–211 (2022)
8. Karaağaçlı, T., Özgüven, H.N.: Experimental modal analysis of geometrically nonlinear structures by using response-controlled stepped-sine testing. In: Proceedings of the 39th International Modal Analysis Conference (IMAC), Orlando, FL, USA (2021)
9. Koyuncu, A., Karaağaçlı, T., Şahin, M., Özgüven, H.N.: Experimental modal analysis of nonlinear amplified piezoelectric actuators by using response-controlled stepped-sine testing. Exp. Mech. **62**, 1579–1594 (2022)
10. Karaağaçlı, T., Özgüven, H.N.: Experimental modal analysis of structures with high nonlinear damping by using response-controlled stepped-sine testing. In: Proceedings of the 41st International Modal Analysis Conference (IMAC), Austin, TX, USA (2023)
11. Teloli, R.O., Butaud, P., Chevallier, G., da Silva, S.: Good practices for designing and experimental testing of dynamically excited jointed structures: the Orion beam. Mech. Syst. Signal Process. **163**, 108172 (2022)
12. Teloli, R.O., Butaud, P., Chevallier, G., da Silva, S.: Dataset of experimental measurements for the Orion beam structure. Data Brief. **39**, 107627 (2021)

Chapter 11
Towards Exact Statistically Independent Nonlinear Normal Modes via the FPK Equation

Max D. Champneys, Timothy J. Rogers, Nikolaos Dervilis, and Keith Worden

Abstract The nonlinear extension of linear modal analysis is a problem that has received a great deal of attention in the literature. A recently proposed framework casts the problem of nonlinear modal analysis within a machine-learning framework that generates modes that are statistically independent from each other. Thus far, several techniques from machine learning have been applied to learn the nonlinear modal transformation, including a multinomial expansion and a neural-network model. Recent effort has been given to understand the nonlinear modal dynamics within the statistically independent framework from a theoretical perspective; of particular interest are ways that the nonlinear transformations might be specified exactly from the equations of motion. This paper uses the Fokker-Planck-Kolmogorov (FPK) equation to construct a transformation in the reduced single degree-of-freedom nonlinear case; in this way, the dynamics can be made to respect an arbitrary target distribution. It is furthermore shown that setting the target distribution to the Gaussian distribution corresponding to the underlying linear dynamics (whereby all of the nonlinear elements are removed) is not sufficient to produce global amplitude invariance in the modal transformation.

Keywords Nonlinear normal modes · FPK equation · Nonlinear structural dynamics

11.1 Introduction

Linear modal analysis (LMA) is ubiquitous in both industrial and research settings for the consideration of linear structural dynamics. LMA is so prevalent that modal properties (natural frequencies, damping ratios and mode shapes) have become the *lingua* franca for descriptions of structural dynamics and beyond.

It is lamentable that nonlinearity is so destructive to LMA. The principle of superposition (a necessary and sufficient condition for a system to be linear [1]) does not hold generally for the nonlinear case.

The presence of nonlinearity in real-world structural dynamics is becoming increasingly difficult to ignore. As the demands of complex engineering structures grow ever more towards the lightweight and carbon-efficient, the materials, geometries and fixtures employed lead inevitably towards increasingly nonlinear dynamics.

Given the immense utility of linear modal analysis, it is without wonder that a great deal of research effort has been expended in the pursuit of extensions to the method that might be applied in the presence of nonlinearity—so-called nonlinear normal modes (NNM) of vibration. The first of these, from Rosenberg [2, 3], extends the coherent motion property of the linear mode shape to non-planar relationships in the configuration space of the dynamic system. Since its proposal in the 1960s, the Rosenberg framework has been extended by many authors to address shortcomings such as non-conservative forces and internal resonances. Surveys of the method at various waypoints can be found in [4–6].

A geometrically more general definition of an NNM was later offered by Shaw and Pierre in a series of papers in the 1990s [7–10]. This approach lifts the Rosenberg NNM into the phase space of the dynamics, whereby each mode is defined by an *invariant manifold* upon which motion, if initiated, remains for all time without exciting any of the other modes. The

M. D. Champneys (✉)
Industrial Doctorate Centre in Machining Science, Advanced Manufacturing Research Centre with Boeing, University of Sheffield, Sheffield, UK

Dynamics Research Group, Department of Mechanical Engineering, University of Sheffield, Sheffield, UK
e-mail: mdchampneys1@sheffield.ac.uk

T. J. Rogers · N. Dervilis · K. Worden
Dynamics Research Group, Department of Mechanical Engineering, University of Sheffield, Sheffield, UK
e-mail: tim.rogers@sheffield.ac.uk; n.dervilis@sheffield.ac.uk; k.worden@sheffield.ac.uk

M. R. W. Brake et al. (eds.), *Nonlinear Structures & Systems, Volume 1*, Conference Proceedings
of the Society for Experimental Mechanics Series, https://doi.org/10.1007/978-3-031-36999-5_11

Shaw-Pierre formulation of an NNM relies on an appeal to centre manifold theory [11], and as such, the NNMs are valid *locally*, with each NNM being tangential to the corresponding linear mode at the equilibrium.

Since these theoretical frameworks, a new class of NNM, based on the notion of statistical independence, was proposed [12]. The new approach takes a purely data-driven view of nonlinear modal analysis in order to try to replicate the utility of *experimental modal analysis* (EMA). The physical displacements $\mathbf{y}$ of the nonlinear dynamics are projected onto modal coordinates $\mathbf{u}$ by the application of a nonlinear forward transformation:

$$\mathbf{u} = f(\mathbf{y}) \tag{11.1}$$

The approach takes a machine-learning view of the modal decomposition, using several *inductive biases* to ensure that the modal dynamics are *useful* by some measure. In the original formulation [12], a multinomial transformation for f was taken with the inductive biases of linear statistical independence and orthogonality enforced by penalty terms in the objective function. Since then, the statistically independent framework has been extended by a number of authors including approaches such as non-parametric learners [13], nonlinear correlation metrics [14], normalising flows [15] and neural-network models [16, 17]. Recently, specific attention has been paid to the nature of the underlying modal dynamics in [18].

Although the statistically independent NNM (SI-NNM) framework has been shown to be effective in a number of data-driven numerical and experimental case-study examples, there remains an interest in how the nonlinear modal transformation f might be learned directly from the equations of motion (EOMs).

There are several motivations for attempting to compute the nonlinear modal mapping directly from the EOMs. A key motivation is that it is manifestly possible in the linear case. It is therefore argued here that access to a modal mapping in the case of perfect system knowledge (even in the Single-input single-output (SISO) case) is an important theoretical result in support of the SI-NNM framework. Another important motivation is the reduction in computational cost that can be made by avoiding the need to optimise the parameters of a nonlinear modal transformation.

11.2 The Fokker-Planck-Kolmogorov Equation

The approach to generating the modal map in this work is inspired by the Fokker-Planck-Kolmogorov (FPK) equation. The FPK equation is a partial differential equation, the solution of which is the so-called *stationary probability density*, $p(\mathbf{y}, \dot{\mathbf{y}}|\mathbf{x})$, of a dynamic system. The *stationary probability density* can be interpreted as the probability of observing a given system state over the entire time history of the system response, subject to some input $\mathbf{x}$. In the context of statistically independent NNMs, the *stationary probability density* is of particular interest. With access to $p(\mathbf{y}, \dot{\mathbf{y}}|\mathbf{x})$, the problem of specifying the modal transformation becomes the specification of a map f such that:

$$f(\mathbf{y}) = \mathbf{u} \tag{11.2}$$

$$\mathbf{y} \sim p(\mathbf{y}, \dot{\mathbf{y}}|\mathbf{x}) \tag{11.3}$$

$$\mathbf{u} \sim \prod_{i}^{n} \alpha_i(u_i|\mathbf{x}) \tag{11.4}$$

where the α_i are target distributions that can be selected arbitrarily to promote independence. For example, one might require that the modal map decomposes displacements into independent Gaussian distributions. The map can then be specified either by exact reasoning or by the application of the change-of-variables equation. For example, in the one-dimensional case, the change-of-variables equation is given by:

$$p_y(y) = p_u(u) \left| \frac{\mathrm{d}u}{\mathrm{d}y} \right| \tag{11.5}$$

Now, substituting in the required form of the transformation:

$$p_y(y) = p_u(f(y)) \left| \frac{\mathrm{d}f(y)}{\mathrm{d}y} \right| \tag{11.6}$$

$$\left|\frac{\mathrm{d}f(y)}{\mathrm{d}y}\right| = \frac{p(u)}{p(f(y))} \tag{11.7}$$

One has an ODE that, if solved (directly or otherwise), yields the nonlinear transformation from the stationary density to some arbitrary target distribution as required.

Important results regarding the derivation of stationary probability densities for a class of second-order dynamic systems with polynomial-stiffness nonlinearities were developed by Caughey in [19]. The full derivation of the results used here goes beyond the scope of the current investigation, but the interested reader is directed to [19] for a thorough reference.

The salient result in the context of the present investigation is for a nonlinear system of the form:

$$\ddot{\mathbf{y}} + C\dot{\mathbf{y}} + \mathbf{F}(\mathbf{y}) = \mathbf{x}(t) \tag{11.8}$$

where C is a diagonal matrix of damping coefficients and where $\mathbf{x}(t) \sim \mathbb{N}(\mathbf{0}, \sigma_x^2 I)$. The *stationary probability density* is given by:

$$p_s(\mathbf{y}, \dot{\mathbf{y}}) = A \times \exp\left[-\frac{2c}{D}\left[\frac{1}{2}\dot{\mathbf{y}}^2 + \int_0^y \mathbf{F}(\zeta)\,\mathrm{d}\zeta\right]\right] \tag{11.9}$$

where D is the spectral density level of the white-noise Gaussian input. For discrete data, D can be related to the variance of the input and the sampling period (Δ_t) by:

$$D = \sigma_x^2 \Delta_t \tag{11.10}$$

11.3 Direct NNMs in a Single Dimension

It may at first seem weird to perform nonlinear modal analysis on a SISO system (and—as is the theme of this year's conference—indeed it is!), but the authors make the argument that the results established here provide an important theoretical illustration for the statistically independent NNM framework.

Before blindly applying machine learning to the problem of learning $f(\mathbf{y})$, it is a worthwhile endeavour to consider which inductive biases are sufficient to induce the desired properties of a nonlinear modal decomposition. One such property is the extent to which the stationary distributions of nonlinear dynamic systems can be altered by static maps. Another is the way in which these static maps vary with nonlinear intensity and excitation level. Understanding these properties is key to understanding which inductive biases should be built into the machine-learning framework for nonlinear modal analysis.

The proposed approach is to directly learn the modal transformation from the FPK and a target distribution (chosen arbitrarily to be a Gaussian). The approach is demonstrated here in the SISO case for a Duffing-type nonlinear system with the equation of motion:

$$\ddot{y} + c\dot{y} + ky + \epsilon y^3 = x(t) \tag{11.11}$$

where $x(t) \sim \mathbb{N}(0, \sigma_x^2)$ is a Gaussian, white-noise excitation, with variance σ_x^2.

Starting with the stationary density for a second-order dynamic system with a stiffness nonlinearity (11.9), and substituting in:

$$F = y + \epsilon y^3 \tag{11.12}$$

one finds:

$$p(y, \dot{y}) = A \times \exp\left[-\frac{c}{D}\left[\dot{y}^2 + ky^2 + \frac{\epsilon}{2}y^4\right]\right] \tag{11.13}$$

which is the joint *stationary probability density* of the displacement and velocity up to some constant A.[1]

[1] A closed form expression for A is available in terms of parabolic cylinder functions and other higher-order transcendental functions. However in practice, a numerical approximation can be taken—here, a quadrature-based numerical solver is employed—with no damage to the results presented here.

To recover the density of the displacement only, one notices that the above can be re-written as:

$$p(y, \dot{y}) = p_s(y)p_s(\dot{y}) \tag{11.14}$$

where the densities of the velocities and displacements are independent. Now marginalising over the velocities, one has:

$$p_s(y) = \int_{\dot{y}} p_s(\dot{y}, y)\, \mathrm{d}y \tag{11.15}$$

or equivalently,

$$p_s(y) = A \times \exp\left[-\frac{c}{D}\left[ky^2 + \frac{\epsilon}{2}y^4\right]\right] \int_{-\infty}^{\infty} \exp\left[-\frac{c}{D}\dot{y}^2\right] \mathrm{d}y \tag{11.16}$$

Because the integral above has the form of a Gaussian distribution, one can use the result that the infinite integral over the distribution is equal to unity to recover:

$$p_s(y) = A \times \exp\left[-\frac{c}{D}\left[ky^2 + \frac{\epsilon}{2}y^4\right]\right] \sqrt{\frac{D\pi}{c}} \tag{11.17}$$

Now let,

$$A' = A \times \sqrt{\frac{D\pi}{c}} \tag{11.18}$$

Then the *stationary probability density* of the displacement of the nonlinear Duffing equation can be recovered as:

$$p_s(y) = A' \times \exp\left[-\frac{c}{D}\left[ky^2 + \frac{\epsilon}{2}y^4\right]\right] \tag{11.19}$$

A similar approach can be taken to recover an expression for the *stationary probability density* of the velocities, yielding:

$$p_s(\dot{y}) = A'' \times \exp\left[-\frac{c}{D}\dot{y}^2\right] \tag{11.20}$$

which is clearly a Gaussian distribution. In order to validate the expressions derived here, they are compared to the stationary distributions estimated empirically from simulated data. The data are generated using a fixed-step fourth-order Runge-Kutta scheme. Parameters pertaining to the simulation are collected in Table 11.1. Figure 11.1 depicts the Power spectral density (PSDs) (estimated by the Welch method), for the linear (obtained by setting $\epsilon = 0$) and nonlinear data generated for this investigation. In the figure, there is clear evidence of nonlinearity, including a hardening effect on the resonance peak and a visible harmonic at three times the principal resonance.

The stationary distribution for the displacements derived above is plotted against numerical results in Fig. 11.2 for the Duffing equation and the equivalent linear system. As can be seen from the figures, there is excellent agreement between the numerical results and those obtained from the FPK equation.

Table 11.1 Parameters used to simulate the toy dynamics data

Parameter	Symbol	Value
Mass	m	1
Viscous damping	c	20
Linear stiffness	k	1
Cubic stiffness	ϵ	100
Input excitation level	σ_x^2	1
Runge-Kutta method order		4
Sampling frequency (Hz)	f_s	10
Dataset size	N	10^6

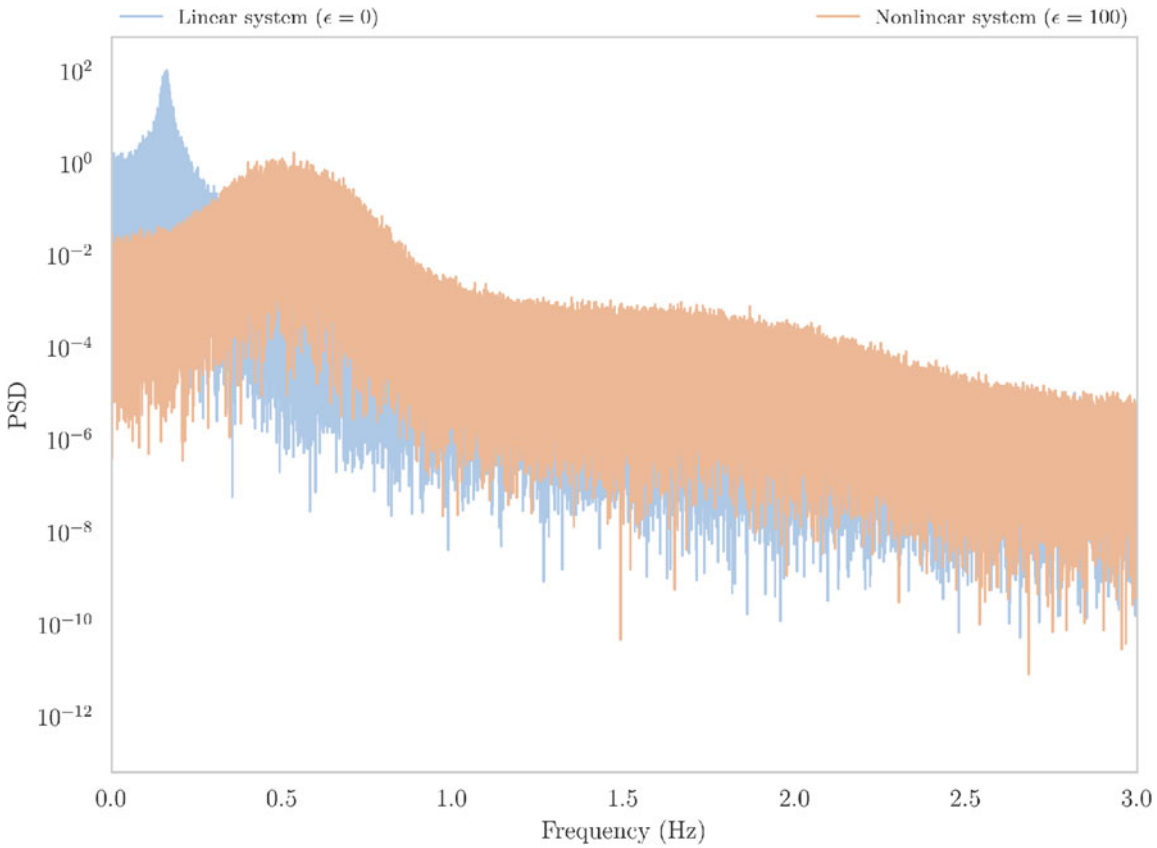

Fig. 11.1 PSD of linear versus nonlinear system

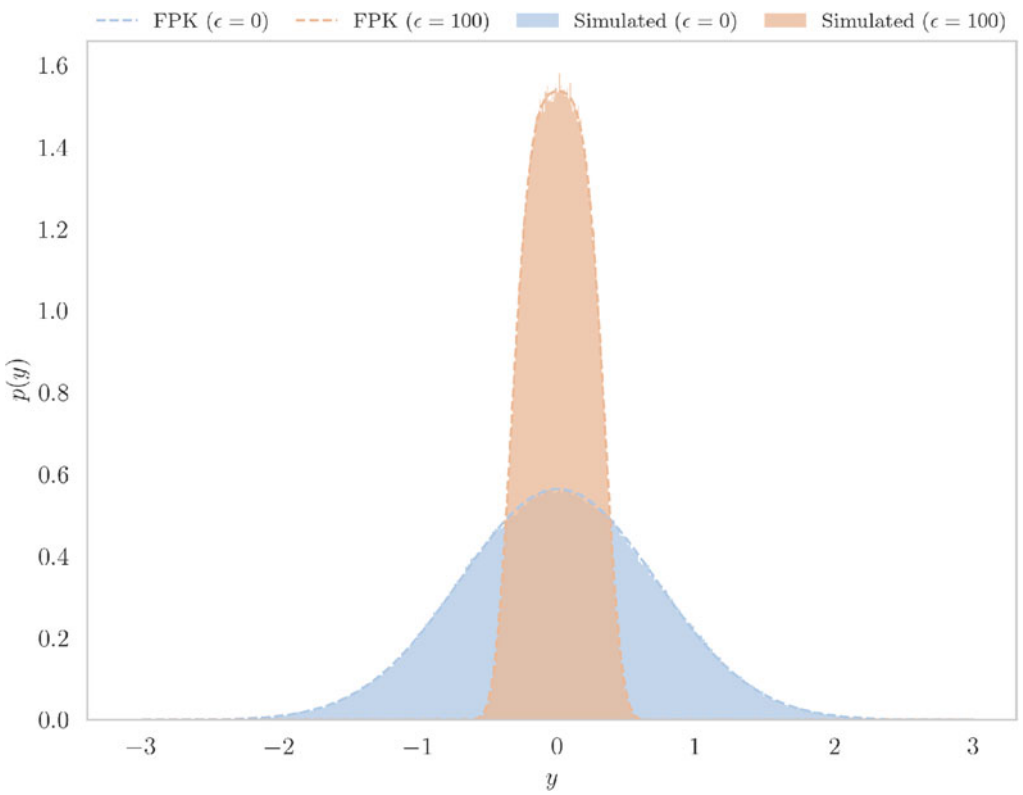

Fig. 11.2 Stationary densities of simulated data versus predictions from the FPK

It is now interesting to consider a static nonlinear map that renders the transformed displacement Gaussian. In the context of the statistically independent framework, this is akin to the statistical-independence criterion (albeit trivially in a single dimension for now). The desired forward modal transformation has the form:

$$f(y) = u, \quad u \sim \mathbb{N}\left(\mu_u, \sigma_u^2\right) \tag{11.21}$$

It is required that $f : y \rightarrow u$ be a static, continuous and invertible map; one can thus apply the change-of-variables equation and write:

$$\left|\frac{\mathrm{d}f(y)}{\mathrm{d}y}\right| = \frac{p(u)}{p(f(y))} \tag{11.22}$$

If f is additionally constrained to be a monotonic function,

$$\frac{\mathrm{d}f(y)}{\mathrm{d}y} > 0 \quad \forall y \tag{11.23}$$

then,

$$\frac{\mathrm{d}f(y)}{\mathrm{d}y} = \frac{p(u)}{p(f(y))} \tag{11.24}$$

Substituting in the definition of $p(y)$ and replacing $p(u)$ with the required form of a Gaussian distribution gives:

$$\frac{df(y)}{dy} = \frac{A'}{\sqrt{2\sigma_u^2\pi}} \times \exp\left[-\frac{(f(y)-\mu_u)^2}{2\sigma_u^2} + \frac{c}{D}\left[ky^2 + \frac{\epsilon}{2}y^4\right]\right] \tag{11.25}$$

where the parameters of the target distribution are set to:

$$\sigma_u^2 = \frac{ck}{2D} \tag{11.26}$$

$$\mu_u = 0 \tag{11.27}$$

The above is a first-order nonlinear ODE in $f(y)$. Although the ODE is separable in f and y, the integral in f is intractable analytically and so a numerical solution must be adopted. Since all the distributions considered here are symmetric, it is sufficient to only consider the half-plane IVP with $y > 0$ and $f(0) = 0$ as an initial condition. The full map can then be recovered by reflecting the positive solution about $y = 0$. In this investigation, a fixed-step Runge-Kutta IVP algorithm is used to solve (11.25). The integration provides a discrete representation of f that is interpolated linearly to form a continuous mapping. Finally, the nonlinear displacements are transformed onto the modal displacements u that now obey the target distribution.

Although a Gaussian target distribution has been selected for $p(u)$, in practice there is no restriction on the form of the target (besides independence). The author envisages that the choice of $p(u)$ will depend on physical insights (i.e. bounding, distribution support) that one might be able to make about the nonlinear system under investigation.

Figure 11.3 depicts histograms of the simulated nonlinear and transformed modal data against the original and target distributions. As can be seen in the figure, the quality of the transformation is excellent, and the modal data fits the target distribution exactly.

It is of interest at this stage to consider the effects of varying nonlinearity and excitation level on the modal transformations. In Fig. 11.4, the physical and transformed modal data are plotted and compared over a range of values for the nonlinear stiffness parameter. Also plotted are third-order polynomial fits to the forward modal transformations in each case. As expected, with $\epsilon = 0$ the modal transformation is the trivial unity map. As the level of nonlinearity increases, the cubic structure of the required modal transformation becomes more pronounced. The data (obtained from integrating equation (11.25) forward in time) are used to fit polynomial models of the modal transformation. Examination of the least-squares polynomial models of these data is of interest, as some insight can be gleaned as to the form of the mapping.

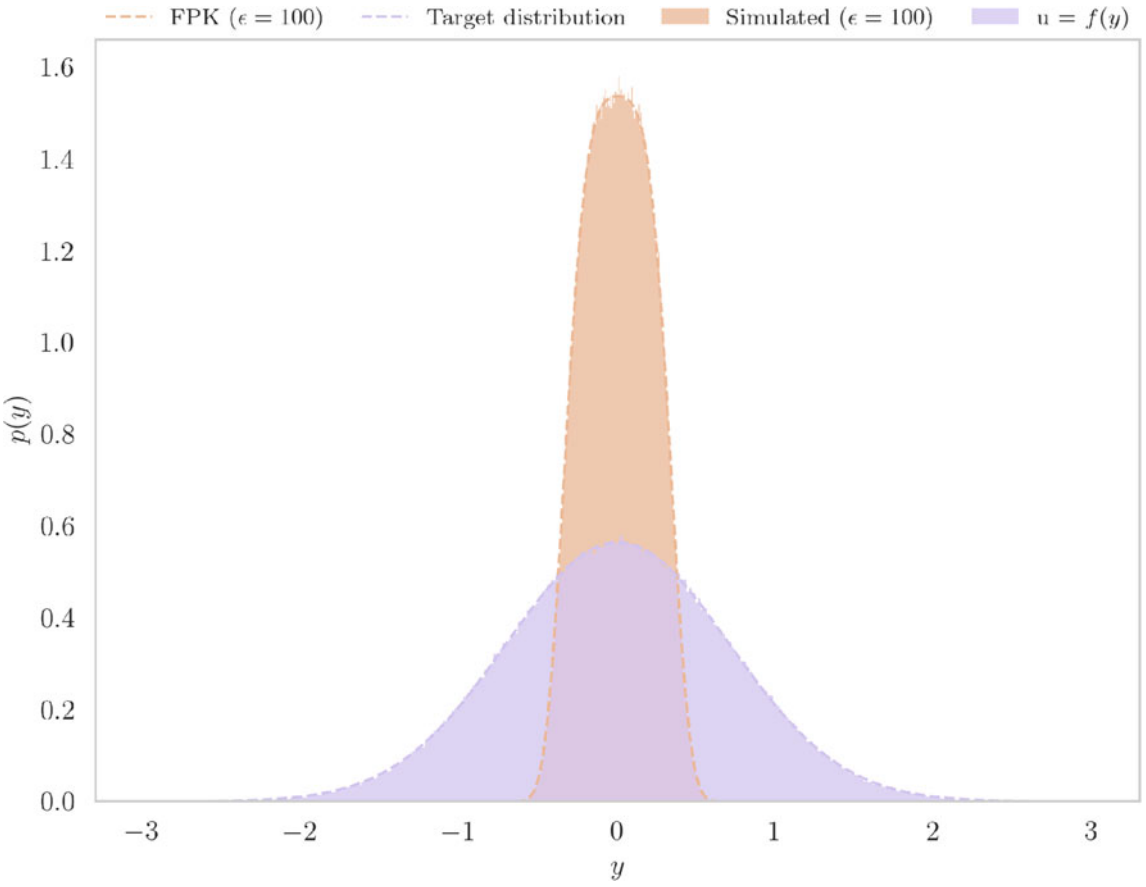

Fig. 11.3 Histograms of physical and modal displacements compared to FPK prediction and target distribution

In several cases, towards the edges of the distributions, the measured samples are seen to deviate from the least-squares polynomial fit. The authors reason that these discrepancies are caused by numerical issues in the evaluation of (11.25). As the magnitude $|y| \to \infty$, the numerator and denominator of the change-of-variables equation both rapidly approach zero, leading to instability in the numerical integration procedure. Note however that these errors do not cause any visible damage to the quality of the fit in Fig. 11.3; this is because the instability only affects the very extremes of the distributions, where very few samples are observed.

Another important consideration at this stage is the amplitude invariance of the proposed approach. Figure 11.5 depicts the forward modal transformation and the corresponding least-squares polynomial fit, calculated at a range of excitation levels. It is interesting to note that the modal transformations are not independent of amplitude. This result implies that amplitude invariance cannot be guaranteed under the SI-NNM framework using only a Gaussian target distribution. In order to achieve a modal transformation with amplitude invariance, additional inductive biases must be introduced to the framework. Despite this, it is promising to see that over two orders of magnitude the variation in the exact modal decomposition is small. This result might indicate that some *local* amplitude invariance might be expected; however, additional investigation will be required to confirm this.

11.3.1 A Cautionary Result

The choices of $\sigma_u^2 = \frac{ck}{2D}$ and $\mu_u = 0$ in the analysis above were not arbitrary, but deliberate. Consider the effect of taking $\epsilon = 0$ in Eq. (11.19).

$$p_s(y) = A' \times \exp\left[-\frac{c}{D}\left[ky^2 + \frac{0}{2}y^4\right]\right]$$

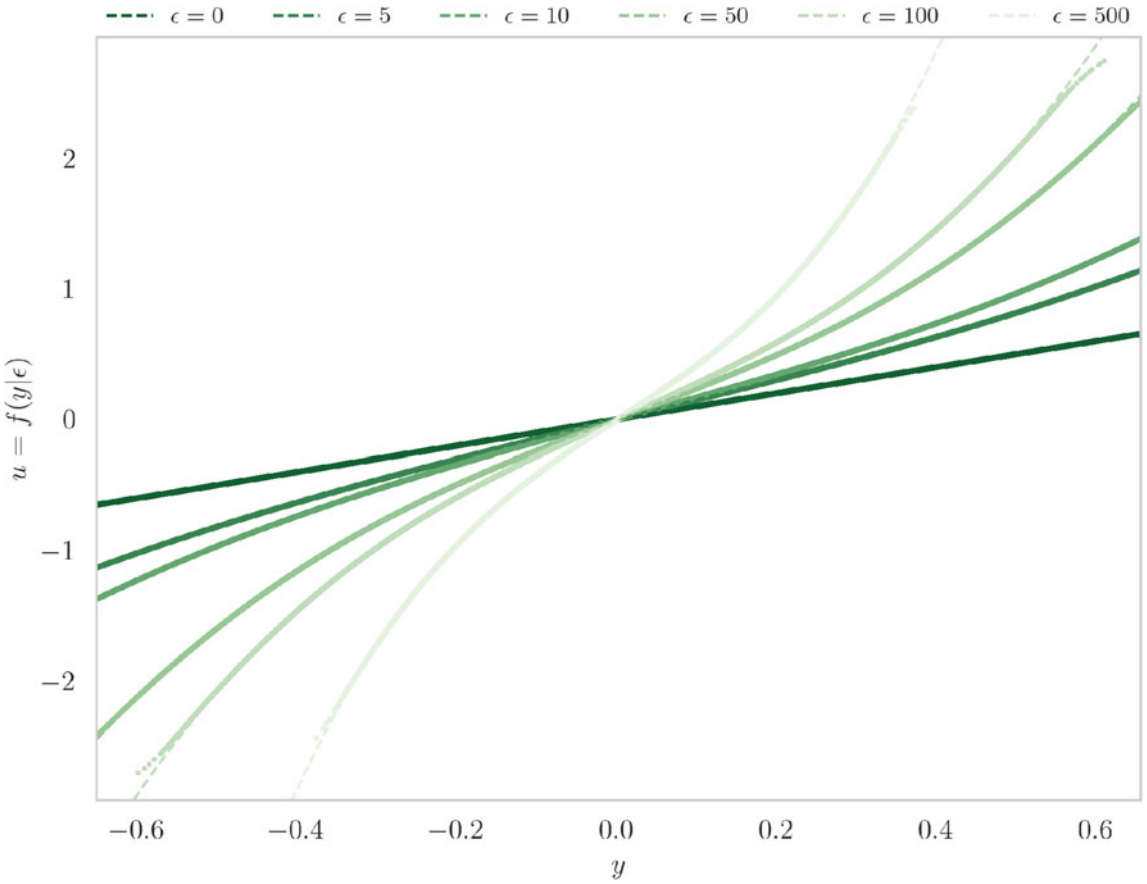

Fig. 11.4 Comparison of the modal mapping $f(y)$ with varying nonlinear stiffness ($\sigma_x^2 = 1$)

$$p_s(y) = A' \times \exp\left[-\frac{ck}{D}y^2\right] \tag{11.28}$$

which is a Gaussian distribution with mean 0 and variance $\frac{ck}{2D}$. In effect, the map f projects the density of the nonlinear displacements onto a distribution wherein there is no effect from the nonlinearity.

The following line of reasoning is now a tempting (but erroneous) one. Because the *stationary probability density* of $u = f(y)$ is the same as that of the underlying linear system (with $\epsilon = 0$) given the same white-noise input, the dynamics of $x \to u$ should therefore be linear.

Certainly, the converse argument is true. However a disproof of the above is straightforward. One begins by substituting the map f into the equation of motion for the Duffing oscillator.

$$\frac{\mathrm{d}^2}{\mathrm{d}t^2}g(u) + c\frac{\mathrm{d}}{\mathrm{d}t}g(u) + kg(u) + \epsilon g(u)^3 = x(t) \tag{11.29}$$

where,

$$g(u) = f^{-1}(u) = y \tag{11.30}$$

Evaluating the time derivatives of $g(u)$,

$$\frac{\mathrm{d}}{\mathrm{d}t}g(u) = \frac{\mathrm{d}g}{\mathrm{d}u}\frac{\mathrm{d}u}{\mathrm{d}t} = g'(u)\dot{u} \tag{11.31}$$

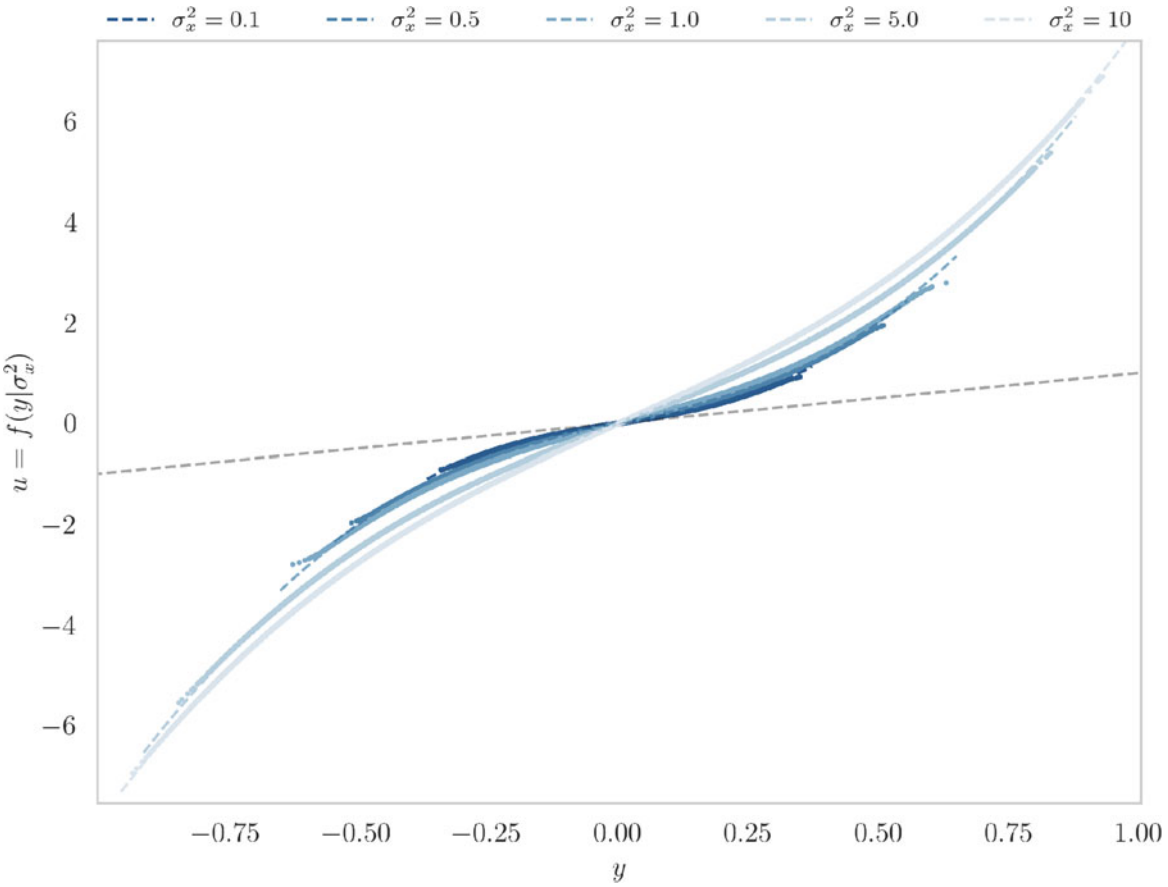

Fig. 11.5 Comparison of the modal mapping $f(y)$ with varying excitation level ($\epsilon = 100$)

$$\frac{\mathrm{d}^2}{\mathrm{d}t^2} g(u) = \frac{\mathrm{d}}{\mathrm{d}t}\left[g'(u)\dot{u}\right] = g''(u)\dot{u}^2 + g'(u)\ddot{u} \tag{11.32}$$

and substituting into the equation of motion gives:

$$g''(u)\dot{u}^2 + \ddot{u}g'(u) + cg'(u)\dot{u} + kg(u) + \epsilon g(u)^3 = x(t) \tag{11.33}$$

which, despite a Gaussian stationary density for x and u, is clearly a nonlinear ODE.

11.4 Towards Direct MDOF NNMs

Although it has been shown that a modal transformation (of sorts) is available in the SISO case, it is of no practical interest for performing nonlinear modal analysis. Unfortunately, the method presented above cannot be trivially extended to the higher-dimensional case. The principal issue is the form of the change-of-variables equation for higher-dimensional mappings. For n degrees of freedom, the static forward modal transformation $f(\mathbf{y}) = \mathbf{u}$ is a function with n inputs and n outputs. The change-of-variables equation is thus:

$$\left|J_f\right| = \frac{p(\mathbf{u})}{p(f(\mathbf{y}))} \tag{11.34}$$

where J_f is the Jacobian of f and $|\cdot|$ denotes the determinant operation. The above expression cannot be uniquely solved for f and once again a machine-learning approach must be adopted. However, for nonlinear systems where the equations of

motions are known exactly, the above expression can be used as an objective function whereby the quantity:

$$J_{\mathrm{FPK}}(f, \mathbf{y}) = \left|J_f\right| - \frac{p(\mathbf{u})}{p(f(\mathbf{y}))} \tag{11.35}$$

can be minimised within an optimisation framework to enforce an arbitrary target distribution in the modal space. Formulating the machine-learning problem in this way bears a close resemblance to the method of normalising flows (NF) [20]. Indeed, a NF approach to generating the statistically independent NNMs has been presented in the literature [15], with comparable results to other approaches.

Given the difficulty in solving (11.34), direct access to the modal transformation is not considered further at this stage. However, there are still promising avenues for further investigation, including the inclusion of the change-of-variables equation in the objective function when the stationary density of the physical displacements can be accessed (analytically from the FPK equation or otherwise).

11.5 Discussion

In this work, the problem of specifying exact modal transformations under the statistically independent framework has been treated. An approach to constructing the maps using the FPK equation and the change-of-variables equation is presented. In the limited SISO case, it is shown that the modal transformation can be specified by the numerical solution of a nonlinear ODE. This has furthermore been demonstrated on a simulated benchmark dataset. It is shown that the modal transformations specified in this way depend globally on the level of input excitation, although variation between local excitation levels is small.

It is interesting to imagine whether there might exist a choice of $p(u)$ (parametrised by the input excitation) that permitted an amplitude-invariant forward modal transformation (excluding of course the trivial $p(u) = p(y)$). It is certainly hard to imagine that this would be possible in general for nonlinear dynamic systems. However, this is an interesting avenue for further investigation.

Also considered in this paper is the extension of the method to the multiple degree-of-freedom case. It is shown that the differential equation arising from the change-of-variables equation in this case cannot be directly solved for the modal transformation f. Instead, a machine-learning approach is envisaged that uses the Jacobian of the modal transformation in the objective function to encourage conformance with a target distribution in the modal coordinates.

Overall, the results presented here offer some theoretical insight into how the SI-NNMs correspond to the underlying equations of motion. Although results are only given for the limited SISO case, there remain promising avenues for extension to the MDOF case.

Acknowledgments MDC would like to acknowledge the support of the EPSRC grant EP/L016257/1.

TJR would like to acknowledge the support of the EPSRC grant EP/W002140/1.

References

1. Worden, K., Tomlinson, G.R.: Nonlinearity in Structural Dynamics: Detection, Identification and Modelling. IOP, New York (2001)
2. Rosenberg, R.: On nonlinear vibrations of systems with many degrees of freedom. In: Advances in Applied Mechanics, vol. 9. Elsevier, Amsterdam (1966)
3. Rosenberg, R.M.: The normal modes of nonlinear n-degree-of-freedom systems. J. Appl. Mech. **29**, 7–14 (1962)
4. Kerschen, G., Peeters, M., Golinval, J.-C., Vakakis, A.F.: Nonlinear normal modes, part I: A useful framework for the structural dynamicist. Mech. Syst. Signal Process. **23**(1), 170–194 (2009)
5. Peeters, M., Viguié, R., Sérandour, G., Kerschen, G., Golinval, J.-C.: Nonlinear normal modes, part II: Toward a practical computation using numerical continuation techniques. Mech. Syst. Signal Process. **23**(1), 195–216 (2009)
6. Vakakis, A.: Non-linear normal modes (NNMs) and their applications in vibration theory: an overview. Mech. Syst. Signal Process. **11**(1), 3–22 (1997)
7. Shaw, S.W., Pierre, C.: Normal modes of vibration for non-linear continuous systems. J. Sound Vib. **169**(3), 319–347 (1994)
8. Shaw, S.W.: An invariant manifold approach to nonlinear normal modes of oscillation. J. Nonlinear Sci. **4**, 419–448 (1994)
9. Shaw, S.W., Pierre, C.: Normal modes for non-linear vibratory systems. J. Sound Vib. **164**(1), 85–124 (1993)

10. Shaw, S., Pierre, C.: Non-linear normal modes and invariant manifolds. Sound Vib. **150**(1), 170–173 (1991)
11. Carr, J.: Applications of Centre Manifold Theory, vol. 35. Springer Science & Business Media, Berlin (2012)
12. Worden, K., Green, P.L.: A machine learning approach to nonlinear modal analysis. Mech. Syst. Signal Process. **84**, 34–53 (2017)
13. Dervilis, N., Simpson, T.E., Wagg, D.J., Worden, K.: Nonlinear modal analysis via non-parametric machine learning tools. Strain **55**(1), e12297 (2018)
14. Champneys, M.D., Worden, K., Dervilis, N.: Nonlinear modal analysis based on complete statistical independence. In: Nonlinear Vibrations, Localisation and Energy Transfer, vol. 160 (2019)
15. Bull, L.A., Gardner, P.A., Dervilis, N., Worden, K.: Normalising flows and nonlinear normal modes. In: IFAC-PapersOnLine, vol. 54. Elsevier, Amsterdam (2021)
16. Tsialiamanis, G., Champneys, M.D., Dervilis, N., Wagg, D.J., Worden, K.: On the application of generative adversarial networks for nonlinear modal analysis. Mech. Syst. Signal Process. **166**, 108473 (2022)
17. Simpson, T., Tsialiamanis, G., Dervilis, N., Worden, K., Chatzi, E.: On the use of variational autoencoders for nonlinear modal analysis. In: IMAC 2022. ETH Zurich, Institute of Structural Engineering, New York (2022)
18. Champneys, M., Tsialiamanis, G., Rogers, T., Dervilis, N., Worden, K.: On the dynamic properties of statistically-independent nonlinear normal modes. Mech. Syst. Signal Process. **181**, 109510 (2022)
19. Caughey, T.K.: Derivation and application of the fokker-planck equation to discrete nonlinear dynamic systems subjected to white random excitation. J. Acoust. Soc. Am. **35**(11), 1683–1692 (1963)
20. Kobyzev, I., Prince, S.J., Brubaker, M.A.: Normalizing flows: An introduction and review of current methods. IEEE Trans. Pattern Anal. Mach. Intell. **43**(11), 3964–3979 (2021)

Chapter 12
Simulating Nonlinear Beating Phenomena Induced by Dry Friction in Dynamic Systems

Iyabo G. Lawal, Michael R. Haberman, and Keegan J. Moore

Abstract Self-excitation and beating phenomena are the result of nonlinear constitutive behavior of vibrating structures with nonlinear components. These behaviors require externally supplied excitation and can be induced by the combination of near equilibrium damping and nonlinear damping operating far from equilibrium. In this study, dry friction, a mechanism known for producing self-excitation in structures, is explored as a mechanism for producing beat phenomena in structures. The system consists of two masses connected via a linear spring with one of the masses damped via a grounded dashpot that is modeled using a five-parameter friction contact model. The system is modeled and solved using the RK-4 time-integration scheme. We perform system parameter identification of experimental data using the STFT (short-time Fourier transform) and wavelet-bounded empirical mode decomposition (WBEMD) to determine system model variables that may simulate the self-excitation and beat phenomena observed in the structural dynamics. Beat phenomena may also be a result of the existence of two or more closely separated damped natural frequencies. We also investigate the degree to which self-excitation in the structure is driving the nonlinear beat phenomenon as opposed to it being caused by choosing closely separated damped natural frequencies. We address this question using nonlinear normal modes (NNM) analysis which provides frequency-energy dependence of the modes as system parameters change. The approach developed here is useful for the design of energy harvesting and vibration isolation systems that are subjected to sliding friction.

Keywords Beating phenomena · Empirical mode decomposition · Friction · Mode lock-in · Self-excitation

12.1 Introduction

The emergence of "beating" has been observed in structures and depends on their stiffness and damping properties. In several studies, "beating" phenomena has been observed to be a result of closely separated modes in the structure, which in a linear system would produce a similar effect. It could also be caused by harmonic interactions driven by nonlinearities in the contact interface or by self-excitation within the structure. The root cause of this "beating" phenomena is not yet fully understood. The motivation in modeling this phenomena is to understand what set of parameters generate this effect in a 2-DOF mass system that consists of a driven linear oscillator and a nonlinear module with damping elements. This configuration of elements has also been known to produce targeted energy transfer (TET) from the linear oscillator to the strongly nonlinear module, known as a nonlinear energy sink (NES) [1, 2]. Kerschen and others [1] found that "beat phenomena" was a more efficient means of energy transfer than the reliance of either fundamental or sub-harmonic resonance capture. The efficiency of energy pumping or one-way energy transfer increases when "beating" phenomena is present. Another self-excitation effect is caused by friction-induced vibrations, where substructures separated by frictional contacts create self-excitation in the overall structure and in some cases may produce "brake squeal" [3]. This phenomena is identified as "mode lock-in" by the structural dynamics community. Prior studies explore how viscous elements can produce passive energy suppression in structures [4]. In this work, we explore another angle, by looking at friction as a dissipative element for TET. Friction has the

I. G. Lawal (✉) · M. R. Haberman
Department of Mechanical Engineering, University of Texas at Austin, Austin, TX, USA
e-mail: iyabo@utexas.edu; haberman@utexas.edu

K. J. Moore
Department of Mechanical & Materials Engineering, University of Nebraska–Lincoln, Lincoln, NE, USA
e-mail: kmoore@unl.edu

M. R. W. Brake et al. (eds.), *Nonlinear Structures & Systems, Volume 1*, Conference Proceedings
of the Society for Experimental Mechanics Series, https://doi.org/10.1007/978-3-031-36999-5_12

additional challenge in that it can also be a cause of self-excitation in the structure, particularly with "stick-slip" contact [5]. At high velocities, it acts in a dissipative capacity; however, if the right system parameters are chosen, it can also produce self-excitation and the emergence of "beating" phenomena.

12.2 Background

The 2-DOF lumped parameter model with spring and viscous damping is shown in Fig. 12.1a. An alternative 2-DOF lumped parameter model is shown in Fig. 12.1b, where energy dissipation is from a frictional contact element represented with a Bouc-Wen contact model [6].

12.2.1 Lumped Parameter Model

Two systems are considered: one that is viscous damped and the other friction damped with the use of a BW element. The two systems are shown in Fig. 12.1. The driven mass behaves as a linear oscillator and is externally driven, while the dissipative element is either a viscous or friction element.

The characteristic equation for both cases is shown. The parameters can be tuned to produce the beating phenomena. The goal is to determine the set of parameters that generate "beating" phenomena. F_{ex} is the external driving force, and F_D is the friction force generated in the BW dissipation element. The viscous-damped model parameters are $\mathrm{m}_1 = m_2 = 1.2\,\mathrm{kg}$, $\mathrm{k}_1 = 1.4\,\mathrm{N/\mu m}$, $\mathrm{k}_2 = 200\,\mathrm{N/\mu m}$, $k_3 = 29\,\mathrm{N/\mu m}$, and $c = 250\,\mathrm{kN/mm \cdot s}$. In the Bouc-Wen model, the same parameters were used in addition to the five model parameters: $\mathrm{P_n} = 60\,\mathrm{N}$, $\mathrm{n} = 2$, $\mathrm{k_t} = 270\,\mathrm{N/\mu m}$, $\sigma = 0.5$, $\mu = 0.5$, $\rho = \mathrm{k_t}/\mu|\mathrm{P_n}|$.

Viscous Damping

$$\ddot{x_1} = \frac{1}{m_1}\left[F_{ex}(t) - k_2(x_1 - x_2) - k_1 x_1 - c_1\dot{x}_1\right]$$

$$\ddot{x_2} = \frac{1}{m_2}\left[k_2(x_1 - x_2) - k_3 x_2 - c_3\dot{x}_2\right]$$

BW Friction Damping

$$\ddot{x_1} = \frac{1}{m_1}\left[F_{ex}(t) - k_2(x_1 - x_2) - k_1 x_1 - c_1\dot{x}_1\right]$$

$$\ddot{x_2} = \frac{1}{m_2}\left[k_2(x_1 - x_2) - F_D(x_2, \dot{x}_2)\right]$$

$$\text{where} \quad F_D(x_2, \dot{x}_2) = \mu P_N \xi(t) \quad \text{and} \quad \dot{\xi} = \rho\left[1 - (\sigma \dot{x}_2 sgn(\xi) + 1 - \sigma)|\xi|^n\right]\dot{x}_2. \tag{12.1}$$

The matrix form of the equation of motion and the state-space representation of the viscous-damped system are shown with **F**, representing the external forcing vector.

$$\mathbf{M}\ddot{x}(t) + \mathbf{C}\dot{x}(t) + \mathbf{K}x(t) = \mathbf{F}(t) \tag{12.2}$$

$$\mathbf{z} = \begin{pmatrix} \mathbf{x} \\ \dot{\mathbf{x}} \end{pmatrix}, \quad \dot{\mathbf{z}} = \mathbf{g}(\mathbf{z}) \quad \text{and} \quad \mathbf{g}(\mathbf{z}) = \begin{pmatrix} \dot{\mathbf{x}} \\ \mathbf{M}^{-1}\left[\mathbf{F}(t) - \mathbf{K}\mathbf{x}(\mathbf{t}) - \mathbf{C}\dot{\mathbf{x}}(t)\right] \end{pmatrix} \tag{12.3}$$

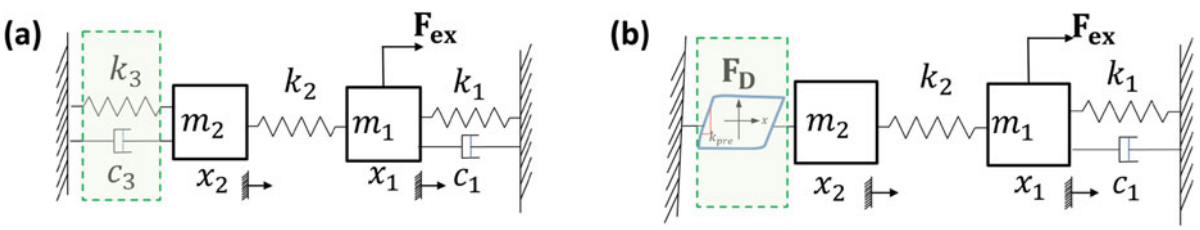

Fig. 12.1 Lumped parameter model with (**a**) representing viscous-damped system and (**b**) representing friction-damped system

12.3 Analysis

In the case where the system is being driven with an excitation force, F_{ex}, one technique to obtain the displacement and velocities is to use a numerical approach using implicit time-integration schemes such as Newark, Wilson, and Runge-Kutta (RK4) methods to get the displacements and velocities of a nonlinear system. A time-integration scheme based on Runge-Kutta is developed in MATLAB to determine the displacement and velocities in both systems. The simulation was completed over a 10-second interval and with a 0.01 time discretization for 10 seconds. The velocities of the masses are shown in Fig. 12.2 where the "beating" phenomena is observed in the viscous damped, but not the friction-damped system. For both models, the response of the displacement has a similar pattern to the velocity, with differences due to magnitudes.

A frequency domain analysis of the displacement in both systems is shown in Fig. 12.3. Figure 12.3a shows sub-harmonic interactions in the spectra. Analysis was done with a short-time Fourier transform (STFT) with six Gaussian windowing functions.

12.3.1 Numerical Integration Scheme

Beating phenomena was observed in the viscous-damped case. There also appears to be some energy transfer between the harmonics in the case of viscous damping. This can be seen clearly in Fig. 12.3a where the peak frequency at 0.03 Hz is transferring its energy into the other modes of the system. Beat phenomena occurred here when the difference between the damped frequencies, $\Delta\omega = \omega_1 - \omega_2$, is quite small. ω_1 represents the frequency with the highest amplitude for m_1 and ω_2 is the frequency with the highest amplitude for m_2. $\Delta\omega_{visc}$ was 0.001. This is different from the friction dissipated model, which at the given parameters did not demonstrate "beating" phenomena. $\Delta\omega_{BW}$ was 0.03. The other observation made from Fig. 12.3a is the presence of closely spaced frequencies near the peak frequency, ω_1.

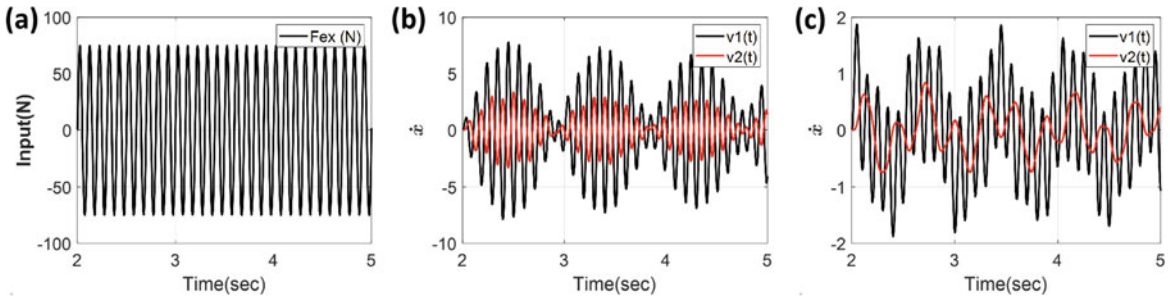

Fig. 12.2 Input excitation force shown in (**a**) with amplitude of 75 and $T = 0.1$. The viscous-damped system velocities ($\dot{\mathbf{x}}$) are shown in (**b**) and the friction-damped velocities ($\dot{\mathbf{x}}$) are shown in (**c**)

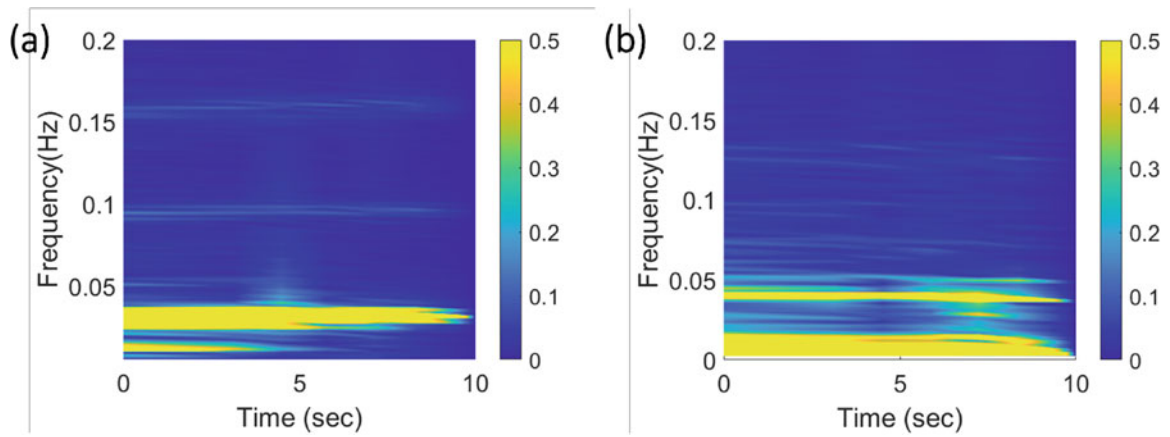

Fig. 12.3 STFT of the displacement, x_2, for (**a**) viscous-damped system and (**b**) friction-damped system with Bouc-Wen friction element with maximum frequency of 0.2 Hz

12.4 Conclusion

If the "beating" phenomena is caused by self-excitation in the structure, it can be suppressed by changing damping and stiffness parameters. Lu and others [4] achieve this by including stiffness and damping elements in directions orthogonal or at an angle to the direction of motion. In a friction element, both dissipative properties and self-excitation in the structure may emerge. Self-excitation from friction elements has been observed experimentally in structures; however, it isn't clear where the switch from self-excitation to dissipation or the reverse occurs in the structure. Chatterjee found that for the LuGre friction model, there exists a critical normal load modulation factor that reduces "stick-slip" behavior in the assembly [5]. In that study, cyclical normal force, P_N, present was used to reduce "stick-slip"-based oscillations. Future studies will explore how cyclical normal force, P_N, in the BW module can be used to reduce "stick-slip"-based oscillations and even possibly understand where the shift from self-excitation to dissipation occurs in the structure.

The use of normal modes (NNM) using the arc-length continuation method [7, 8] may help to evaluate energy transfer within the system. As observed in the viscous-damped case, there seems to be some level of sub-harmonic transfer when "beating" phenomena is present. However, there might also be an energy transfer mechanism, known as targeted energy transfer (TET), present as well. In TET, energy transfer between the linear oscillator and the dissipative element occurs passively. To ascertain if this mechanism is present, the use of NNM is needed to generate energy-frequency curves and to see the interactions between the two masses in the system [9, 10].

References

1. Kerschen, G., Lee, Y.S., Vakakis, A.F., McFarland, D.M., Bergman, L.A.: Irreversible passive energy transfer in coupled oscillators with essential nonlinearity. SIAM J. Appl. Math. **66**(2), 648–679 (2006)
2. Quinn, D.D., Gendelman, O., Kerschen, G., Sapsis, T.P., Bergman, L.A., Vakakis, A.F.: Efficiency of targeted energy transfers in coupled nonlinear oscillators associated with 1:1 resonance captures: Part I. J. Sound Vib. **311**(3–5), 1228–1248 (2008)
3. Allgaier, R., Gaul, L., Keiper, W., Willner, K.: Mode lock-in and friction modelling. Trans. Eng. Sci. **24**, 35–47 (1999)
4. Lu, Z.Q., Li, J.M., Ding, H., Chen, L.Q.: Analysis and suppression of a self-excitation vibration via internal stiffness and damping nonlinearity. Adv. Mech. Eng. **9**(12), 12 (2017)
5. Chatterjee, S.: Non-linear control of friction-induced self-excited vibration. Int. J. Non-Linear Mech. **42**(3), 459–469 (2007)
6. Guo, K., Zhang, X., Li, H., Hua, H., Meng, G.: A new dynamical friction model. Int. J. Mod. Phys. B **22**(8), 967–980 (2008)
7. Peeters, M., Viguié, R., Sérandour, G., Kerschen, G., Golinval, J.C.: Nonlinear normal modes, Part II: Toward a practical computation using numerical continuation techniques. Mech. Syst. Signal Process. **23**(1), 195–216 (2009)
8. Wallen, S.P., Haberman, M.R., Lu, Z., Norris, A., Wiest, T., Seepersad, C.C.: Static and dynamic non-reciprocity in bi-linear structures. In: Proceedings of Meetings on Acoustics, vol. 34. Acoustical Society of America (2018)
9. Vakakis, A.F., Bergman, L.A., McFarland, D.M., Lee, Y.S., Kurt, M.: Current efforts towards a non-linear system identification methodology of broad applicability. Proc. Inst. Mech. Eng. C: J. Mech. Eng. Sci. **225**(11), 2497–2515 (2011)
10. Moore, K.J., Kurt, M., Eriten, M., McFarland, D.M., Bergman, L.A., Vakakis, A.F.: Wavelet-bounded empirical mode decomposition for measured time series analysis. Mech. Syst. Signal Process. **99**, 14–29 (2018)

Chapter 13
Case Study on the Effect of Nonlinearity in Dynamic Environment Testing

Brennen Clark, Matthew S. Allen, and Ben Pacini

Abstract While recent research has greatly improved our ability to test and model nonlinear dynamic systems, it is rare that these studies quantify the effect that the nonlinearity would have on failure of the structure of interest. While several very notable exceptions certainly exist, such as the work of Hollkamp et al. on the failure of geometrically nonlinear skin panels for high speed vehicles (see, e.g., Gordon and Hollkamp, Reduced-order models for acoustic response prediction. Technical Report AFRL-RB-WP-TR-2011-3040, Air Force Research Laboratory, AFRL-RB-WP-TR-2011-3040, Dayton, 2011. Issue: AFRL-RB-WP-TR-2011-3040AFRL-RB-WP-TR-2011-3040), other studies have given little consideration to failure. This work studies the effect of common nonlinearities on the failure (and failure margins) of components that undergo durability testing in dynamic environments. This context differs from many engineering applications because one usually assumes that any nonlinearities have been fully exercised during the test.

Keywords Dynamic environment · Reliability · Quasi-linear

13.1 Introduction

Dynamic environment testing usually considers components that are fixed to a vehicle at their base. An environment is typically created that seeks to envelope the worst-case base accelerations that the component is expected to experience in operation. Then, the part is tested by replaying that environment on a large shaker and then checking whether the component is still functional. If the component survives, one typically repeats the tests with the environment increased to see if failure occurs. This continues until the part fails or until the shaker system is no longer able to exert sufficient force to increase the environment further. The difference between the environment at which the component fails (or the maximum tested environment) and the actual environment defines a margin; if the environment changes as more information becomes available this margin can be used to justify avoiding additional testing.

In this work, we consider cases in which the environmental testing is performed at various levels relative to that at which a nonlinearity becomes activated, to understand the consequences. To simplify the analysis, we consider quasi-linear behavior, in which one can define a linear model for a certain vibration level by choosing a constant value for the coefficients in

Sandia National Laboratories is a multimission laboratory managed and operated by National Technology and Engineering Solutions of Sandia, LLC., a wholly owned subsidiary of Honeywell International, Inc., for the US Department of Energy's National Nuclear Security Administration under contract DE-NA-0003525. This paper describes objective technical results and analysis. Any subjective views or opinions that might be expressed in the paper do not necessarily represent the views of the U.S. Department of Energy or the US Government.

B. Clark
Mechanical Engineering Department, Brigham Young University, Provo, UT, USA
e-mail: bclark42@byu.edu

M. S. Allen (✉)
Department of Mechanical Engineering, Brigham Young University, Provo, UT, USA
e-mail: matt.allen@byu.edu

B. Pacini
Structural Dynamics Department, Sandia National Laboratories, Livermore, CA, USA
e-mail: brpacin@sandia.gov

M. R. W. Brake et al. (eds.), *Nonlinear Structures & Systems, Volume 1*, Conference Proceedings of the Society for Experimental Mechanics Series, https://doi.org/10.1007/978-3-031-36999-5_13

an amplitude-dependent linear model. Measurements from a representative nonlinear structure are then used to predict the consequences on the environment testing.

13.2 Setting of Problem

We construct our model to match the behavior of the S4 benchmark beam structure [2]. For this study we assume a single degree-of-freedom modal model with the generalized coordinate being the displacement of Mode 2. This mode of vibration exhibits noticeable nonlinearity based on the data from [3], and is shown as the blue dots in Fig. 13.1. This model was then fit to a single-degree-of-freedom modal model with a mass, linear spring, linear damper, and an Iwan joint in order to be able to extrapolate the behavior to higher amplitudes (green dashed line in Fig. 13.1).

Approximating the system with a quasi-linear modal model, the equation of motion can be written in terms of the amplitude-dependent natural frequency $\omega_n(A)$ and damping ratio $\zeta(A)$ where A is the amplitude of the response q, i.e., $q = A\sin(\omega t - \phi)$. We assume a broad-band base excitation model for the force $F(t)$ so that the resonance frequency will be excited even if the natural frequency shifts at higher amplitude. Our modal equation of motion is

$$\ddot{q} + 2\zeta(A)\omega_n(A)\dot{q} + \omega_n^2(A)q = F(t) \tag{13.1}$$

The response of the system to a harmonic force is then given by the well-known equation, which gives the peak velocity in modal coordinates.

$$q(t) = Re\left[\frac{-F_p}{(\omega_n^2 - \omega^2) + i(2\zeta\omega_n\omega)}e^{i\omega t}\right] \quad \rightarrow \quad V_p = \frac{F_p}{2\zeta\omega_n}. \tag{13.2}$$

Now suppose that we know the response V_{p1} due to a force F_{p1} and we wish to find the response V_{p2} to a different force $F_{p2} = \alpha F_{p1}$. Using the prior equation, while allowing the damping and frequency to differ at each point because they are amplitude dependent, we obtain the following:

$$V_{p2} = \frac{\alpha F_{p1}}{2\zeta_2\omega_{n2}} = \alpha V_{p1}\left(\frac{\zeta_1}{\zeta_2}\right)\left(\frac{\omega_{n1}}{\omega_{n2}}\right) = V_{LinPred}\left(\frac{\zeta_1}{\zeta_2}\right)\left(\frac{\omega_{n1}}{\omega_{n2}}\right) \tag{13.3}$$

This equation must be solved iteratively because ζ_2 is a function of the amplitude V_{p2}. In doing so, one can discover how the response of the system changes as the force (i.e., the environment) increases or decreases. This can then be compared

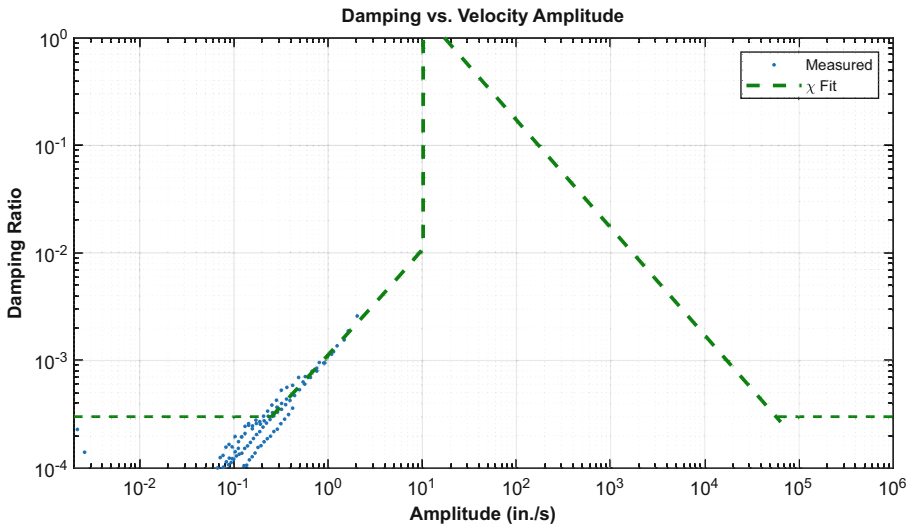

Fig. 13.1 Damping vs. velocity amplitude measurements from [3] and fit to an SDOF system with an Iwan element

to what one would obtain if the system were linear, i.e., $V_{LinPred} = \alpha V_{p1}$, as this is the behavior that is typically assumed when the nonlinearity in a system is not characterized.

13.3 Results

Several possible cases are presented in Table 13.1. In our analogy, the force or the factor α represents how much the force is amplified compared to that for the reference point. The force is analogous to the strength of the vibration environment, which is typically quantified as the base acceleration in environmental testing; the base acceleration on a component translates into an inertial force that can excite its modes of vibration. In the case considered here the system has only one mode of vibration.

The first lesson learned from the results in Table 13.1 is that, for this type of nonlinearity, the response and hence the stress can increase very slowly relative to the environment. For example, in Case C we began with a response level $V_1 = 0.1$ in/s and then the environment was increased by a factor of 1000 ($\alpha = 1000$), and yet the response V_{2NL} (and hence the stress in the part) increased by only a factor of $5.3/0.1 \approx 53$. A typical test might actually only involve an environment that was 20 dB or an order of magnitude above the expected environment, in which case the stresses in the part may not increase much beyond those in the expected environment. As a result, one should be wary in using linear thinking (i.e., that a 10x environment equates to 10x stress) when assessing environments. On the other hand, this case study also shows that a system with friction nonlinearity can have very high robustness, being capable of experiencing very large environments without large increases in stress. Conversely, if analysts were to take this nonlinearity into account ,then they might be able to exploit it to reduce the mass and cost of the component quite significantly.

The situation is worse in Cases D–F, where the test was performed with the system on the verge of macroslip. In Case D, increasing the environment by a factor of 10 increases the response by a factor of $9.54/2 \approx 3.2$, but then increasing the environment by a further factor of 100 (Case F) results in a further increase of only $10.25/9.54 \approx 7\%$. Once again the system would have great ability to increase in the level of the environment so that the tests would do little to increase the stresses in the part. While this is desirable, one is on the verge of catastrophe. From Case F, if the amplitude of the environment is increased by a factor of 2 (i.e., to a total of 2000), then Case G shows that the response would suddenly increase by more than a factor of 6000! In such a case, we would expect the part to break very quickly and fail the environmental test. One might then increase the strength of the part by an order of magnitude and repeat the test only to see it fail again.

Cases with $\alpha < 1$ in Table 13.1 are also particularly relevant to environment testing because one usually presumes that the test was performed at a higher level than the field environment. For example, Case K states that if testing was performed at a very high level (i.e., beyond the macroslip regime), that decreasing the response by a factor of 10 ($\alpha = 0.1$) reduces the response by a factor of 1000 (i.e., to 10.23 instead of 10,000). Hence, the environment test would be dramatically over-conservative. While 100,000 in/s may sound like a tremendously large environment for the S4 Beam, one should bear in mind that the curve above can shift a lot if the design of the bolts is changed or if they are just tightened less. Hence, small levels of base excitation could be needed to achieve this phenomenon in a different structure.

Table 13.1 Data comparing the response at higher input amplitude predicted by the linear model versus the nonlinear model. All of these results assume that $\omega_{n1} = \omega_{n2}$ in Eq. 13.3

Case	V_1	ζ_1	α	ζ_2	V_{2Lin}	V_{2NL}
A	0.1	0.0003	10	0.0006	1	0.5
B	0.1	0.0003	100	0.0018	10	1.65
C	0.1	0.0003	1000	0.00566	100	5.3
D	3	0.00324	10	0.01	30	9.54
E	3	0.00324	100	0.095	300	10.25
F	3	0.00324	1000	0.95	3000	10.25
G	3	0.00324	2000	0.0003	6000	65000
H	10.25	0.95	2	0.0003	20.5	65000
I	3	0.00324	0.1	0.001	0.3	0.928
J	3	0.00324	0.01	0.00034	0.03	0.286
K	100000	0.0003	0.1	0.29	10000	10.23

13.4 Conclusions

This paper has highlighted the danger in applying linear thinking to a nonlinear system and has also demonstrated a procedure by which the damping versus amplitude behavior of a system can be used to obtain more reliable estimates of the response of a system as its environment changes. Even if the test drives the structure well into the nonlinear regime, nonlinearity affects how the stresses in the part increase or decrease in response to that environment, and one should be aware of that when determining what environment to test to and when interpreting the results.

While it was not discussed here, the results could be even more serious if testing is performed at low levels and then that model is used to predict the response at higher levels. That extrapolation can be highly over-conservative or highly under-conservative depending on whether the joints are exercised above or below macroslip.

For the conference presentation, these case studies will be investigated further, including quantifying the effect on fatigue life, and additional case studies will be presented for a bilinear contact nonlinearity.

References

1. Gordon, R.W., Hollkamp, J.J.: Reduced-order models for acoustic response prediction. Technical Report AFRL-RB-WP-TR-2011-3040, Air Force Research Laboratory, AFRL-RB-WP-TR-2011-3040, Dayton, 2011. Issue: AFRL-RB-WP-TR-2011-3040 AFRL-RB-WP-TR-2011-3040
2. Singh, A., Scapolan, M., Saito, Y., Allen, M.S., Roettgen, D., Pacini, B., Kuether, R.J.: Experimental Characterization of a new Benchmark Structure for Prediction of Damping Nonlinearity. Orlando, 2018
3. Estakhraji, S.I.Z., Wall, M., Capito, J., Allen, M.S.: A thorough comparison between measurements and predictions of the amplitude dependent natural frequencies and damping of a bolted structure. J. Sound Vib. **544**, 117397 (2023)

Chapter 14
Strategies for Improving the Comparison of Frequency Response Functions with Similarity Metrics

Hunter R. Kramer, Levi H. Manring, John F. Schultze, Sandra J. Zimmerman, and Brian P. Mann

Abstract Determining the similarity of an existing structure with a reference structure is an important problem in structural dynamics. For this purpose, many metrics have been developed to quantify the similarity of frequency spectra, such as two transfer functions. However, these approaches yield an aggregate or single numerical score for the similarity over an entire frequency range. This paper, instead, applies these common similarity metrics across a range of frequencies and plots the results to illustrate instances where counterintuitive results can occur. For example, the highest degree of similarity often occurs at a frequency where the two frequency spectra appear to diverge.

The result is that counterintuitive cases can be corrected by applying a log frequency shift to the response, enabling better comparisons. Additionally, a similarity metric that compares the phase of the frequency spectra can be applied to make further comparisons. This paper seeks to verify the new methods presented in Manring et al. (J Sound Vib 539:117255, 2022) using a modified experiment and proposes a windowing method as another tool for comparing similar transfer functions. The authors investigate these approaches while applying historical measures of similarity, to provide a more intuitive result for a similarity score. While the shifted frequency spectra can now provide more intuitive comparisons of the degree of similarity, the degree of shifting the frequency segments provides an additional opportunity to quantify the differences in the frequency spectra. The developed approaches were applied to both theoretical and experimental systems.

Keywords Frequency response · Vibration · Metric · Log frequency shift · Phase similarity metric

14.1 Introduction

In the field of engineering and design, there are numerous applications of random vibration testing. Industries such as automotive, aerospace, and manufacturing leverage their understanding of vibrations to study critical system dynamics and increase the robustness of designs. One common way of capturing the dynamics of a vibrating system is to measure its frequency response function (FRF). FRFs are a measure of system behavior in response to some external force. FRFs are unique to classes of systems and comparing similar FRFs can exemplify key differences between the systems in question.

Tools that quantitatively compare FRFs are commonly referred to as similarity metrics. These metrics take two FRF signals, one for reference and one for comparison, and compare the value of the FRFs at each spectral line. Using this data, the metrics compute a single value that describes the similarity between them. There are several methods by which this can be done, such as the use of scaled inner products. This type of method is especially useful at comparing the amplitudes of two FRFs and has the added benefit of producing a normalized value between 0 and 1 (0 being least similar and 1 being most similar).

H. R. Kramer (✉) · L. H. Manring · B. P. Mann
Department of Mechanical Engineering and Materials Science, Pratt School of Engineering Duke University, Durham, NC, USA
e-mail: hunter.kramer@duke.edu; levi.manring@duke.edu; brian.mann@duke.edu

J. F. Schultze · S. J. Zimmerman
Los Alamos National Laboratory, Los Alamos, NM, USA
e-mail: schultze@lanl.gov; szimmerman@lanl.gov

M. R. W. Brake et al. (eds.), *Nonlinear Structures & Systems, Volume 1*, Conference Proceedings
of the Society for Experimental Mechanics Series, https://doi.org/10.1007/978-3-031-36999-5_14

The use of scaled inner products can be seen in the frequency response assurance criterion, or FRAC [1] which is given by

$$\text{FRAC} = \frac{\left|\sum_{k=1}^{N_k}[\mathbf{H}_A(f_k)^H \cdot \mathbf{H}_B(f_k)]\right|^2}{\sum_{k=1}^{N_k}[\mathbf{H}_A(f_k)^H \cdot \mathbf{H}_A(f_k)]\sum_{k=1}^{N_k}[\mathbf{H}_B(f_k)^H \cdot \mathbf{H}_B(f_k)]} \tag{14.1}$$

where $\mathbf{H}_A$ is the reference FRF, $\mathbf{H}_B$ is the comparison FRF, N_k is the number of spectral lines to compare, and f_k is the frequency at spectral line k. The superscript ^{H} indicates the Hermitian transpose of the preceding vector. The FRAC excels at comparing the amplitude of two FRFs but is prone to scaling issues. To remedy this a modified version of FRAC, called MFRAC, scales the result by the ratio of minimum to maximum powers for each FRF.

Some similarity metrics utilize other methods besides scaled inner products. The magnitude-shape similarity function (MSSF) is a combined comparison metric that compares not only magnitude but phase information [2]. One unique feature of MSSF is its use of the hyperbolic tangent function. For this paper, only the magnitude comparison of MSSF will be studied, which is called M_α and is given by

$$M_\alpha(f) = 1 - \tanh\left(\frac{\ln(3)\left|20\log_{10}|H(f)|\right|}{2\alpha}\right). \tag{14.2}$$

M_α uses a scaling factor α and a complex transfer function between two FRFs $H(f)$, as opposed to a scaled inner product.

Another interesting metric is the frequency response function similarity metric (FRFSM) [3]. This method differs from the previous metrics in its use of a probability density function to compare decibel scaled magnitudes of two FRFs. The process of using FRFSM is done using three equations. The first is the probability density function given by g as

$$g(x, \mu, \sigma^2) = \frac{1}{\sigma\sqrt{2\pi}}\exp\left(-\frac{1}{2}\left(\frac{x-\mu}{\sigma}\right)^2\right) \tag{14.3}$$

wherein σ is the standard deviation, x is the variable of interest, and μ is the mean. The next equation is ϵ which describes the decibel scaled magnitude of the two FRFs of interest given as

$$\epsilon(f) = \left|10\log_{10}\|\mathbf{H}_A(f)\|^2 - 10\log_{10}\|\mathbf{H}_B(f)\|^2\right|. \tag{14.4}$$

In Eq. 14.4, f is the frequency where the FRF signals are being applied. The final expression for FRFSM is given by

$$\text{FRFSM}(f) = \frac{g(\epsilon(f), 0, \sigma_0^2)}{g(0, 0, \sigma_0^2)}. \tag{14.5}$$

In Eq. 14.5, the mean μ is taken to be 0 for both probability density functions. Additionally, σ_0^2 is a reference value used to scale the metric. This value was recommended to be 6 dB by the authors of [3].

Up to this point, we have only described metrics that compare the amplitudes of FRFs with no consideration of phase. There exist several metrics that include or specifically study phase, but this paper focuses on the phase similarity metric (PSM) [4]. This metric, which is based on FRFSM, utilizes the probability density function g with one key difference. PSM introduces the phase error metric, $\angle H_w$, defined as

$$\angle H_w = |W(\angle H_e)| \tag{14.6}$$

where H_e is the difference between the phases of the two FRFs and W is a function that wraps the resultant phase from $-\pi$ to π radians. The equation for PSM then follows the form of FRFSM, given by

$$\text{PSM}(f) = \frac{g(\angle H_w, 0, \sigma_0^2)}{g(0, 0, \sigma_0^2)}. \tag{14.7}$$

To properly scale the result from Eq. 14.7 between 0 and 1, the value of σ_0^2 was chosen to be $\pi/4$ by the authors of [4].

One method by which the previously discussed metrics can be made more useful is the log frequency shifting (LFS) method [4]. This method can be used to shift the FRF of a comparison signal linearly in the frequency domain to resemble a reference signal more closely. This can be particularly useful because many different factors can shift the relevant features, such as the resonant frequencies of FRFs. This can lead to inaccurate comparisons of similar signals or even signals from the same system. This method can be used in two ways, using a single shift or using several different shifts centered around the resonant frequencies of the reference FRF. This paper applies a single shift to align similar FRFs. An in-depth description of how this method works can be found in reference [4].

14.2 Simulation

This section applies the previously described metrics to an idealized system. For this study, an Euler-Bernoulli beam with point excitation and point measurement was analyzed. The excitation and measurement were both located at the end of the beam to produce and capture a large system response. The beam characteristics used in this study are representative of the beam used in the later Experimental Validation section. The simulation parameters used are listed in Table 14.1 of the Appendix.

The LFS technique is useful in aligning signals that have similar features but may be shifted in the frequency domain. To demonstrate this technique, the beam response was simulated for various lengths. The equation for the resonant frequencies of an Euler-Bernoulli beam is

$$\omega_n = \sqrt{\frac{EI}{\rho A}}\beta_n^2 \tag{14.8}$$

where ω_n is the resonant frequency, E is the Young's modulus, I is the area moment of inertia, ρ is the beam density, and A is the cross-sectional area [5]. The value of β_n can be attained by solving the transcendental equation for an Euler-Bernoulli beam with fixed-free boundary conditions.

By changing the beam length by some constant, γ, we can alter the resonant frequencies of the beam by a measurable amount. Rearranging Eq. 14.8 slightly gives

$$\omega_{n,\gamma} = \sqrt{\frac{EI}{\rho A(\gamma L)^4}}(\beta_n L)^2 \tag{14.9}$$

which allows us to see this behavior directly [4]. In Eq. 14.9, L is the beam length. For the nth value of $\beta_n L$, it becomes evident that the resonant frequency $\omega_{n,\gamma}$ will change as a factor of $1/\gamma^2$ (assuming the other variables are constant). Applying linearly spaced values of γ to our beam produces linearly spaced FRFs, perfect for demonstrating the LFS technique. Figure 14.1 shows these FRFs plotted on a log scale for the first three resonant frequencies. Note that the magnitude of these FRFs is dimensionless throughout this paper.

Upon visual inspection, these FRFs are clearly similar. This is more difficult to describe mathematically, as historical metrics of FRF comparison can lack visual intuition. These metrics are generally applied using one of two methods. The first method is to compare signals over the entire frequency spectra giving a single, overall score of similarity. The second is by applying the metric at each spectral line, called the "point-to-point" method. While this is more useful in some cases, it ignores the overall behavior of the curves in question. Thus, applying classic FRF comparison metrics in these ways can often be misleading. For example, consider two of the signals from Fig. 14.1 that are shown in Fig. 14.2a. If the FRFs for gamma values of $\gamma = 1.0$ (reference) and $\gamma = 1.05$ are compared using the similarity metric FRFSM without LFS, the results are very confusing. To elaborate, the FRFSM provides a value of unity between the resonant frequencies. Conversely, while near the resonant frequencies, the value varies. One way to mitigate this effect is to use a windowed approach. This approach applies the desired comparison metric to a window of a predetermined size that shifts from the beginning to the end of the signal. This provides a "middle ground" between the single score and point-to-point methods. Figure 14.2 gives the FRFSM score between the two FRFs for varying window sizes.

A few more notable behaviors can be observed in Fig. 14.2. One is that all these similarity metrics are at a maximum at the points where the FRFs cross paths. This makes sense mathematically because the value of the FRFs is equal to the corresponding frequencies. This result falls victim to the metrics' lack of intuition, however, because the FRFs are diverging

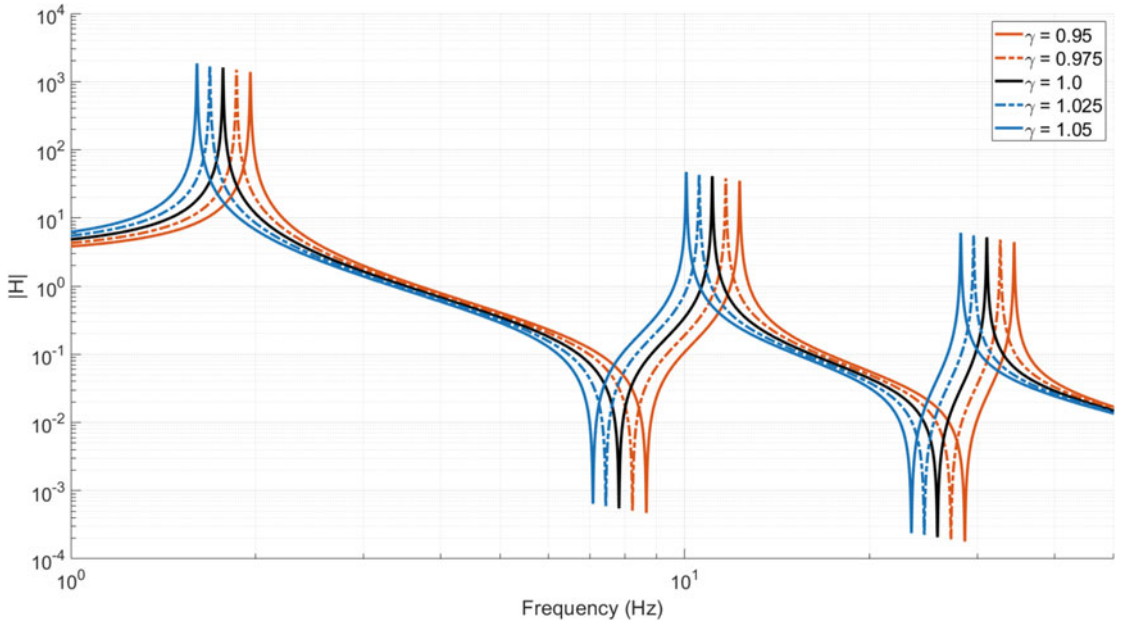

Fig. 14.1 The FRFs for simulated Euler-Bernoulli beams of differing length

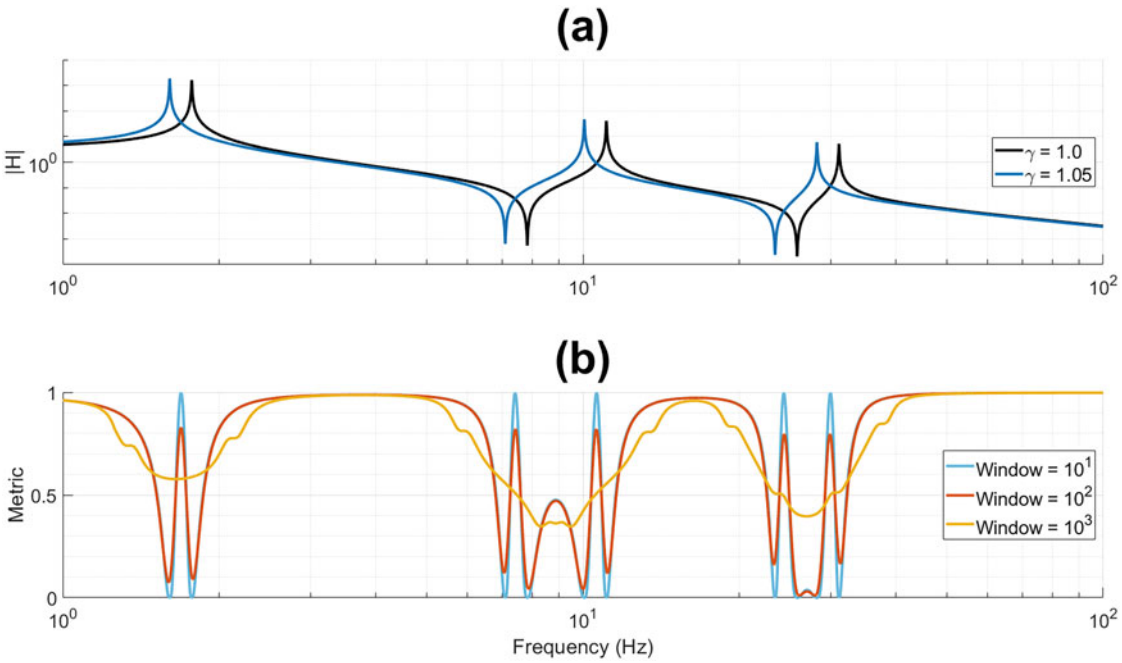

Fig. 14.2 A demonstration of the advantages of using a windowed approach with varying window sizes. (**a**) shows the FRF amplitudes for $\gamma = 1.05$ and the baseline FRF. (**b**) shows the performance of FRFSM on the reference signal and the baseline signal using various window sizes

at these points. By varying the selected window size, a different result can be seen. In Fig. 14.2 three window sizes are used: 10^1, 10^2, and 10^3 spectral lines. Note that the frequencies simulated in this study are spaced on a logarithmic scale as opposed to a linear scale. This ensures that the effect of the window size is applied evenly to logarithmically scaled spectra. As the window size increases, the sensitivity of the applied metrics decreases. This can be useful for attenuating out sharp spikes in the signal but can also cause the metric to be insensitive to important behaviors. The extreme case of this is in the single score method, where the window size is equal to the size of the FRF, leading to one comparison value. In Fig. 14.2, a window size of 10^2 is a good compromise as it preserves the rises and falls of the metric without excessive peaks or attenuation. For the remainder of this section, the figures use this window size when calculating similarity metrics.

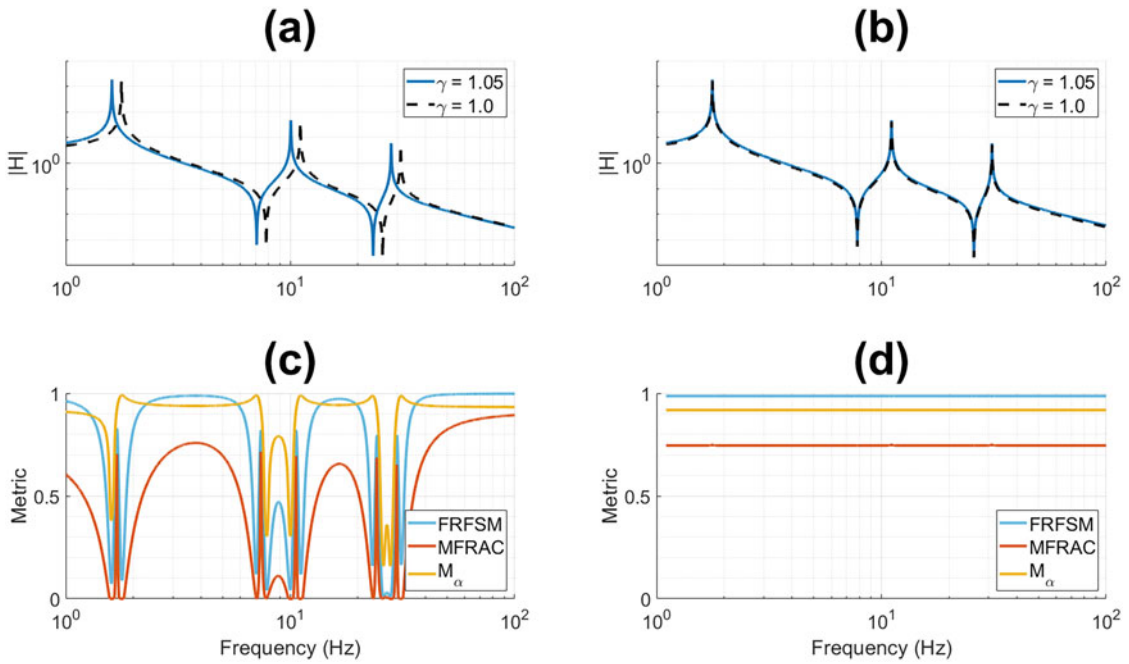

Fig. 14.3 An amplitude comparison of the FRFs for $\gamma = 1.05$ and the reference FRF. (**a**) shows the comparison FRF for $\gamma = 1.05$ and the baseline FRF. (**b**) shows the LFS comparison and reference FRFs. (**c**) shows the performance of several metrics applied to the non-shifted FRFs. (**d**) shows the performance of the shifted FRFs

In conjunction with windowing, LFS can be utilized to further improve these mathematical comparisons. Figure 14.3 shows the three different comparison metrics, MFRAC, FRFSM, and M_α, applied to the two FRFs from Fig. 14.2a.

Applying the similarity metrics before log shifting results in some useful information. Like the previous case, the metrics represent the similarity well between the resonant frequencies but perform with varying accuracy near them. Once the reference FRF is log shifted, all three metrics become constant. FRFSM becomes nearly unity, showing an almost perfect correlation, while M_α and particularly MFRAC are lower in value. This is due to how MFRAC scales its value by the ratio of the maximum to minimum powers. From this analysis, it can be concluded that LFS is beneficial in the comparison of amplitudes of FRF functions.

Another useful tool in FRF comparisons is to compare the phase. Historically, there are a limited number of metrics that include the phase as part of the comparison. This paper studies the phase similarity metric or PSM [4]. PSM is successful in capturing the phase behaviors of the comparison signal about the reference. This metric has been applied to the two FRFs from Fig. 14.2a and can be seen in Fig. 14.4c. To further enhance the comparison, LFS can be applied to align the phase shifts of the signals. The resulting curve can be seen in Fig. 14.4d.

As with the amplitude comparison, a few notable behaviors can be observed. Before LFS, the PSM metric is near unity for most of the signal. Large jumps in the metric occur at the phase shifts, however, because of the slight delay that increasing the length creates. After applying LFS, the signals are aligned such that the curves are indistinguishable. As a result, the PSM metric becomes constant and attains a value of unity. Figure 14.4 exemplifies the advantages of using LFS in conjunction with PSM. Applying LFS allows for the PSM metric to provide a more useful result in contrast to when it is used alone.

14.3 Experimental Validation

In the previous section, the LFS method and PSM were applied to the simulated response of a beam (in Figs. 14.3 and 14.4, respectively). This section applies these methods to test data from a simple experimental setup. Figure 14.5 shows a picture of the experimental system. An APS dynamics vertical shaker used to study the response of a thin metal beam is shown. The physical characteristics of this beam have been listed in Table 14.2 of the Appendix. To vary the dynamics of this system, an adaptor with an integral magnet was designed to allow for the addition of magnetic weights. A control accelerometer (denoted A) was added to the base of the beam behind the fasteners to capture the movement of the shaker. Additionally,

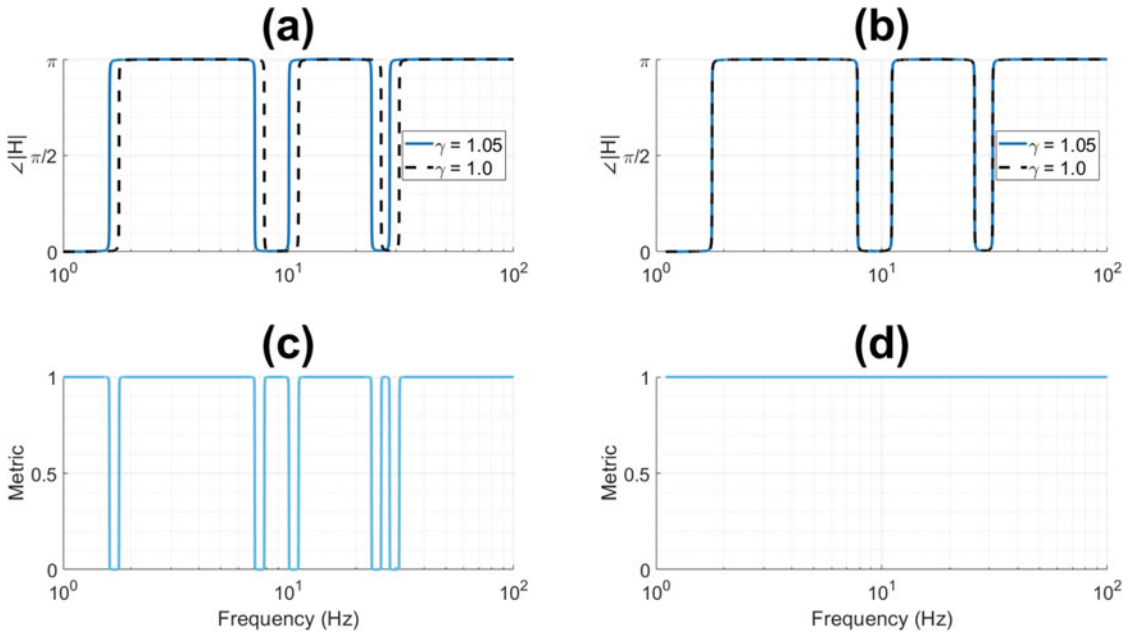

Fig. 14.4 A demonstration of phase comparison for a reference and comparison FRF. (**a**) shows the comparison phase for $\gamma = 1.05$ and the baseline phase. (**b**) shows the LFS comparison and reference phases. (**c**) shows the performance of PSM applied to the non-shifted phases. (**d**) shows the performance of the shifted phase

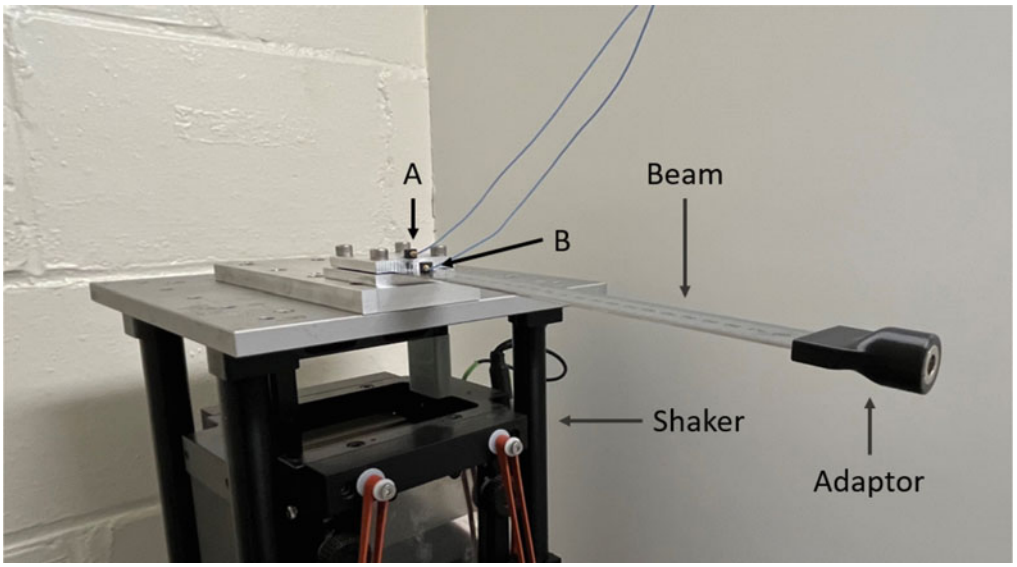

Fig. 14.5 The experimental fixed-free beam used for validation testing. The setup consisted of two accelerometers (denoted A and B), a vertical shaker, a thin metal beam, and an adaptor with integral magnet to vary the system response

a measurement accelerometer (denoted B) was added in front of the fasteners, directly on the beam to capture the beam's response. This location was chosen to mitigate the system noise incurred during testing. This differed from the simulated case where experimental noise was not considered and thus the response was measured at the end of the beam. An NI PXIe-1082 real-time controller was used with a LabView script to conduct the random vibration testing.

The weights added to the beam had a mass of approximately 9.1 grams each. To get a baseline reading, the beam was first tested without any added mass. Individual masses were then added to the end of the beam and tested using a random vibration study. The masses were approximately $1/6$ of the overall mass of the beam. While this is greater than what is commonly used for system perturbations, it is useful for examining extreme cases. From the data collected using the control and measurement accelerometers, the FRF for the system was derived. This was done via a Fourier transform of the time series. Each experimental case consisted of 20 trials, from which the data was averaged and smoothed using Gaussian smoothing.

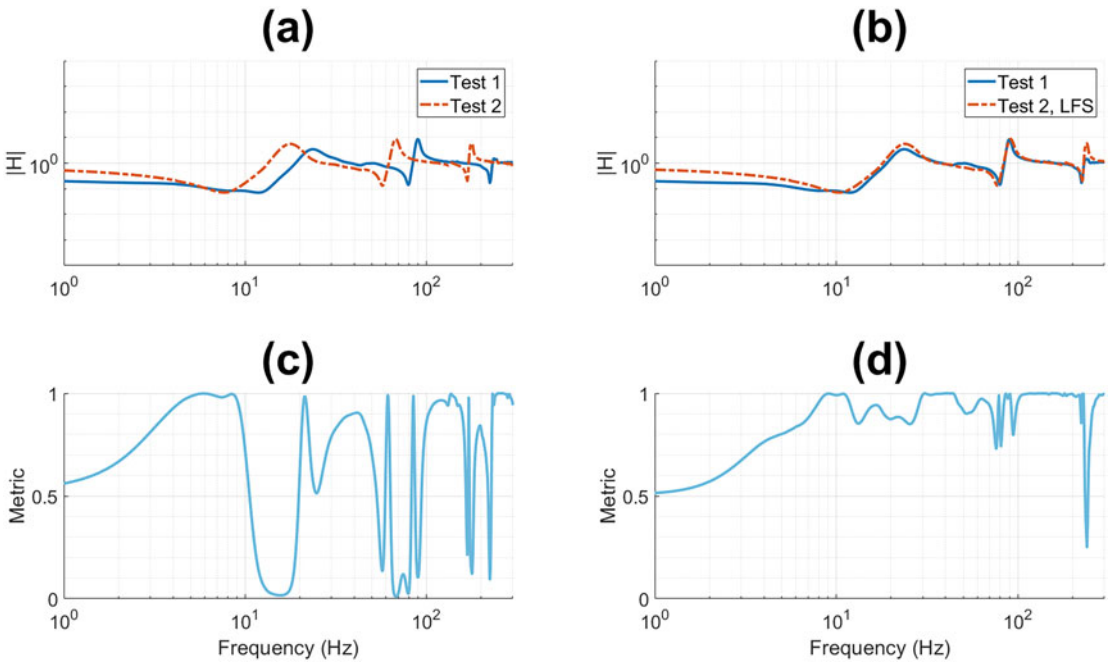

Fig. 14.6 A comparison of the magnitude of the FRFs for the beam with no added mass (Test 1) and the beam with added adaptor (Test 2). (**a**) shows the original FRFs. (**b**) shows the shifted comparison FRF with the original reference FRF. (**c**) shows the FRFSM applied to the original FRFs. (**d**) shows the FRFSM applied to the shifted comparison FRF and the original reference FRF

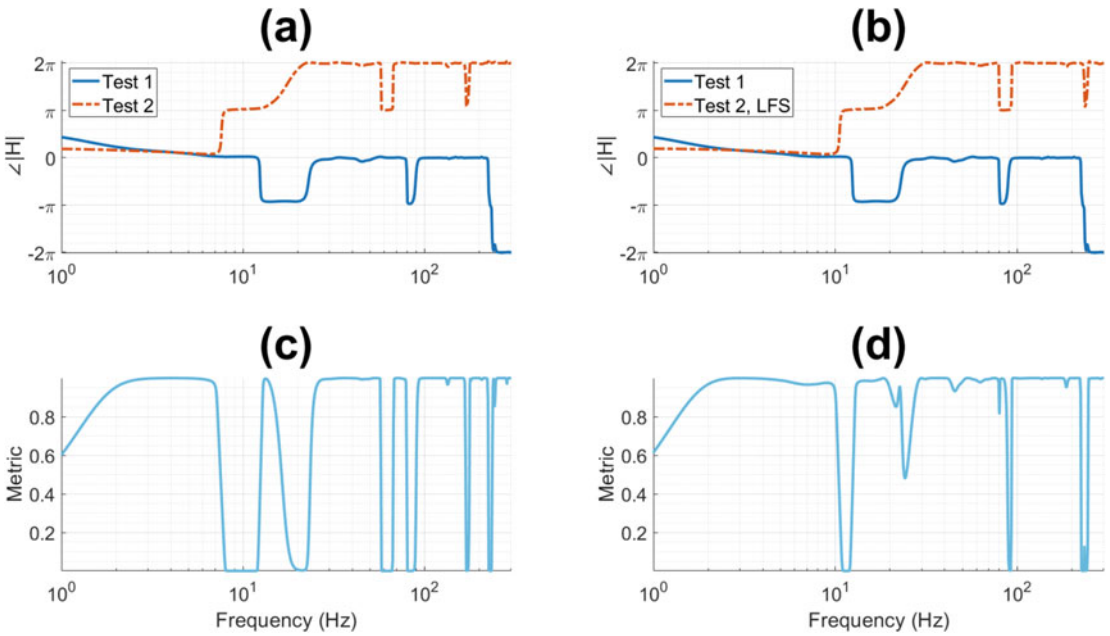

Fig. 14.7 A comparison of the phase of the FRFs for the beam with no added mass (Test 1) and the beam with added adaptor (Test 2). (**a**) shows the original FRFs. (**b**) shows the shifted comparison FRF with the original reference FRF. (**c**) shows the FRFSM applied to the original FRFs. (**d**) shows the FRFSM applied to the shifted comparison FRF and the original reference FRF

A comparison of the processed FRFs was done using the LFS and PSM methods. Figure 14.6 shows the results of applying the LFS method to the first and second tests (no mass and 18.8 grams, respectively). Additionally, FRFSM was applied to compare the similarity of the signals before and after LFS.

While the FRFs from these two tests are similar, it can be observed that adding mass to the end of the beam shifts the resonant frequencies down, conversely to our simulated case. The resulting curve from applying FRFSM resembles the simulated case. From the experimental data, however, there is much more variance in general at the location of the resonant frequencies. After the implementation of LFS, the value of FRFSM is close to unity for a majority of the frequencies studied.

The one notable exception is the third resonant frequency. Here, the response from the weighted beam is much greater than from the unweighted beam. When there is no mass, the higher frequency modes dampen out quickly, leading to this result.

Next, the phase of the above FRFs was studied. The phase of the FRFs was unwrapped for clarity and then log shifted using the LFS method. The resultant curves shared similar features but were separated by a shift of 2π which can be seen in Fig. 14.7. This shift exemplifies the usefulness of the LFS and PSM methods. While LFS succeeds in aligning resonant frequencies, it still preserves the unique features of each curve.

PSM was then applied to the shifted and unshifted curves. Studying the resulting curves reveals that before LFS there are more jumps between 0 and 1. This makes the signals more difficult to compare and masks the similar features. After applying LFS, the PSM curve still has several jumps between 0 and 1, but they make more sense intuitively. Aligning these features allows for a more direct comparison of the shape of the curves by mitigating the differences caused by the frequency shift. This information is still preserved, however, in the value of the lag factor. The lag factor describes how much the frequency of the comparison FRF must be shifted to align with the reference FRF. This value is derived by maximizing the cross-correlation between the two FRFs, with further details described in [4].

14.4 Conclusions

This paper demonstrated the advantages of using the LFS method in conjunction with existing FRF similarity metrics. An Euler-Bernoulli fixed-free beam was simulated with different length parameters to generate similar FRF signals. An experimental beam was studied on a vertical shaker with varying tip masses to validate the LFS method on physical system responses. Similarity metrics were applied to the resulting FRFs of these systems with and without LFS to gain insight into its advantages.

When LFS was applied with the similarity metrics, the results showed a greater correlation between the FRFs. Aligning the peaks of the comparison FRF to the reference FRF leads to more intuitive results while quantifying the shift in the frequency domain. Selecting a suitable window size reduced large peaks in simulation while still preserving important feature information. We find these methods presented in [4] and the proposed windowing method to be beneficial for comparing similar FRFs.

Acknowledgments This research is supported by the Delivery Environments program under the Office of Engineering and Technology Maturation at Los Alamos National Laboratory (LA-UR-22-31189).

Appendix

Table 14.1 Simulation parameters

Parameter	Symbol	Value	Unit
Young's modulus	E	10^{11}	N/m^2
Density	ρ	10^3	kg/m^3
Area moment of inertia	I	10^{-12}	m^4
Cross-sectional area	A	10^{-5}	m^2
Beam length	L	1.0	m
Measurement location	x_a	1.0	m
Excitation location	x_h	1.0	m
Damping	ζ	10^{-3}	

Table 14.2 Experimental beam characteristics

Parameter	Value	Unit
Young's modulus	180	GPa
Density	7750	kg/m^3
Approximate mass	0.056	kg
Length	0.254	m
Width	0.029	m
Height	0.001	m
Measurement location	0.010	m

References

1. Pascual, R., Golinval, J.-C., Razeto, M.: A frequency domain correlation technique for model correlation and updating. Proceedings of the International Modal Analysis Conference—IMAC (1997)
2. Shin, K.: An alternative approach to measure similarity between two deterministic transient signals. J. Sound Vib. **371**, 434–445 (2016)
3. Lee, D., Ahn, T.-S., Kim, H-S.: A metric on the similarity between two frequency response functions. J. Sound Vib. **436**, 32–45 (2018)
4. Manring, L.H., Schultze, J.F., Zimmerman, S.J., Mann, B.P.: Improving magnitude and phase comparison metrics for frequency response functions using cross-correlation and log-frequency shifting. J. Sound Vib. **539**, 117255 (2022)
5. Meirovitch, L., Parker, R.G.: Fundamentals of vibrations. Appl. Mech. Rev. **54**(6), B100–B101 (2001)

Chapter 15
Resonant Characterization of Nonlinear Structures in the Co-existence of Multiple Resonant Components

Nidish Narayanaa Balaji, Matthew R. W. Brake, D. Dane Quinn, and Malte Krack

Abstract The study of nonlinear normal modes has become a very popular subdiscipline in the structural dynamics community. This is principally due to the fact that they allow for a practical generalization of the concept of spectral invariant manifolds in linear dynamics. There have been a lot of analytical successes achieved in this area through the application of the method of multiple scales which decomposes the response of a nonlinear oscillator into fast-changing dynamics occurring on a slowly varying manifold. Numerical calculations have also been carried out using a periodic ansatz (with resonance-based constraints). Most of such investigations in the past have focused on cases where a single nonlinear mode is studied in isolation. Although this alone provides very interesting results, such as invariant manifold characterization and internal resonance detection, these are usually not sufficient to study the coupling between multiple nonlinear modes. Recent experimental studies have shown that such coupling can lead to very nontrivial trends in the resonant characteristics, making it difficult to correlate computational realizations with experimental measurements. The present paper takes a computational approach frequency-domain numerical simulations conducted using quasi-periodic harmonic balance to obtain numerical insights into the steady-state multi-resonant behavior. These results are compared with signal processing conducted on transient ringdown responses to determine the ramifications of commonly employed signal processing techniques like frequency-domain filtering for mode isolation. Analytical results are also computed using multiple scales for comparisons. Results are presented for a simplified system with two kinds of nonlinearities: geometric and dry friction.

Keywords Nonlinear resonance · Quasi-periodic oscillations · Modal coupling · Method of multiple scales · Nonlinear structural dynamics

15.1 Introduction

Resonance of nonlinear structures is an area that has been undergoing increasing interest in the structural dynamics community over the last few decades [1]. Nonlinear normal modes (NNMs) generalize the concept of resonance in linear dynamics to nonlinear systems. Unlike linear systems, in which the resonance is an invariant feature of the dynamics irrespective of the amplitude of response (or excitation), the presence of nonlinearity implies a strong amplitude dependence of the resonance characteristics (resonant frequency, damping, mode shapes, etc.). Consequently, there have been several computational as well as analytical techniques that have been successfully applied for the estimation of these NNMs in terms of amplitude-dependent resonant characterization (see, for instance, [2–4]).

Apart from the theoretical interest in the NNMs, the practical interest stems from the fact that, like modal representations in linear vibrations, these NNMs allow for the construction of reduced-order nonlinear modal models. Such models provide a computationally very efficient representation of a potentially much larger system. Stemming from the single nonlinear mode

N. N. Balaji (✉) · M. R. W. Brake
Department of Mechanical Engineering, Rice University, Houston, TX, USA
e-mail: nidish.balaji@ila.uni-stuttgart.de; brake@rice.edu

D. Dane Quinn
Department of Mechanical Engineering, The University of Akron, Akron, OH, USA
e-mail: quinn@uakron.edu

M. Krack
Institute of Aircraft Propulsion Systems, University of Stuttgart, Stuttgart, Germany
e-mail: malte.krack@ila.uni-stuttgart.de

M. R. W. Brake et al. (eds.), *Nonlinear Structures & Systems, Volume 1*, Conference Proceedings of the Society for Experimental Mechanics Series, https://doi.org/10.1007/978-3-031-36999-5_15

theory [5], this idea has been successfully applied for the synthesis of both the free and the forced responses of nonlinear structures [6, 7]. In these studies, after the relevant NNM is computed, the complexification-averaging (CX-A) technique is employed to derive the governing equations for the so-called slow dynamics, representing the instantaneous amplitude and phase of the response. Since the frequencies are known, the "fast dynamics" is reconstructed as a harmonic response enveloped by the slow dynamics. The interested reader is directed to [6, 7] for details.

Most of the abovementioned studies employ the singe nonlinear mode theory [5], i.e., resonant characteristics of a single nonlinear mode taken in isolation is employed for the syntheses (other modes, if included, are only taken as linear contributors to the response). While being a very powerful and widely used approach, this limits the domain of accuracy to scenarios where the excitation/response is close to the chosen mode (in frequency). Multiple modes may interact in a real structure through internal resonances (occurring at amplitude ranges where modal frequencies are commensurate) and through mode coupling (coupling that does not require commensurate frequencies) (see [8] for an analytical treatment covering both these aspects for a nonlinear structure).

The current paper proposes a nonlinear modal analysis approach which allows for the consideration of multiple modes together. The first complication this introduces is that the solutions for which the equations of motion are solved for are not periodic but are quasi-periodic since the frequencies corresponding to the different modes are not necessarily commensurate. Multi-frequency harmonic balance is therefore used as the computational technique of choice. A two-degree-of-freedom (DOF) model is used for demonstrating the technique numerically, with amplitude ranges chosen in such a manner so as to avoid any internal resonances.

15.2 Methodology

This section first describes the quasi-periodic formalism proposed for resonant characterization of multiple modes at the same time. Throughout the rest of the paper, the terminology "multi-resonant" will be adopted to denote response cases where the response consists of multiple modes that are resonant (and at a specified amplitude).

Given a nonlinear system of equations of the form

$$\underline{\underline{\mathrm{M}}}\,\underline{\ddot{u}} + \underline{\underline{\mathrm{C}}}\,\underline{\dot{u}} + \underline{\underline{\mathrm{K}}}\,\underline{u} + \underline{f}_{nl}(\underline{u}, \dots) = \underline{0} \tag{15.1}$$

the extended periodic motion concept [2] (EPMC) constrains the response to be periodic by introducing a periodic ansatz. Since the system could have dissipative components, the formulation also introduces a negative damping term of the form $\xi \underline{\underline{\mathrm{M}}}\,\underline{\dot{u}}$ (with an unknown coefficient ξ) that is meant to cancel out the dissipation by supplying sufficient energy over a cycle of oscillation. The equations of motion for EPMC is

$$\underline{\underline{\mathrm{M}}}\,\underline{\ddot{u}} + \underline{\underline{\mathrm{C}}}\,\underline{\dot{u}} + \underline{\underline{\mathrm{K}}}\,\underline{u} + \underline{f}_{nl}(\underline{u}, \dots) - \xi \underline{\underline{\mathrm{M}}}\,\underline{\dot{u}} = \underline{0}\,. \tag{15.2}$$

The "modal amplitude" is defined as the cyclic amplitude q such that $\oint \underline{u}^T \underline{\underline{\mathrm{M}}}\,\underline{u} dt = q^2$ (other amplitude definitions also exist), which is user-specified. It is to be noted that a practical implementation will involve a phase constraint, whereby all of the unknowns can then be parameterized by the modal amplitude q and the phase θ. Solving this system of equations will give a complex multi-harmonic mode shape $\underline{\Psi}$, a natural frequency ω, and the effective dissipation coefficient ξ, each of which is parameterized by the modal amplitude q.

Considering the case where a multi-resonant response is desired that has more than one resonant frequency component, the response will have to be quasi-periodic in general. So opting for a quasi-periodic multi-harmonic ansatz must provide sufficient flexibility for such a study. Unlike the previous case, there will have to be at least as many independent damping terms as the number of resonant components under consideration. We use the so-called Caughey series of matrices to generate sets of matrices to serve as coefficient matrices for the damping terms. It must be stressed at this point that, in general, the exact choice of the sequence of matrix should not change the results, i.e., this should not constrain the system in any manner. This claim will have to be verified for the current choice, but is deferred for future investigations and this is taken to be a fact for the current investigation. The negative damping terms are hereby

$$\underline{f}_{nd} = \left(\xi_1 \underline{\underline{\mathrm{M}}} + \xi_2 \underline{\underline{\mathrm{K}}} + \xi_3 \underline{\underline{\mathrm{K}}}\,\underline{\underline{\mathrm{M}}}^{-1}\underline{\underline{\mathrm{K}}} + \dots\right)\underline{\dot{u}}$$

$$= \sum_{i=1} \xi_i \underbrace{\underline{\underline{\mathrm{M}}} \left(\underline{\underline{\mathrm{M}}}^{-1} \underline{\underline{\mathrm{K}}} \right)^{i-1}}_{} \dot{\underline{u}}$$

$$= \sum_{i=1} \xi_i \underline{\underline{\mathrm{C}}}_i \dot{\underline{u}}\,, \tag{15.3}$$

where $\underline{\underline{\mathrm{C}}}_i$ are the Caughey matrices. Similar to EPMC, the idea here is to use proportional negative damping to cancel out the dissipative components in a hyper-cyclic (cyclic in hyper-time) sense.

The equations of motion for this case will be

$$\underline{\underline{\mathrm{M}}}\,\ddot{\underline{u}} + \underline{\underline{\mathrm{C}}}\,\dot{\underline{u}} + \underline{\underline{\mathrm{K}}}\,\underline{u} + \underline{f}_{nl}(\underline{u}, \dots) - \sum_i \xi_i \underline{\underline{\mathrm{C}}}_i \dot{\underline{u}} = \underline{0}\,. \tag{15.4}$$

In this case, the definition of the modal amplitudes of the individual resonant components come from the first harmonic coefficients of each frequency component. Solving this system will result in a quasi-periodic deflection shape with multiple harmonic components: the resulting resonant components $\omega_1, \omega_2, \dots$; and the damping coefficients $\xi_1, \xi_2, \dots$, all parameterized by modal amplitudes $q_1, q_2, \dots$.

15.3 Numerical Illustrations on a Two-DOF System

The above-developed formulation is applied to a two-DOF nonlinear oscillator that has previously been considered in the literature (see [2], for instance). The governing equations for this are taken to be

$$\begin{bmatrix} 1 & 0 \\ 0 & 1 \end{bmatrix} \begin{Bmatrix} \ddot{x}_1 \\ \ddot{x}_2 \end{Bmatrix} + \begin{bmatrix} 0.02 & -0.01 \\ -0.01 & 0.02 \end{bmatrix} \begin{Bmatrix} \dot{x}_1 \\ \dot{x}_2 \end{Bmatrix} + \begin{bmatrix} 2 & -1 \\ -1 & 2 \end{bmatrix} \begin{Bmatrix} x_1 \\ x_2 \end{Bmatrix} + \frac{1}{2} \begin{Bmatrix} x_1^3 \\ 0 \end{Bmatrix} = \begin{Bmatrix} 0 \\ 0 \end{Bmatrix}. \tag{15.5}$$

Two modes are studied concurrently; therefore, two independent frequency components need to be considered. Figure 15.1 shows, in graphical form, the list of harmonics selected for the quasi-periodic ansatz. The harmonic (n, m) corresponds to an ansatz of the form $\cos(n\omega_1 t + m\omega_2 t) + j \sin(n\omega_1 t + m\omega_2 t)$. Truncation is carried out in such a manner that $|n| + |m| \leq H_{max}$ with $H_{max} = 7$.

Figure 15.2 shows the natural frequencies of the two modes of this system as a function of the two modal amplitudes Q_1 and Q_2. These simulations are conducted by setting H_{max} to 7. It must be noted here that since there are two control parameters Q_1, Q_2, traditional numerical continuation is not applicable (designed for single parameter continuation). For the purposes of the current study, an additional constraint is enforced of the form $(Q_1, Q_2) = Q(\cos\theta, \sin\theta)$ and single parameter continuation is carried out in the parameter Q. This is repeated for different θ values so as to traverse the solution

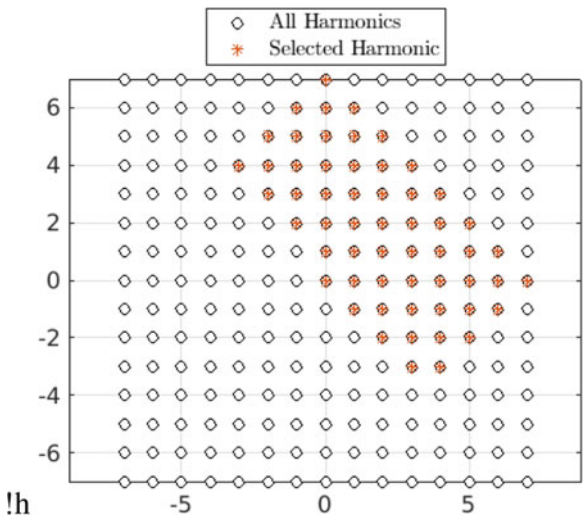

Fig. 15.1 Selected harmonics for two frequency components and $H_{max} = 7$ (Redundant indices removed)

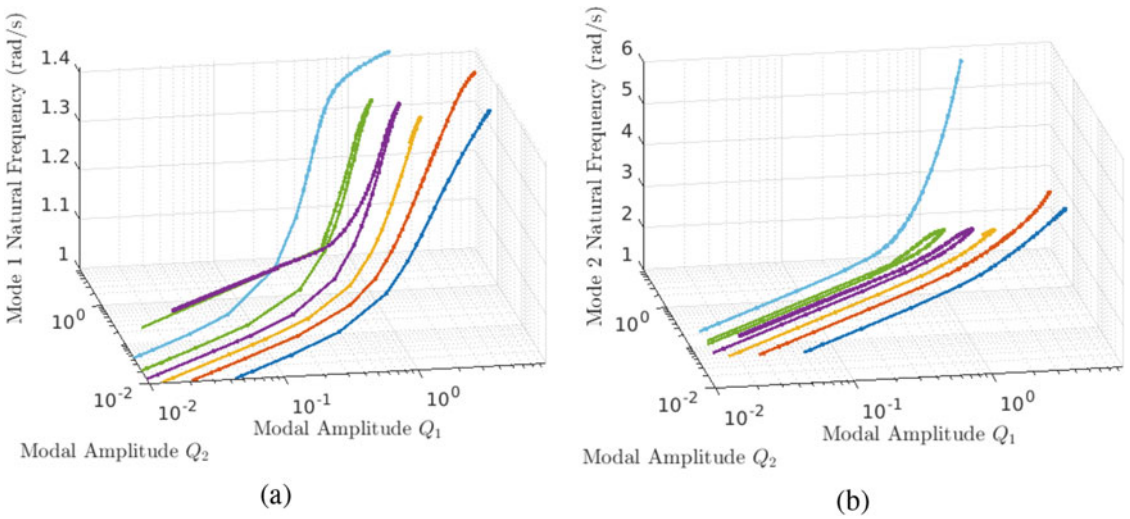

Fig. 15.2 Results from the seven-harmonic QP simulation, plotting the (**a**) first and (**b**) second natural frequencies as functions of the modal amplitudes Q_1, Q_2

domain (which is a planar region) through single lines. The results shown in Fig. 15.2 demonstrate that beyond a certain amplitude, the frequency backbone seems to change direction, indicating strong presence of modal interactions/couplings. Little can be said about such phenomena with the continuation scheme employed presently, since the constraint enforced above for the continuation may end up artificially constraining the system, rendering these features on the backbone plot to have limited physical meaning. One will have to resort to multi-parameter continuation techniques in order to fully explore such features.

For the purposes of this study, the following analyses will be restricted to single harmonic simulations. Although this has limited physical significance, it will, at the minimum, enable a better understanding of modal interactions that are not related to internal resonances (which necessarily require a multi-harmonic ansatz).

15.3.1 Two-Component Single Harmonic Balance Results

For the system at hand, it must be noted that one may employ the method of multiple scales (MMS, as in [8]) in order to obtain analytical expressions for the nonlinear natural frequency (and damping) characteristics. For the system at hand, the expressions for the natural frequencies are

$$\omega^{(1)} = \omega_0^{(1)} + \epsilon \frac{3\alpha}{8}(Q_1^2 + 2Q_2^2), \text{ and} \tag{15.6a}$$

$$\omega^{(2)} = \omega_0^{(2)} + \epsilon \frac{3\alpha}{8}(2Q_1^2 + Q_2^2). \tag{15.6b}$$

Note that these expressions are derived using MMS considering just a single harmonic, thereby enabling direct comparison to the numerical results generated by the quasi-periodic harmonic balance (QP-HB) approach developed above. ϵ represents the book-keeping parameter used in the perturbation analysis. The above expressions correspond to the analysis carried up to an $\mathcal{O}(\epsilon)$ accuracy. Figure 15.3 shows a comparison of the resonant frequency backbone surfaces (since these are functions of both the modal amplitudes) computed using the numerical approach (QP-HB) and the analytical approach (MMS). A close match can be observed, especially for small amplitudes.

Another aspect can be highlighted by constructing vertical contour sets on the above modal surfaces. These are contour levels drawn for different values of Q_1 and Q_2, as shown in Fig. 15.4. These highlight the fact that even when the mode 1 amplitude is fixed (and nonzero), the mode 1 frequency can vary purely due to the changes in the mode 2 amplitude (vice versa for the mode 2 frequency). This fact is also reflected by the analytical dependence in Eq. 15.6. This seems to suggest that in a practical setting, the employment of data from hammer impact tests (which provides a broad spectrum and therefore

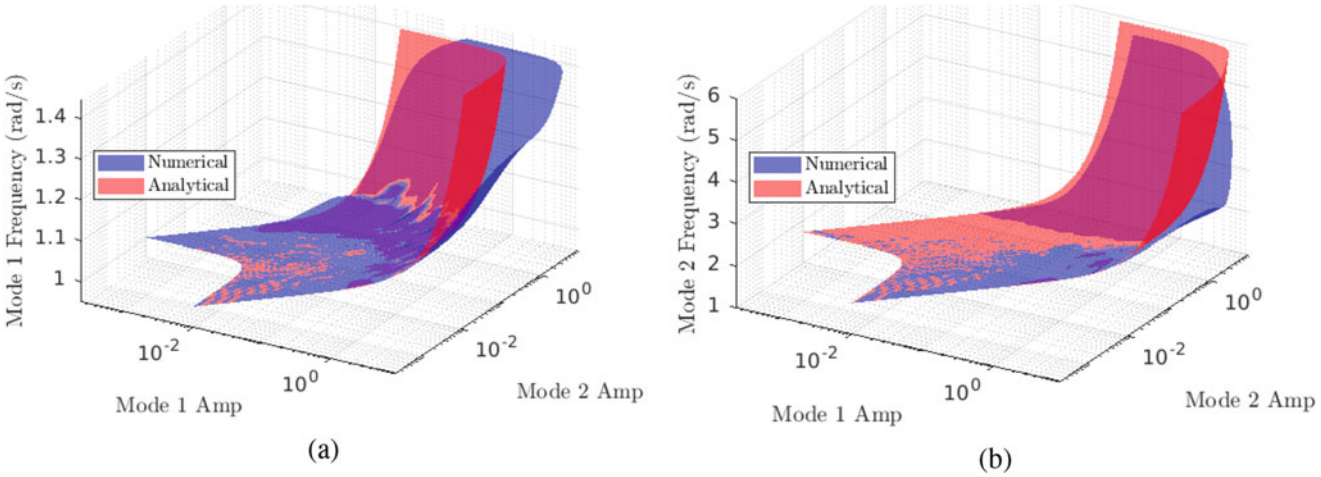

Fig. 15.3 Surfaces of the (**a**) first and (**b**) second mode natural frequencies as a function of the two modal amplitudes, numerical and analytical predictions

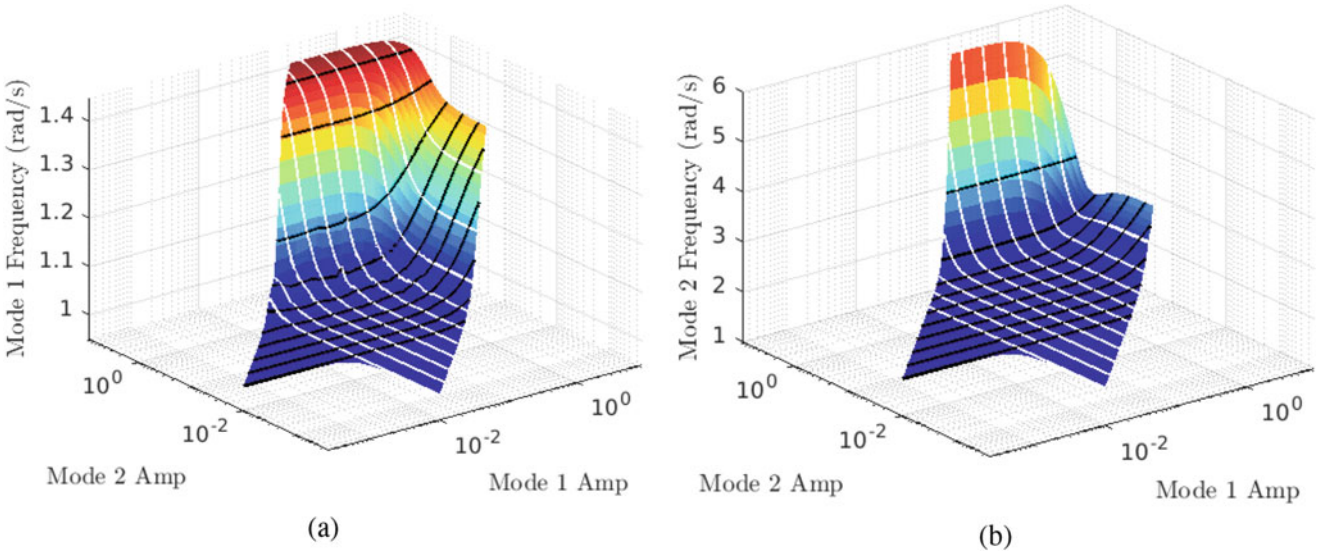

Fig. 15.4 Surfaces of the (**a**) first and (**b**) second mode natural frequencies as a function of the two modal amplitudes, showing vertical contours

multimodal excitation) could possibly be of questionable reliability. In the literature, similar observations have been made experimentally in [9].

As a first step in assessing the acuteness of this issue, a transient simulation is conducted wherein the initial condition is provided as a mix of the two mode shapes at a sufficiently high amplitude level so as to exhibit nonlinear free decay (but not too high so as to avoid internal resonance phenomena). The PFF approach [10] is used to postprocess the ringdown data into modal backbones. Figure 15.5a presents the transient ringdown data in time as well as frequency domains, showing the raw acceleration data extracted from DOF 2 (x_2). In Fig. 15.5b, the characteristics of the mode 1 frequency are plotted against the DOF 2 acceleration amplitude along contour levels corresponding to different values of Q_2 (the other mode in the system). The first observation that can be made is that at higher amplitudes of Q_2, there seems to be a very nontrivial relationship between the second mode amplitude and the first mode frequency (this is also verified for mode 2, but not shown). Here, the MMS results corresponding to the same amplitude levels as the contours are plotted as dash-dotted lines—the match is once again very good at low amplitude levels, but becomes inaccurate as either Q_1 or Q_2 becomes large. Also plotted (in black) is the frequency backbone post-processed from the transient ringdown data using PFF. There seems to be some disagreement between the transient result and any of the contour levels in the nonlinear regimes.

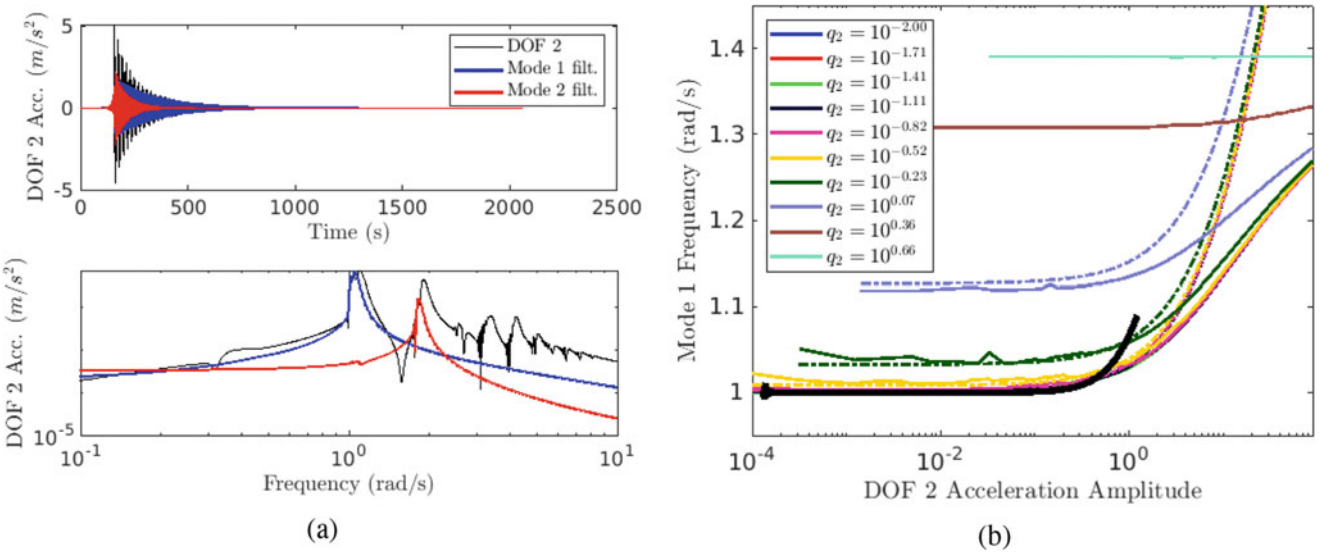

Fig. 15.5 (**a**) Time and frequency-domain representations of the ringdown data (before and after filtering and **b**) contour curves from the mode 1 backbone surface (Fig. 15.4a), shown as solid lines, along with their analytical counterparts (using MMS), shown as dash-dotted lines. Also plotted in (**b**) is the mode 1 backbone post-processed from the transient data in (**a**)

15.4 Conclusions

A new computational approach based on the extended periodic motion concept (EPMC) has been proposed for the study of nonlinear multi-resonant dynamics. Resonant backbones have been computed for a two-DOF oscillator with a cubic nonlinearity. The results show that the proposed approach is capable of diagnosing both modal interactions as well as modal coupling. Some areas that have been identified for future research are:

- The viability of multi-parameter continuation for the investigation of the resonant backbone manifolds in the presence of modal interactions must be explored.
- The generizability of the assumed negative damping form needs to be understood better.
- Modal coupling (away from the internal resonance regimes) needs to be studied in more detail, as a way of determining how much inaccuracies are incurred while employing hammer impact test-based data in an experimental setting.

Apart from these, it is remarked that the presented approach can potentially allow the direct detection of modal interactions through bifurcation tracking. This is possible due to the fact that when the two frequencies become commensurate, the Jacobian matrix of the system of equations being solved for the QP-HB approach becomes singular, i.e., indicating a bifurcation.

Furthermore, the practical utility of this approach will be greatly enhanced if it becomes possible to derive slow flow equations of motions for the amplitude and phase coordinates of multiple modes concurrently (such as the developments in [6, 7]). This will enable the construction of nonlinear modal reduced-order models, leading to potentially faster computations for large systems.

References

1. Vakakis, A.F.: Non-linear normal modes (NNMs) and theirapplications in vibration theory: an overview. Mech. Syst. Signal Process. **11**(1), 3–22 (1997). ISSN: 0888-3270. https://doi.org/10.1006/mssp.1996.9999
2. Krack, M.: Nonlinear modal analysis of nonconservative systems: extension of the periodic motion concept. Comput. Struct. **154**, 59–71 (2015). ISSN: 00457949. https://doi.org/10.1016/j.compstruc.2015.03.008
3. Balaji, N.N., Brake, M.R.W.: A quasi-static non-linear modal analysis procedure extending rayleigh quotient stationarity for non-conservative dynamical systems. Comput. Struct. **230**, 106184 (2020). ISSN: 00457949. https://doi.org/10.1016/j.compstruc.2019.106184
4. Dane Quinn, D.: Modal analysis of jointed structures. J. Sound Vib. **331**(1), 81–93 (2012). ISSN: 0022-460X. https://doi.org/10.1016/j.jsv.2011.08.017

5. Szemplińska-Stupnicka, W.: The modified single mode method in the investigations of the resonant vibrations of non-linear systems. J. Sound Vib. **63**(4), 475–489 (1979). ISSN: 0022460X. https://doi.org/10.1016/0022-460X(79)90823-X
6. Krack, M., Panning-von Scheidt, L., Wallaschek, J.: On the computation of the slow dynamics of nonlinear modes of mechanical systems. Mech. Syst. Signal Process. **42**(1), 71–87 (2014). ISSN: 0888-3270. https://doi.org/10.1016/j.ymssp.2013.08.031
7. Krack, M., Panning-von Scheidt, L., Wallaschek, J.: A method for nonlinear modal analysis and synthesis: application to harmonically forced and self-excited mechanical systems. J. Sound Vib. **332**(25), 6798–6814 (2013). ISSN: 0022460X. https://doi.org/1016/j.jsv.2013.08.009
8. Mathis, A.T., Dane Quinn, D.: Transient dynamics, damping, and mode coupling of nonlinear systems with internal resonances. Nonlinear Dyn. **99**(1), 269–281 (2020). ISSN: 0924-090X, 1573-269X. https://doi.org/10.1007/s11071-019-05198-w
9. Moldenhauer, B.J. et al.: Influences of modal coupling on experimentally extracted nonlinear modal models. In: G. Kerschen, M.R.W. Brake, L. Renson (eds.) Nonlinear Structures and Systems, vol. 1. Conference Proceedings of the Society for Experimental Mechanics Series, pp. 189–204. Springer, Cham (2020). ISBN: 978-3-030-12391-8. https://doi.org/10.1007/978-3-030-12391-8_25
10. Jin, M. et al.: Identification of instantaneous frequency and damping from transient decay data. J. Vib. Acoust. **142**(5) (2020). ISSN: 1048-9002. https://doi.org/10.1115/1.4047416

Chapter 16
Derivative-Less Arclength Control-Based Continuation for the Experimental Identification of Nonlinear Frequency Responses

Gaëtan Abeloos and Gaëtan Kerschen

Abstract This study focuses on the continuation process that is inherent to control-based continuation. Existing continuation procedures can be separated in two families. Similarly to numerical continuation, derivative-based methods find the solution of an objective function, the derivatives of which are estimated using finite differences. In mapping-based methods, the input parameter space is exhaustively or partially explored during the experiment. The features of interest can then be extracted during a post-processing phase or in parallel to the experiment. A novel arclength continuation procedure is developed in this paper. It requires neither the estimation of derivatives nor the identification of responses outside the features of interest, thus simplifying and accelerating the continuation process. The method is demonstrated numerically using a Duffing oscillator.

Keywords Nonlinear vibration · Control-based continuation · Arclength continuation · Duffing oscillator · Frequency responses

16.1 Arclength Continuation: The Basic Idea

The objective of this paper is to develop a continuation procedure which is simple to conceptualize and to implement and which avoids the need for post-processing or offline computations. The method is inspired by (i) the numerical arclength continuation procedure [1, 2], during which a control parameter is changed until it reaches the desired equilibrium, and (ii) the adaptive filtering-based online CBC experiment [3].

Because the sought frequency response curve (FRC) is one-dimensional in the input parameter space, a sufficiently small ellipse centered on the branch intersects it twice, as illustrated by the red markers in Fig. 16.1. One intersection is a previously identified response, and the other one is the next response to be identified. Successive responses on the FRC can thus be identified by increasing the arc angle α on the ellipse until the system reaches the next intersection. The response lies on the FRC if the excitation amplitude p given by the CBC controller equals the targeted excitation amplitude p^*. For illustration, Fig. 16.2 depicts the value of p depending on the arc angle α along the ellipse in Fig. 16.1. The ellipse intersects the FRC twice, because p reaches the target value p^* twice.

The continuation procedure is detailed in Fig. 16.3. We only need to know two responses on the FRC to identify a third one; the current one is denoted (Ω_c, X_c^*), and the previous one (Ω_p, X_p^*). An ellipse with semi-major axes $\Delta\Omega$ and ΔX_1^* is centered at the current point. The slope angle β between the current and previous points approximates the FRC slope. The input parameters (Ω, X_1^*) are set on the ellipse with an arc angle α from the previous point. The arc angle α is increased progressively from an initial angle α_0 sufficiently far away from the previous point until p reaches p^*, up to a certain tolerance tol_p.

In practice, we advise to identify the backbone curve before using the arclength continuation method to identify an FRC. In doing so, the experimenter can estimate the intervals in which the frequency and amplitude vary, and, in turn, adimentionalize the input parameter space (Ω, X_1^*) such that the eccentricity of the ellipse is close to unity, i.e., $\Delta\Omega \approx \Delta X_1^*$. Additionally, knowing the backbone allows to decrease the rate of change of the arclength when approaching the resonance peak, the region where transients can have the greatest effect on accuracy. The resonance peak can also be localized by looking at the evolution of the phase lag. An arc angle margin α_0 is chosen to ensure a sufficient distance with previously identified

G. Abeloos · G. Kerschen (✉)
Aerospace and Mechanical Engineering Department, University of Liège, Liège, Belgium
e-mail: gaetan.abeloos@uliege.be; g.kerschen@uliege.be

M. R. W. Brake et al. (eds.), *Nonlinear Structures & Systems, Volume 1*, Conference Proceedings
of the Society for Experimental Mechanics Series, https://doi.org/10.1007/978-3-031-36999-5_16

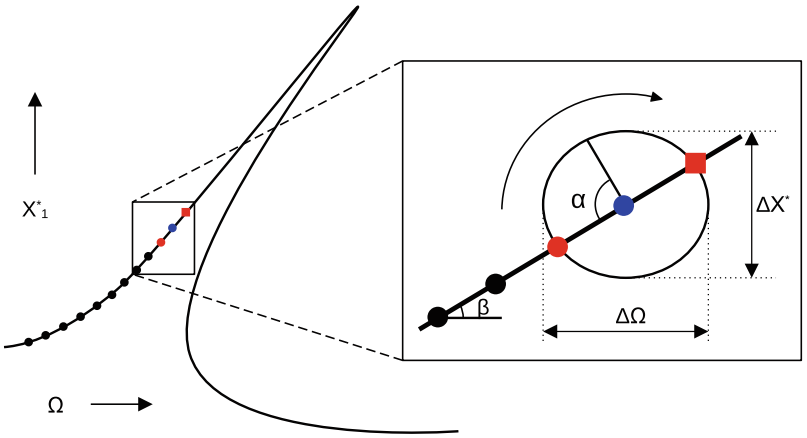

Fig. 16.1 The proposed arclength continuation procedure. Previously identified responses: circles; next response to be identified: square, center of the arc (blue) and responses on the arc (red)

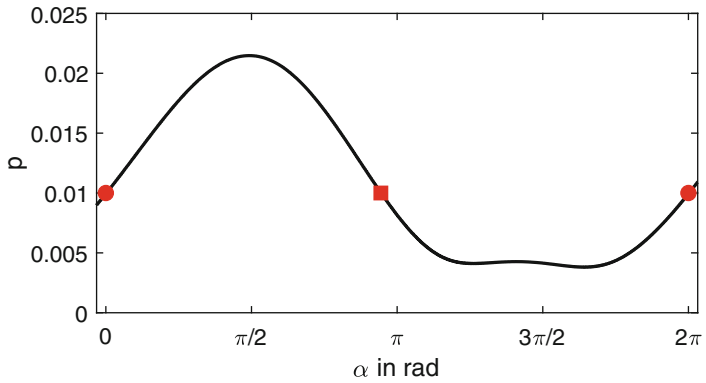

Fig. 16.2 Force amplitude p during the CBC experiment (Table 16.2) along the arc centered at $X^* = 0.02$, $\Omega = 40.8$ with the continuation parameters in Table 16.3 and excitation amplitude target $p^* = 0.01$. Previously identified response, circles, and next response: square

Algorithm 6.1 Arclength continuation for CBC experiment

1: $(\Omega_\mathrm{p}, X^*_\mathrm{p})$ and $(\Omega_\mathrm{c}, X^*_\mathrm{c})$ defined by user
2: **loop**
3: $\quad\alpha \leftarrow \alpha_0$
4: $\quad\beta \leftarrow \mathrm{atan2}(X^*_\mathrm{c} - X^*_\mathrm{p}, \Omega_\mathrm{c} - \Omega_\mathrm{p})$
5: $\quad(\Omega, X^*_1) = (\Omega_\mathrm{c} + \Delta\Omega\cos(\beta + \pi - \alpha), X^*_\mathrm{c} + \Delta X^* \sin(\beta + \pi - \alpha))$
6: $\quad$Wait a duration t_wait for steady state
7: $\quad$**while** $|p - p^*| > \mathrm{tol}_p$ **do**
8: $\quad\quad$Increase α with chosen method (see Section 6.4.1)
9: $\quad$**end while**
10: $\quad(\Omega_\mathrm{p}, X^*_\mathrm{p}) \leftarrow (\Omega_\mathrm{c}, X^*_\mathrm{c})$
11: $\quad(\Omega_\mathrm{c}, X^*_\mathrm{c}) \leftarrow (\Omega, X^*_1)$
12: **end loop**

Fig. 16.3 Arclength continuation for CBC experiment

responses on the FRC. Finally, a cooldown time t_wait is needed for damping the transients resulting from sudden changes in input parameters.

16.2 Numerical Example

In this section, the arclength continuation method is demonstrated numerically using the Duffing oscillator in Table 16.1 with the parameters in Tables 16.2 and 16.3. N is the number of harmonics considered in the harmonic balance method used to calculate the reference FRCs, μ is the internal parameter of the adaptive filter, and k_d is the differential gain.

During a CBC experiment, the reference derivative $\dot{x}^*$ appears in the differential controller. It is usually equivalent to define the reference signal x^*, then differentiate it to obtain $\dot{x}^*$, or to define $\dot{x}^*$ directly. However, for arclength continuation, because the reference amplitude follows an ellipse in the input parameter space, the path is different if the fundamental amplitude of x^*, X_1^*, or the fundamental amplitude of $\dot{x}^*$, ΩX_1^*, is considered, especially when the frequency Ω changes significantly during the experiment. In this section, we implement the CBC experiment by defining $\dot{x}^*$ directly. The reference amplitudes are therefore displayed as ΩX_1^*.

Three strategies for moving along the ellipse and reaching the force target p^* are introduced. The first method is to sweep at a constant rate $\dot{\alpha} = \eta_\alpha$ until the excitation amplitude tolerance tol_p is reached. The path followed in the input parameter space is represented in Fig. 16.4. Figure 16.5 shows that the system is not in steady state when p^* is reached. Transients both in the system response and in the adaptive filters thus decrease the accuracy of the identified FRC, which is slightly shifted compared to the harmonic balance reference in Fig. 16.4.

The impact of changes in the sweep rate η_α or the semi-major axes $(\Delta\Omega, \Delta X^*)$ is plotted in Fig. 16.6. As expected, decreasing the sweep rate reduces the transients, which, in turn, increases the accuracy. However, this comes at the cost of a longer testing time (Table 16.4). When increasing the sweep rate, the more important transients may prevent the estimated force amplitude from reaching p^*. In this case, the continuation procedure is looping indefinitely and fails to go across the fold bifurcation. Reducing the size of the arc allows the experimenter to identify more points on the FRC, as confirmed in Fig. 16.6. Additionally, smaller arcs reduce the magnitude of the transients. Eventually, the accuracy is improved, whereas testing time is increased (Table 16.4).

Table 16.1 Parameters of the Duffing oscillator

m	c	k	$f_{\text{nl}}(x)$
0.05	0.2	57	$2 \times 10^8 x^3$

Table 16.2 Simulation parameters of the CBC experiment

N	f_s in kHz	μ	k_d
5	5	0.001	2

Table 16.3 CBC continuation parameters

tol_p	α_0	η_α	k_i	$\Delta\Omega$	ΔX^*	t_{wait}
$p^*/100$	$\pi/4$	$\pi/15$	75	0.5	0.002	2

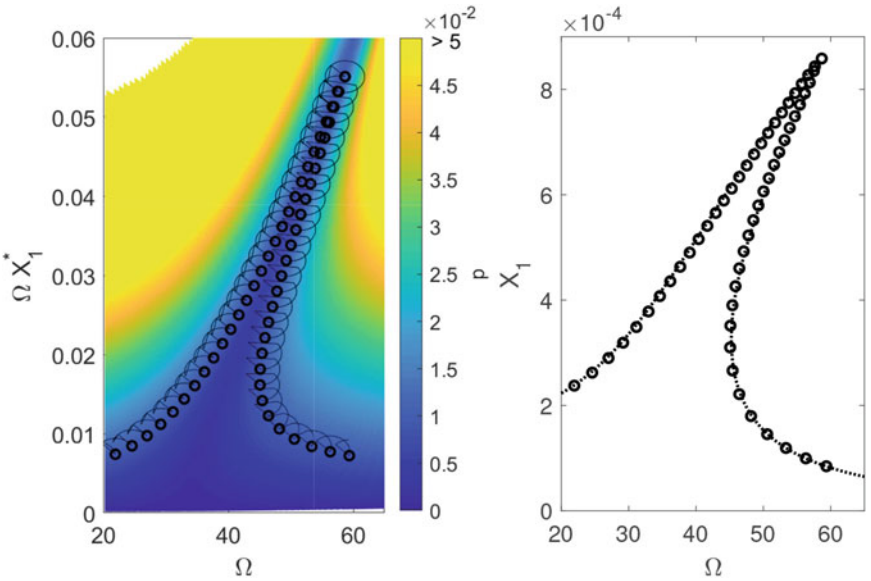

Fig. 16.4 Arclength continuation of a cubic oscillator with arclength sweep. The accepted points are marked by circles. (**a**) Input parameter space and (**b**) FRC at $p = 0.01$ (harmonic balance in dotted curve)

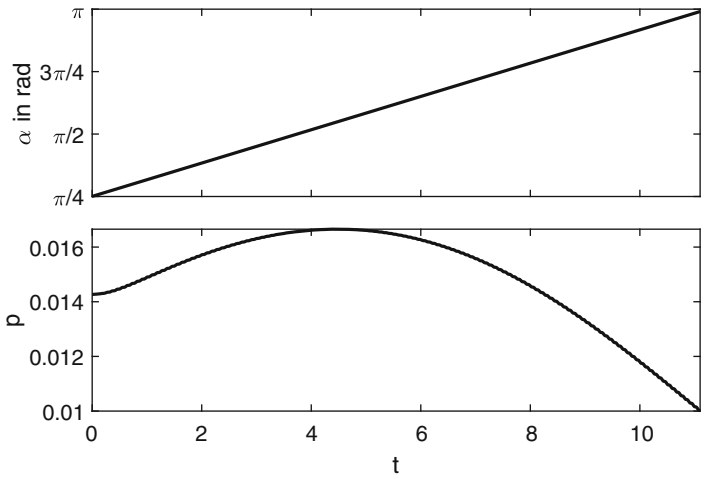

Fig. 16.5 Time series of the arc angle α (arc sweep) and force amplitude p along an arc centered at $\Omega X^* = 0.02$, $\Omega = 6.5$

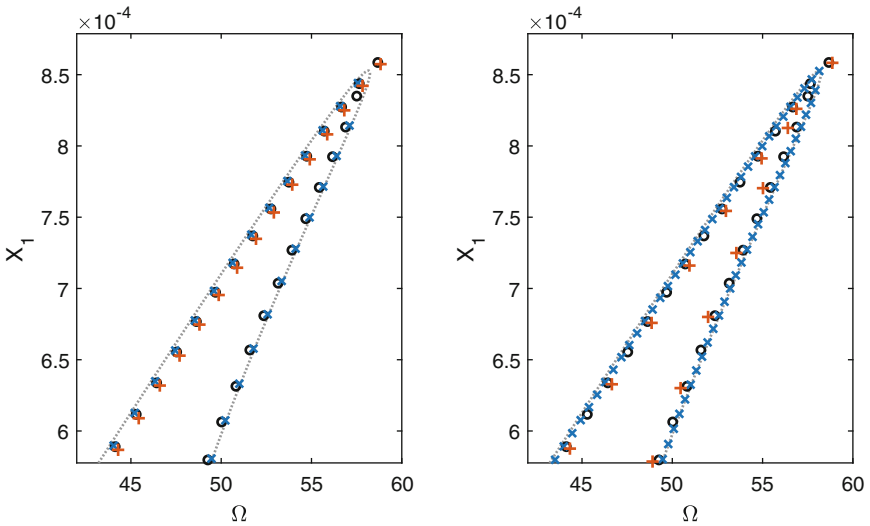

Fig. 16.6 Parametric study varying (**a**) the sweep rate $\eta_\alpha = \pi/30$ (blue $\times$), $\pi/15$ (black $\circ$), and $2\pi/15$ (orange $+$) or (**b**) the semi-major axes $(\Delta\Omega, \Delta X^*) = (0.25, 0.001)$ (blue $\times$), $(0.5, 0.002)$ (black $\circ$), and $(1, 0.004)$ (orange $+$). The dotted curve represents harmonic balance results

Table 16.4 Time (s) to reach the amplitude peak of the cubic oscillator

	Arc sweep	Arc control
Reference	365	259
Slower	650	500
Faster	*210	*153
Smaller arc	908	1486
Larger arc	180	*73

The reference parameters are $(\Delta\Omega, \Delta X^*) = (0.5, 0.002)$, $\eta_\alpha = \pi/30$, and $k_\mathrm{i} = 75$. The slower and faster runs correspond to $\eta_\alpha/2 - k_\mathrm{i}/2$ and $2\eta_\alpha - 2k_\mathrm{i}$, respectively. Smaller and larger arcs correspond to half and twice the reference semi-major axes. An asterisk means CBC failed to go across the fold bifurcation

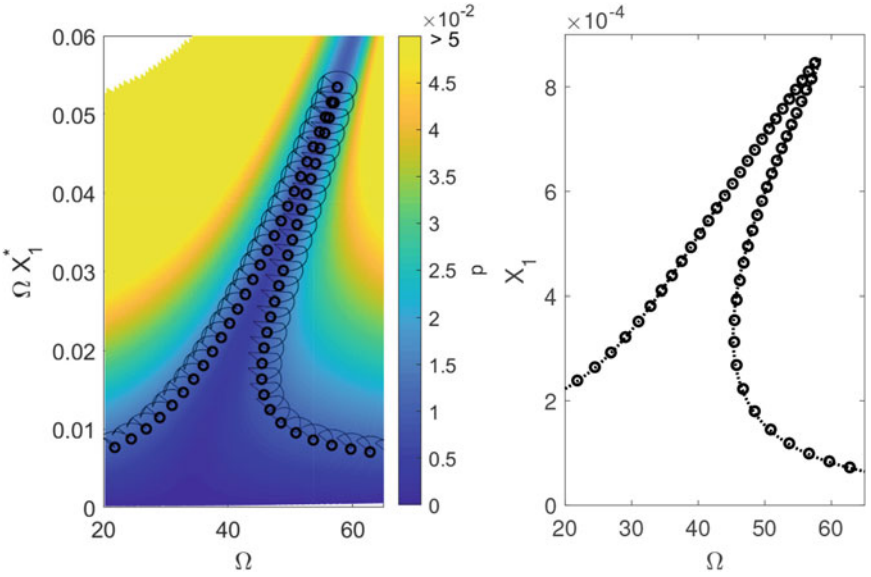

Fig. 16.7 Arclength continuation of a cubic oscillator with arclength integral control. The accepted points are marked by circles. (**a**) Input parameter space and (**b**) FRC at $p = 0.01$ (harmonic balance in dotted curve)

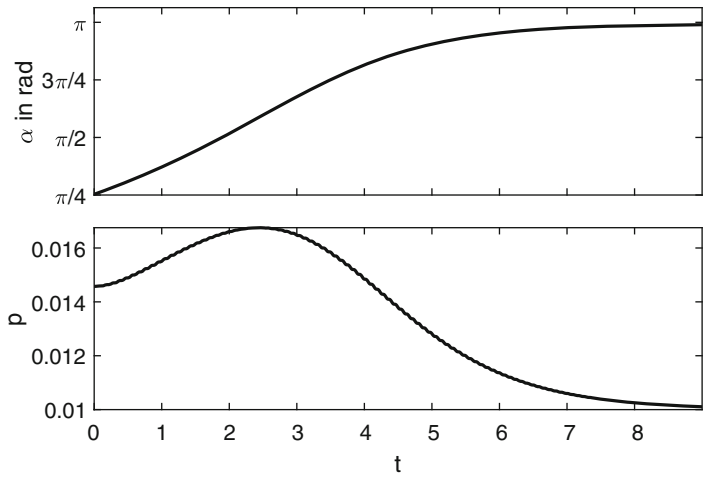

Fig. 16.8 Time series of the arc angle α (integral control) and force amplitude p along an arc centered at $\Omega X^* = 0.02$, $\Omega = 6.5$

The second arclength strategy is to use an integral controller acting on the arc angle α with the excitation amplitude error as the input, i.e., $\dot{\alpha} = k_\mathrm{i}(p - p^*)$. The path followed in Fig. 16.7 is similar to that in Fig. 16.4, because the arcs have the same dimensions. The effects of the transients are, however, diminished as the arc angle gently converges toward its target, as displayed in Fig. 16.8. The identified FRC in Fig. 16.7 is thus more accurate.

The influence of the integral gain k_i is similar to that of the sweep rate η_α. For instance, decreasing k_i leads to a longer (Table 16.4) but more accurate experiment (Fig. 16.9). Figure 16.9 evidences one drawback of the integral controller, namely, the arclength evolution depends on the force amplitude error. Input parameters further away from the desired values mean a greater force amplitude error and therefore faster evolution of the arclength. Decreasing the semi-major axes causes the experiment to last much longer (Table 16.4), but leads to excellent accuracy (Fig. 16.9). We note that a PID controller could also be considered. In theory, the proportional and differential gains could decrease the settling time and the overshoot. However, we think that a single control law cannot be optimal for the identification of the complete FRC, because the settling time would increase far away from resonance, whereas the overshoot would increase close to resonance.

The third arclength strategy combines both arc sweep and integral control. The arc is first swept at a constant rate η_α. This has the advantage that the arc's semi-major axes are decoupled from the rate at which the arclength evolves. When p^* is reached, the sweep is interrupted, and an integral controller is activated, allowing a gentle convergence toward p^*. Figure 16.10 plots the results for this strategy.

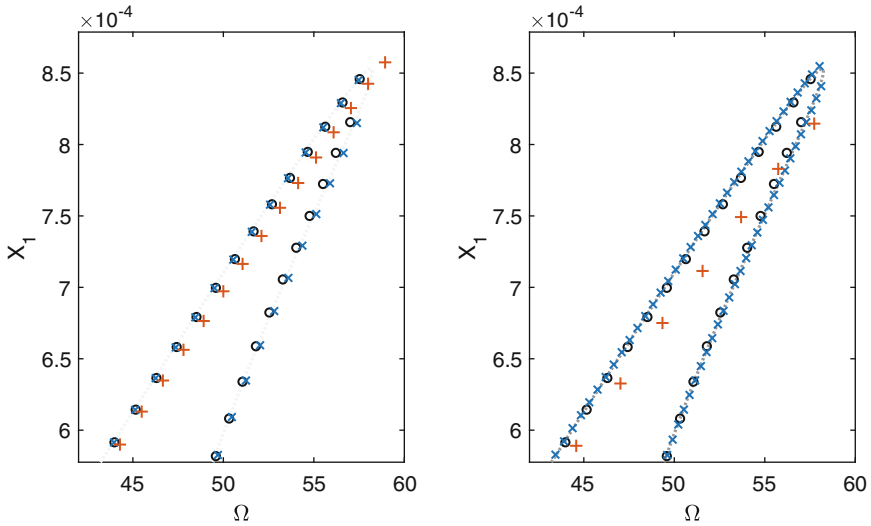

Fig. 16.9 Parametric study varying (**a**) the integral gain $k_\mathrm{i} = 40$ (blue ×), 75 (black ∘), and 150 (orange +) or (**b**) the semi-major axes $(\Delta\Omega, \Delta X^*) = (0.25, 0.001)$ (blue ×), (0.5, 0.002) (black ∘), and (1, 0.004) (orange +). The dotted curve represents harmonic balance results

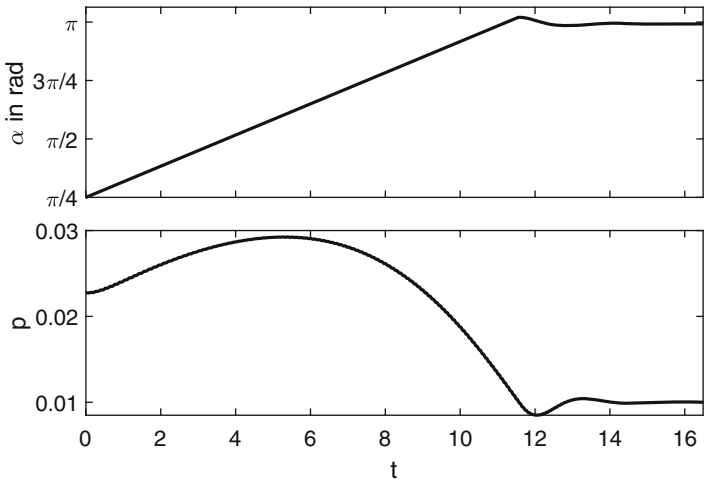

Fig. 16.10 Time series of the arc angle α (arc sweep+integral control) and force amplitude p along an arc centered at $\Omega X^* = 0.02$, $\Omega = 6.5$

16.3 Conclusion

This paper has introduced a novel experimental continuation method for FRCs requiring neither the estimation of derivatives nor the approximation of the response surface. One underlying assumption is that the input parameter space has no more than two dimensions. At the root of the method is an arclength continuation process during which the experiment follows an elliptic arc (centered on a previously identified response on the FRC) until it intersects the FRC again. Thanks to adaptive filtering, the continuation does not need to be halted, rendering the complete process fully online. The arclength continuation procedure was successfully validated numerically using a Duffing oscillator.

Acknowledgments The authors are grateful to « FONDS POUR LA FORMATION A LA RECHERCHE DANS L'INDUSTRIE ET DANS L'AGRICULTURE » (FRIA) for the financial support of G. Abeloos' thesis.

References

1. Riks, E.: An incremental approach to the solution of snapping and buckling problems. Int. J. Solids Struct. **15**, 529–551 (1979)
2. Crisfield, M.A.: A fast incremental/iterative solution procedure that handles "snap-through" (1981)
3. Abeloos, G., Renson, L., Kerschen, G.: Stepped and swept control-based continuation using adaptive filtering. Nonlinear Dyn. **104**, 3793–3808 (2021)

Chapter 17
Experimental Modal Analysis of Structures with High Nonlinear Damping by Using Response-Controlled Stepped-Sine Testing

Taylan Karaağaçlı and H. Nevzat Özgüven

Abstract In the last decade, various promising nonlinear modal identification techniques have been developed based on the nonlinear normal mode (NNM) concept. Most of these techniques rely on the phase resonance testing approach where the identification of nonlinear modal damping is still an unresolved issue. The response-controlled stepped-sine testing (RCT) framework provides a convenient way of accurately quantifying nonlinear modal damping by applying standard linear modal analysis techniques to frequency response functions (FRFs) measured at constant displacement amplitude levels with standard modal test equipment. Various studies by the authors have shown that these constant-response FRFs come out in quasi-linear form even in the case of a high degree of nonlinearities. The RCT approach has been validated so far on several systems including a real missile structure with moderate damping nonlinearity mostly due to bolted connections and a micro-electromechanical device with a stack-type piezo-actuator. This study makes a step further by validating the method on a real control fin actuation mechanism that exhibits very high and nonlinear modal damping; the maximum value of viscous modal damping ratio goes up to 15% and the percentage change of the damping with respect to vibration amplitude is about 70%.

Keywords High nonlinear damping · Nonlinear experimental modal analysis · Response-controlled stepped-sine testing · Control fin actuation mechanism · Unstable branch

17.1 Introduction

The ever-growing industrial competition always favors higher speed, lower energy consumption, and longer service life in aircraft and turbomachinery. In the achievement of these high-performance goals, lightweight design becomes an important objective. However, the lightweight design naturally results in more flexible structures that may exhibit large amplitude oscillations under dynamic loads, which may eventually lead to dynamic instabilities such as the aeroelastic flutter [1] or the limit cycle oscillation (LCO) [2].

Structural damping plays a key role in the suppression of aeroelastic instabilities [3, 4]. Therefore, accurate modeling of the damping mechanism is vital for the determination of realistic instability envelopes and for pushing the limits in the design process. However, under large amplitude oscillations as in the case of aeroelastic instabilities, the structural damping exhibits highly nonlinear behavior, which makes its identification a challenging task.

Almost all structural damping mechanisms in aircraft and turbomachinery are mainly due to friction. Friction and backlash in the actuation mechanisms of aircraft control surfaces, and special dissipative elements such as under-platform dampers in turbomachinery, are among important sources of structural damping. Another important source of damping common to both aircraft and turbomachinery is friction in mechanical joints. Identification of all these nonlinear damping mechanisms is already a difficult task as mentioned above. Another factor that complicates the identification process even more is the variability of nonlinear dynamics in mechanical joints in repeated testing [5].

The recent work of Al-Habibi et al. [6] gives a comprehensive review of the state-of-the-art techniques that can be used in the identification of nonlinear structural damping. Although it is possible to categorize these techniques in various ways, as is

T. Karaağaçlı (✉)
The Scientific and Technological Research Council of Turkey, Defense Industries Research and Development Institute, TÜBİTAK-SAGE, Mamak, Ankara, Turkey
e-mail: taylan.karaagacli@tubitak.gov.tr

H. Nevzat Özgüven
Department of Mechanical Engineering, Middle East Technical University, Ankara, Turkey

M. R. W. Brake et al. (eds.), *Nonlinear Structures & Systems, Volume 1*, Conference Proceedings of the Society for Experimental Mechanics Series, https://doi.org/10.1007/978-3-031-36999-5_17

done in the review paper, the methods can simply be divided into two main groups: nonmodal and modal techniques. Several important examples of nonmodal methods are the restoring force surface (RFS) [7] method, the nonlinear auto-regressive moving average with exogenous input (NARMAX) method [8], the wavelet transform [9], and the describing surface method (DSM) [10]. Although these techniques give satisfactory results in the case of local nonlinearities, their extension to general nonlinear multi-degree-of-freedom (MDOF) systems is not practical in general. The main advantage of modal methods over nonmodal approaches is that they are capable of quantifying the resultant effect of multiple nonlinearities spread over a nonlinear MDOF structure. The last decade witnessed the development of various promising nonlinear modal identification techniques. In 2011, Peeters et al. [11] extended the phase resonance testing approach to nonlinear systems and successfully isolated a single NNM during the experiment. In 2015, Londono et al. [12] adapted the nonlinear resonant decay method (NLRDM) [13] to extract the backbone curves of nonlinear systems. A year later, Renson et al. [14] implemented the control-based-continuation (CBC) [15] to trace out the NNM backbone curves. In 2017, Peter and Leine [16] proposed another experimental continuation technique based on the phase-locked-loop (PLL) control strategy commonly used in electrical engineering. A very recent NNM backbone curve identification technique is the one proposed by Kwarta and Allen [17], where near-resonant steady-state harmonic responses measured by open-loop sine testing are processed by using the single nonlinear mode formula [18]. Another very recent nonlinear modal identification technique is the velocity feedback approach proposed by Scheel [19].

All the modal approaches mentioned above successfully identify NNM backbone curves. However, the identification of nonlinear modal damping is still an unresolved issue for many of them [11, 14, 16]. Although in recent papers [17, 19, 20], a special emphasis is placed on nonlinear modal damping, its identification is still a difficult problem especially when the degree of nonlinearity is very high. However, in the RCT method [21], the nonlinear modal damping is very conveniently identified by applying standard linear modal analysis techniques to constant-response FRFs that are measured in the quasi-linear form. The quasi-linearity of these FRFs is achieved by keeping the displacement amplitude of the driving point constant throughout the frequency sweep. The RCT approach has been validated so far on a benchmark beam with local cubic stiffness nonlinearity and a real missile structure with moderate damping nonlinearity mostly due to bolted connections [21], a double-clamped beam that exhibits strong geometrical nonlinearity [22, 23], a micro-electromechanical device with a stack-type piezo-actuator [24], and a benchmark beam with a bolted lap joint [25]. The main contribution of this chapter is to show that the RCT method is capable of identifying a very high and nonlinear modal damping; the maximum value of viscous modal damping ratio goes up to 15% and the percentage change of the damping with respect to vibration amplitude is about 70%. The mechanism exhibits not only a high degree of damping nonlinearity but also a high degree of stiffness nonlinear that results in a 50% shift of the natural frequency, which is also successfully identified by the RCT technique.

17.2 Nonlinear Experimental Modal Analysis with the RCT-HFS Framework

Nonlinear experimental modal analysis by using response-controlled stepped-sine testing (RCT) [21] consists of the following steps:

1. Measure constant-response FRFs at several different displacement amplitude levels by keeping the displacement amplitude of the driving point constant throughout the stepped-sine testing at each level.
2. Extract modal parameters (modal constant, natural frequency, and modal damping ratio) at each displacement amplitude level by applying standard linear modal analysis techniques to constant-response FRFs that come out in the quasi-linear form. Construct the nonlinear modal model by expressing the identified modal parameters as functions of the modal amplitude.
3. Synthesize required constant-force FRFs by using the identified nonlinear modal parameters in a Newton-Raphson solution scheme with the arc-length continuation algorithm.

The quasi-linearity of constant-response FRFs mentioned in step 2 is theoretically based on the following receptance formula derived from the Nonlinearity Matrix concept [26] and the single nonlinear mode theory [18] as explained in [21]:

$$\alpha_{jk}(\omega, q_r) = \frac{\overline{A}_{jkr}(q_r)}{\overline{\omega}_r^2(q_r) - \omega^2 + i2\overline{\xi}_r(q_r)\,\omega\overline{\omega}_r(q_r)} \tag{17.1}$$

where α_{jk} is the near-resonant receptance corresponding to the displacement at point j for a given excitation at point k, and ω denotes the excitation frequency. $\overline{A}_{jkr}(q_r)$, $\overline{\omega}_r(q_r)$, and $\overline{\xi}_r(q_r)$ are the modal constant, natural frequency, and viscous modal damping ratio corresponding to the r th nonlinear mode, respectively.

All the modal parameters shown in Eq. (17.1) are functions of a single parameter: the modal amplitude q_r. Therefore, if the modal amplitude is kept constant throughout the stepped-sine testing, the measured FRFs come out in the quasi-linear form. In [21], it is shown that in the case of single-point excitation, the constant modal amplitude condition can be achieved by keeping the displacement amplitude of the driving (excitation) point constant in closed-loop control. It is important to note that the constant displacement amplitude condition does not necessarily require a displacement transducer as the control sensor. In most of the applications of the RCT method conducted so far, the accelerometer has been used as the control sensor due to its popularity and availability. The constant displacement amplitude condition can be achieved indirectly by feeding the closed-loop controller with an appropriate acceleration profile.

An important merit of the RCT method is that it is based on frequency sweep at constant amplitude and therefore it can be implemented by using standard modal test equipment available in the market (e.g., LMS SCADAS & LMS Test Lab). This is an important advantage of the RCT approach over state-of-the-art techniques such as CBC [15] and PLL [16]. CBC technique, which is based on amplitude sweep at constant frequency, and the PLL technique, which is based on phase control, cannot be implemented with standard equipment.

The validation of the nonlinear modal parameters identified by the RCT method can be achieved by using the harmonic force surface (HFS) concept proposed by the authors in [21]. The prominent feature of the HFS is the accurate identification of the turning points and unstable branches of constant-force frequency response curves, directly from the experiment. This makes the HFS a valuable tool to accurately determine the backbone curves of strongly nonlinear structures [27]. The HFS technique consists of the following steps:

1. Measure harmonic excitation force spectra at several different constant displacement amplitude levels by keeping the displacement amplitude of the driving point constant throughout the stepped-sine testing at each level.
2. Construct the HFS by merging the measured harmonic excitation force spectra and using linear interpolation.
3. Extract constant-force frequency response curves by cutting the HFS with constant-force planes.

The third step of the HFS technique provides a model-less identification of stable and unstable branches of constant-force frequency response curves. Theoretically, these curves should be the same as the curves synthesized in the third step of the RCT method and therefore can be used to validate the nonlinear modal model identified by RCT. It is important to note that the harmonic excitation force spectra used to construct the HFS are the ones measured during RCT and used to construct the constant-response FRFs. Therefore, since no additional test is required, the construction of the HFS can be regarded as an integral part of the RCT method together with the identification of the nonlinear modal model. In this context, the RCT-HFS can be regarded as a self-validating framework.

17.3 Experiment

Control fins play an important role in the aeroelastic behavior of guided missiles [28, 29]. For realistic aeroelastic analyses, the accurate modeling of the structural dynamics of control fins is of vital importance. Unfortunately, backlash and friction between various moving parts in the actuation mechanism of a control fin may result in a very complex nonlinear behavior. The identification of such a high and complex nonlinearity is a very challenging problem for the current state of the art.

Figure 17.1 shows the sketch of the experimental setup used to identify the nonlinear behavior of a real control fin actuation mechanism. The casing of the actuation mechanism is rigidly fixed to the ground. The control fin is instrumented with 10 miniature accelerometers (Dytran 3225M23). The structure is excited at point 1 in the z-direction with a stinger attached to an electrodynamic shaker (B&K). The excitation force is measured with a force transducer (Dytran 1022V) attached between the stinger and the control fin.

In this study, the vibration mode of interest is the first mode of the control fin actuation mechanism assembly which is a torsional mode. Preliminary broadband random test results indicate that the fin surface acts as a rigid body in that mode. Therefore, it can be concluded that this mode simply results from the nonlinear dynamics of the actuation mechanism. Accordingly, the system is treated as an SDOF rotational system and the nonlinear system identification is accomplished simply by using the driving point FRFs of the system.

Similar to the previous applications of the RCT method, all the data acquisition and closed-loop control tasks are accomplished by using the LMS SCADAS Mobile data acquisition system and the LMS Test Lab. software package. The upper and lower frequency limits of the stepped-sine tests covering the mode of interest are determined based on preliminary broadband random tests. The frequency step used in stepped-sine testing is 0.125 Hz.

In a recent study by the authors [27], the NNM backbone curve corresponding to the first mode of the control fin actuation mechanism has been successfully identified by using the HFS technique as shown in Fig. 17.2. The evolution of the backbone

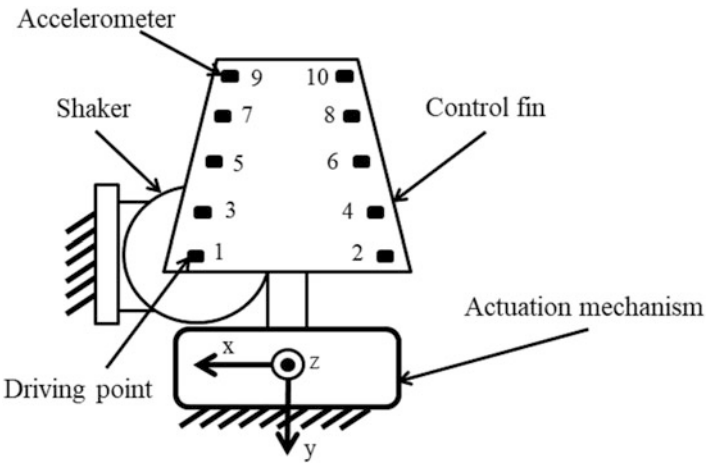

Fig. 17.1 Sketch of the experimental setup for the nonlinear system identification of the control fin and its actuation mechanism

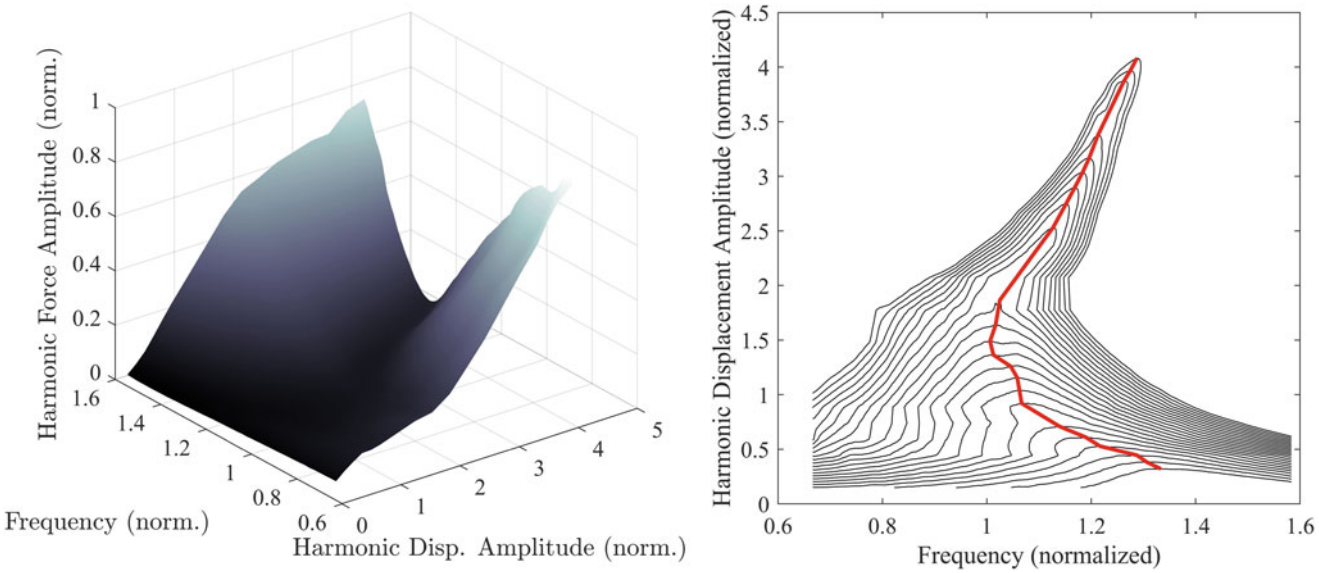

Fig. 17.2 Identification of the NNM backbone curve of the control fin actuation mechanism by using the HFS technique [27]: (**a**) harmonic force surface (HFS) (**b**) driving point constant-force frequency response curves (black) extracted from the HFS and the NNM backbone curve (red)

curve demonstrates the complexity of the nonlinear behavior: the resonance frequency first decreases until it reaches a minimum value and then it increases monotonically. The initial softening effect could be related to the stick-to-slip transition and succeeding hardening behavior is probably related to backlash.

Unfortunately, the identification of the NNM backbone curve only reveals the evolution of the stiffness nonlinearity of the control fin actuation mechanism, but it does not say anything about the damping nonlinearity. The main contribution of this chapter is the accurate identification of nonlinear modal damping.

In order to identify the nonlinear modal model of the control fin actuation mechanism, first of all, the constant-response receptances of the system are measured at 15 different displacement amplitude levels (labeled D1 to D15) by using the RCT strategy. For the sake of clarity, Fig. 17.3 shows the receptance curves corresponding to only 10 different constant displacement amplitude levels.

In the second step, the constant-response receptance curves measured at each displacement amplitude level are subjected to linear modal analysis with LMS PolyMAX. The outcome of each modal analysis is a specific set of modal parameters (modal constant, natural frequency, and modal damping ratio). The good overlap between the linear receptance curves synthesized from each set of modal parameters and the corresponding constant-response receptance curves validates the quasi-linearity of receptances shown in Fig. 17.3. The variations of the modal parameters (identified at 15 different displacement amplitude levels) with respect to the modal amplitude are shown in Figs. 17.4 and 17.5.

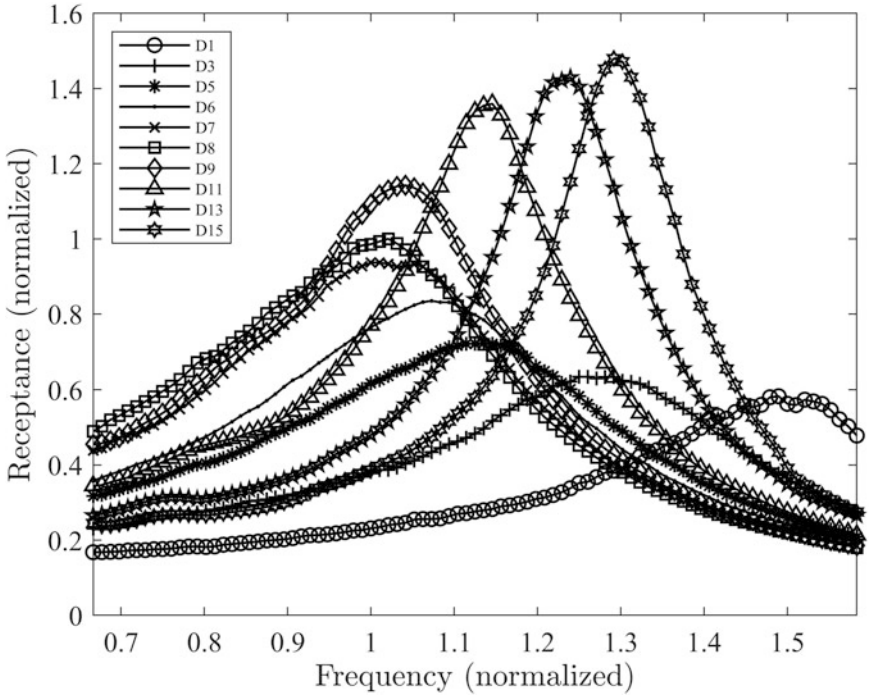

Fig. 17.3 Constant-response receptances of the control fin actuation mechanism measured at the driving point by RCT

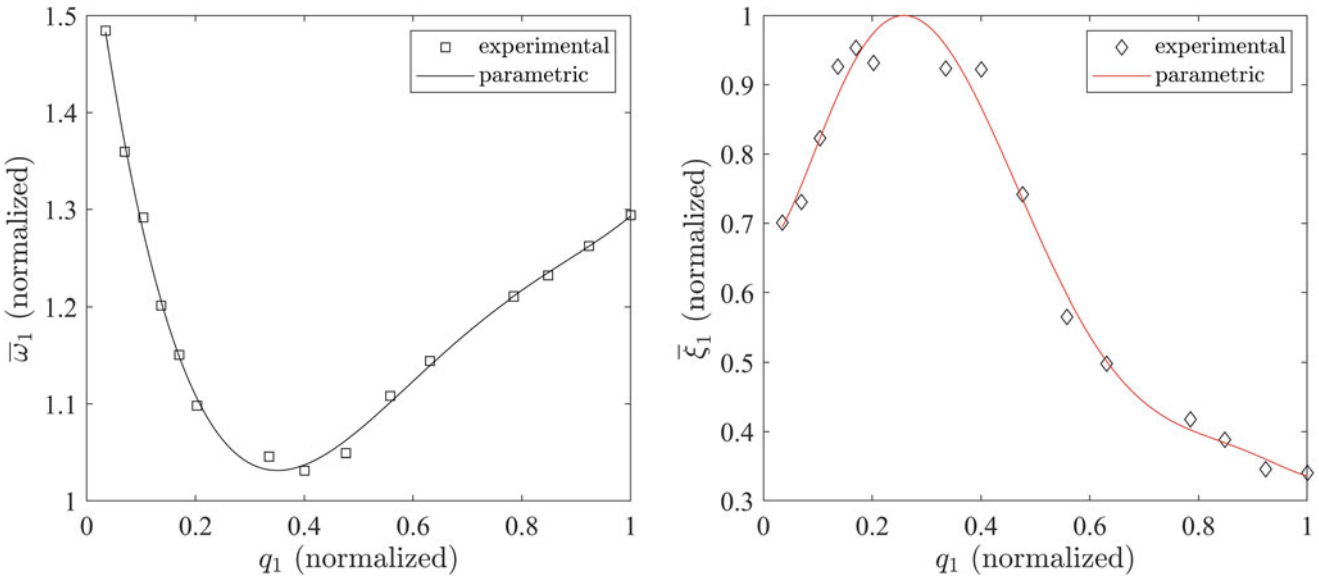

Fig. 17.4 Variation of the modal parameters with modal amplitude: (**a**) natural frequency (**b**) modal damping ratio

In Fig. 17.4, about a 50% change in the natural frequency and a 70% change in the modal damping ratio indicate a very high degree of stiffness and damping nonlinearities that cannot be reached in many studies. In Fig. 17.4b, the modal damping ratio is given in the normalized form; the actual value of the viscous damping ratio goes up to 15%. This means that not only the damping nonlinearity but also the value of damping itself is very high. All these results clearly demonstrate the power of the RCT method.

In order to achieve the validation, first of all, constant-force receptances are synthesized from the identified modal parameters in a Newton-Raphson solution scheme with the arc-length continuation algorithm at four different force levels: F1, F2, F3, and F4 in ascending order. Then, these synthesized receptances are compared with the ones extracted from the HFS as shown in Fig. 17.6. As can be seen from the figure, the match between the synthesized and extracted receptances is almost perfect, which shows that the identified nonlinear modal parameters are very accurate.

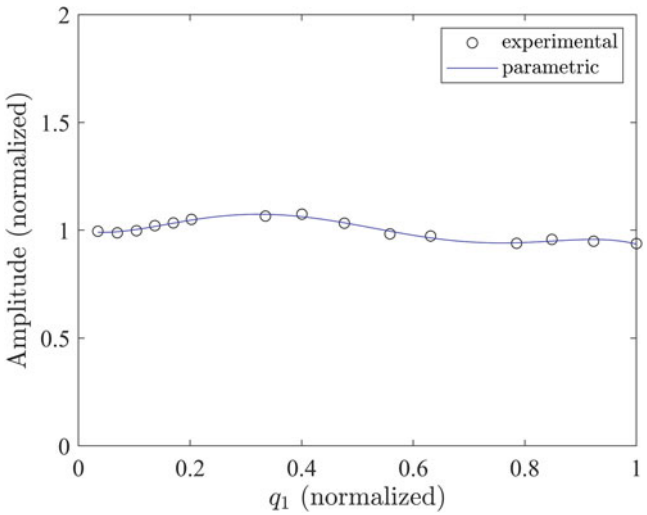

Fig. 17.5 Variation of the modal constant with modal amplitude

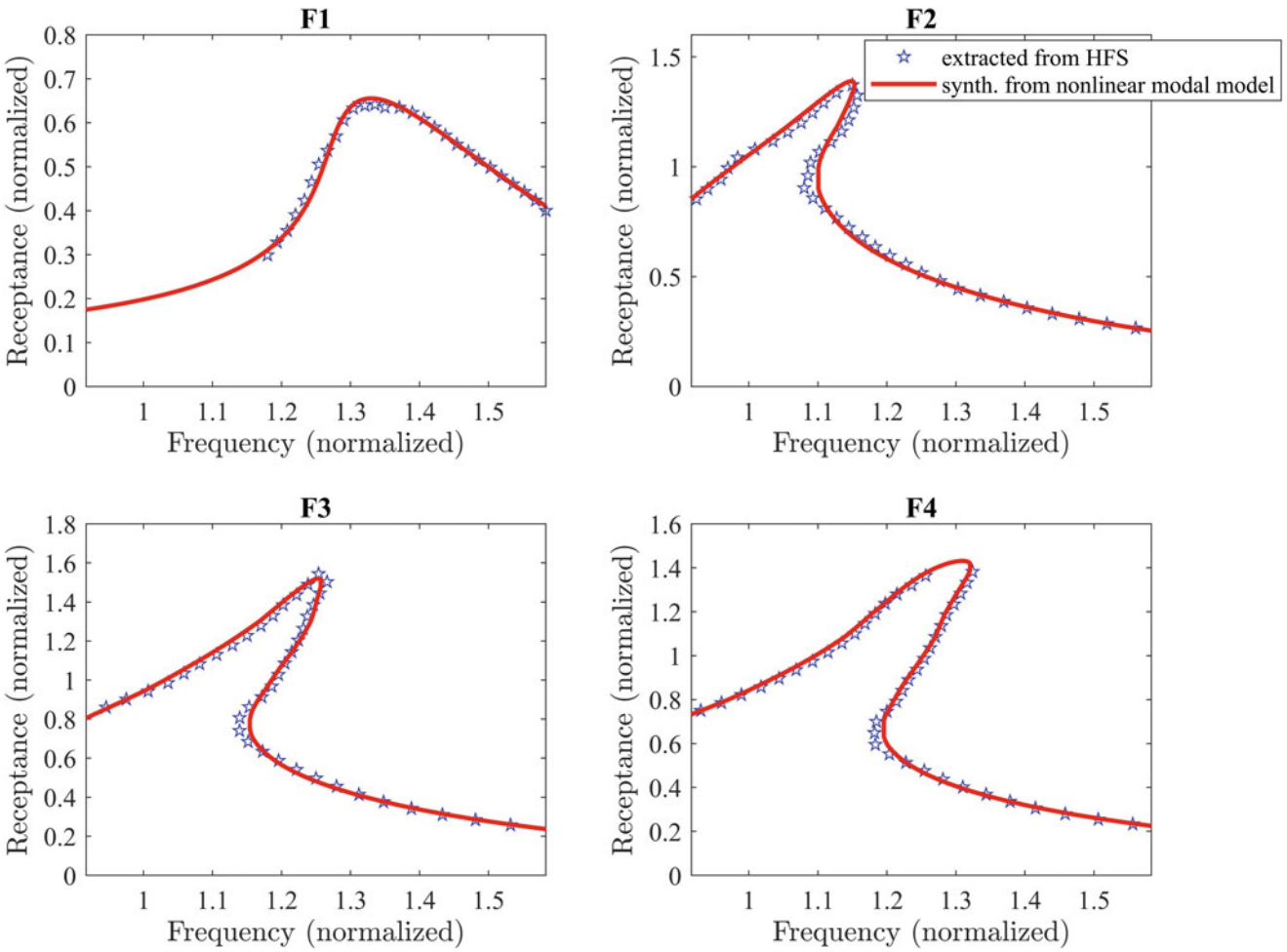

Fig. 17.6 Validation of the identified nonlinear modal model by comparing the driving point receptances synthesized from the model with the ones extracted from the HFS

17.4 Discussions and Conclusions

In the last decade, very promising experimental continuation techniques have been developed based on the nonlinear normal mode (NNM) concept. Most of these techniques proved to be successful in the accurate identification of NNM backbone curves. However, the rigorous mathematical treatment and the accurate identification of nonlinear modal damping is still a very challenging task for most of the state-of-the-art techniques, especially in the case of very high and nonlinear damping. However, the response-controlled stepped-sine testing (RCT) method provides a very convenient and accurate way of identifying nonlinear modal damping by applying standard linear modal analysis techniques to constant-response FRFs that are measured in the quasi-linear form. The quasi-linearity of these FRFs is achieved by keeping the displacement amplitude of the driving point constant throughout the stepped-sine testing. The RCT method has been successfully applied so far on various systems including a real missile structure with moderate damping nonlinearity mostly due to bolted connections and a micro-electromechanical device with a stack-type piezo-actuator. This study makes a step further by validating the method on a real control fin actuation mechanism that exhibits a very high and nonlinear modal damping; the maximum value of viscous damping ratio goes up to 15% and the percentage change of the damping with respect to vibration amplitude is about 70%. The mechanism exhibits not only a high degree of damping nonlinearity but also a high degree of stiffness nonlinear that results in a 50% shift of the natural frequency, which is also successfully identified by the RCT technique. The perfect match between the constant-force FRFs synthesized from the identified modal parameters and the ones directly extracted from the experiment by using the harmonic force surface (HFS) technique shows that the nonlinear modal parameters are very accurately identified.

Acknowledgments The provision of TÜBİTAK-SAGE for modal testing and analysis capabilities is gratefully acknowledged.

References

1. Waite, J.J., Kielb, R.E.: Shock structure, mode shape, and geometric considerations for low-pressure turbine flutter suppression. In: Proceedings of ASME Turbo Expo, Seoul, South Korea (2016)
2. Bunton, R.W., Denegri Jr., C.M.: Limit cycle oscillation characteristics of fighter aircraft. J. Aircr. **37**(5), 916–918 (2000)
3. Denegri Jr., C.M., Sharma, V.K., Northington, J.S.: F-16 limit cycle oscillation analysis using nonlinear damping. J. Aircr. **53**(1), 243–250 (2016)
4. Chen, P.C., Zhang, Z., Zhou, Z., Wang, X.Q., Mignolet, M.P.: Limit cycle oscillation prediction for aircraft with external stores. In: International Forum on Aeroelasticity and Structural Dynamics, IFASD-2019, Savannah, GA, USA (2019)
5. Brake, M.R.W., Schwingshackl, C.W., Reu, B.P.: Observations of variability and repeatability in jointed structures. Mech. Syst. Signal Process. **129**, 282–307 (2019)
6. Al-Hababi, T., Cao, M., Saleh, B., Alkayem, N.F., Xu, H.: A critical review of nonlinear damping identification in structural dynamics: methods, applications, and challenges. Sensors. **20**(24), 7303 (2020)
7. Masri, S.F., Caughey, T.K.: A nonparametric identification technique for nonlinear dynamic problems. J. Appl. Mech. **46**, 433–447 (1979)
8. Worden, K., Barthorpe, J.: Identification of hysteretic systems using NARX models, part I: evolutionary identification. In: Proceedings of the 30th International Modal Analysis Conference (IMAC), Jacksonville, FL, USA (2012)
9. Garibaldi, L., Ruzzene, M., Fasana, A., Piombo, B.: Identification of non-linear damping mechanisms using the wavelet transform. Mecanique Industrielle et Materiaux. **51**, 92–94 (1998)
10. Karaağaçlı, T., Özgüven, H.N.: A frequency domain nonparametric identification method for nonlinear structures: describing surface method. Mech. Syst. Signal Process. **144**, 106872 (2020)
11. Peeters, M., Kerschen, G., Golinval, J.C.: Dynamic testing of nonlinear vibrating structures using nonlinear normal modes. J. Sound Vib. **330**, 486–509 (2011)
12. Londono, J.M., Neild, S.A., Cooper, J.E.: Identification of backbone curves of nonlinear systems from resonance decay responses. J. Sound Vib. **348**, 224–238 (2015)
13. Platten, M.F., Wright, J.R., Cooper, J.E., Dimitriadis, G.: Identification of a nonlinear wing structure using an extended modal model. AIAA J. Aircraft. **46**(5), 1614–1626 (2009)
14. Renson, L., Gonzalez-Buelga, A., Barton, D.A.W., Neild, S.A.: Robust identification of backbone curves using control-based continuation. J. Sound Vib. **367**, 145–158 (2016)
15. Sieber, J., Krauskopf, B.: Control-based bifurcation analysis for experiments. Nonlinear Dyn. **51**, 356–377 (2008)
16. Peter, S., Leine, R.I.: Excitation power quantities in phase resonance testing of nonlinear systems with phase-locked-loop excitation. Mech. Syst. Signal Process. **96**, 139–158 (2017)
17. Kwarta, M., Allen, M.S.: Nonlinear Normal Mode backbone curve estimation with near-resonant steady state inputs. Mech. Syst. Signal Process. **162**, 108046 (2022)
18. Szemplinska-Stupnicka, W.: The modified single mode method in the investigations of the resonant vibrations of nonlinear systems. J. Sound Vib. **63**(4), 475–489 (1979)

19. Scheel, M.: Nonlinear modal testing of damped structures: velocity feedback vs. phase resonance. Mech. Syst. Signal Process. **165**, 108305 (2022)
20. Scheel, M., Weigele, T., Krack, M.: Challenging an experimental nonlinear modal analysis method with a new strongly friction-damped structure. J. Sound Vib. **485**, 115580 (2020)
21. Karaağaçlı, T., Özgüven, H.N.: Experimental modal analysis of nonlinear systems by using response-controlled stepped-sine testing. Mech. Syst. Signal Process. **146**, 107023 (2021)
22. Karaağaçlı, T., Özgüven, H.N.: Experimental quantification and validation of modal properties of geometrically nonlinear structures by using response-controlled stepped-sine testing. Exp. Mech. **62**, 199–211 (2022)
23. Karaağaçlı, T., Özgüven, H.N.: Experimental modal analysis of geometrically nonlinear structures by using response-controlled stepped-sine testing. In: Proceedings of the 39th International Modal Analysis Conference (IMAC), Orlando, FL, USA (2021)
24. Koyuncu, A., Karaağaçlı, T., Şahin, M., Özgüven, H.N.: Experimental modal analysis of nonlinear amplified piezoelectric actuators by using response-controlled stepped-sine testing. Exp. Mech. **62**, 1579–1594 (2022)
25. Gürbüz, M.F., Karaağaçlı, T., Özer, M.B., Özgüven, H.N.: Bypassing the repeatability issue in nonlinear experimental modal analysis of jointed structures by using the RCT-HFS framework. In: Proceedings of the 41st International Modal Analysis Conference (IMAC), Austin, TX, USA (2023)
26. Tanrıkulu, Ö., Kuran, B., Özgüven, H.N., Imregün, M.: Forced harmonic response analysis of nonlinear structures using describing functions. AIAA J. **31**(7), 1313–1320 (1993)
27. Karaağaçlı, T., Özgüven, H.N.: Experimental identification of backbone curves of strongly nonlinear systems by using response-controlled stepped-sine testing (RCT). Vibration. **3**(3), 266–280 (2020)
28. Shin, W.H., Lee, I.: Nonlinear aeroelastic analysis for a control fin with actuator. J. Aircraft. **44**(2), 597–605 (2007)
29. Ning, Y., Nan, W., Xin, Z., Wei, L.: Nonlinear flutter wind tunnel test and numerical analysis of folding fins with freeplay nonlinearities. Chin. J. Aeronaut. **29**(1), 144–159 (2016)

Chapter 18
The TRChallenge: Experimental Quantification of Nonlinear Modal Parameters and Confrontation with the Predictions

Arati Bhattu, Nidhal Jamia, Svenja Hermann, Florian Müller, Maren Scheel, H. Nevzat Özgüven, Christoph Schwingshackl, and Malte Krack

Abstract In recent years, the prediction of the behavior of structures with high-level nonlinearities has been a challenging area of research. In 2021, the Tribomechadynamics Research Challenge was proposed to evaluate the current state of the art in modeling in the community of jointed structures: the task was a blind prediction of the nonlinear dynamic response of a system including a frictional and a geometric nonlinearity. Participants of the challenge were given only the technical drawings, including material and surface specifications required to manufacture and assemble the system and were asked to predict the frequency and damping ratio of the lowest-frequency elastic mode as function of the amplitude. The behavior of the real system was experimentally characterized during the Tribomechadynamics Research Camp 2022. This contribution presents the experimental work performed during the research camp. As the nature of the structure requires a base excitation, two recently developed nonlinear testing techniques have been explored to extract the modal parameters: the response-controlled testing method and the phase-resonant testing method. The results obtained with the different methods are compared and the blind predictions are confronted with the experimental results in order to assess their accuracy.

Keywords Frictional and geometric nonlinearity · Backbone curve · Phased-locked-loop · Tribomechadynamics

18.1 Introduction

The benchmark structure of the Tribomechadynamics Research Challenge 2021 [1] consists of a thin plate, called panel, which is mounted between two pillars of a support structure and two blades via six M5 bolts and washers on each side. The contact between panel, blade, and support is expected to introduce contact nonlinearity and friction damping. The panel has a thickness of 1.5 mm and is arched by an angle of 2° since the contact surfaces of the pillars are misaligned. The preload is expected to introduce geometric nonlinearity in the form of bending-stretching coupling. Thin curved panels are widely used in aircraft, space, and wind turbine industries to achieve high strength-to-weight ratios. However, these slender

A. Bhattu
Rice University, Houston, TX, USA
e-mail: aab27@rice.edu

N. Jamia (✉)
Swansea University, Swansea, UK
e-mail: nidhal.jamia@swansea.ac.uk

S. Hermann
FEMTO-ST Institute, Besançon, France
e-mail: svenja.hermann@femto-st.fr

F. Müller · M. Scheel · M. Krack
University of Stuttgart, Stuttgart, Germany
e-mail: florian.mueller@ila.uni-stuttgart.de; maren.scheel@ila.uni-stuttgart.de; malte.krack@ila.uni-stuttgart.de

H. N. Özgüven
Middle East Technical University, Ankara, Turkey
e-mail: ozguven@metu.edu.tr

C. Schwingshackl
Imperial College London University, London, UK
e-mail: c.schwingshackl@imperial.ac.uk

M. R. W. Brake et al. (eds.), *Nonlinear Structures & Systems, Volume 1*, Conference Proceedings
of the Society for Experimental Mechanics Series, https://doi.org/10.1007/978-3-031-36999-5_18

Table 18.1 Research groups that participated in the Tribomechadynamics Research Challenge in 2021

Research group	Abbreviation	References
Brigham Young University/the University of Wisconsin-Madison	(BYU/UW)	[2]
University of Erlangen-Nuremberg Germany	(FAU)	
Imperial College London	(ICL)	[3]
Northwestern Polytechnical University China	(NWPU)	
Sandia National Laboratories USASU	(SNL)	
Swansea University UK	(SU)	
University of Stuttgart	(USTUTT)	

structures are subjected to geometric and frictional nonlinearities because of large deformation and mechanical fasteners. The participants of the research challenge (Table 18.1) were provided with a CAD model and technical drawings of the system, including material and surface specifications. The participants had the total freedom to choose between different approaches and analysis to model the given system. This led to a wide variation of assumptions and methods used in the different models performed. A significant discrepancy is found in the predictions of the modal properties on the center point of the panel. The linear natural frequency predictions varies from 65 Hz to 120 Hz. The variation of the natural frequency of the lowest-frequency elastic mode does not follow the same trend for the different predictions: some groups predict no evolution, other results show a significant frequency decrease (-20%, softening of the structure) followed by a frequency increase (hardening, up to $+20\%$), and a purely hardening behavior of the structure of approximately 75% was also obtained. The amplitude-dependent damping ratios show a variation of several orders of magnitude between the different predictions ranging from 0.003% up to approximately 1%.

The aim of this work is to identify the actual behavior of the manufactured structure, so that the modeling results can be put into context and potential model updating can take place in the future. The nature of the structure makes it necessary to provide the dynamic loading in the form of base excitation via a large shaker. Thus, the excitation forces cannot be directly measured, which makes it impossible to quantify the damping directly from backbone curves. Therefore, two recently developed nonlinear testing techniques are used to extract the amplitude-dependent modal properties of the system: the response-controlled testing (RCT) method and the phase-resonant testing method. A validation of the linearized modal basis is performed by comparing the results of low-amplitude tests with the results of random vibration tests. The amplitude-dependent modal parameters obtained by both test methods are compared to each other and to the blind predictions.

18.2 Experimental Setup and Test Strategies

The support structure is connected to a shaker table and the system is tested under base excitation. A differential laser Doppler vibrometer (LDV) is considered to measure the relative velocity at the center of the panel with respect to the left blade. The base velocity is measured using an additional LDV pointed to the right blade. These sensors are specifically used for controlling excitation and response signals. In addition a multi-point vibrometer (MPV) is used to acquire velocity measurements from different locations along the support and the panel. A set of 15 points positioned in a 5×3 grid on the surface of the plate is considered as shown in Fig. 18.1. The dynamic behavior of the structure is evaluated based on the MPV measurement data.

Different experimental techniques are applied to the test structure to quantify the impact of the frictional and geometric nonlinearity. Initially, a validation of the linearized modal basis is performed. Therefore, the linear responses of the structure for small vibration levels obtained by random tests and by the different testing strategies are compared. Afterwards, the nonlinear behavior around the first resonance mode at higher vibration levels is investigated. The response-controlled testing (RCT) method [4] is used to obtain quasi-linear responses of the structure for a controlled displacement of the panel center with respect to the support structure. The phase lag between excitation and response is stepped from 75° to 105°, maintaining constant response amplitude. The quasi-linear frequency response curves generated from steady state solution are used to find frequency and damping using circle fit method. These results are compared to the phase-resonant testing method. The backbone curve is tracked using a phased-locked-loop (PLL) controller in order to extract the amplitude-dependent frequency and damping. During PLL tests, the shaker voltage is stepped, maintaining constant phase lag of 90° to generate the backbone curve. The damping ratio is determined by a model-free approach from the balance of supplied and dissipated power in the

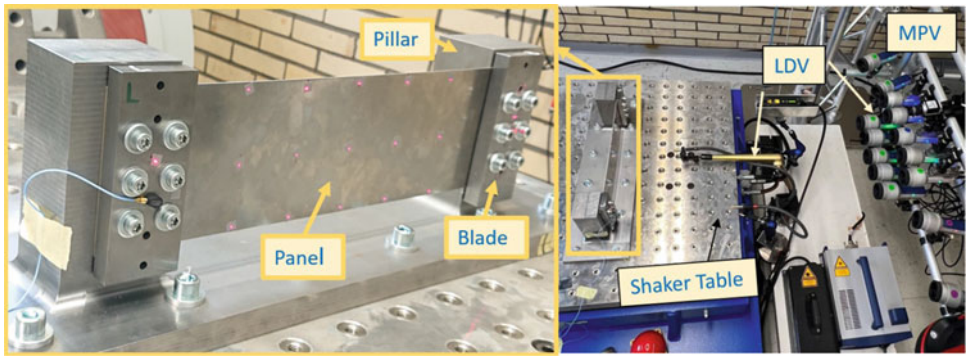

Fig. 18.1 Experimental setup: (**a**) different parts of the dynamic system and (**b**) components of the setup

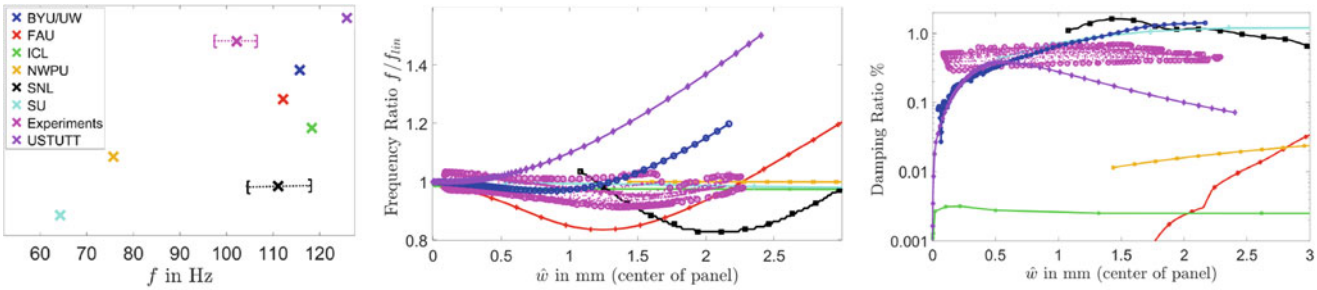

Fig. 18.2 Modal properties of first resonance mode: (**a**) linear natural frequency f_{lin}, (**b**) normalized natural frequency f/f_{lin} vs. displacement amplitude $\hat{\omega}$, and (**c**) damping ratio vs. displacement amplitude $\hat{\omega}$

system [5]. Repeatability tests are carried out to ensure the robustness of the measurements. Finally, the experimentally extracted amplitude-dependent natural frequencies and damping are compared to each other, and the results are compared to the model predictions, carried out by the different research groups in the context of the 2021 Tribomechadynamics Research Challenge.

18.3 Results

The linear response obtained from a random vibration test with small vibration amplitudes showed a good agreement with the results obtained from RCT and PLL testing at lower vibration amplitudes. Furthermore, the RCT results are comprised of the uncertainty interval of the PLL results for most of the tested cases up to a displacement amplitude of 2.1 mm. Figure 18.2 shows a comparison between the experimental results obtained by PLL (pink) and the predictions. The SNL predictions show a good agreement with the experimental linear natural frequency (f_{lin}) results as shown in Fig. 18.2a. Figure 18.2b shows the evolution of the normalized natural frequency of the first resonance mode (f/f_{lin}) with the relative displacement at the center of the panel ($\hat{\omega}$). The experimental results identified a softening then a hardening behavior of the structure. A similar trend was obtained by the predictions from SNL, BYU/UW, and FAU teams. However, the variation of the frequency is higher in the predictions (0.8–1.2) than in the experiments (0.95–1.05). The experimentally obtained damping ratios, shown in Fig. 18.2c, are comprised of between 0.2% and 0.7% and increase with $\hat{w}$. Concerning the predicted outcomes, the results of four groups are in the same order of magnitude (SNL) and within the uncertainty interval of the measurement results (SU, USTUTT, BYU/UW). The different nonlinear testing approaches work well for small to medium displacement amplitudes. Amplitudes higher than 2.1 mm were not tested because of difficulty to control, stresses exceeding elastic regime, temperature sensitivity, and limitation of the MPV measurement range.

18.4 Conclusion

The results of the work show that the two different nonlinear testing approaches, RCT and PLL, allow to extract the modal parameters of a structure under base excitation. The experimental results allow to confront the different predictions to the behavior of the real structure as a follow-up to the 2021 Tribomechadynamics Research Challenge.

Acknowledgments This work presents the results of the Tribomechadynamics Research Camp (TRC). The authors thank MTU Aero Engines for sponsoring the TRC 2022.

References

1. Krack, M., Schwingshackl, C., Brake, M.R.: The tribomechadynamics research challenge. InL Proceedings of IMAC 40. Orlando (2022)
2. Shetty, D., Park, K., Payne, C., Allen, M.S.: Predicting nonlinearity in the TMD benchmark structure using QSMA and SICE. In: Nonlinear Structures & Systems, vol. 1, pp. 281–287. Springer, Berlin (2023)
3. Lasen, M., Salles, L., Dini, D., Schwingshackl, C.W.: Tribomechadynamics challenge 2021: a multi-harmonic balance analysis from Imperial College London. In: Nonlinear Structures & Systems, vol. 1, pp. 79–82. Springer, Berlin (2023)
4. Karaağaçlı, T., Özgüven, H.N.: Experimental modal analysis of nonlinear systems by using response-controlled stepped-sine testing. Mech. Syst. Signal Process. **146**, 107023 (2021)
5. Müller, F., Woiwode, L., Gross, J., Scheel, M., Krack, M.: Nonlinear damping quantification from phase-resonant tests under base excitation. Mech. Syst. Signal Process. **177**, 109170 (2022)

Chapter 19
Using Abaqus with Python to Perform QSMA on the TMD Structure

Brennan Bahr, Drithi Shetty, and Matthew S. Allen

Abstract Automotive and aerospace structures are increasingly making use of thin panels to reduce weight while seeking to maintain durability and minimize noise transmission. These panels can exhibit geometrically nonlinear behavior due to bending-stretching coupling. Additionally, the use of mechanical fasteners results in nonlinear hysteretic behavior due to friction between the contact surfaces. The Tribomechadynamics benchmark structure, consisting of a thin panel clamped at the ends using bolted joints, was developed as part of a research challenge to test the ability of the nonlinear dynamics community to predict the dynamic behavior of a structure with both friction and geometric nonlinearity. Simulating the dynamic response of a high-fidelity nonlinear FE model is highly computationally expensive, even for such a small-scale structure. Therefore, quasi-static methods have been gaining popularity. This paper builds on our previous efforts to predict the amplitude-dependent frequency and damping of the first bending mode of this structure using quasi-static modal analysis (QSMA). A 3D FE model of the TMD structure was analyzed. The paper shows how Python, an open-source programming language, can be integrated with a commercial finite element package to perform QSMA. This minimizes file input/output compared to our previous approach and speeds up the process. We also investigate using the pseudo-inverse of the mode shape matrix, rather than the mass matrix times the mode shape matrix, to further accelerate the computations. The QSMA results are used to fit a reduced-order model to the structure, which comprises a single DOF implicit condensation and expansion (or SICE) ROM for geometric nonlinearity and an Iwan model to characterize friction nonlinearity. This model is able to reproduce the nonlinear modal behavior with high fidelity while significantly reducing the computational cost.

Keywords Friction · Geometric Nonlinearity · Reduced-order modeling · Contact · Hysteresis

19.1 Introduction

Thin panels are commonly used in the design of lightweight, high-speed structures that are assembled together using mechanical fasteners. These panels exhibit nonlinear behavior due to bending-stretching coupling at large deformations [1, 2]. Additionally, friction at the interfaces that are fastened together results in energy dissipation which has a nonlinear effect on the system dynamics [3]. The industry standard is often to make linear approximations to create a computationally efficient finite element model. Such simplifications lead to conservative designs that need to be iterated on, resulting in greater cost of prototyping and dynamic testing. However, simulating the dynamic response of a high-fidelity nonlinear finite element model can be highly computationally expensive, with the cost increasing with complexity [4]. Therefore, reduced-order modeling approaches have been developed as a more efficient alternative [5, 6].

One such approach that has been gaining traction in the structural dynamics community is the method of quasi-static modal analysis [7, 8], or QSMA. In this method, the nonlinear FE model under consideration is statically excited in the shape of the mode of interest. The corresponding displacement can then be calculated using any finite element package. This is done over a range of load amplitudes to obtain the force-displacement backbone curve. The results can then be used to quantify the modal dynamic response of the structure over the amplitude range of interest, typically by estimating the

B. Bahr (✉) · M. S. Allen
Department of Mechanical Engineering, Brigham Young University, Provo, UT, USA
e-mail: matt.allen@byu.edu

D. Shetty
Department of Mechanical Engineering, UW-Madison, Madison, WI, USA
e-mail: ddshetty@wisc.edu

M. R. W. Brake et al. (eds.), *Nonlinear Structures & Systems, Volume 1*, Conference Proceedings
of the Society for Experimental Mechanics Series, https://doi.org/10.1007/978-3-031-36999-5_19

amplitude-dependent frequency and damping behavior. Lacayo and Allen [8] showed that QSMA can be used to calculate the force-displacement relation for a nonlinear mode of a jointed structure consisting only of friction nonlinearity. Park and Allen [9] derived a similar relation for a single mode of a geometrically nonlinear structure. QSMA has been tested on different benchmark systems [10, 11], producing results that are in fairly good agreement with dynamic response predictions at a fraction of the computational cost. Furthermore, the method has been successfully applied to real-world structures [12].

Although QSMA offers a clear computational advantage over nonlinear dynamic analyses, some bottlenecks in its implementation still exist, especially in the case of larger 3D FE models. Efforts have been made to address these challenges. For instance, Jewell et al. [10] found that the contact and solver settings need to be iterated on to improve solution convergence and reduce solve time. Zare and Allen [13] proposed a contact algorithm that speeds up the quasi-static simulations, especially in the case of 3D models that comprise a two-dimensional friction problem. Another bottleneck, which is the main focus of this paper, is the extraction of the structural mass and mode shape matrices from the commercial FE package. The implementation of QSMA requires the mass and mode shape matrices, obtained by a linear eigenvalue analysis, in order to calculate the distributed static load to be applied. Since QSMA is not currently a standard procedure in commercial FE software, the static load must be externally calculated and fed to the FE package. Thus, the structural mass matrix and/or the mode shape matrix must be extracted from the FE software, which can grow quite large as the complexity of the model increases. In the past, Matlab scripts were created that would call on an FEA software, such as Abaqus, to perform a linear or static analysis. Due to the differences in syntax between the two programs, an additional step of translating the collected data into the appropriate language is needed if QSMA is to be performed. Skipping this additional step is desirable as the translation process takes up a significant amount of time while performing QSMA.

In our prior works, the steps above were performed using Matlab scripts that called upon a set of Python scripts to interface with Abaqus. However, Python has much of the same capability as Matlab so it was suggested to eliminate Matlab and perform all of the necessary analysis within Python. This paper presents a procedure to directly interface with the Python scripting language that is built into the commercial FEA software Abaqus in order to reduce the time that is needed to complete an analysis using QSMA. This is partly enabled by recent upgrades to Abaqus that incorporate newer and more complete versions of Python. While eliminating Matlab speeds up the file input-output, it was still necessary to write the mass matrix to a text file and read that into Python, and it became clear that doing so was an additional major bottleneck. Hence, a study was performed to see if the pseudo-inverse of the first m columns of the mode shape matrix could be used to obtain an adequate approximation of the distributed loading needed for QSMA.

The proposed improvements have been tested on a simplified 2D FE model of the TMD benchmark structure [14]. The TMD benchmark structure [15] consists of a thin, curved panel that is clamped at the ends with the help of bolts, thus potentially consisting of both geometric and frictional nonlinearity. Additionally, a 3D, high-fidelity FE model of the TMD structure has been considered. While loading the mass matrix of this model using the previous approach would take days, this paper shows how the new approach results in significant computational savings. In both case studies, the reduced-order modeling approach presented by Shetty et al. [14] has been used to estimate the overall changes in damping and frequency.

The following section reviews the major steps required to implement QSMA on a finite element model and discusses the Python scripts that are needed to implement this. The proposed approach is then applied to a simple two-dimensional model of two cantilevered beams that are bolted at their free ends, to verify the method. The scripts for this example are found in the Appendix and should enable others to test this approach and implement it on their systems. Then the new approach is applied to the TMD benchmark structure and its relative merits are investigated.

19.2 Theory

The QSMA process that was first presented in [8] is detailed below; see [8, 10] for additional details. The FE equations of motion for a N-degree of freedom (MDOF) system are given below, including the pre-stress in the joints $\mathbf{F}_{pre}$ and the joint force, $\mathbf{F}_J(\mathbf{x}, \boldsymbol{\theta})$, where $\boldsymbol{\theta}$ captures the stuck/slip state of each pair of contact nodes in the FEM.

$$\mathbf{M}\ddot{\mathbf{x}} + \mathbf{K}\mathbf{x} + \mathbf{F}_J(\mathbf{x}, \boldsymbol{\theta}) = \mathbf{F}_{ext} + \mathbf{F}_{pre} \tag{19.1}$$

The nonlinear term is approximated as $\mathbf{K}_0\mathbf{x}$ for small displacements about the preloaded state and the following eigenvalue problem is solved to find the linearized modes:

$$\left(\mathbf{K} + \mathbf{K}_0 - \omega_r^2\mathbf{M}\right)\boldsymbol{\phi}_r = \mathbf{0} \tag{19.2}$$

where ω_r and $\boldsymbol{\phi}_r$ are the natural frequency and eigenvector for the rth mode.

In prior works, the quasi-static force $\mathbf{M}\boldsymbol{\phi}_r\alpha$ was applied to excite only the rth mode, so that the quasi-static problem solved by the FEA software was the following:

$$\mathbf{K}\mathbf{x} + \mathbf{F}_J(\mathbf{x}, \boldsymbol{\theta}) = \mathbf{M}\boldsymbol{\phi}_r\alpha \tag{19.3}$$

Once the solution $\mathbf{x}$ was obtained, the modal response $q_r(\alpha)$ was obtained using $q_r(\alpha) = \boldsymbol{\phi}_r^{\mathrm{T}}\mathbf{M}\mathbf{x}(\alpha)$. While the above is theoretically exact, for large models it can be quite cumbersome to extract the mass matrix from the software so that the products $\boldsymbol{\phi}_r^{\mathrm{T}}\mathbf{M}$ and $\mathbf{M}\boldsymbol{\phi}_r$ can be evaluated. (For the 3D model discussed later, it could take more than a day to write the mass matrix to a text file and then to read that into Matlab.) Hence, this paper explores the following alternative.

The product $\boldsymbol{\phi}^{\mathrm{T}}\mathbf{M}$ is the inverse of the mode shape matrix, and so $\boldsymbol{\phi}_r^{\mathrm{T}}\mathbf{M}$ is simply the rth column of that inverse. Hence, it can be estimated by taking the pseudo-inverse of the mode shape matrix $\boldsymbol{\phi}$. In practice, one typically only computes a finite number of columns of the mode shape matrix, so the pseudo-inverse is denoted

$$\boldsymbol{\phi}^{L,m} = pinv\left(\boldsymbol{\phi}(:, 1:m)\right) \tag{19.4}$$

where $(:, 1:m)$ denotes the first m columns of the matrix. Once the pseudo-inverse has been computed, one can extract the rth column for the mode of interest, which is denoted $\boldsymbol{\phi}_r^{L,m}$ and is a $1 \times N$ vector. The matrix $\boldsymbol{\phi}$ is easily extracted from the Abaqus *.odb files into Python, and so one can easily compute the loading as $\mathbf{M}\boldsymbol{\phi}_r\alpha \approx \left(\boldsymbol{\phi}_r^{L,m}\right)^{\mathrm{T}}\alpha$ in Python. Then, Abaqus can be called to solve the following quasi-static problem:

$$\mathbf{K}\mathbf{x} + \mathbf{F}_J(\mathbf{x}, \boldsymbol{\theta}) = \left(\boldsymbol{\phi}_r^{L,m}\right)^{\mathrm{T}}\alpha \tag{19.5}$$

Once the nonlinear quasi-static solution $\mathbf{x}$ has been obtained, this can be converted into the rth modal displacement using $q_r(\alpha) \approx \left(\boldsymbol{\phi}_r^{L,m}\right)^{\mathrm{T}}\mathbf{x}(\alpha)$. Hence, the variables that need to be saved or exported are much smaller than the length N vectors and $N \times N$ matrices that are saved and imported into Matlab using our prior approach [10]. A validation of this new method is described in Sect. 19.3.2 of this work.

19.2.1 Using Python to Perform QSMA

This subsection outlines the proposed Python approach and contrasts it to our prior approach. As is stated in the previous section, the natural frequency and eigenvalues of various modes are needed in order to perform QSMA, and these should be obtained about the preloaded state. Hence, the procedure below assumes that one has already performed a nonlinear static analysis to preload the joints and has then performed linear modal analysis about that state, and that the output *.odb file from that analysis is available.

Once that is complete, one can run the first Python script, designated "InputWriter.py," as this script will use the data from the linear analysis to calculate and apply a quasi-static load to be used in the QSMA nonlinear static analysis, as is outlined in Fig. 19.1. This script creates two additional input files. The first file, designated "model_force," will contain the information needed for the QSMA static analysis step. This includes the typical parameter settings used to control the convergence of the model, as well as the forces and moments to be applied, which are given in the right-hand side of Eq. (19.5). The second file, designated "model_staticforce," is a simple script that combines the original input file, which contains the model definition, with the "model_force" input file that was just created.

The "model_staticforce" input file can also be used to specify that a restart analysis is to be run. When this capability is used, Abaqus simply resumes the model that was run earlier (i.e., when doing preload and linear modal analysis), and so the model does not need to be assembled again and the preload step does not need to be repeated. The use of restarts in Abaqus is discussed later in this work as it was found to significantly decrease the time that is spent performing QSMA.

The second Python script, "PostProcessing.py," is used to extract the static response $\mathbf{x}$ in Eq. (19.5) that was found during the QSMA static analysis and then to convert it to modal coordinates q_r. Then, a small number of modal coordinates are written to a *.mat file for storage. The authors currently bring this data into Matlab for any further analysis but this step is fast now because the data to be written is small as one is typically not interested in more than a few tens of modes. One could compute the amplitude-dependent frequency and damping from only one mode, the mode that is directly excited in

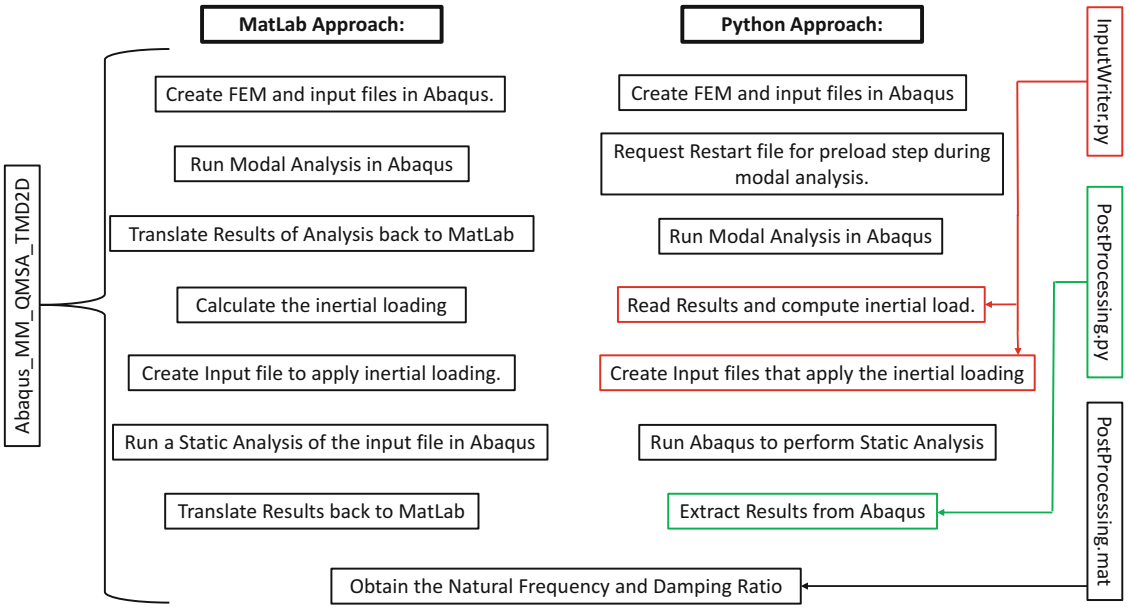

Fig. 19.1 Flowchart representation of the two methods that are discussed in this work. The names of the scripts are given on the far sides of the flowchart, with Matlab on the left and Python on the right

Eq. (19.5), but other modes are also typically imported in order to see how much they were statically coupling to the mode in question.

19.2.1.1 Using Abaqus's Restarts

Restarts were used frequently while analyzing various models to reduce the time needed. Restarts allow the user to resume an analysis at a specified step if the requisite files for the previous steps have been created. This was very useful in the context of QSMA because any QSMA analysis starts with a preload. Using restarts one can run preload only once and then perform QSMA for as many modes as needed or as many load levels as needed. The disadvantage is that the files needed for the restart consume quite a bit of disk space. A description of how to create and use restart files can be found in [16].

19.2.1.2 Rough Friction vs. Lagrange Friction

As is discussed later in this work, the TMD benchmark structure is particularly difficult to solve due to the fact that it consists of both geometric and frictional nonlinearity. The nonlinearity that arises due to friction occurs due to micro-slip between the bolts and the assembly. Geometric nonlinearity comes about as the panel bends due to bending-stretching coupling. As is explained in [14], one way to distinguish the effects of the two types of nonlinearity is to run an analysis with both types of nonlinearity enabled and then to run a separate analysis in which the nonlinearity due to friction is eliminated. This can be done by setting the coefficient of friction to infinity so as to ensure that no micro-slip will arise during the analysis. The data from these different runs are then collected and processed as outlined in [14].

To implement this, one only needs to edit the portion of the Abaqus input file where the interaction property is defined and to set that to what Abaqus designates as "rough" friction [16]. This effectively sets the coefficient of friction to infinity to ensure that nothing will slip in the analysis. An example of this type of analysis is shown in Fig. 19.2, where the modal load-displacement curves are shown for both types of analyses.

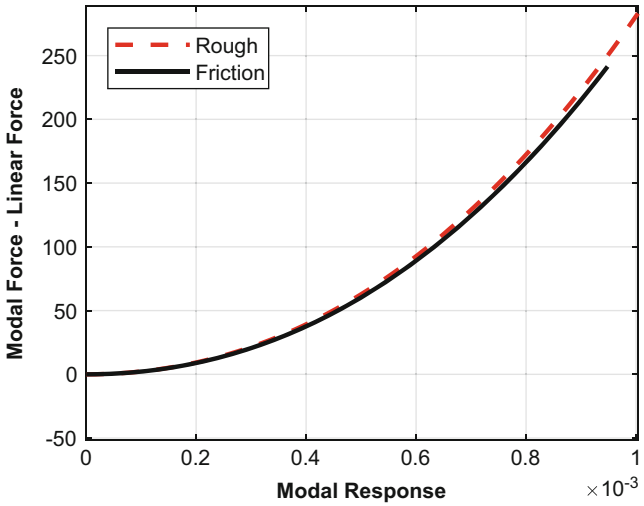

Fig. 19.2 Load-displacement curves for 2D TMD benchmark model with an infinite coefficient of friction (i.e., "rough" contact in Abaqus) and Lagrange friction with $\mu = 0.6$

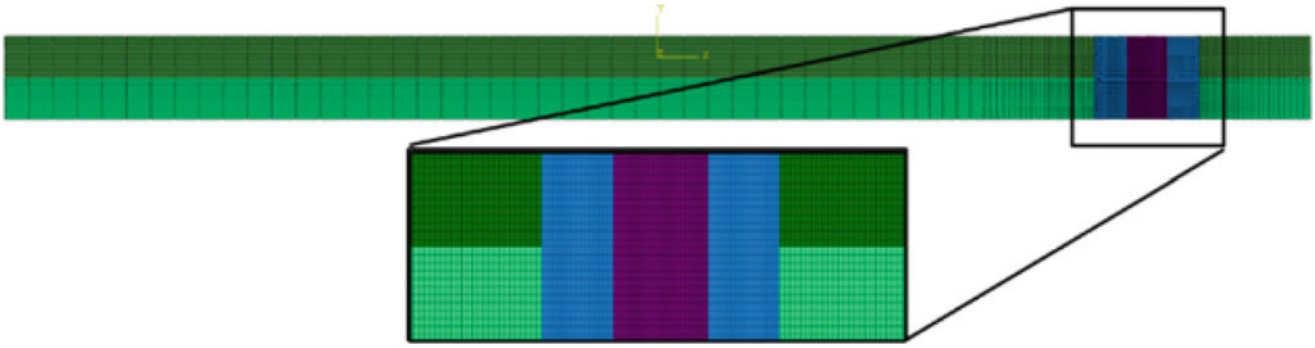

Fig. 19.3 Visual representation of the stacked beam model that is used in Sect. 19.3. The magnified portion of the figure represents the pressure load that is implemented to represent a bolt that holds the two plates together

19.3 Case Study 1: Stacked Beam

To test the efficacy of using Python to perform QSMA, the abovementioned scripts were used to analyze the same simple two-dimensional model that was used in [10]. QSMA was performed using Python to extract the amplitude-dependent variables of the first mode of vibration, and the results were compared to those obtained by using the previous method.

The model consists of two cantilever beams that are bolted together at one end as is seen in Fig. 19.3. Each beam is 203 mm long, 6.35 mm thick, and infinite in width due to the plane strain elements that were used during analysis. A fixed boundary condition was applied to the left side of the two beams, and the bolt that fastened the two beams together was modeled as a pressure load on the top and bottom of the beam 25.44 mm from the right side of the structure. The pressure load applied to the system is 288 Newton meters in magnitude distributed across 6.35 mm to mimic the effect of a bolt with a 6.35 mm diameter fastened with 4450 N of preload. For a more detailed description of the meshing and materials that were used, see [10]. It is worth mentioning that the material that was used to construct the beam is linearly elastic, which means that the only damping in the system is due to Coulomb friction between the bolt and the beams.

19.3.1 Application of Quasi-static Modal Analysis

The first step in the analysis was to solve for the preload in the bolt and to perform linear modal analysis. The input file for this step is available from the authors upon request. This analysis results in the computation of the linearized mode shapes

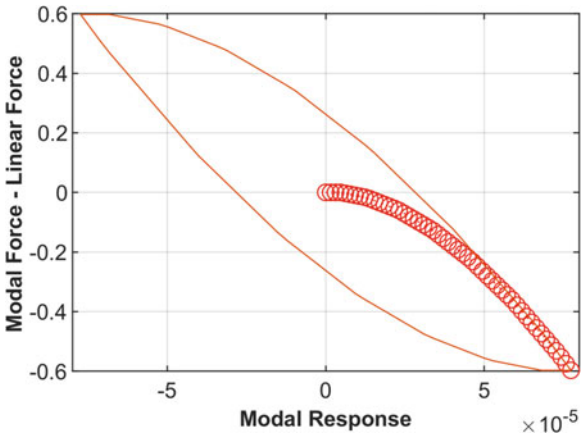

Fig. 19.4 Example of a modal force-displacement result for the 2D beam, as well as the resulting hysteresis loop that is formed by using Masing's rules. As is mentioned in [8], the slope of the secant line of the force-displacement backbone is used to calculate the natural frequency of the system, and the area enclosed in the hysteresis loop is used to find the damping ratio of the system

in Eq. (19.2). The first 20 modes of the assembly are considered, as a greater number of eigenvalues calculated result in a more orthogonal matrix when computing the pseudo-inverse in Eq. (19.4), as is discussed in Sect. 19.3.2 of this work. These modes are also used after the QSMA analysis to determine if modal coupling is present in the results.

After the modal analysis was completed, the first Python script is run. This script extracts the mode shapes that were evaluated during the analysis and calculates the inertial load that is to be applied to each node using Eq. (19.5). An input file is then created that specifies the magnitude and direction of the load on each node.

If various tests were to be performed, then restart files were created before submitting the new input files for analysis. The restart functionality does little to speed up this small model, but this model is a good test bench for debugging the restart procedure.

19.3.1.1 Post-Processing Results from the Static Analysis

The second Python script is initiated, either from the command line or from the Abaqus GUI after the static analysis has concluded to extract the modal displacements of each mode due to the preload and inertial load. Note that even though it is a Python script, it must be run within Abaqus because it makes use of libraries that are only available within the Python installation that exists within Abaqus. As mentioned previously, that second script saves modal load-displacement data, such as that shown in Fig. 19.2. This force-displacement backbone curve can then be used to form a hysteresis loop using Masing's rules. This practice was utilized in [8] in connection with quasi-static modal analysis to calculate the natural frequency and damping of the structure. The same procedure is used in this work to find the natural frequency and damping of the nonlinear structure being examined. An example of the force-displacement backbone curve, as well as the resultant hysteresis loop, is shown in Fig. 19.4.

The calculated values for the natural frequency and damping are then graphed with respect to peak modal velocity. The results are then compared to the graphs that were created using the previous method in Fig. 19.5

19.3.2 Validation of Pseudo-inverse Approach

This section explores the feasibility of using the pseudo-inverse method to perform QSMA. As mentioned previously, this method was desired over using $\mathbf{M}\boldsymbol{\phi}$ due to the time that is needed to pull the mass matrix into either Matlab or Python in order to compute the product. In order to test the viability of the pseudo-inverse method, QSMA was performed on the stacked beam structure [10] using both approaches. A summary of the comparison is provided below, as well as recommendations for using the $pinv$ function in the future.

The accuracy of the pseudo-inverse $\boldsymbol{\phi}^{L,m}$ was compared with that of the traditional approach by multiplying the matrix by $\boldsymbol{\phi}$. The result can then be compared with that of the $\boldsymbol{\phi}_r^T \boldsymbol{M}$ matrix to assess the accuracy. It is worth noting that the Python script that was used to calculate $\boldsymbol{\phi}^{L,m}$ used Numpy's $pinv$ function. The Python library Scipy also has a pseudo-inverse function, but Numpy's pseudo-inverse approximation uses less memory than Scipy's as Scipy's $pinv$ function uses a least squares approximation, while Numpy's $pinv$ function uses an SVD to approximate the inverse. This made Numpy's $pinv$ function more desirable as it takes less time to compute while still giving reliable results.

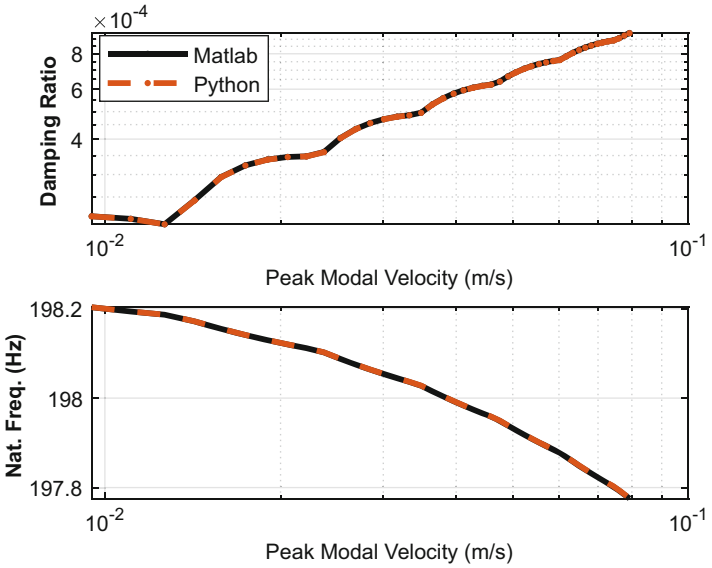

Fig. 19.5 Comparison of the natural frequency and damping ratio obtained using the Python scripts that are described in this work and the previous Matlab script for the stacked beam model. The results differ only in the third decimal place

Table 19.1 The product of $\boldsymbol{\phi}^{L,m}$ and $\boldsymbol{\phi}$ for the 2D stacked beam structure [10]. The pseudo-inverse was computed using 20 modes, but the table only shows the first five columns and rows of the product

	Mode 1	Mode 2	Mode 3	Mode 4	Mode 5
Mode 1	1	6.14e-16	−3.95e-16	−1.49e-15	1.94e-16
Mode 2	8.34e-16	1	8.70e-16	2.15e-15	−3.07e-16
Mode 3	1.17e-15	−9.86e-16	1	−7.14e-16	5.10e-16
Mode 4	7.43e-17	−3.91e-16	−6.31e-18	1	−4.68e-17
Mode 5	−4.17e-16	−1.19e-16	−2.70e-15	−2.57e-16	1

As seen in Table 19.1, the pseudo-inverse provides an excellent approximation to the inverse $\boldsymbol{\phi}$. In fact, the off-diagonal values were lower using this approach than using the more rigorous $\mathbf{M}\boldsymbol{\phi}$. Hence, it seems that this is a viable approach for calculating the inertial load that is to be applied in QSMA.

When testing this approach, it was found that the method lost accuracy if too small a number of mode shapes was used, yet using 20 mode shapes as done above gave excellent results and it was not very expensive to compute that many modes even for the larger models considered later.

19.4 Case Study 2: 2D TMD Benchmark Structure

The advantages of using the python approach become much clearer when studying a larger model. The model that is studied in this section is known as the Tribomechadynamics benchmark structure [14]. The benchmark structure is comprised of a 1.5 mm thick panel that is attached to two blocks, known as blades. The panel is fastened to both blades by two rows of three bolts. The surface of the support that is in contact with the panel has an inclination of 1^o on both sides, which results in slight curvature of the panel, as seen in Fig. 19.6. Due to the assembly of the panel, the structure will experience geometric nonlinearity, as well as nonlinearity due to friction. The structure will also behave differently depending on the direction in which the inertial load is applied, which is to be accounted for if a full analysis of the structure is needed.

Because this system has both geometric and friction/slip nonlinearity, the standard QSMA approach must be augmented. Shetty et al. [14] proposed an extension that was found to give excellent results for this structure, but to implement their method one must perform at least three analyses: two analyses with the friction disabled (i.e., the surfaces are glued together) in which the structure is deformed in positive and negative directions, and a third with both friction and geometric nonlinearity present. Hence, the use of restart files was quite beneficial for this particular model as it allowed the first two steps of the analysis to be run only once. Those first two steps required about an hour for this model. It is also worth noting that the static was performed using a Riks analysis (rather than Abaqus's static, general method). The Riks analysis was found to provide

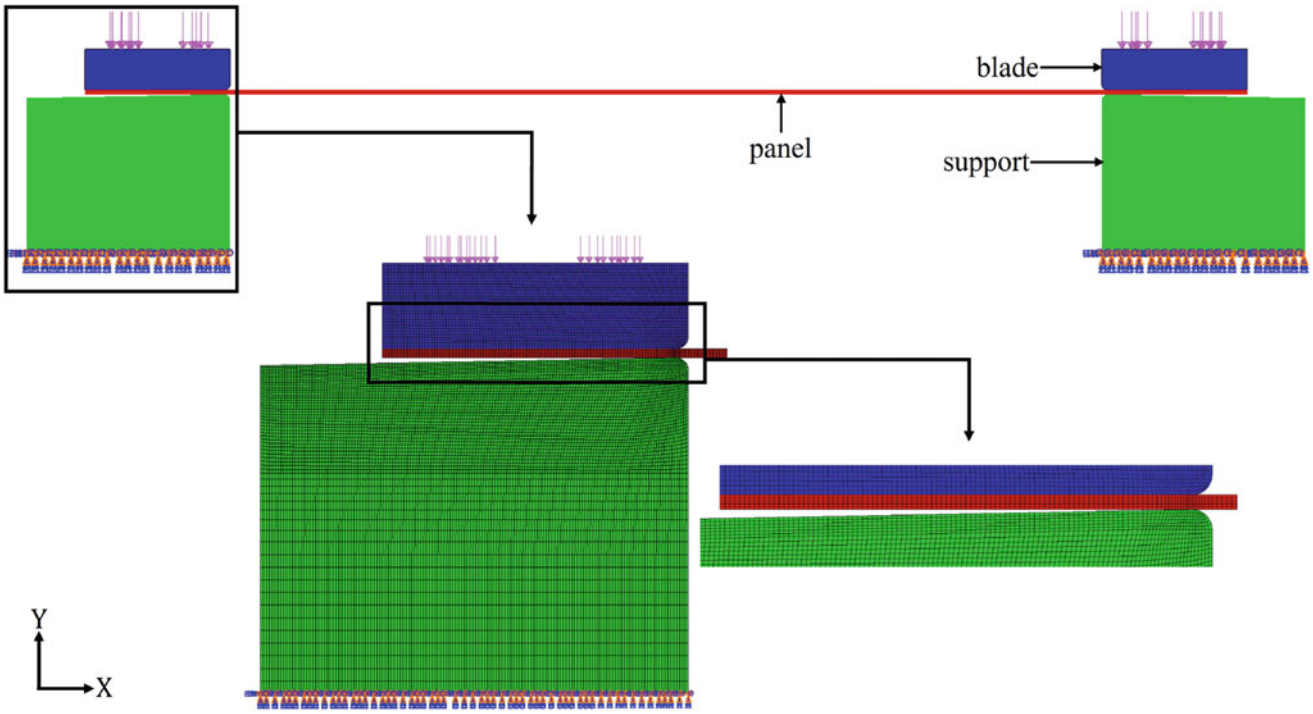

Fig. 19.6 2D FE model of the TMD structure, with a magnified version of the left-hand side interface showing the mesh density at contact, from [14]

greater accuracy over the range of loads in the study in [14], whereas the static general analysis only meets the specified tolerances for the largest loads in each analysis.

Once the linear analysis had been completed, one can proceed to calculate the inertial load. In the Python script in the Appendix, the load scale factor determines both the magnitude and the sign of the load applied to the beam. Because the mode can have an arbitrary sign, some care is needed. In the script shown some checks are included to ensure that a load scale factor of positive one applies the inertial load in the positive y direction, while a load scale factor of negative one applies the inertial load in the $-y$ direction. The maximum displacement of the panel is also specified by indicating that a node located at the middle of the panel should not be displaced more than 4.2 mm, or double the thickness of the panel, in either direction. The maximum load proportionality factor could also be specified in place of the maximum displacement of a chosen node. Once these variables have been defined, the first Python script can then be run in Abaqus to calculate the forces and moments that are to be applied at each node and to write those to an input file.

Abaqus is then called to run the QSMA static analysis. Once the static analysis has finished running, the results can be extracted from the *.odb file for post-processing using the second Python script. Two more analyses are then run in which slip at the joint is eliminated by setting the contact to "rough" in Abaqus. This analysis is repeated with a positive and negative load scale factor.

19.4.1 Results

The results obtained using the new Python based approach were once again indistinguishable from those presented in [14], and so they are not repeated here. Table 19.2 compares the time required for each step when using each method.

The three QSMA static analyses mentioned previously are denoted A through C in Table 19.2. Analyses A and B had "rough" contact (no slip), with the load applied in the $-y$ and $+y$ directions, respectively. Analysis C was run with Lagrangian friction with $\mu = 0.6$ and with the quasi-static load applied in the $-y$ direction. The preload analysis, linear analysis, and frequency and damping computation all follow the same process and therefore should have similar times as is shown. The main differences between the two methods are the time needed to load the mass and stiffness matrices from the Abaqus output file and the time needed to process the QSMA output. It takes less time to process the QSMA output using

Table 19.2 Time taken to estimate the frequency and damping of the TMD 2D FE model using the Matlab [14] compared to the Python approach proposed in this work

Analysis	Matlab scripts	Python scripts with restarts
Preload analysis	2911 s (≈49 min.)	3301 s (≈55 min.)
Linear modal analysis	4 s	4 s
Calculation and application of inertial load	84.2 s	47.5 s
QSMA—analysis A	530 s (≈9 min.)	486 s (≈ 8 min.)
QSMA—analysis B	530 s (≈9 min.)	532 s (≈9 min.)
QSMA—analysis C	673 s (≈11 min.)	632 s (≈11 min.)
Post-processing QSMA output	$(3 \times 2123) = 6369$ s (≈1.77 h)	$(3 \times 1894) = 5682$ s (≈1.6 h)
Frequency and damping computation	63 s	16 s
Total time taken	3.12 h	3.06 h

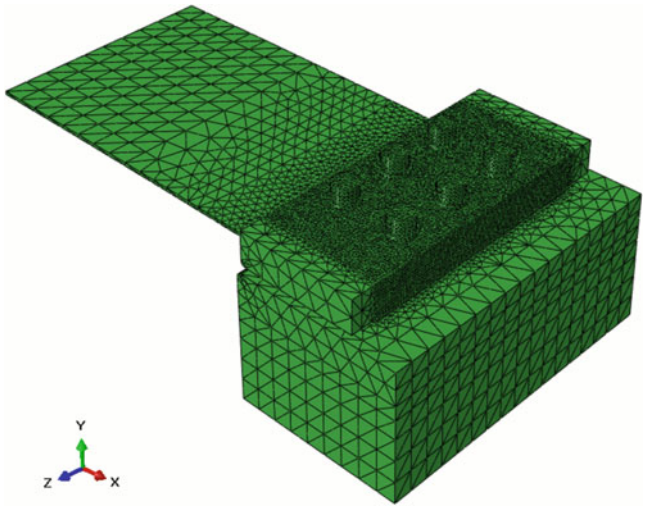

Fig. 19.7 3D FE model of the support, blades, and panel, dubbed here the partial assembly because half-symmetry was employed

the Python scripts as all of the information is processed in Python and only a small set of results are written to disk. While the difference in time taken may not be huge in this case study, it grows significantly when larger FE models are considered. The frequency and damping estimated by this method are identical to the results presented in [14] and have therefore not been shown here for brevity.

19.5 Case Study 3: 3D TMD Benchmark Structure

A 3D version of the TMD benchmark structure [14] has also been created, and the proposed approach has been instrumental in running analyses on this model. The same process that was used for the 2D version of the model is currently being used, but the analyses take much longer to solve due to the complexity of the model. It is hoped that the new methods described in this paper will significantly decrease the amount of time needed for analysis. To date, the preload analysis has been completed using restart, and several static analyses have been completed. As an example, it takes 2–3 days to extract the mass matrix from the 3D model and to load it into Abaqus, but this step is no longer needed when the $pinv$ method described in Sect. 19.4 is implemented. Each static analysis takes 5–7 days to complete and they frequently crash, so the Python workflow proposed here is optimal as it is easy to restart if interrupted and doesn't require Matlab to be open (Fig. 19.7).

19.6 Conclusions

This paper has presented a new approach for performing QSMA that makes use of Python to minimize file input/output and the associated computational costs. While the changes to the workflow are quite elementary, it is hoped that the exposition can serve as a tutorial for any researchers interested in performing QSMA. The new workflow appears to be quite promising when large models need to be studied, and is relatively easy to implement.

The interested reader can copy and paste the Python scripts provided in the Appendix and apply this approach to a wide range of finite element models with minimal modification. These scripts are provided without warranty, and they will likely be improved in the coming months and those improvements can also be made available upon request. We also welcome any improvements that any readers may make.

The conference presentation will cover the results obtained on the 3D TMD structure, which have been enabled by this new and more efficient workflow.

Appendix

InputWriter.py

```
import timeit
tic = timeit.default_timer()
from odbAccess import *
from abaqusConstants import *
import copy
import sys
import numpy
import scipy
from scipy.io import savemat
import section
import regionToolset
import displayGroupMdbToolset as dgm
import part
import material
import assembly
import step
import interaction
import load
import mesh
import optimization
import job
import sketch
import visualization
import xyPlot
import displayGroupOdbToolset as dgo
import connectorBehavior
import math

#Values that need to be changed based on the model, jobname, and
#mode number to be analyzed.
modelname = 'TMDbenchmark-2D-riks'
requestedMode = 1
jobName = "TMDbenchmark-2D-refine_matmodes"
part = 'PART-1-1'          #'PART-1-1' is default
loadSclFactor = 1.0        #constant taken from previous code
thick = 1.5                #constant taken from previous code
```

```
requested_disp = loadSclFactor*thick
lastStep = 'BoltPreload'  #Last step before adding quasi-static load
Modal = False
#Does the input file have a modal analysis step that is not needed?

odbFileName= jobName + ".odb"
db = openOdb(odbFileName)


setName='mode'
step_names=db.steps.keys()
step_name=step_names[-1]

myStep=db.steps[step_name]
numFrames=len(myStep.frames)-1
numValues=len(myStep.frames[0].fieldOutputs['U'].values)

#   print numFrames
#   print numValues

# frames[0] is the base state, really have numFrames-1 numFrames
freq=numpy.zeros((numFrames,1),dtype=float);
disp=numpy.zeros((6*numValues,numFrames),dtype=float);
dof =numpy.zeros((6*numValues, 1), dtype=float); # JDS Modification
descript=[]

v=0
while v < numFrames:
    myMode=myStep.frames[v+1]
    freq[v]=myMode.frequency
    descript.append(myMode.description)
    n=0
    while n < numValues:
        #
        try:
            data=myMode.fieldOutputs['U'].values[n].data
        except OdbError:
             data=myMode.fieldOutputs['U'].values[n].dataDouble
        #
        # Add displacements
        disp[6*n+0][v]=data[0]
        disp[6*n+1][v]=data[1]
        if len(data) > 2:
            disp[6 * n + 2][v] = data[2]
        else:
            disp[6 * n + 2][v] = 0.
        #
        #
        # Add DOF to DOF vector using [node.1, node.2, node.3, ...] convention
        if v == 0:
            dof[6*n + 0] = myMode.fieldOutputs['U'].values[n].nodeLabel + 0.1
            dof[6*n + 1] = myMode.fieldOutputs['U'].values[n].nodeLabel + 0.2
            dof[6*n + 2] = myMode.fieldOutputs['U'].values[n].nodeLabel + 0.3
        #
        if myMode.fieldOutputs.has_key('UR'):
```

```
            #
            try:
                data=myMode.fieldOutputs['UR'].values[n].data
            except OdbError:
                data=myMode.fieldOutputs['UR'].values[n].dataDouble
            #
            # Add displacements
            disp[6*n + 3][v] = data[0]
            disp[6*n + 4][v] = data[1]
            if len(data) > 2:
                disp[6*n + 5][v] = data[2]
            else:
                disp[6*n + 5][v] = 0.
            #
            # Add DOF
            if v == 0:
              dof[6*n + 3] = myMode.fieldOutputs['UR'].values[n].nodeLabel + 0.4
              dof[6*n + 4] = myMode.fieldOutputs['UR'].values[n].nodeLabel + 0.5
              dof[6*n + 5] = myMode.fieldOutputs['UR'].values[n].nodeLabel + 0.6
                #
            elif myMode.fieldOutputs.has_key('UR3'): # ? need to add else?
              else: #
                #
                try:
                    data=myMode.fieldOutputs['UR3'].values[n].data
                except OdbError:
                    data=myMode.fieldOutputs['UR3'].values[n].dataDouble
                #
                disp[6*n + 5][v]=data
                if v == 0:
                    dof[6*n + 5] = myMode.fieldOutputs['UR3'].values[n].
                      nodeLabel + 0.6
        n+=1
    v+=1

"""
Creating the Scale Factor to multiply with disp to get the correct force to add
to the model before analysis
"""

"""
modesOfInterest = [1]

if (modeNum > 1) :
for i in range(1,modeNum) :
modesOfInterest.append(i + 1)
"""

modeNum = requestedMode
N = numpy.size(dof)

phi = copy.deepcopy(disp)

P = numpy.size(phi[:,modeNum - 1])
```

```
#taking the pseudoinverse of phi
mPhi = numpy.linalg.pinv(phi)

#find translational displacements using dof
tempDof = copy.deepcopy(dof)
for i in range(0,N):
        if ((float(dof[i]) - floor(dof[i])) < 0.35):
            tempDof[i] = 1.0
        else:
            tempDof[i] = 0.0

#need to make a fake array as to not change the values of phi
#we need to find the max of the translation values in phi
fakePhi = copy.deepcopy(phi)

#find values of phi that match translational displacements
for i in range(0,P):
        fakePhi[i,modeNum-1] = abs((float(phi[i, modeNum-1])) * (float
          (tempDof[i])))
        #print(tempDof[i],phi[i,modeNum-1],fakePhi[i,modeNum-1])
        # ^^^ Use to check values if needed

#find max value of translational displacements for scale factor
phi_max = float(max(fakePhi[:,modeNum-1]))

#find index of phi_max
phi_max_ind = numpy.argmax(fakePhi[:,modeNum - 1])

#Ensures the sign of loadSclFactor is independent of an arbitrary modeShape sign
loadSclFactor = ((loadSclFactor) * (float(numpy.sign(phi[phi_max_ind,
  modeNum-1]))))

#Calculating Scale Factor to apply to mPhi
alpha = ((float(freq[modeNum-1])*2*math.pi)**2)*loadSclFactor*thick/phi_max

fshape = alpha * mPhi[modeNum-1,:]

"""
sign command in matlab is the same as numpy.sign() command in python
** is the same as ^ for python
numpy.linalg.pinv(phi) - finds the pseudoinverse of phi
numpy.where - finds the index of the argument in ()
copy.deepcopy - creates a copy of the array without using a pointer to the data
like phi = disp
"""

with open(modelname + '_force.inp','w') as f:
    f.write('*STEP, inc=10000000, nlgeom=YES, NAME=STATIC\n')
    f.write('*STATIC, riks, stabilize, factor=0.0002, allsdtol=0.00,
      continue=NO\n')
    f.write('**InitArcLenInc, EstTotArcLen, MinArcLenInc, MaxArcLenInc, Max LPF,
        NodeRegion, DOF, MaxDisp\n')
    f.write('1e-3, 12., 1e-8, 1e-1, , MaxDispNode, 2, 4.2\n')
    f.write('*CLOAD, OP=new\n')
    for i in range(0,N):
```

```
            dofi = float(dof[i])
            nodeNum = int(dofi)
            dirval = int(round((dofi-nodeNum)*10))
            force = fshape[i]
            if (nodeNum == 0 or abs(force) < 1.0e-15):
                continue
            elif (dirval == 1):
                f.write(str(nodeNum)+', 1, ')
                f.write(str(force)+'\n')

            elif (dirval == 2):
                f.write(str(nodeNum)+', 2, ')
                f.write(str(force)+'\n')

            elif (dirval == 3):
                f.write(str(nodeNum)+', 3, ')
                f.write(str(force)+'\n')

            elif (dirval == 4):
                f.write(str(nodeNum)+', 4, ')
                f.write(str(force)+'\n')

            elif (dirval == 5):
                f.write(str(nodeNum)+', 5, ')
                f.write(str(force)+'\n')

            elif (dirval == 6):
                f.write(str(nodeNum)+', 6, ')
                f.write(str(force)+'\n')

            else:
                continue
        f.write('*END STEP\n')

    with open(modelname + '_staticforce.inp','w') as f:
        f.write('** Static Force\n')
        f.write('**\n**\n')
        f.write('*Restart, read, step=1\n')
        f.write('** ----------------------------------------------------------------
          -----\n')
        f.write('**\n')
        f.write('** ----------------------------------------------------\n')
        f.write('** ------ STEP data for SUBCASE 1\n')
        f.write('** ----------------------------------------------------\n')
        f.write('*INCLUDE, INPUT=' + modelname + '_force.inp')

    mdic = {'alpha':alpha, 'Mphi': mPhi, 'fn':freq, 'phi_max_ind':phi_max_ind,
        'phi_max':phi_max}
    savemat("VariablesFromModal", mdic, True)

    numpy.save("Mphi",mPhi)

    toc = timeit.default_timer()

    print(toc - tic)
```

PostProcessing.py

```
import timeit
tic = timeit.default_timer()
from odbAccess import *
from abaqusConstants import *
import copy
import sys
import numpy
import scipy
from scipy.io import savemat
import section
import regionToolset
import displayGroupMdbToolset as dgm
import part
import material
import assembly
import step
import interaction
import load
import mesh
import optimization
import job
import sketch
import visualization
import xyPlot
import displayGroupOdbToolset as dgo
import connectorBehavior
import math

jobName = "TMDbenchmark-2D-riks_staticforce"
odbFileName= jobName + ".odb"
matFileName = jobName + "_FromAbaqus"
db = openOdb(odbFileName)


setName='mode'
step_names=db.steps.keys()
step_name=step_names[-1]

myStep=db.steps[step_name]
numFrames=len(myStep.frames)
numValues=len(myStep.frames[0].fieldOutputs['U'].values)

#   print numFrames
#   print numValues

# frames[0] is the base state, really have numFrames-1 numFrames
staticDisp=numpy.zeros((6*numValues,numFrames),dtype=float);
dof =numpy.zeros((6*numValues, 1), dtype=float); # JDS Modification
descript=[]

"""
Getting disp, dof, and freq arrays
"""
```

```
v=0
while v < numFrames:
    myMode=myStep.frames[v]
    descript.append(myMode.description)
    n=0
        while n < numValues:
        #
        try:
            data=myMode.fieldOutputs['U'].values[n].data
        except OdbError:
            data=myMode.fieldOutputs['U'].values[n].dataDouble
        #
        # Add displacements
        staticDisp[6*n+0][v]=data[0]
        staticDisp[6*n+1][v]=data[1]
        if len(data) > 2:
            staticDisp[6 * n + 2][v] = data[2]
        else:
            staticDisp[6 * n + 2][v] = 0.
        #
        #
        # Add DOF to DOF vector using [node.1, node.2, node.3, ...] convention
        if v == 0:
            dof[6*n + 0] = myMode.fieldOutputs['U'].values[n].nodeLabel + 0.1
            dof[6*n + 1] = myMode.fieldOutputs['U'].values[n].nodeLabel + 0.2
            dof[6*n + 2] = myMode.fieldOutputs['U'].values[n].nodeLabel + 0.3
        #
        if myMode.fieldOutputs.has_key('UR'):
            #
            try:
                data=myMode.fieldOutputs['UR'].values[n].data
            except OdbError:
                data=myMode.fieldOutputs['UR'].values[n].dataDouble
            #
            # Add displacements
            staticDisp[6*n + 3][v] = data[0]
            staticDisp[6*n + 4][v] = data[1]
            if len(data) > 2:
                staticDisp[6*n + 5][v] = data[2]
            else:
                staticDisp[6*n + 5][v] = 0.
            #
            # Add DOF
            if v == 0:
              dof[6*n + 3] = myMode.fieldOutputs['UR'].values[n].nodeLabel + 0.4
              dof[6*n + 4] = myMode.fieldOutputs['UR'].values[n].nodeLabel + 0.5
              dof[6*n + 5] = myMode.fieldOutputs['UR'].values[n].nodeLabel + 0.6
                #
            elif myMode.fieldOutputs.has_key('UR3'): #? need to add else? else:#
                #
                try:
                    data=myMode.fieldOutputs['UR3'].values[n].data
                except OdbError:
                    data=myMode.fieldOutputs['UR3'].values[n].dataDouble
                #
```

```
                staticDisp[6*n + 5][v]=data
                if v == 0:
                    dof[6*n + 5] = myMode.fieldOutputs['UR3'].values[n].
                     nodeLabel + 0.6
        n+=1
    v+=1

mPhi = numpy.load("Mphi.npy")
#loads in mPhi from the previous script.

LPF = numpy.array(db.steps['STATIC'].historyRegions['Assembly Assembly-1']
    .historyOutputs['LPF'].data)
#Extracts the Load Proportionality Factor.

#Extracts the modal displacement calculated from the Static Analysis.
u_nls = numpy.squeeze(staticDisp)
R = numpy.size(u_nls[:,0])
u_prel= numpy.zeros((R,1),dtype = float)
#Creates an array with the displacements calculated from the Preload Step.
for i in range (0,R):
    u_prel[i,0] = u_nls[i,0]

C = numpy.size(u_nls[0,:])
tempArray = numpy.ones((1,C), dtype = float)
m = numpy.matmul(u_prel,tempArray)
#Separates the displacements from the Preload Step from the displacements
#from the Static Step.
u_nls = u_nls - m

tempDisp = copy.copy(u_nls)
u_nls = numpy.zeros((R,(C-1)),dtype = float)
for i in range (0,C-1):
    for j in range (0,R):
            u_nls[j,i] = tempDisp[j,i+1]

q_nls = numpy.matmul(mPhi,u_nls)

mdic = {"u_nls":u_nls,"u_prel":u_prel,"q_nls":q_nls,"LPF":LPF}
savemat("VariablesFromStatic",mdic,True)

toc = timeit.default_timer()
print(toc-tic)
```

References

1. Woinowsky-Krieger, S.: The effect of an axial force on the vibration of hinged bars. J. Appl. Mech. **17**(1), 35–36 (2021)
2. Raju, I.S., Venkateswara Rao, G., Kanaka Raju, K.: Effect of longitudinal or inplane deformation and inertia on the large amplitude flexural vibrations of slender beams and thin plates. J. Sound Vib. **49**(3), 415–422 (1976)
3. Ungar, E.E.: The status of engineering knowledge concerning the damping of built-up structures. J. Sound Vib. **26**(1), 141–154 (1973)
4. Kuether, R.J., Najera, D.A., Ortiz, J., Khan, M.Y., Miles, P.R.: 2021 tribomechadynamics research challenge: Sandia National Laboratories high-fidelity FEA approach. Presented at 40th International Modal Analysis Conference (IMAC-XL) (2022)
5. Mignolet, M.P., Przekop, A., Rizzi, S.A., Michael Spottswood, S.: A review of indirect/non-intrusive reduced order modeling of nonlinear geometric structures. J. Sound Vib. **332**(10), 2437–2460 (2013)
6. Segalman, D.J., Gregory, D.L., Starr, M.J., Resor, B.R., Jew, M.D., Lauffer, J.P., Ames, N.M.: Handbook on Dynamics of Jointed Structures. Technical report, Sandia National Laboratories, Albuquerque, 2009

7. Festjens, H., Chevallier, G., Dion,J.-L.: A numerical tool for the design of assembled structures under dynamic loads. Int. J. Mech. Sci. **75**, 170–177 (2013)
8. Lacayo, R.M., Allen, M.S.: Updating structural models containing nonlinear Iwan joints using quasi-static modal analysis. Mech. Syst. Signal Process. **118**, 133–157 (2019)
9. Park, K., Allen, M.S.: Quasi-static modal analysis for reduced order modeling of geometrically nonlinear structures. J. Sound Vib. **502**, 116076 (2021)
10. Jewell, E., Allen, M.S., Zare, I., Wall, M.: Application of quasi-static modal analysis to a finite element model and experimental correlation. J. Sound Vib. **479**, 115376 (2020)
11. Wall, M., Zare, I., Allen, M.S.: Predicting S4 Beam Joint Nonlinearity Using Quasi-Static Modal Analysis. Springer, Berlin (2020)
12. Allen, M.S., Schoneman, J.D., Scott, W., Sills, J.W.: Application of Quasi-Static Modal Analysis to an Orion Multi-Purpose Crew Vehicle Test. Houston (2020)
13. Zare, I., Allen, M.S.: Adapting a contact-mechanics algorithm to predict damping in bolted joints using quasi-static modal analysis. Int. J. Mech. Sci. **189**, 105982 (2021)
14. Shetty, D., Allen, M.S., Park, K.: A new approach to model a system with both friction and geometric nonlinearity. J. Sound Vib. **552**, 117631 (2023)
15. Krack, M., Schwingshackl, C., Brake, M.R.: The tribomechadynamics research challenge. In 40th International Modal Analysis Conference (IMAC-XL), p. 3 (2022)
16. Abaqus Analysis User's Guide (2014)

Chapter 20
A Novel Approach for Local Structural Modification of Nonlinear Structures

E. Ceren Ekinci, M. Bülent Özer, and H. Nevzat Özgüven

Abstract Structural modification methods provide powerful tools to calculate the dynamic behavior of a modified structure from that of the original one. In general, either the modal properties or responses of the original structure are used to calculate the responses of the modified system. These methods reduce the computational efforts drastically compared to a complete system re-analysis, especially when the modification is local. However, such methods do not apply to nonlinear systems due to response-dependent nature of the frequency response functions (FRFs). One of these methods for linear systems, called the "matrix inversion method," uses the FRFs of the original structure and the spatial properties of the modification to estimate the FRFs of the modified system. Recently, a new method utilizing the response-controlled step-sine testing (RCT) approach was proposed for obtaining the quasi-linear FRFs and response-dependent modal properties of nonlinear structural systems. Full-duality between the quasi-linear constant amplitude FRFs and the nonlinear constant force FRFs was shown around the nonlinear structure's resonance frequencies. In this chapter, a novel structural modification approach is proposed, which utilizes the matrix inversion method (so far used to modify only linear systems) and the RCT-based quasi-linear FRFs of the nonlinear structure. This approach enables obtaining the modified structure's quasi-linear FRFs, similar to the linear system structural modification problem. Combining the matrix inversion method for linear systems with the RCT approach enables the efficient calculation of receptances of structures with local nonlinearities placed around response-controlled degree of freedom, or when the modifications are such that the mode shapes do not change significantly, even if the nonlinearity is distributed.

Keywords Nonlinear structural modification · Modified system response · Structural nonlinear re-analysis · Response-controlled step-sine testing

20.1 Introduction

Although almost every mechanical structure displays some degree of nonlinearity, in most cases, when the response levels are low, nonlinearities can be disregarded. Hence, for practical simplicity, the system is analyzed as if it is linear. For linear systems, analysis at one forcing level is sufficient to calculate receptances. However, for nonlinear systems, the response is amplitude-dependent and a different response behavior can occur for different forcing levels, making the analysis of nonlinear systems quite burdensome [1–7]. Similarly, experimental studies on systems with structural nonlinearities also have some difficulties. With traditional experimental methods, system responses are measured through a frequency sweep under the action of a constant force. This procedure runs into difficulties around the jump regions, which may be observed in the frequency response of nonlinear systems. In that case, the frequency resolution of the experiment should be increased around the jump frequency, and sophisticated control and measurement devices should be used especially if the unstable region of the response needs to be captured. In a recent work of Karaağaçlı and Özgüven [8], a new technique for the determination of nonlinear system behavior is developed. With this method, the experiment is conducted under constant response amplitude of the excitation point, and the corresponding force is measured. The proposed method results in quasi-linear receptances and full-duality between constant response and constant forcing receptances have been demonstrated. This method allows a better understanding of jump frequencies and unstable regions than the other experimental methods with much less complicated control and measurement equipment.

E. Ceren Ekinci (✉) · M. Bülent Özer · H. Nevzat Özgüven
Department of Mechanical Engineering, Middle East Technical University, Ankara, Turkey
e-mail: ceren.ekinci@metu.edu.tr; ozerb@metu.edu.tr; ozguven@metu.edu.tr

M. R. W. Brake et al. (eds.), *Nonlinear Structures & Systems, Volume 1*, Conference Proceedings of the Society for Experimental Mechanics Series, https://doi.org/10.1007/978-3-031-36999-5_20

It is very common in engineering practice that the numerical model is updated as a result of experimental identification of a structural system or sometimes due to changes needed on the physical structure. It is computationally highly advantageous not to perform a full-scale resolution of the model due to updates in the model. For linear systems, these changes in the system can be implemented on the response with modification techniques through either modal parameters [9, 10] or frequency response functions in a computationally efficient manner [11]. The direct applications of these efficient updating approaches on nonlinear structural models are not straightforward [12–16]. Arslan and Özgüven [12] proposed a method for updating nonlinear structures when the nonlinearity is localized. This chapter intends to extend Arslan and Özgüven's work through application of the method to local and distributed nonlinearities. This is achieved by merging the RCT approach with the matrix inversion method [12]. Since RCT allows one to obtain the quasi-linear FRFs of the original system, the matrix inversion method can be employed on the constant response level quasi-linear frequency responses. With the use of modal properties of each response level, the response of the system under the action of the constant force is calculated. The approach is verified with a case study, which includes a system with more than one nonlinear element in the updated structural model. The method works accurately and efficiently around a modified system mode when the modifications do not significantly change the mode shape of the original system.

20.2 Theory

The equation of motion of an MDOF nonlinear system is as follows:

$$[M]\ \{\ddot{x}\} + [C]\ \{\dot{x}\} + [K]\{x\} + \{f_N(x)\} = \{f\} \tag{20.1}$$

where $[M]$, $[C]$, $[K]$ are mass, damping, and stiffness matrices; $\{f_N(x)\}$ is the nonlinear internal force vector and $\{f\}$ is external forcing vector.

From describing function method [3], a matrix $[\Delta]$ to represent the nonlinear forces as an equivalent (response level dependent) stiffness can be obtained.

$$[M]\ \{\ddot{x}\} + [C]\ \{\dot{x}\} + [K]\{x\} + [\Delta]\{x\} = \{f\} \tag{20.2}$$

When a harmonic excitation $\{f\}$ is applied to the system, the response $\{x\}$ will also be harmonic with the same frequency. Then, the equation of motion can be arranged as follows:

$$\{f\} = \{F\} \cdot e^{i\omega t} \tag{20.3}$$

$$\{x\} = \{X\} \cdot e^{i\omega t} \tag{20.4}$$

$$\left[-\omega^2 \cdot [M] + i\ \omega\ [C] + [K] + [\Delta]\right]\{x\} = \{F\} \tag{20.5}$$

With response-controlled step-sine testing, $[\Delta]$ becomes constant in operating frequency and acts like a stiffness term. As a result, quasi-linear FRFs of the corresponding response level are formed.

When the nonlinearity is only on the response-controlled DoF (degree of freedom), modifications do not induce a change in $[\Delta]$ for each response level. Similarly, when the mode shapes do not change significantly after the alterations, there are no major variations on modified system's describing function $[\Delta]$. As a result, when the structural modification affects the linear elements, structural modification methods can be applied to quasi-linear FRFs.

According to the method proposed by Özgüven [13], when a linear system is subjected to structural modifications, the FRFs of the modified system can be found with the help of unmodified system FRFs and modification matrix or dynamic stiffness matrix, which consists of the changes in stiffness, mass, and damping.

$$[\gamma] = [[I] + [\alpha]\ [\Delta D]]^{-1}\,[\alpha] \tag{20.6}$$

In case the modification is local, receptance and modification matrices are rearranged and divided into four parts, corresponding to modified and unmodified DoFs. Thus, the computational effort is reduced significantly due to inversion of a smaller matrix.

$$[\alpha] = \begin{bmatrix} [\alpha_{mm}] & [\alpha_{mu}] \\ [\alpha_{um}] & [\alpha_{uu}] \end{bmatrix} \tag{20.7}$$

$$[\Delta D] = \left[[\Delta K] - \omega^2 \ [\Delta M] + i \ \omega \ [\Delta C] \right] \tag{20.8}$$

$$[\Delta D] = \begin{bmatrix} [\Delta D]_{mm} & 0 \\ 0 & 0 \end{bmatrix} \tag{20.9}$$

$$[\gamma_{mm}] = \left[[I] + [\alpha_{mm}] \ [\Delta D]_{mm} \right]^{-1} [\alpha_{mm}] \tag{20.10}$$

After obtaining quasi-linear FRFs of the modified system, modal properties corresponding to each response level are computed. From peak amplitude method, resonance peak value and resonance peak frequency are obtained. From the peak value, half power points are also detected. Thus, modal damping and modal constant of the r-th mode is

$$\gamma_r = \frac{\omega_1^2 - \omega_2^2}{2 \cdot \omega_r^2} \tag{20.11}$$

$$A_{ij_r} = \left|\alpha_{ij}\right|_{\max} \cdot \gamma_r \cdot \omega_r^2 \tag{20.12}$$

where γ_r and A_{ij_r} are modal damping and modal constant values of r-th mode, ω_1 and ω_2 are the frequencies of half power points, ω_r is the resonance frequency of r-th mode, $|\alpha_{ij}|_{\max}$ is the maximum value of the receptance on the corresponding mode.

For an n-DoF system, the receptance of any DoF can be obtained as follows:

$$\alpha_{ij}(w, x_i) = \sum_{r=1}^{n} \frac{A_{ij_r}}{\left((\omega_r(x_i))^2 - \omega^2 + i \ \left((\omega_r(x_i))^2\right) \cdot \gamma_r(x_i)\right)} \tag{20.13}$$

As long as the modes are well separated, single mode theory can be assumed. FRFs around the first natural frequency become

$$\alpha_{ij}(w, x_i) = \frac{A_{ij}}{\left((\omega_r(x_i))^2 - \omega^2 + i \ \left((\omega_r(x_i))^2\right) \cdot \gamma_r(x_i)\right)} \tag{20.14}$$

Once the modal properties related to each response level are known, receptances for a specific forcing can be calculated iteratively over a frequency range.

20.3 Case Studies

For the validation of the suggested method, a simulated experiment is conducted for the following 5 DoF system with local cubic stiffness nonlinearities. Mass and stiffness of the first and second DoFs are exposed to modifications.

The system parameters are given as follows:

$$[M] = \begin{bmatrix} 1 & 0 & 0 & 0 & 0 \\ 0 & 1 & 0 & 0 & 0 \\ 0 & 0 & 1 & 0 & 0 \\ 0 & 0 & 0 & 1 & 0 \\ 0 & 0 & 0 & 0 & 1 \end{bmatrix} \text{ kg}, \qquad [C] = \begin{bmatrix} 10 & -5 & 0 & 0 & 0 \\ -5 & 10 & -5 & 0 & 0 \\ 0 & -5 & 10 & -5 & 0 \\ 0 & 0 & -5 & 10 & -5 \\ 0 & 0 & 0 & -5 & 10 \end{bmatrix} \frac{\text{N.s}}{\text{m}}$$

$$[K] = \begin{bmatrix} 2 & -1 & 0 & 0 & 0 \\ -1 & 2 & -1 & 0 & 0 \\ 0 & -1 & 2 & -1 & 0 \\ 0 & 0 & -1 & 2 & -1 \\ 0 & 0 & 0 & -1 & 2 \end{bmatrix} \times 10^4 \frac{\mathrm{N}}{\mathrm{m}}$$

The nonlinear element on the system is a cubic stiffness with the value

$$k^* = 1 \times 10^6 \frac{\mathrm{N}}{\mathrm{m}^3}$$

The modifications implemented on the system, which is shown with red lines in Fig. 20.1, are as follows:

$$[\Delta M] = \begin{bmatrix} 0.5 & 0 \\ 0 & 0.5 \end{bmatrix} \mathrm{kg} \qquad [\Delta K] = \begin{bmatrix} 10000 & -5000 \\ -5000 & 5000 \end{bmatrix} \frac{\mathrm{N}}{\mathrm{m}}$$

A simulated experiment for the system is carried out for a range of constant response amplitudes, and quasi-linear FRFs are calculated for each response level of the original system (system without the red components in Fig. 20.1). Receptance of each response level is placed in structural modification with matrix inversion equation (Eq. 20.6), and receptance of the modified system is computed accordingly. Modal damping, resonance frequency, and modal constant values are extracted from the quasi-linear FRFs.

To verify the results represented in the case study, a full re-analysis of the modified system (with the red components in Fig. 20.1) is conducted through response-controlled step-sine testing method with a simulated experiment. The results of the modified system's response obtained with the response-controlled step-sine testing method are labeled as "Calculated with RCT method" in Figs. 20.2 and 20.3. Resonance frequencies are calculated with both response-controlled step-sine testing and structural modification for nonlinear systems method, which is proposed in this chapter and is labeled as "Calculated with matrix inversion method." Change of resonance frequency with respect to constant response level due to nonlinear elements is given in Fig. 20.2. As seen from this figure, the method provides a good estimate for local nonlinearities.

Previously, it was mentioned that full-duality between the constant response amplitude FRFs and constant force amplitude FRFs is possible. Hence, using the modal properties calculated with the method for each response level, the direct point FRF of the first mode of the modified system for different excitation forcing levels can be calculated. Figure 20.3 represents the calculated constant forcing amplitude FRFs at forcing levels between 10 N and 50 N. The constant forcing FRFs are calculated using the RCT solver with the mass and stiffness matrices of the modified system, and also using the structural modification with matrix inversion method, which modifies the original system's receptance matrix with a modification matrix **[D]** expressed in terms of dynamic stiffness matrix of the modifying system. It can be clearly seen from Figs. 20.2 and 20.3 that the agreement between the results is pretty good, which shows that quasi-linear receptance matrices obtained from the RCT method enable one to implement structural modification with matrix inversion method, which has significant computational advantages, especially when the nonlinear system is large and modifications affect a small number of DoFs.

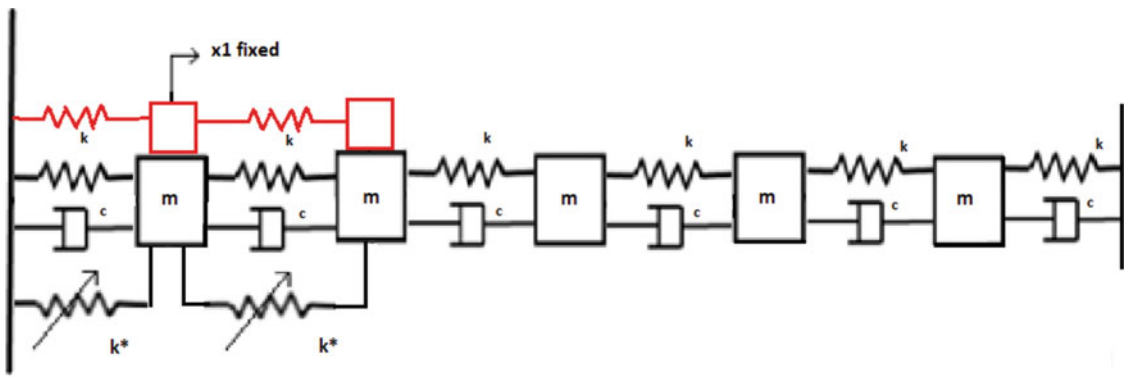

Fig. 20.1 The system analyzed in case study

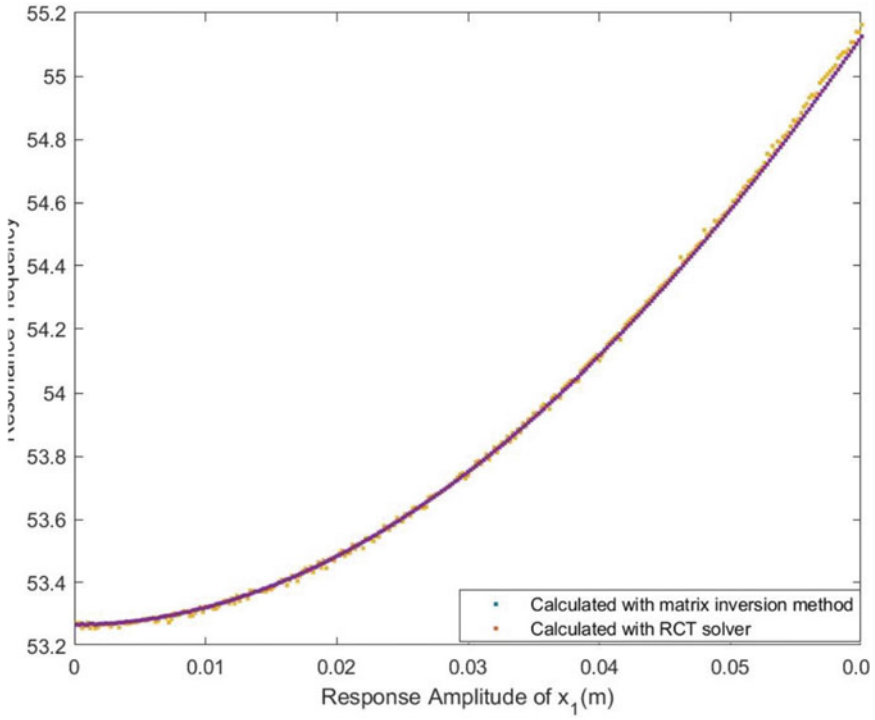

Fig. 20.2 Resonance frequency with respect to response level

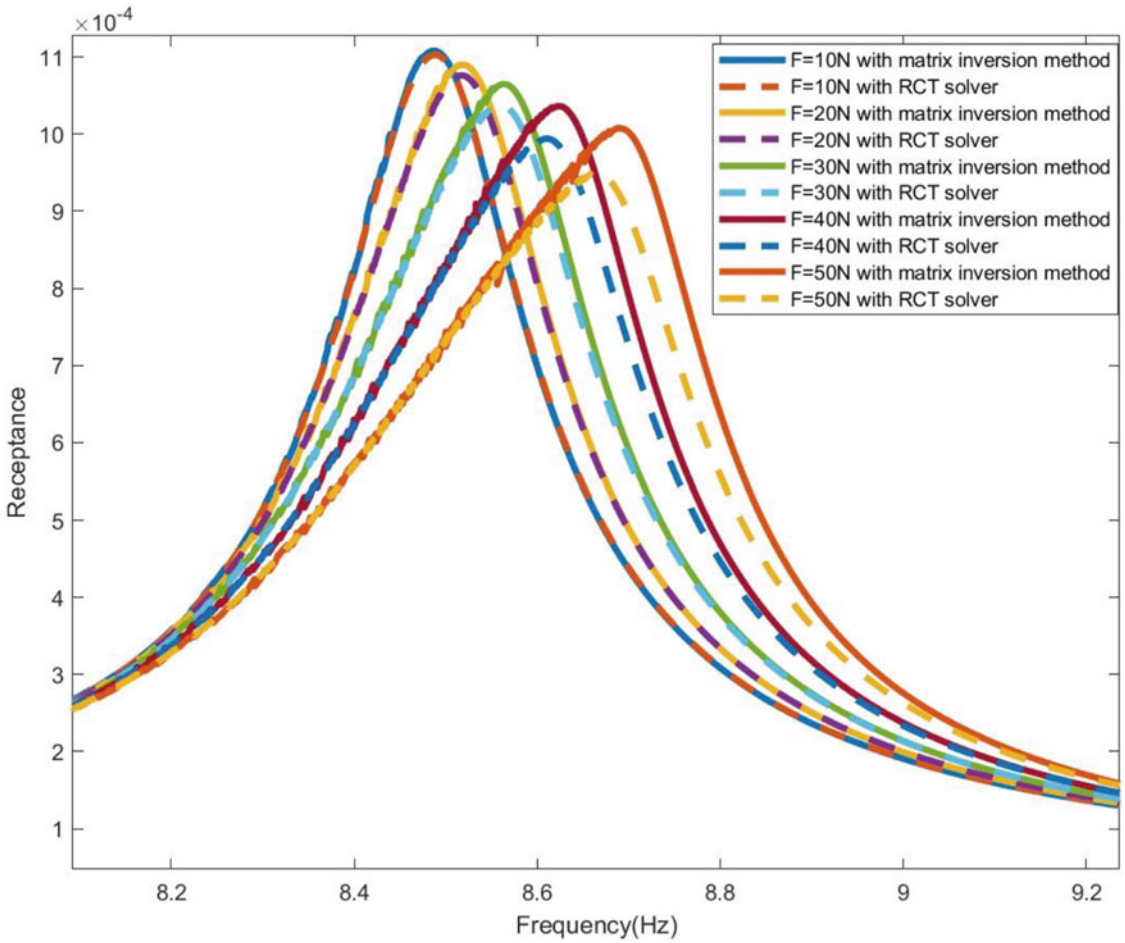

Fig. 20.3 FRF of modified system around resonance frequency

20.4 Conclusions

In [12], it is shown that when there is only one nonlinear element in a linear system, and the response control step-sine testing is conducted from the nonlinear DoF, response found from structural modification with matrix inversion method is exact, when there is more than one nonlinearity in the system, which is placed locally around the controlled DoF, as shown in the case study, the method proposed in this study gives a good estimate for the modified system's response with the use of quasi-linear receptances obtained from response-controlled step-sine testing (RCT) approach. Consequently, the proposed method gives quite accurate results even if there is more than one nonlinearity in the system provided that the modifications in the system do not change the mode shape of the corresponding mode significantly. The slight differences in the responses obtained by direct analysis of the modified system and by applying the structural modification method proposed in this study are believed to be due to minor changes in the mode shape of the original system due to employed structural modifications.

References

1. Worden, K.: Nonlinearity in Structural Dynamics: Detection, Identification and Modelling. CRC Press, Boca Raton (2019)
2. Özer, M.B., Özgüven, H.N., Royston, T.J.: Identification of structural nonlinearities using describing functions and the Sherman–Morrison method. Mech. Syst. Signal Process. **23**(1), 30–44 (2009)
3. Tanrikulu, O., Kuran, B., Ozguven, H.N., Imregun, M.: Forced harmonic response analysis of nonlinear structures using describing functions. AIAA J. **31**(7), 1313–1320 (1993)
4. Krack, M., Gross, J.: Harmonic Balance for Nonlinear Vibration Problems. Springer, Cham (2019)
5. Noël, J., Kerschen, G.: Nonlinear system identification in structural dynamics: 10 more years of progress. Mech. Syst. Signal Process. **83**, 2–35 (2017)
6. Kuran, B., Özgüven, H.: A modal superposition method for nonlinear structures. J. Sound Vib. **189**(3), 315–339 (1996)
7. Ferhatoglu, E., Cigeroglu, E., Özgüven, H.N.: A novel modal superposition method with response dependent nonlinear modes for periodic vibration analysis of large MDOF nonlinear systems. Mech. Syst. Signal Process. **135**, 106388 (2020)
8. Karaağaçlı, T., Özgüven, H.N.: Experimental modal analysis of nonlinear systems by using response-controlled stepped-sine testing. Mech. Syst. Signal Process. **146**, 107023 (2021)
9. Herrada, F., García-Martínez, J., Fraile, A., Hermanns, L., Montáns, F.: A method for performing efficient parametric dynamic analyses in large finite element models undergoing structural modifications. Eng. Struct. **131**, 625–638 (2017)
10. Khader, N.: Structural dynamic modification to predict modal parameters of multiple beams. In: Residual Stress, Thermomechanics & Infrared Imaging, Hybrid Techniques and Inverse Problems, vol. 8, pp. 365–377. Springer, Cham (2013)
11. Nevzat Özgüven, H.: Structural modifications using frequency response functions. Mech. Syst. Signal Process. **4**(1), 53–63 (1990)
12. Arslan, Ö., Özgüven, H.: Modal identification of non-linear structures and the use of modal model in structural dynamic analysis. In: Conference Proceedings of the Society for Experimental Mechanics Series (2008)
13. Kalaycıoğlu, T., Özgüven, H.: Dynamic decoupling of nonlinear systems. In: 35th International Modal Analysis Conference – IMAC 35. Springer, Cham (2017)
14. Kalaycıoğlu, T., Özgüven, H.: Experimental verification of a recently developed FRF decoupling method for nonlinear systems. In: Dynamics of Coupled Structures. Springer, Cham (2018)
15. Kalaycıoğlu, T., Özgüven, H.: Nonlinear structural modification and nonlinear coupling. Mech. Syst. Signal Process. **46**, 289 (2014)
16. Chong, Y., Imregun, M.: Coupling of non-linear substructures using variable modal parameters. Mech. Syst. Signal Process. **14**(5), 731–746 (2000)

Chapter 21
Model Validation of a Modular Foam Encapsulated Electronics Assembly with Controlled Preloads via Additively Manufactured Silicone Lattices

Tanner Ballance, Bryce Lindsey, Daniel Saraphis, Moheimin Khan, Kevin Long, Sharlotte Kramer, and Christine Roberts

Abstract Traditional electronics assemblies are typically packaged using physically or chemically blown potted foams to reduce the effects of shock and vibration. These potting materials have several drawbacks including manufacturing reliability, lack of internal preload control, and poor serviceability. A modular foam encapsulation approach combined with additively manufactured (AM) silicone lattice compression structures can address these issues for packaged electronics. These preloaded silicone lattice structures, known as foam replacement structures (FRSs), are an integral part of the encapsulation approach and must be properly characterized to model the assembly stresses and dynamics. In this study, dynamic test data is used to validate finite element models of an electronics assembly with modular encapsulation and a direct ink write (DIW) AM silicone FRS. A variety of DIW compression architectures are characterized, and their nominal stress-strain behavior is represented with hyperfoam constitutive model parameterizations. Modeling is conducted with Sierra finite element software, specifically with a handoff from assembly preloading and uniaxial compression in Sierra/Solid Mechanics to linear modal and vibration analysis in Sierra/Structural Dynamics. This work demonstrates the application of this advanced modeling workflow, and results show good agreement with test data for both static and dynamic quantities of interest, including preload, modal, and vibration response.

Keywords Electronics packaging · Additive manufacturing · Foams · Model validation · Vibration

21.1 Introduction

Electronic assemblies are among the most sensitive engineering hardware and their performance can be impacted heavily by damage induced by shock and vibration. Traditionally, techniques to protect electronic assemblies in harsh vibration environments typically involve the use of physically or chemically blown potted foams. While these techniques can be robust against vibration damage, some sacrifices are made for this protection. First, once an electronic assembly is potted, servicing the assembly in the cases of short circuits, loose contacts, or broken solders can be difficult or impossible as the assembly is completely encased by the potting material. Another downfall of this technique is manufacturing reliability. During the potting, many factors can play a role on how the assembly will respond to vibrations including curing temperature, chemical composition, and stresses generated by the curing or blowing of the potting material. Optimizing all these factors to achieve a desired response under vibrations poses a complex problem. If the blown foam generates too high of a pressure within the assembly, either through improperly chosen temperatures, densities, or chemistry, unwanted preload of the electronics can occur. With a lack of control on the preload of the electronics, mode shapes and resonances will be impossible to predict. To address these issues, a modular encapsulation approach is utilized in conjunction with additively manufactured (AM) silicone

T. Ballance
Purdue University, West Lafayette, IN, USA

B. Lindsey
Oklahoma State University, Stillwater, OK, USA

D. Saraphis
The University of North Carolina at Charlotte, Charlotte, NC, USA

M. Khan (✉) · K. Long · S. Kramer · C. Roberts
Sandia National Laboratories, Albuquerque, NM, USA
e-mail: mkhan@sandia.gov

M. R. W. Brake et al. (eds.), *Nonlinear Structures & Systems, Volume 1*, Conference Proceedings of the Society for Experimental Mechanics Series, https://doi.org/10.1007/978-3-031-36999-5_21

lattice compression structures, also known as foam replacement structures (FRSs) [1]. The modular encapsulation approach offers three major advantages: (1) reduces the effort required to access assembled electronics, (2) drastically increases manufacturing repeatability, and (3) provides reasonable control on the preload conditions experienced by the electronics. This approach accomplishes these objectives by taking advantage of AM techniques and design-oriented packaging.

Before these structures can be used in place of traditional techniques, the silicone lattice FRS must be properly characterized under preloaded conditions. Being a vital part of this alternative encapsulation technique, the FRS behavior will dictate the stresses and dynamics in the assembly. Essentially acting as a control input, the lattice structure and thickness of the silicone elastomeric material can affect not only the frequency of the dominant modes but also the magnitude of the response. Modifying the FRS thickness, lattice spacing, and angle can result in a different stiffness and as a result a different modal and vibration response

In this work, finite element (FE) models of an electronic assembly of microcontrollers (Raspberry Pi's) with modular encapsulation and direct ink write (DIW) printed silicone structures are validated with static and dynamic test data. To ensure a reasonable computation time, the silicone lattice structures were homogenized as a bulk hyperfoam material. A variety of FRSs are analyzed to ensure the hyperfoam model parameters properly capture the nominal stress-strain behavior of the DIW FRS. The modeling was conducted using the Sierra finite element software suite, where uniaxial compression was carried out in Sierra/Solid Mechanics (Sierra/SM) [2] and linear modal and vibration analysis was carried out in Sierra/Structural Dynamics (Sierra/SD) [3]. The structure of this chapter is as follows: description of the hardware used in modeling and experiments, material parameterization, experimental methods, the specific simulations carried out along with results, and, finally, discussion and conclusions made about the validity of the finite element model.

21.2 Geometry

The assembly of interest is composed of an aluminum enclosure consisting of a housing and lid, with electronics components encapsulated within the enclosure and by hyperelastic foams. The assembly is roughly 7 inches by 7 inches by 4 inches and is shown in Fig. 21.1.

Figure 21.2 shows a cross section of the assembly with the individual components labeled.

The layout of the electronics within the assembly can be seen in Fig. 21.3. Stripping away the middle foam layers shows the four Raspberry Pi Zeros and cable connectors. The Pi's are mounted at each corner using steel rods that extend from the

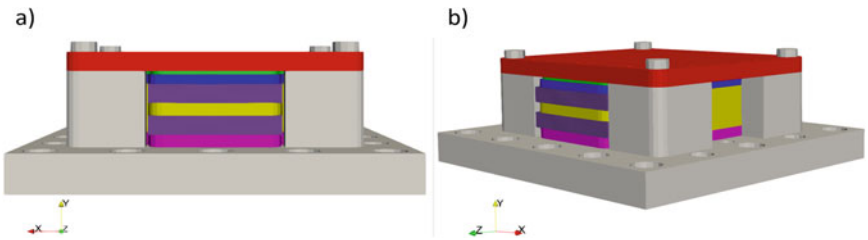

Fig. 21.1 Assembly side view (**a**) and isometric view (**b**)

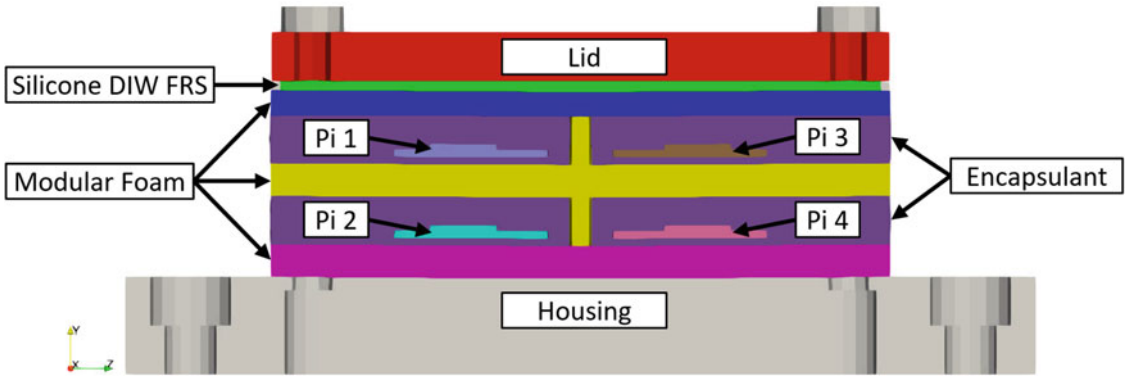

Fig. 21.2 Assembly cross section with labeled components

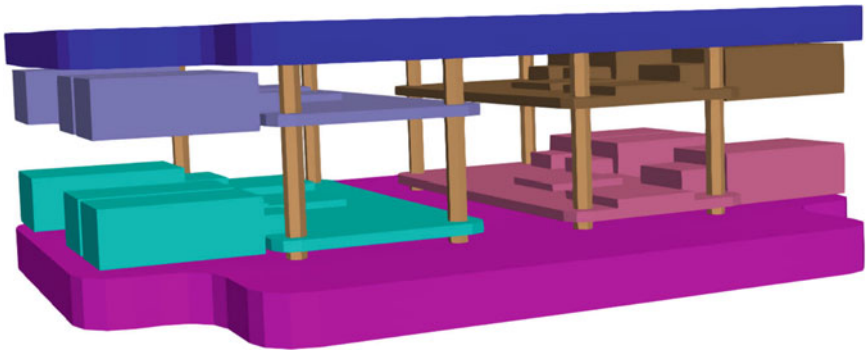

Fig. 21.3 Raspberry Pi's (4) within the assembly

Table 21.1 Material elastic properties

Name	Material	Young's modulus (psi)	Poisson ratio
Enclosure	Aluminum	10×10^6	0.33
Raspberry Pi	FR4	4.35×10^6	0.30
Modular foam	PMDI	12.8×10^3	0.25
Encapsulation	Sylgard(R)184	366	0.4995

housing plate. The Pi's are protected by the modular foam layers and an elastomeric encapsulant. The assembly is closed using the DIW FRS under pressure to maintain layer contact.

21.3 Materials

Several materials with very different mechanical properties are used within the assembly. All materials are treated as homogenous continua including the DIW lattices (as direct numerical simulation of the lattice struts was prohibitively computationally expensive). Table 21.1 summarizes some of the nominal elastic properties of the materials used in the analyses.

For both the Sierra/SM and Sierra/SD simulations, the aluminum enclosure material is modeled as linear elastic. The encapsulated Raspberry Pi's and connectors are approximated as a single linear isotropic FR4 circuit board material, and details of individual circuit elements, connectors, and solder connections are ignored.

The rigid internal foams are also treated as linear elastic with properties that correspond to an 11 pound per cubic foot rigid polymeric methylene diisocyanate (PMDI) foam. It is worth noting that the rigid foams studied here have yield strengths depending on density, so our analyses are only valid for stress states below yield of approximately 400 psi at room temperature [4]. The DIW lattice material is modeled with a hyperelastic, compressible Ogden model (hyperfoam), which is suitable for representing the rate independent mechanical behavior of compressible materials [5]. Rate effects from viscoelasticity or pneumatic effects (air flow through the lattice) are not considered. We note that the lattice structures are always at most of cubic symmetry or lower, but we are focused on the uniaxial preloading response in this work and think an isotropic representation is reasonable. Details of the hyperfoam fit are provided in the following section. In the Sierra/SM simulation, the solid siloxane encapsulation was modeled with the Gent model [6] using a locking parameter of 3.65. This was simplified to a hyperelastic Neo-Hookean model for the structural dynamic simulations, which we think is suitable, since the encapsulation is only expected to achieve moderate strains. The bulk and shear moduli for the Sylgard(R) 184 encapsulation were obtained from [7]. Finally, we note that the material properties and constitutive models are fully consistent between the structural mechanics and structural dynamics simulations for the hyperfoam models. A linearized material tangent stiffness based on the hyperfoam parameters from the material fit is utilized such that no new properties are defined when handing off the preloaded state to perform the modal and frequency response analyses.

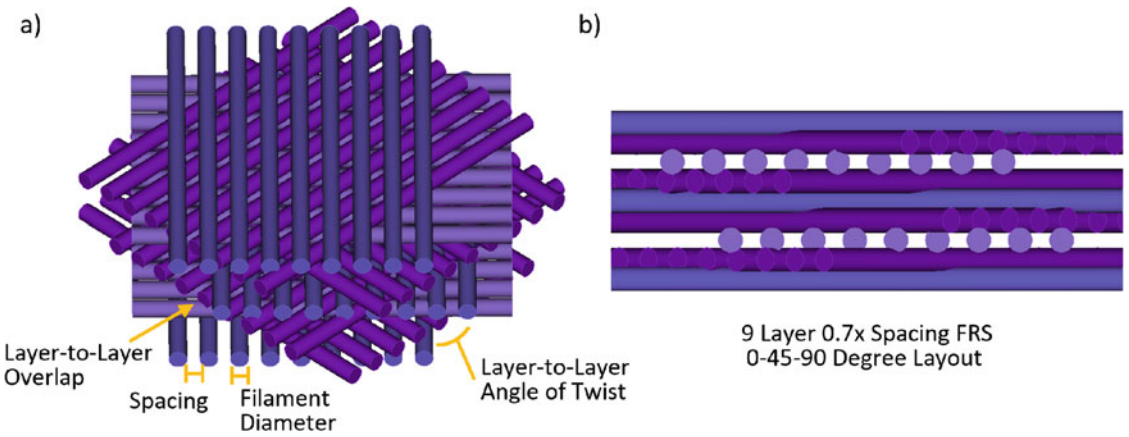

Fig. 21.4 Direct ink write silicone lattice structures (**a**) isometric view showing the printing parameters and (**b**) side view of 9 layer 0.7× spacing and 20% overlap 0-45-90-degree FRS

21.4 Homogenized Material Paramaterization for DIW Lattice Structures

A sufficiently accurate model for the 3D printed DIW silicone lattice structures that can represent preloads and the steady-state vibration response of the assembly is required. Ideally, direct numerical simulation of the lattice would be included in the assembly model whereby the solid material would be represented either as a solid elastomer continuum or as a collection of beams. Either form of direct numerical simulation (DNS) was too expensive or full of additional challenges (beam on beam contact as well as short beam formulations). So, our approach was to homogenize the mechanical behavior of the DIW silicone lattice structures with the hyperfoam model mentioned in the previous section. That is, we fit the experimental uniaxial compression stress versus strain (engineering) data at slow strain rates with the hyperfoam model. This exercise is trivial, but optimized parameter outputs often are unstable (lead to imaginary sound speeds as evidenced by negative eigenvalues of the acoustic tensor). So, we followed a procedure to fit each individual lattice separately and during the fitting process to check extensively if, under many different states of deformation, the material would have an acoustic tensor with negative or zero eigenvalues. Our procedure followed prior work detailed in [8].

A schematic of the DIW lattice structures with associated design parameters is shown in Fig. 21.4 which defines the printing parameters that control the lattice construction: the filament diameter, filament spacing, overlap, angle of each layer, and the number of layers in the thickness direction.

Lattices analyzed here have a specific layup wherein each subsequent layer is rotated 45 degrees from the previous layer along the thickness direction. In all cases, 8-, 9-, and 11-layer structures were printed following the procedure outlined in [1]. Stiffer structures were of interest, so the filament spacing considered ranged from 0.7 to 0.9 times the filament diameter, and in certain cases, overlap between layers (which is nominally around 20%) was decreased to 12%. Despite different geometries, the different lattices showed two families of responses as shown in Fig. 21.5a with several repeats with highly stiff lattices realized for the 8-layer, 0.7 spacing and more compliant lattices realized for the other printing parameters. Although close, it is worth noting that the lattice structures are not size converged. That is, for the same filament diameter and layer spacing, different numbers of layers produce slightly different nominal stress versus strain relations. Consequently, each set of printing parameters must be fit with an individual model. All curves in Fig. 21.5a were fit following the procedure in [8], and a curve of relevance used in the experiments is shown in Fig. 21.5b.

21.5 Experimental Methods

Several units in various assembly configurations were tested, two of which are discussed here. These two nominally identical units were tested to assess unit-to-unit variability. Both quasistatic and dynamic testing was done to experimentally characterize the assemblies. First, the units were assembled and preloaded using a uniaxial testing machine. Load-displacement behavior of each assembly was recorded for various thicknesses of the DIW silicone lattice FRS as shown in Fig. 21.6. The 0.0875-inch thick FRSs are the focus of this work.

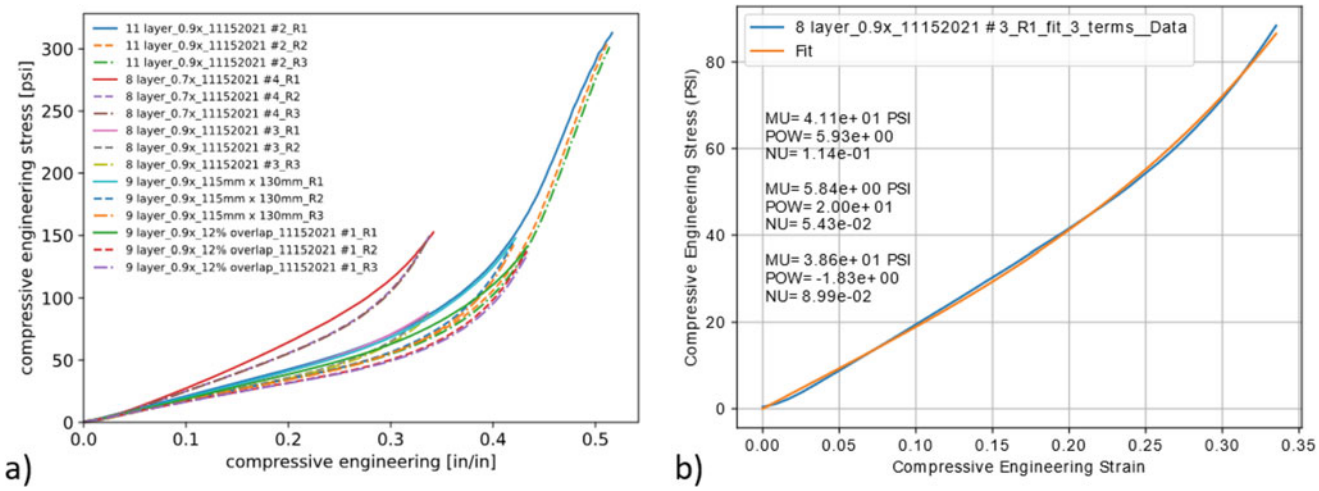

Fig. 21.5 0-45-90 layups of 8-, 9-, and 11-layer lattice structures with different layer spacings, layer-to-layer overlaps, and repeats (**a**). A stabilized hyperfoam fit of the 8-layer, 0.9 spacing lattice used in subsequent subassembly preload and steady-state vibration simulations (**b**)

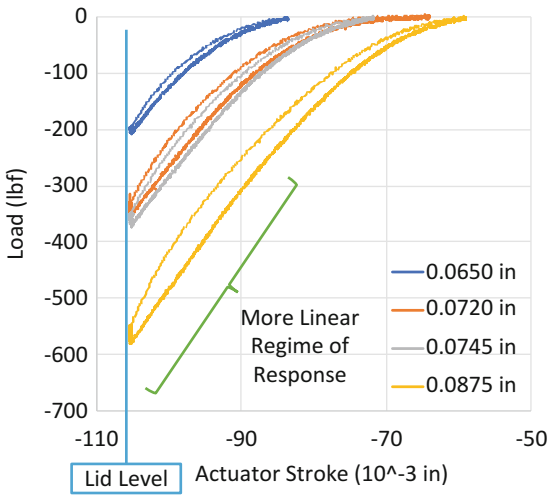

Fig. 21.6 Test load-displacement curves for various FRS thicknesses

Following the compression to lid level, the bolts for each of the units were torqued down to retain the lid preload. After the assembly preload, free-free modal testing was conducted. Triaxial accelerometers were placed on the external metal housing as well as a single uniaxial accelerometer on each of the four Raspberry Pi's, as shown in Fig. 21.7. The first three experimentally measured free-free mode frequencies and damping ratios are summarized in Table 21.2. The second mode (bottom plate drumming) is emphasized as it is the primary mode of interest for this work.

Uniaxial vibration testing was also conducted on each assembly using an electrodynamic shaker. An image of the test setup is shown in Fig. 21.8. A low-level random vibration was applied to the base of the assembly, corresponding to the *Y*-direction in Fig. 21.2. The in-axis acceleration response of the Raspberry Pi's was measured using the same uniaxial sensor as in the modal test.

21.6 Finite Element Analysis

A finite element model of the assembly was developed to match the as-tested configurations and the experimental data was used to validate the model. Both static and dynamic simulations were performed based on the experimental procedures discussed in the prior section. A nonlinear Sierra/SM finite element model was used to perform the preloading, and linear modal and random vibration analyses were subsequently performed with Sierra/SD. Figure 21.9 demonstrates this analysis workflow.

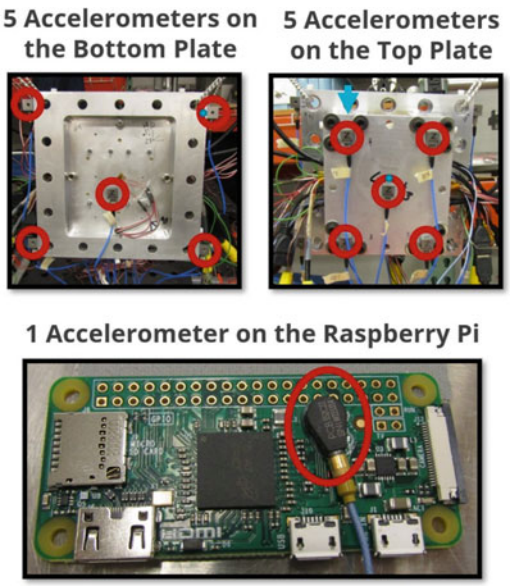

Fig. 21.7 Modal test setup and accelerometer placement

Table 21.2 Free-free modal results for tested units

Mode	Description	Unit 1 freq. (Hz)	Unit 1 damp. (%)	Unit 2 freq. (Hz)	Unit 2 damp. (%)
1	Board out-of-phase bouncing	1233	9.97	1458	6.54
2	Bottom plate drumming	1390	4.84	1526	5.84
3	Assembly torsion	1720	1.02	1716	0.85

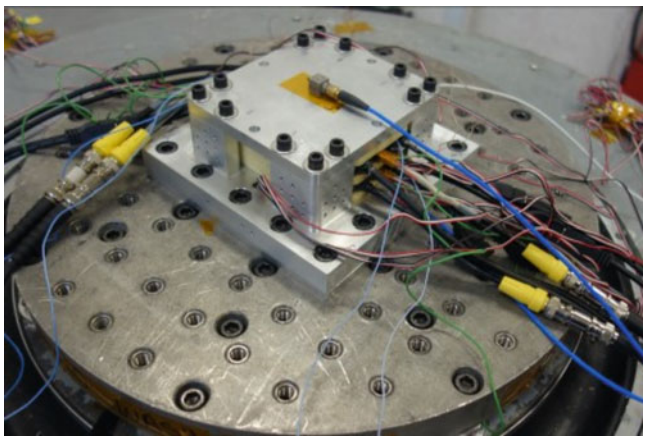

Fig. 21.8 Vibration testing setup

In the SM finite element model, the bottom surface of the assembly was fixed in the direction of loading, and a cosine ramp function was used to prescribe the lid displacement required to close the gap created by the homogenized FRS. Then, an artificial strain was applied to the bolt shanks to close the gap. The SM model is considered quasistatic in that the preload is applied over a long enough time such that the kinetic energy is small with respect to internal energy. The finite element model uses an explicit time-marching algorithm to resolve the preload on the FRS. A selective deviatoric solid element formulation was adopted for the eight-node hexahedral (Hex8) elements defined as solid sections. The strain incrementation was defined to be strongly objective. The model contains approximately 73,000 Hex8 elements for a total of 105,000 nodes. A reference image of the assembly showing the scale of the element size is provided in Fig. 21.10. CUBIT meshing software was used to mesh the assembly [9].

The resulting state of the preloaded SM simulation is handed off and linearized to perform SD simulations. Namely, the material tangent stiffnesses are updated, and the eigenfrequencies, eigenmodes, and system accelerations due to a random input are determined. The boundary condition used in the SD simulation is an applied acceleration to the bottom surface of the enclosure, which coincides with the direction of the height of the assembly. The acceleration is applied to the bottom

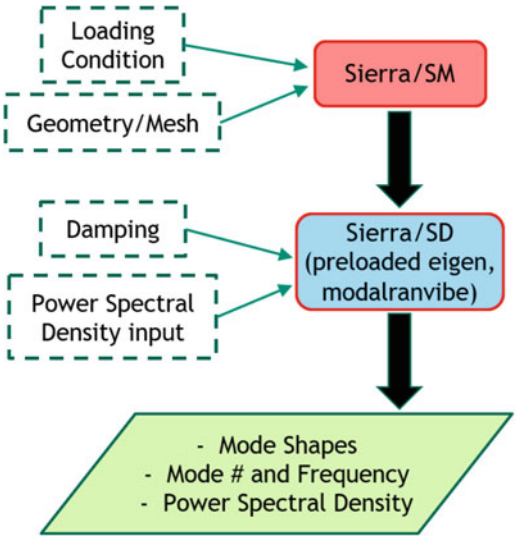

Fig. 21.9 FEA workflow

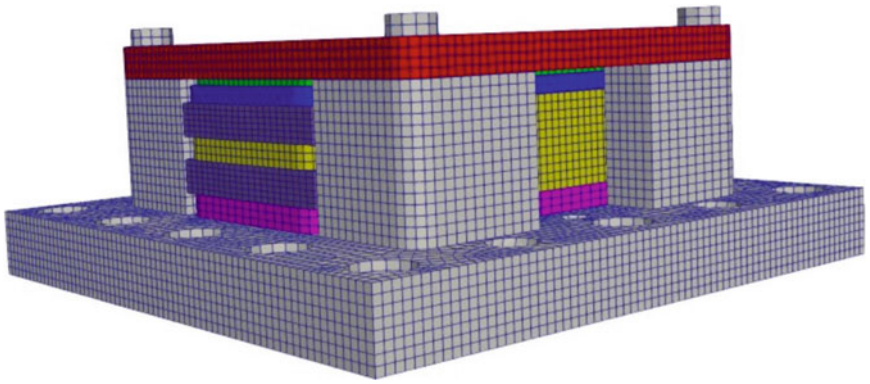

Fig. 21.10 Meshed assembly showing element size relative to total size

surface via a point mass attached to the surface by a rigid bar. The acceleration is specified by assigning a specific mass and magnitude to the point mass. The applied acceleration is modulated between 0 and 2000 Hz with a spectral density amplitude of 0.01 g^2/Hz. The applied acceleration matches the excitation used for experimentation on the assemblies. Fixed-base eigenfrequencies and mode shapes are computed up to 3000 Hz to reduce the effects of modal truncation in the random vibration solution.

The main interest of this work is to validate the model workflow and investigate the effects of preloading the assembly with the DIW FRS on the dynamic response of the electronics. To this end, the main results of interest in the SM simulation were checks to see if the loading and boundary conditions were satisfactory when compared to data from the quasistatic experiments, namely, that the forces used to compress the assembly were consistent with those from experiments. The key information gathered in the SM simulations was comparing force and lid displacement, as well as checks on the contact enforcement, such as contact force and status. As for the subsequent SD analyses, the free-free modes can be compared to the test data for each unit, along with comparisons of acceleration response of the Raspberry Pi's due to fixed-base random vibration input.

21.7 Results

As discussed previously, the focus of the SM analysis was to ensure proper preload of the assembly. This preload was quantified by computing the internal reaction force of the lid as it closed the gap. This force can be compared to the experimentally measured load-displacement behavior, specifically the final preload force. Figure 21.11 shows the lid force versus time and force-displacement behavior during preloading. Results were filtered to 4 kHz using a 4th order Butterworth filter.

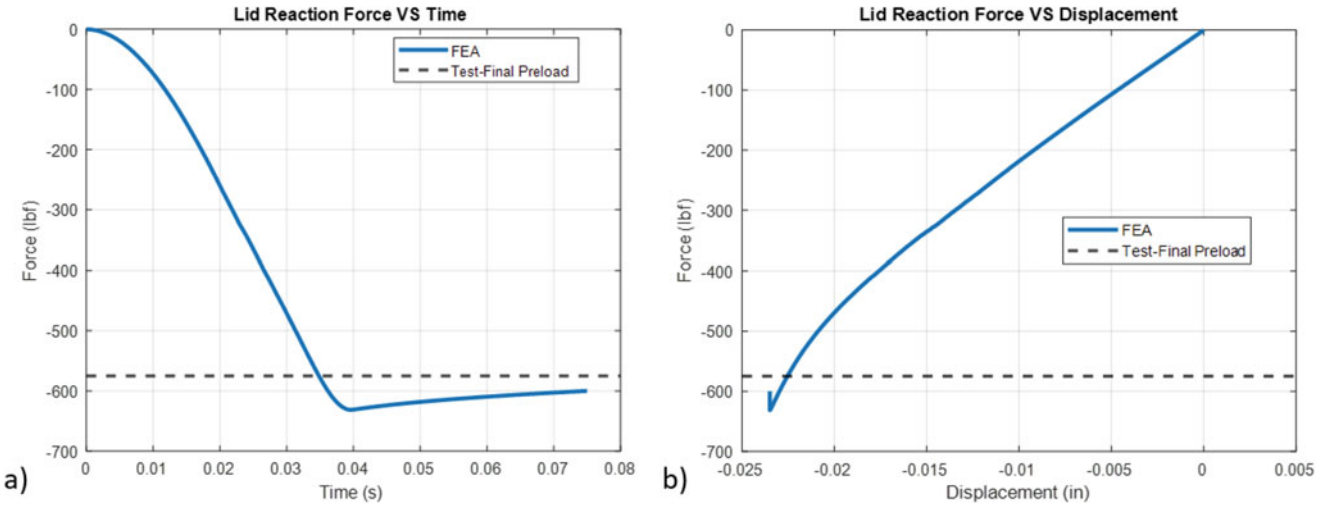

Fig. 21.11 Lid force versus time (**a**) and lid reaction force versus displacement (**b**)

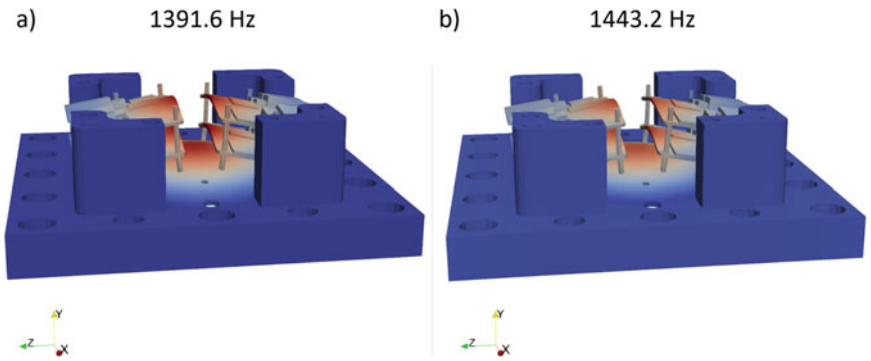

Fig. 21.12 Preloaded fixed-base (**a**) and free-free (**b**) housing drumming mode

At the end of the preloading portion, the lid reaction force reaches close to 650 lb_f and eventually falls back to around 600 lb_f after the settling step of the simulation. Note that longer relaxation of the materials was not considered due to computational limitations; however, this omission would affect the final preload value. Still, the preload value from the SM simulations is close to the experimentally measured value of 575 lb_f for the 0.0875-inch FRS, as given in Fig. 21.6 in the experimental methods section. In addition, the shape of the force-displacement curve resembles test data. Along with the lid force-displacement information, contact checks were performed to ensure proper gap closure, and the resulting preloaded state from the SM simulation was determined to be satisfactory.

Next, the final step from the Sierra/SM simulation was handed off to Sierra/SD, which linearized the preloaded state for computing the modal analysis. Figure 21.12 shows the preloaded fixed-base and free-free housing plate drumming modes of the assembly. The free-free value of 1443 Hz is comparable to the experimental results for the test units 1 and 2- 1390 Hz and 1526 Hz, respectively.

The fixed-base FE modal solution was then used to perform the random vibration analysis using the test loading discussed previously. A value of 2% uniform damping was used in the analysis, with added damping based on the modal test values, for example, with 5% damping applied specifically to the drumming mode of interest. Figure 21.13 shows the comparisons between the FE model and the test data for each unit. Results are presented for two Raspberry Pi's, one at the top (Pi 3) and one at the bottom (Pi 2) of the assembly, matching the layout shown in Fig. 21.2.

The acceleration response of the FE model for both Pi 2 and Pi 3 is consistent with the experimental data for both units. The plots highlight the dominant in-axis response of the drumming mode discussed previously, and the simulation captures that behavior well. Table 21.3 summarizes the free and fixed frequencies for this mode, using the modal data along with peak response frequency as an estimate.

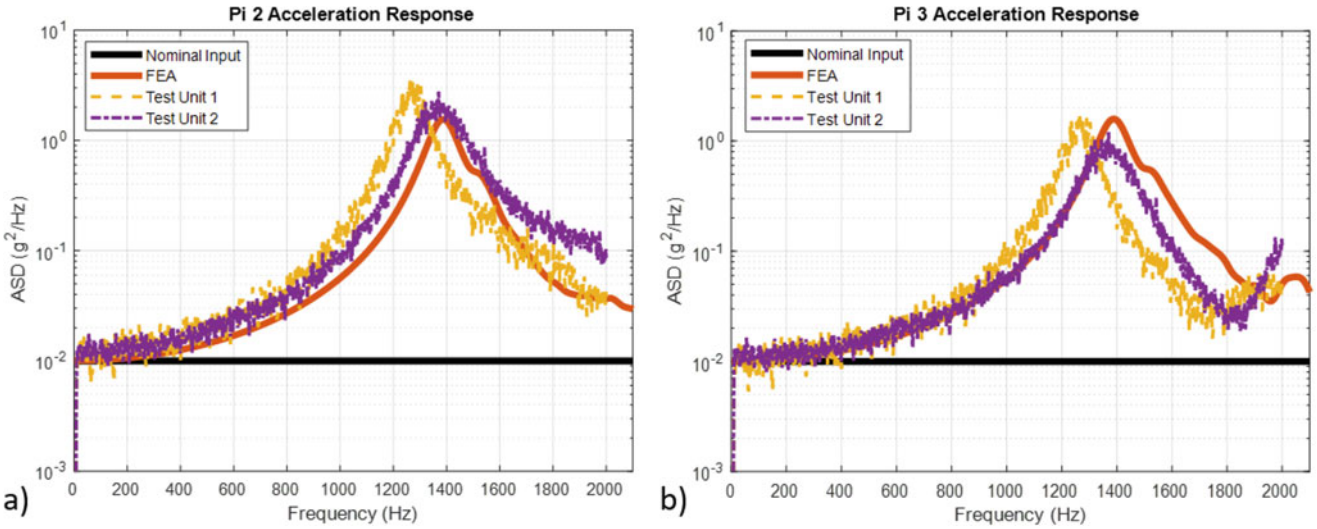

Fig. 21.13 Pi 2 (**a**) and Pi 3 (**b**) acceleration response comparisons

Table 21.3 Drumming mode frequency comparison

Unit	Free-free frequency (Hz)	Fixed-base frequency (Hz)
FE Model	1443	1392
Test unit 1	1390	~1265
Test unit 2	1526	~1370

Although the simulation results do not track either of the tested units exactly, the initial and peak responses are in-family, especially given the observed unit-to-unit variability in the drumming mode frequency and damping. There are some discrepancies at higher frequencies for Pi 3, but it is difficult to make further comparisons, since the vibration data stops at 2 kHz.

It is important to note that the geometry and material simplifications could have contributed to the model being slightly stiff. However, both the static and dynamic analysis results tracked well with the experimental data, providing good validation for the presented modeling workflow for modular foam assemblies with DIW silicone lattices.

21.8 Conclusion

This work presents model validation for an analysis workflow involving an electronics assembly with a modular encapsulation and additively manufactured silicone lattice foam replacement structures. Using homogenized representations of the AM FRS, hyperfoam parameterizations were obtained, and a nonlinear Sierra/SM model was developed, which showed comparable load-displacement behavior to test data during preloading. The preloaded state was handed off to a linearized Sierra/SD model, which accounted for updated material stiffnesses and showed modal and vibration results that matched well with experimental data.

The modular approach for electronic assemblies discussed in this work demonstrates advantages over the traditional techniques due to the ability to control the dynamic response of the electronics. Future work will explore various thicknesses and designs of the lattice structures and investigate the effect of varying levels of preload on the static and dynamic responses of the assembly. Furthermore, additional correlation and test activities could help address the observed discrepancies and improve the model representation.

Acknowledgments This research was conducted at the 2022 Nonlinear Mechanics and Dynamics Research Institute supported by Sandia National Laboratories and hosted by the University of New Mexico. The authors would also like to thank Janelle Lee and Brian Owens for their work on initial design, modeling, and simulation, Steven Carter for the modal testing, and Matthew Campisi for the vibration testing of the assembly.

References

1. Roach, D.J., et al.: Utilizing computer vision and artificial intelligence algorithms to predict and design the mechanical compression response of direct ink write 3D printed foam replacement structures. Addit. Manuf. **41**, 101950 (2021). https://doi.org/10.1016/j.addma.2021.101950. ISSN 2214-8604
2. Sierra Solid Mechanics Team: Sierra/Solid Mechanics 5.10 User's Guide. United States. https://doi.org/10.2172/1886996. https://www.osti.gov/servlets/purl/1886996 (2022)
3. Sierra Structural Dynamics Team: Sierra/SD – User's Manual – 5.10. United States. https://doi.org/10.2172/1887938. https://www.osti.gov/servlets/purl/1887938
4. Lame Team: Library of Advanced Materials for Engineering 5.6, SAND2022-3247 (2022)
5. Storakers, B.: On material representation and constitutive branching in finite compressible elasticity. J. Mech. Phys. Solids. **34**(2), 125–145 (1986)
6. Gent, A.N.: A new constitutive relation for rubber. Rubber Chem. Technol. **69**(1), 59–61 (1996)
7. Long, K.N., Brown, J.A.: A Linear Viscoelastic Model Calibration for Sylgard 184, SAND2017-4555
8. Long, K.N., Hamel, C.M.: Stabilized Hyperfoam Modeling of the General Plastics EF4003 (3 PCF) Flexible Foam. SAND2022-7395R
9. CUBIT Development Team: CUBIT Geometry and Mesh Generation Toolkit 15.8 User Documentation, 2021, SAND2021-5152 W

Chapter 22
Characterizing the Dynamic Response of a Foam-Based Testbed with Material, Geometric, and Experimental Uncertainties

Tariq Abdul-Quddoos, Patrick Lee, Cole Zemelka, Thomas Roberts, Samantha Ceballes, and Scott Ouellette

Abstract Closed-cell polymer foams are commonly employed as support structures to absorb shock and vibration in mechanical systems. Engineering analysts responsible for system designs that incorporate these foams must understand the effects that intrinsic and extrinsic conditions have on their dynamic responses. Parameters intrinsic at the system level, such as preloading and material properties, along with extrinsic environmental parameters, such as forcing energy and frequency, have the potential to drive the system into nonlinear or chaotic regimes. A suite of simulation-based studies is performed utilizing finite element (FE) analysis to investigate both intrinsic and extrinsic model parameters to understand such effects on the nonlinear system dynamics. A high-fidelity FE model of the mass-foam testbed needs to be developed to perform two tasks – implicitly determine stress states from precompression in the foam and explicitly solve for the system's response when subject to various dynamic inputs. Using prior knowledge of stochastic quantities in the model, input parameter distributions will be generated to quantify the influences on the system's dynamic response behavior. An existing testbed consisting of a mass suspended by two pieces of closed-cell polymer foam will be used to perform various experiments for model validation. This project aims to explore the parameter spaces to predict, validate, and confidently bound the nonlinear dynamic behaviors of a system.

Keywords Closed-cell polymer foam · SX358 · Dynamic response · Finite element analysis · Model validation

22.1 Introduction

Closed-cell polymer foams are commonly used in mechanical systems as support structures for shock and vibration absorption. Cellular polydimethylsiloxane (PDMS) produced via room-temperature vulcanization in a blown foam form is one commonly utilized silicone foam material [1]. Silicone foams are produced for nominal compression, so varying compression speed and strain are of interest. Foams exposed to considerable compressive force can exhibit chaotic nonlinear dynamic responses, making their behavior less predictable and harder to model. System level parameters (such as preloading, excitation amplitude, and frequency), along with material and geometric properties (such as thickness and density), have shown to be contributing factors in the nonlinear response of the foam in both simulations and experimental analysis [2].

Multiple analytical methods exist to model the mechanical response and extract characteristics exhibited by foam when exposed to dynamic loading. Curve fitting is a popular method for estimating parameters for analytical models. Hereditary models and fractional derivative models are examples of curve fitted models and have been proposed in characterizing the dynamic response of flexible polyurethane foams [3]. Hereditary models have also been applied in other work for closed-

T. Abdul-Quddoos
Department of Electrical & Computer Engineering, Prairie View A&M University, Prairie View, TX, USA

P. Lee
Department of Civil and Environmental Engineering, University of California – Los Angeles, Los Angeles, CA, USA

C. Zemelka
Department of Mechanical and Aerospace Engineering, The Ohio State University, Columbus, OH, USA

Los Alamos National Laboratory, Los Alamos, NM, USA

T. Roberts (✉) · S. Ceballes · S. Ouellette
Los Alamos National Laboratory, Los Alamos, NM, USA
e-mail: tproberts@lanl.gov

M. R. W. Brake et al. (eds.), *Nonlinear Structures & Systems, Volume 1*, Conference Proceedings
of the Society for Experimental Mechanics Series, https://doi.org/10.1007/978-3-031-36999-5_22

cell polymer foams using Prony's method for parameter estimation and a Prony series embedded in the models governing equation [4]. Models have also been proposed that derive analytical representations of foams dynamic response from physical models, where the foams are represented as combination of nonlinear elements [5].

Another prominent method for predicting the foam response is the use of finite element (FE) analysis software to predict engineering structure responses. Both constitutive models – requiring calibration of the model parameters to recreate experimentally observed deformation behavior – and physics-based models – which take advantage of physical deformation phenomenon to inform the response – are common methods used to capture the foam response [2]. Previous efforts to predict the material response of commonly utilized closed-cell polymer foams have highlighted the limitations of constitutive models, including generalized hyperfoam formulation. The possibility of unstable model response when strains above the calibration data range applied to the foam, due to the lack of information, were captured relative to deformation mechanics, material properties, or material characteristics [6]. Physics-based models, including those designed specifically for hyperelastic closed-cell polymer foams, such as CHIPFoam, utilize deformation mechanics and material characteristics for material model parameter calibration [1]. Analysis of CHIPFoam model responses and uncertainty associated with material characteristics and environmental conditions were conducted previously to understand effects on the dynamic response of a structure incorporating nonlinear foams. Uncertainty in material manufacturing yielded 71% variation in fundamental frequency, while preload and loading uncertainty yielded 185% and 16% variation in fundamental frequency, respectively [2].

In this work, a closed-cell polymer foam, SX358, is embedded in an existing dynamics testbed from the TRUST (Testbeds to Reduce Uncertainties in Simulations and Tests) project [7], for a suite of experimental and simulated studies. The testbed is excited at small-amplitudes vertically, and the dynamic response of the testbed is analyzed. This study explores the frequency response of the testbed with variations of prestrain, foam thicknesses, and foam densities, with the intent of characterizing the response across parameter spaces using finite element analysis methods. The testbed will be modeled using the ABAQUS FEA software and compared to experimental results for model validation. Sources of uncertainty will also be analyzed for model and experimental refinement.

22.2 Methods

A suite of experiments is carried out with the testbed for validation of the simulated model by utilizing the experimental workflow diagram in Fig. 22.1. Here, the frequency response of the testbed is compared to the simulation across material and system parameter spaces. The experiment is carried out by applying a Gaussian white noise signal to the testbed with the intent of exciting a large range of frequencies. A digital-to-analog converter from a PXIe 4463 applies a voltage signal to a PA-138 amplifier that outputs a current proportional to the input voltage that drives the shaker the testbed is on. A PXIe 4499 sound and vibration module is used to sample the signals from two accelerometers on the testbed baseplate and the six from the testbed center mass, reading in the acceleration as standard-gravity (g's). For measuring the preload, a PXIe 4330 strain/bridge input module is used to measure the load in pounds (lbf), applied to the loadcell. A LabVIEW script serves as the control script for the experiment, using the NI-DAQmx instrument drivers for interfacing with hardware. The LabVIEW script uses a producer/consumer architecture, this architecture divides the code into two parallel loops, one for controlling the system input (producer) and the other for acquiring data (consumer). The producer loop preps the excitation signal for the digital-to-analog converter and the consumer loop samples signals of interest using the sound and vibration module at a sample frequency of 6 kHz and saves them into the TDMS file format.

The frequency response function (FRF) of the accelerometers Z-axis signals are used to analyze the testbed response up to 3 kHz. The FRF is generated by dividing the cross power spectral density by the input auto power spectral density, where the baseplate accelerometers are system input and center mass accelerometers are system output. Modal frequencies are detected by applying a peak detection algorithm to the FRF and extracting prominent peaks. The suite of experiments is carried out with foams of thicknesses 2, 5, and 10 mm, densities of 0.35, 0.40, 0.45, and 0.5 g/cc, and preloads of 44.4, 133.4, and 222.4 N.

A defeatured version of the testbed was modeled using commercial FEA software ABAQUS 2021 (Dassault Systemes). Counterbored holes and associated fasteners were approximated as solid geometries and tied surfaces, respectively, to aid in simplification of modeling of the geometry and reduce computation times. No components of the shaker itself were modeled, with the baseplate of the testbed being the lowest piece in the assembly that was recreated. Figure 22.2 shows an isometric view of the initial model. Different material assignments are highlighted using different colors.

As a result of the defeaturing, a total of 26-part instances were required to construct the 3D-model used in FEA simulation, including the primary components of threaded vertical tie-rod, load cell, washers, nuts, accelerometers and mounting blocks,

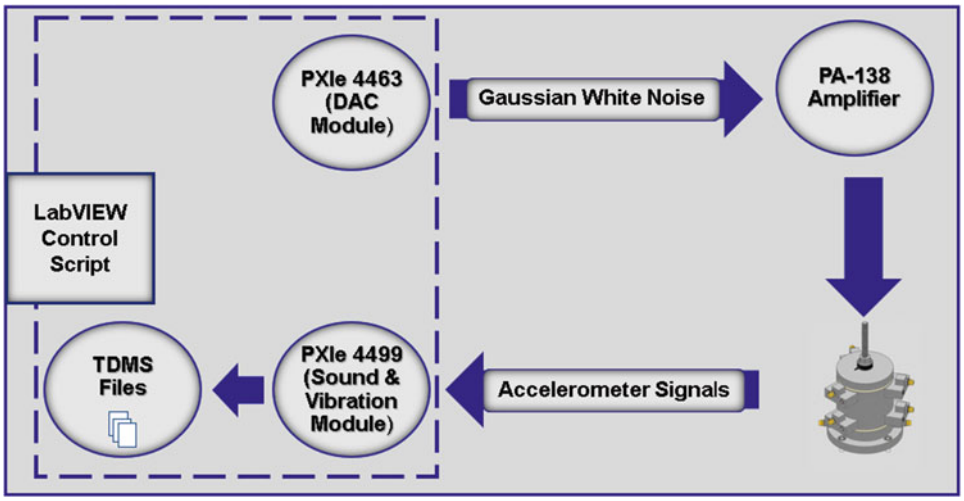

Fig. 22.1 Experimental workflow diagram

Fig. 22.2 Initial 3D ABAQUS Model

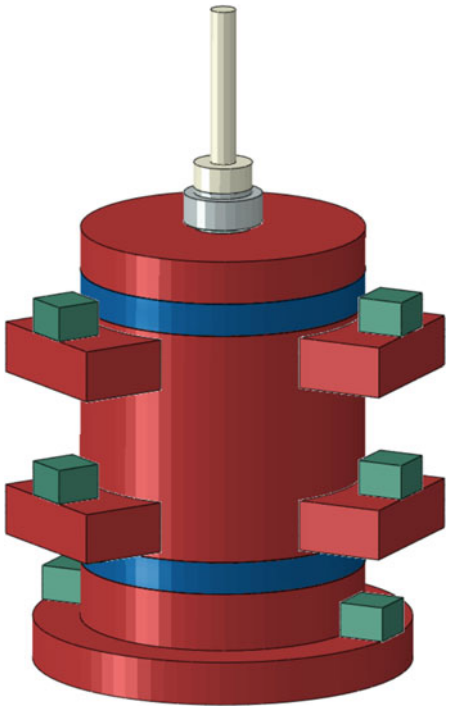

baseplate, baseplate riser, center mass, testbed cap, and two SX358 foam pad punch-outs (shown in blue). The model itself was meshed using C3D8R brick elements, and general contact was implemented into the model to prevent penetration during initial loading steps. The global seed size was initially chosen such that all major components of the assembly had at least three elements through its thickness (z-axis stacking direction). All surfaces that were designed to be in contact with each other were tied using surface-to-surface based definitions.

To recreate the boundary conditions of the testbed while on the shaker table, the bottom surface of the baseplate was fixed in all degrees-of-freedom. Figure 22.3 highlights the boundary conditions used in the model and shows the cross-section of the initial 3D ABAQUS model.

The overall simulation consists of three steps – the first being a general, static step that included application of the preload on the load cell and gravity on the entire structure along the negative z-direction (vertical, axial). Figure 22.3 also shows the *PRETENSION SECTION and concentrated load (ABAQUS-specific terminology) that was applied to the structure to replicate the load applied on the testbed via tightening of the top bolt. The second step was the modal analysis step (*FREQUENCY), completed using a linear perturbation step-type. The Lanczos solver was used. All modal frequencies

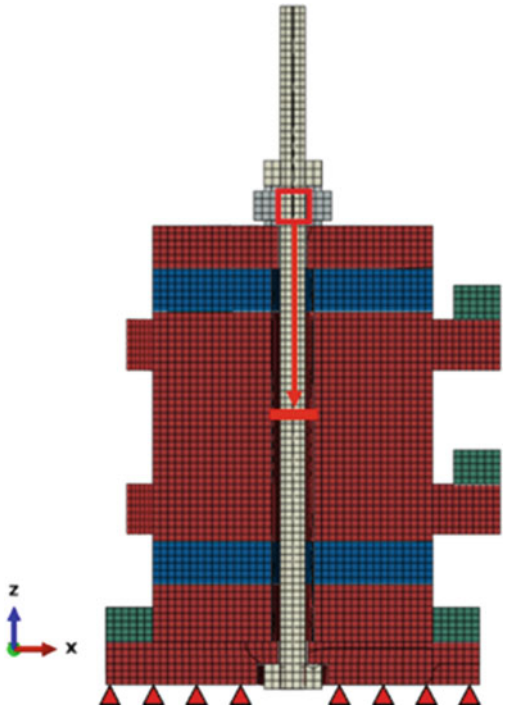

Fig. 22.3 Boundary conditions and loading of testbed model

were requested in the range of 0–3000 Hz – a range that was expected to capture most of the significant modes excited during white noise testing. After modal analysis was completed, a random response step was performed. This step required input acceleration into the system as well as the associated direction. Structural damping of 1% across all modes was utilized. To replicate the experimental testing, a power spectral density (PSD) of the baseplate acceleration generated during white noise application was constructed and provided as an input to the model. The acceleration was specified to occur in the *z*-direction (per Fig. 22.3). Acceleration in the form of another PSD was extracted from the center mass accelerometers that were created in the ABAQUS model. A ratio of the output to input PSDs was used to create frequency response functions (FRFs) for analysis purposes.

Six material models were required for modeling of the defeatured testbed assembly. Linear elastic models were used for four of the six materials, with *HYPERFOAM being used for the two foam pad layers. Table 22.1 displays the materials, assignments, as well as material properties used (where applicable). The Mock Accelerometer elastic properties were assumed to be equivalent to the load cell, and density was calculated using the mass and volume of the part itself. The density of the foams was reduced by two orders of magnitude compared to the nominal densities reported for the parts. This was to remove all foam-dominated modes from the frequency range of interest. Since all steps were implicit and the foam was of negligible mass compared to the metal components that made up most of the system, the stress-strain responses of the foams were not affected due to this modification.

YAML files and associated dictionaries contained instructions for construction of the simulation files, as well as parameterization of all files. ABAQUS Python journal files were responsible for the creation of parts and their associated geometry, partitioning of the parts for mesh control and set creation, and subsequent meshing of the parts. ABAQUS input files contained general details about materials, assembly creation, boundary conditions, and output requests.

As briefly mentioned above, nearly all aspects of the geometry, assembly construction, and loading are parameterized and easily modifiable during execution. This enabled the initiation of batch simulations with varied geometric and loading parameters – useful for determining the limits of the response of the assembly when utilizing different foam thickness, foam densities, and preload. Overall, the simulation process was determined by the selected foam pads used during physical experimentation of the testbed. Foam pad responses to compression were characterized using an MTS 880 servo-hydraulic frame. The quasistatic stress-strain response was fit to the *HYPERFOAM material model in ABAQUS and incorporated directly into the model. Due to the goal of the project being aligned with bounding the overall response of the center mass based on variability in preload and foam pad properties, the bounding limits of the responses – or lowest and highest frequency for a given mode – were the focus of simulation result analysis. During modal analysis steps and subsequent data extraction processes, the modal frequencies were extracted and compared to the experimentally observed frequencies. As described briefly above, random response step analysis consisted of extraction of the center mass-mounted accelerometer

Table 22.1 Simulation material assignments

Material name	Assignments	Model type	Density, ρ (Mg/mm^3)	Poisson's ratio, ν	Young's modulus, E (MPa)	Test data type	Model order, n
Aluminum 6061-T6	Accelerometer Mount Blocks, Baseplate, Baseplate Riser, Center Mass, Baseplate Cap	Linear Elastic	2.71263×10^{-9}	0.33	6.82581×10^{4}	N/A	
Stainless Steel 440C	Washers, Load cell		7.79936×10^{-9}	0.28	1.99750×10^{5}		
Alloy Fe-9Ni	Nuts, Threaded rod		7.83331×10^{-9}	0.31	2.04039×10^{5}		
Mock Accelerometer	Accelerometers		5.33087×10^{-9}	0.28	1.99750×10^{5}		
SX358 Lower	Lower foam pad	Hyperfoam	VARIED	N/A		Uniaxial Test Data	2
SX358 Upper	Upper foam pad						

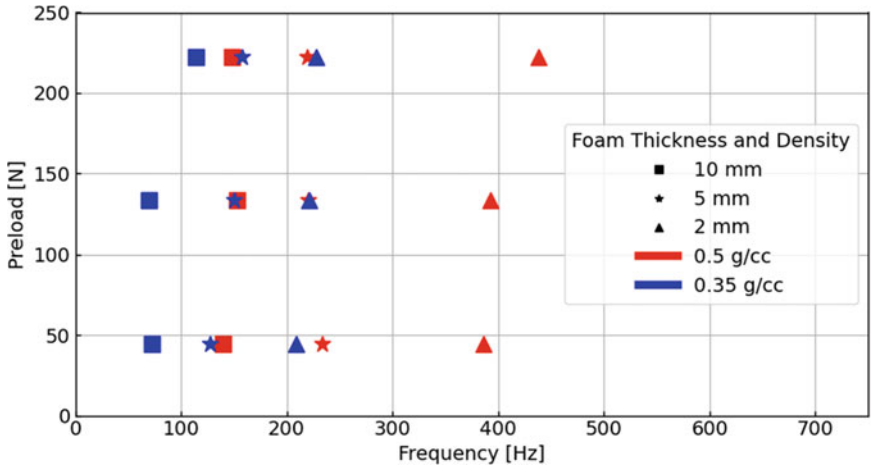

Fig. 22.4 First excited experimental modal frequencies

accelerations and calculation of the modal frequencies based on a frequency-domain analysis – which followed the same process as the experimental query using white noise.

22.3 Results and Analysis

Figure 22.4 shows the first excited modal frequencies that were extracted during experimental data processing.

A summary of results from the conducted experiments can be seen in Fig. 22.4, where only first detected modal frequency in the vertical direction is shown for varying preloads, foam densities, and foam thicknesses. Results show an emphasis toward the foam material properties having a prominent effect on the frequency response of the testbed. Preloads in the range experimented on showed small impact compared to material properties on the systems response, with the largest change in the first modal frequency occurring for 2 mm, 0.5 g/cc foam with the frequency at 44.4 N of preload being at 386 Hz and increasing to 438 Hz at 222.4 N preload. The testbed response with respect to changes in the foam's material properties shows a constant trend: as foams stiffen, their first modal frequency increases. For foams with a constant density, the experimental findings show that increases in the thickness of the foam specimens lead to a frequency decrease. For example, in foam with a density of 0.5 g/cc and a 44.4 N preload, the first modal frequency for 2 mm is 386 Hz, then decreases to 234 Hz for 5 mm, and then decreases to 140 Hz for 10 mm foam. For foam with a constant thickness and changing density, as density increases

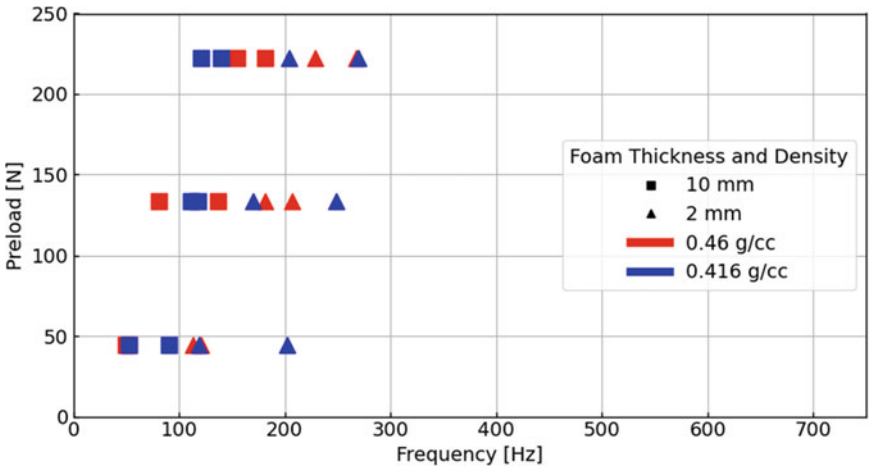

Fig. 22.5 First excited simulation modal frequencies

so does the first modal frequency, for example, with the 2 mm foam and a 44.4 N preload, at 0.35 g/cc the first mode is at 209 Hz and increases to 386 Hz with a density of 0.5 g/cc.

Figure 22.5 shows the first excited modal frequencies that were computed from the ABAQUS simulations and subsequent processing. The two bounding cases of 2- and 10-mm pad thicknesses with low and high densities, values of 0.416 and 0.46 g/cc, respectively, are captured along with the three variations in preload.

Like the experimental results in Fig. 22.4, preload applied on the structure during simulations did appear to have impacts on the frequency of the first excited mode. The most significant shift observed within one parameter set was the 2 mm high-density case, where the frequency increased from 121 to 268 Hz when moving from 44.4 to 222.4 N preload on the setup. As discussed above when referencing the experimental results, the same conclusions with respect to foam thickness and density are observed. For any constant preload and foam thickness combination, the sample with the highest density typically had the higher modal frequency – suggesting a stiffer material. This conclusion is supported by referencing the stress-strain curves that were utilized in the ABAQUS *HYPERFOAM model, shown in Fig. 22.6. At any given level of preload-dictated strain for the region of interest for these foams, the higher density foam typically has a higher local modulus. The overall variation in modal frequency due to density increases were not as pronounced in the simulations as it was in the experimental results. The largest increase was for the case with 2 mm foams at a preload of 44.4 N with an increase in frequency of 81 Hz when moving from low- to high-density foams.

Another consistent trend, like the results from the experimental analysis, shows that as the foam thickness decreases and both preload and density remain the same, the modal frequencies increase. This was consistent across all six pairs of simulations that were generated. The reduction in modal frequency associated with thickness decreases while maintaining the same density and preload were also less pronounced when compared to experimental results – like the trend with densities discussed immediately above this section. The largest decrease in modal frequency was for the low-density case at 133.4 N preloading, with a drop in frequency of 131 Hz when moving from the 2- to 10-mm sample. This also reinforced the idea that the thinner foam specimens are generally stiffer and less compliant than their thicker counterparts.

FRFs constructed using the *RANDOM RESPONSE simulation output are also compiled in Fig. 22.7.

All 24 simulations are captured in Fig. 22.7. Colors are associated estimations of the local moduli depending on where the loaded assembly fell on the stress-strain curve in Fig. 22.6. The first modal frequency extracted corresponded to the first and most exaggerated peak that appears at the lower frequency portions of the curves. To reinforce the conclusions established previously and to better understand the patterns in the data, three additional figures shown below, from Figs. 22.8, 22.9, and 22.10, compare cases of similar preloads, densities, and foam thicknesses; respectively.

In Fig. 22.8, there is a clear trend when comparing sets of 44.4, 133.4, or 222.4 N preload on the structure. As the preload on the structure is increased from 44.4 to 222.4 N, the first excited modal frequency increases while the foam is further compressed.

No clear trends can be pulled from Fig. 22.9 with the boxplot visualization. The overall range of the first excited modal frequency is approximately equal between the two sets of densities, and the overall distribution of frequencies is also similar.

Figure 22.10 also displays clearly identifiable trends in relation to the parameter impacts on the modal frequencies. Looking at variations in foam pad thickness in Fig. 22.10 reinforces the trends identified in the previous figures as well, with

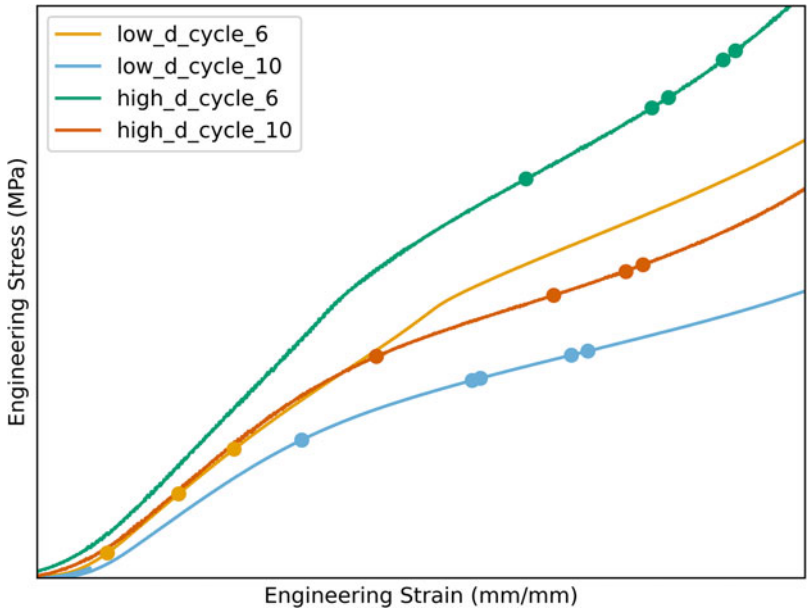

Fig. 22.6 Portion of stress-strain curves used in ABAQUS material models

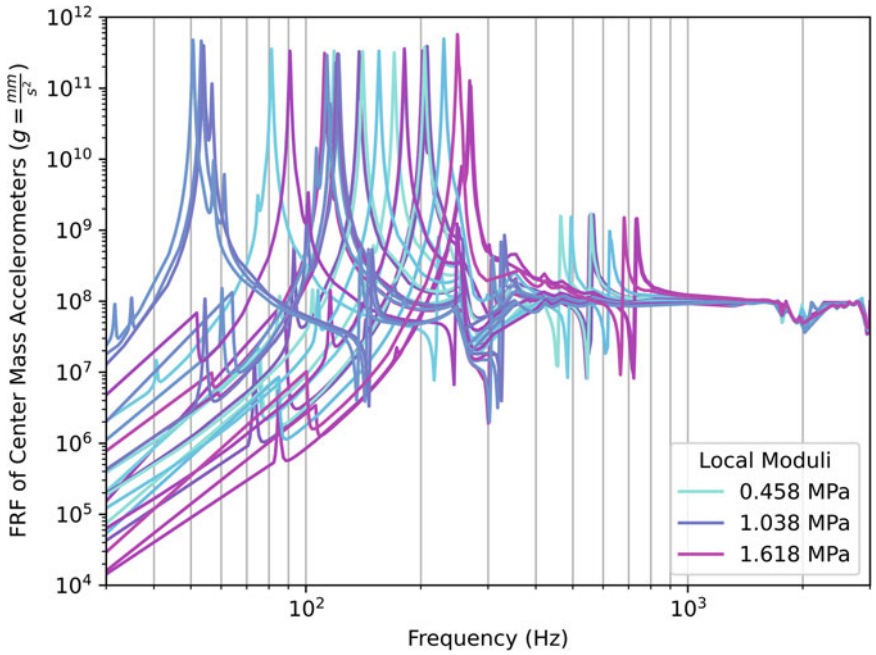

Fig. 22.7 FRFs for all simulations

thinner specimens having higher modal frequencies when compared to the thicker specimens, corresponding to an overall stiffer foam with thinner specimens.

Figure 22.11 shows the experimental and simulation results comparison for the low- and high-density foams, with both 2- and 10-mm pad thickness, for all preload cases described in earlier sections.

The central dashed line demonstrates the ideal simulation and experiment comparison results, with the first excited modal frequency being the same from both sources. The lighter gray region is a band of acceptable simulation results, which is an arbitrary 50 Hz range above and below the ideal case. There is, however, a clear deviation from the central line among all four groups of constant-parameter sets. As established above when discussing the trends observed among variations in foam pad thicknesses, the simulation and experimental results allowed for the same conclusion to be reached when comparing parameters: as the pad thickness decreases, the associated localized foam stiffness increases. The previously observed overlap

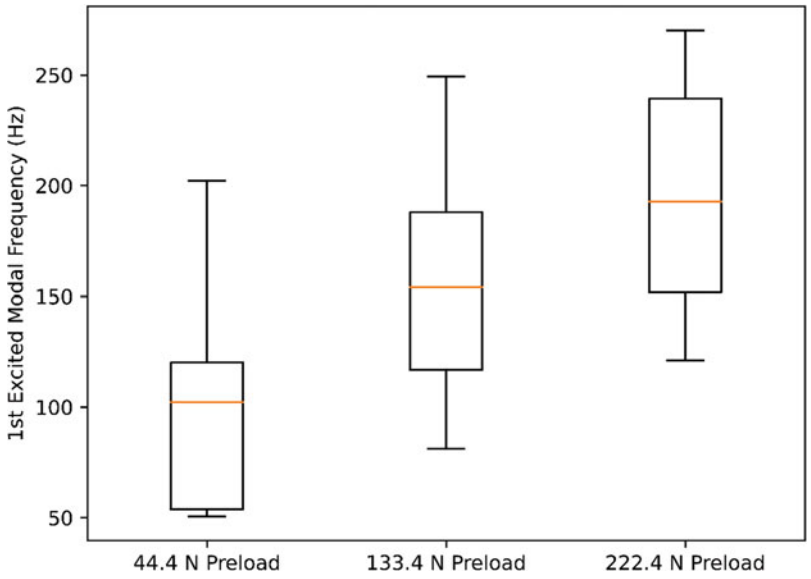

Fig. 22.8 Boxplots of first excited modal frequency for shared preloads

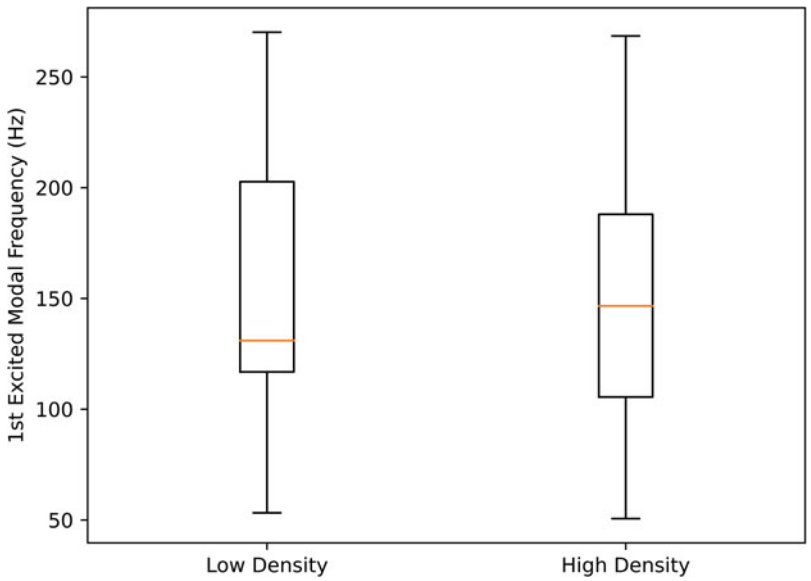

Fig. 22.9 Boxplots of first excited modal frequency for shared densities

in modal frequencies when comparing different densities in the simulation results is also observed again. The overall trend in Fig. 22.11 is a rightward skew in the data as the stiffer foams were tested. Due to modal frequencies being proportional to the stiffness and mass in a single degree of freedom system as shown below in Eq. 22.1, and the experimentally observed frequencies being greater than those extracted from simulation results, it can be concluded that the foam specimens used in the experimental test setup were stiffer than the stand-in material models utilized in the ABAQUS simulations – most notably for the thin and high-density case.

$$\omega = \sqrt{k/m} \tag{22.1}$$

where ω is the resonant frequency, k is the stiffness of the spring, and m is the mass of the mass.

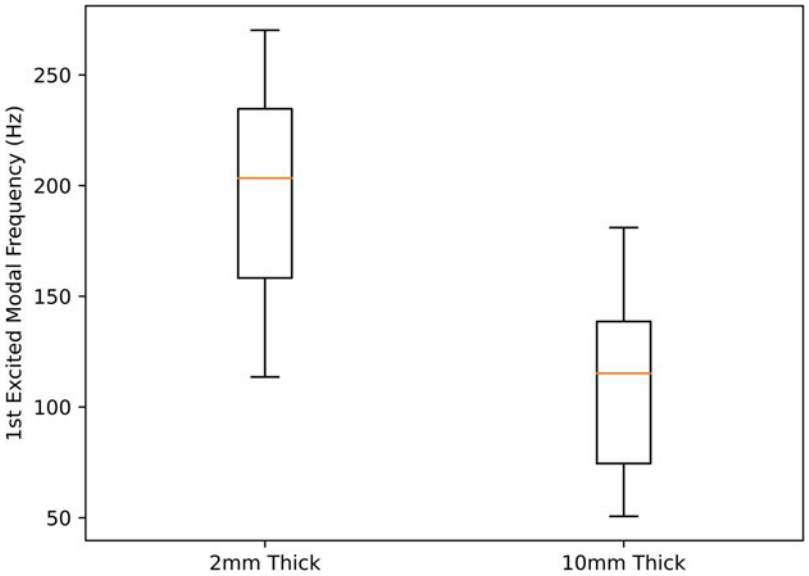

Fig. 22.10 Boxplots of first excited modal frequency for shared pad thicknesses

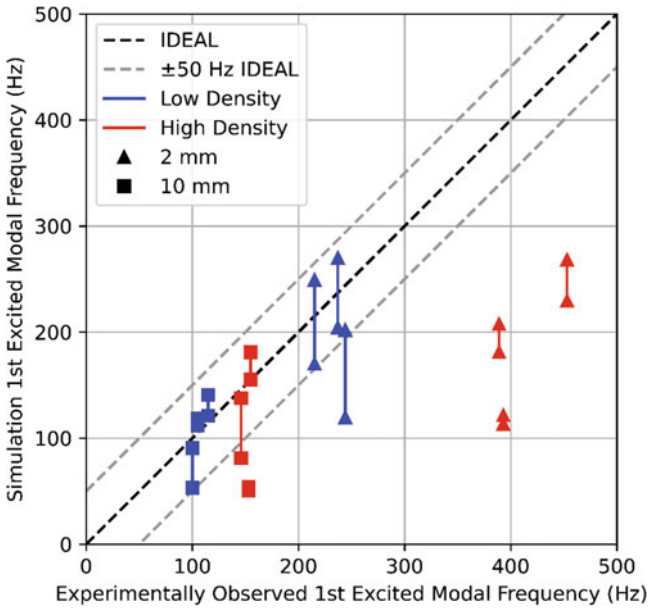

Fig. 22.11 Comparison of first excited modal frequencies from simulations and experiments

22.4 Discussion

The most significant source of uncertainty is within the calibration step of the testbed. The three uncertainties we are testing for are thickness and density, of the foam, and preload, of the testbed. When testing for uncertainties, a suite of experiments was considered, but the material and equipment also carry inherent uncertainties. Thickness of the foam is relatively accurate and precise with the measurements that was obtained and can be found in the appendix. The density varies, but for the relatively thicker (above 2 mm) foams, density seems to be more consistent. This can also be seen in the appendix. SX358 varies depending on the batch production, so it may not be applicable for all batches of foam to have similar consistencies. Our 1 mm samples showed how a section may or may not have the expected air (void) content. The material uncertainty can be determined to be less significant, with small contributions, so the best foams were selected based on both thickness and density, which can be seen by the color-coding in the appendix. SX358 is sensitive to temperature: when temperature

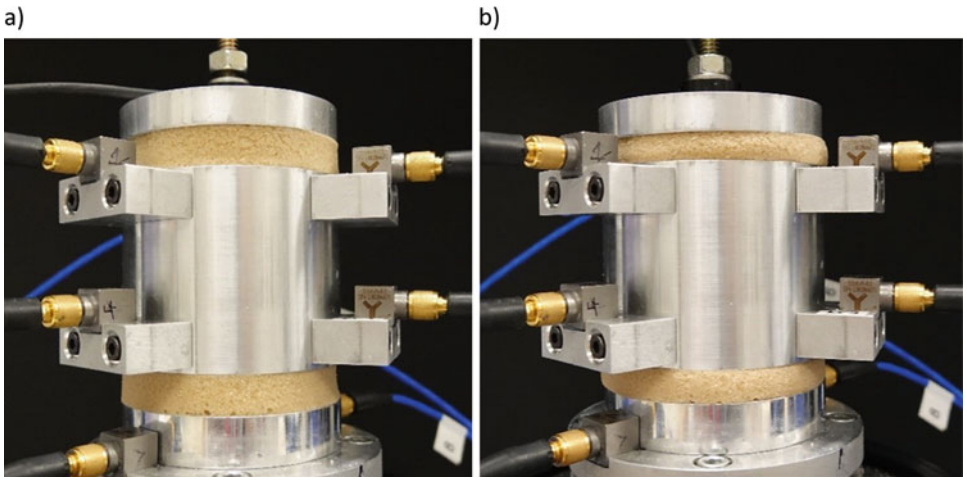

Fig. 22.12 (**a**) Unbarreled state: the preload was not applied, and the foam is relaxed. (**b**) Foam in compression, barreled state: the preload was applied to about 50 pounds

increases, the compression set also increases [8]. Humidity is also significant, because SX358 contains diatomaceous earth (DE) filler, which is immensely drawn to moisture, and causes uncertainty in the material properties [9–11].

Preload is the most significant source of error, because the preload varies on judgment and the load cell being used when it is inaccurate for the application. The load cell has a capacity of 22,241 N. However, the measurements of interest only reach up to 222 N. During the tests, the load cell offset (zeroing the loadcell) can be up to 222 N, depending on when the test is being run. The drift after zeroing the value can range up to 13 N and an additional 13 N of drift is likely due to the compression of the foam.

Another interesting phenomenon observed in the experiments was barreling. The more thick and less dense the material, the more likely it is for barreling to occur. This phenomenon can be observed in Fig. 22.9. Barreling results in the load cell to read a load, drop significantly, and return to reading the increase in preload. The drop in preload measurement makes sense, since during the preload, bending and buckling of the foam's cell walls can occur. It should be mentioned that the current finite element model requires updates to be able to demonstrate barreling. A minor contribution to the load cell uncertainty is the threaded rod with two nuts does not provide enough friction for the setup to tighten itself, so each layer is able to "spin." With a minor tap, the load cell can change up to +/− two pounds due to loosening or tightening from one of the many components that are smooth (Fig. 22.12).

22.5 Conclusion

Closed-cell polymer foams are a nonlinear material and under excitation can give a complicated system response. SX358, a closed-cell polymer foam, is embedded in an existing dynamics testbed for a suite of simulation and experimental studies to characterize the dynamic response of the testbed with respect to changes in foam thickness, foam density, and applied preload. The testbed is excited with gaussian white noise, and the first modal frequency is compared between simulated and experimental results for model validation. Both experimental and simulated results show the trend of a positive shift in the first detected modal as the foams stiffen. Also, as the foam stiffens, the simulated results deviate from the experimental results, with the simulated model results showing its foam to be stiffer than the physical foam. A source of uncertainty is the applied preload as the load cell is not suited well for a range up to 222.4 N, giving rise to variation in the actual applied preload across experiments, which is more evident the more compliant the foams.

Future work involves improvements to the model by using material data directly from samples and resizing the maximum capacity of the load cell to increase precision and accuracy. Furthermore, the mechanical response of SX358 with respect to changing humidity has not yet been explored.

Acknowledgments This research was funded by Los Alamos National Laboratory (LANL) through the Engineering Institute's Los Alamos Dynamics Summer School. The Engineering Institute is a research and education collaboration between LANL and the University of California San Diego's Jacobs School of Engineering. This collaboration seeks to promote multidisciplinary engineering research that develops and integrates advanced predictive modeling, novel sensing systems, and new developments in information technology to address LANL mission relevant problems.

The primary authors would like to give appreciation out to three LANL mentors: Dr. Scott Oullette, Dr. Samantha Ceballes, and Thomas Roberts, as well as faculty mentor Dr. James Gibert of Purdue for their guidance in this work. Also, the authors are tremendously thankful to Dr. Charles Farrar and Dr. Adam Wachtor for their assistance in the laboratory.

Appendix

To help characterize a suspended mass setup, the bottom of the test apparatus consists of a shaker that provides the excitation, which is secured to the table using magnets. A nut, washer, and threaded rod are attached below the bottom base plate of the testbed, which is machined to provide a groove for the hex nut and a surface for two accelerometers [7, 8]. Above the bottom plate, a typical hole was drilled for the threaded rod to pass through each component. For the foams, holes were punched. A cylindrical spacer is placed above the plate with a typical radius to the rest of components above. First piece of foam specimen is placed on cylindrical spacer. The suspended mass is then placed on top of the foam. In the suspended mass, typical three holes are drilled at 120° apart to allow for sensor blocks to be attached to the setup. These are fastened with two bolts and a notch that fits into the middle hole of the typical holes. For the platforms, machining is done for the accelerometers to fit tightly on the mass. The second foam specimen is placed on top of the suspended mass. The testbed top cap is then placed on top of the foam. A washer, load cell, washer, and nut are placed on top of the top cap. All components for the testbed are shown in Tables 22.2 and 22.3.

A thin layer of wax is applied to the accelerometers, which helps them stick to the notches in the baseplate and platforms. The triaxial BNC cables are connected to each accelerometer, which is labeled to keep track of position, and to the BNC rack. The BNC rack is connected to the BNC rack module

Table 22.2 Experimental hardware for testbed

Part number	Description	Quantity	Material
–	Washer, Flat, No. 10	2	Stainless Steel
09S8Y-025	Washer, Flat, ¼–20 UNC	1	ASTM F436, Yellow Zinc
McMaster 91251A342 or Equivalent	Socket HD cap screw, #10–32 UNC × .500 LG	4	ASTM A574
McMaster 90128A151 or Equivalent	Socket HD cap screw, #6–32 UNC × .75 LG	12	ASTM A574
08G8CY-025	Nut, Hex, ¼–20 UNC	2	Medium Carbon Alloy Steel, Yellow Zinc, Grade 8
08FNCZ-025	Nut, Hex, ¼–20 UNC	1	Zinc
3313N11	Threaded rod, ¼–20 UNC	1	Zinc Yellow-Chromate Plated Steel, Grade 8
–	Testbed Sensor Block	6	Aluminum, 6061-T6
–	Testbed Top Cap	1	Aluminum, 6061-T6
–	Testbed Center Mass	1	Aluminum, 6061-T6
–	Testbed Spacer	1	Aluminum, 6061-T6
–	Testbed Base Plate	1	Aluminum, 6061-T6

Table 22.3 Experimental hardware for excitation and data collection

Part number	Description	Quantity
2075E	Modal Shop Shaker, Vibration Test Shaker, 75 lbf	1
010G10	PCB 3 BNC to 1 accelerometer, shielded, FEP cable, 10 ft	9
PXIe-1092	Data acquisition system chassis	1
PXIe-8861	Data acquisition system	1
TB-4330	Signal conditioner block	1
PXIe 4330	Load cell module	1
BNC-2144	BNC Rack	1
054104-1502	PCB load cell	1
PCB 356A43, Adhesive Mount	Accelerometer, Triaxial ICP 10 mV/g, 500 g, .250-28	9
PXIe 4463	Signal Generation, Shaker, PXI Sound, and Vibrations Module	1
PXIe 4499	BNC Rack Module, PXI Sound, and Vibration Module	2
PA-138	LabWorks Inc, 25 V, 500 VA	1
197516A-01	National Instruments, 4× InfiniBand to InfiniBand Cable, 1 m, NI 449x/BBC-2144	4

Table 22.4 Measurements of the thicknesses example

Specimen	Thickness 1 (mm)	Thickness 2 (mm)	Thickness 3 (mm)	Average Thickness (cm)
1	0.91	0.93	1.00	0.095
2	1.04	1.05	1.06	0.105
3	1.12	1.20	1.10	0.114
4	1.06	1.06	1.09	0.107
5	1.48	1.03	1.01	0.117
6	1.03	1.02	1.00	0.102
7*	1.01	1.03	1.04	0.103
8	1.02	1.03	1.00	0.102

Table 22.5 Density calculation sample

Specimen	R1 (mm)	R2 (mm)	Mass (g)	V1 (cm^3)	V2 (cm^3)	Total Volume (cm^3)	Density (g/cm^3)
1	4.43	31.90	1.200	0.058	3.0	3.0	0.40
2	4.76	30.87	1.242	0.0747	3.14	3.07	0.405
3	4.74	31.06	1.246	0.0805	3.46	3.37	0.369
4	4.80	30.98	1.195	0.0773	3.23	3.15	0.379
5	4.74	30.96	1.239	0.0828	3.53	3.45	0.359
6	4.72	30.87	1.206	0.0712	3.04	2.97	0.406
7*	4.69	31.02	1.215	0.0709	3.10	3.03	0.401
8	4.67	30.92	1.177	0.0697	3.05	2.98	0.394

Table 22.6 Sample of values used for testing

Specimen	Average Thickness (mm)	Density (g/cm^3)	2.00 mm & 0.35 g/cm^3	Specimen	Average Thickness (mm)	Density (g/cm^3)	10.00 mm & 0.50g/cm^3
1	**2.007**	**0.357**	**TEST**	**1**	**10.087**	**0.495**	**TEST**
2	2.080	0.364		**2**	**10.087**	**0.504**	**TEST**
3	**2.133**	**0.357**	**TEST**	**3**	10.197	0.514	
4	2.137	0.363		**4**	10.153	0.495	
5	**2.100**	**0.359**	**TEST**	**5**	**10.103**	**0.504**	**TEST**
6	2.070	0.374		**6**	10.167	0.499	
7	2.223	0.360		**7**	**10.123**	**0.501**	**TEST**
8	**2.133**	**0.363**	**TEST**	**8**	10.140	0.493	

If an accelerometer becomes detached, then a plastic scraper is used to remove the residual wax from the accelerometer and the notch with assistance of isopropyl alcohol and wiped with Kimwipes. New wax is applied afterward to reattach the accelerometer. When switching the foams, isopropyl alcohol will be used to ensure none of the foams are still on the surfaces of contact. A 3D printed component is used to make sure the experiments are run consistently with minimal changes with each run. The components discussed in this paragraph can be referenced in Table 22.3.

Average thicknesses were determined with a caliper and measured in three locations radially. A sample is shown in Table 22.4. The red row is an indication that some of the samples were destroyed and removed from the data due to the difficulty of working with such delicate samples.

Density was calculated using the outer and inner radii at the same location and measured on a scale to three decimal places. These values are then divided by the average thickness, which determines the experimental density. These values can be seen in Table 22.5.

Samples of the 2.00 mm with 0.35 g/cm^3 and 10.00 mm with 0.50 g/cm^3 are shown for examples for selecting four sets for testing. These sample average thicknesses and densities are shown in Table 22.6. The values are color coded: green with ideal, yellow with acceptable, and red with unacceptable conditions. Both thickness and density are used to determine if the specimen should be tested. Only the two best specimens were tested due to the time constraints with the other two as backups.

References

1. Lewis, M.: A robust, compressible, hyperelastic constitutive model for the mechanical response of foamed rubber. Tech. Mech. **36**(1–2), 88–101 (2016)
2. Roberts, T., et al.: Dynamics of a Non-linear Oscillator: Dependencies on Extrinsic Conditions and Model Form Uncertainty. LANL, LA-UR-20-30141 (2020)
3. Deng, R., et al.: Flexible polyurethane foam modelling and identification of viscoelastic parameters for automotive seating applications. J. Sound Vib. **262**, 391 (2003)
4. Singh, R.: Estimation of the dynamical properties of polyurethane foam through use of Prony Series. J. Sound Vib. **264**, 1005 (2003)
5. Patten, W.: A vibration model of open celled polyurethane foam automotive seat cushions. J. Sound Vib. **217**, 145 (1998)
6. Siranosian, A., et al.: Developing an Abaqus *HYPERFOAM model for M9747 (4003047) Cellular Silicone Foam. LANL, LA-UR-12-20871 (2012)
7. Sheera, S., et al.: TRUST Nonlinear Dynamics (ND) Report. LANL, LA-UR-21-30732 (2021)
8. Labouriau, A., et al.: Aging mechanisms in RTV polysiloxane foams. Polym. Degrad. Stab. **121**, 60 (2015)
9. Yang, D.: Effect of Sample Size on Mechanical Properties of SX358 foam. LANL, LA-UR-12-26494 (2012)
10. Jia, Z.: Study on hydrophobicity transfer of RTV coatings based on a modification of absorption and cohesion theory. IEEE Trans. Dielectr. Electr. Insul. **13**, 1317 (2006)
11. Rutherford, S.W.: Water sorption in silicone foam containing diatomaceous earth. J. Colloid Interface Sci. **306**, 228 (2007)

Chapter 23
Experimental Investigation on Frictional Interfaces of a Bolted Flange System

Nidhal Jamia, Matthew S. Bonney, Hassan Jalali, Michael I. Friswell, Hamad Haddad Khodaparast, and Robin S. Mills

Abstract The coupling between the frictional energy dissipation and the dynamic response at the joint interface leads to mechanisms that are challenging to identify relying mainly on numerical data. The need for experimental analyses of such mechanisms is vital for better understanding of the inherent features in the contact interface dynamic response and for creating models that can evolve with changes in the system and environment. This work looks to gain insights about the different frictional mechanisms in the contact interface such as micro-vibro-impacts and micro-slip and macro-slip under different resonance modes and different environmental conditions. A bolted flange system was designed and manufactured at the Laboratory of Verification and Validation (LVV). Two main sensing systems are used for the testing using accelerometers and displacement sensors. All tests were performed in an environmental control chamber that contains a large multi-axial shaker. The interest in this work focuses on the hysteresis information near resonance which provides insight into the interaction between two substructures along with the contact interface.

Keywords Hysteresis · Frictional mechanisms · Contact interface

23.1 Introduction

Bolted joints play a key role in the damping behaviour of assembled structures. Despite their simplicity, the inherent dynamics of bolted joints are too complex to be accurately modelled. The energy dissipation in the contact interface is highly nonlinear and complicated to analyse. Under cyclic loading, a tangential micro- and macro-slip can develop at the contact interface leading to hysteretic behaviour. The formed hysteresis loops quantify the energy dissipated in the contact interface. This hysteretic behaviour is strongly affected by the nonlinear mechanisms occurring in the contact interface. The micro-vibro-impacts and the frictional slips present the dominant nonlinear mechanisms in the contact interface. The vibro-impact mechanism occurs in the normal direction and alters the distribution of normal forces in the contact interface, hence the slip behaviour in the tangential direction changes. The high level of complexity of such mechanisms made the understanding of the dynamic behaviour of the joints challenging. Jamia et al. [1] proposed an equivalent model to predict the micro-slip behaviour in terms of hysteresis loops. Ahmadian and Jalali [2] proposed the use of the generic element to model a bolted lap-joint. A comparison of hysteresis curves at resonance frequencies was considered to validate the proposed model. Recently, Jalali et al. [3] proposed a generalised Valanis model with the ability to generate non-symmetric hysteresis loops for friction contact interface modelling and identification. In addition, bolted flange joints are widely used in the assembling of mechanical structures, and they have been investigated by many researchers [4, 5]. In this work, an experimental investigation is carried out to gain further understanding of the inherent nonlinear mechanisms in the contact interface and their effect on the hysteretic behaviour of the joint under a harmonic load.

N. Jamia (✉) · M. I. Friswell · H. H. Khodaparast
Faculty of Science and Engineering, Swansea University, Swansea, UK
e-mail: nidhal.jamia@swansea.ac.uk

M. S. Bonney · R. S. Mills
Department of Mechanical Engineering, University of Sheffield, Sheffield, UK

H. Jalali
Department of Mechanical & Construction Engineering, Northumbria University, Newcastle Upon Tyne, UK

M. R. W. Brake et al. (eds.), *Nonlinear Structures & Systems, Volume 1*, Conference Proceedings
of the Society for Experimental Mechanics Series, https://doi.org/10.1007/978-3-031-36999-5_23

23.2 Experimental Setups

An L-shape flange with a 100 × 100 mm^2 area of contact interface is proposed. The main interest in this work is the torsion mode. Hence, a rod clamped to the end of flange with an offset was considered to excite the torsion mode within the shaker frequency range. Two different excitation systems were used in this work to test a bolted flange under base excitation. In the first configuration, the test rig is clamped to a large multi-axial shaker. Two main sensing configurations are used in the testing. The first one consists of ten uni-axial accelerometers attached to the two sides of the flange along the longitudinal direction of the flange. The second configuration consists of two laser displacement sensors pointed to the contact interface in the normal and tangential directions, as shown in Fig. 23.1. A second configuration was considered where an electrodynamic shaker is used. A laser Doppler vibrometer system was used to measure the velocity at 22 points from the flange and the base velocity. An additional laser displacement was pointed to the contact interface in the normal direction to monitor the opening and closing behaviour of the joint contact as shown in Fig. 23.2. All tests were performed in an environmental control chamber located in the LVV. This room provides the ability to accurately control the temperature and the humidity. In addition, a thermocouple is used to assess the temperature of the structure during testing.

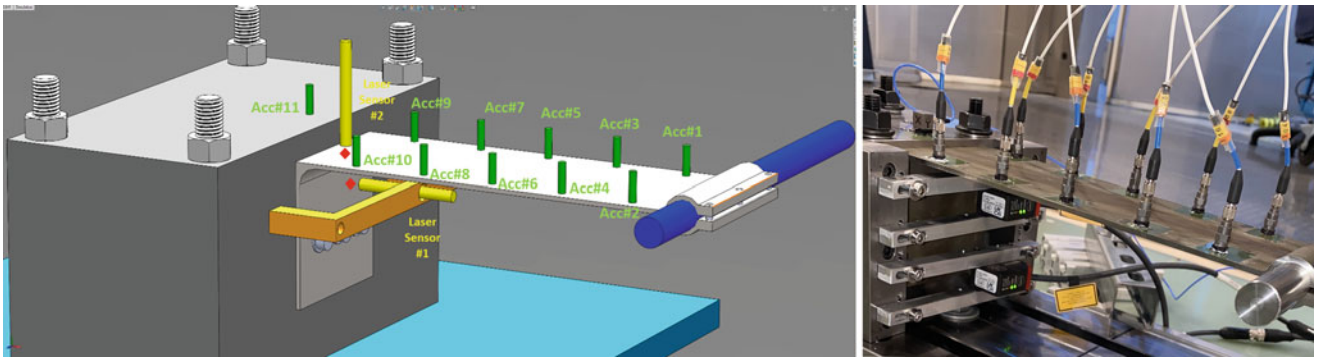

Fig. 23.1 Setup of configuration 1

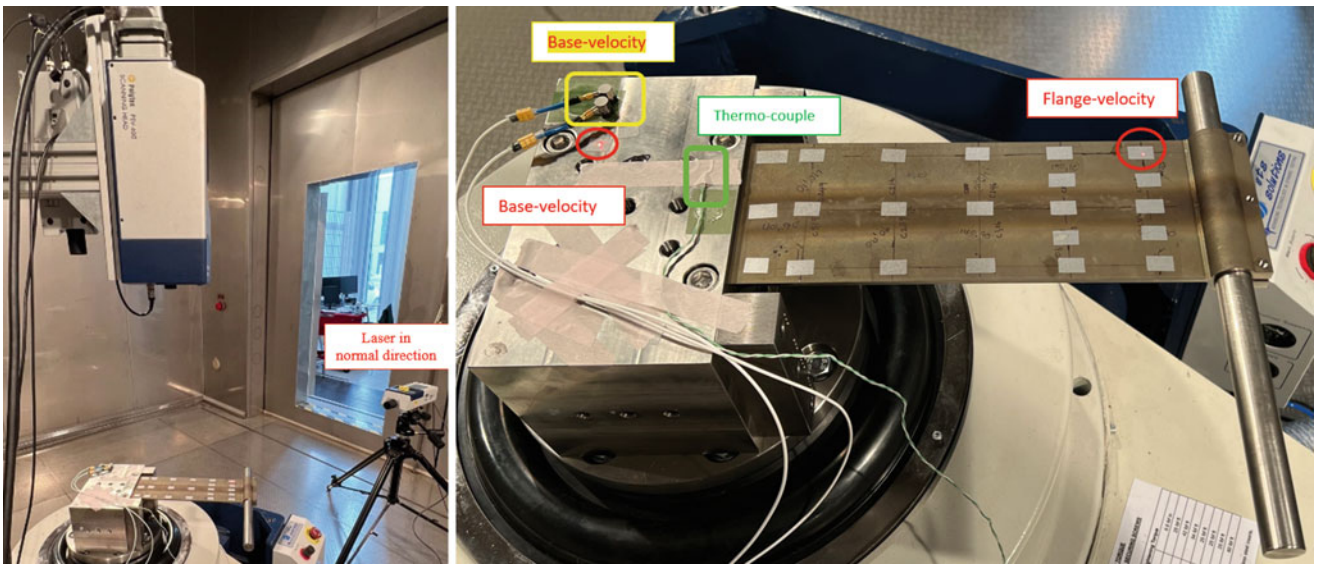

Fig. 23.2 Setup of configuration 2

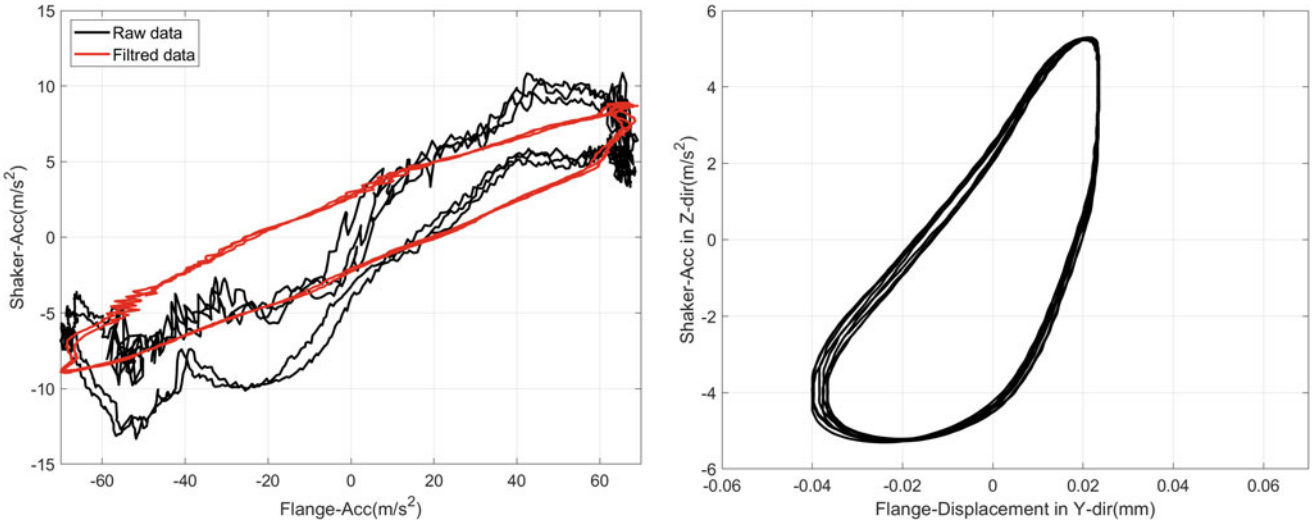

Fig. 23.3 Equivalent to hysteresis loops at excitation frequency $\omega = 29.8$ Hz using raw data (black) filtered data (red) obtained from (**a**) accelerometer 8 (**b**) laser sensor 1

23.3 Results and Discussion

To represent hysteresis information near resonance in the contact interface, loops equivalent to the conventional hysteresis loops are used. To generate these loops, the base response is plotted against the flange response under a single frequency excitation. Initially, a linear modal analysis of the flange system was performed to identify natural frequencies and mode shapes. The results obtained showed a fundamental mode that has a natural frequency of 9.45 Hz, which is the first bending mode, and a second mode at 29.85 Hz, which is the first torsional mode. The system was excited at a frequency of 29.8 Hz under a base excitation amplitude of 4 m/s^2. All signals were acquired at a sampling rate of 25.6 kHz for a period of 10 seconds. The responses from an accelerometer close to the clamp mounting and the base are used to plot the equivalent to the hysteresis loops, and these are shown in Fig. 23.3a. Due to the high level of noise in the acquired data, the data was filtered using a low pass filter with a cutoff frequency of 100 Hz to produce less noisy plots. Despite the reduction of the noise level, the filtering altered the results and limited the nonlinear features that can be extracted from the loops. The response acquired from laser 2 (as shown in Fig. 23.1a) is used to plot the equivalent to the hysteresis loop shown in Fig. 23.3b using the raw data collected from the laser pointed into the tangential direction of the contact interface. The results produced loops with less noise that can be used to identify the nonlinear characteristics of the joint. In Fig. 23.4, the raw data output of the two laser sensors measuring the tangential and opening-closing behaviour of the contact interface is plotted against the shaker acceleration at three excitation frequencies close to the torsional natural frequency. The results show the effect of the contact interface impact on the friction. The loops in Fig. 23.4a show a more regular shape of hysteresis loops around the resonance. This can be explained by the fact that the sensor pointing to the contact interface in the normal direction only measures the opening and closing behaviour. The loops in Fig. 23.4b correspond to the second laser sensor measuring the tangential direction of the contact interface (laser 2 in Fig. 23.1). The shape indicates a superposition of two mechanisms: the micro-vibro-impacts and the micro-slip mechanism in the torsional mode.

23.4 Conclusion

In this work, extensive experimental testing was performed on a bolted flange joint under base excitation. Two sensing systems were used to extract the hysteresis behaviour of the system. The analyses of the different features of the equivalent to hysteresis loops of the contact interface were conducted to provide further understanding of the inherent phenomena in the joint contact due to the micro-vibro-impact and slip mechanisms.

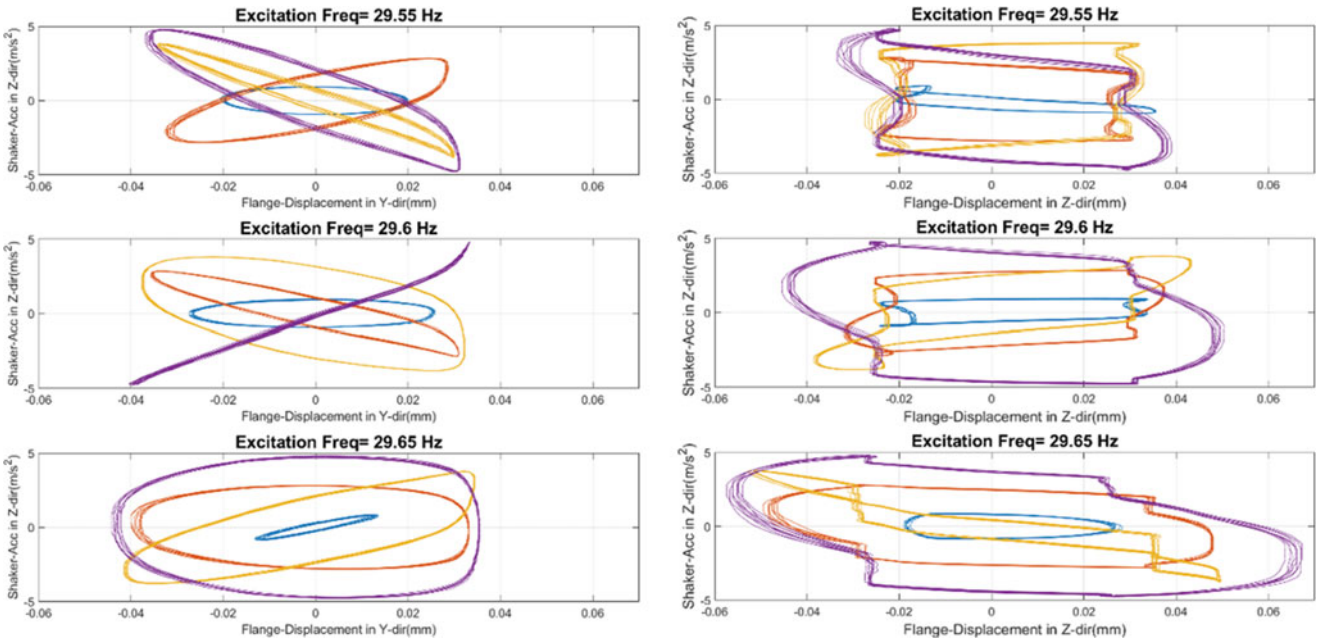

Fig. 23.4 Equivalent to hysteresis loop close to the torsional mode: base excitation against displacement of contact interface in (**a**) normal direction (**b**) tangential direction

Acknowledgements The authors gratefully acknowledge the support of the Engineering and Physical Sciences Research Council through the award of the Programme Grant "Digital Twins for Improved Dynamic Design", grant number EP/R006768/1.

References

1. Jamia, N., Jalali, H., Taghipour, J., Friswell, M.I., Haddad Khodaparast, H.: An equivalent model of a nonlinear bolted flange joint. Mech. Syst. Signal Process. **153** (2021). https://doi.org/10.1016/j.ymssp.2020.107507
2. Ahmadian, H., Jalali, H.: Generic element formulation for modelling bolted lap joints. Mech. Syst. Signal Process. **21**, 2318–2334 (2007)
3. Jalali, H., Jamia, N., Friswell, M.I., Haddad, K.H., Taghipour, J.: A generalization of the Valanis model for friction modelling. Mech. Syst. Signal Process. **179**, art. No. 109339 (2022)
4. Beaudoin, M.A., Behdinan, K.: Analytical lump model for the nonlinear dynamic response of bolted flanges in aero-engine casings. Mech. Syst. Signal Process. **115**, 14–28 (2019)
5. Yin, T., Wang, X., Zhu, H.: Probabilistic approach for the detection of bolt loosening in periodically supported structures endowed with bolted flange joints. Mech. Syst. Signal Process. **128**, 588–616 (2019)

Chapter 24
Estimation of Wheel Center Forces of a Car, Without Neither Load Sensor Nor Strain Gauge Measurements When Crossing a Groove on the Road

Alexandre Débarbouillé, Zoran Dimitrijevic, Franck Renaud, Denis Chojnacki, Laurent Rota, and Jean-Luc Dion

Abstract To design a vehicle suspension the knowledge of wheel loads is required. These loads are due to road unevenness and can be identified thanks the acquisition of measurements during vehicle rolling on roads or tracks. Some offline methods are used to identify them; most of these methods are based on transfer functions between points of measurements and consider the hypothesis of linear dynamic behavior of the vehicle. This hypothesis leads to misestimation of the exceptional load. We propose an approach based on a nonlinear multi-body model of the half-vehicle and an extended Kalman filter augmented and constrained for the data fusion with measurements from accelerometers, gyrometer, tachometer, and GPS. This half vehicle model lies in a 2D plane. The Kalman state vector is composed of positions and velocities of each solid, the road/track loads are unknown but estimated by the filter, and the state prediction is constrained by kinematic links between bodies.

Keywords Extended Kalman filter · Numeric twin · Nonlinear 2D model · Load estimation · Constrained method

24.1 Introduction

Designing elements of vehicle suspension needs the knowledge of loads due to road unevenness. To estimate loads we can use measurements done in vehicle rolling on roads or tracks. Most methods use some transfer functions between points of measurements. However, the description of end tail distribution of the loads is misestimated with such linear approaches. We propose a method based on a twin numerical model of the car (multi-body model of car body and bodies of the ground connection) and a specific Kalman filter [1]. In this approach the nonlinear behavior of the suspension is implemented in our model and the Kalman filter; the data fusion uses measurements from accelerometers, gyrometer, tachometer, and GPS. One can find in [2] a virtual sensing approach for estimating wheel center forces. A simplified multi-body suspension system taking into account only few solids was used to estimate loads at wheel center in the three directions. They propose to improve their approach by the implementation of nonlinearities [3]. In our study a complete multi-body vehicle dynamic system is developed with fully nonlinear geometric behavior. We present here the methodology to estimate the longitudinal and vertical wheel center forces of the 2D multi-body model with a few sensors and an extended Kalman filter [4] to correct the predictions. The Kalman filter is used in several domains like the estimation of attitude. In aerospace domain [5] a Kalman filter is implemented with differential equation for the state model based on the relation between gyrometer and quaternion for the attitude representation. Some works in heavy vehicle domain use the Kalman filter to predict vehicle attitude to improve the techniques of fuel savings [6]. A new branch of study makes investigation on health monitoring [7]. In general, the attitude estimation is done by the measurement of one accelerometer and a magnetometer in the measurement model and

A. Débarbouillé (✉)
Équipe Vibroacoustique, Structures et Formes Mécaniques, Laboratoire Quartz - EA 7393, ISAE, Supméca, Paris, France

Stellantis, Technical center of Vélizy, Vélizy, France
e-mail: alexandre.debarbouille@isae-supmeca.fr

Z. Dimitrijevic · D. Chojnacki · L. Rota
Stellantis, Technical center of Vélizy, Vélizy, France
e-mail: zoran.dimitrijevic@stellantis.com; denis.chojnacki@mpsa.com; laurent.rota@stellantis.com

F. Renaud · J.-L. Dion
Équipe Vibroacoustique, Structures et Formes Mécaniques, Laboratoire Quartz - EA 7393, ISAE, Supméca, Paris, France
e-mail: franck.renaud@supmeca.fr; jean-luc.dion@supmeca.fr

M. R. W. Brake et al. (eds.), *Nonlinear Structures & Systems, Volume 1*, Conference Proceedings
of the Society for Experimental Mechanics Series, https://doi.org/10.1007/978-3-031-36999-5_24

the state model uses a gyrometer [8]. In the automobile domain, an odometer or a GPS is added to the measurement model [9] to improve these estimations. When quaternion is used for describing attitude, the normalization of the quaternion must be integrated to the process of the Kalman filter as a constrained equation. It can be applied differently like in [8] where the quaternion is reevaluated after each iteration step. Other approaches add constraints in the measurement model [10] and [11], then called the perfect measurement. According to [11] this approach has a numerical issue: the constraints uncertainty is equal to zero and the covariance matrix of the measurement is singular. Another approach changes the Kalman gain [12] in order to respect the constraints equation in the estimation state. The last approach to take account the constraints in a Kalman filter consists of obtaining the constrained estimation by a projection of the unconstrained estimation of the Kalman filter into the surface of constraints. We implement our Kalman filter with this approach, called estimate projection [11], in the article. We implement an augmented and constrained extended Kalman filter with position, speed, attitude, and first derivation of the attitude in the state vector, and we augment the state by unknown loads and forces in the plan without the torque. The constraints are implemented with the hypothesis of estimate projection. This work is still in progress and we aim at dealing with full 3D systems quite soon. Dealing with 2D is the first step towards the 3D; moreover, 2D models are more convenient for future real-time application. Actually we apply our method to rolling measures simulated with Simpack on digitalized roadtracks and also to real rolling measures on our proving grounds (roadtracks).

24.2 Background

24.2.1 Rotation Representation

We defined the attitude of every body by an axis of rotation given by the unit vector $\underline{\mathbf{u}}$ and an angle of rotation θ in a three-dimensional system. This representation allows us to avoid issues of singularity encountered with Euler or Cardan angles after derivating the rotation matrix in the space or time domain. The quaternion $\underline{\mathbf{p}}$ [13] is defined with $\underline{\mathbf{u}}$ and θ and is given by:

$$\underline{\mathbf{p}} = \cos\left(\frac{\theta}{2}\right) + i\underline{\mathbf{u}}\sin\left(\frac{\theta}{2}\right) \tag{24.1}$$

It denotes the rotation between the reference marker and the solid considered. The quaternion $\underline{\mathbf{p}}$ is a number with four dimensions, three of which are purely imaginary $\underline{\mathbf{p}} = \left[p_0,\ \underline{\mathbf{p}}_v^t\right]^t$ with p_0 the real part and $\underline{\mathbf{p}}_v^t$ the imaginary part. By definition, $\underline{\mathbf{p}}^t\underline{\mathbf{p}} = 1$. In order to process similarly the 2D models and 3D models, the 2D-quaternion $\underline{\mathbf{p}}$ is thus simplified as follows: $\underline{\mathbf{p}} = \left(\cos\left(\frac{\theta}{2}\right)\ ,\ \sin\left(\frac{\theta}{2}\right)\right)^t = [p_0\ ,\ p_1]^t$. To build the model with 2D-quaternion representation for the prediction step of the Kalman filter, we define specific operator applied on 2D-quaternion in [14].

24.2.2 Multi-body Equations

Let $\underline{\mathbf{x}}_k$ be the position of the gravity center position $\mathcal{G}_k$ in the terrestrial reference frame and $\underline{\mathbf{p}}_k$ the attitude of the solid $\mathcal{S}_k$. Let $\underline{\mathbf{q}}_k = (\underline{\mathbf{x}}_k^t \quad \underline{\mathbf{p}}_k^t)^t$ be the state vector of the rigid body $\mathcal{S}_k$. To compute accelerations $\underline{\ddot{\mathbf{q}}}_k$ in the Kalman prediction, we use the principle of virtual power adapted to the 2D-quaternion representation. First, a description of the virtual kinematic and kinetic energy is given according to the 2D-quaternion. The virtual power of loads and virtual power of accelerations are then calculated. Finally, we identify the virtual power of loads to the virtual power of accelerations. In addition, we have to take the kinematic and 2D-quaternion constraints into account to properly compute accelerations for the multi-body model. The method to obtain the acceleration for a rigid body is given in [14]. The unconstrained accelerations are $\underline{\ddot{\mathbf{q}}}_k$, where $\underline{\mathfrak{M}}_k$ is the mass matrix, $\underline{\mathcal{J}}_k$ is an inertial term, $\underline{\mathbf{F}}_{k,j}$ is all forces and torques applied on the point j onto the body k, and $\underline{\mathbf{D}}_{k,j}$ is a matrix depending on the state vector and geometry.

$$\underline{\mathfrak{M}}_k\underline{\ddot{\mathbf{q}}}_k = \sum_j\left(\underline{\mathbf{D}}_{k,j}\underline{\mathbf{F}}_{k,j}\right) - \underline{\mathcal{J}}_k \tag{24.2}$$

24.2.3 The Constraints Equations

In the multi-body model, there are constraints between bodies. In addition other constraints are introduced by the need to have a normalized 2D-quaternion to calculate rotation matrix, rotation rate, $\underline{\mathcal{J}}_k$, and $\underline{\mathfrak{M}}_k$. We choose the method of Lagrange multiplier in order to take the constraints into account. The dynamic model with 2D-quaternion constraints is :

$$\underline{\mathcal{M}}_k \begin{pmatrix} \ddot{\underline{\mathbf{q}}}_k \\ \lambda_{\underline{\mathbf{p}},k} \end{pmatrix} = \underline{\mathbf{F}}_k \quad \text{With} \quad \underline{\mathcal{M}}_k = \begin{bmatrix} \underline{\mathfrak{M}}_k & \mathbb{G}^t_{\underline{\mathbf{p}},k} \\ \mathbb{G}_{\underline{\mathbf{p}},k} & 0 \end{bmatrix} \quad \text{and} \quad \underline{\mathbf{F}}_k = \begin{pmatrix} \sum_j \left(\mathbf{D}_{k,j} \underline{\mathbf{F}}_{k,j} \right) - \underline{\mathcal{J}}_k \\ L_{\underline{\mathbf{p}},k} + \mathcal{W}_{\underline{\mathbf{p}},k} \end{pmatrix} \tag{24.3}$$

where $\lambda_{\underline{\mathbf{p}},k}$ is the Lagrange multiplier. The stabilization term $\mathcal{W}_{\underline{\mathbf{p}},k}$ added in Eq. (24.3) tends to compensate the deviation thanks to Baumgarte's stabilization method, with parameters chosen according to [15]. The term $\mathcal{W}_{\underline{\mathbf{p}},k}$ represents stabilization term of constraint of 2D-quaternion norm based on $g_{\underline{\mathbf{p}}_k}$ and $\dot{g}_{\underline{\mathbf{p}}_k}$, the constraints function and its derivative. $L_{\underline{\mathbf{p}},k}$ and $\mathbb{G}_{\underline{\mathbf{p}},k}$ are linked by $\ddot{g}_{\underline{\mathbf{p}}\,k}(\underline{\mathbf{q}}) = \mathbb{G}_{\underline{\mathbf{p}},k} \ddot{\underline{\mathbf{q}}} - L_{\underline{\mathbf{p}},k}$.

The constraints between bodies defined by $\underline{\mathbf{g}}_B(\underline{\mathbf{q}})$ are added to the equation system defined by Eq. (24.3) of each body $\mathcal{S}_k$. Finally, the state vector of the multi-body system is $\underline{\mathbf{q}} = (\underline{\mathbf{q}}_1^t \ \cdots \ \underline{\mathbf{q}}_{k_S}^t)^t$ with k_S the body number. The constraint accelerations $\ddot{\underline{\mathbf{q}}}$ of the multi-body system are given the following equation, where $\overset{\mathbf{o}}{\underline{\mathbf{R}}} = (\ (\ddot{\underline{\mathbf{q}}}_1^t \ \lambda_{\underline{\mathbf{p}},1})^t \ \cdots \ (\ddot{\underline{\mathbf{q}}}_{k_S}^t \ \lambda_{\underline{\mathbf{p}},k_S})^t \ )^t$ and where $\underline{\lambda}_B$ are the Lagrangian multipliers for the constraints between bodies and $\underline{\mathcal{W}}_B$ is the Baumgarte's stabilization term of constraint $\underline{\mathbf{g}}_B$.

$$\begin{bmatrix} \mathbf{M} & \mathbb{G}^t_B \\ \mathbb{G}_B & \mathbf{0} \end{bmatrix} \begin{pmatrix} \overset{\mathbf{o}}{\underline{\mathbf{R}}} \\ \underline{\lambda}_B \end{pmatrix} = \begin{pmatrix} \underline{\mathbf{F}} \\ \underline{\mathbf{L}}_B + \underline{\mathcal{W}}_B \end{pmatrix} \quad \text{With} \quad \underline{\mathbf{M}} = \begin{bmatrix} \underline{\mathcal{M}}_1 & & \\ & \ddots & \\ & & \underline{\mathcal{M}}_{k_S} \end{bmatrix} \quad \text{and} \quad \underline{\mathbf{F}} = \begin{pmatrix} \underline{\mathbf{F}}_1 \\ \vdots \\ \underline{\mathbf{F}}_{k_S} \end{pmatrix} \tag{24.4}$$

24.3 Kalman Filtering of the Multi-body Model

24.3.1 The Augmented and Constrained Extended Kalman Filter (ACEKF)

In this section, we introduce the following notations for s, a given symbol: $\overline{s}$ denotes the prediction of states and $\hat{s}$ denotes the Kalman estimation. The Kalman filter is a commonly used method to make an estimation of a linear dynamic system with two steps: A prediction, denoted $\overline{\mathbf{X}}$, is computed by the known state variable at time step n using Eq. (24.9), i.e.: $\overline{\underline{\mathbf{X}}}^{n+1} = \underline{\mathbf{f}}\left(\hat{\underline{\mathbf{X}}}^n\right)$ where $\underline{\mathbf{f}}$ is the function of prediction model. A correction of the estimation is done based on the measurement Eq. (24.11) at the time n+1, i.e.: $\overline{\underline{\mathbf{Y}}}^{n+1} = \underline{\mathbf{h}}\left(\overline{\underline{\mathbf{X}}}^{n+1}\right)$, where $\underline{\mathbf{h}}$ is the function of measurement model and $\overline{\underline{\mathbf{Y}}}$ is the measurement vector. $\hat{\underline{\mathbf{X}}}$ is the state estimation of the Kalman filter. $\hat{\underline{\mathbf{X}}}$ is assumed Gaussian. The covariance matrix of state error noted $\hat{\underline{\mathbf{P}}}$ is estimated by the Kalman filter. $\underline{\mathbf{f}}$ and $\underline{\mathbf{h}}$ are nonlinear functions of the states. The extended Kalman filter (EKF) is an approach to study the nonlinear formulation. The prediction $\overline{\underline{\mathbf{X}}}_n$ is computed using the system of Eqs. (24.9) and (24.10).

$$\begin{array}{ccc} \text{Prediction} & \text{Correction} & \text{Notation} \\ \begin{cases} \overline{\underline{\mathbf{X}}}^{n+1} = \underline{\mathbf{f}}(\hat{\underline{\mathbf{X}}}^n) \\ \overline{\underline{\boldsymbol{P}}}^{n+1} = \mathbb{F} \hat{\underline{\boldsymbol{P}}}^n \mathbb{F} + \underline{\mathbf{Q}} \end{cases} & \begin{cases} \hat{\underline{\mathbf{X}}}^{n+1} = \overline{\underline{\mathbf{X}}}^n - \underline{\mathbf{K}} \left(\underline{\mathbf{h}}(\overline{\underline{\mathbf{X}}}^n) - \underline{\mathbf{Y}}^n \right) \\ \hat{\underline{\boldsymbol{P}}}^{n+1} = \left(\underline{\mathbf{I}}_{ns} - \underline{\mathbf{K}} \mathbb{H} \right) \overline{\underline{\boldsymbol{P}}}^n \end{cases} & \begin{cases} \underline{\mathbf{K}} = \overline{P}^n \mathbb{H}^t (\mathbb{H} \overline{P}^n \mathbb{H}^t + \underline{\mathbf{R}})^{-1} \\ \mathbb{F} = \frac{\partial \underline{\mathbf{f}}}{\partial \underline{\mathbf{X}}} \left(\underline{\mathbf{X}}^n \right) \\ \mathbb{H} = \frac{\partial \underline{\mathbf{h}}}{\partial \underline{\mathbf{X}}} \left(\overline{\underline{\mathbf{X}}}^{n+1} \right) \end{cases} \end{array} \tag{24.5}$$

where $\underline{\mathbf{Y}}$ is the vector of real measurements, $\underline{\mathbf{Q}}$ and $\underline{\mathbf{R}}$ are the covariance matrices of prediction and measurement model. The CEKF is a EKF where the estimated state $\hat{\underline{\mathbf{X}}}$ is conditioned to follow exact equation represented by the function $\underline{\mathbf{g}}_K\left(\underline{\mathbf{X}}\right) = \underline{\mathbf{0}}_{N_c \times 1}$. The equations of constraints are nonlinear. We use the method of estimate projection [11] to implement the constraints in the CEKF. The EKF returns an estimation $\hat{\underline{\mathbf{X}}}$ of the real state vector $\underline{\mathbf{X}}$, then $\hat{\underline{\mathbf{X}}}$ is projected onto the surface of constraints. The constrained estimation $\hat{\underline{\mathbf{X}}}_c$ is then written as:

$$\begin{cases} \hat{\underline{\mathbf{X}}}_c = \hat{\underline{\mathbf{X}}} - \underline{\mathbf{J}}\,\underline{\mathbf{g}}_c\left(\hat{\underline{\mathbf{X}}}\right) \\ \hat{\underline{\mathbf{P}}}_c = \left(\underline{\mathbf{I}} - \underline{\mathbf{J}}\,\underline{\mathbb{G}}\right)\left(\hat{\underline{\mathbf{P}}}\right) \end{cases} \quad \text{with} \quad \underline{\mathbf{J}} = \hat{\underline{\mathbf{P}}}\underline{\mathbb{G}}^t\left(\underline{\mathbb{G}}\hat{\underline{\mathbf{P}}}\underline{\mathbb{G}}^t\right)^{-1} \quad \text{and} \quad \underline{\mathbb{G}} = \frac{\partial \underline{\mathbf{g}}}{\partial \underline{\mathbf{X}}}\left(\hat{\underline{\mathbf{X}}}\right) \tag{24.6}$$

Here, the multi-body model, a car, is excited by external environment, the road. We choose to characterize the road by the strength ζ according to the horizontal and vertical directions which exited directly the wheel center. The equation describing this strength in the prediction model is given by:

$$\zeta^{n+1} = \underline{\mathbf{A}}_\zeta \zeta^n + \underline{\mathbf{B}}_\zeta \tag{24.7}$$

24.3.2 Kalman Prediction

We use the constant time step dt to describe the time evolution equations of the state space model. They are given by the following discrete-time equations:

$$\begin{cases} \underline{\mathbf{q}}_k^{n+1} = \underline{\mathbf{q}}_k^n + dt\ \dot{\underline{\mathbf{q}}}_k^n + \frac{dt^2}{2}\ \ddot{\underline{\mathbf{q}}}_k^n \\ \dot{\underline{\mathbf{q}}}_k^{n+1} = \dot{\underline{\mathbf{q}}}_k^n + dt\ \ddot{\underline{\mathbf{q}}}_k^n \end{cases} \tag{24.8}$$

Let be $\underline{\mathbf{X}} = (\underline{\mathbf{q}}^t \quad \dot{\underline{\mathbf{q}}}^t \quad \underline{\zeta})^t$ the state of the multi-body system where n_s is the size of state vector and $\underline{\zeta}$ the vector of unknown parameters describing some characteristics of the multi-body system. Consider f as the function describing the relation between consecutive time steps based on Eq. (24.8) for $\underline{\mathbf{q}}$ and $\dot{\underline{\mathbf{q}}}$. In addition, we introduce a noise denoted $\underline{\epsilon}_X$ on the model estimation and its covariance matrix $\underline{\mathbf{Q}}$, assumed independent of time. Then:

$$\underline{\mathbf{X}}^{n+1} = \underline{\mathbf{f}}(\underline{\mathbf{X}}^n) + \underline{\epsilon}_X \qquad \text{with} \quad \underline{\mathbf{f}}(\underline{\mathbf{X}}^n) = \begin{bmatrix} \underline{\mathbf{I}} & dt\underline{\mathbf{I}} & \underline{\mathbf{0}} \\ \underline{\mathbf{0}} & \underline{\mathbf{I}} & \underline{\mathbf{0}} \\ \underline{\mathbf{0}} & \underline{\mathbf{0}} & \underline{\mathbf{A}}_\zeta \end{bmatrix} \underline{\mathbf{X}}^n + \begin{pmatrix} \begin{Bmatrix} \frac{dt^2}{2} \\ dt \end{Bmatrix} \otimes \ddot{\underline{\mathbf{q}}}^n \\ \underline{\mathbf{B}}_\zeta \end{pmatrix} \tag{24.9}$$

where $\otimes$ is the Kronecker product and $\underline{\mathbf{A}}$ is the matrix describing the parameter evolution. The Jacobian of $\underline{\mathbf{f}}$, denoted $\underline{\mathbb{F}}$, is given by:

$$\underline{\mathbb{F}} = \begin{bmatrix} \underline{\mathbf{I}} & dt\underline{\mathbf{I}} & \underline{\mathbf{0}} \\ \underline{\mathbf{0}} & \underline{\mathbf{I}} & \underline{\mathbf{0}} \\ \underline{\mathbf{0}} & \underline{\mathbf{0}} & \underline{\mathbf{A}} \end{bmatrix} + \begin{pmatrix} \begin{Bmatrix} \frac{dt^2}{2} \\ dt \end{Bmatrix} \otimes \frac{\partial \ddot{\underline{\mathbf{q}}}^n}{\partial \underline{\mathbf{X}}^n} \\ \underline{\mathbf{0}} \end{pmatrix} \quad \text{with} \quad \begin{Bmatrix} \frac{\partial \overset{\mathbf{o}}{\underline{\mathbf{q}}}^n}{\partial \underline{\mathbf{X}}^n} \\ \frac{\partial \underline{\lambda}_B^n}{\partial \underline{\mathbf{X}}^n} \end{Bmatrix} = -\overset{\mathbf{o}}{\underline{\mathbf{M}}}^{-1}\left[\frac{\partial \overset{\mathbf{o}}{\underline{\mathbf{M}}}}{\partial \underline{\mathbf{X}}^n}\begin{pmatrix} \overset{\mathbf{o}}{\underline{\mathbf{q}}}^n \\ \underline{\lambda}_B \end{pmatrix} + \frac{\partial}{\partial \underline{\mathbf{X}}^n}\left(\begin{Bmatrix} \underline{\mathbf{F}} \\ \underline{\mathbf{L}} + \underline{\mathcal{W}} \end{Bmatrix}\right)\right] \tag{24.10}$$

24.3.3 Kalman Correction

In our issue, let the solid $\mathcal{S}_1$ be the car body and O the center of the terrestrial reference frame. The observation of the state space model is given by sensors, such as biaxial accelerometer, biaxial gyrometer, GPS, and tachometer. The gyrometer measures the rotation's rate of the car body, denoted y_{gyro}, defined in the marker $\mathcal{B}_1$. The biaxial accelerometers measure accelerations $\underline{\mathbf{y}}_{acc}$ on several non-coplanar points $\mathcal{P}_{k_1,j_1}$ on the car body, given in the marker $\mathcal{B}_1$. The accelerometers measure the acceleration of the car body plus the constant gravity vector, denoted as $\underline{\mathbf{a}}_{grav}$. The position $\underline{\mathbf{y}}_{GPS}$ of the car body is measured by the GPS. The tachometer measure the longitudinal speed of the car body denoted $\underline{\mathbf{y}}_{tacho}$. In the case of a car rolling without sliding, the speed on the other directions is considered as noise without bias. We assume that measurement noises $\underline{\epsilon}_{acc}$, ϵ_{gyro}, $\underline{\epsilon}_{GPS}$, and $\underline{\epsilon}_{tacho}$ are zero-mean white Gaussian and uncorrelated. We introduce the function $\underline{\mathbf{h}}$ based in Eq. (24.11):

$$\underline{\mathbf{Y}} = \begin{pmatrix} \underline{\mathbf{y}}_{acc,1} \\ \vdots \\ \underline{\mathbf{y}}_{acc,n_{acc}} \\ y_{gyro} \\ \underline{\mathbf{y}}_{GPS} \\ \underline{\mathbf{y}}_{tacho} \end{pmatrix} = \underline{\mathbf{h}}(\underline{\mathbf{X}}) + \underline{\epsilon}_Y \begin{cases} \underline{\mathbf{y}}_{acc} & = \underline{\mathbf{R}}_{0,1}\left(\ddot{\underline{\mathbf{x}}}_1 + 2\left(\overset{+}{\underline{\mathbf{p}}}_1 \overset{+}{\ddot{\underline{\mathbf{p}}}}_1 + \overset{+}{\dot{\underline{\mathbf{p}}}}_1 \overset{+}{\dot{\underline{\mathbf{p}}}}_1\right)\mathcal{GP}_j^1 + \underline{\mathbf{a}}_{grav}\right) + \underline{\epsilon}_{acc} \\ y_{gyro} & = \underline{\psi}^{\underline{\mathbf{p}}_1}\dot{\underline{\mathbf{p}}}_1 + \epsilon_{gyro} \\ \underline{\mathbf{y}}_{GPS} & = \underline{\mathbf{x}}_1 + \underline{\epsilon}_{GPS} \\ \underline{\mathbf{y}}_{tacho} & = \underline{\mathbf{R}}_{0,1}\dot{\underline{\mathbf{x}}}_1 + \underline{\epsilon}_{tacho} \end{cases} \tag{24.11}$$

where $\underline{\epsilon}_Y = \left(\underline{\epsilon}_{acc,1}^{\ t} \cdots \underline{\epsilon}_{acc,n_{acc}}^{\ t}\ \epsilon_{gyro}\ \underline{\epsilon}_{GPS}^t\ \underline{\epsilon}_{tacho}^t\right)^t$ t denotes the noise measurement vector. Its covariance matrix $\underline{\mathbf{R}}$ is assumed independent of time. Finally, we obtain the formulation of the extended Kalman filter used to estimate the state of the nonlinear problem. However, in our study, the multi-body model is defined with constraints such as the 2D-quaternion norm and the kinematic constraints between bodies.

24.3.4 Kalman Modifications

The reference Kalman filter is augmented with wheel center loads in 2D plan; the first modification is implementation of a filter on the measurement in order to reduce high-frequency signal given by the sensor (above 50 Hz). A large part of this signal doesn't represent dynamic information. And the second one is another way of filtering measurement by identifying sinus signal in accelerometer measurement with parameters a, b, ω to identify by the Kalman filter.

$$\underline{\mathbf{y}}_{acc}^{kal} = \underline{\mathbf{y}}_{acc}^{mes} + a.\cos(\omega t) + b.\sin(\omega t) \tag{24.12}$$

24.4 Analysis

24.4.1 Model Studied

In this section, we describe the study case used to evaluate the robustness of the algorithm presented below. To get simulated measures to feed Kalman filter, a numerical simulation of a car rolling at 40 km/h on a track of more than 65 meters has been done. A pothole of 1 m large is put on the road. First, a simulation with Simpack with a 3D model of car is computed to generate virtual measurements, then measurements are noised with the characteristics in Table 24.1 and the ACEKF is implemented with noised measurements to estimate state and loads (Fig. 24.1).

Table 24.1 Parameter of measurement noises

Sensors	$E(\epsilon)$	$\sqrt{V(\epsilon)}$
Accelerometer	0	0.1 m/s^2
Gyrometer	0	0.1 rad/s
GPS	0	1 m
Tachometer	0	0.1 m/s

Fig. 24.1 Figurative road profile

The sensor measurements and sensor positions are imported into our algorithm computed in Matlab environment. Covariance matrix of measurement noises $\underline{\mathbf{R}}$ and covariance matrix of state model noises $\underline{\mathbf{Q}}$ are diagonal. Let $\underline{\mathbf{D}}_Q$ and $\underline{\mathbf{D}}_R$, respectively, represent the vector of diagonal terms in $\underline{\mathbf{Q}}$ and in $\underline{\mathbf{R}}$ (Table 24.2):

	Car body	Front wheel	Rear wheel	Front junction
$-\log_{10}(\underline{\mathbf{D}}_Q)$ $\underline{\mathbf{x}}/\underline{\mathbf{p}}/\underline{\dot{\mathbf{x}}}/\underline{\dot{\mathbf{p}}}$	24/26/19/21	20/22/15/17	20/28/15/17	20/22/15/17

	Accelerometer	GPS	Gyrometer	Tachometer
$-\log_{10}(\underline{\mathbf{D}}_Q)$	15	14	14	10

The covariance matrix at the step time 0 is $\hat{\underline{\mathbf{P}}}^0 = 10^{-2}\,\underline{\mathbf{Q}}$ and we initialize the estimated state $\hat{\underline{\mathbf{X}}}^0 = (\underline{\mathbf{q}}^{0\,t}\ \ \underline{\dot{\mathbf{q}}}^{0\,t}\ \ \underline{\zeta}^{0\,t})^t$ with $\underline{\dot{\mathbf{q}}}_k^0 = \underline{\zeta}^0 = \underline{\mathbf{0}}_{4\times 1}$. The first estimated model is given by Eq. (24.5) and the measurement model is given by the system of Eqs. (24.11) (Figs. 24.2, 24.3, and 24.4).

Table 24.2 Characteristics of bodies

Name bodies	Mass [kg]	Inertia [kg/m^2]
Car body	750	1000
Front wheel	40	20
Rear wheel	30	20
Front junction	15	1

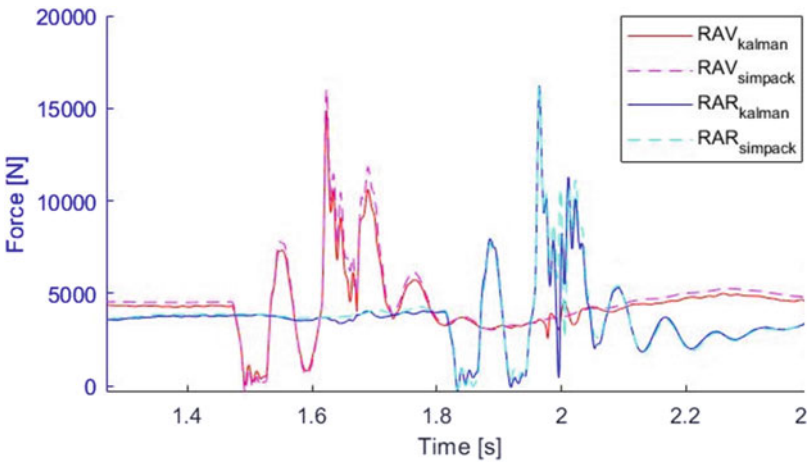

Fig. 24.2 Load identification with simulated measurement

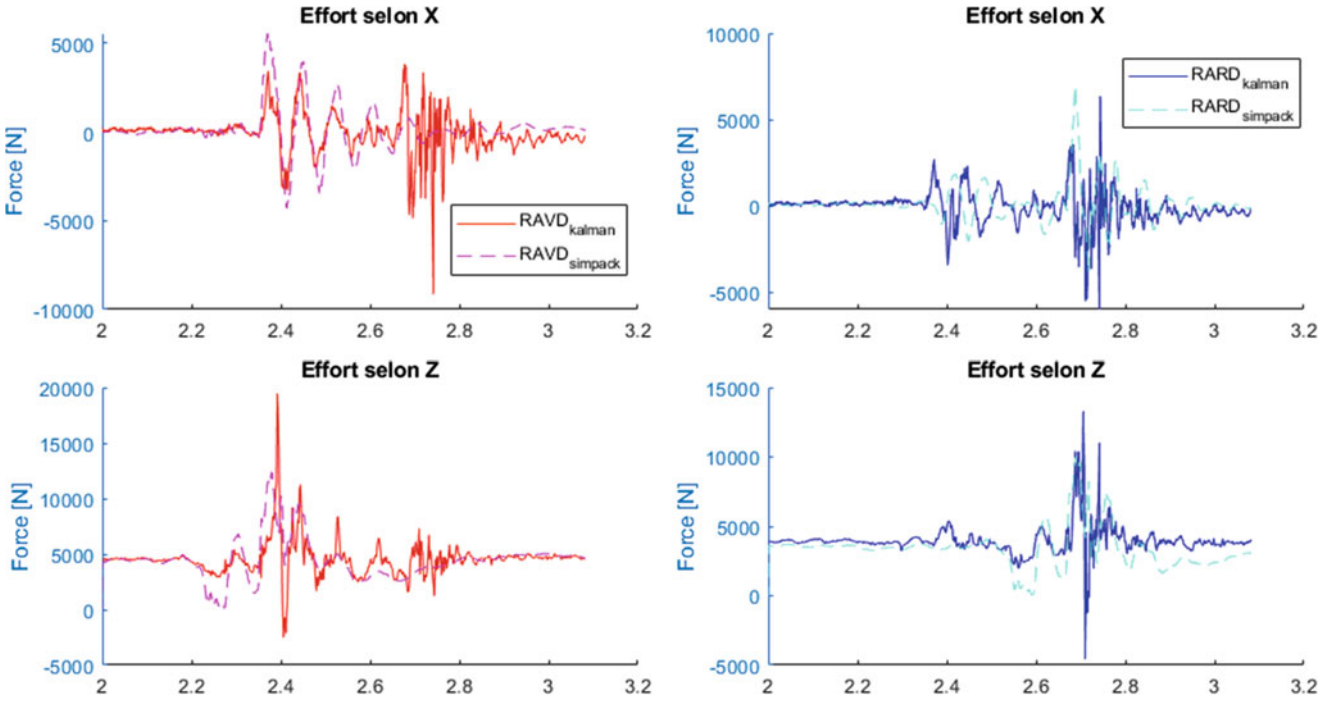

Fig. 24.3 Load identification with real measurement when sinus is added to the accelerometer equation of the measurement model

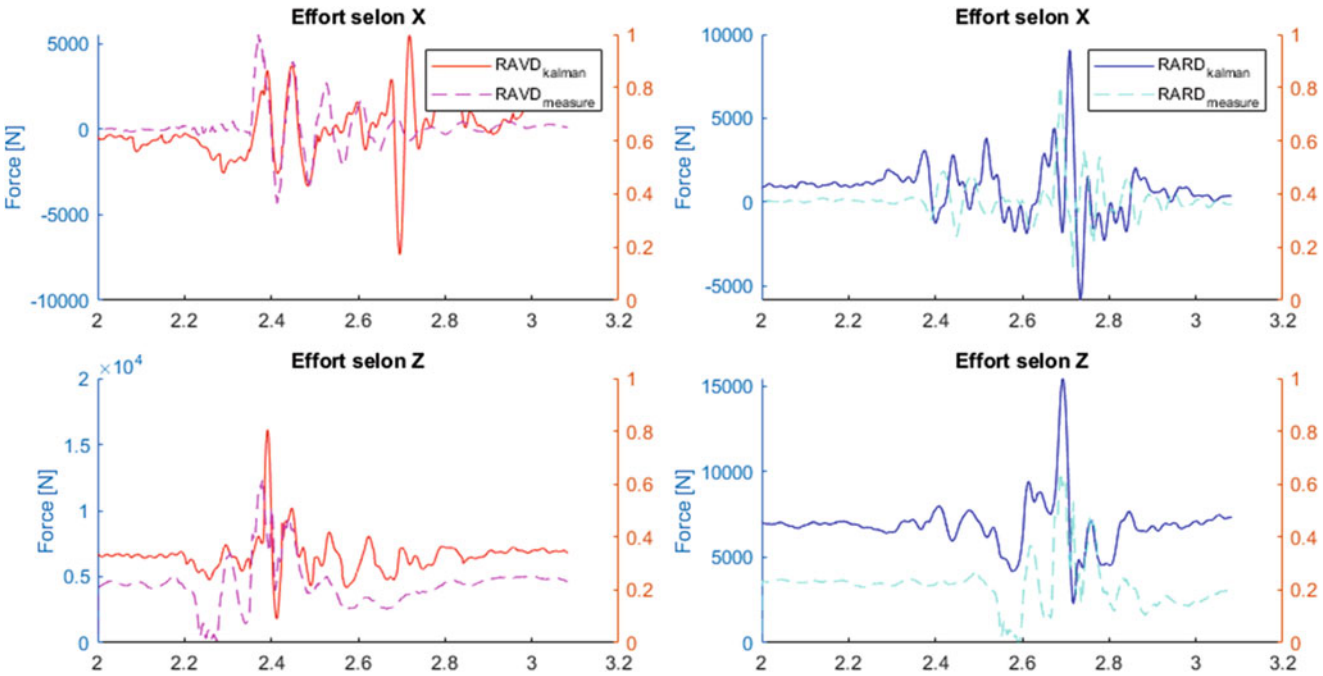

Fig. 24.4 Load identification with real measurement when measures are filtering above 50 Hz

24.4.2 Experimentation of Alternative Kalman Filters

24.5 Conclusion

We have implemented an augmented and constrained extended Kalman filter adapted to a multi-body 2D model of vehicle. Even if we deal here with 2D, the implementation choices are oriented to easily adapt the approach to a 3D model of vehicle. This approach takes into account constraint equations and nonlinearities due to the prediction and measurement models. This ACEKF is designed to estimate the wheel center load when the vehicle is rolling on a real road. The road profile is unknown but the Kalman estimator is augmented by load parameters and then can identify it. The wheel center load is well estimated in vertical direction. The combination of measurement from accelerometers, gyrometer, tachometer, and GPS was identified as a set of sensors sufficient to estimate the attitude of a car body and this study confirms the feasibility to identify wheel center loads with the same set.

References

1. Kalman R.E.: A new approach to linear filtering and prediction problems". Trans. ASME J. Basic Eng. **82**, 35–45 (1960)
2. Risaliti, E., Van Cauteren, J., Tamarozzi, T., Cornelis, B., Desmet, W.: Virtual sensing of wheel center forces by means of a linear state estimator. In: Proceedings of ISMA (2016)
3. Risaliti, E., Tamarozzi, T., Cornelis, B., Desmet, W.: Virtual sensing of wheel center loads on a mcpherson suspension. In: International Conference on Noise and Vibration Engineering (2018)
4. Ribeiro, M.I.: Kalman and extended Kalman filters: concept, derivation and properties (2004)
5. Markley, F.L., Shuster, M.D. Leffens, E.J.: Kalman filtering for spacecraft attitude estimation. J. Guidance Control Dyn. **5**, 417–429 (1982)
6. Brétaille, D., Peyret, F., Joly, C.: Comparative study of non-linear filtering techniques applied to real time 2d. traitement du signal **25**, 201–220 (2008)
7. Zhou, Z., Zhao, L., Wan, C., Tang, H., Xue, S., Xie, L.: Parameter identification for structural health monitoring with extended Kalman filter considering integration and noise effect. Appl. Sci. **8**, 2076–3417 (2018)
8. Makni, A.: Fusion de données inertielles et magnétiques pour l'estimation de l'attitude sous contrainte énergétique d'un corps rigide accéléré. traitement du signal et de l'image. Thesis, Université Grenoble Alpes (2016)
9. Salaün, E., Martin, P.: Generalized multiplicative extended Kalman filter for aided attitude and heading reference system. In: Guidance Navigation, and Control Conference (2010)
10. Yang, Y.: Robust Kalman filtering with constraints: a case study for integrated navigation. J. Geodesy **84**, 373–381 (2010)
11. Simon, D.: Kalman filtering with state constraints: a survey of linear and nonlinear algorithms. Control Theory Appl. **4**, 1303–1318 (2010)
12. Chandrasekar, J., Palanthandalam-Madapusi, H.J., Otávio, B., Teixeira, S.: Gain-constrained kalman filtering for linear and nonlinear systems. Trans. Signal Process. **56**, 4113–4123 (2008)
13. Chou, J.C.K.: Quaternion kinematic and dynamic differential equations. Trans. Robot. Autom. **8**, 53–64 (1992)
14. Débarbouillé, A., Renaud, F., Dimitrijevic, Z., Chojnacki, D., Rota, L., Dion, J.-L.: Wheel forces estimation with an augmented and constrained extended Kalman filter applied on a nonlinear multi-body model of a half vehicle. Proc. Struct. Integr. **38**, 342–351 (2022). Fatigue Design 2021, International Conference Proceedings, 9th Edition
15. Flores, P., Machado, M., Seabra, E., Tavares da Silva, M.: A parametric study on the Baumgarte stabilization method for forward dynamics of constrained multi-body systems. J. Comput. Nonlinear Dyn. (2011)

Chapter 25
Nonlinear Dynamics, Continuation, and Stability Analysis of a Shaft-Bearing Assembly

Brian Evan Saunders, Robert J. Kuether, Rui M. G. Vasconcellos, and Abdessattar Abdelkefi

Abstract In this work, the frequency response of a simplified shaft-bearing assembly is studied using numerical continuation. Roller-bearing clearances give rise to contact behavior in the system, and past research has focused on the nonlinear normal modes of the system and its response to shock-type loads. A harmonic balance method (HBM) solver is applied instead of a time integration solver, and numerical continuation is used to map out the system's solution branches in response to a harmonic excitation. Stability analysis is used to understand the bifurcation behavior and possibly identify numerical or system-inherent anomalies seen in past research. Continuation is also performed with respect to the forcing magnitude, resulting in what are known as S-curves, in an effort to detect isolated solution branches in the system response.

Keywords Nonlinear dynamics · Contact/impact · Harmonic balance · S-curves · Stability

25.1 Introduction

Mechanical systems are often operated in complex engineering environments such as random excitations and shock loading, which reveal nonlinear phenomena such as large or plastic deformations, friction, and intermittent contact between parts. Mechanical operating environments are generally sorted into two classes: relatively low-amplitude, long time duration such as vibrating systems, and high-amplitude, short time duration such as systems undergoing mechanical shock. System environments that operate in the linear regime benefit from faster and more accurate solution analysis (i.e., modal superposition) than nonlinear systems. Well-known methods like linear modal analysis do not hold for nonlinear systems unless the nonlinearity is weak and can be linearized with acceptable accuracy.

Some nonlinearities such as contact/impact cannot be linearized easily, or only in certain limits as the contact gaps and stiffnesses become sufficiently large or small [1]. Contact behavior operating within these limits, large-amplitude vibrations, and mechanical shock all tend to cause strongly nonlinear responses; so, approximations with linear modal analysis will still miss out on extremely important behaviors. These behaviors may be desirable or undesirable, depending on the application. A clearance between moving parts, for example, can be taken advantage of in the form of targeted energy transfer to mitigate the effects of mechanical shock [2]. Conversely, isolas are an undesirable behavior, since a perturbation can cause a system to suddenly jump from a low-amplitude response to a high-amplitude response. Isolas can be present near the primary resonances of a system, subharmonic resonances, and elsewhere in the frequency response [3]. Other considerations are also important for accurately capturing the nonlinear behavior in an engineering system, such as any inherent symmetries in the system, accurate damping behavior when possible, or the variation of a parameter(s) due to wear [4, 5].

In this work, we study the nonlinear frequency response of a simplified model of a shaft-bearing assembly. The system of interest was previously developed by Goldberg et al. [6] and studied using nonlinear modal analysis, finite element analysis, and experimental transient ringdown to approximate the system's response to shock-type loadings. A major goal of this work is to study the formation of nonlinear behaviors, such as chaos or superharmonic, subharmonic, and isolated resonances, with

B. E. Saunders (✉) · A. Abdelkefi
Mechanical & Aerospace Engineering Department, New Mexico State University, Las Cruces, NM, USA
e-mail: bevan343@nmsu.edu

R. J. Kuether
Sandia National Laboratories, Albuquerque, NM, USA

R. M. G. Vasconcellos
Campus of São João da Boa Vista, São Paulo State University, São João da Boa Vista, Brazil

M. R. W. Brake et al. (eds.), *Nonlinear Structures & Systems, Volume 1*, Conference Proceedings of the Society for Experimental Mechanics Series, https://doi.org/10.1007/978-3-031-36999-5_25

respect to parameters such as contact stiffness and gap sizes. Another goal is to explore the effects of asymmetries in the system, such as unequal contact stiffnesses or contact gap sizes. Both time integration and multiharmonic balance (MHB) simulations are utilized to detect all motions whether periodic, quasiperiodic, chaotic, or isolated, and to continue periodic solution branches, respectively. Stability analysis is used to understand bifurcation behavior, and anomalies seen in past research are also explored further. Continuation with respect to the system forcing magnitude, resulting in what are known as S-curves, are also computed in an effort to detect and better understand isolas in the system response.

25.2 System Modeling and Numerical Methods

Goldberg et al. studied a simplified bearing-and-shaft assembly [6]. Their experimental setup consisted of an impact beam representing a shaft, with the contact effects of bearing clearances represented by modal hammer tips. The impact tips have variable gap heights and impact stiffnesses. Compression springs on both ends are used to hold the impact beam within a box frame and are meant to represent soft suspension springs such that the lowest frequency modes imitate those of pseudo rigid body modes. The impact tips are also mounted to the frame structure. A 3 DOF model is used for simulations with the following assumptions: gravity is ignored, equal linear viscous damping is applied to each DOF, and a monoharmonic excitation is applied to the center DOF.

$$\begin{bmatrix} m_1 & 0 & 0 \\ 0 & m_2 & 0 \\ 0 & 0 & m_3 \end{bmatrix} \begin{bmatrix} \ddot{x}_1 \\ \ddot{x}_2 \\ \ddot{x}_3 \end{bmatrix} + \begin{bmatrix} c & 0 & 0 \\ 0 & c & 0 \\ 0 & 0 & c \end{bmatrix} \begin{bmatrix} \dot{x}_1 \\ \dot{x}_2 \\ \dot{x}_3 \end{bmatrix} + \begin{bmatrix} 2\kappa_s + \frac{k}{L^2} & \frac{-2k}{L^2} & \frac{k}{L^2} \\ \frac{-2k}{L^2} & \frac{4k}{L^2} & \frac{-2k}{L^2} \\ \frac{k}{L^2} & \frac{-2k}{L^2} & 2\kappa_s + \frac{k}{L^2} \end{bmatrix} \begin{bmatrix} x_1 \\ x_2 \\ x_3 \end{bmatrix} + \begin{bmatrix} f_g(x_1) \\ 0 \\ f_g(x_3) \end{bmatrix} = \begin{bmatrix} 0 \\ p_2 \\ 0 \end{bmatrix} \cos(\omega t) \# \tag{25.1a}$$

$$f_g(x) = \begin{cases} k_g(x+g), & x < -g \\ 0, & -g \le x \le g \# \\ k_g(x-g), & x > g \end{cases} \tag{25.1b}$$

25.3 Frequency Response Analysis

Frequency response analysis shows the contact stiffness is the dominant parameter controlling formation of nonlinear behaviors. This is true even for asymmetric configurations, where the left- and right-side spring and contact parameters are unequal. The contact gap size and forcing magnitude are the next most influential parameters. Figure 25.1 shows the response near the system's third resonance for a moderate contact stiffness (as compared to "soft" or "hard" contact). The resonance peak extends to approximately 707 Hz due to hardening from the contact elements, and a cloud of isolas exists with subharmonic orders of 5, 7, 9, 10, 11, 12, and 13. The isolas appear in symmetry-complementing pairs. Two isolas

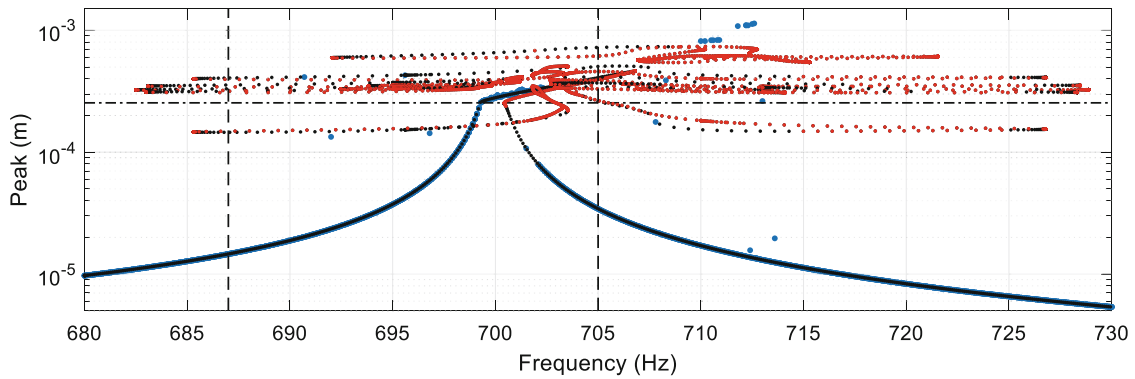

Fig. 25.1 Floquet stability results for DOF x_1 near the third resonance. Blue dots: time integration results. Black dots: stable MHB. Red dots: unstable MHB. Dash-dot line: upper contact boundary. Vertical lines: 687 Hz and 705 Hz, analyzed in the final conference presentation

of quasiperiodic motions also exist and can only be captured currently using time integration methods. Stability analysis on the MHB solution shows a majority of each isola is unstable, and study of the basins of attraction in these frequency ranges revealed that the system tends to the lower-amplitude main solution branch more so than to any of the isolas. At low frequency, there exist superharmonic resonances, symmetry-breaking bifurcations, regions of chaos, and quasiperiodic isolas. Isolas were not observed for the system's nominal, hard value of contact stiffness, but large regions of chaotic behavior were observed.

25.4 Conclusions

In this work, we studied the nonlinear frequency response of a simplified model of a shaft-bearing assembly. Overall, the contact stiffness is the most dominant nonlinear parameter in the system, and asymmetries in the contact stiffnesses and gap sizes lead to the most significant changes in behavior for a modified system. Superharmonic resonances, isolas, quasiperiodic, and chaotic behaviors were formed and observed. An accurate damping model would be valuable, since even minor changes in models showed noticeable effects. Valuable future work could apply harmonic balance techniques to capture low-frequency responses with complete or incomplete chatter behavior. Other valuable areas include improving the detection of isolas, especially in densely packed clouds of isolas, and further development of harmonic balance continuation techniques to capture isolas of quasiperiodic responses.

Acknowledgments The authors B. Saunders and A. Abdelkefi gratefully acknowledge the support from Sandia National Laboratories. This study describes objective technical results and analysis. Any subjective views or opinions that might be expressed in the paper do not necessarily represent the views of the U.S. Department of Energy or the United States Government. This work was supported by the Laboratory Directed Research and Development program at Sandia National Laboratories, a multimission laboratory managed and operated by National Technology and Engineering Solutions of Sandia LLC, a wholly owned subsidiary of Honeywell International Inc. for the U.S. Department of Energy's National Nuclear Security Administration under contract DE-NA0003525. SAND2022-14739 C. R. Vasconcellos acknowledges the financial support of the Brazilian agency CAPES (grant 88881.302889/2018-01).

References

1. Herrera, C.A., McFarland, D.M., Bergman, L.A., Vakakis, A.F.: Methodology for nonlinear quantification of a flexible beam with a local, strong nonlinearity. J. Sound Vib. **388**, 298–314 (2017). https://doi.org/10.1016/j.jsv.2016.10.037
2. Gzal, M., Fang, B., Vakakis, A.F., Bergman, L.A., Gendelman, O.V.: Rapid non-resonant intermodal targeted energy transfer (IMTET) caused by vibro-impact nonlinearity. Nonlinear Dynam. **101**(4), 2087–2106 (2020). https://doi.org/10.1007/s11071-020-05909-8
3. Kuether, R.J., Renson, L., Detroux, T., Grappasonni, C., Kerschen, G., Allen, M.S.: Nonlinear normal modes, modal interactions and isolated resonance curves. J. Sound Vib. **351**, 299–310 (2015). https://doi.org/10.1016/j.jsv.2015.04.035
4. Smith, S., Bilbao-Ludena, J.C., Catalfamo, S., Brake, M.R.W., Reuß, P., Schwingshackl, C.W.: The effects of boundary conditions, measurement techniques, and excitation type on measurements of the properties of mechanical joints. In: Nonlinear Dynamics, Volume 1, Conference Proceedings of the Society for Experimental Mechanics Series, pp. 415–431. Springer, Cham (2016)
5. Xu, M., Han, Y., Sun, X., Shao, Y., Gu, F., Ball, A.D.: Vibration characteristics and condition monitoring of internal radial clearance within a ball bearing in a gear-shaft-bearing system. Mech. Syst. Signal Process. **165**, 108280 (2022). https://doi.org/10.1016/j.ymssp.2021.108280
6. Goldberg, N.N., Demsky, S., Youssef, A.A., Carter, S.P., Fowler, D., Jackson, N., Kuether, R.J., Steyer, A.: Experimental and computational investigation of nonlinear dynamics of a simplified bearing-and-shaft assembly. 40th International modal analysis conference (IMAC XL), Orlando, FL, Feb 7–10, 2022

Chapter 26
Quantification of Amplitude- and Rotation Speed-Dependent Nonlinearity of Machine Tool Spindles

Meng-Huan Hsieh and Yum-Ji Chan

Abstract Stiffness of spindles, which are high-speed rotors, has to be determined accurately for precision metal cutting. Dependence of rotor natural frequencies and damping on both amplitude and rotation speed is studied experimentally. The spindle shaft is excited using a noncontact electromagnetic exciter: the excitation suddenly stops for free vibration after the response reaches steady state. The peak finding and picking (PFF) method is used to determine the amplitude-dependent natural frequency and damping. It is found that the nonlinearity trends obtained from different excitation methods are similar.

Keywords Rotordynamics · Nonlinear vibration · Nonlinear identification · Electromagnetic excitation · Ringdown test

26.1 Introduction

High-speed spindles in machine tools are widely used in the manufacturing industry for rapid manufacturing. Dynamic properties of machine tool spindle determine precision, accuracy, and cutting stability of a machine tool [1]; thus, it is desirable to determine them accurately. It is known that spindle bearing stiffness decreases with increasing rotating speed [2], and both rolling bearings and internal joints of spindles display nonlinear properties.

Speed-dependent nonlinear spindle models have been built to study cutting stability [3], but there are little experimental evidence. Traditional excitation methods in experimental modal analysis (EMA) are not applicable to high-speed spindles, because excitation has to be noncontact. Some noncontact exciters evolve from active magnetic bearings (AMB) for excitation in both bending directions [4]. Noncontact excitation and measurement system were introduced to carry out EMA on rotating spindles [5, 6]. Both the frequency response function (FRF) [7] and the time-domain free decay can be used to quantify the nonlinear characteristics of a system, such as amplitude-dependent natural frequency and damping. In time-domain signal processing, zero-crossing counts [8] and Hilbert transform [9] were proposed to estimate the instantaneous frequencies, and damping ratio is usually obtained from the envelope of time-domain free decay.

This study obtains amplitude-dependent natural frequencies and damping ratios of the first three modes of a spindle (Fig. 26.1) experimentally for rotation speed up to 11,000 rpm. After using impact hammers to obtain the ranges of natural frequencies in a nonrotating spindle, electromagnetic exciter excites the spindle near a natural frequency to steady state, before it is turned off to achieve free-decay response. Response is measured using a Laser Doppler Vibrometer (LDV). Nonlinear characteristics is identified by using the peak finding and fitting (PFF) method [10]. The PFF method, which is formulated with single degree-of-freedom (SDOF) systems, can be applied to multiple degrees-of-freedom (MDOF) systems by filtering the response by bandpass filter.

26.2 Selected Results

EMA on nonrotating spindle with standardized impact excitation shows that the first two flexural natural frequencies become lower under higher impact force (Fig. 26.2). After initial tests, electromagnetic exciter is used to carry out ringdown testing to obtain free-decay response of the spindle. PFF analysis shows similar dependence of the first two natural frequencies

M.-H. Hsieh · Y.-J. Chan (✉)
Department of Mechanical Engineering, National Chung Hsing University, Taichung, Taiwan
e-mail: yjchan@nchu.edu.tw

M. R. W. Brake et al. (eds.), *Nonlinear Structures & Systems, Volume 1*, Conference Proceedings
of the Society for Experimental Mechanics Series, https://doi.org/10.1007/978-3-031-36999-5_26

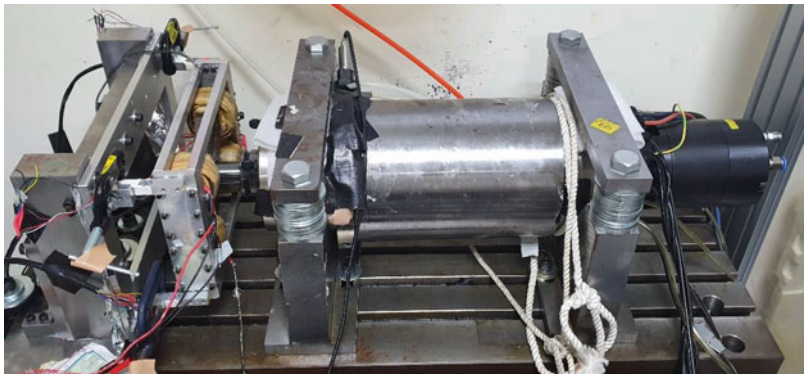

Fig. 26.1 Spindle tested in this study

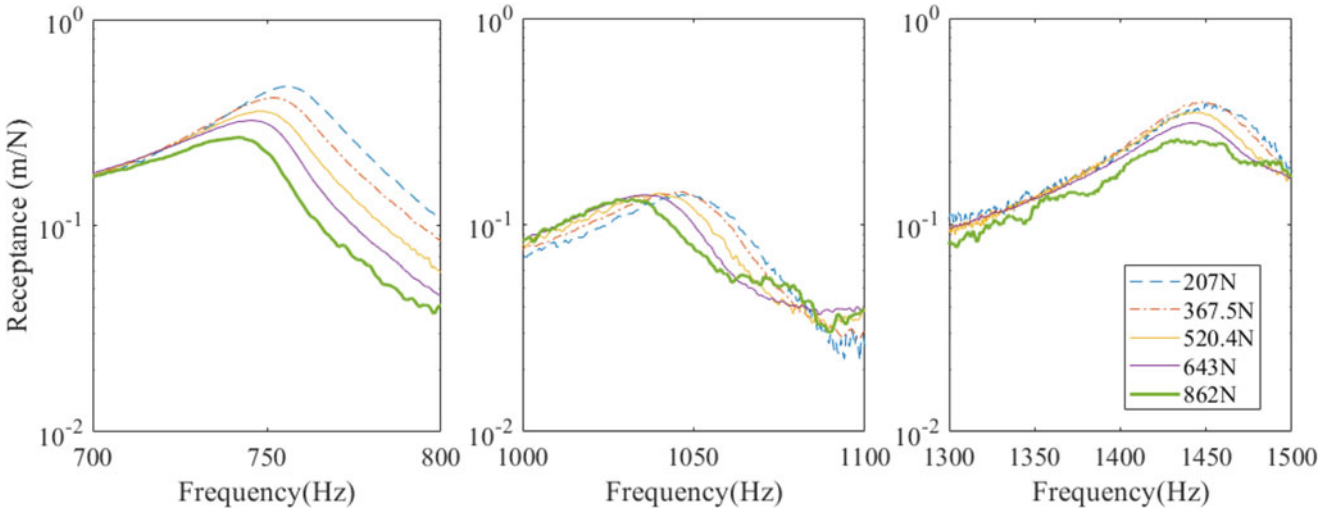

Fig. 26.2 Receptance FRFs under various levels of impact excitation near to (left) first (center), second (right), and third flexural natural frequencies

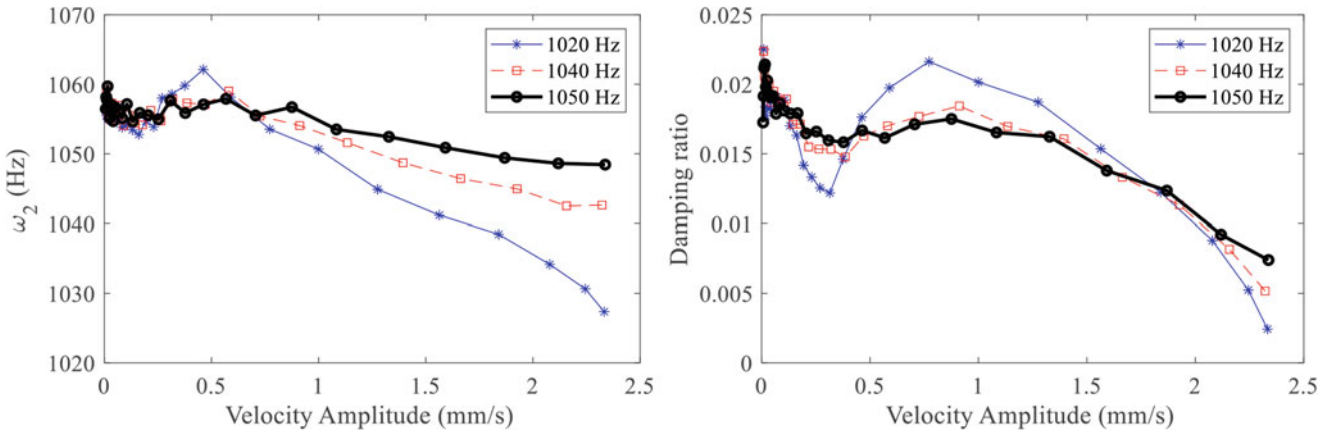

Fig. 26.3 Amplitude-dependent properties of (left) second natural frequency and (right) associated damping ratio under different initial excitation frequencies

on amplitude, although the results at high amplitude depend on initial excitation frequency (Fig. 26.3). The third natural frequency does not depend on amplitude because of its structure (Fig. 26.4).

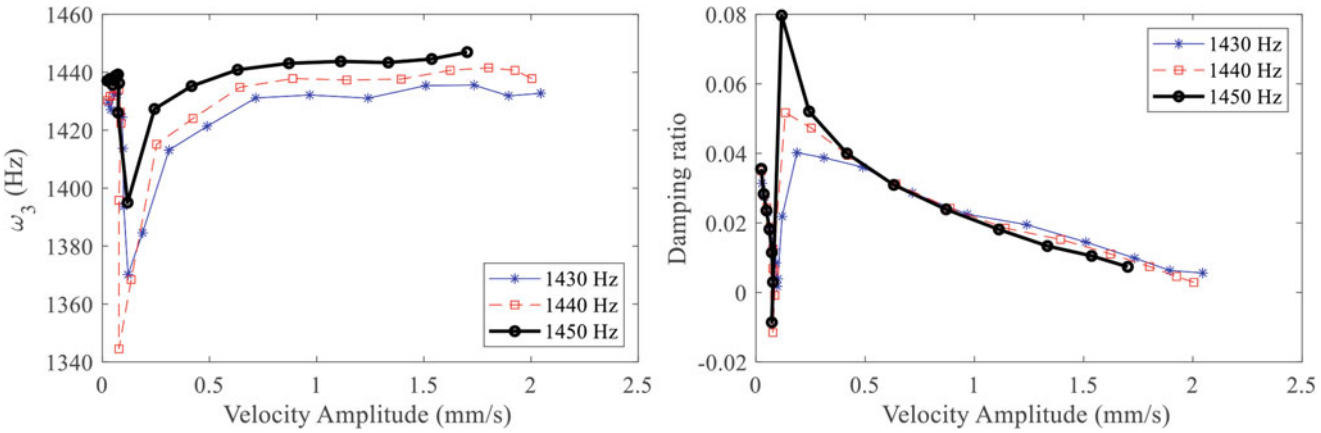

Fig. 26.4 Amplitude-dependent properties of (left) third natural frequency and (right) associated damping ratio under different initial excitation frequencies

Results for spindles rotating at 2000, 5000, and 10,000 rpm have been shown in the presentation. In summary, PFF analysis on the free decay shows large fluctuation in natural frequencies, and negative instantaneous damping ratio occurs more often.

26.3 Conclusions

By considering the first three flexural natural frequencies of a spindle, the proposed method with electromagnetic exciter and PFF nonlinear identification method gives similar nonlinear characteristics to traditional method, which involves impact hammer and observation of FRF peak shift. It is noted that nonlinear characteristics of rotating spindles fluctuate with amplitude, partly because of the interaction between the close natural frequencies.

Acknowledgments The research is generously supported by National Science and Technology Council grant number NSTC 111-2221-E-005-052-MY2.

References

1. Abele, E., Altintas, Y., Brecher, C.: Machine tool spindle units. CIRP Ann. Manuf. Technol. **59**, 781–802 (2010)
2. Chen, J.-S., Hwang, Y.-W.: Centrifugal force induced dynamics of a motorized high-speed spindle. Int. J. Adv. Manuf. Technol. **30**, 10–19 (2006)
3. Xu, K., Wang, B., Zhao, Z., Zhao, F., Kong, X., Wen, B.: The influence of rolling bearing parameters on the nonlinear dynamic response and cutting stability of high-speed spindle systems. Mech. Syst. Signal Process. **136**, 106448 (2020)
4. Tlalolini, D., Ritou, M., Rabréau, C., Loch, S.L., Furet, B.: Modeling and characterization of an electromagnetic system for the estimation of frequency response function of spindle. Mech. Syst. Signal Process. **104**, 294–304 (2018)
5. Rantatalo, M., Aidanpää, J.-O., Göransson, B., Norman, P.: Milling machine spindle analysis using FEM and non-contact spindle excitation and response measurement. Int. J. Mach. Tools Manuf. **47**, 1034–1045 (2007)
6. Kono, D., Nishio, S., Yamaji, I., Matsubara, A.: A method for stiffness tuning of machine tool supports considering contact stiffness. Int. J. Mach. Tools Manuf. **90**, 50–59 (2015)
7. Dhupia, J.S., Powalka, B., Ulsoy, A.G., Katz, R.: Effect of a nonlinear joint on the dynamic performance of a machine tool. J. Manuf. Sci. Eng. **129**, 943–950 (2007)
8. Londoño, J.M., Neild, S.A., Cooper, J.E.: Identification of backbone curves of nonlinear systems from resonance decay responses. J. Sound Vib. **348**, 224–238 (2015)
9. Feldman, M.: Hilbert transform in vibration analysis. Mech. Sys. Signal Proc. **25**, 735–802 (2011)
10. Jin, M., Chen, W., Brake, M.R.W., Song, H.: Identification of instantaneous frequency and damping from transient decay data. J. Vib. Acoust. **142**, 1 (2020)

Chapter 27
Toward Active Control of Limit Cycle Oscillations in an Aeroelastic Wing Using a Variable Frequency Flow Disturbance Generator

Michael T. Hughes, Daniel Hall, Ashok Gopalarathnam, and Matthew Bryant

Abstract Limit cycle oscillations (LCOs) in nonlinear aeroelastic systems can be problematic for aircraft and structures, but can also be exploited for energy-harvesting applications. In the presence of constant flow conditions and structural characteristics, once initiated, aeroelastic LCO can persist indefinitely. However, the introduction of external forces from impinging vortices injected upstream of the wing has been shown to modulate the self-sustaining LCO. Under the right conditions, a static bluff body placed upstream of an aeroelastic wing has been experimentally shown to annihilate preexisting LCO and produce a cessation of oscillation. However, the exact conditions and characteristics of both the bluff body and the aeroelastic system must be tailored to produce this behavior. A rotation-oscillating cylinder with an attached splitter plate actuated by a servomotor is capable of producing a well-defined von Kármán vortex street at a range of oscillation frequencies. This system has been shown to both excite and annihilate LCO in a downstream aeroelastic wing when oscillated just below the inherent LCO frequency of the wing. Using real-time sensing on the aeroelastic wing to measure pitch angle and heave displacement, a controller can be designed to trigger the appropriate motion of the disturbance generator to inject prescribed disturbances if wing LCOs are detected. The variable frequency disturbance generator can then be used to either enhance or reduce the wing LCO amplitude or cancel out the LCO entirely. The controller will be designed using state machine control theory. The state machine determines whether the wing is not in LCO, entering LCO, in LCO, or exiting LCO. In this chapter, we present wind tunnel experiments that demonstrate and characterize the ability of an automatically controlled upstream flow disturbance generator to produce or suppress LCO in an aeroelastic wing. The experiments provide insight into how controlled interactions between the aeroelastic wing and prescribed flow disturbances can be used to produce desired LCO behavior and may spur follow-on development of energy-harvesting enhancement devices and on-wing disturbance generator devices that could be implemented in flight vehicles.

Keywords Aeroelasticity · Limit cycle oscillations · Wing-wake interaction · Flow disturbance · Active control

27.1 Introduction

Aeroelasticity and its effects on structures, lifting surfaces, and other bodies have been studied extensively over the last century. Samuel Langley's prototype aircraft failed due to aeroelastic divergence [1], resulting in his loss in the race to heavier-than-air flight to the Wright Brothers who utilized wing warping effects to steer the Wright Flyer [2]. As the fledgling aviation industry continued to grow, early pioneers continued to encounter instances of aeroelastic behavior. In 1935, Theodorsen penned his foundational study, *General Theory of Aerodynamic Instability and the Mechanism of Flutter* [3], for the National Advisory Committee on Aeronautics (NACA) marking the beginning of academic study of aeroelastic phenomena. The simplest strategy to avoid the destructive effects of aeroelasticity is to design the vehicle so that the flutter speed lies beyond the range of the flight envelope. However, nonlinearities due to structural components [4, 5], added external stores [6, 7], and unsteady aerodynamics [8] present more complex situations, which cannot always be predicted by linear flutter analysis. To address these instances of destructive aeroelasticity, a number of approaches have been taken including the addition of nonlinear energy sinks (NES) [9, 10] and adaptive control of existing aircraft control surfaces [11].

In addition to aviation applications, some modern studies have explored using aeroelastic phenomena in renewable energy harvesting. Bryant and Garcia [12] proposed a system, which used piezoelectric devices attached to an aeroelastic wing

M. T. Hughes (✉) · D. Hall · A. Gopalarathnam · M. Bryant
Department of Mechanical and Aerospace Engineering, North Carolina State University, Raleigh, NC, USA
e-mail: mthughe2@ncsu.edu

M. R. W. Brake et al. (eds.), *Nonlinear Structures & Systems, Volume 1*, Conference Proceedings
of the Society for Experimental Mechanics Series, https://doi.org/10.1007/978-3-031-36999-5_27

with degrees of freedom in pitch and heave. Further studies by Bryant and Garcia [13] built on the previous system and experimentally characterized the power output and flutter response over a large range of freestream conditions and with both a flat plate and an airfoil. Zhao and Yang [14] showed that the addition of a beam stiffening device resulted in effective power generator for aeroelastic systems experiencing galloping instabilities, vortex-induced vibrations, and flutter. Other methods of power enhancement of such aeroelastic systems have focused on wing-wake interactions resulting from upstream bodies. Kirschmeier and Bryant [15] showed that tandem oscillating wings can be tuned to enhance the energy transfer from the wake into the downstream wing.

This chapter will discuss the application of a state-machine control scheme to automatically control aeroelastic behavior in a two degree-of-freedom (2DOF) aeroelastic wing using vortices produced by an upstream variable frequency disturbance generator. The remainder of this chapter will walk through the development of the aeroelastic wing and the disturbance generator experimental hardware, discuss the state-machine control scheme, present preliminary results, and discuss progress toward incorporating a recurrent neural network (RNN) machine learning model in the aeroelastic control approach.

27.2 Methodology

Experimental testing was performed in the North Carolina State University (NCSU) Subsonic Wind Tunnel, which is a closed-return tunnel with a test section measuring 0.81 m by 1.14 m by 1.17 m. A variable pitch fan driven by a three-speed electric motor provides flow in the tunnel, measured by dynamic pressure, which is controlled by changing the blade pitch at each of the three motor speeds. The maximum dynamic pressure in the tunnel test section is 720 Pa, corresponding to a flow velocity of approximately 40 m/s at nominal temperature and atmospheric pressure.

The aeroelastic wing apparatus presented in this work was initially developed by Gianikos et al. [16] and described in more detail there and in Kirschmeier et al. [17]. The apparatus (please refer Fig. 27.1) includes the main wing section, two mounting carriages, and a support structure. The main wing section consists of a decambered SD7003 airfoil with a chord length of 15 cm and a span of 60 cm. The wing was constructed from 3D printed ABS plastic with two internal support rods to improve the strength of the wing and reduce deflection along the span. The ends of the wing were capped with flat, elliptical plates of length 45 cm to reduce tip effects and allow the wing section to emulate 2D flow based on the work of Visbal and Garman [18]. The mounting carriages were placed above and below the wind tunnel test section along a sliding rail mounted to the support structure. The wing section was mounted vertically in the test section and attached to the carriages

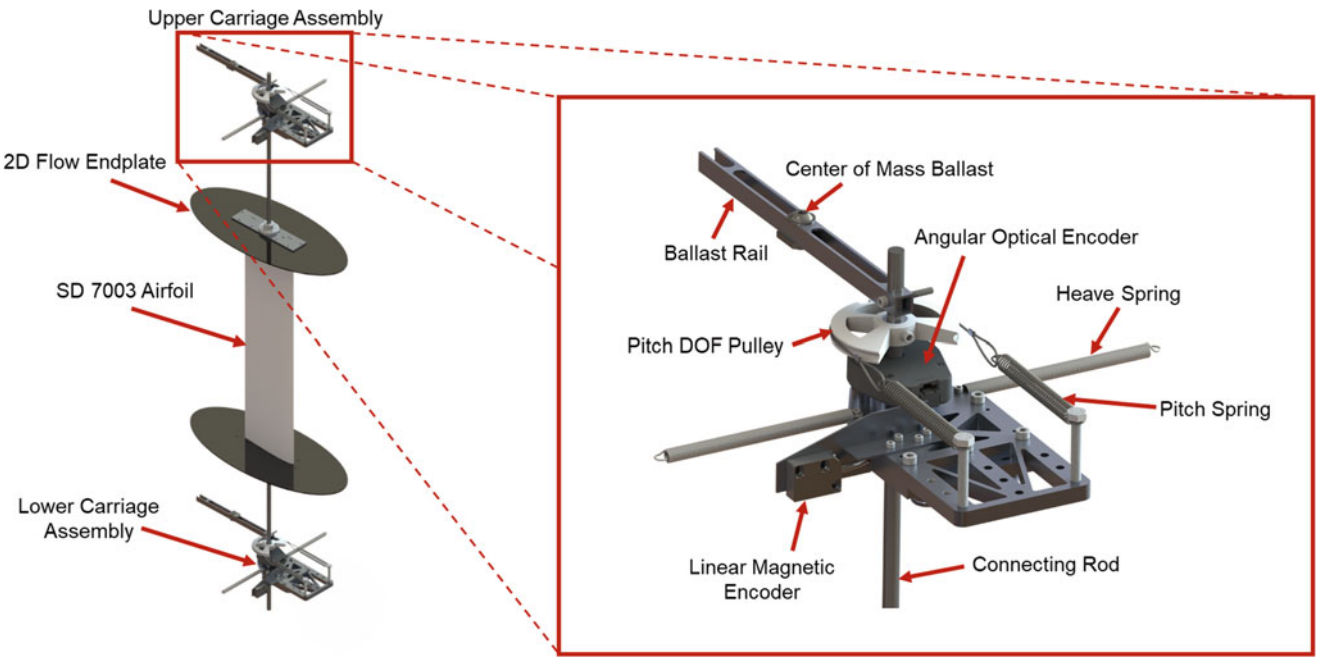

Fig. 27.1 CAD rendering of the aeroelastic wing apparatus showing the wing section and mounting carriages with key components labeled. The external support structure and linear rails are not shown

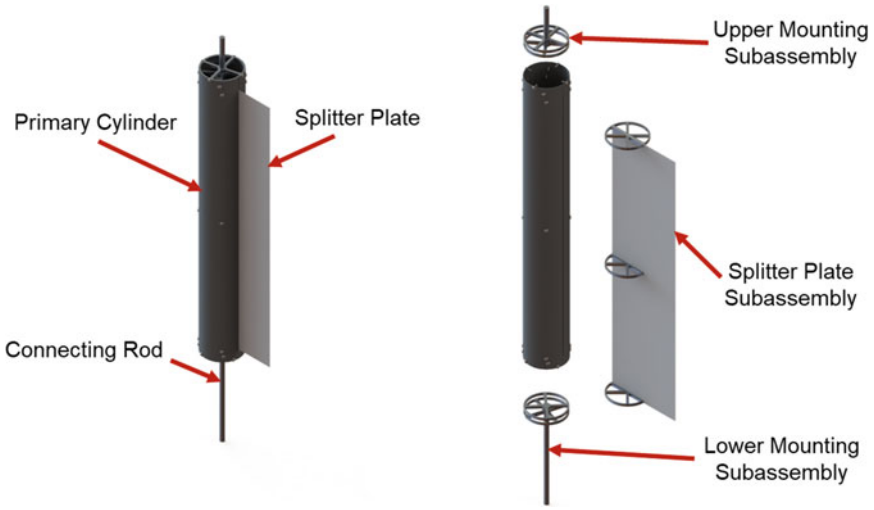

Fig. 27.2 Fully assembled and exploded view of the variable frequency disturbance generator showing the major components and subassemblies used during construction

via steel rods. The sliding rail allowed the wing to translate, or heave, perpendicular to the direction of flow, while bearings in the carriages allowed the wing to rotate about its midchord. The support structure to which the rails were attached was constructed around the wind tunnel section using T-slotted aluminum framing. No components of the support structure were attached to the wind tunnel structure to avoid any unwanted vibrations being transferred into the experimental apparatus. The elastic properties of the system were supplied by attaching linear extension springs to the mounting carriages. The extension springs providing stiffness in the heave degree of freedom were attached to either side of each carriage and a fixed point on the support structure. Springs providing stiffness in the pitch degree of freedom were mounted on the carriages themselves and attached to a pulley connected to the steel rod connecting the wing and carriage. This allowed the pitch springs to translate with the carriage as it moved along the linear mounting rail. In total, eight springs were used, four for each degree of freedom split between the upper and lower carriages.

The variable frequency flow disturbance generator, shown in Fig. 27.2, was designed to produce a well-defined von Karman vortex street with shed vortices being produced at rates from less than 1 Hz to at least 8 Hz. The main body of the disturbance generator was constructed from a 10.48 cm diameter cylinder made of braided carbon fiber produced by DragonPlate™ (Elbridge, NY, USA). Research by Rockwood and Medina [19] showed that while an oscillating cylinder can produce a locked-in vortex wake with a shedding frequency equal to its oscillation frequency, the inclusion of a trailing edge splitter plate resulted in a more well-defined wake for the same range of oscillation frequencies. For this work, the splitter plate was constructed from a 1.5875 mm thick carbon fiber and birch composite material produced by DragonPlate™ (Elbridge, NY, USA), which extended one cylinder diameter from the trailing edge. The rotational axis of the disturbance generator was placed at the central axis of the primary cylinder. A SureServo SVL-210b produced by AutomationDirect (Cumming, GA, USA) was used to drive the rotation of the disturbance generator and controlled using a Copley Control (Canton, MA, USA) Xenus XTL-230-18. A maximum continuous torque of 3.3 Nm and maximum instantaneous torque of 9.9 Nm was provided by the servomotor. While the Xenus controller provided direct control of the servomotor, an analog voltage trajectory sinusoid was supplied to the Xenus by a Keysight (Santa Rosa, CA, USA) 33500B Waveform Generator with the output controlled by the main data acquisition and control virtual instrument (VI).

National Instruments (NI) LabVIEW was run on a NI PXIe-1078 data acquisition computer and used to construct a VI to gather real-time data and control the output status of the disturbance generator trajectory. Wing pitch and disturbance generator angle were recorded with US Digital (Vancouver, WA, USA) E6-10000 optical encoders. The disturbance generator encoder was placed just above the servomotor mount and the wing encoders were place both above and below the wing and the average angle used in all calculations to mitigate effects from structural twist in the wing. Linear displacement of the wing was measured using a Renishaw (West Dundee, IL, USA) LM10 magnetic linear encoder.

Control of the disturbance generator was performed entirely within the LabVIEW VI used to run the experiment and record data. There were two methods of control used in the course of this work. The first method, User Control, allowed the researchers to manually set the oscillation amplitude and frequency and to start and stop the disturbance generator oscillation at-will. The second method, Automatic LCO Control, used preset oscillation amplitude and frequency and was started and stopped using wing pitch amplitude thresholds, allowing this control scheme to function as a rudimentary state machine

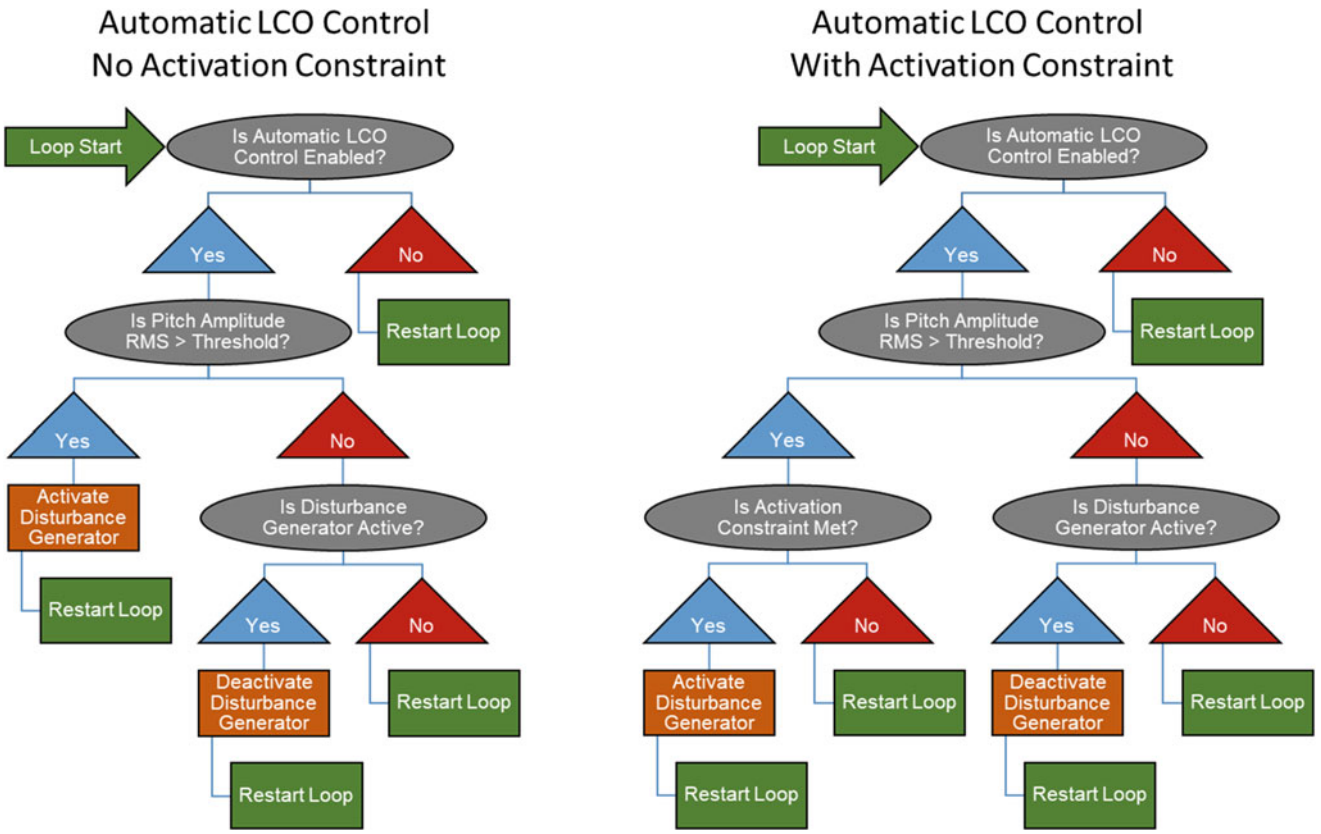

Fig. 27.3 Decision diagrams for the Automatic LCO Control scheme used to detect and annihilate LCO in the downstream wing

within the LabVIEW VI. An additional activation constraint was added to the Automatic LCO Control scheme based on the instantaneous wing pitch value to control the phase between the disturbance generator and wing at activation. A simplified model of the Automatic LCO Control scheme, both with and without the activation constraint, is shown in Fig. 27.3.

Experiments were run to test the effectiveness of the Automatic LCO Control scheme in the NCSU Subsonic Wind Tunnel. For all tests, the disturbance generator was placed at a distance of eight cylinder diameters upstream of the aeroelastic wing measured from the wing quarter-chord to cylinder central axis. Additionally, test section dynamic pressure was set to 720 Pa (1.0 lb/ft^2). To initially trigger LCO in the wing, researchers used the User Control scheme and oscillated the disturbance generator in a sinusoidal trajectory with a frequency of 3.88 Hz $\pm$ 0.01 Hz, lying just below the inherent LCO frequency of the aeroelastic wing apparatus of 3.93 Hz at this dynamic pressure, and an amplitude of approximately 25 degrees. Preset frequencies used with the Automatic LCO Control scheme to attempt LCO annihilation included 3.5 Hz, 3.7 Hz, 3.8 Hz, 4.0 Hz and 4.5 Hz, all with amplitudes of approximately 25 degrees. This range of frequencies was selected to test disturbance generator oscillation frequencies both above and below and near and far from the inherent LCO frequency.

27.3 Results and Analysis

During each test, the disturbance generator was first used to excite the aeroelastic wing apparatus with the User Control scheme. After initializing the oscillations, the wing displayed periodic amplitude growth and decay with maximum amplitude values fluctuating between approximately 0° and 50°. By stopping the disturbance generator oscillations near the peak pitch amplitude in the wing, the system would remain at high amplitude and enter into self-sustaining LCO. This persisted until manually attenuated by reducing the freestream dynamic pressure or using the disturbance generator to annihilate the LCO. The Automatic LCO Control scheme was used to attempt annihilation in the downstream wing using disturbance generator oscillation frequencies of 3.5 Hz, 3.7 Hz, 3.8 Hz, 4.0 Hz, and 4.5 Hz. The rms amplitude threshold used to stop the disturbance generator oscillations was set to 20° in all test cases. LCO annihilation was observed for all disturbance generator frequencies except the 3.5 Hz and 4.5 Hz cases. Disturbance generator oscillation frequencies of 3.8 Hz resulted in time-to-annihilation

Table 27.1 Results from test cases, which resulted in successful LCO annihilation

Test number	Disturbance generator frequency	Instantaneous wing pitch activation constraint	Time to annihilation
1	3.8 Hz	–	15.15 s
2	3.8 Hz	–	19.38 s
3	3.8 Hz	–	15.91 s
4	3.8 Hz	–	13.75 s
5	3.8 Hz	–	13.34 s
6	3.7 Hz	–	7.98 s
7	3.8 Hz	$\theta > 30°$	16.96 s
8	3.8 Hz	$\theta > 30°$	12.84 s
9	4.0 Hz	$\theta > 30°$	12.10 s
10	4.0 Hz	$\theta > 30°$	7.40 s
11	3.8 Hz	$-5° < \theta < 5°$	17.02 s
12	3.8 Hz	$-5° < \theta < 5°$	7.86 s
13	4.0 Hz	$-5° < \theta < 5°$	20.16 s
14	4.0 Hz	$-5° < \theta < 5°$	19.06 s

(TTA) values ranging from 13.34 seconds to 19.375 seconds as shown in Table 27.1. Figure 27.4 provides an example of the pitch and heave time histories of one such test.

Following the initial tests to verify that the Automatic LCO Control scheme could successfully annihilate preexisting LCO in the downstream wing, additional constraints were added to the disturbance generator activation conditions. Using the instantaneous wing pitch angle, an activation constraint was applied to force a defined phase difference between the disturbance generator and the downstream wing. The first constraint required that the instantaneous wing pitch must be greater than 30 degrees while the second activation constraint required an instantaneous wing pitch angle between −5 degrees and 5 degrees. For these tests, disturbance generator frequencies of both 3.8 Hz and 4.0 Hz were used to annihilate LCO. As shown in Table 27.1, TTA ranged from 7.40 seconds to 20.16 seconds, with the shortest average TTA found when the oscillation frequency was set to 4.0 Hz and the activation constraint requiring wing pitch greater than 30 degrees.

Spectral analysis on the wing pitch and heave motion was performed using MATLAB's Fast-Fourier Transform (FFT) tool. The results from the FFT performed on the wing response when the disturbance generator was annihilating the LCO show a relationship between the difference in pitch and heave frequency and TTA, as seen in Fig. 27.5. For the tests with the shortest TTA, the difference between the pitch and heave frequencies is large, whereas the opposite is true for tests with longer TTA. Additionally, it is important to note that the three tests with the fastest TTA each represent a different disturbance generator oscillation frequency (3.7, 3.8, and 4.0 Hz), suggesting that the disturbance generator oscillation frequency is not directly responsible for the reduced TTA. These three cases also show both pitch and heave frequencies below the inherent LCO frequency (i.e., the oscillation frequency when the wing is exhibiting LCO while the disturbance generator is stationary).

27.4 Planned Future Work

To further develop the controller for the disturbance generator and oscillating wing system, the use of machine learning models is being explored. Specifically, a recurrent neural network (RNN) is being developed to take in time history data from these wind tunnel experiments and learn the system's behavior. Due to their architecture, RNNs can utilize the time history dependency of data to recognize the trends in the response of a system, as was shown by Chen et al. [20]. This group utilized a type of RNN known as a long short-term memory (LSTM) neural net to predict wind speeds and flow [20]. A simple RNN model schematic can be seen in Fig. 27.6. RNNs function similarly to other neural networks by taking in the input vector x for each time step, applying matrix transformations on the input vector in the hidden layer h, and generating a predicted output y. Unlike other neural networks, though, RNNs "remember" the hidden layer of the previous time step to be used as another input for the current time step, thus allowing them to identify time history trends.

In order to proceed with training the model, the aeroelastic data from the wind tunnel tests had to be analyzed and prepared to feed to the model. Specifically, this meant labeling each dataset with the appropriate states of buffeting, growth, decay, and LCO. To do so, the envelope of the pitch amplitude was observed, and the critical points of that curve were calculated. These data points were then divided into four groups using the statistical method of k-means clustering, which utilizes a

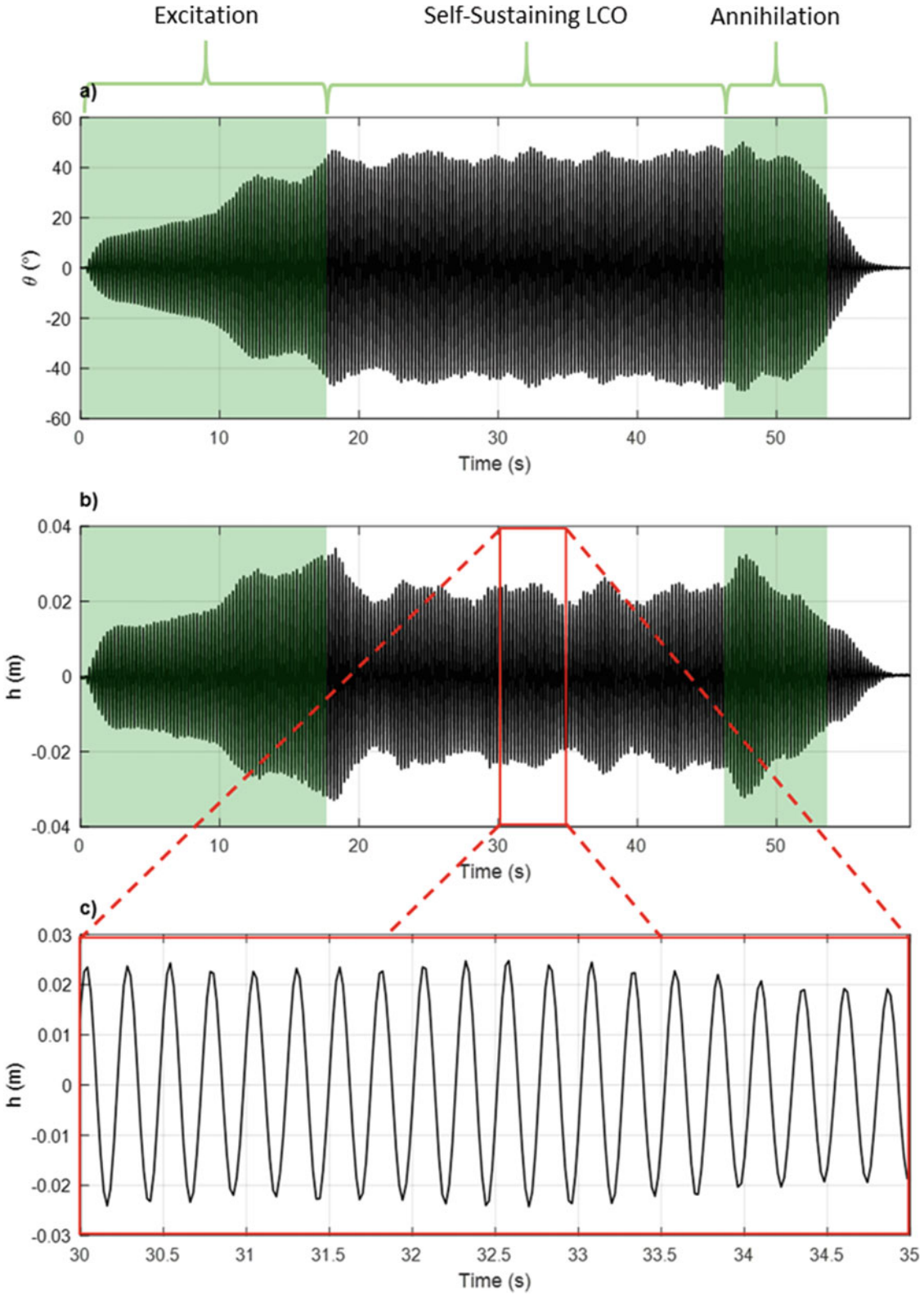

Fig. 27.4 Time histories for (**a**) pitch, (**b**) heave, and (**c**) zoomed-in heave for an Automatic LCO Control test with the disturbance generator frequency set to 3.8 Hz. The green shaded areas represent time when the disturbance generator oscillations are active

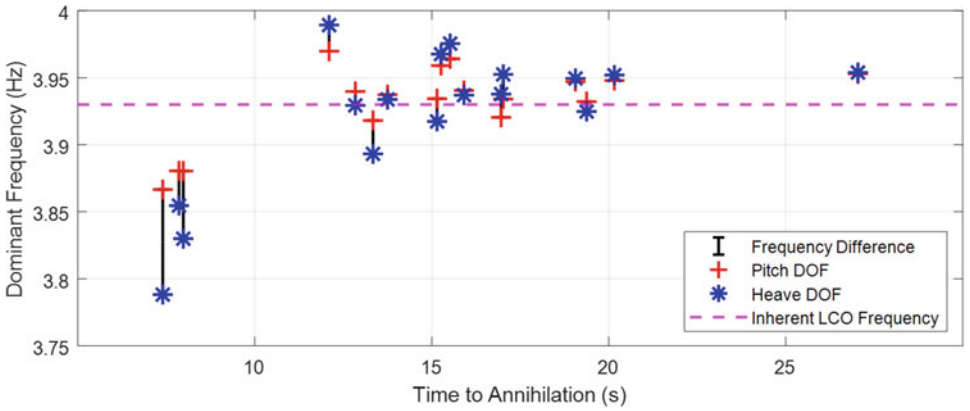

Fig. 27.5 Dominant frequency during LCO annihilation found using FFT on the pitch and heave response in the wing. Larger gaps between the pitch and heave frequencies appear to reduce the TTA

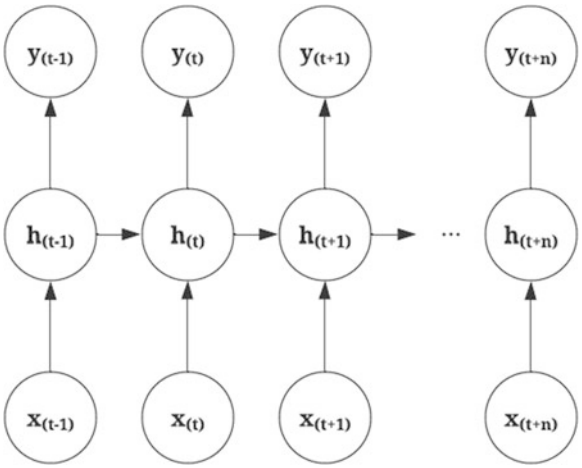

Fig. 27.6 Schematic of a basic recurrent neural network model, which evaluates the function output at each time step and utilizes the hidden layers from the previous time step in the current time step's calculation

randomized group of *n* centroids to divide the data points based on proximity. These four groups were then used to label their associated states. Since the states were not always sequential, it was important to make sure the model will have a uniform chance of selecting each state; therefore, a one-hot encoding method was used so that there would be a uniform distance between each state vector. Rather than labeling the data with numerical states 1–4 for buffeting-LCO, this method uses unit vectors to label the data. As such, the labeling for each data point consisted of an appended vector of [1, 0, 0, 0] for buffeting, [0, 1, 0, 0] for growth, [0, 0, 1, 0] for decay, and [0, 0, 0, 1] for LCO. Using k-means to cluster the data showed that some similarities exist between the growth and LCO regions, as the upper portion of the growth regions is grouped into the LCO label. This agrees with the experimental results, as manual LCO excitation via controlling the disturbance generator occurs most consistently in this higher amplitude portion of the growth region. A full labeled time history of the wing pitch can be seen in Fig. 27.7, showing the grouping of high amplitude growth with LCO. With the labeled data, the RNN model can be trained and its hyperparameters tuned to accurately predict outcomes for the updated controller.

Once the neural network is fully trained, it will be implemented in the controller in place of the amplitude cutoff in the current state machine. The trained RNN will read in the wing motion data in real time, allowing it to identify the state of the system and forecast the control action needed to drive the wing to the desired LCO behavior more quickly. The controller will utilize the RNN for a two-fold purpose of increasing the efficiency of LCO excitation and annihilation. Specifically for the process of annihilation, the controller will take in the initial wing response during LCO via the rotary and linear encoders, and then feed the data to the neural network model. This planned implementation method for the RNN in the controller is shown in Fig. 27.8. Next, the RNN will predict whether or not and when the wing's response is trending toward decay, which will indicate the optimal time to begin the annihilation procedure. If it predicts the desired behavior, the disturbance generator will be activated so that the wing LCO can be canceled out, returning the wing to equilibrium in the same fashion as the current state machine. Otherwise, the disturbance generator remains inactivated until the decay state is predicted.

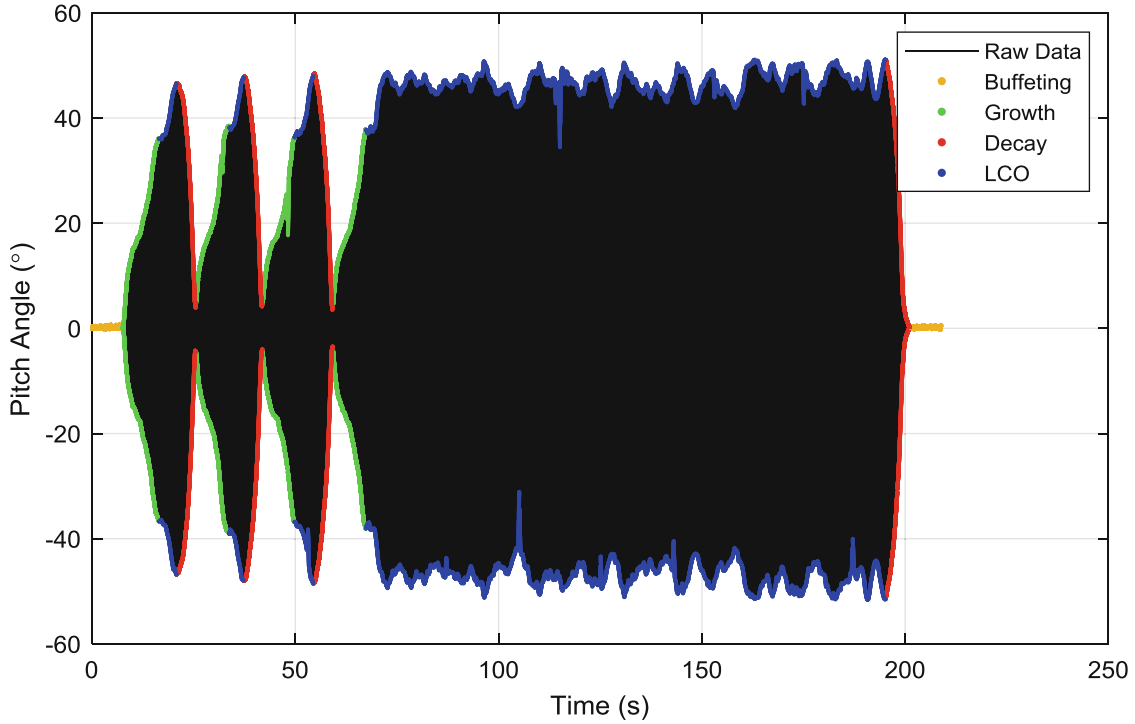

Fig. 27.7 Labeled data for a test case with disturbance generator frequency of 3.87 Hz. The yellow regions denote the buffeting label in the envelope curve, green denotes growth, red denotes decay, and blue denotes LCO

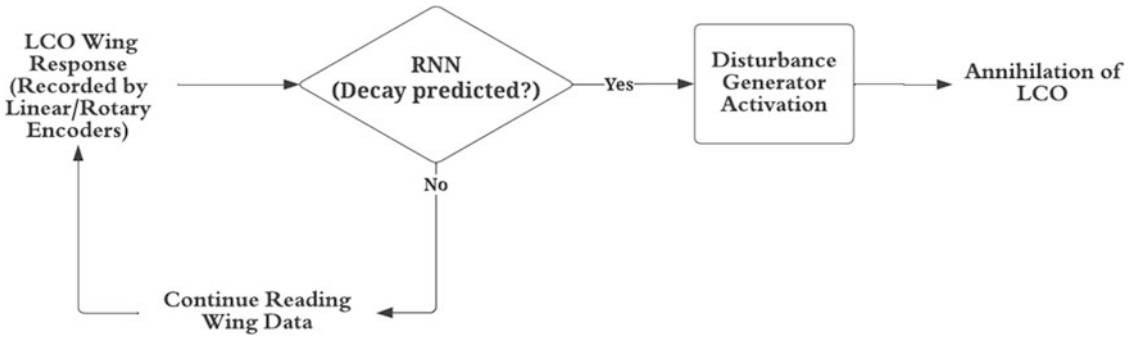

Fig. 27.8 Simple block diagram for the controller with implemented RNN model used to annihilate LCO in the downstream wing

27.5 Conclusions

This chapter has shown that a state-machine control scheme can be used with a variable frequency flow disturbance generator to automatically control limit cycle oscillations (LCOs) in a two degree-of-freedom (2DOF) aeroelastic wing. In its current form, the control scheme uses preset oscillation frequencies near the inherent LCO frequency of the aeroelastic wing to annihilate preexisting LCO. However, moving forward, the disturbance generator oscillation frequency could be set as a variable based on real-time sensing of the wing LCO frequency and coupled with a feedback control scheme to drive the time to annihilation (TTA) toward zero. Additionally, the researchers have begun to investigate the use of a recurrent neural network (RNN) model to identify the real-time state of the system. This could be used alongside the existing control scheme to forecast LCO before the wing begins exhibiting large-amplitude oscillation. Coupled with the RNN, the controller could be tuned to drive the wing to the desired LCO behavior more quickly.

Acknowledgments The authors would like to thank Dr. Shreyas Narispur and Dr. Mingtai Chen for their guidance and training on operation of the NCSU Subsonic Wind Tunnel and undergraduate student Ethan Sites for his preparation of testing hardware and tunnel operation.

Funding Sources Funding for this research is provided by the National Science Foundation for its financial support of this study under Award No. CMMI-2015983, which is managed by Dr. Robert Landers.

References

1. Garrick, I.E., Reed, W.H.: Historical development of aircraft flutter. J. Aircr. **18**(11), 897–912 (1981)
2. Ricketts, R.H.: Experimental aeroelasticity history, status and future in brief, NASA Technical Report, TM-102651, April 1990
3. Theodorsen, T.: General theory of aerodynamic instability and the mechanism of Flutter, Tech. Rep. 496, NACA, 1935
4. Patil, M.J., Hodges, D.H.: On the importance of aerodynamic and structural geometrical nonlinearities in aeroelastic behavior of high-aspect-ratio wings. J. Fluids Struct. **19**, 905–915 (2004)
5. O'Neil, T., Gilliatt, H., Strganac, T.W.: Investigations of aeroelastic response for a system with continuous structural nonlinearities. Proc. AIAA 37th structure, structural dynamics and materials, April 1996
6. Goodman, C., Hood, M., Reichenbach, E., Yurkovich, R.: An analysis of the F/A-18C/D Limit cycle oscillation solution. 44th AIAA/ASME/ASCE/AHS/ASC structures, structural dynamics, and materials conference, 2003
7. Hayes, W.B., Sisk, K.: Prevention of External Store Limit Cycle Oscillations on the F/A-18E/F Super Hornet and EA-18G Growler Aircraft.," Tech. Rep. RTO-MP-AVT-152,. North Atlantic Treaty Organization/Science and Technology Organization (2008)
8. Dowell, E.H., Tang, D.: Nonlinear aeroelasticity and unsteady aerodynamics. AIAA J. **40**(9), 1697–1707 (2002)
9. Pidaparthi, B., Missoum, S.: Stochastic optimization of nonlinear energy sinks for the mitigation of limit cycle oscillations. AIAA J. **57**(5), 2134–2144 (2019)
10. Bichiou, Y., Hajj, M.R.: Effectiveness of a nonlinear energy sink in the control of an aeroelastic system. Nonlinear Dynamics. **86**, 2161–2177 (2016)
11. Strganac, T.W., Ko, J., Thompson, D.E., Kurdila, A.J.: Identification and control of limit cycle oscillations in aeroelastic systems. J. Guid. Control. Dyn. **23**(6), 1127–1133 (2000)
12. Bryant, M., Garcia E.: Development of an aeroelastic vibration power harvester. Proc. SPIE 7288, active and passive smart structures and integrated systems, April 2009
13. Bryant, M., Garcia E.: Energy harvesting: a key to wireless sensor nodes. Proc. 7493, Second international conference on smart materials and nanotechnology in engineering, Oct 2009
14. Zhao, L., Yang, Y.: Enhanced aeroelastic energy harvesting with a beam stiffener. Smart Mater. Struct. **24**(3), 032001 (2015)
15. Kirschmeier, B., Bryant, M.: Experimental investigation of wake-induced aeroelastic limit cycle oscillations in tandem wings. J. Fluids Struct. **81**, 309–324 (2018)
16. Gianikos, Z.N., Kirschmeier, B.A., Gopalarathnam, A., Bryant, M.: Limit cycle characterization of an aeroleastic wing in a bluff body wake. J. Fluids Struct. **95**, 102986 (2020)
17. Kirschmeier, B.A., Gianikos, Z., Gopalarathnam, A., Bryant, M.: Amplitude annihilation in wake-influenced aeroelastic limit-cycle oscillations. AIAA J. **58**(9), 4117–4127 (2020)
18. Visbal, M.R., Garmann, D.J.: Numerical investigation of Spanwise end effects on dynamic stall of a pitching NACA 0012 Wing. Proc. 55th AIAA aerospace sciences meeting, Jan 2017
19. Rockwood, M., Medina, A.: Controlled generation of periodic vortical gusts by the rotational oscillation of a circular cylinder and attached plate. Exp. Fluids. **61**(3), 65 (2020)
20. Chen, Y., Zhang, S., Zhang, W., Peng, J., Cai, Y.: Multifactor spatio-temporal correlation model based on a combination of convolutional neural network and long short-term memory neural network for wind speed forecasting. Energy Convers. Manag. **185**, 783–799 (2019)

Chapter 28
Experimental Parameter Identification of Nonlinear Mechanical Systems via Meta-heuristic Optimisation Methods

Cristiano Martinelli, Andrea Coraddu, and Andrea Cammarano

Abstract Meta-heuristic optimisation algorithms are high-level procedures designed to discover near-optimal solutions to optimisation problems. These strategies can efficiently explore the design space of the problems; therefore, they perform well even when incomplete and scarce information is available. Such characteristics make them the ideal approach for solving nonlinear parameter identification problems from experimental data. Nonetheless, selecting the meta-heuristic optimisation algorithm remains a challenging task that can dramatically affect the required time, accuracy, and computational burden to solve such identification problems. To this end, we propose investigating how different meta-heuristic optimisation algorithms can influence the identification process of nonlinear parameters in mechanical systems. Two mature meta-heuristic optimisation methods, i.e. particle swarm optimisation (PSO) method and genetic algorithm (GA), are used to identify the nonlinear parameters of an experimental two-degrees-of-freedom system with cubic stiffness. These naturally inspired algorithms are based on the definition of an initial population: this advantageously increases the chances of identifying the global minimum of the optimisation problem as the design space is searched simultaneously in multiple locations. The results show that the PSO method drastically increases the accuracy and robustness of the solution, but it requires a quite expensive computational burden. On the contrary, the GA requires similar computational effort but does not provide accurate solutions.

Keywords Experimental nonlinear analysis · Nonlinear dynamics · Parameter identification · Meta-heuristic optimisation · Nonlinear frequency response

28.1 Introduction

The increasing demand for lightweight, high-performance, and flexible structures shows the ultimately nonlinear nature of mechanical systems, prompting the study of nonlinear dynamics in many fields of science [1]. In the literature, many techniques have been proposed for identifying the parameters of nonlinear systems [2, 3]; between them, there are linearisation methods, time-domain methods, frequency-domain methods, time-frequency methods, modal methods, black-box methods, and model updating methods. The latter methods try to extract information from the experimental data to update a numerical/analytical model [3]. Meta-heuristic optimisation algorithms lend themselves to similar tasks and can be adopted for model updating processes [4–7], minimising the difference between the experimental and numerical data. Such algorithms can efficiently search the design space of the optimisation problem [8] by seeking a near-optimal solution.

Many examples of similar optimisation processes are available in the scientific literature. Pelteret et al. [5] applied five different meta-heuristic algorithms for the parameter identification of nonlinear constitutive laws that describe coupled, magnetic-field responsive materials. The authors demonstrated that, for the class of problem and with the adopted setting, the genetic algorithm (GA) provided the best performance in terms of the accuracy of the predicted parameters. Yousri et al. [6]

C. Martinelli (✉)
Naval Architecture, Ocean & Marine Engineering Department, University of Strathclyde, Glasgow, UK
e-mail: cristiano.martinelli@strath.ac.uk

A. Coraddu
Department of Maritime & Transport Technology, Delft University of Technology, Delft, The Netherlands
e-mail: a.coraddu@tudelft.nl

A. Cammarano
James Watt School of Engineering, University of Glasgow, Glasgow, UK
e-mail: andrea.cammarano@glasgow.ac.uk

M. R. W. Brake et al. (eds.), *Nonlinear Structures & Systems, Volume 1*, Conference Proceedings
of the Society for Experimental Mechanics Series, https://doi.org/10.1007/978-3-031-36999-5_28

investigated the performance of several meta-heuristic optimisation algorithms for the parameter identification of fractional order chaotic systems, combining the optimisation procedures with different objective functions. The authors numerically demonstrated that, between the considered algorithms and objective functions, the flower pollination algorithm with integral of squared error represents the most effective combination for identifying the parameters. Recently, Safari et al. [7] presented a semi-parametric identification framework for nonlinear systems. The framework is based on optimisation strategies which allow identifying both the parameters and the type of nonlinear characteristics that better describe the system. The authors proved the efficacy of the proposed methodology by applying the framework to numerical and experimental examples. The significant number of works available in the literature [9–21] demonstrates the solid scientific interest in the parameter identification of nonlinear systems via meta-heuristic optimisation.

However, the definition of the objective function and the selection of the optimisation algorithm can drastically change the number of required iterations to reach the solution, hence the computational burden [6]. In some instances, the adoption of one method rather than another can prevent the attainment of a correct solution, as demonstrated in many works [5, 6]. Therefore, it is not completely clear which meta-heuristic algorithm provides the best performance for the identification process of nonlinear systems. In this paper, we propose the performance comparison of two mature meta-heuristic optimisation algorithms, i.e. the PSO and the GA, for parameter identification problems of nonlinear mechanical systems. These naturally inspired algorithms are based on the definition of a population, which initially colonises the whole design space of the problem, and they are chosen as they advantageously increase the chances of identifying the optimum solution to the identification problem. A clamped-clamped nonlinear two-degrees-of-freedom system is studied, and its parameters are identified from the experimental data. Firstly, the linear parameters are deduced with the Kennedy-Pancu method [22]. Then, the nonlinear parameters of the model are identified via an error minimisation process using the two meta-heuristic algorithms mentioned above. Finally, the performance of the two methods is compared in terms of computational burden, required time, and accuracy.

28.2 Experimental Test Rig and Nonlinear Analysis

The nonlinear system is constituted of two adjustable masses and two supports. One support is fixed on the vibration isolation table and blocks the structure on the ground, while the second is attached to a shaker (LDS-V403) and excites the system. The masses and the supports are made in PLA (polylactic acid) and are obtained through FDM (filament deposition modelling), a common additive manufacturing process. Two parallel beams in stainless steel sustain the masses, allowing them to oscillate in the horizontal plane. Such a configuration provides a hardening nonlinear stiffness characteristic to the model: when the masses move from the resting position, the beams are subjected to both bending and axial deformation. The latter changes the bending stiffness resulting in a hardening cubic characteristic.

The main dimensions of the components of the system are reported in Table 28.1. The two masses are separated by a distance of 160 mm, while each mass is 90 mm apart from the adjacent constraint. Moreover, the support beams are separated by a distance of 35 mm. Figure 28.1 shows the experimental test rig and the configuration set-up to obtain the data: two accelerometers are connected to the masses (PCB Piezotronics Model: 352C22) while a laser vibrometer (Polytec PVD 100) is used to measure the velocity of the base.

The nonlinear analysis is performed by recording the acceleration time histories of the two masses when a voltage input signal is provided to the shaker. The sinusoidal input signal is produced by the National Instruments (NI) unit NI-9263, and it is designed to smoothly change frequency every 30 s. This allows the creation of forward/backwards sweep frequency signals from 11 Hz to 16 Hz with a variation of frequency of 0.1 Hz. The acquired raw time signal is recorded with the unit NI-9234 and it is post-processed with the following steps: the signal is divided into time portions corresponding to a well-defined frequency, each block is filtered and integrated to obtain the displacement and the velocity of the masses, and then the transient is removed from each portion of the signal. Finally, the amplitude of each steady-state signal block is computed from the averaged peaks. The resulting transfer functions[1] (TFs) are described by Fig. 28.2. The figure shows the

Table 28.1 Dimensions of the masses and the distances between the masses and the supports

Component	Length	Width	Height
Beams	500 mm	0.5 mm	20 mm
Mass	50 mm	55 mm	50 mm

[1] For transfer function of nonlinear system, we mean the frequency response curve of the system for a given input.

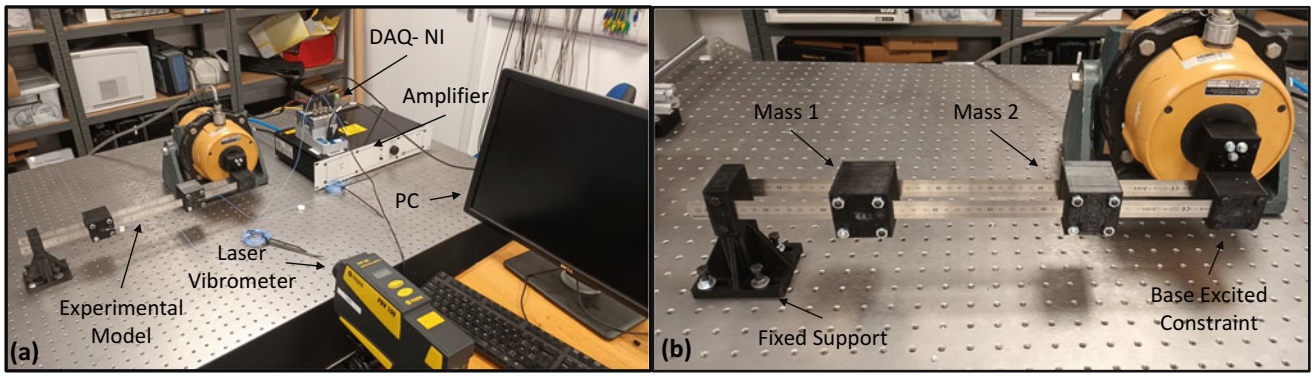

Fig. 28.1 Experimental set-up for the analysis of the two-mass system (**a**) and model description (**b**)

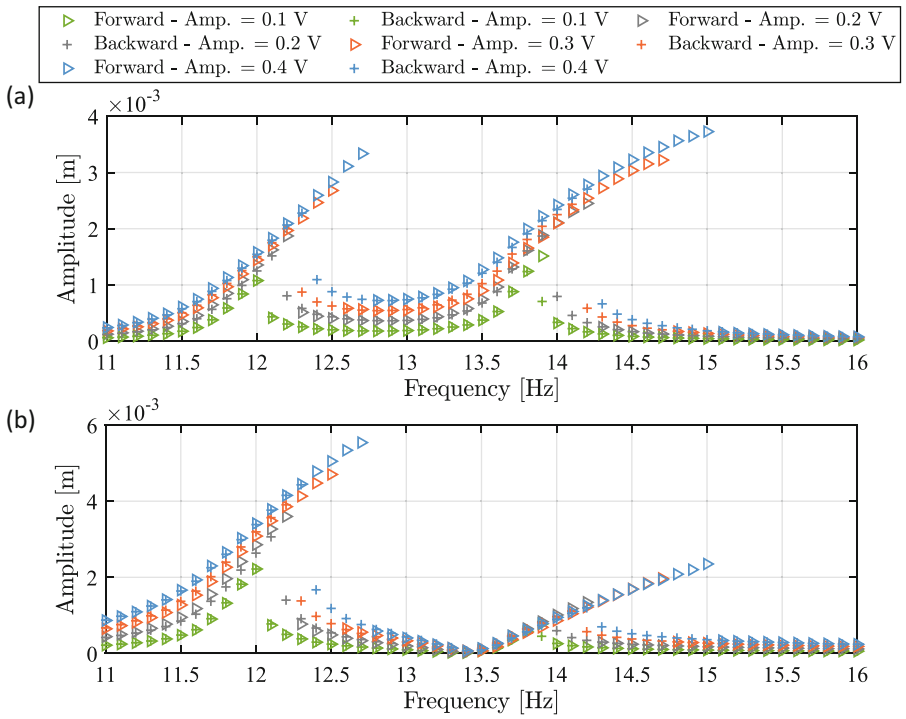

Fig. 28.2 Nonlinear transfer function between the voltage input and the first mass displacement (**a**) and the second mass displacement (**b**). The TFs are computed at different amplitudes of input voltages to show the effect of the external excitation

TFs from the input voltage signal to the output displacement of the masses; when the signal input amplitude is small, the system behaves almost linearly, while at high input amplitudes, the typical jump phenomena occur in the forward frequency sweeps after the system resonances. The backward frequency sweeps, instead, show the low-amplitude dynamics of the system. Finally, it is worth remembering that these TFs include the dynamics of the shaker; thus, the following numerical analyses need to take this aspect into account.

28.3 Model Updating of the Underlying Linear System

The experimental system can be mathematically described with a lumped parameter model with asymmetrical coefficients. The model is graphically represented by Fig. 28.3, where k_1, k_2, and k_3 denote the linear stiffness, c_1, c_2, and c_3 are the viscous damping coefficients, μ_1, μ_2, $\mu_{2,b}$, and μ_3 represent the cubic stiffness coefficients, m indicates the mass of the system, and y is the displacement of the moving constraint. Given the nature of the nonlinearities, the equations of motion contain unsymmetrical cubic stiffness coefficients, as described by Eq. 28.1.

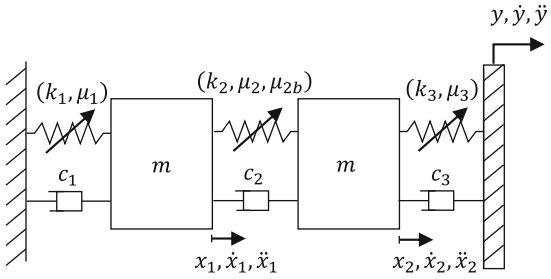

Fig. 28.3 Lumped parameter model representing the experimental test rig

$$m\ddot{x}_1 + c_1\dot{x}_1 + k_1x_1 + \mu_1x_1^3 + c_2(\dot{x}_1 - \dot{x}_2) + k_2(x_1 - x_2) + \mu_2x_1^3 - \mu_{2,b}x_1^2x_2 + \mu_{2,b}x_1x_2^2 - \mu_2x_2^3 = 0 \tag{28.1a}$$

$$m\ddot{x}_2 + c_3(\dot{x}_2 - \dot{y}) + k_3(x_2 - y) + \mu_3(x_2 - y)^3 - c_2(\dot{x}_1 - \dot{x}_2) - k_2(x_1 - x_2) - \mu_2x_1^3 + \mu_{2,b}x_1^2x_2 - \mu_{2,b}x_1x_2^2 + \mu_2x_2^3 = 0 \tag{28.1b}$$

The linear behaviour of the system can be easily described by the linear part of Eq. 28.1; by considering a sinusoidal input signal y with constant acceleration amplitude and through mathematical manipulation, the linear receptance[2] H can be represented as follows:

$$H_1 = \frac{X_1}{\ddot{Y}} = \frac{X_2k_2 + i\Omega X_2c_2}{\ddot{Y}(k_1 + k_2 - \Omega^2m + \Omega i(c_2 + c_1))} \tag{28.2a}$$

$$H_2 = \frac{X_2}{\ddot{Y}} = \frac{X_1k_2 - \frac{\ddot{Y}k_3}{\Omega^2} + i\Omega X_1c_2 - \frac{i\ddot{Y}c_3}{\Omega}}{\ddot{Y}(k_2 + k_3 - \Omega^2m + \Omega i(c_2 + c_3))} \tag{28.2b}$$

where X_1 and X_2 are the complex amplitudes of the mass displacement, $\ddot{Y}$ represents the complex amplitude of the acceleration input, and Ω denotes the forcing frequency of the excitation.

The experimental linear behaviour of the system is evaluated by measuring the TF of the underlying linear system. This can be achieved by exciting the system with random vibrations; indeed, such an excitation attenuates the effect of the system nonlinearities and allows obtaining an averaged linear TF [22, 23]. The underlying linear TF is acquired with the unit *DataPhysics Abacus 901*(DP-901) and with the aid of the commercial software *SignalCalc 900 Series*. The linear TF is determined by considering the motion of the excited constraint as the input signal and the mass displacement as the output signal, and then an averaging process is adopted to reduce the effect of the noise. Such a linear TF represents the experimental counterpart of the receptance mathematically described in Eq. 28.2.

In order to identify the linear coefficients of the system, the experimental linear transfer functions are exploited; the Kennedy-Pancu method [22] represents a straightforward, effective tool to extract the natural frequencies ω_n, modal damping ratios ζ, and the modal matrix Ψ of MDOF mechanical systems. The modal damping ratios and the natural frequencies can be organised in matrix form as follows:

$$\mathbf{Z} = \begin{bmatrix} 2\zeta_1\omega_{n,1} & 0 \\ 0 & 2\zeta_2\omega_{n,2} \end{bmatrix} \tag{28.3a}$$

$$\mathbf{W}_n = \begin{bmatrix} \omega_{n,1}^2 & 0 \\ 0 & \omega_{n,2}^2 \end{bmatrix} \tag{28.3b}$$

The matrices of Eq. 28.3 can be used to obtain the stiffness and damping linear coefficients of the system, as follows:

$$\mathbf{M} = \begin{bmatrix} m & 0 \\ 0 & m \end{bmatrix} \tag{28.4a}$$

$$\mathbf{C} = \begin{bmatrix} c_1 + c_2 & -c_2 \\ -c_2 & c_2 + c_3 \end{bmatrix} = (\mathbf{\Psi}^T)^{-1}(\mathbf{\Psi}^T\mathbf{M}\mathbf{\Psi}\mathbf{Z})(\mathbf{\Psi})^{-1} \tag{28.4b}$$

[2] For receptance, the authors mean the transfer function between input acceleration and the output displacement.

Table 28.2 Identified linear coefficients of the underlying linear system: initial set of coefficients (obtained from Kennedy-Pancu method) and optimised set of coefficients (obtained from the optimisation process)

Component	c_1 [Ns/m]	c_2 [Ns/m]	c_3 [Ns/m]	k_1 [N/m]	k_2 [N/m]	k_3 [N/m]
Initial coefficients	0.0454	0.0069	0.0370	726.3	85.5	621.5
Optimised coefficients	0.0454	0.0075	0.0366	714.9	89.6	624.9

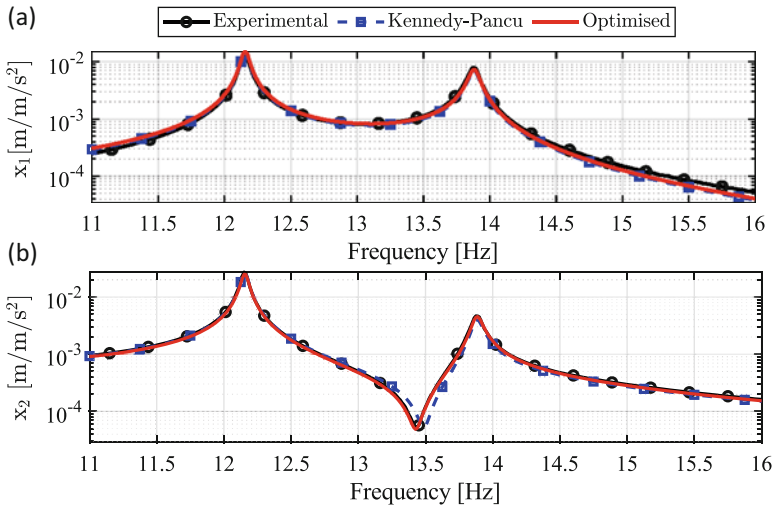

Fig. 28.4 Comparison between the experimental and analytical receptances of the first (**a**) and the second (**b**) degree of freedom of the system

$$\mathbf{K} = \begin{bmatrix} k_1 + k_2 & -k_2 \\ -k_2 & k_2 + k_3 \end{bmatrix} = (\boldsymbol{\Psi}^T)^{-1}(\boldsymbol{\Psi}^T \mathbf{M} \boldsymbol{\Psi} \mathbf{W}_n)(\boldsymbol{\Psi})^{-1} \tag{28.4c}$$

where M represents the diagonal mass matrix, C is the linear damping matrix, and K denotes the linear stiffness matrix. Now, considering that both the masses of the system are equal to 0.113 kg, the unknown coefficients of the underlying linear system, i.e. c_1, c_2, c_3 , k_1, k_2, and k_3, can be evaluated with the Kennedy-Pancu method and by exploiting Eqs. 28.3 and 28.4. The obtained set of coefficients represents a rough but effective approximation of the linear part of the system; thus, it is used as a starting point for an optimisation procedure. The optimisation aims to minimise the difference between the experimental and analytical receptances in terms of amplitude and phase, allowing a more accurate definition of the linear coefficients of the system. Equations 28.2a and 28.2b can be solved to obtain the analytical expression of the amplitude and phase of the system receptances and their differences with respect to the experimental data can be minimised with the *lsqnonlin* MATLAB function, which is used in the optimisation process. The results of the optimisation process are reported in Table 28.2.

The results of Table 28.2 show that the identified initial coefficients are already a very good approximation of the linear system; however, the additional optimisation process allows for reaching a more accurate definition of the linear parameters which is beneficial for the following nonlinear parameter identification. Figure 28.4 shows the experimental and analytical receptances for the two sets of coefficients. The figure demonstrates that the Kennedy-Pancu prediction is very near to the optimal configuration, but a small difference in the anti-resonance response is still present. The optimised TFs, instead, can better fit the experimental data, proving to be a good approximation, even at low amplitude responses.

28.4 Nonlinear Model Updating

Once the linear coefficients are known, the nonlinear system can be identified with the aid of the meta-heuristic optimisation algorithms, namely, GA and PSO. Both the algorithms are based on the definition of a population; the GA [24–26] initialises the domain with a random initial population, whose size is defined by the user. Then, the algorithm creates the next generation of individuals starting from the current population, which is assessed on the base of the objective function value of each individual. Some individuals, generally with low objective function values, are selected as parents according to the selection criteria and used to create new individuals. The children are created in three different ways: elite individuals survive the

generational change as they have the lowest values of the objective function, crossover children are obtained by combining the genes of the parents according to the selected crossover function, and mutated children are generated by introducing random mutation to a single parent. The algorithm stops when the change in the objective function is less than the prescribed tolerance. The PSO [27, 28], instead, is based on swarm intelligence. Similarly to the GA, the algorithm begins uniformly populating the whole domain. The algorithm randomly assigns the initial position and velocity to the particles and computes the objective function of each particle. At this point, the algorithm can identify the best position d associated with the best function value b, and all the particle positions are stored in the matrix p. Then the iteration process starts: for each particle i, a random subset S of N particles is chosen. This set does not include the particle i-th. The best position g and the best function value f are identified in the subset S whose objective function values are already known. With this information, the algorithm can compute the new velocity and position with the following expressions:

$$v(i) = Wv(i) + y_1u_1(p(i) - x(i)) + y_2u_2(g - x(i)) \tag{28.5a}$$

$$x(i) = x(i) + v(i) \tag{28.5b}$$

where $x(i)$ and $v(i)$ represent the position and the velocity of the i-th particle, y_1, y_2, u_1, and u_2 are PSO tuning coefficients, and W represents the inertia coefficient. The updated position $x(i)$ is, now, used to evaluate again the objective function $F(x(i))$ and if its value is lower than $F(p(i))$ the optimal position $p(i)$ is updated with new identified position $x(i)$. Finally, if $F(x(i)) < b$ then the optimal value b is updated and the neighbourhood N is modified accordingly. At each iteration, the bounds are enforced, and the process is repeated until the change in the objective function is less than the prescribed tolerance.

For both methods, the optimisation procedure tries to minimise the following objective function:

$$F(x) = \sum_{j=1}^{P} \sum_{i=1}^{R} (|T_{num}(x) - T_{exp}|) \tag{28.6}$$

where x is the design variable vector, constituted of the nonlinear unknown coefficients μ_1, μ_2, $\mu_{2,b}$, and μ_3, R is the number of discrete frequencies at which the function is evaluated, P is the number of degrees of freedom of the problem, and T_{exp} and T_{num} represent, respectively, the experimental and numerical transfer functions between the shaker input voltage and the mass displacement. The numerical transfer function T_{num} is computed via numerical integration of Eq. 28.1 with the aid of the MATLAB built-in function *ode45*; such procedure must be performed by utilising the experimental displacement and velocity of the moving constraint. This is necessary to account for the dynamics of the shaker, which could not be considered otherwise. The optimisation procedure is performed by using the MATLAB built-in functions *ga* and *particleswarm* with the default options. The optimisation processes are repeated three times to generate more robust results, and a multi-core computer (32 cores—Intel(R) Xeon(R) Silver 4214 CPU @ 2.10 GHz, RAM 129 Gb) is used to perform the analyses with parallel computing. The largest amplitude responses of the experimental TFs are used to compute the considered objective function: this guarantees to better represent the nonlinear characteristic of the experimental data. Therefore, the optimisation is carried out considering the experimental data generated by a voltage input amplitude of 0.4 V for the forward sweep of discrete frequencies in the ranges from 11.6 Hz to 12.7 Hz and from 13.6 Hz to 15.0 Hz, i.e. where the system shows the resonances. Finally, the lower and upper boundaries of the optimisation are set, respectively, at $\mu = 10^3$ N/m^3 and $\mu = 10^8$ N/m^3, for all the design variables.

The results of the optimisations with the two meta-heuristic algorithms are reported in Tables 28.3 and 28.4. The tables show that the PSO accurately converges to the same optimal condition for three different cases with a similar amount of time and iterations. The minimum objective function value is 2.458e-3 which represents the best-optimal identified condition. On the contrary, the GA requires less time to perform the optimisation, but it identifies three very different optimal conditions. Moreover, these optimal conditions are associated with higher-objective function values. Figure 28.5 provides a graphical interpretation of the optimisation results of Tables 28.3 and 28.4, showing the comparison between the optimised numerical TFs and the experimental ones. Figure 28.5a and b show the numerical TFs for the first and second degree of freedom of the system for the best solution of the PSO algorithm. The figures demonstrate that the PSO numerical results can fit the experimental TFs with high fidelity. Conversely, the GA optimal results generate poorly converged numerical TFs, as shown in Fig. 28.5c and d. The results of Tables 28.3, 28.4, and Fig. 28.5 demonstrate the robustness of the PSO and its ability to solve identification problems of nonlinear systems, confirming its superiority with respect to the GA when common default options are used in the optimisation procedure. Moreover, these results agree with previous studies [4, 12, 14, 21] which, differently from this case, adopted time data to identify the system parameters.

Table 28.3 Optimisation results for the identification process with the PSO algorithm. The optimisations are carried out with a swarm size of 40 particles

PSO	Time [min]	Iterations	Func. counts	μ_1 [N/m^3]	μ_2 [N/m^3]	$\mu_{2,b}$ [N/m^3]	μ_3 [N/m^3]	Func. value
Test 1	566.1	77	3120	2.653e6	1.314e6	8.889e6	7.071e6	2.461e-3
Test 2	524.7	74	3000	2.732e6	1.324e6	8.850e6	7.069e6	2.458e-3
Test 3	591.8	87	3520	2.651e6	1.312e6	8.891e6	7.074e6	2.461e-3

Table 28.4 Optimisation results for the identification process with the GA. The optimisations are carried out with a population of 50 individuals

GA	Time [min]	Iterations	Func. Counts	μ_1 [N/m^3]	μ_2 [N/m^3]	$\mu_{2,b}$ [N/m^3]	μ_3 [N/m^3]	Func. Value
Test 1	471.8	55	2638	1.259e7	1.685e7	9.162e6	3.104e6	40.705e-3
Test 2	489.3	54	2591	8.093e6	1.785e7	1.446e6	3.363e6	38.705e-3
Test 3	497.5	57	2732	1.002e3	8.612e6	3.537e5	1.296e7	22.668e-3

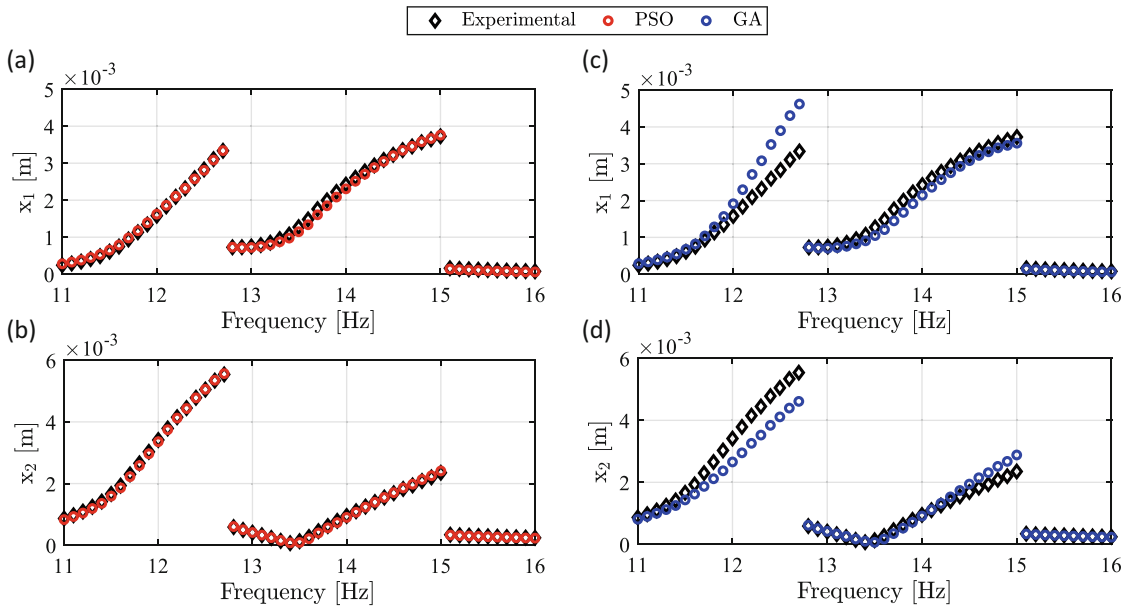

Fig. 28.5 Comparison between the experimental transfer function and the numerical optimised transfer functions with PSO (**a**–**b**) and with GA (**c**–**d**). The results are obtained by using the experimental transfer function with a voltage input amplitude of 0.4 V

Finally, the optimal results are experimentally validated: a different set of experimental data, i.e. the TFs associated with an input voltage amplitude of 0.3 V and 0.4 V, is used to validate the identified nonlinear coefficients with the PSO method. Figure 28.6 shows the comparison between such experimental results and the numerical transfer functions with the optimal PSO coefficients identified in the *Test* 2 of Table 28.3. The figure demonstrates that the experimental and numerical TFs are in extreme agreement even for different sets of experimental data, validating the identified numerical model.

28.5 Conclusion

This paper presents the experimental parameter identification of a nonlinear two-degrees-of-freedom system via meta-heuristic optimisation procedures. Firstly, the experimental test rig and the adopted methodology for acquiring the experimental data are presented. Then, the identification of the linear parameters is described, and, finally, two mature meta-heuristic optimisation methods, i.e. PSO and GA, are introduced and used in the identification process of the nonlinear parameters. The optimisation analyses show that the PSO is able to identify the nonlinear parameters from experimental data with great accuracy and repeatability. Contrarily, the GA requires less computational effort but provides sparse and poor accurate solutions which result in the identification of the wrong nonlinear parameters. Finally, the PSO optimal parameters are experimentally validated. The comparison demonstrates that the obtained coefficients are valid not only for the first set of experimental data but also for other sets of experimental data which are obtained at different excitation conditions. This

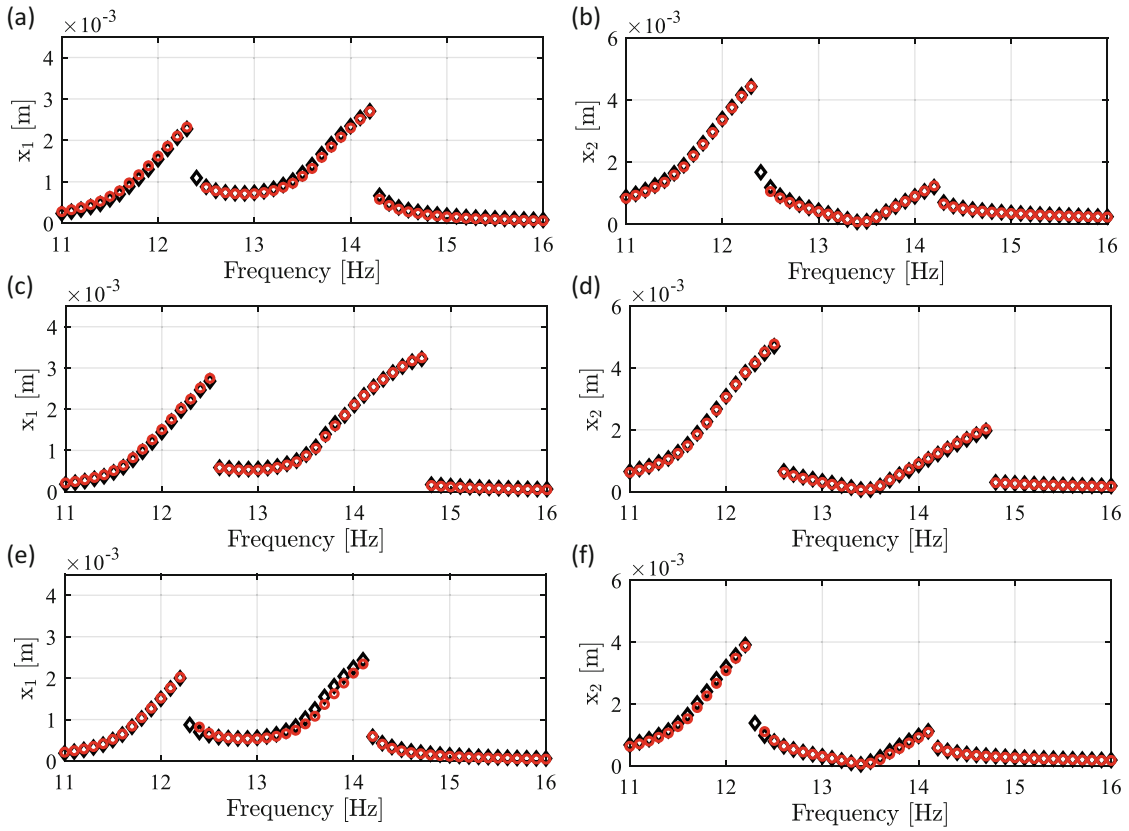

Fig. 28.6 Validation of the optimal nonlinear coefficients with the following experimental transfer functions: backward frequency sweep with an input voltage amplitude of 0.4 V (**a**–**b**), forward frequency sweep with an input voltage amplitude of 0.3 V (**c**–**d**), and backward frequency sweep with an input voltage amplitude of 0.3 V (**e**–**f**). The experimental results are denoted by the black diamond, while the numerical results with optimal PSO coefficients are identified by a red circle

validates the experimental identification procedure and demonstrates that the PSO can be successfully adopted for nonlinear parameter identification of mechanical systems.

Acknowledgments The authors would like to acknowledge the Institution of Engineering and Technology (IET) and the following NERC and EPSRC grants: GALLANT,Glasgow as a Living Lab Accelerating Novel Transformation (No. NE/W005042/1), RELIANT, Risk EvaLuatIon fAst iNtelligent Tool for COVID19 (No. EP/V036777/1).

Data Availability: The experimental data are available at the following DOI [29]

References

1. Wagg, D., Neild, S.: Nonlinear Vibration with Control: For Flexible and Adaptive Structures, vol. 218, 2nd edn. (2015)
2. Kerschen, G., Worden, K., Vakakis, A.F., Golinval, J.C.: Past, present and future of nonlinear system identification in structural dynamics. Mech. Syst. Signal Process. **20**, 505–592 (2006)
3. Noël, J.P., Kerschen, G.: Nonlinear system identification in structural dynamics: 10 more years of progress. Mech. Syst. Signal Process. **83**, 2–35 (2017)
4. Quaranta, G., Lacarbonara, W., Masri, S.F.: A review on computational intelligence for identification of nonlinear dynamical systems. Nonlinear Dyn. **99**, 1709–1761 (2020)
5. Pelteret, J.P., Walter, B., Steinmann, P.: Application of metaheuristic algorithms to the identification of nonlinear magneto-viscoelastic constitutive parameters. J. Magn. Magn. Mater. **464**, 116–131 (2018)
6. Yousri, D.A., AbdelAty, A.M., Said, L.A., Elwakil, A.S., Maundy, B., Radwan, A.G.: Parameter identification of fractional-order chaotic systems using different meta-heuristic optimization algorithms. Nonlinear Dyn. **95**, 2491–2542 (2019)
7. Safari, S., Monsalve, J.M.L.: Direct optimisation based model selection and parameter estimation using time-domain data for identifying localised nonlinearities. J. Sound Vib. **501**, 6 (2021)

8. Kaveh, A., Bakhshpoori, T.: Metaheuristics: Outlines, MATLAB Codes and Examples. Springer, Berlin (2019)
9. Ha, J.-L., Kung, Y.-S., Fung, R.-F., Hsien, S.-C.: A comparison of fitness functions for the identification of a piezoelectric hysteretic actuator based on the real-coded genetic algorithm. Sensors Actuators A: Phys. **132**(2), 643–650 (2006)
10. Kwok, N.M., Ha, Q.P., Nguyen, M.T., Li, J., Samali, B.: Bouc—Wen model parameter identification for a MR fluid damper using computationally efficient GA. ISA Trans. **46**, 167–179 (2007)
11. Chen, C.M., Hsu, Y.C., Fung, R.F.: System identification of a Scott–Russell amplifying mechanism with offset driven by a piezoelectric actuator. Appl. Math. Model. **36**, 2788–2802 (2012)
12. Charalampakis, A.E., Dimou, C.K.: Comparison of evolutionary algorithms for the identification of Bouc–Wen hysteretic systems. J. Comput. Civil Eng. **29**, 5 (2015)
13. Bartkowski, P., Zalewski, R., Chodkiewicz, P.: Parameter identification of Bouc–Wen model for vacuum packed particles based on genetic algorithm. Arch. Civil Mech. Eng. **19**, 322–333 (2019)
14. Modares, H., Alfi, A., Fateh, M.M.: Parameter identification of chaotic dynamic systems through an improved particle swarm optimization. Expert Syst. Appl. **37**(5), 3714–3720 (2010)
15. Ye, M., Wang, X.: Parameter estimation of the Bouc–Wen hysteresis model using particle swarm optimization. Smart Mater. Struct. **16**(6), 2341 (2007)
16. Talatahari, S., Rahbari, N.M., Kaveh, A.: A new hybrid optimization algorithm for recognition of hysteretic non-linear systems. KSCE J. Civil Eng. **17**(5), 1099–1108 (2013)
17. Qin, H., Bu, N., Chen, W., Yin, Z.: An asymmetric hysteresis model and parameter identification method for piezoelectric actuator. Math. Probl. Eng. **2014** (2014)
18. Quaranta, G., Marano, G.C., Greco, R., Monti, G.: Parametric identification of seismic isolators using differential evolution and particle swarm optimization. Appl. Soft Comput. **22**, 458–464 (2014)
19. Barbieri, N., Barbieri, R., da Silva, R.A., Mannala, M.J., Barbieri, L.D.S.A.V.: Nonlinear dynamic analysis of wire-rope isolator and Stockbridge damper. Nonlinear Dyn. **86**, 501–512 (2016)
20. Quaranta, G., Monti, G., Marano, G.C.: Parameters identification of van Der Pol–Duffing oscillators via particle swarm optimization and differential evolution. Mech. Syst. Signal Process. **24**, 2076–2095 (2010)
21. Irakoze, R., Yakoub, K., Kaddouri, A.: Identification of Piezoelectric LuGre Model Based on Particle Swarm Optimization and Real-Coded Genetic Algorithm, pp. 1451–1457. Institute of Electrical and Electronics Engineers (2015)
22. Ewins, D.J.: Modal Testing: Theory, Practice and Application. Wiley, New York (2009)
23. Worden, K., Tomlinson, G.R.: Nonlinearity in Structural Dynamics: Detection, Identification and Modelling. CRC Press, Boca Raton (2001)
24. Holland, J.H.: Adaptation in Natural and Artificial Systems. Ann Arbor (1975)
25. Goldberg, D.E.: Genetic Algorithms in Search, Optimization & Machine Learning. Addison-Wesley, Reading (1989)
26. Bosworth, J.L., Foo, N.Y., Zeigler, B.P.: Comparison of genetic algorithms with conjugate gradient methods. Technical report, NASA, 1972
27. Kennedy, J., Eberhart, R.: Particle swarm optimization. In: Proceedings—International Conference on Neural Networks, vol. 4, pp. 1942–1948. IEEE (1995)
28. Yuhui Shi and Russell Eberhart. A modified particle swarm optimizer. In: 1998 IEEE International Conference on Evolutionary Computation Proceedings. IEEE World Congress on Computational Intelligence (Cat. No. 98TH8360), pp. 69–73. IEEE (1998)
29. Martinelli, C., Coraddu, A., Cammarano, A.: Experimental analysis of a nonlinear piecewise multi-degrees of freedom system [data collection], Enlighten Research Data (2023). http://dx.doi.org/10.5525/gla.researchdata.1471

Chapter 29
Investigation of the Nonlinear Dynamics of a Particle-Damped Slender Beam by Experimental Continuation

Gleb Kleyman and Sebastian Tatzko

Abstract In the present study, experimental continuation is applied to investigate the dynamic behavior of a slender steel beam with an attached particle damper. The slender beam is excited to vibration amplitudes at which it behaves geometrically nonlinear by which multiple coexisting vibration states are possible. The forced response curves are measured while the excitation force is held harmonic. To this end, the higher harmonic components of the excitation voltage are controlled using a Newton algorithm. In addition the backbone curve is measured and a nonlinear modal damping is identified.

Keywords Experimental continuation · Experimental bifurcation analysis · Particle damping · Backbone curves · Nonlinear frequency curves

29.1 Introduction

Particle dampers are local attachments that have gained popularity due to their high potential for vibration mitigation. However, their damping behavior is strongly nonlinear and thus depends significantly on the vibration amplitude of the base structure [1]. Different states of particle motion can be identified as a function of the vibration amplitude leading to a shift in both resonance frequency and damping of the base structure. Vibration levels at which damping becomes maximal are difficult to reach experimentally as established experimental methods, e.g., linear modal analysis, do not provide accurate estimates of the resonance frequency and damping for strongly nonlinear systems.

This becomes even more challenging when a particle damper is applied to an already nonlinear base structure. Often, thin structures such as plates or slender beams are highly prone to vibrations. At vibration amplitudes in the order of the material thickness, they become geometrically nonlinear. These two nonlinear effects are then superimposed, which significantly complicates vibration analysis.

Experimental continuation is a fairly novel method for identifying nonlinear systems. It relies on stabilizing feedback control and numerical path continuation techniques that, unlike linear methods, allow for monitoring backbone curves (evolution of resonance frequency and damping factor versus vibration level) and multivalued frequency response curves of strongly nonlinear structures. In the past, it has been shown that the experimental continuation is applicable to various problems, including geometrical nonlinearity [2].

Compared to this early stage we have improved our implementation towards a Newton-based approach, which allows to individually adjust the harmonic components of the excitation force. The method has been recently tested on a slender, geometrically nonlinear beam [3].

29.2 Theoretical Background of Experimental Continuation

The experimental continuation method relies on a three-step procedure: stabilization of unstable branches, selective control of higher harmonic components, and path continuation. The stabilization is achieved by a feedback control exploiting a differential controller. A detailed description would be beyond the scope of this study; see [4] for details. The selective

G. Kleyman (✉) · S. Tatzko
Department of Mechanical Engineering, Institute of Dynamics and Vibration Research, Leibniz University Hannover, Hannover, Germany
e-mail: kleyman@ids.uni-hannover.de; tatzko@ids.uni-hannover.de

M. R. W. Brake et al. (eds.), *Nonlinear Structures & Systems, Volume 1*, Conference Proceedings
of the Society for Experimental Mechanics Series, https://doi.org/10.1007/978-3-031-36999-5_29

control of harmonic components is performed by a decomposition of the control signal u_e into N harmonic components split into sine and cosine parts:

$$\vec{U}_\mathrm{e} = \left[u_{\mathrm{sin},1},\, u_{\mathrm{cos},1},\, \ldots,\, u_{\mathrm{cos,N}}\right]^\top. \tag{29.1}$$

In order to trace the response curve by an arc-length continuation algorithm, the excitation angular frequency Ω is handled as an additional unknown parameter:

$$\vec{Y}_k = \left[\vec{U}_\mathrm{e}\ \Omega\right]^\top. \tag{29.2}$$

For each point on the solution curve the unknown parameters are found iteratively by Newton's algorithm:

$$\vec{Y}_{k,j+1} = \vec{Y}_{k,j} - \mathbf{J}^{-1}\vec{R}(\vec{Y}_{k,j}), \tag{29.3}$$

where the Jacobian $\mathbf{J}$ is estimated from a finite difference procedure. The residual vector is composed of the residuals $\vec{r}_\mathrm{frc}$ for forced response curves or $\vec{r}_\mathrm{bbc}$ for backbone-curve measurements and an arc-length constraint r_par:

$$\vec{R} = \begin{bmatrix} \vec{r}_\mathrm{frc/bbc} \\ r_\mathrm{par} \end{bmatrix}. \tag{29.4}$$

The constraint equation enforces the algorithm to accept only solutions perpendicular to a secant vector $\vec{Y}'_{k-1}$. The present formulation of the residuals imposes the higher harmonics of the excitation force to become zero (within the scope of experimental precision):

$$\vec{r}_\mathrm{frc} = \left[f_{\mathrm{sin},1} - f_0,\, f_{\mathrm{cos},1},\, \ldots,\, f_{\mathrm{cos,N}}\right]^\top \qquad \vec{r}_\mathrm{bbc} = \left[\varphi_{f,x} - \pi/2,\, x_{\mathrm{cos},1},\, f_{\mathrm{sin},2},\, \ldots,\, f_{\mathrm{cos,N}}\right]^\top. \tag{29.5}$$

However, any other signal can also be controlled by this approach. Once a solution is found, an initial guess is calculated for the next solution point on the branch:

$$\vec{Y}_\mathrm{p} = \vec{Y}_{k-1} + \mathrm{ds}\vec{Y}'_{k-1}. \tag{29.6}$$

29.3 Experimental Setup

The presented algorithm was implemented via user-defined Matlab function blocks in Simulink and runs on a dSpace MicroLabBox hardware. A shaker was used to excite the steel beam (dimensions 370x40x1.5 mm). The beam was clamped to a vibration isolation table on both of its ends. A plastic container was filled to approximately 40% of its volume with ceramic granular material and glued to the beams center. Compare Fig. 29.1 for a photograph and schematic representation of the experimental setup. The forced response curves for different excitation levels and the backbone curve were measured. For all measurements the second and third harmonic of the excitation force were eliminated as described above. The first mode of the beam was investigated for which the modal damping factor was estimated using the power balance method described in [5].

29.4 Results

Figure 29.2 shows the forced response curves for excitation levels between 0.1 N and 0.7 N along with the backbone curve in logarithmic scale to the left and for better interpretation the backbone curve and corresponding modal damping curve in linear scale to the right. Two different classes of nonlinear behavior can be derived: From 60 Hz to 65 Hz the system response is mainly dominated by the particle damper. Due to the decreasing effective mass (increasing relative motion of the particles), the resonance peak shifts toward higher frequencies while the damping increases. The damping factor reaches its maximum value at a modal amplitude of about 0.1 mm$\sqrt{\mathrm{kg}}$ (0.2 mm displacement amplitude at driving point). At higher amplitudes the

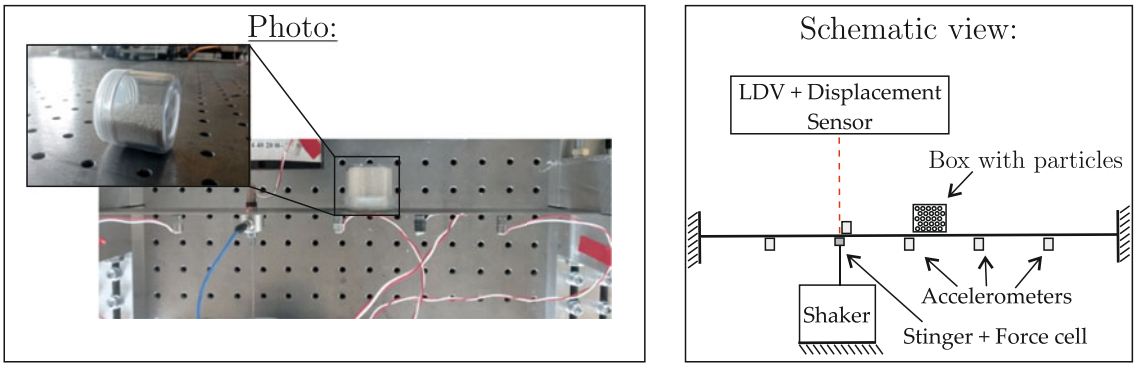

Fig. 29.1 Experimental setup of the particle damped slender beam

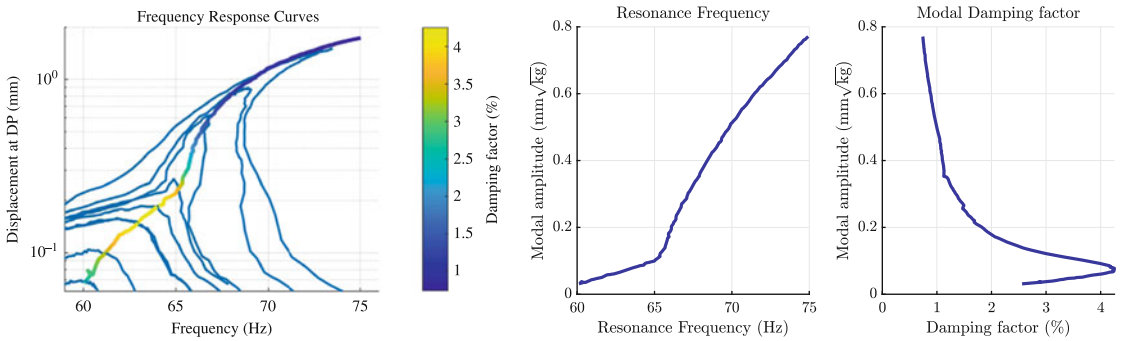

Fig. 29.2 Measurement results: forced response curves (left) and nonlinear resonance frequency and damping (right)

damping factor asymptotically decreases. Here, the system approaches the so-called gas-like regime [6], where all particles are moving relative to the container walls. At oscillation levels higher than 0.1 mm$\sqrt{\text{kg}}$ the geometric nonlinearity of the beam begins to dominate the structural response. Thus, the resonance frequency further increases as a result of the hardening effect (midplane stretching). As the damping decreases at higher amplitudes, multivalued forced response curves arise. The maximum measured frequency shift is 15 Hz which is already a difference of 25 % compared to resonance frequency of the system at low-level excitation. However, it is expected that the resonance frequency further increases when the excitation level is increased.

Acknowledgments The authors thank the German Research Foundation (DFG) for the support within the priority program SPP 1897 Calm, Smooth, and Smart.

References

1. Ehlers, T., Tatzko, S., Wallaschek, J., Lachmayer, R.: Design of particle dampers for additive manufacturing. Addit. Manuf. **38**, 101752 (2021)
2. Kleyman, G., Paehr, M., Tatzko, S.: Application of control-based-continuation for characterization of dynamic systems with stiffness and friction nonlinearities. Mech. Res. Commun. **106**, 103520 (2020)
3. Kleyman, G., Tatzko, S.: Application of experimental continuation to a geometrically nonlinear beam. In: ISMA 2022 (2022)
4. Kleyman, G., Tatzko, S.: Optimal controller gain for the control based continuation of a duffing-oscillator. In: ENOC 2022 (2022)
5. Scheel, M., Peter, S., Leine, R.I., Krack, M.: A phase resonance approach for modal testing of structures with nonlinear dissipation. J. Sound Vib. **435**, 56–73 (2018)
6. Saluena, C., Esipov, S.E., Poeschel, T., Simonian, S.S.: Dissipative properties of granular ensembles. In: SPIE, pp. 19–26 (1998)

Chapter 30
Identification of Nonlinear Characteristics of an Additive Manufactured Vibration Absorber

Cristiano Martinelli, Rohit Avadhani, and Andrea Cammarano

Abstract Additive manufacturing has become increasingly popular in the last decades and has shown great potential for designing and manufacturing innovative design solutions. Recently it has been demonstrated that additive manufacturing can be used to create monolithic compliant mechanisms that can avoid assembly and relative movement between components, showing considerable advantages in their use in harsh environments (i.e. space applications). In this paper, we explore the possibility of adopting 3D-printed compliant mechanisms as tuned-mass vibration absorbers: the challenge is to identify the characteristics of an equivalent nonlinear oscillator that can be used to assess the performance of the absorber. The experimental and numerical results show that the proposed compliant mechanism offers a complex nonlinear dynamic behaviour and it can effectively act as a vibration absorber for a simple cantilever beam.

Keywords Nonlinear parameter identification · Nonlinear dynamics · Additive manufacturing · Compliant mechanisms · Tuned vibration absorber

30.1 Introduction

Compliant mechanisms are monolithic flexible structures that achieve the desired motion thanks to their deformation [1–3]. Such flexible structures can effectively bypass the main disadvantages of classical rigid mechanisms [4–7], i.e. reduced fatigue life, increased stress singularities at edges, difficulty in fabrication, and difficulty in the assembly, allowing the design of more complex and effective shapes [3, 6, 8, 9] that can efficiently work even in harsh environments, like in space applications or in surgical operations [6].

Thanks to these characteristics, they find practical applications in many fields of engineering, e.g. in the aerospace sector [2, 6, 10, 11], where compliant mechanisms are used to produce flexible hinges and to dampen the high level of vibrations during spacecraft take-off; in the medical sector [12, 13], where compliant mechanisms are used as surgical devices/tools with the intent to improve the compatibility with soft tissues; in piezoelectric energy harvesting applications [14], where compliant mechanisms can be practically combined with piezoelectric transducers to extract energy from the deformation of the mechanism; and in robotic applications [15], where compliant mechanisms are used to create force/motion amplifiers. However, the compliant mechanisms cannot be fabricated with classical industrial processes, but additive manufacturing procedures are needed to produce these devices [6, 16]. Such processes allow producing more complex shapes and designs which are inevitably accompanied by induced nonlinear behaviours, due to both the geometry and the material properties, as shown in many examples available in the literature [17, 18]. In this context, the knowledge about the nonlinear dynamic behaviour of 3D-printed complaint mechanisms is still very limited and needs to be better investigated by the scientific community. Thus, we propose the experimental investigation of a nonlinear compliant mechanism with a hexagonal profile which is produced by FDM (filament deposition modelling), a classical additive manufacturing procedure, and acts as a tuned-mass vibration absorber for a simple cantilever beam. Firstly, the nonlinear mechanical properties of the complaint mechanism are experimentally identified with the restoring force surface method

C. Martinelli (✉)
Naval Architecture, Ocean & Marine Engineering Department, University of Stratchlyde, Glasgow, UK
e-mail: cristiano.martinelli@strath.ac.uk

R. Avadhani · A. Cammarano
James Watt School of Engineering, University of Glasgow, Glasgow, UK
e-mail: 2696886a@student.gla.ac.uk; andrea.cammarano@glasgow.ac.uk

M. R. W. Brake et al. (eds.), *Nonlinear Structures & Systems, Volume 1*, Conference Proceedings
of the Society for Experimental Mechanics Series, https://doi.org/10.1007/978-3-031-36999-5_30

(RFSM). Then, an equivalent nonlinear oscillator is used to experimentally validate the identified nonlinear characteristics. Finally, the ability of the compliant dynamic absorber is experimentally shown. The results demonstrate that the proposed compliant mechanism can act as a nonlinear vibration absorber for a simple cantilever beam and that the chosen geometry can effectively induce the generation of nonlinear damping and stiffness characteristics in the mechanism.

30.2 Experimental Test Rig

The experimental test rig consists of a base-excited cantilever beam, made of stainless steel, and a compliant mechanism produced in TPU (thermoplastic polyurethane) via FDM. This material provides the necessary flexibility to the compliant mechanism, allowing the system to vibrate. Both structures have a tip mass attached to their end. The compliant mechanism has a complex hexagonal geometrical shape, as shown in Fig. 30.1, and it acts as vibration absorbed for the cantilever beam: when excited, it vibrates, dampening the response of the beam. Nonetheless, during the induced deformation, it changes its shape, triggering a complex nonlinear dynamic behaviour.

The experimental system is analysed in three different configurations: the cantilever beam (primary structure) with the compliant mechanism (secondary structure) attached to its free end, the cantilever beam without the compliant mechanism, and the compliant mechanism alone. In all the configurations, the system is base-excited and the attention is focused on the nonlinear dynamic behaviour of the compliant mechanism. A shaker (LDS-V403) is used to excite the system, as shown in Fig. 30.1, while two piezoelectric accelerometers (PCB Piezotronics Model:352C22) are used to record the accelerations of the tip of the primary and secondary structure, in the three proposed configurations. Finally, a laser vibrometer (Polytec PDV-100) is used to measure the velocity of the base which excites the system.

30.3 Linear System Characterisation

This section describes the linear characterisation of the primary and secondary structure and the adopted methodology. The experimental transfer function (TF) between the velocity of the base and the acceleration of the tip mass of the structure is recorded with the aid of the software *SignalCalc* and the unit *DataPhysics Abacus 901* (DP-901). The shaker receives a random input voltage signal which allows obtaining an averaged linear TF, limiting the effect of the structural nonlinearities [19, 20]. In this way, it is possible to identify an equivalent underlying linear system even for nonlinear systems, like the complaint mechanism. Then, the linear TFs are used to extract the natural frequencies ω_n and the damping

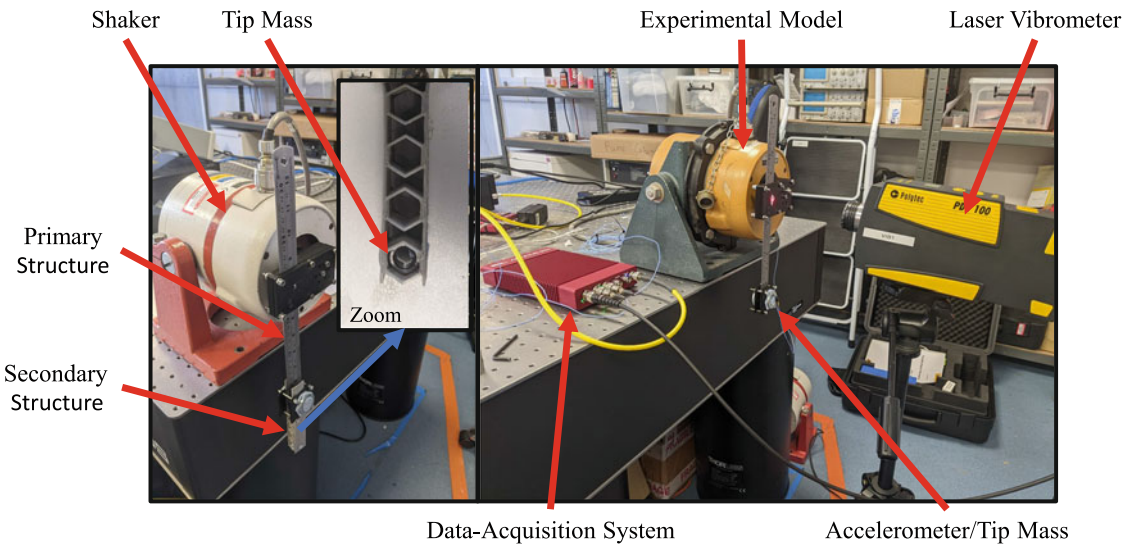

Fig. 30.1 Experimental test rig with primary and secondary structure (left) and experimental set-up with only the primary structure (right). The zoom shows the hexagonal shape of the complaint mechanism. The laser vibrometer is used to collect the base velocity, while the two accelerometers record the accelerations of the tip masses

Table 30.1 Mass of the primary structure, secondary structure, and tip masses

Mass	Primary structure	Secondary structure
Component mass m_s [g]	200.0	9.3
Tip mass m_{tip} [g]	70.0	5.2

Table 30.2 Natural frequencies, damping ratios, and associated coefficients of the primary and secondary structures

Parameter	Primary structure	Secondary structure
Natural frequency ω_n [Hz]	11.3	11.4
Damping ratio ζ [%]	0.36	4.78
Equivalent stiffness k_1 [N/m]	687.4	42.6
Equivalent damping c_1 [Ns/m]	0.0706	0.0568

ratios ζ of the primary and secondary structure by using classical linear identification methods, like the -3 dB method and the Kennedy and Pancu method [20]. Once the modal parameters, i.e. ω_n and ζ, are obtained, the linear stiffness k_1 and damping c_1 coefficients of an equivalent SDOF mechanical oscillator are computed by taking into account the following expressions: $k_1 = \omega_n^2 m$ and $c_1 = 2\omega_n \zeta m$, where the dynamic mass m is expressed as $m = m_{tip} + 1/3 m_s$, with m_{tip} denoting the tip mass, and m_s representing the mass of the considered component. The values of the masses m_{tip} and m_s are reported in Table 30.1, while the results of the linear identification are outlined in Table 30.2.

The primary structure shows low damping and a linear dynamic behaviour for the range of investigated input amplitudes; thus, its equivalent coefficients can be considered identified. On the contrary, the compliant mechanism reveals a nonlinear dynamic behaviour and high damping level which could undermine the correct identification of the linear properties, especially the identification of the natural frequency ω_n. Therefore, an additional optimisation procedure, which aims to improve the value of the identified linear stiffness k_1, is performed. The minimisation is carried out with the MATLAB built-in function *lsqnonlin*, which performs a nonlinear mean square minimisation between the amplitude and the phase of the numerical and experimental TFs. The considered TF can be mathematically described in complex form as:

$$T_{an} = \frac{i\Omega k_1 - c_1 \Omega^2}{k_1 - m\Omega^2 + i c_1 \Omega} \tag{30.1}$$

where T_{an} denotes the complex analytical transfer function, Ω is the forcing frequency, and i represents the imaginary unit. Such a TF represents the analytical counterpart of the experimental TF, previously adopted to identify the linear coefficients. Therefore, the objective function of the associated optimisation problem can be represented with the following expression:

$$\mathbf{F}(k_1) = |\mathbf{T}_{exp} - \mathbf{T}_{an}(k_1)|, \tag{30.2}$$

where $\mathbf{F}(k_1)$ is objective function, $\mathbf{T}_{exp}$ represents the complex experimental TF in vector form, and $\mathbf{T}_{an}$ denotes the complex analytical TF in vector form. The optimisation procedure generates an optimal linear stiffness coefficient $k_{1,opt}$ equal to 43.5 N/m and the results are graphically described by Fig. 30.2 where the experimental, the analytical original, and the analytical optimised TFs of the compliant mechanism are reported. The figure shows that the experimental and optimised TFs are in good agreement; thus, the underlying linear system of the secondary structure can be considered identified by the following coefficients: m, $k_{1,opt}$, and c_1.

30.4 Nonlinear System Characterisation

In this section, the nonlinear behaviour of the compliant mechanism is characterised by using the RFSM. The method is utilised to identify the nonlinear damping and stiffness coefficients of an equivalent nonlinear SDOF base-excited oscillator which is represented in Fig. 30.4. The RFSM is based on the second Newton's law which is used to define the restoring force R_f as follows:

$$R_f = -m\ddot{x} = c(\dot{z})\dot{z} + k(z)z \tag{30.3}$$

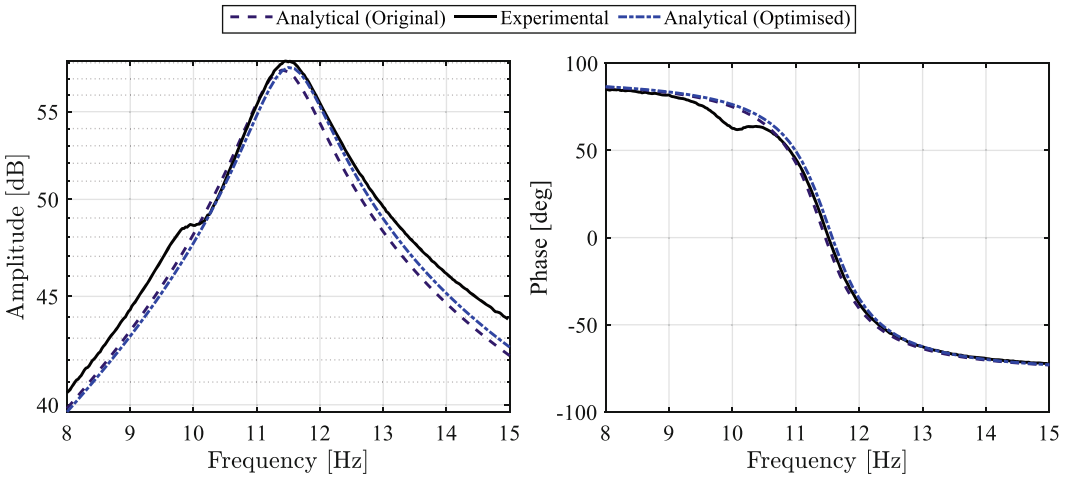

Fig. 30.2 Comparison between the experimental and analytical TFs for the amplitude (left) and phase (right) of the complaint mechanism. The original analytical transfer function is computed with the coefficients of Table 30.2, while the optimised transfer function is computed with the same coefficients but the optimal stiffness $k_{opt,1}$

Table 30.3 Damping and stiffness coefficients identified from the RFS. The polynomial fitting is performed with a third-degree polynomial

Parameter	First degree coeff.	Second degree coeff.	Third degree coeff.
Stiffness	$k_{1,RFS} = 40.9\,\text{N/m}$	$k_{2,RFS} = -248.3\,\text{N/m}^2$	$k_{3,RFS} = -49271.0\,\text{N/m}^3$
Damping	$c_{1,RFS} = 0.0548\,\text{Ns/m}$	$c_{2,RFS} = 0.0500\ \text{Ns/m}^2$	$c_{3,RFS} = 0.0387\,\text{Ns/m}^3$

where x represents the absolute displacement of the compliant mechanism tip, z is the relative displacement of the compliant mechanism tip with respect to the base, $c(\dot{z})$ and $k(z)$ denote the nonlinear damping and stiffness coefficients, and m is the dynamic mass of the oscillator equal to 0.0083 Kg. This equation can be used to create the restoring force surface (RFS) from which it is possible to identify the nonlinear damping $c(\dot{z})$ and the nonlinear stiffness $k(z)$ by considering, respectively, the intersection of the RFS and the plane passing for $z = 0$ and for $\dot{z} = 0$. The RFS is obtained by considering 20 different experimental tests—each test is performed by providing a sinusoidal voltage input to the shaker with a frequency of 10.7 Hz and different voltage input amplitudes, namely, an input amplitude of 0.686 V with the following amplification factors: 0.1, 0.2, 0.3, 0.4, 0.5, 0.6, 0.7, 0.8, 0.9, 1.0, 1.1, 1.2, 1.3, 1.4, 1.5, 1.6, 1.7, 1.8, 1.9, and 2.0. For each input condition, an accelerometer measures the absolute acceleration of the tip mass, while the laser measures the absolute velocity of the compliant mechanism base with the *National Instruments* unit NI-9234. Then, the recorded signals are integrated, derived, filtered, and manipulated to obtain the absolute acceleration $\ddot{x}$, the relative velocity $\dot{z}$, and the relative displacement z of the system. Such quantities can be used to create the RFS with the definition of Eq. 30.3, and the resulting nonlinear properties are reported in Fig. 30.3. The figure shows the presence of a symmetric cubic softening stiffness which reduces the stiffness of the system when large deformations are imposed. On the other hand, the damping reveals an asymmetric quadratic characteristic which produces high damping at positive relative velocities and low asymptotic damping at negative relative velocities. This behaviour could be triggered by the imperfect shape of the compliant mechanisms which is due to the fabrication process [6, 21, 22]: indeed, during the vibration, the system is not deforming in the same way in the two oscillation directions, inducing the generation of an asymmetric nonlinear characteristic in the system response. The identified nonlinear characteristics show a continuous shape, which is easily fitted with a third-degree polynomial using the MATLAB function *polyfit*. The results of the fitting process are numerically and graphically reported in Table 30.3 and in Fig. 30.3.

The values of the first-order parameters of Table 30.3, i.e. $k_{1,RFS}$ and $c_{1,RFS}$, are very similar to the linear coefficients $k_{1,opt}$ and c_1 previously identified for the compliant mechanism; this confirms the robustness of results of the RFSM and allows using the identified higher-order coefficients in the validation process. The nonlinear validation is performed by adopting sets of nonlinear experimental data which are completely different from the one adopted in the identification process. Such data represent the TFs[1] between the shaker voltage input and the displacement output signal of the tip mass. A discrete frequency sweep from 10.5 Hz to 11.5 Hz with an increment of 0.1 Hz is considered for the analysis, along with different excitation amplitudes, precisely equal to 0.686 V with amplification factors of 0.9, 1.2, 1.5, 1.6, 1.7, 1.8, 1.9, 2.0, and

[1] For transfer function of nonlinear system, we mean the frequency response curve of the system for a given input.

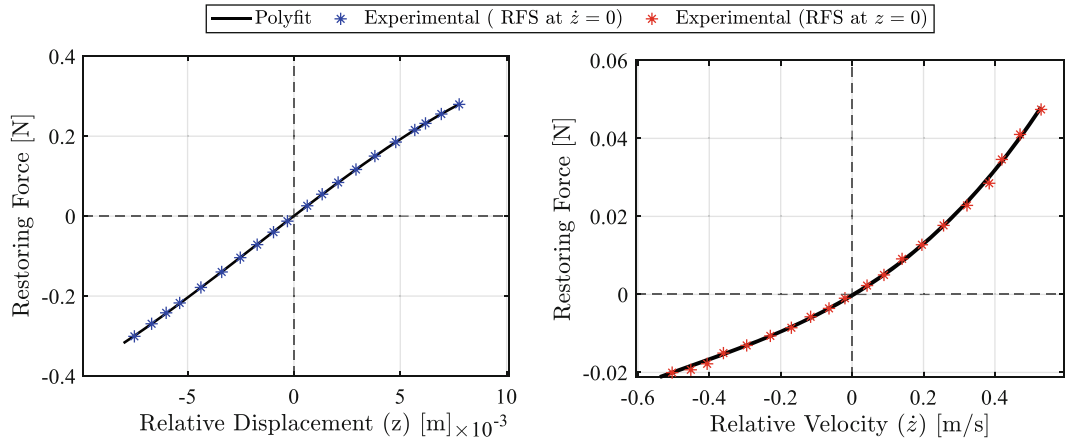

Fig. 30.3 Nonlinear stiffness (left) and damping (right) characteristics of the complaint mechanism. The nonlinear properties are obtained by collecting the data of the restoring force surface at $z = 0$ for the damping and at $\dot{z} = 0$ for the stiffness

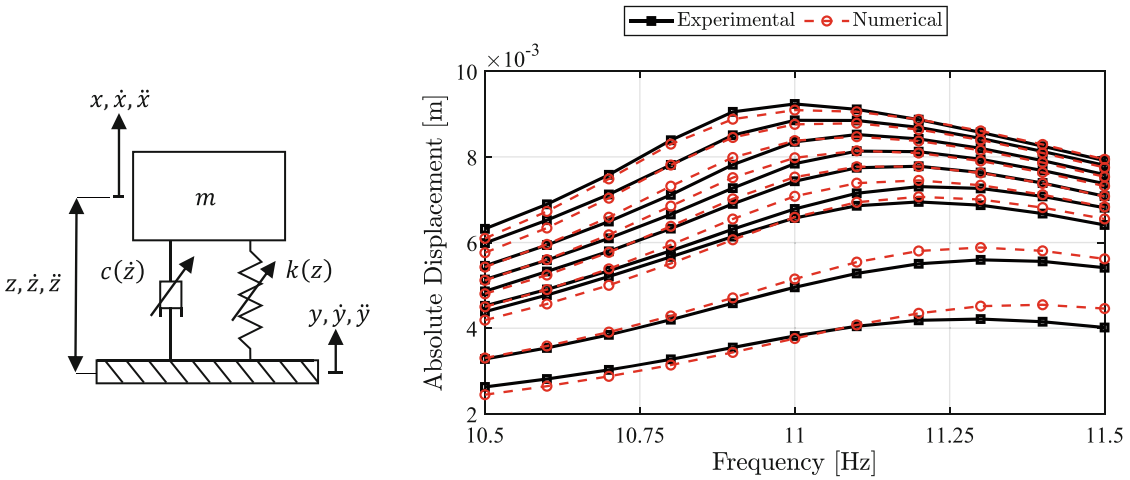

Fig. 30.4 Nonlinear equivalent SDOF oscillator (left) and experimental validation (right) of the identified model. The numerical solution is compared with the experimental data in the frequency range between 10.5 and 11.5 Hz for different excitation amplitudes

2.1. At each set-up, the input and output signals are recorded for about 10 seconds after reaching the steady-state condition. Then, the signal is filtered and integrated, and its peaks are averaged to estimate the amplitude of the system response. This process is repeated for each frequency and each input amplitude and it allows for measuring the nonlinear experimental TFs in different conditions. However, it is worth noticing that the output of the shaker, hence the base excitation of the system, is influenced by the dynamics of the complaint system. This results in the necessity of using the recorded experimental motion of the base as numerical input to numerically compute the dynamic response of the equivalent SDOF oscillator. Thus, the numerical integration is performed with the MATLAB function *ode45* which is adopted to solve the following equation of motion, representing the nonlinear oscillator described in Fig. 30.4:

$$m\ddot{x} + c_1(\dot{x} - \dot{y}) + c_{2,RFS}(\dot{x} - \dot{y})^2 + c_{3,RFS}(\dot{x} - \dot{y})^3 + k_{1,opt}(x - y) + k_{2,RFS}(x - y)^2 + k_{3,RFS}(x - y)^3 = 0 \qquad (30.4)$$

where y represents the experimental base displacement; $\dot{y}$ denotes the experimental base velocity; $k_{1,opt}$ and c_1 are linear coefficients of the secondary structure, described in Table 30.2 and Sect. 30.3; $k_{2,RFS}$, $k_{3,RFS}$, $c_{2,RFS}$, and $c_{3,RFS}$ represent the cubic and quadratic coefficients, identified in Table 30.3; and m is the dynamic mass of the oscillator. The numerical and experimental TFs are reported on the right side of Fig. 30.4: the experimental data shows the typical reduction of resonance frequency at high excitation amplitudes, confirming the softening nature of the compliant mechanism stiffness. Moreover, the numerically computed nonlinear dynamic response is in good agreement with experimental data at both high and low response amplitudes; therefore, the identified equivalent oscillator and its coefficients can be considered validated.

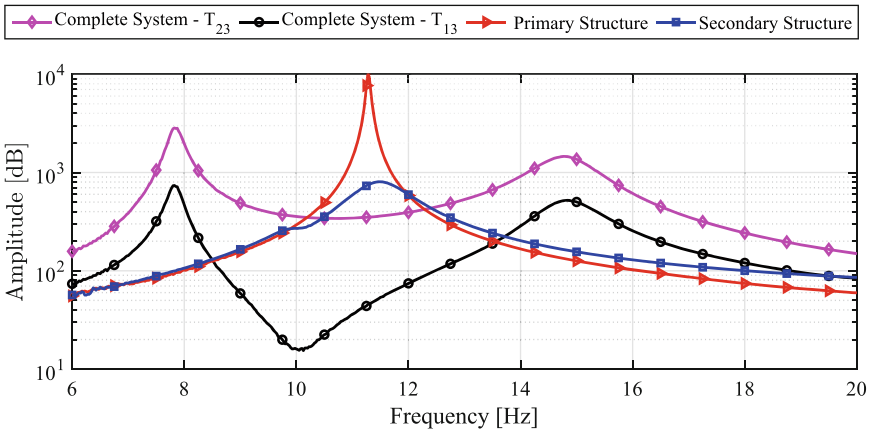

Fig. 30.5 Experimental linear TFs between the input base velocity and the acceleration of the tip masses for the three considered configurations: complete system (primary + secondary structure), primary structure, and secondary structure. TFs of the complete system, i.e. $T_{1,3}$ and $T_{2,3}$, consider, respectively, the acceleration of the tip mass of the primary and the secondary structure as an output signal

Finally, the efficacy of the compliant mechanism as a nonlinear vibration absorber is experimentally tested. The linear TF between the velocity of the base and the absolute acceleration of the tip masses is recorded again with random excitation and the unit *DataPhysics Abacus 901* for the primary structure, the secondary structure, and the complete system with primary and secondary structure. The results are reported in Fig. 30.5 and demonstrate that the compliant nonlinear mechanism is able to reduce the response amplitude of the beam around the resonance frequency of the primary structure, hence acting as a nonlinear vibration absorber.

30.5 Conclusion

In this paper, the experimental analysis and the nonlinear characterisation of a compliant mechanism with a complex hexagonal shape which acts as a nonlinear vibration absorber of a simple cantilever beam are performed. Firstly, the linear properties of the primary and secondary structures are identified by using the averaged linear TF. Then, the RFSM is implemented to identify the nonlinear stiffness and damping characteristics of an equivalent SDOF oscillator, representing the compliant mechanism. These properties are fitted with a third-degree polynomial and the resulting quadratic and cubic coefficients of damping and stiffness are adopted in the validation process. Finally, the identified nonlinear SDOF oscillator is validated by comparing the numerical and experimental results in terms of amplitude response at different frequencies and excitation amplitudes.

The RFS of the compliant mechanism shows interesting stiffness and damping nonlinear properties. Surprisingly, the system offers a softening stiffness characteristic which reduces the resonance frequency of the system when the excitation amplitude is increased. On the other hand, the damping shows an asymmetric quadratic behaviour with respect to the relative velocity $\dot{z}$ which could be due to small imperfections in the compliant mechanism. Such imperfections could be generated by the 3D-printing process, resulting in an asymmetric deformation of the mechanism which is responsible for the associated asymmetric damping characteristic. Moreover, the outlined identification process is shown to be effective in identifying an equivalent nonlinear SDOF oscillator, as demonstrated by the experimental validation. Finally, the system is experimentally tested in the three proposed configurations and the compliant mechanism capabilities to dampen the dynamic response of a simple steel beam are successfully demonstrated.

Acknowledgments The authors would like to acknowledge the Institution of Engineering and Technology (IET) and the following NERC and EPSRC grants: GALLANT, Glasgow as a Living Lab Accelerating Novel Transformation (No. NE/W005042/1), RELIANT, Risk EvaLuatIon fAst iNtelligent Tool for COVID19 (No. EP/V036777/1).

References

1. Fowler, R.M., Howell, L.L., Magleby, S.P.: Compliant space mechanisms: a new frontier for compliant mechanisms. Mech. Sci. **2**(2), 205–215 (2011)
2. Merriam, E.G., Jones, J.E., Howell, L.L.: Design of 3d-printed titanium compliant mechanisms. In: The 42nd Aerospace Mechanism Symposium (2014)
3. Kota, S., Joo, J., Li, Z., Rodgers, S.M., Sniegowski, J.: Design of compliant mechanisms: applications to mems. Analog Integr. Circuits Signal Process. **29**(1), 7–15 (2001)
4. Cao, L., Dolovich, A.T., Schwab, A.L., Herder, J.L., Zhang, W.: Toward a unified design approach for both compliant mechanisms and rigid-body mechanisms: module optimization. J. Mech. Design **137**(12), 122301 (2015)
5. Yu, Y.-Q., Howell, L.L., Lusk, C., Yue, Y., He, M.-G.: Dynamic modeling of compliant mechanisms based on the pseudo-rigid-body model. J. Mech. Design **127**(4), 760–765 (2005)
6. Howell, L.L.: Compliant mechanisms. In: 21st Century Kinematics, pp. 189–216. Springer, Berlin (2013)
7. Pucheta, M.A., Cardona, A.: Design of bistable compliant mechanisms using precision–position and rigid-body replacement methods. Mech. Mach. Theory **45**(2), 304–326 (2010)
8. Wang, M.Y.: Mechanical and geometric advantages in compliant mechanism optimization. Front. Mech. Eng. China **4**(3), 229–241 (2009)
9. Greenberg, H.C., Gong, M.L., Magleby, S.P., Howell, L.L.: Identifying links between origami and compliant mechanisms. Mech. Sci. **2**(2), 217–225 (2011)
10. Saudan, H., Kiener, L., Perruchoud, G., Kruis, J., Vaideeswaran, K., Dadras, M.M., Cochet, F., Liberatoscioli, S.: Compliant mechanisms and space grade product redesign based on additive manufacturing. In: Advances in Optical and Mechanical Technologies for Telescopes and Instrumentation III, vol. 10706, pp. 829–844. SPIE (2018)
11. Dewalque, F., Schwartz, C., Denoél, V., Croisier, J.L., Forthomme, B. and Brüls, O.: Experimental and numerical investigation of the nonlinear dynamics of compliant mechanisms for deployable structures. Mech. Syst. Signal Process. **101**, 1–25 (2018)
12. Thomas, T.L., Kalpathy Venkiteswaran, V., Ananthasuresh, G.K. and Misra, S.: Surgical applications of compliant mechanisms: a review. J. Mech. Robot. **13**(2), 020801 (2021)
13. Moritoki, Y., Furukawa, T., Sun, J., Yokoyama, M., Shimono, T., Yamada, T., Nishiwaki, S., Kageyama, T., Fukuda, J., Mukai, M. et al.: 3d-printed micro-tweezers with a compliant mechanism designed using topology optimization. Micromachines **12**(5), 579 (2021)
14. Liang, H., Hao, G., Olszewski, O.Z.: A review on vibration-based piezoelectric energy harvesting from the aspect of compliant mechanisms. Sensors Actuators A: Phys. **331**, 112743 (2021)
15. Hricko, J., Havlík, Š.: Compliant mechanisms for motion/force amplifiers for robotics. In: International Conference on Robotics in Alpe-Adria Danube Region, pp. 26–33. Springer, Berlin (2019)
16. Garaigordobil, A., Ansola, R., Veguería, E., Fernandez, I.: Overhang constraint for topology optimization of self-supported compliant mechanisms considering additive manufacturing. Comput.-Aided Design **109**, 33–48 (2019)
17. Qiu, K., Wang, Z., Zhang, W.: The effective elastic properties of flexible hexagonal honeycomb cores with consideration for geometric nonlinearity. Aerospace Sci. Technol. **58**, 258–266 (2016)
18. Pellicano, F., Amabili, M., Paıdoussis, M.P.: Effect of the geometry on the non-linear vibration of circular cylindrical shells. Int. J. Non-Linear Mech. **37**(7), 1181–1198 (2002)
19. Worden, K., Tomlinson, G.R.: Nonlinearity in Structural Dynamics: Detection, Identification and Modelling. CRC Press, Boca Raton (2001)
20. Ewins, D.J.: Modal Testing: Theory, Practice and Application. Wiley, New York (2009)
21. Ngo, T.D., Kashani, A., Imbalzano, G., Nguyen, K.T., Hui, D.: Additive manufacturing (3d printing): a review of materials, methods, applications and challenges. Comp. B: Eng. **143**, 172–196 (2018)
22. Abdulhameed, O., Al-Ahmari, A., Ameen, W., Mian, S.H.: Additive manufacturing: Challenges, trends, and applications. Adv. Mech. Eng. **11**(2), 1687814018822880 (2019)

Chapter 31
Resonant Vibration Absorbers with Impacts

Mihai Cimpuieru, Sean T. Kelly, and Bogdan I. Epureanu

Abstract Methods to reduce the vibration amplitude of blisks are essential to ensure the safe operation of turbomachinery. Resonant vibration absorbers (RVAs) can be used to mitigate vibrations of structures through energy transfer and absorption. Specifically, an RVA is a friction damper with possible impacts that is tuned to the natural frequency of the blisk, allowing energy transfer from the beam to the damper. The state of the art for blisk nonlinear dynamics includes contact models that capture the energy dissipation from friction dampers. Several recent studies have focused on modeling Coulomb friction and repetitive impacts to analyze their effects on reducing vibration amplitudes in blisks. This chapter explores the effectiveness of RVAs in dissipating energy in blisks through impacts. To do so, methods combining finite element modeling, reduced order modeling, and nonlinear structural dynamics are used to analyze the forced response of a beam that resembles a blade in a blisk equipped with an RVA. Specifically, an RVA is attached near the root of the beam where the beam experiences only small displacements similar to locations under the rim of blisks. The RVA device provides impacts at two surfaces connected to the host structure, namely, the beam. The dynamics of the system is analyzed using the harmonic balance method to account for nonlinear impact forces. Dynamic effects of impacts are simulated with a novel microscopic model that captures local material elasticity and viscosity. Results show that increasing the local stiffness of the impact areas shifts the first resonance of the beam tip response to higher frequencies. In addition, increasing the damping of the material at the impact areas decreases the beam response amplitude at resonance. Furthermore, a reduction in the impact time per cycle is observed with increasing material damping. Finally, the best RVA performance is observed when the beam and damper are moving out of phase.

Keywords Turbomachinery · Blisk · Nonlinear · Impact · Damping

31.1 Introduction

Blisks are turbomachinery components that are paramount to the well functioning of gas turbines. These low damping structures excited by high fluctuating aerodynamic forces experience large vibration amplitudes that can ultimately cause blisk failure. In addition, blisks have inherent sector to sector differences in their material properties, a characteristic defined as mistuning. Several studies have shown that mistuning can also cause high blisk vibrations [1] that can affect the safe operation of these turbomachinery components. Thus, multiple studies have focused on mitigating blisk vibrations. In particular, resonant vibration absorbers (RVAs) have been used to absorb energy from a host structure and further enhance the reduction through energy dissipation. Energy absorption is achieved by tuning the RVA to the frequency of its host structure, while energy can be dissipated through friction [2] or impact contacts [3]. For blisks, applications involved placing a damper in the disk region to enhance energy absorption and dissipate energy through Coulomb friction contacts close to the blade root [4].

This chapter focuses on studying the effects of RVAs with impact contacts in blisks. Impacts are modeled microscopically with a spring and a damper at each contact node pair. To perform this study, a simpler computational beam is designed to mimic a blisk blade. The RVA is clamped close to the blade's root, similar to the approach in [2]. The absorber is then tuned to the first natural frequency of the beam and forcing is applied close to the beam root. To analyze the effectiveness of the RVA, the harmonic balance method (HBM) is implemented to calculate the beam tip response reductions. Results show

M. Cimpuieru (✉) · S. T. Kelly · B. I. Epureanu
Department of Mechanical Engineering, University of Michigan, Ann Arbor, MI, USA
e-mail: mcimpi@umich.edu

M. R. W. Brake et al. (eds.), *Nonlinear Structures & Systems, Volume 1*, Conference Proceedings
of the Society for Experimental Mechanics Series, https://doi.org/10.1007/978-3-031-36999-5_31

a reduction in beam response with increased damping coefficient and a stiffening effect due to the spring force at impact. Additionally, the highest reduction is obtained when the RVA and the beam move out of phase.

31.2 Methodology

To demonstrate the effectiveness of the RVA (Fig. 31.1, green), a computational finite element (FE) model is developed using a beam as host structure as presented in Fig. 31.1. The beam-RVA system is modeled using a number of approximately 741,387 degrees of freedom (DOF), which is reduced using a Craig-Bampton reduced order model with 5 primary nodes and 70 secondary modes. As described in the introduction section, the RVA absorbs energy from the host structure (i.e., the beam) and further dissipates energy through nonlinear impact contacts. Impact contacts between the RVA and the host structure occur at the left and right sides of the "U" shape component present in Fig. 31.1 (red), 2, and 3. The forcing is applied in the proximity of the beam's root and the response is measured at the free end of the beam. The RVA is tuned to ensure high-energy absorption from the host structure and large nonlinear impact forces for energy dissipation. Thus, the first natural frequency of the RVA is tuned to match the target frequency of the host structure, resulting in two cantilever beam modes: one where the beam and the RVA move in phase with each other (Fig. 31.2), and the other one with the two moving out of phase (Fig. 31.3). The harmonic balance method (HBM) [5] with an alternating frequency-time domain (AFT) procedure is implemented to calculate the beam response. The mass and stiffness matrices of the linear system (i.e., no impact contacts) are obtained through the Craig-Bampton reduction, while the nonlinear forces are calculated within the AFT procedure. The nonlinear forces at impact are calculated in the time domain using a novel microscopic model at each contact node pair. Within the AFT scheme, the forces at impact are converted to the frequency domain using a fast Fourier transformation (FFT) applied over one oscillation cycle. Multiple contact nodes per impact can be added for a more accurate contact model. For each contact node pair, a virtual spring and a virtual damper are used to model the impact contact as exemplified in Fig. 31.4. For the analysis in this chapter, both left and right impacts are modeled as point contacts (i.e., one node pair per contact interface) due to the geometry of the RVA and of the "U" shape component. While the spring models the elastic deformation of the bodies during contact, the damping force dissipates energy during impacts by acting in the opposite direction of the relative motion between the contacting bodies (i.e., contact between the left/right wall and the left/right side of the RVA). The corresponding spring and damping forces are calculated in the time domain as part of the AFT procedure as follows:

$$\boldsymbol{f}_{\text{nonlinear } j} = \begin{cases} k_i \left(\mathbf{x}_{\text{left wall},j} - \mathbf{x}_{\text{RVA left},j}\right) + c_i \left(\dot{\mathbf{x}}_{\text{left wall},j} - \dot{\mathbf{x}}_{\text{RVA left},j}\right) \\ 0 \end{cases}, \tag{31.1}$$

$$\text{switch condition} : k_i \left(\mathbf{x}_{\text{left wall},j} - \mathbf{x}_{\text{RVA left},j}\right) + c_i \left(\dot{\mathbf{x}}_{\text{left wall},j} - \dot{\mathbf{x}}_{\text{RVA left},j}\right) = 0$$

where $\mathbf{x}_{\text{RVA left},j}$ is the vector of coordinates (i.e., x,y,z) of the node on the RVA's left side corresponding to contact pair j. $\mathbf{x}_{\text{left wall},j}$ is the vector of coordinates of the node placed on the left wall of the "U" component part of contact pair j. Similarly, Eq. 31.1 is used to model the right-side impacts.

31.3 Results and Discussion

To analyze the influence of the RVA on the host structure's response, it is paramount to understand the effect of the stiffness and damping forces during impact on the beam's response. In Fig. 31.5, the beam tip response when the damper moves freely (i.e., no contact at the left or right walls) shows two peaks corresponding to the two modes that result after tuning. A shift in resonance frequency can be observed for both modes when impacts occur. This phenomenon is attributed to the stiffening effect caused by the virtual spring accounting for the elastic deformation at impact. The damping force causes the amplitude reduction of the beam response through energy dissipation. It can be noticed that for both modes the amplitude reduction is increasing with higher damping value coefficients (c_i). However, the response corresponding to the mode at 32.04 Hz when the damper and the host structure are moving in phase shows a smaller amplitude reduction. The reason for this phenomenon is the smaller relative velocity between the damper and the beam that causes lower forces opposing the relative motion of the absorber and the host and therefore less energy dissipation within the system. Finally, Figs. 31.6 and 31.7 show the impact

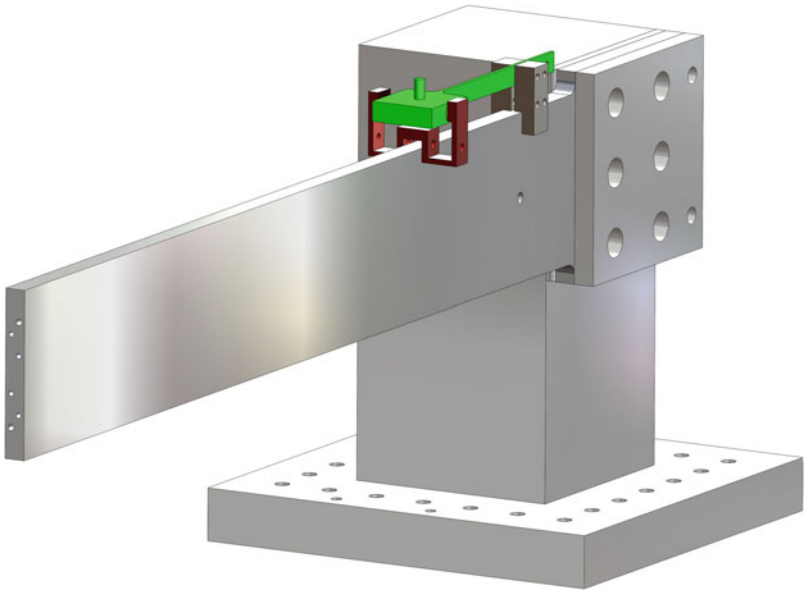

Fig. 31.1 Beam with damper attached

Fig. 31.2 Mode shape in phase

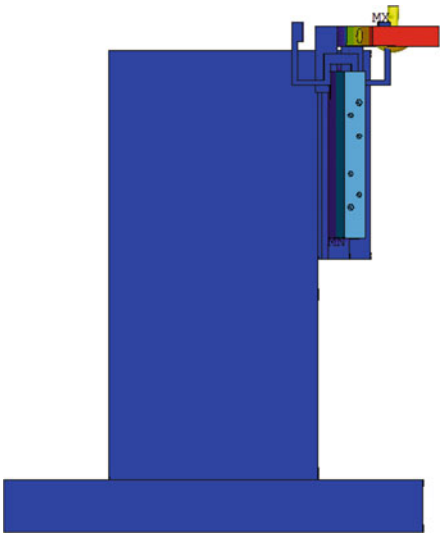

time during an oscillation cycle period for each forcing frequency. More explicitly, the impact time during a cycle period is defined as the number of steps within that cycle when the impact force is nonzero (i.e., the RVA is impacting the left or right wall). An important observation is that the total impact time decreases with higher damping coefficients due to a reduced relative velocity that eventually causes less contact between the RVA and the beam. It is important to mention that there is slightly less impact time at the right wall than at the left one due to the asymmetric equilibrium distances between the walls and the RVA (i.e., right wall is 0.2 mm further away from the RVA than the left wall is at equilibrium position).

31.4 Conclusions

A new resonant vibration absorber (RVA) using impacts for energy dissipation has been designed and studied computationally using a novel microscopic contact modeling technique. This technique captures local material elasticity and viscosity through a virtual spring and damper at each contact node pair. Using a beam as host structure and an RVA connected to the root of the beam, an analysis was performed on the beam tip response reductions due to energy absorption and enhanced through

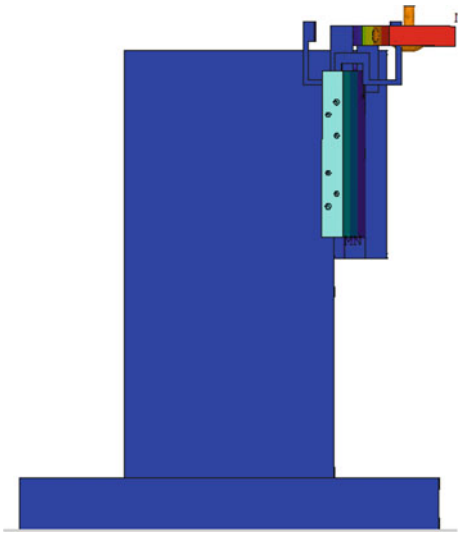

Fig. 31.3 Mode shape out of phase

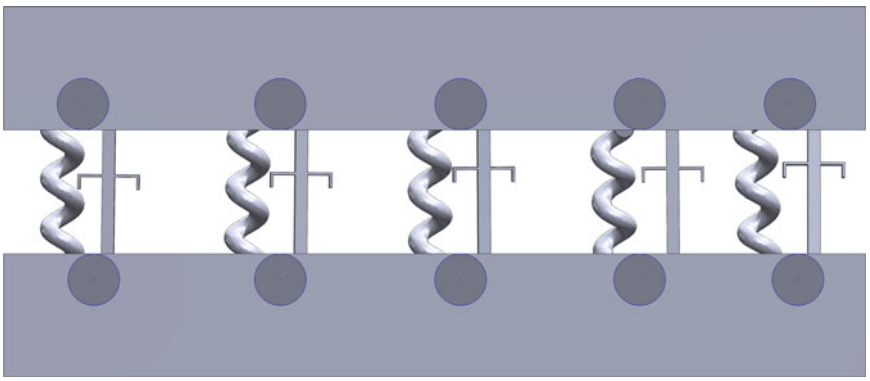

Fig. 31.4 Microscopic impact contact model

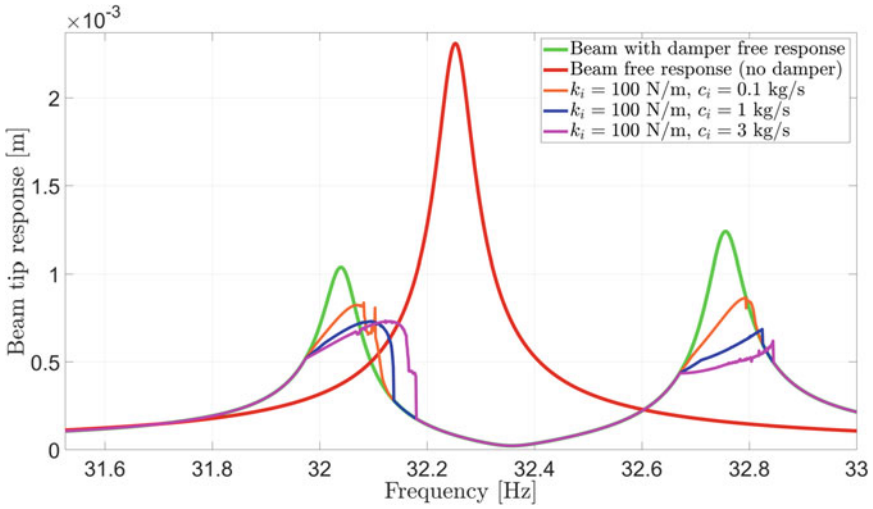

Fig. 31.5 Forced response measured at beam tip

impacts causing energy dissipation. The behavior of the system exhibits stiffening effects due to the elastic deformation at impact, and increasing beam amplitude reductions and less contact times with higher damping coefficients.

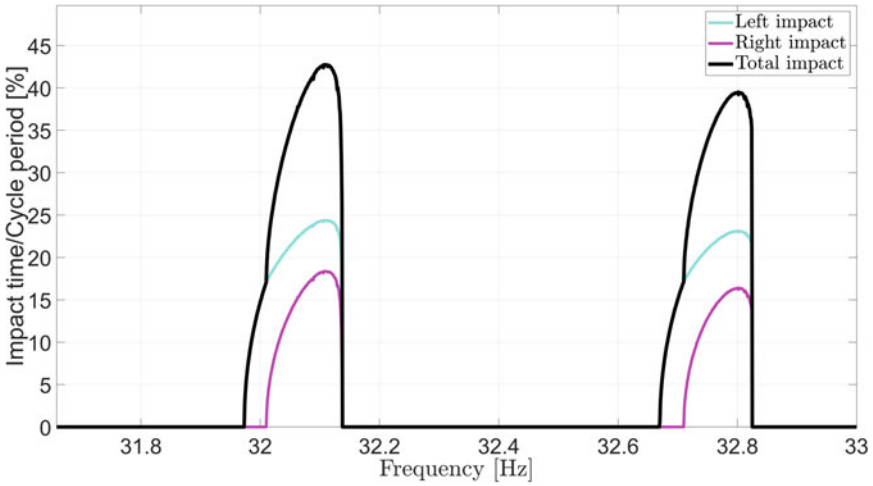

Fig. 31.6 Impact time $c_i = 1$ kg/s

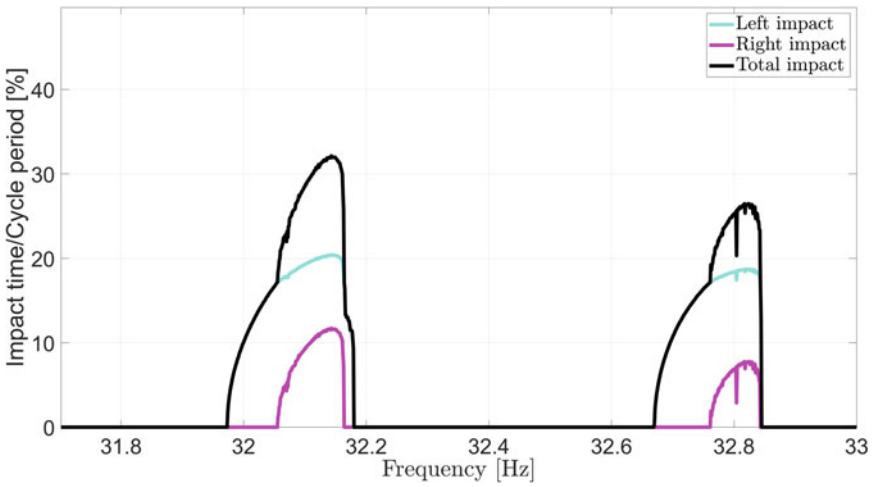

Fig. 31.7 Impact time $c_i = 3$ kg/s

Acknowledgments The authors would like to gratefully acknowledge the generous support offered by the GUIde 6 consortium toward their investigation research in this topic.

References

1. Kelly, S.T., Lupini, A., Epureanu, B.I.: Data-driven approach for identifying mistuning in As-Manufactured Blisks. J. Eng. Gas Turbines Power. **144**(5), 051006 (2022)
2. Lupini, A., Shim, J., Epureanu, B.I.: Experimental and computational study of a tuned damper with frictional contacts. AIAA J. **58**(8), 3607–3613 (2020)
3. Li, T., Seguy, S., Berlioz, A.: Optimization mechanism of targeted energy transfer with vibro-impact energy sink under periodic and transient excitation. Nonlinear Dyn. **87**(4), 2415–2433 (2017)
4. Lupini, A., Epureanu, B.I.: A friction-enhanced tuned ring damper for bladed disks. J. Eng. Gas Turbines Power. **143**(1), 011002 (2021)
5. Krack, M., Gross, J.: Harmonic Balance for Nonlinear Vibration Problems. Springer International Publishing, Cham (2019)

Chapter 32
Modeling and Verifying the Dynamic Response of Layered Plate Damping Systems

Greg Dorgant, Dana Figueroa, Zach Rogers, Jonathan Hower, Adam Bouma, Tyler Schoenherr, and David Soine

Abstract The dynamic response of plate systems in which similar size plates are joined with bolts is modeled. Specifically, the modal response of analytical, numerical, and experimental models is compared and is shown to vary with respect to bolt pattern, number of joint interfaces, plate thickness, and bolt preload. The contrast between the numerical (validated with experimental data through model updating) and the analytical models quantifies the complexity of a joined plate system as opposed to a homogenous plate. Comparing and accurately modeling these configurations further the understanding of the dynamic response of layered joined plates.

Keywords Model updating · Bolted plates

32.1 Introduction

Bolted plate systems exist in the real world in many forms—from pipe flanges to spacecraft, and structural I-beams to consumer products like microwaves. As such, it is critical to fully understand the dynamic behavior of these omnipresent systems. Beginning in the 1950s, researchers have studied the effect of critical factors such as bolt spacing, bolt preload, and impact amplitude on the modal response of systems incorporating bolt connections [1–4] both numerically in finite element and experimentally. In finite element analysis, bolted connections have been modeled as nonlinear contact surfaces defined by frictional interfaces [5, 6]. Continuing research in this area has focused on simplifications aimed at reducing computational cost while maintaining accuracy. For example, Kim et al. showed that a model consisting of 1D beam elements rigidly connected and given an applied stress dependent on preload provided similar accuracy while reducing computational time [7].

G. Dorgant (✉)
George W. Woodruff School of Mechanical Engineering, Georgia Institute of Technology, Atlanta, GA, USA
e-mail: gdorgant3@gatech.edu

D. Figueroa
Department of Mechanical Engineering, New Mexico Institute of Mining and Technology, Socorro, NM, USA

Z. Rogers
Mechanical and Aerospace Engineering, University of Central Florida, Orlando, FL, USA

J. Hower
Department of Energy's Kansas City National Security Campus Managed by Honeywell, Kansas City, MO, USA

A. Bouma · T. Schoenherr · D. Soine
Sandia National Laboratories, Albuquerque, NM, USA

M. R. W. Brake et al. (eds.), *Nonlinear Structures & Systems, Volume 1*, Conference Proceedings
of the Society for Experimental Mechanics Series, https://doi.org/10.1007/978-3-031-36999-5_32

We aim to examine how bolt preload, number of layers, excitation amplitude, and total thickness affect the modal response of bolted plate systems through experimental testing in a full factorial experimental design coupled with a finite element model. The full factorial experimental design examines five factors over two levels to determine the influence of each of these factors: natural frequency, mode shape, and modal damping. We compare the experimental results with a simplified finite element model.

32.2 Background

Besides the material damping, the bolts provide the dominant damping mechanism through frictional slip at the interface between layers [8, 9]. Two regions (no-slip and microslip) generally exist around bolts when the system is excited perpendicularly to the bolt's axis. Figure 32.1 illustrates these two regions as they range from the bolt shank.

Nearest to the bolt, the no-slip region, wherein the clamping force sufficiently constrains the interface, prevents all slip. Further from the bolt, the clamping force is not sufficient to keep the interface from slipping. For most systems, the motion of this slip is small and localized, thus inspiring the description of microslip. The bolted plate system acts nonlinearly with respect to amplitude—as the system excitation increases, the microslip region increases. When exciting the system parallel to the bolt's axis, a region of separation may also exist in which the constitutive plates lose contact if the impact amplitude is sufficiently large. In a similar manner, for sufficient amplitude, the no-slip region will disappear, and the plate will be a macroslip region. While the impacts examined herein will not be sufficient to trigger macroslip, small interfacial regions may separate in configurations of low coupling.

From this understanding of the mechanisms introduced by the bolted connections, we predict that both the number of interfaces and bolt spacing will share a direct relationship with the modal damping. As more interfaces are introduced, more microslip interfaces and thus more damping will exist. Similarly, as the bolt spacing increases, more area will be susceptible to microslip and separation; therefore, more nonlinear damping will be introduced into the system. The relationship between total thickness (h) and the modal frequency (f_i) of a square plate is given by

$$f_i = \frac{\lambda_i}{2\pi a^2}\left[\frac{Eh^3}{12\gamma\left(1-\nu^2\right)}\right]^{\frac{1}{2}} = \frac{\lambda_i}{2\pi a^2}\left[\frac{E}{12\rho\left(1-\nu^2\right)}\right]^{\frac{1}{2}} h \tag{32.1}$$

where λ_i describes the mode shape, a is the plate's side length, E is the elastic modulus, γ is the mass density per unit area, ν is the Poisson's ratio, and ρ is the mass density per unit volume [10]. Zaman et al. [1] compared the modal response of bolted joints and monolithic joints created by welding and found out that the bolted joint displayed reduced natural frequencies but increased damping. Saito and Suzuki [2] investigated the effect of bolt preload on the natural frequencies and modal damping of plastic plates with bolted joints. They found that natural frequencies will increase asymptotically, while damping will decrease asymptotically as bolt torque is increased. Ungar [3] *found that while fewer* bolts generally correlate with higher damping. Brons et al. [4] observed higher damping ratios for higher impact amplitudes. Table 32.1 summarizes the relationships shared by each of the studied factors and the modal frequency and damping.

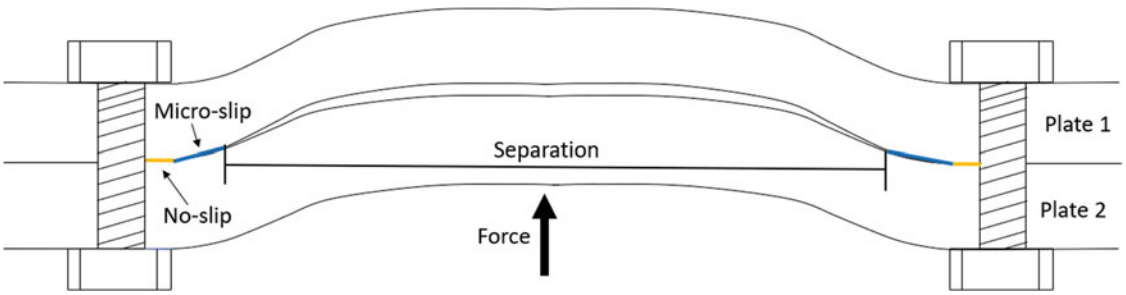

Fig. 32.1 Illustration of the areas of slip

Table 32.1 Expected relationships between experimental factors and measured responses

	Relationship shared with frequency	Relationship shared with damping
Bolt spacing	Unknown	Direct [3]
Bolt preload	Asymptotically direct [2]	Asymptotically inverse [2]
Total thickness	Direct [10]	None
Number of interfaces	Unknown	Direct
Impact amplitude	Unknown	Direct [4]

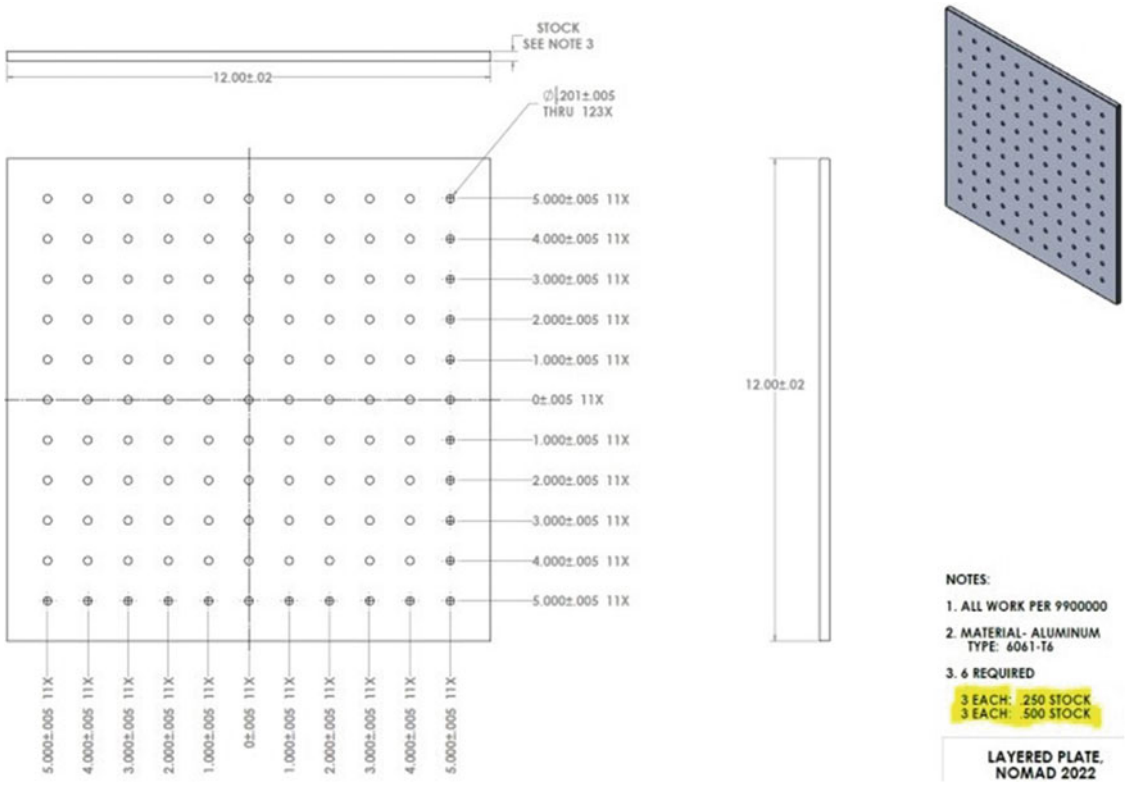

Fig. 32.2 Plate drawing

32.3 Experimental Testing Methodology

32.3.1 Test Setup and Considerations

The test setup consists of a layered plate configuration made up of one or more square 6061-T6 aluminum plates coupled with 10–24 bolts. Figure 32.2 displays the base plate schematic. The dimensions are 12″ x 12″ and either 0.25″ or 0.5″ in thickness with an 11 × 11 grid of 0.2″ diameter through holes.

There are five bolt patterns possible for an 11 × 11 grid while maintaining a bolt in each corner of the plate and a four-fold symmetry for the bolts. These two requirements properly constrain the number of bolt patterns and maintain the pre-existing symmetry of the square plate. Figure 32.3 displays the bolt patterns labeled one through five in ascending order of the number of bolts required. We choose to focus our tests on bolt patterns one and three to represent a high and low bolt spacing, respectively, and 12 plate configurations are represented in Table 32.2. We define our joined plate systems with two factors: total thickness and the number of interfaces. For the two plate thicknesses present (0.25 and 0.5 inch), these two factors uniquely define every plate system.

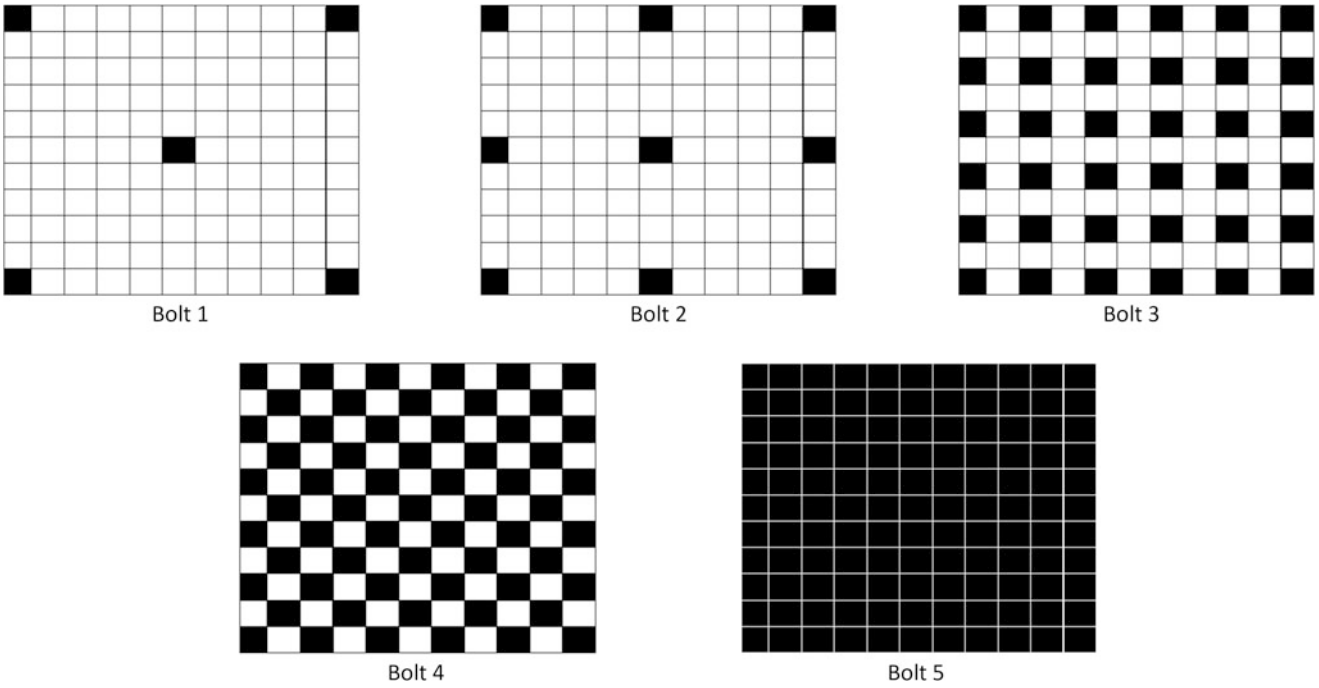

Fig. 32.3 Bolt patterns 1–5 (black indicates a filled through hole)

Table 32.2 All 12 plate configurations tested

Configuration	Layer 1	Layer 2	Layer 3	Layer 4	Total thickness (in)	Number of interfaces
1	0.25	–	–	–	0.25	0
2	0.5	–	–	–	0.5	0
3	0.25	0.25	–	–	0.5	1
4	0.25	0.5	–	–	0.75	1
5	0.5	0.5	–	–	1	1
6	0.25	0.25	0.25	–	0.75	2
7	0.25	0.5	0.25	–	1	2
8	0.5	0.25	0.5	–	1.25	2
9	0.5	0.5	0.5	–	1.5	2
10	0.25	0.5	0.5	0.25	1.5	3
11	0.5	0.25	0.25	0.5	1.5	3
12	0.5	0.25	0.5	0.25	1.5	3

32.3.2 Test Procedure

Each plate configuration is created to test if the order in which plates of varying thicknesses are placed as well as the number of interfaces affects the systems natural frequencies and damping values. For each plate configuration, the bolt pattern, the bolt preload, and the excitation amplitude are changed to see if those variables have any effects on natural frequencies and damping as well. A plastic-tipped modal hammer (PCB086C03) is used for all test runs. We excite the test specimen using a roving-hammer test with three input locations using three impacts at each. Figure 32.4 illustrates the antinodal lines of the first four modes, which informs our choice of input locations.

These locations correspond to accelerometers 1, 9, and 6 (highlighted in yellow) in the 3 × 3 grid of triaxial 10 mV accelerometers shown in Fig. 32.5a. Figure 32.5b depicts the way bungee cords suspend a test specimen from a test frame constructed from 80-20 aluminum beams to best simulate free boundary conditions. Each plate configuration is suspended on a test frame made of 80-20 aluminum beams by bungee cords to best simulate free-free conditions.

Siemens SCADAS Mobile is used to collect the accelerations and Siemens LMS to process the data into the modal information. LMS uses the add-in PolyMax, in which a curve-fitting algorithm (a polyreference least-squares complex frequency domain method [11]) estimates the modal parameters from one or more FRFs. Figure 32.6 displays the stabilization

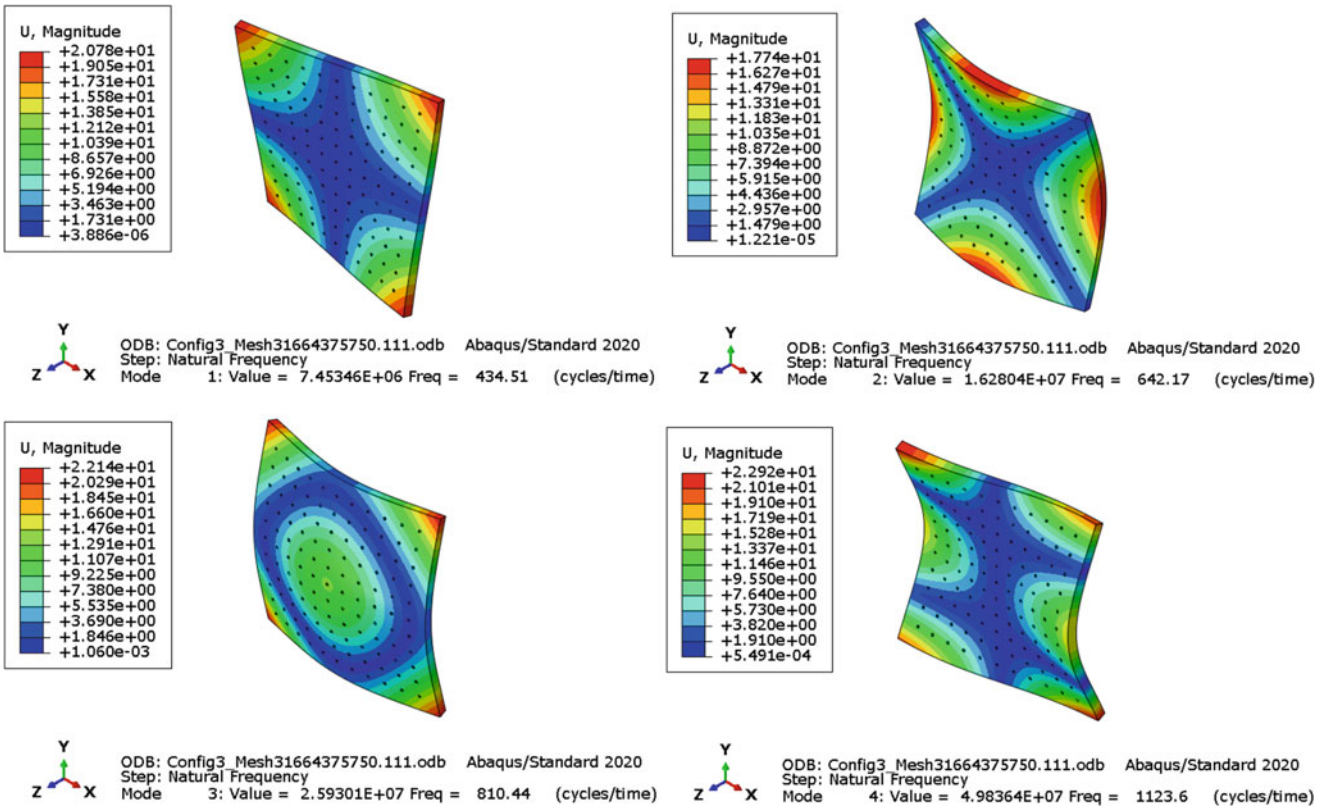

Fig. 32.4 Finite element depiction of the first four modes

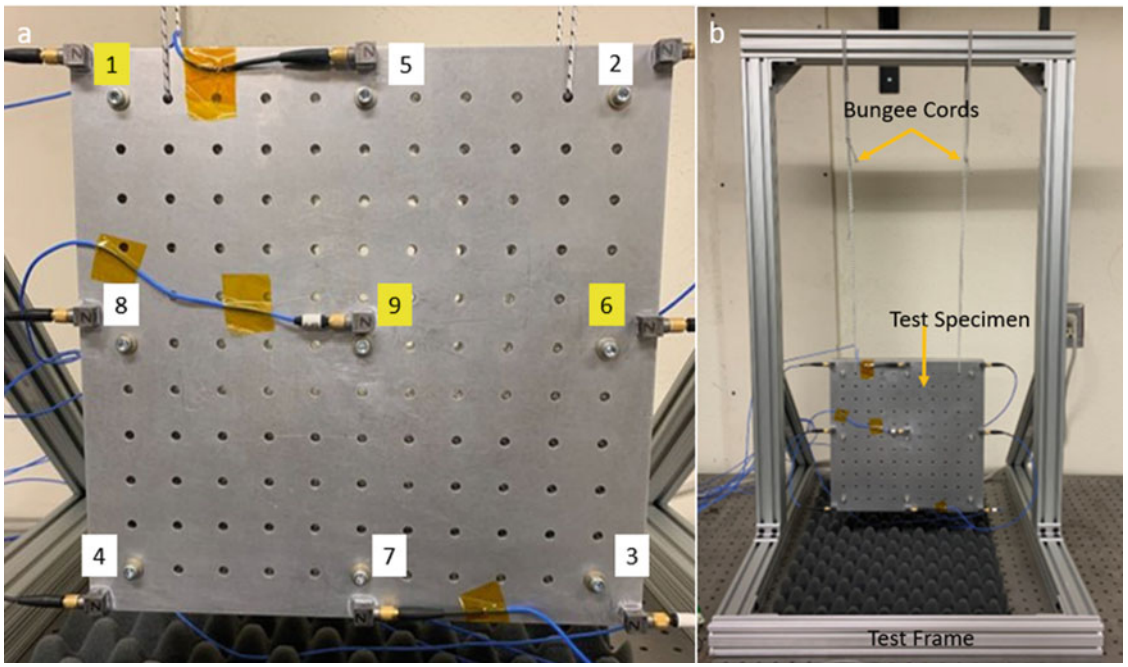

Fig. 32.5 (**a**) Accelerometer placement on a test specimen and (**b**) the testing frame with specimen

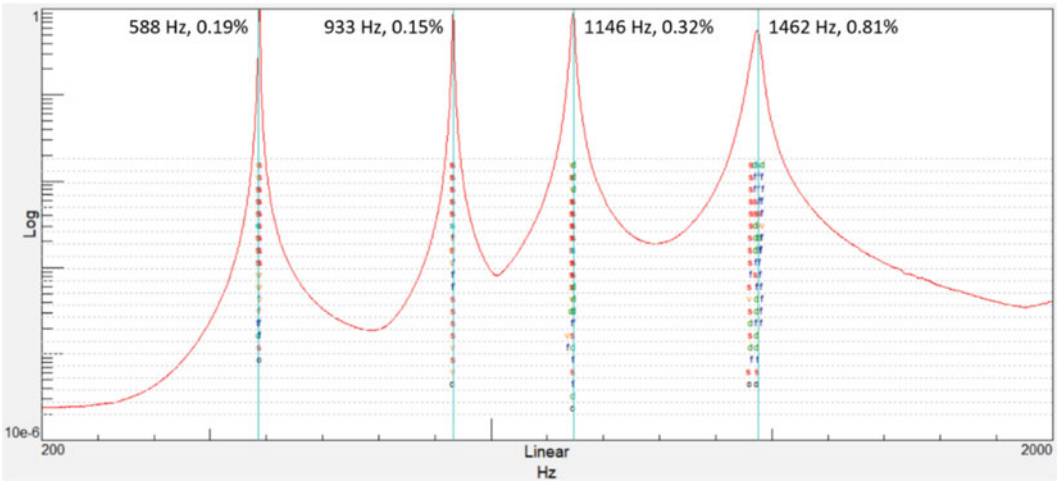

Fig. 32.6 Stabilization diagram from one of the systems tested

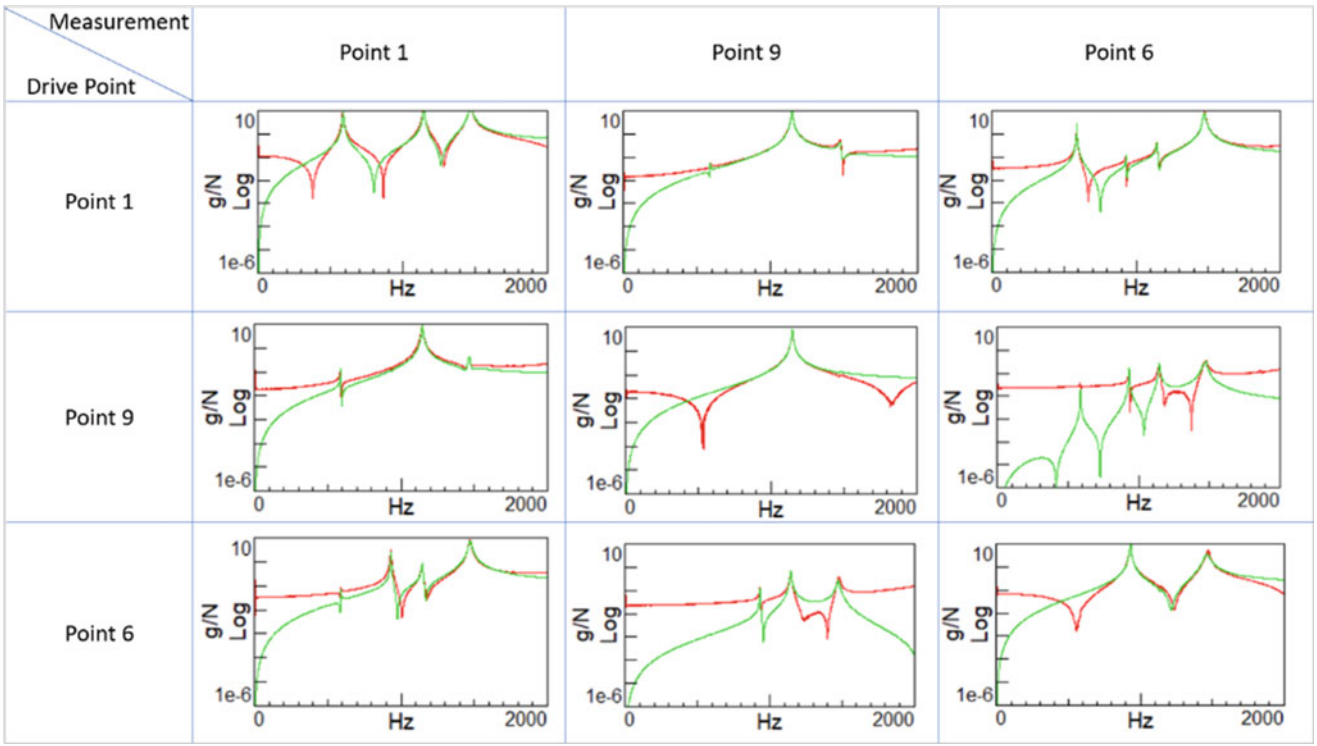

Fig. 32.7 Comparisons between the resynthesized and measured FRFs. The column and row refer to the measurement and drive points

diagram of the complex modal indicator function (MIF) from one of the roving-hammer tests. This diagram, constructed in LMS PolyMax from the frequency response functions (FRFs) using the measured force and accelerations, allows us to extract the frequency, damping, and shape of a mode. We gain assurance in our modal selection by resynthesizing the FRFs using the selected modes and comparing the resynthesized and measured FRFs as Fig. 32.7 demonstrates.

32.4 Finite Element Procedure

32.4.1 Model Setup

Figure 32.8a shows the model setup for configuration six with bolt pattern three, while Fig. 32.8b demonstrates the simplification in bolt geometry the assumption of axisymmetry.

Bolted joints have been represented in literature with four models: solid bolt, coupled bolt, spider bolt, and no-bolt [7]. These models vary in the accuracy of their representation of the bolted connection and the computational effort required; as one improves the representation accuracy, the computational cost increases. We render our system using the spider bolt model wherein the bolt is represented by beam elements and the bolt's geometry is translated to the beam elements' properties. Using tie constraints, the degrees of freedom of slave nodes (below the surface of the plate) are constrained to those of master nodes (red intersections in Fig. 32.9). We repeat these constraints on the connecting surface(s) between multiple bolted media. Figure 32.9 depicts this model with the bolted medium in blue, bolt in cyan, and tie constraints in red.

32.4.2 Mesh Convergence and Material Property Estimation

We first perform a mesh convergence study on a monolithic plate to identify the ideal number of elements and to ensure efficiency and simulation accuracy. With the ideal number of elements, the model displays eigenfrequencies with less than two percent difference when compared to the experimentally determined natural frequencies. Figure 32.10 displays the results of this study, thus leading us to use 75,000 elements in our model in future simulations.

From a determined mesh, we determine the material properties of the single bolt-less aluminum plate by fitting its eigenfrequencies and eigenmodes with its experimentally determined natural frequencies and mode shapes. Similarly, matching the finite element determined eigenfrequencies and modes of a bolted single plate with its experimental counterparts yields the bolts' material properties. The properties of both parts are shown in Table 32.3 and were kept consistent for the remainder of trials.

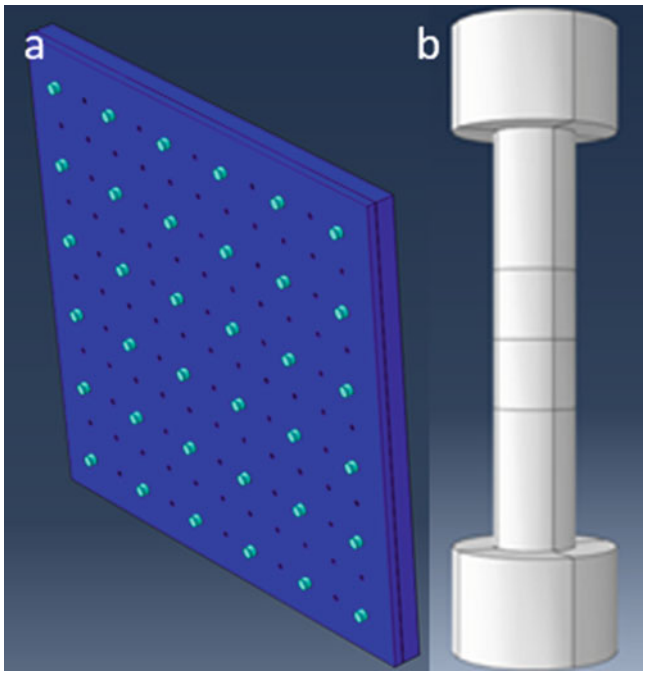

Fig. 32.8 (**a**) Finite element model of configuration six with bolt pattern three setup and (**b**) the simplified bolt model

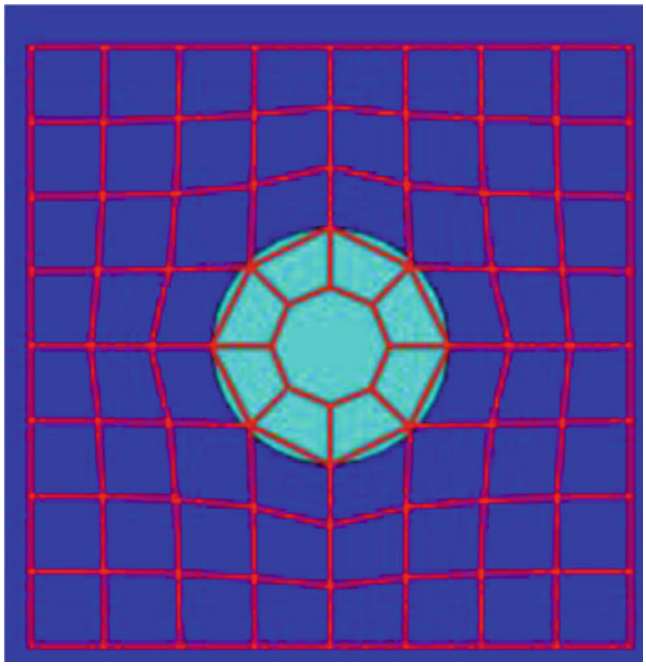

Fig. 32.9 Tie constraint elements shown in red

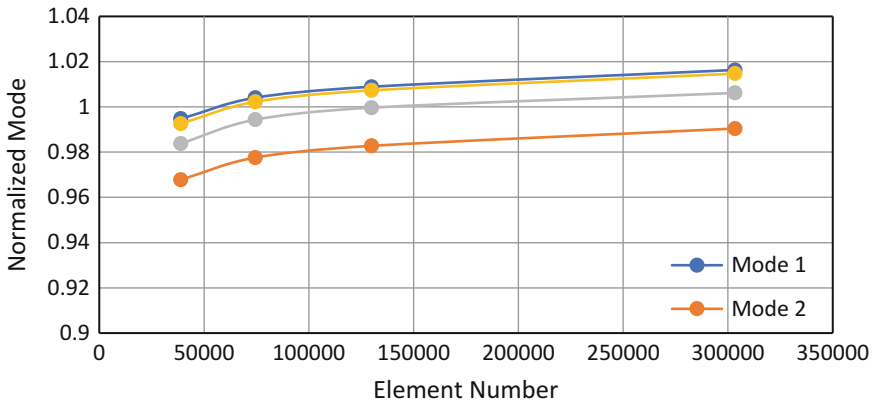

Fig. 32.10 Mesh convergence

Table 32.3 Material properties of numerical model

	Aluminum (plate)	Steel (bolts)
Elastic modulus (psi)	1.0×10^7	2.9×10^7
Density $\left(\frac{\text{lb}}{\text{in}^3}\right)$	0.093	0.28
Poisson ratio	0.33	0.29

32.4.3 Simulation Steps

Prior to solving natural frequencies, bolt preloads are applied. Preload force is determined using Eq. 32.2 relating the preload tension to preload torque (T), bolt diameter (d), and a coefficient based on the conditions of the bolt (K) [12]. For all simulations, a value of 0.2 is used for K.

$$F = \frac{T}{K_i * d} \tag{32.2}$$

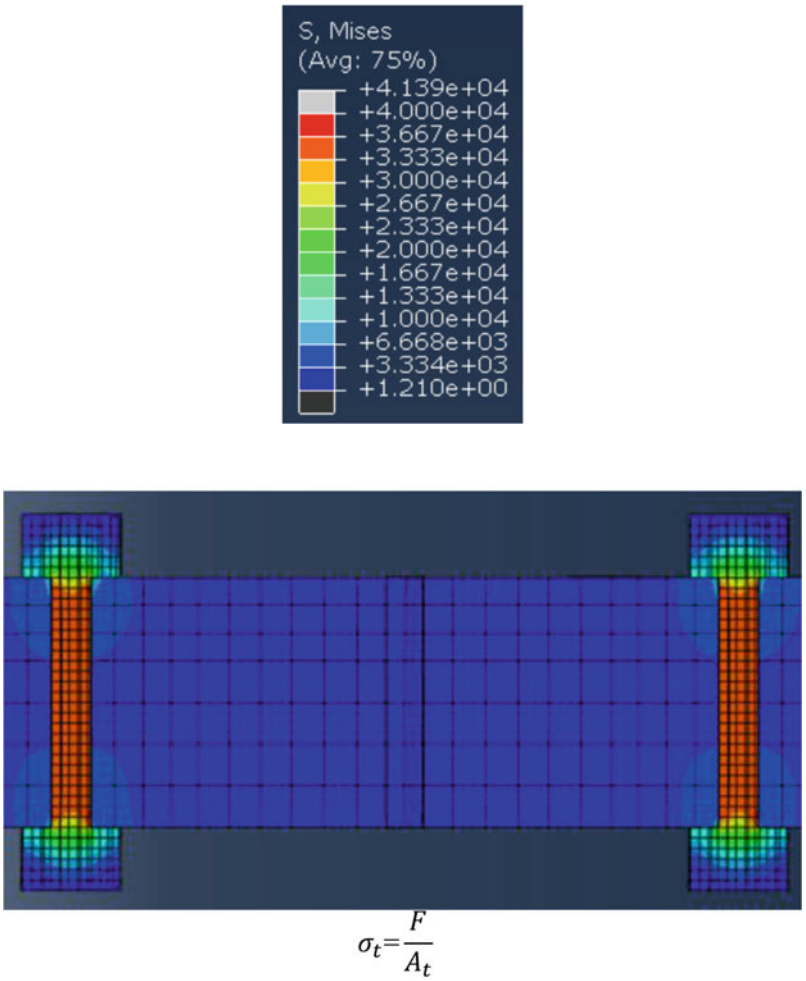

Fig. 32.11 Preload stress for configuration 6 bolt pattern 3

Preload application is verified by examining stress levels in the plate and bolt shank. Figure 32.11 shows the stress after preload in which the maximum stress level is given approximately by Eq. 32.3.

$$\sigma_{\mathrm{t}} = \frac{F}{A_{\mathrm{t}}} \tag{32.3}$$

We determine the first ten eigenfrequencies of the system to include the six rigid body modes and first four elastic modes. Inclusion of rigid body modes is necessary for accurate correlation of FRFs, as without these modes, response asymptotically approaches zero at low frequencies. We thus calculate the FRFs in a frequency range including up to the fourth elastic mode using a modal steady-state dynamics step in Abaqus. Experimentally determined modal damping values is applied for elastic modes and a two percent modal damping is applied for rigid body modes.

We adjust the tie constraint lengths to fit the experimental natural frequencies. These tie constraints are displayed in Table 32.4 for a number of systems. We note from Table 32.4 that the least number of bolts, bolt configuration 2, had the largest tie length implying that tie length is inversely correlated with number of bolts. We also see that coupling will reach an asymptotic limit as more bolts are added to the setup. Past this point, the difference in natural frequency observed will be more dependent on the increase in mass of the system from adding extra bolts, which explains the lack of change in tie length seen in the 6-3 and 6-4 columns of Table 32.4.

Table 32.4 Tie side length used for experimental setups tested

Configuration-bolt pattern	6-3	6-4	4-3	5-3	3-3	5-2	6-2
Tie length	0.38	0.38	0.40	0.8	1	1.4	1.2

Table 32.5 MAC and natural frequency agreement values

Configuration	Mode	Percent difference FE vs. Exp natural frequency (%)	MAC (%)
3	1	0.464	99.5
4	1	1.95	99.7
5	1	−0.81	98.7
6	1	1.13	99.1
3	2	−2.239	99.9
4	2	1.13	99.9
5	2	−2.08	100
6	2	−1.21	99.8
3	3	−0.564	99.4
4	3	1.08	99.7
5	3	−1.14	99.5
6	3	0.07	99.6
3	4	0.228	12.8
4	4	1.45	63.3
5	4	−1.9	84.5

32.5 Results

32.5.1 Numerical and Experimental Comparison

We first compare the experimentally determined mode shapes and natural frequencies to those derived numerically by calculating the Modal Assurance Criterion (MAC) values. Table 32.5 displays the values representing the similarity between the experimentally and numerically determined mode shapes and the percent difference between the natural frequencies from experiments and finite element.

The first three elastic modes show good agreement between experimental and numerical solutions, both in terms of natural frequency and mode shape. Outside of the bare monolithic plate, MAC values for the fourth mode are all low in comparison to the first three modes. The MAC value drops from 95.8% to 52.4% with the addition of bolts to the bare plate. We attribute this discrepancy to the degeneracy of the fourth mode, which is not present for the first three modes. Along with natural frequency and mode shape correlation, the numerical model was used to predict FRFs for three different experimental setups. Figures 32.12, 32.13, and 32.14 compare the experimental and numerical natural frequencies.

The nonlinearities owed to bolted connections explain the discrepancies in Figs. 32.12, 32.13, and 32.14 described in Section 32.2. As the model does not include contact constraints nor frictional penalties, the contact interface cannot account for the nonlinearities at the interface—microslip and separation. These phenomena are especially noticeable in regions with low coupling (i.e., fewer bolts) between plates. The low coupling explains the increased disparity in the FRFs at the top left and middle right locations at which the plates are most loosely coupled. Similarly, the FRFs at the middle accelerometer consistently agree more than the other two locations as this location is less affected by nonlinearities. As the number of bolts increases, the plates become more coupled, thus improving accuracy between numerical and experimental results from the reduction of nonlinearities and frictional effects.

Preload was not seen to have much of an effect on natural frequencies and mode shapes with this model setup. This is due to the coupling caused by the tie constraints overpowering the effect of preload. During analysis, the preload step was the most computationally expensive. Thus, one advantage of this model is the ability to increase computational efficiency without affecting the final result.

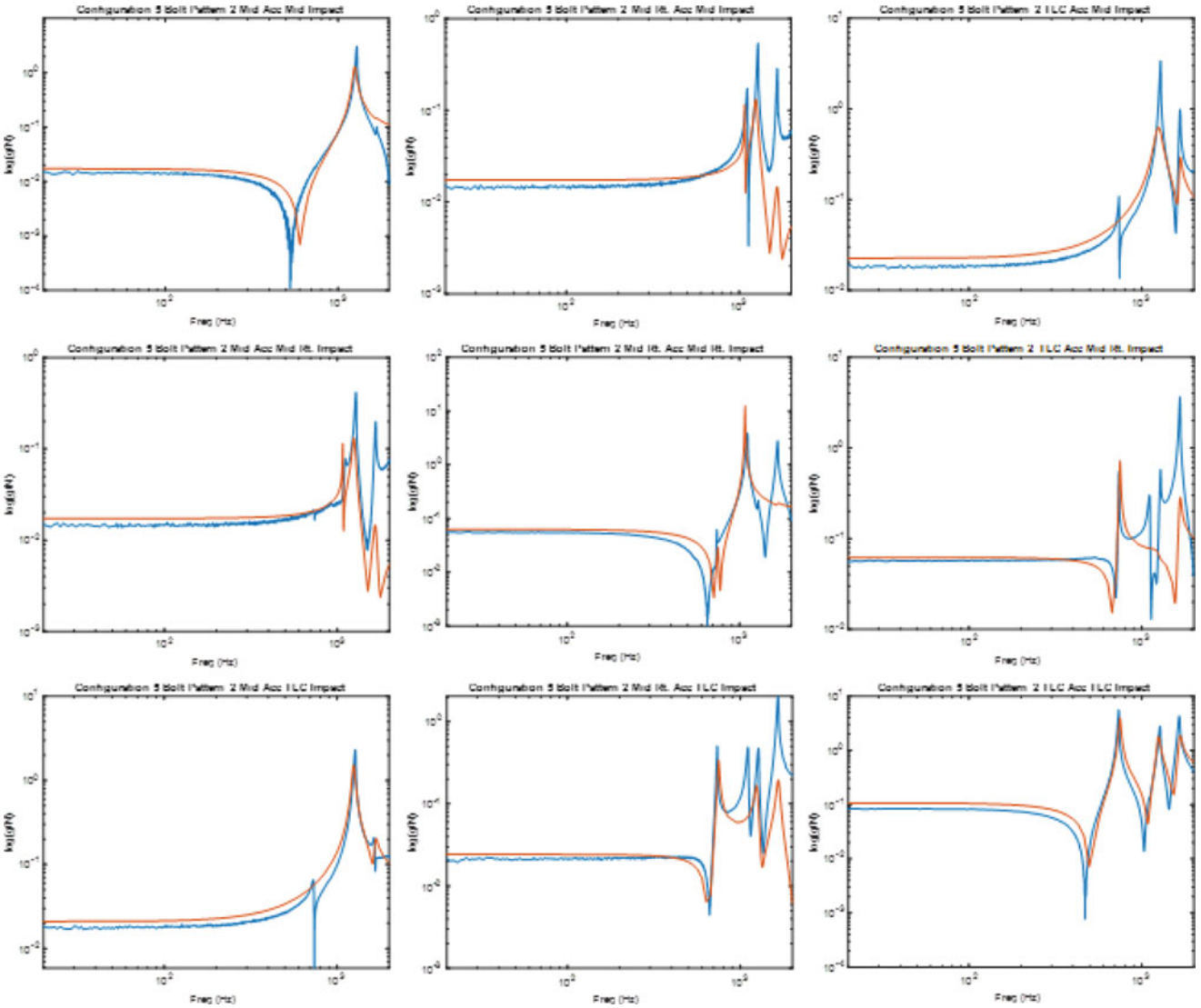

Fig. 32.12 Numerical versus experimental frequency response functions for configuration five bolt pattern two

32.5.2 Experimental Analysis

We conduct our experimental analysis by first determining the factors influential to our responses. Then, we display the data graphically based on the critical factors. We finish our analysis with a regression using Minitab.

We determine the importance of each factor in predicting each of the eight measured responses with a full factorial design in Minitab. Figures 32.15 and 32.16 display the contribution of each of the factors as well as the 2- and 3-factor interactions in predicting the modes' frequency and damping. Figure 32.15 details that only bolt spacing, total thickness, and the number of interfaces significantly affect the natural frequencies, while Fig. 32.16 shows that all factors except thickness significantly influence the modal damping. Both figures indicate that the bolt spacing is the most important factor in both natural frequency and modal damping models. The thickness's lack of influence on the modal damping indicates that material damping is negligible and reinforces the assumption that the bolted connection provides most—if not all—the damping present in these systems. The bolt preload's negligible effect on natural frequency disagrees with past findings that the natural frequency should asymptotically increase with preload. This discrepancy can be explained if the two preloads tested herein translated to frequencies already close to the asymptote to which the natural frequency would converge with large amounts of preload. The impact amplitude's lack of contribution suggests the natural frequency is linear in this impact range for these systems. The figures also demonstrate the significance of factor interactions for both natural frequency and modal damping. It is to be noted that the modal damping factor interactions are much greater than those for natural frequency.

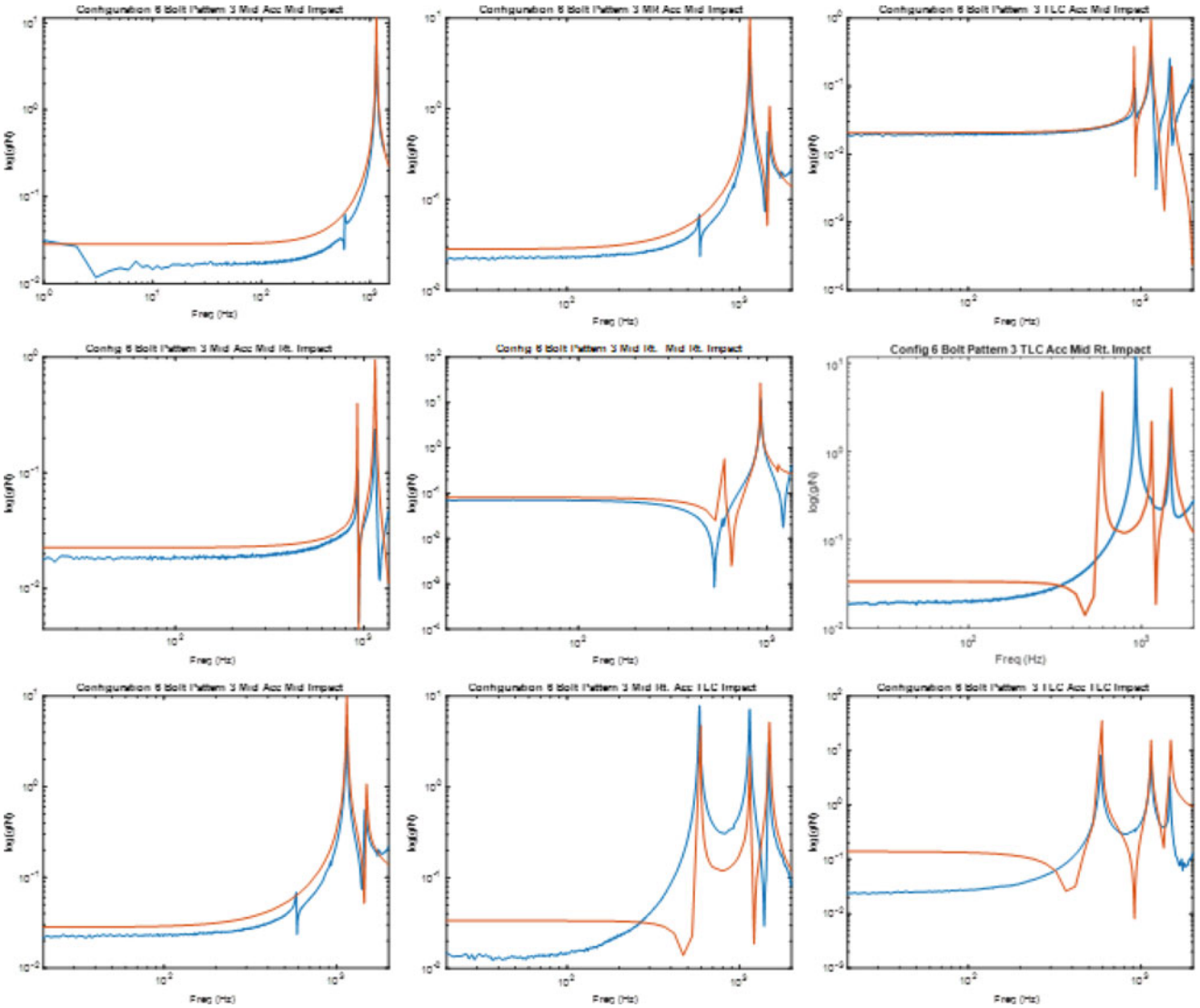

Fig. 32.13 Numerical versus experimental frequency response functions for configuration six bolt pattern three

Now that we understand what factors influence which responses, we organize the responses as they vary with the influential factors identified in Figs. 32.15 and 32.16. Figure 32.17 visualizes the four modal frequencies over changes in thickness, bolt spacing, and number of interfaces. We observe from Fig. 32.17 a direct relationship between bolt spacing and modal frequency and an inverse relationship between the number of interfaces and modal frequency. Preload does not have much of an effect on the frequencies, but in Fig. 32.18, increasing the bolt preload decreases the damping of each mode.

We also use Minitab to quantify the relationships between the factors and the response metrics in a linear regression. Figure 32.19 demonstrates the linear relationship between the thickness and frequency of each mode, further validating the prediction given in Eq. 32.1. We note that the quantitative relationship given in Eq. 32.1 does not match the data in Fig. 32.19, which we attribute to the mass loading provided by the bolts.

32.6 Conclusions

This chapter studies the effects of the bolt spacing, bolt preload, number of interfaces, total thickness, and impacting amplitude on the modal response of multilayered bolted plates through a full factorial experimental design matched with a finite element validation. Focusing on the damping and frequency of the first four modes, we determine that the bolt

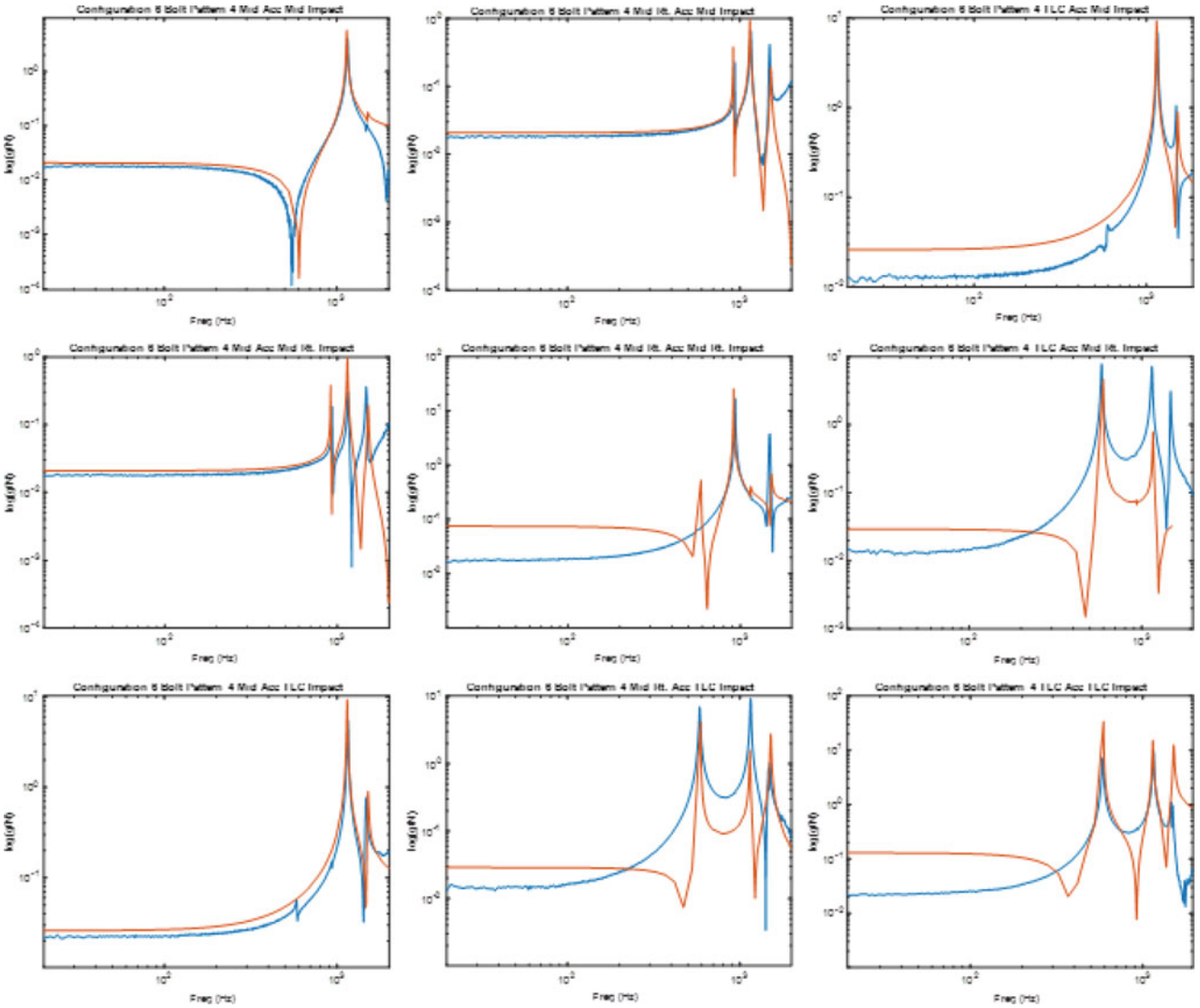

Fig. 32.14 Numerical versus experimental frequency response functions for configuration six bolt pattern four

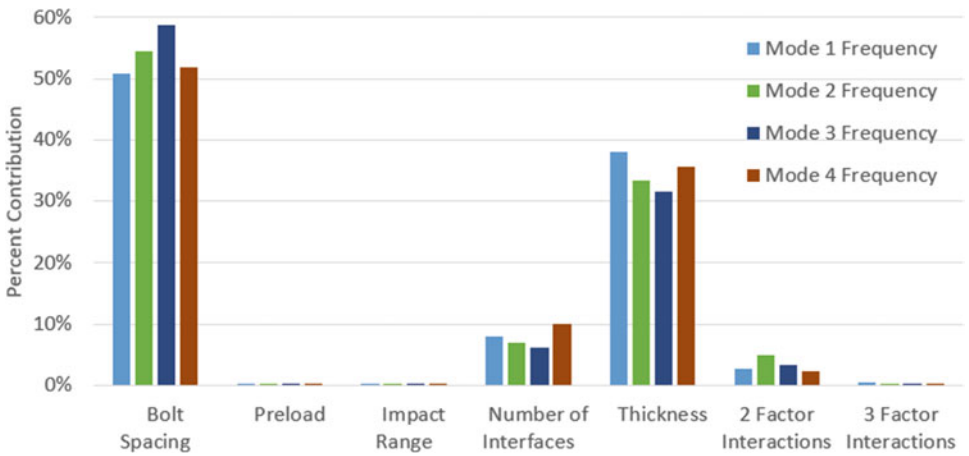

Fig. 32.15 Factor contributions to modal natural frequencies

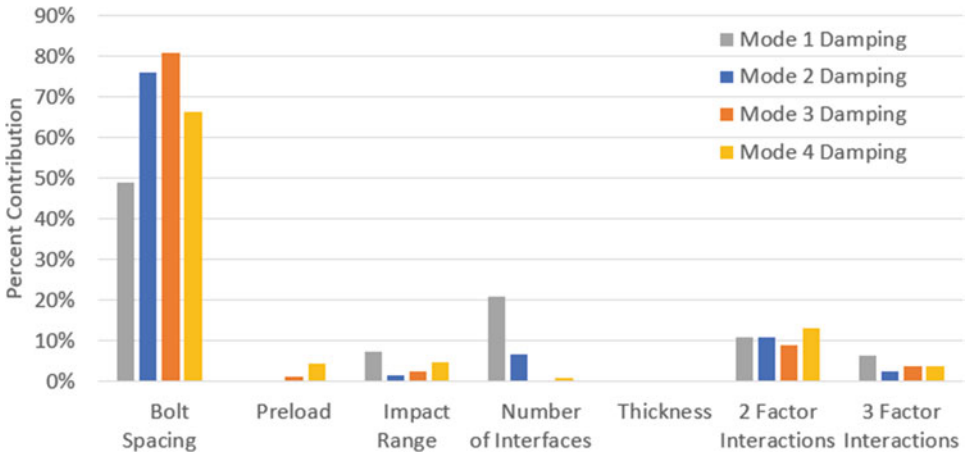

Fig. 32.16 Factor contributions to modal damping

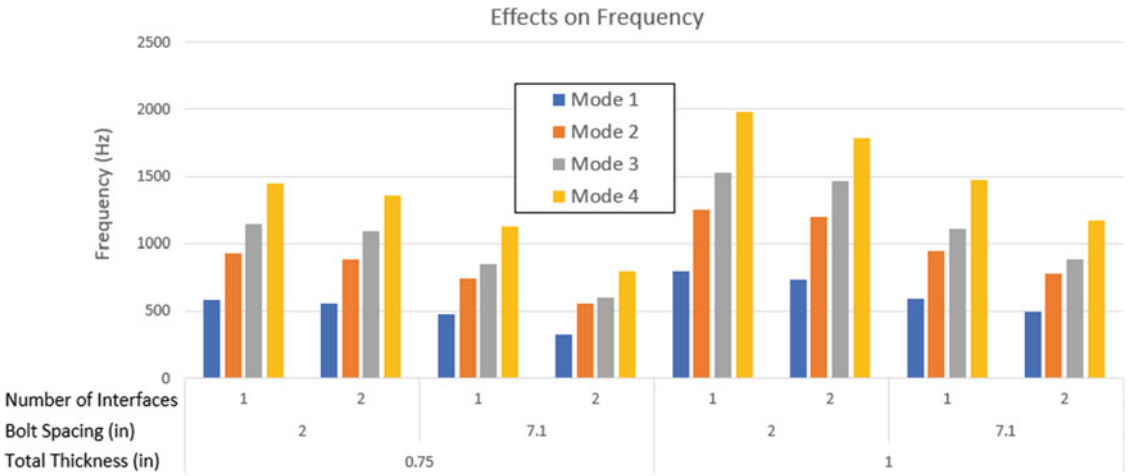

Fig. 32.17 Pivot chart showing general trend of the factor effects on frequency

spacing and thus number of bolts is the most significant parameter leading to the conclusion that the number of inter-plate coupling components dominates the modal response. The findings herein are not only a starting point on which design and analysis of bolt connections may rely but also a basis from which further parametric studies may extend.

This chapter also examines the modeling of bolted joints with tie constraints of varying length. This methodology matches experimental natural frequencies and mode shapes well by modifying the length of tie constraints (thus changing the effective stiffness). This result reduces the need for the preload step, significantly cutting down computational time thus highlighting the greatest advantage of this methodology—reduction of computational cost and contact interactions.

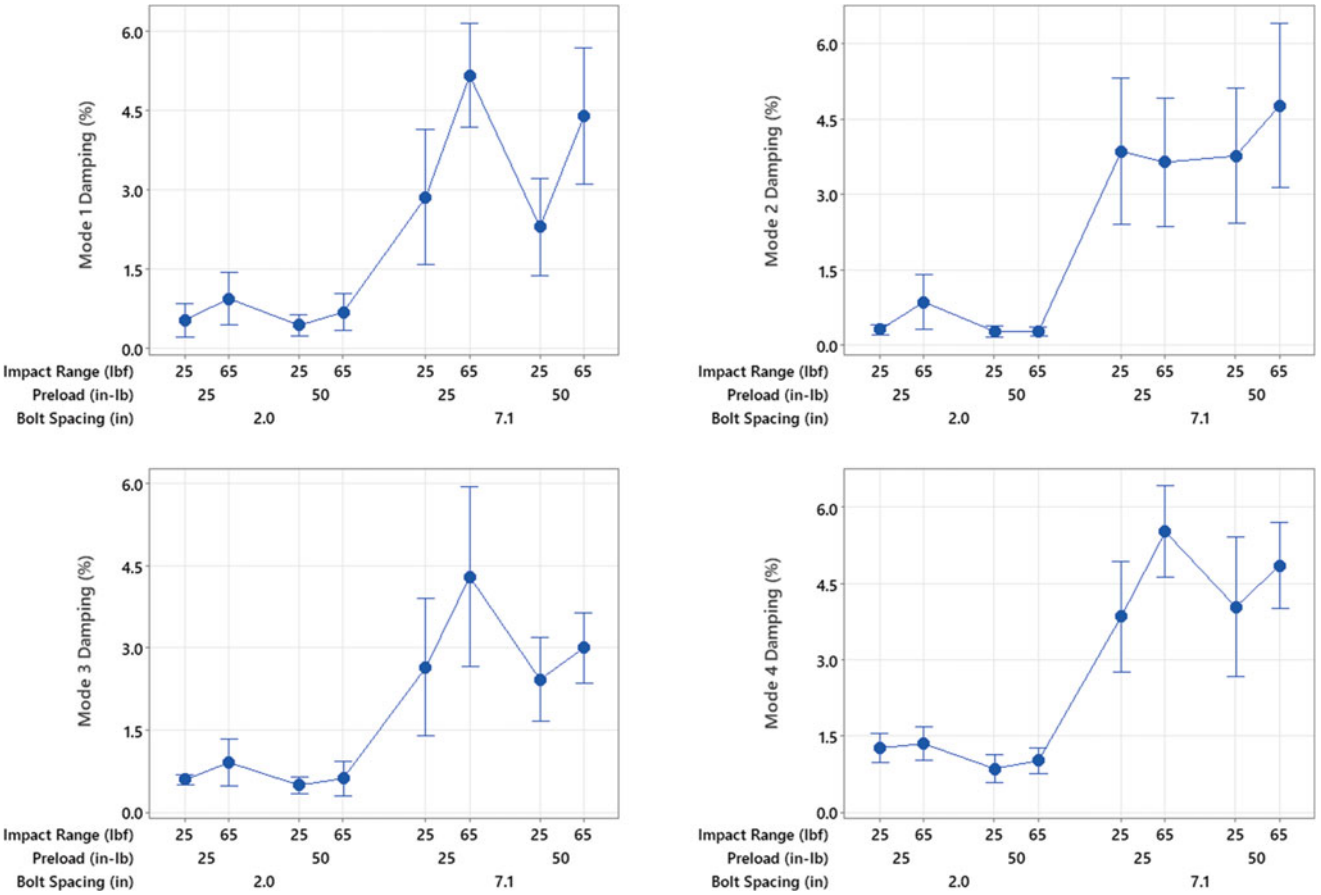

Fig. 32.18 Chart showing general trend of the factor effects on modal damping

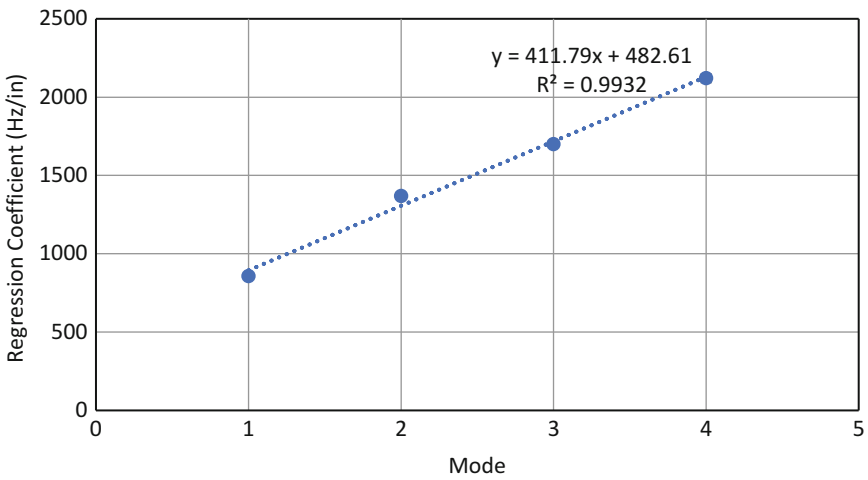

Fig. 32.19 Relationship between the total thickness and modal frequency

References

1. Zaman, I., Khalid, A., Manshoor, B., Araby, S., Ghazali, M.I.: The effects of bolted joints on dynamic response of structures. IOP Conf. Ser. Mater. Sci. Eng. **50**, 012018 (2013)
2. Saito, A., Suzuki, H.: Dynamic characteristics of plastic plates with bolted joints. ASME. J. Vib. Acoust. **142**(1), 011002 (2019) https://doi.org/10.1115/1.4044865
3. Ungar, E.E.: Energy dissipation at structural joints; mechanisms and magnitudes, Technical Documentary Report No. FDL-TDR-64-98, Air Force Flight Dynamics Laboratory, Wright-Patterson Air Force Base, Ohio, 1964
4. Brøns, M., Thomsen, J.J., Sah, S.M., Tcherniak, D., Fidlin, A.: Estimating bolt tension from vibrations: transient features, nonlinearity, and signal processing. Mech. Syst. Signal Process. **150**, 107224., ISSN 0888-3270 (2021). https://doi.org/10.1016/j.ymssp.2020.107224
5. Yorgun, C., et al.: Finite element modeling of bolted steel connections designed by double channel. Comput. Struct. **82**(29–30), 2563–2571 (2004). https://doi.org/10.1016/j.compstruc.2004.04.003
6. Liao, X., et al.: Analytical model of bolted joint structure and its nonlinear dynamic characteristics in transient excitation. Shock. Vib. **2016**, 1–11 (2016). https://doi.org/10.1155/2016/8387497
7. Kim, J., et al.: Finite element analysis and modeling of structure with bolted joints. Appl. Math. Model. **31**(5), 895–911 (2007). https://doi.org/10.1016/j.apm.2006.03.020
8. Chen, W., Deng, X.: Structural damping caused by micro-slip along frictional interfaces. Int. J. Mech. Sci. **47**(8), 1191–1211., ISSN 0020-7403 (2005). https://doi.org/10.1016/j.ijmecsci.2005.04.005
9. Segalman, D.J.: An Initial Overview of Iwan Modeling for Mechanical Joints. Sandia National Lab.(SNL-NM), Albuquerque (2001. Web.). https://doi.org/10.2172/780307
10. Blevins, R.D.: Formulas for Natural Frequency and Mode Shape. Van Nostrand Reinhold Co, New York (1979)
11. Peeters, B., Van der Auweraer, H., Guillaume, P., Leuridan, J.: The PolyMAX Frequency-Domain method: a new standard for modal parameter estimation? Shock. Vib. **11**, Article ID 523692. 15 pages (2004). https://doi.org/10.1155/2004/523692
12. Budynas, R.G., et al.: Shigley's Mechanical Engineering Design. McGraw-Hill Education (2021)

Chapter 33
State-Space Modeling of Nonlinear Electrostatic Transducers and Experimental Characterization Using LDV

Yuqi Meng, Xiaoyu Niu, Randall P. Williams, Ehsan Vatankhah, Zihuan Liu, and Neal A. Hall

Abstract Electrostatic speakers and ultrasound transmitters, including capacitive micromachined ultrasound transducers (CMUTs), may be thought of as systems with applied voltage as the input variable and diaphragm displacement and sound pressure as the output variables. These electrostatically actuated systems are inherently nonlinear. Electrostatic pressure is proportional to the square of the applied voltage and is inversely proportional to the cube of the time-varying diaphragm-backplate gap spacing. The squeeze film damping coefficient is also dependent on the time-varying gap spacing. For large diaphragm displacement, strain stiffening of the diaphragm can also affect the transducer dynamics. These nonlinear systems are most commonly driven in a linear regime, whereby the moving diaphragm is biased to an operating point with a large static voltage and a relatively small dynamic signal voltage is superimposed to provide actuation of the diaphragm. In recent work, we have demonstrated advantages of exploiting the full operating range of electrostatic transducers, not restricted to a linear operating regime. Our recent focus has been on using commonly available MEMS microphone structures as airborne ultrasonic projectors at frequencies of up to 100 kHz. Although designed as receivers to work in the audible range, these commercial devices are effective as ultrasound transmitters. A large dynamic input voltage is applied to force the diaphragm to traverse the full diaphragm-backplate gap, typically 2 μm. Electrostatic pull-in,whereby the diaphragm contacts the backplate,can be exploited as a braking feature to instantaneously eliminate diaphragm ring-down and increase the bandwidth of generated waveforms. Having an accurate model for these nonlinear devices is advantageous. A state-space model based on a segmented diaphragm approach has recently been summarized in prior work. The model is suitable for time-domain simulations of the movement of the diaphragm in response to input drive signals and addresses the nonlinear system aspects listed above. In this work, diaphragm waveforms in response to various input signals are measured using a laser doppler vibrometer (LDV) and compared against simulation results to verify the model's accuracy.

Keywords Nonlinear · CMUT · Ultrasound · Pull-in

33.1 Introduction

Capacitive micromachined ultrasound transducers (CMUTs) and piezoelectric micromachined ultrasound transducers (PMUTs) have the ability to address many air-coupled ultrasound applications. These include gesture recognition [1], sensing, imaging [2], range finding [3], and haptics [4]. Achievable transmit pressure is a key figure of merit for many applications. Achieving high transmit pressure requires large diaphragm displacement. Electrostatic actuation is approximately linear only over a small displacement range, and therefore linearly operated electrostatic actuators in air are limited in their achievable diaphragm displacement and SPL. Many innovative sensing and transmit schemes have been explored for immersion CMUTs including collapse mode [5–7], deep collapse mode, collapse-snapback mode [8], and several others [9–11]. These schemes target improvements in either receive sensitivity or transmit pressure. Applications of

Yuqi Meng and Xiaoyu Niu contributed equally to this work.

Y. Meng (✉) · X. Niu · E. Vatankhah · Z. Liu · N. A. Hall
Chandra Department of Electrical and Computer Engineering, The University of Texas at Austin, Austin, TX, USA
e-mail: yuqimeng@utexas.edu; xyniu@utexas.edu; e.vatankhah@utexas.edu; zihuanliu@utexas.edu; nahall@mail.utexas.edu

R. P. Williams
Applied Physics Laboratory, University of Washington, Seattle, WA, USA

M. R. W. Brake et al. (eds.), *Nonlinear Structures & Systems, Volume 1*, Conference Proceedings
of the Society for Experimental Mechanics Series, https://doi.org/10.1007/978-3-031-36999-5_33

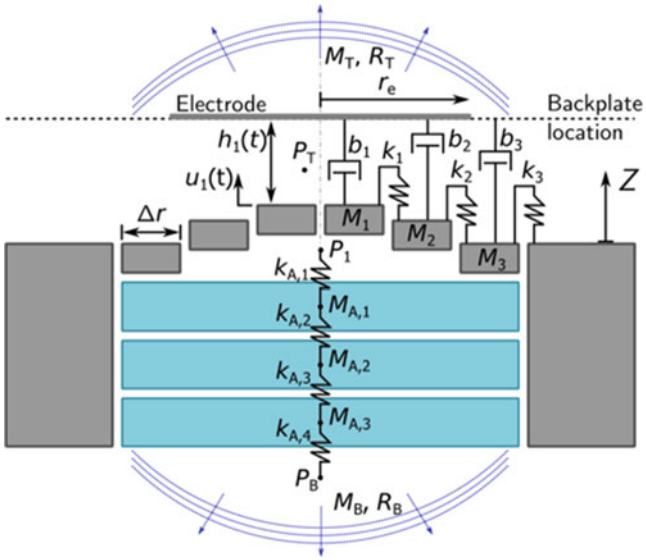

Fig. 33.1 Schematic illustration of segmented model domain (from [16])

such techniques are less explored for air-coupled devices, with a few notable exceptions [12–14]. We recently demonstrated the generation of ultrasound in air using a commercial MEMS microphone structure [15]. The MEMS transducer was driven with high-amplitude tone-burst waveforms, with peak amplitudes exceeding the static pull-in voltage of the device. In the work summarized herein, we present additional measurements on this MEMS transducer using tone-burst waveforms of varying frequencies. Our goal is to showcase the variety of large-displacement waveforms achievable with this large signal drive technique, and also to evaluate the accuracy of a computational model that predicts the dynamics of these transducers in response to large drive signals. The model was summarized in detail in [16] and uses a segmented diaphragm approach as summarized in Fig. 33.1, borrowed from reference [16]. State variables are defined as the instantaneous velocity of each diaphragm ring and the displacement of each ring relative to neighboring rings. A region of air beneath the diaphragm is also segmented and introduces additional state variables. These are the instantaneous velocity of each air segment and the instantaneous rarefaction of each air parcel. The input to the system is the instantaneous electric potential applied to all rings in parallel. In the state-space formulation, the time rate of change of each state variable is a function of the instantaneous state variables and the input to the system. This relation can be generally written as

$$\dot{\vec{X}} = \dot{\vec{X}}(\vec{X}, \vec{U}(t)) \tag{33.1}$$

where $\vec{X}$ is a vector housing the state variables and $\vec{U}(t)$ is a vector housing the inputs to the system at time t. No assumptions of linearity are required in the formulation. The first-order rate equations are ideal for numerical simulations that march forward in time to yield $\vec{X}(t)$. The state variables can then be post-processed if necessary to yield the desired outputs of the system. In the case of the MEMS transducer, we are interested in the distributed displacement of the diaphragm as a function of time in response to large dynamic electrical signals. The state equations can be determined by inspection for simple systems, and with the aid of systematic formulation tools such as bond graphs for highly interconnected systems. In our case, a bond graph formulation facilitated the formulation. Reference [16] summarizes the individual state equations that form Eq. (33.1). The formulation takes into account the nonlinear relationship between electrostatic pressure and voltage, the nonlinear relationship between electrostatic pressure and instantaneous ring-electrode spacing defined as $h_i(t)$ in Fig. 33.1, and the dependence of damping coefficient on gap spacing $b(h_i)$.

33.2 Analysis

The device under evaluation is a MEMS microphone with a diaphragm diameter of approximately 1 mm, 400 nm thickness, and comprised of tensioned silicon nitride with approximately 48.8 MPa residual stress. A 60 nm thick layer of aluminum on the diaphragm serves as the electrode. The device has a packaged fundamental resonance frequency equal to 45 kHz. A schematic of the transducer cross section is provided in Fig. 33.2, borrowed from reference [15]. Given the thin profile of

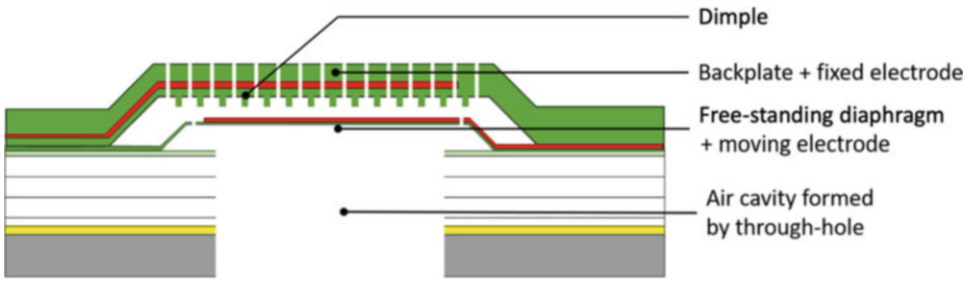

Fig. 33.2 A cross-sectional schematic of the electrostatic MEMS transducer [15]

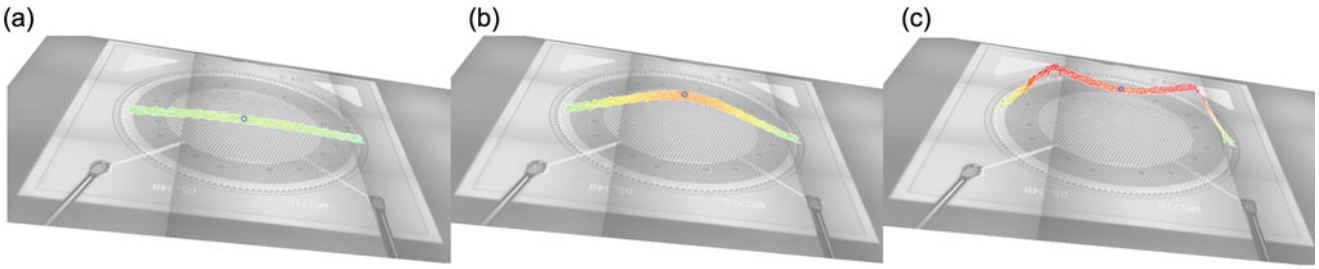

Fig. 33.3 Diaphragm deflection profiles measured using the scanning LDV at zero volts, at an intermediate voltage less than the collapse voltage, and at a voltage greater than the pull-in voltage

the diaphragm and the relatively high residual tensile stress, the diaphragm is stress-dominated rather than bending-stiffness dominated, such that the diaphragm behaves as a membrane rather than a plate. In an initial measurement, the diaphragm is actuated with a low-frequency triangle waveform that ramps from 0 V to 20 V and back down. The result of this experiment is presented in Fig. 33.3 which is a segmented scan of the transducer's diaphragm displacement obtained at different voltages. The images are captured using a Polytec MSA-050 scanning laser doppler vibrometer (LDV) system. Image (a) shows the diaphragm status at 0 volts. Image (b) shows the diaphragm at an intermediate voltage, less than the pull-in voltage, and Image (c) presents the diaphragm profile after pull-in. In this pull-in state, approximately 70 percent of the diaphragm is in contact with the backplate and the diaphragm has a flat profile across the central region. Pull-in for this transducer occurs at 18 V and subsequent snapback at 13 V [15].

Next, the transducer is driven with a 4-cycle square wave burst with the signal value ranging from 0 V to +20 V and with frequency equal to 4 kHz, 36 kHz, and 96.8 kHz. Figure 33.4a, b, and c presents the drive signal and the measured and simulated center-point diaphragm displacement. The high-frequency oscillations in the square wave excitation signal are experimental artifacts and are not significant. Interesting and noteworthy features are as follows. In Fig. 33.4a, for each excitation cycle the diaphragm traverses the full 1.8 μm diaphragm-backplate gap, pulls in, and subsequently rings down when released. In Fig. 33.4b the period of the excitation is shorter, and the diaphragm's ring-down is interrupted by each subsequent pull-in cycle. In Fig. 33.4c the half-period of the excitation is shorter than the transient pull-in time of the diaphragm, and the diaphragm therefore never pulls into contact with the backplate. The model predicts this phenomenon accurately. Furthermore, it is interesting to note that the diaphragm displacement is slightly different in each excitation cycle, showing some degree of ramp-up. This subtlety is also accurately predicted by the model.

Figures 33.4d, e, and f presents the diaphragm displacement in response to excitation signals that are the complement of the those in (a), (b), and (c). The actuation voltage begins and ends at 20 V and is held at 20 V in between burst cycles. Comparing image (a) against (d) and (b) against (e), the only significant difference is that the ring down of the diaphragm at the end of the burst is prevented in the complementary drive case, as the diaphragm is pulled-in against the backplate to prevent ring-down. Comparing (c) against (f), however, the results are quite different. The peak-to-peak displacement in response to the waveform in (c) is approximately 1 μm while that of complementary tone burst is approximately 2 μm. In the complementary case, the diaphragm begins the cycle in a pulled-in state with stored elastic potential energy, and this energy results in larger amplitude oscillations when the diaphragm is released from pull-in. Here again, the model does an exceptional job at predicting these important characteristics.

A second commercial MEMS microphone structure was also used as an actuator. This microphone is a Knowles model SPM0687LR5H-1. Figure 33.5 presents a scanning electron micrograph (SEM) of the chip which comprises two diaphragms electrically connected in parallel. The transducer was driven as an ultrasound transmitter near 70 kHz using a unipolar

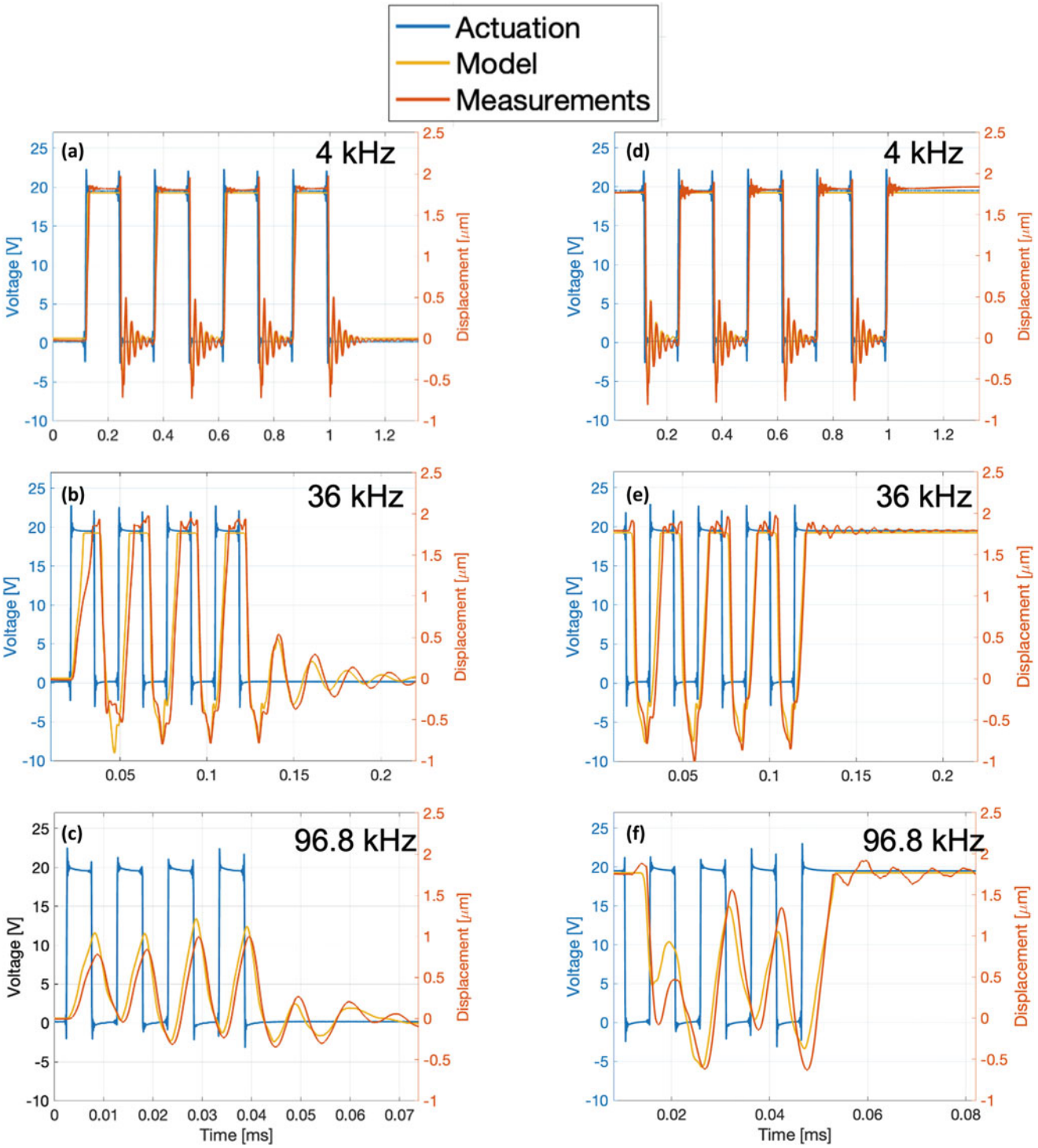

Fig. 33.4 Comparison of simulated and measured center-point diaphragm displacement at (**a**, **d**) 4 kHz, (**b**, **e**) 36 kHz, and (**c**, **f**) 96.8 kHz

4-cycle tone-burst signal with a peak-to-peak voltage of 70 volts. The frequency of 70 kHz chosen for this demonstration corresponds to the fundamental resonance frequency of the diaphragm. The actuator signal and the resulting center-point diaphragm displacement of the MEMS diaphragm are presented in Fig. 33.6b. The diaphragm ramps up to a steady-state peak-to-peak displacement of 6.2 μm. Referring to the rightmost axis in Fig. 33.6b, the positive displacement cycle (i.e., upward displacement) is approximately 2.7 μm, at which point the diaphragm makes physical contact with the backplate. The negative (i.e., downward) displacement reaches a value greater than 3.0 μm as the momentum of the diaphragm carries

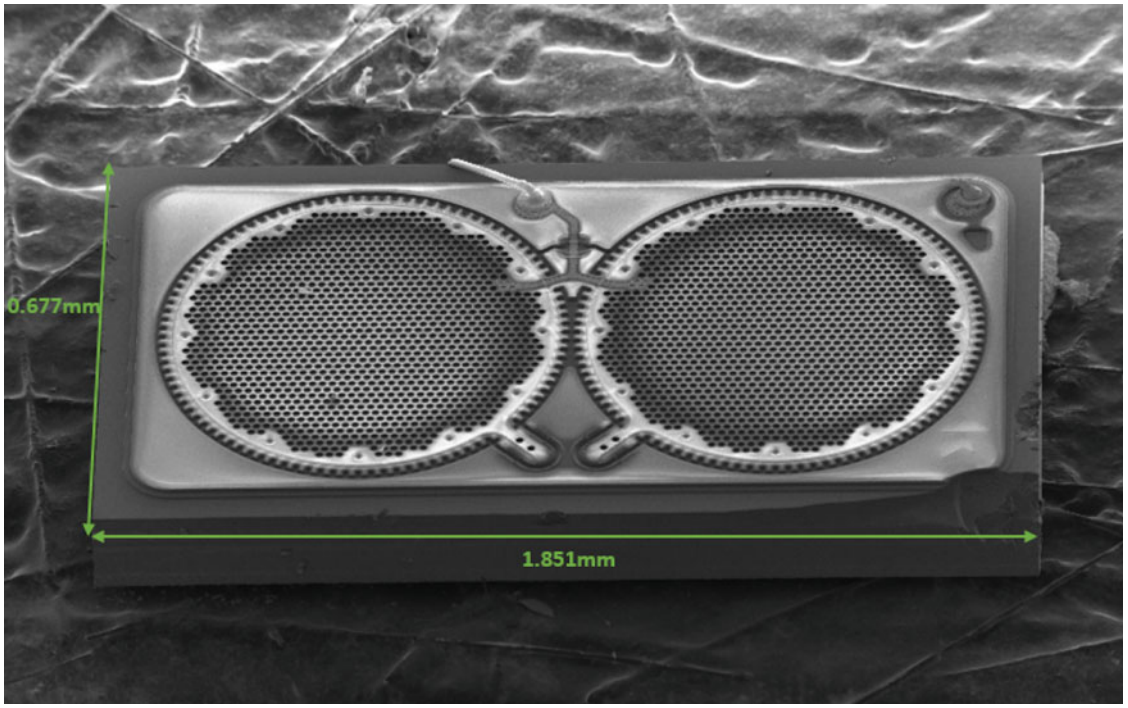

Fig. 33.5 Scanning electron micrograph of a MEMS microphone die from a Knowles microphone model SPM0687LR5H-1

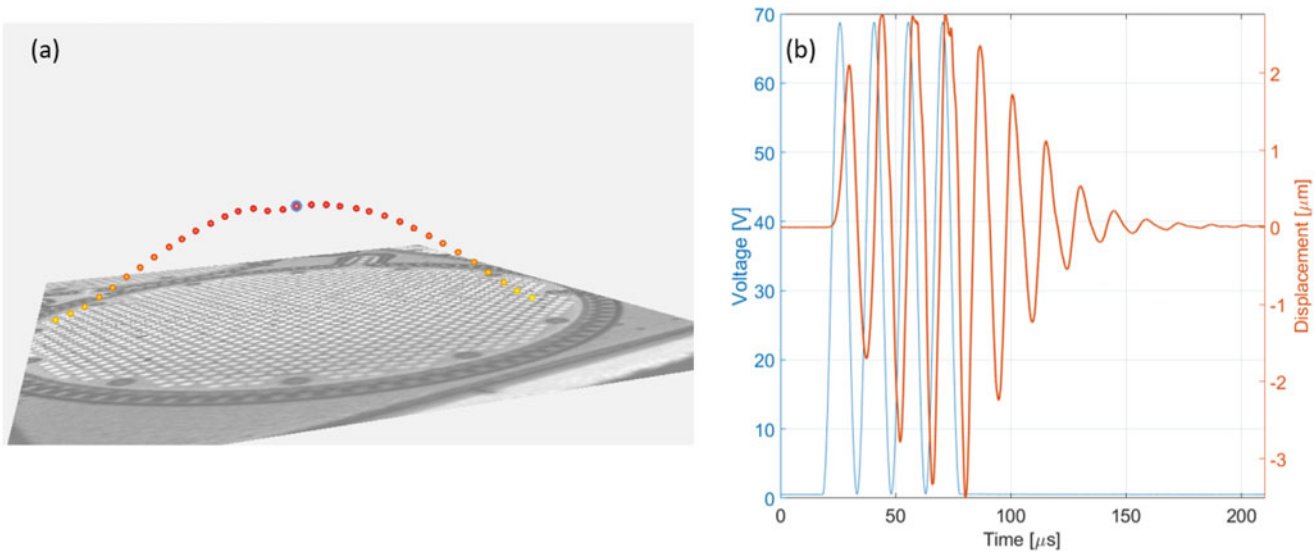

Fig. 33.6 (**a**) Profile of the Knowles diaphragm at pull-in and (**b**) Measured center-point diaphragm displacement

it past its equilibrium or rest position. Figure 33.6a shows a line scan of the diaphragm displacement at an instant in time corresponding to peak positive displacement, where the diaphragm is in contact with the backplate at its center.

To provide context and to emphasize the technological significance of the displacement amplitude achieved by both actuators studied in this work, the so-called surface pressure of the actuator can be computed as $p = Z_o \times v$ where Z_o is the acoustic impedance of air and v is the diaphragm velocity. The surface pressure is the acoustic pressure that would be realized at the surface of a transducer if the transducer were vibrating with uniform velocity v and generating planar waves. A 1 μm displacement amplitude at 100 kHz, as achieved by the first device demonstrated, corresponds to a surface pressure equal to 261 Pa, or a sound pressure level (SPL) equal to approximately 140 dB. These levels are significantly loud, and transducers capable of generating such levels may be considered for interesting ultrasonic applications in air such as acoustic micro-tapping and parametric arrays [17, 18].

33.3 Conclusions and Future Work

When used as actuators, MEMS microphones have been shown to be effective at generating peak-to-peak diaphragm displacements greater than 2 μm across a range of frequencies. The state-space model, which addresses several nonlinear system aspects, predicts the large-signal dynamics of MEMS microphones accurately. Given the proven capabilities of the model, we now wish to apply the model to design dense arrays of CMUT transducers for the generation of high-amplitude ultrasound in air (e.g., SPL $>$ 140 dB). Before doing so, we will add bending stiffness to the model equations. The first generation of the model, as is used for the simulations presented herein, is limited to stress-dominated membranes. Many transducers are bending-dominated and we wish to explore this design space as well.

References

1. Horsley, D.A., Przybyla, R.J., Kline, M.H., Shelton, S.E., Guedes, A., Izyumin, O., Boser, B.E.: Piezoelectric micromachined ultrasonic transducers in consumer electronics: the next little thing? In: Proceedings of the 29th IEEE International Conference on Micro Electro Mechanical Systems (MEMS), pp. 145–148. IEEE, Piscataway (2016)
2. Zhang, H., Liang, D., Wang, Z., Ye, L., Rui, X., Zhang, X.: Fabrication and characterization of a wideband low-frequency CMUT array for air-coupled imaging. IEEE Sensors J. **20**(23), 14090–14100 (2020)
3. Przybyla, R.J., Shelton, S.E., Guedes, A., Krigel, R., Horsley, D.A., Boser, B.E.: In-air ultrasonic rangefinding and angle estimation using an array of ALN micromachined transducers. (2012)
4. Halbach, A., Gijsenbergh, P., Jeong, Y., Devriese, W., Gao, H., Billen, M., Torri, G.B., Chare, C., Cheyns, D., Rottenberg, X. et al.: Display compatible PMUT array for mid-air haptic feedback. In: Proceedings of the 20th International Conference on Solid-State Sensors, Actuators and Microsystems & Eurosensors XXXIII (TRANSDUCERS 2019 & EUROSENSORS XXXIII), pp. 158–161. IEEE, Piscataway (2019)
5. Apte, N., Park, K.K., Nikoozadeh, A., Khuri-Yakub, B.T.L Bandwidth and sensitivity optimization in CMUTs for airborne applications. In: Proceedings of the 2014 IEEE International Ultrasonics Symposium, pp. 166–169. IEEE, Piscataway (2014)
6. Park, K.K., Oralkan, O., Khuri-Yakub, B.T.: Comparison of conventional and collapse-mode CMUT in 1-D array configuration. In: Proceedings of the 2011 IEEE International Ultrasonics Symposium, pp. 1000–1003. IEEE, Piscataway (2011)
7. Olcum, S., Yamaner, F.Y., Bozkurt, A., Köymen, H., Atalar, A.: CMUT array element in deep-collapse mode. In: Proceedings of the 2011 IEEE International Ultrasonics Symposium, pp. 108–111. IEEE, Piscataway (2011)
8. Olcum, S., Yamaner, F.Y., Bozkurt, A., Atalar, A.: Deep-collapse operation of capacitive micromachined ultrasonic transducers. IEEE Trans. Ultrason. Ferroelectr. Freq. Control **58**(11), 2475–2483 (2011)
9. Bayram, B., Oralkan, O., Ergun, A.S., Haeggstrom, E., Yaralioglu, G.G., Khuri-Yakub, B.T.: Capacitive micromachined ultrasonic transducer design for high power transmission. IEEE Trans. Ultrason. Ferroelectr. Freq. Control **52**(2), 326–339 (2005)
10. Satir, S., Zahorian, J., Degertekin, F.L.: Transmit optimization of CMUTs in non-collapse mode using a transient array model. In: Proceedings of the 2012 IEEE International Ultrasonics Symposium, pp. 85–88. IEEE, Piscataway (2012)
11. Satir, S., Xu, T., Degertekin, F.L.: Model based drive signal optimization of CMUTs in non-collapse operation and its experimental validation. In: Proceedings of the 2013 IEEE International Ultrasonics Symposium, pp. 295–298. IEEE, Piscataway (2013)
12. Enhos, K., Tasdelen, A.S., Yilmaz, M., Atalar, A., Koymen, H.: Transmitting CMUT arrays without a DC bias. In: Proceedings of the 2019 IEEE International Ultrasonics Symposium, pp. 750–753. IEEE, Piscataway (2019)
13. Khan, T.M., Tasdelen, A.S., Yilmaz, M., Atalar, A., Koymen, H.: Beam steering in a half-frequency driven airborne CMUT transmitter array. In: Proceedings of the 2019 IEEE International Ultrasonics Symposium, pp. 762–765. IEEE, Piscataway (2019)
14. Khan, T.M., Tasdelen, A.S., Yilmaz, M., Atalar, A., Köymen, H.: High-intensity airborne CMUT transmitter array with beam steering. J. Microelectromech. Syst. **29**(6), 1537–1546 (2020)
15. Niu, X., Liu, Z., Meng, Y., Hodges, C.M., Williams, R.P., Hall, N.A.: An air-coupled electrostatic ultrasound transducer using a mems microphone architecture. J. Microelectromech. Syst. **31**(5), 813–819 (2022)
16. Williams, R.P., Vatankhah, E., Hall, N.A.L Multidegree-of-freedom state-space modeling of nonlinear pull-in dynamics of an electrostatic mems microphone. J. Microelectromech. Syst. **31**(4), 589–598 (2022)
17. Gan, W.-S., Yang, J., Kamakura, T.: A review of parametric acoustic array in air (2012). Parametric Acoustic Array: Theory, Advancement and Applications
18. Coutant, Z.A., Adelegan, O., Biliroglu, A.O., Jeng, G.S., Pitre, J.J., Kirby, M.A., Pelivanov, I., Yamaner, F.Y., O'Donnell, M. and Oralkan, Ö.: Wideband air-coupled CMUT arrays for acoustic micro-tapping. In: 2020 IEEE International Ultrasonics Symposium (IUS), pp. 1–3 (2020)